Anomaly Induced Transport And Hall Viscous Effects In 2+1 Space-Time Dimensions

Dissertation zur Erlangung des
Naturwissenschaftlichen Doktorgrades
der Julius-Maximilians-Universität Würzburg

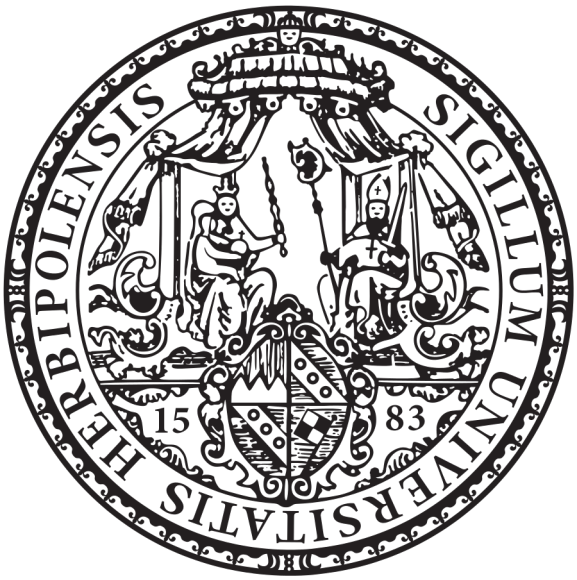

vorgelegt von

Christian Klaus Tutschku

aus Würzburg

Würzburg 2021

Eingereicht am: .....

bei der Fakultät für Physik und Astronomie

1. Gutachter: Prof. Dr. Ewelina M. Hankiewicz
2. Gutachter: Dr. René Meyer
3. Gutachter: .....

der Dissertation

Vorsitzende(r): .....

1. Prüfer: Prof. Dr. Ewelina M. Hankiewicz
2. Prüfer: Dr. René Meyer
3. Prüfer: .....

im Promotionskolloquium

Tag des Promotionskolloquiums: .....

Doktorurkunde ausgehändigt am: .....

To my parents

Abstract

The main goal of this thesis is to elucidate the sense in which recent experimental progress in condensed matter physics, namely the verification of two-dimensional Dirac-like materials and their control in ballistic- as well as hydrodynamic transport experiments enables the observation of a well-known 'high-energy' phenomenon: The parity anomaly of planar quantum electrodynamics (QED_{2+1}). In a nutshell, the low-energy physics of two-dimensional Quantum Anomalous Hall (QAH) insulators like (Hg,Mn)Te quantum wells or magnetically doped (Bi,Sb)Te thin films can be described by combined response of two 2+1 space-time dimensional Chern insulators with a linear dispersion in momentum. Due to their Dirac-like spectra, each of those Chern insulator is directly related to the parity anomaly of planar quantum electrodynamics. However, in contrast to a pure QED_{2+1} system, the Lagrangian of each Chern insulator is described by two different mass terms: A conventional momentum-independent Dirac mass m, as well as a momentum-dependent so-called Newtonian mass term $B|\mathbf{k}|^2$. According to the parity anomaly it is not possible to well-define a parity- and U(1) gauge invariant quantum system in 2+1 space-time dimensions. More precisely, starting with a parity symmetric theory at the classical level, insisting on gauge-invariance at the quantum level necessarily induces parity-odd terms in the calculation of the quantum effective action. The role of the Dirac mass term in the calculation of the effective QED_{2+1} action has been initially studied in Phys. Rev. Lett. 51, 2077 (1983). Even in the presence of Dirac mass, the associated fermion determinant diverges and lacks gauge invariance. This requires a proper regularization/renormalizaiton scheme and, as such, transfers the peculiarities of the parity anomaly to the massive case.
In the scope of this thesis, we connect the momentum-dependent Newtonian mass term of a Chern insulator to the parity anomaly. In particular, we reveal, that in the calculation of the effective action, before renormalization, the Newtonian mass term acts similarly to a parity-breaking element of a high-energy regularization scheme. This calculation allows us to derive the finite frequency correction to the DC Hall conductivity of a QAH insulator. We derive that the leading order AC correction contains a term proportional to the Chern number. This term originates from the Newtonian mass and can be measured via electrical or via magneto-optical experiments. The Newtonian mass, in particular, significantly changes the resonance structure of the AC Hall conductivity in comparison to pure Dirac systems like graphene. In addition, we study the effective action of the aforementioned Chern insulators in external out-of-plane magnetic fields. We show that as a consequence of the parity anomaly the QAH phase in (Hg,Mn)Te quantum wells or in magnetically doped (Bi,Sb)Te thin films survives in out-of-plane magnetic fields, violates the Onsager relation, and can therefore be distinguished from a conventional quantum Hall (QH) response. As a smoking-gun of the QAH phase in increasing magnetic fields, we predict a transition from a quantized Hall plateau with $\sigma_{xy} = -e^2/h$ to a not perfectly quantized plateau which is caused by scattering processes between counter-propagating QH and QAH edge states. This transition is expected to be of significant relevance in paramagnetic QAH insulators like (Hg,Mn)Te/CdTe quantum wells, in which the exchange interaction competes against the out-of-plane magnetic field.
All of the aforementioned results do not incorporate finite temperature effects. In order to shed light on such phenomena, we further analyze the finite temperature Hall response of 2+1 dimensional Chern insulators under the combined influence of a chemical potential and an out-of-plane magnetic field. As we have mentioned above, this non-dissipative trans-

port coefficient is directly related to the parity anomaly of planar quantum electrodynamics. Within the scope of our analysis we show that the parity anomaly itself is not renormalized by finite temperature effects. However, the parity anomaly induces two terms of different physical origin in the effective Chern-Simons action of a QAH insulator, which are directly proportional to its Hall conductivity. The first term is temperature and chemical potential independent and solely encodes the intrinsic topological response. The second term specifies the non-topological thermal response of conduction- and valence band modes, respectively. We show that the relativistic mass m of a Chern insulator counteracts finite temperature effects, whereas its non-relativistic Newtonian mass $B|\mathbf{k}|^2$ enhances these corrections. In addition, we are extending our associated analysis to finite out-of-plane magnetic fields, and relate the thermal response of a Chern insulator therein to the spectral asymmetry, which is a measure of the parity anomaly in out-of-plane magnetic fields.

In the second part of this thesis, we study the hydrodynamic properties of two-dimensional electron systems with a broken time-reversal and parity symmetry. Within this analysis we are mainly focusing on the non-dissipative transport features originating from a peculiar hydrodynamic transport coefficient: The Hall viscosity η_{H}. In out-of-plane magnetic fields, the Hall viscous force directly competes with the Lorentz force, as both mechanisms contribute to the overall Hall voltage. In our theoretical considerations, we present a way of uniquely distinguishing these two contributions in a two-dimensional channel geometry by calculating their functional dependencies on all external parameters. We are in particular deriving that the ratio of the Hall viscous contribution to the Lorentz force contribution is negative and that its absolute value decreases with an increasing width, slip-length and carrier density. Instead, it increases with the electron-electron mean free path in the channel geometry considered. We show that in typical materials such as GaAs the Hall viscous contribution can dominate the Lorentz signal up to a few tens of millitesla until the total Hall voltage vanishes and eventually is exceeded by the Lorentz contribution. Last but not least, we derive that the total Hall electric field has a parabolic form originating from Lorentz effects. Most remarkably, the offset of this parabola is directly characterized by the Hall viscosity. Therefore, in summary, our results pave the way to measure and to identify the Hall viscosity via both global and local measurements of the entire Hall voltage.

Zusammenfassung

Das zentrale Leitmotiv dieser Dissertation besteht darin, zwei unterschiedliche theoretische Konzepte aus verschiedenen Teilbereichen der Physik zu verbinden, um dadurch neue Perspektiven zu erschließen. Im Wesentlichen zielt die Arbeit darauf ab, die quantenfeldtheoretischen Konstrukte der Paritäts- als auch der chiralen Anomalie aus der Hochenergiephysik auf die Festkörperphysik von sogenannten zwei-dimensionalen Quanten Anomalen Hall (QAH) Isolatoren zu übertragen. Die Dirac-artige Bandstruktur dieser neuartigen Materialien ermöglicht es, Effekte freier quantenelektrodynamischer Teilchen in 2+1 Raumzeit Dimensionen im Festkörperlabor direkt messbar zu machen. Um die zentralen Erkenntnisse dieser Arbeit nachvollziehen zu können ist das Verständnis zweier Konstrukte unumgänglich:

(*i*) Unter einer Quantenanomalie versteht man den Symmetriebruch einer klassischen Theorie während des Quantisierungsprozesses. Um eine konsistente Quantentheorie formulieren zu können, ist es in einem quanten-anomalen System nicht möglich, alle klassischen Symmetrien auf der Quantenebene aufrechtzuerhalten.

(*ii*) Unter zwei-dimensionalen QAH Isolatoren versteht man planare Halbleiter mit einer endlichen, transversalen (Hall-) Leitfähigkeit in der Abwesenheit eines externen Magnetfeldes. Derartige Halbleiter werden zum Beispiel in (Hg,Mn)Te/CdTe Schichtsystemen oder in dünnen magnetisierten (Bi,Sb)Te Filmen vorhergesagt und zum Teil bereits experimentell nachgewiesen[a].

Die nieder-energie Theorie um die Bandlücke der oben genannten QAH Systeme wird gemeinsam durch die Physik zweier sogenannter Chern Isolatoren beschrieben. Jeder Chern Isolator besitzt eine lineare Dispersion im Impulsraum und gleicht somit der Theorie quantenelektrodynamischer Teilchen in 2+1 Raumzeit Dimensionen (QED_{2+1}). Darauf basierend ist jeder Chern Isolator für sich direkt mit der Paritätsanomalie verbunden. Um die effektive Bandkrümmung im Festkörper zu charakterisieren unterscheidet sich das Modell eines Chern Isolators von der entsprechenden QED_{2+1} Theorie um einen quadratischen Masse-Term im Impuls, die sogenannte Newtonsche Masse $B|\mathbf{k}|^2$. Zusammen mit dem impulsunabhängigen Dirac Masseterm m definiert jene paritätsbrechende Masse die Energielücke eines Chern Isolators. Wie bereits in (*i*) erwähnt tritt die Paritätsanomalie während der Quantisierung klassisch paritätssymmetrischer Systeme auf. Quantisiert man beispielsweise eine masselose QED_{2+1} Theorie, so induziert man während der Berechnung der Fermion Determinante paritätsbrechende Terme in der zugehörigen effektiven Wirkung. Obgleich eine nichtverschwindende Dirac-Masse die Paritätssymmetrie auf klassischer Ebene bricht, ist die zugehörige Fermion Determinante UV divergent als auch Eichsymmetrie brechend und Bedarf daher eines geeigneten Regularisierung/Renormierungsschemas. Diese Eigenschaft erlaubt es Konsequenzen der Paritätsanomalie ebenfalls in massiven Systemen zu identifizieren. Die Auswirkungen einer Dirac-Masse für die Berechnung der effektiven Wirkung eines QED_{2+1} Systems wurden inertial in der wegweißenden Publikation Phys. Rev. Lett. 51, 2077 (1983) analysiert. Im Rahmen dieser Dissertation eruieren wir die Implikationen der Newtonschen Masse eines Chern Isolators auf die entsprechende Berechnung der Fermion Determinante und beleuchten damit die effektive Bandkrümmung eines Festkörpers im Kontext einer diskreten Raumzeit

[a] Da Mangan paramagnetisch ist, benötigt ersteres System ein schwaches polarisierendes Magnetfeld um eine QAH Phase aufzuweisen.

Anomalie. Wir zeigen insbesondere, dass die Newtonsche Masse vor dem unumgänglichen Renormierungprozess den paritätsbrechenden Elementen verschiedener hochenergetischer Regularisierungsschemata ähnelt, wie zum Beispiel Wilson Fermionen. Mittels dieser Berechnung leiten wir ebenfalls die Wechselstromleitfähigkeit der genannten QAH Isolatoren her. Wir zeigen, dass die führende Frequenzkorrektur in diesen Systemen einen Term proportional zur Chern Zahl enthält. Jener Beitrag basiert auf der zugrundeliegenden Galilei Invarianz und ist insbesondere durch magneto-optische Experimente nachzuweisen. Weiter eruieren wir, dass der genannte Term fundamental die Resonanzstruktur der Hall Leitfähigkeit beeinflusst, sodass diese maßgeblich von der entsprechenden Größe eines puren Dirac Systems wie Graphen abweicht.

Zudem analysieren wir in dieser Arbeit die Physik von 2+1 dimensionalen Chern Isolatoren in externen Magnetfeldern die orthogonal auf der zugrundeliegenden Raum-Mannigfaltigkeit stehen -sogenannte orbitale Magnetfelder. Wir zeigen dass als direkte Konsequenz der Paritätsanomalie die QAH Phase in orbitalen Magnetfelder überlebt, darin die Onsager Relationen bricht und somit von konventionellen QH Systemen unterschieden werden kann, obgleich beide topologischen Phasen durch die selbe Chern Klasse beschrieben sind. Als experimentelle Signatur der QAH Phase in adiabatisch zunehmenden orbitalen Magnetfeldern sagen wir den Übergang eines quantisierten Hall Plateaus mit $\sigma_{\mathrm{xy}} = -\mathrm{e}^2/\mathrm{h}$ zu einem nicht-quantisierten, rauschenden Hall Plateau vorher. Der Mittelwert des letzteren Plateaus hängt stark von Streuprozessen zwischen entgegengesetzt propagierenden QH und QAH Randzuständen ab. Insbesondere in (Hg,Mn)Te/CdTe Schichtsystemen ist der vorhergesagte Übergang von großem Interesse da in jenen Systemen die Austauschwechelwirkung mit dem polarisierenden Magnetfeld konkurriert.

All die oben genannten Ergebnisse vernachlässigen thermische Effekte. Um den Einfluss einer endlichen Umgebungstemperatur auf die Physik von QAH Isolatoren zu untersuchen, analysieren wir im Rahmen dieser Dissertation ebenfalls die Hall Leitfähigkeit 2+1 dimensionaler Chern Isolatoren bei endlicher Temperatur und unter dem Einfluss beliebiger chemischer Potentiale sowie orbitaler Magnetfelder. Wie oben bereits erwähnt hängt dieser nicht dissipative Transportkoeffizient direkt mit der Paritätsanomalie eines masselosen QED_{2+1} Systems zusammen. Wir zeigen mittels unserer Analyse, dass die Paritätsanomalie an sich nicht durch endliche Temperatureffekte beeinflusst wird. Allerdings induziert jene Anomalie in der effektiven Wirkung eines Chern Isolators zwei Beitrage unterschiedlichen physikalischen Ursprungs. Einer der Terme ist unabhängig vom chemischen Potential und der Temperatur da er ausschließlich die intrinsische topologische Phase des Systems codiert. Der andere Term definiert die thermisch angeregten Zustände im Leitungs- bzw. im Valenzband und ist somit nicht-topologischen Ursprungs. Insbesondere zeigen wir, dass in der topologisch nicht trivialen Phase eines Chern Isolators die Dirac Masse den endlichen Temperatureffekten entgegenwirkt, während die nicht-relativistische Newtonsche Masse jene Korrekturen verstärkt. Neben diesen Effekten bei verschwindendem orbitalem Magnetfeld verallgemeinern wir unsere thermischen Betrachtungen hinsichtlich der Effekte quantisierender orbitaler Magnetfelder. Insbesondere verknüpfen wir die Leitfähigkeit von QAH Isolatoren bei endlicher Temperatur zur sogenannten Spektralen Asymmetrie. Diese Größe kann als Signatur der Paritätsanomalie in orbitalen Magnetfeldern interpretiert werden.

Im zweiten großen Kapitel dieser Dissertation analysieren wir den hydrodynamischen Ladungstransport in zwei-dimensionalen Elektronensystemen, in denen sowohl die Zeitumkehr- als auch die Paritätssymmetrie gebrochen sind. Unseren Forschungsschwerpunkt legen wir hierbei vor Allem auf nicht-dissipative Transporteigenschaften, die sich mittels der Hall Viskosität aus den Navier-Stokes Gleichungen ergeben. In orbitalen Magnetfeldern konkurrieren aufgrund dieses paritätsbrechenden Transportkoeffizient zwei transversale Kräfte miteinander: Die sogenannte Hall viskose Kraft und die wohlbekannte Lorentzkraft. Zusammen definieren beide

Kräfte die gesamte Hall Spannung des Systems. In den Ausführungen dieser Arbeit zeigen wir wie die genannten unterschiedlichen Beiträge in zweidimensionalen Transportkanälen anhand ihrer verschiedenen funktionellen Abhängigkeiten von den Systemparametern unterschieden werden können. Wir eruieren, dass das Verhältnis zwischen dem Hall viskosen Beitrag und dem Lorentz basierten Beitrag negativ ist und dessen Absolutbetrag mit zunehmender Kanalbreite, Rutsch-Länge [engl. slip length] und Ladungsträgerdichte abnimmt. Im Gegensatz dazu wächst jener Betrag mit der mittleren Elektron-Elektron Streulänge. Im Rahmen dieser Dissertation zeigen wir, dass in typischen GaAs Fermi Flüssigkeiten der Hall viskose Beitrag das Lorentz Signal bis hin zu einer orbitalen Magnetfeldstärke im zehnstelligen Milli-Tesla Bereich dominieren kann. Im Anschluss nimmt das Verhältnis dieser Größen ab, verschwindet bei einem kritischen Magnetfeld und wird schlussendlich durch das Lorentz Signal dominiert. Zuletzt zeigen wir, dass das transversale elektrische Feld in den genannten Experimenten eine parabolische Form besitzt, welche auf dem Lorentz Beitrag basiert. Im Gegensatz dazu ist der konstante Offset dieser Parabel hauptsächlich durch die Hall Viskosität definiert. Zusammen weisen die hier genannten Eigenschaften einen möglichen Weg zur experimentellen Bestimmung der Hall Viskosität mittels lokaler- oder globaler Spannungsmessungen auf.

Contents

0

Acronyms and Physical Constants

Acronyms	
QH	Quantum Hall
QAH	Quantum Anomalous Hall
QSH	Quantum Spin Hall
QED_{2+1}	Planar Quantum Electrodynamics
BHZ	Bernevig-Hughes-Zhang
2DEG	Two-Dimensional Electron Gas
LL	Landau Level
AC	Alternating Current
DC	Direct Current

Constant	Symbol	Value	
Vacuum Permittivity	$\epsilon_0 = 1 \,/\, c_0^2\, \mu_0$	8.8542×10^{-12}	$C^2\, s^2 / \,kg\, m^3$
Vacuum Permeability	μ_0	1.2566×10^{-6}	$kg\, m \,/\, C^2$
Vacuum Speed of Light	c_0	2.9979×10^{8}	$m \,/\, s$
Planck Constant	$\hbar$	1.0546×10^{-34}	$J\, s$
		6.5821×10^{-16}	$eV\, s$
Elementary Charge	e	1.6022×10^{-19}	C
Fine-Structure Constant	$\alpha = e^2 \,/\, 4\pi\epsilon_0\hbar c_0$	7.2974×10^{-3}	
Boltzmann Constant	k_B	1.3806×10^{-23}	$J \,/\, K$
		8.6173×10^{-5}	$eV \,/\, K$
Electron Rest-Mass	m_e	9.1094×10^{-31}	kg

1 Introduction

In the year 1980 Klaus von Klitzing discovered the so-called quantum Hall (QH) effect [1], which can be understood as a quantum version of the classical Hall effect. In the QH phase the Hall conductivity is a quantized value in units of e^2/h as function of the chemical potential. Only two years later D. J. Thouless, M. Kohmoto, M. P. Nightingale, and M. den Nijs related this experimental finding to an topologically invariant, the so-called TKNN invariant [2]. Based on this concept, a new branch of physics arose, namely the field of topological physics, in which solid-state materials are classified in terms of so-called Chern numbers $\mathcal{C}$ [3–5]. The QH phase belongs to the Chern class $\mathcal{C}_{\mathrm{QH}} \in \mathbb{Z}$. In general, topology is a branch of mathematics. Two objects belong to the same topological class if they can be continuously deformed into each other. For instance, a coffee mug and a conventional doughnut (with one hole only) belong to the same topological class according to their Euler characteristic [6]. In the scope of solid-state physics, two topological phases belong to a different class if their band-structures can not be continuously transformed into each other without closing the corresponding energy gap. Hitherto, several different topological phases of matter have been predicted and measured. For the scope of this thesis, the discovery of topological insulators [7–16] and Weyl- or Dirac [17–22] semimetals is of exceptional relevance. Their experimental verification provides the exceptional opportunity to measure signatures of so-called high-energy anomalies in the solid-state environment [23–30].

In a quantum field theory, an anomaly occurs, whenever a symmetry of a classical theory cannot be maintained on the quantum level [6, 31, 32]. For instance, in 2+1 space-time dimensions the parity anomaly results from the incompatibility of parity- and U(1) gauge symmetry after quantization. More precisely, starting with a parity symmetric theory at the classical level, insisting on gauge-invariance at the quantum level necessarily induces parity-odd terms in the calculation of the quantum effective action. In the 1980s this high-energy concept has been shown for quantum electrodynamics in 2+1 space-time dimensions (QED_{2+1}) [33–39]. A few years later F. D. M. Haldane proposed the first solid-state model of a quantum anomalous Hall (QAH) insulator by adding a parity-breaking[b] Dirac mass term to an otherwise gapless graphene structure [25]. In a nutshell, a QAH insulator is a two-dimensional material with an insulator bulk gap but chiral edge modes at its topological boundary[c]. The name 'anomalous' originates from the fact that such insulators have a quantized Hall conductivity in units of e^2/h even in the absence of Landau levels (LLs), $\mathcal{C}_{\mathrm{QAH}} \in \mathbb{Z}$. Based on these principles, QAH insulators are from a high-energy perspective directly related to the parity-anomaly of planar quantum electrodynamics. Even though Haldane's seminal work is labeled *Model for a Quantum Hall Effect without Landau Levels: Condensed-Matter Realization of the 'Parity Anomaly'*, the nomenclature 'realization' requires further specifi-

[b] The addition of a parity-even Dirac mass term has been initially studied by G. W. Semenoff in Ref. [23].

[c] Here and throughout this thesis, 'n+1-dimensional' always refers to the entire space-time, whereas 'n-dimensional' only encodes the spatial manifold, $n \in \mathbb{N}$.

cation in order to circumvent possible misunderstandings. Strictly speaking, the Haldane model contains two 2+1 dimensional Dirac fermions, as it is based on the hexagonal lattice structure of graphene. By fine-tuning the Haldane mass, one of the Dirac fermion mass gaps can be closed, whereas the other one remains open. In this limit, the entire band-structure contains a single gapless QED_{2+1} system with a non-zero Hall conductivity. Consequently, in the Haldane model one of the Dirac fermions alone is suitable to realize the parity anomaly. Up to date, an experimental realization of the Haldane model has not yet been achieved in crystalline structures[a].

Nevertheless, another type of QAH insulators has been predicted in spin-polarized topological insulators like (Hg,Mn)Te quantum wells [42, 43] or magnetically doped (Bi,Sb)Te thin films [44–48]. In vicinity to the insulating bulk gap, these systems can be effectively described by the superimposed signal of two 2+1 dimensional Chern insulators, which is commonly known as the Bernevig-Hughes-Zhang (BHZ) model, $\mathcal{C}_{\mathrm{BHZ}} \in \mathbb{Z}_2$ [8, 42]. Similar to the Haldane model, the topological gap of one of the Chern insulators in the BHZ model can be closed by magnetically doping the system, whereas at the same time the second Chern insulator remains gapped. In this fine-tuned limit, the gapless Chern insulator realizes the parity anomaly as its contribution to the Hall conductivity is in general non-zero. Based on this property, the analysis of single Chern insulators allows us to study measurable consequences of the parity anomaly in solid-state materials. However, as the aforementioned Chern insulators do describe the low-energy physics of condensed matter materials, they are in contrast to the Dirac fermions in the Haldane model characterized by two different parity-breaking mass terms: A conventional Dirac mass m, as well as momentum-dependent so-called Newtonian mass $B|\mathbf{k}|^2$ [49]. Above, we have already indicated that QAH insulators are directly related to the parity anomaly in 2+1 space-time dimensions. This can be seen clearly by analyzing their Chern number. In the topologically non-trivial regime the Chern number of a QAH insulator results from the Chern number of one of the Chern insulators alone [43, 50]

$$\mathcal{C}_{\mathrm{QAH}} = \mathcal{C}_{\mathrm{CI}} = \left[\mathrm{sgn}(m) + \mathrm{sgn}(B)\right]/2 = \pm 1 \ . \tag{1.1}$$

As a direct consequence of the parity anomaly, this quantity, which is related to the system's parity-odd Hall conductivity

$$\sigma_{\mathrm{xy}} = \mathcal{C}_{\mathrm{CI}}\, \mathrm{e}^2/\mathrm{h} \ , \tag{1.2}$$

does not vanish in parity-symmetric, zero-mass limit. Indicated by this crucial property the Dirac-, as well as the momentum-dependent mass term of a single Chern insulator are both directly related to the parity anomaly. In his seminal work, A. N. Redlich has specified the concrete relation of the Dirac mass term to the parity anomaly by calculating the effective action of a massive QED_{2+1} system [37]. The effective action of Chern insulator in the presence of a momentum-dependent Newtonian mass has not yet been analyzed. To bridge this gap, we calculate in this thesis the polarization operator of a Chern insulator. In the corresponding calculation for a pure, massless QED_{2+1} system, the parity anomaly arises from the particular regularization of the infinite Dirac sea. For instance this has been shown for a lattice regularization with Wilson fermions in Ref. [51], for a Pauli-Villars approach in Refs. [37, 52], for a ζ-function regularization in Ref. [53], and for or higher derivative approachin the Refs. [54, 55]. In the scope of this thesis, we are going to compare the role of the Newtonian mass term in the calculation of the effective action of a Chern insulator to these parity-breaking regularization schemes. The calculation of the effective action allows us to derive the AC Hall conductivity of a QAH insulator. The corresponding analysis for a pure QED_{2+1} system has been executed for instance in the seminal works [56, 57].

[a] Hitherto, this model has only been realized in optical lattices [40, 41].

In the paragraphs above, we have already indicated that both, QH as well as QAH phases are characterized by an integer Chern number $\mathcal{C} \in \mathbb{Z}$. Therefore they belong to the same topological class [3]. This raises a fundamental question: Is it possible to distinguish these two topological phases of matter in external out-of-plane magnetic fields? Especially for QAH insulators which result from paramagnetic doping of two-dimensional topological insulators, such as (Hg,Mn)Te/CdTe quatum wells [42, 43], this question is of particular relevance, as these systems require a polarizing magnetic field to enter the QAH phase. In the scope of this thesis, we demonstrate that QAH phases can in fact be distinguished from conventional QH phases in quantizing out-of-plane magnetic fields, due to their parity-anomaly relation.

Up to date, finite temperature signatures of parity anomaly driven systems have been solely studied in Dirac models with a purely linear spectrum in momentum [36, 57–61]. The quantum effective action of these systems is characterized by a temperature dependent and thus large gauge non-invariant Chern-Simons term originating from the parity anomaly when the fermion determinant is evaluated perturbatively during the quantization process. It has been shown that this non-invariance is absorbed by higher order non-perturbative corrections to the quantum effective action [62–69]. This peculiar feature raises a fundamental question: Does the parity anomaly get renormalized by thermal effects? Within the scope of this thesis we answer this question in detail. We extend the calculations in the aforementioned references to Chern insulators including both, a Dirac-, as well as a Newtonian mass, in the presence and in the absence of quantizing magnetic fields, as well as with and without particle-hole symmetry. Our considerations are of particular relevance for a wide class of QAH insulators. Additionally to the material mentioned above, our calculations will in particular shed light on QAH phases which arise at the interfaces between ferromagnetic insulators and three-dimensional topological insulators, where a proximity-induced interface magnetization has been experimentally observed at high temperatures [70, 71]. In such systems the out-of-plane magnetization implies a gap in the interface Dirac spectrum. This induces a parity anomaly contribution on the surface of the topological insulator and, at the same time, a magneto-electric torque in the Landau-Lifshitz equation [72–74]. A similar effect also occurs on the surface of the recently discovered anti-ferromagnetic topological insulator $MnBi_2Te_4$ [75, 76].

All the aforementioned phenomena do not rely on strong electron-electron interactions. In order to analyze the consequences of electron interactions on the parity- and time-reversal odd transport in 2+1 space-time dimensions, we are going to study the hydrodynamic transport properties of two-dimensional Fermi liquids, as well as Dirac fluids in the second part of this thesis. The idea of describing electrons in solid-state systems via hydrodynamics goes back to the discovery of the Gurzhi effect in (Al)GaAs quantum wires [77–79]. Recently, hydrodynamic transport has received renewed attention due to the accessibility of the hydrodynamic regime in modern materials [80–83]. Two-dimensional systems that violate parity invariance are of special interest, since they are described by novel non-dissipative transport coefficients, such as the Hall viscosity [84–89]. Based on the principles which we have presented above, we are in the scope of this thesis in particular interested in the parity-odd hydrodynamic transport of two-dimensional Dirac materials such as graphene, in which recent experiments have shown that the Hall viscosity may be of the same order of magnitude as the shear viscosity [90–93]. As the current literature [94–97] does not provide a quantitative answer for the functional dependency of Hall viscous transport on all system parameters, we are going to clarify this outstanding issue in the course of this thesis.

Now, having motivated the main questionings of this thesis and embedded them in the current scientific progress, let us make some remarks about the structure of this work:

In Chap. 2, we present a comprehensive overview of several theoretical concepts which are required to understand the outcomes of this thesis. We start with a discussion of the classical- and quantum Hall effect in two spatial dimensions from a solid-state perspective. In order to understand the corresponding physics in terms of a quantum field theory, we construct in the subsequent section a 2+1 dimensional space-time manifold with an associated Clifford algebra. After that, we discuss the classical conservation laws of Dirac systems and explain the formation of quantum anomalies, such as the parity- and the chiral anomaly in suitable space-times. We elucidate the Callan-Harvey mechanism behind the anomaly inflow, and study anomaly driven currents in semi-infinite 2+1 dimensional space-time manifolds. We close this chapter by comparing our findings to conventional quantum Hall phases.

In Chap. 3, we transfer our findings towards QAH insulators in 2+1 space-time dimensions. We explain how these systems can be realized in the solid-state lab. Moreover, we clarify in which sense QAH insulators can be interpreted as solid-state realizations of the parity anomaly. In particular, we relate the Newtonian mass of a QAH insulator to the parity anomaly of massless QED_{2+1} by calculating its effective action. We derive the AC Hall conductivity of these peculiar states of matter and analyze differences to purely linear Dirac systems like graphene. We extend our analysis to finite out-of-plane magnetic fields and include finite temperatures effects as well as a finite particle-hole asymmetry. We clarify how all of these factors affect the signatures of the parity anomaly in QAH insulators.

In Chap. 4, we study the hydrodynamic response of parity- and time-reversal breaking electron systems in two-dimensional channel geometries. We start our considerations by giving a comprehensive introduction into the theory of hydrodynamic transport originating from Fermi fluids, as well as Dirac liquids. We elucidate the corresponding transport coefficients, the relativistic and non-relativistic equations of motion, and the most relevant experiments. Based on these principles we shed light on the role of the Hall viscosity in the hydrodynamic transport of two-dimensional electron systems in external out-of-plane magnetic fields. We support our analytic calculations by numerical simulations and predict possible signatures of this peculiar transport coefficient in materials like GaAs.

In Chap. 5, we summarize our main results and give an outlook over the most interesting future research directions regarding our theoretical findings.

Before we end the introduction, let us make one more statement regarding the structure of this thesis. The outcomes presented in Chap. 3 and Sec. 4.2 are to a large extend based on my publications [P1, P2, P3, P4, P5]. In order to embed the associated results in the line of arguments of the present thesis, these findings are substantially reorganized and extended, such that they include my latest degree of knowledge. However, sometimes it was inevitable to reformulate the line of reasoning and, therefore, I partially adapted some of the contents of the mentioned publications. The corresponding passages are indicated clearly.

2

Hall Physics and Parity Anomaly

Contents

2.1 Classical Hall Effect

The classical Hall effect of a two-dimensional electron gas in an out-of-plane magnetic field describes the formation of a transverse voltage V_H across a Hall bar of width W as a response to an applied longitudinal current I_x. The corresponding experimental setup is schematically shown in Fig. 2.1(a). Before we discuss the theoretical model, let us describe the physical processes which are responsible for this effect. The longitudinal current I_x originates from electrons moving in $-\mathbf{e}_\mathrm{x}$-direction. Due to the out-of-plane magnetic field, these electrons are deviated by the Lorentz force in $\pm\mathbf{e}_\mathrm{y}$-direction towards one of the sample edges (depending on the magnetic field direction). The accumulation of charge carriers at this edge leads to a transverse voltage across the Hall bar. In the steady state, this Hall voltage exactly compensates the Lorentz force, such that electrons moving in -$\mathbf{e}_\mathrm{x}$-direction are not deviated anymore.

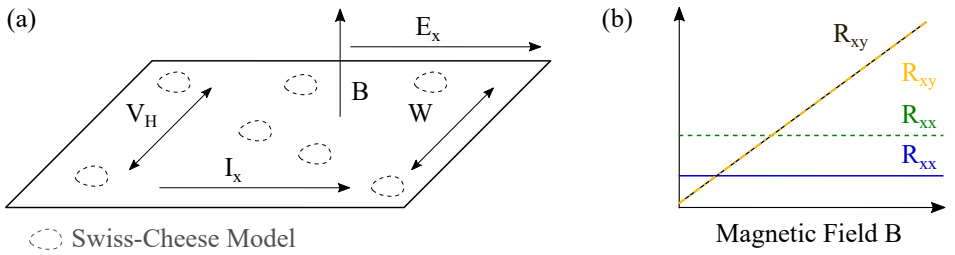

Figure 2.1: (a) Structural setup of a Hall measurement: A two-dimensional electron gas is confined in a crossed electro-magnetic background. While $\mathbf{B}=B\mathbf{e}_\mathrm{z}$ describes an out-of-plane magnetic field, $\mathbf{E}=E_\mathrm{x}\mathbf{e}_\mathrm{x}$ defines a longitudinal electric field, which drives a current I_x in the $\mathbf{e}_\mathrm{x}$-direction. As a response to this current, the system shows a transverse Hall voltage V_H. **(b)** Longitudinal R_xx and off-diagonal R_xy resistance of the two-dimensional electron gas as a function of the magnetic field strength B. While solid lines correspond to a continuous Hall bar, dashed lines indicate the so-called Swiss-Cheese model. In this model, one cuts several holes in the Hall bar, effectively reducing its area. This is also depicted in subfigure **(a)**.

Theoretically, the classical Hall effect can be described by the Drude model [98–100]. In what follows, our line of reasoning will roughly follow the discussions within these references. As stated, let us consider a two-dimensional electron gas under the combined influence of an out-of-plane magnetic field $\mathbf{B}=B\mathbf{e}_\mathrm{z}$[a] and a longitudinal electric field $\mathbf{E}=E_\mathrm{x}\mathbf{e}_\mathrm{x}$, which drives the current I_x in the $\mathbf{e}_\mathrm{x}$-direction. Moreover, we introduce the phenomenological momentum relaxation time scale τ, originating from momentum non-conserving electron scattering processes with impurities, lattice-defects or thermally excited phonons. The classical dynamics of this system is described by the equations of motion [99, 100]

$$m^* \frac{\mathrm{d}\mathbf{v}}{\mathrm{dt}} = -\mathrm{e}\mathbf{E} - \mathrm{e}\mathbf{v}\times\mathbf{B} - \frac{m^*\mathbf{v}}{\tau} \,. \tag{2.1}$$

Here, m^* and $-|e| < 0$ are the electron's effective mass and charge. The left hand side of this equation defines the total force acting on electrons in this system. The right hand side encodes the electric driving force (first term), the Lorenz force (second term), and the phenomenological momentum relaxation (third term). In the steady state, this equation simplifies to

$$\mathbf{v} + \frac{\mathrm{e}\tau}{m^*}\mathbf{v}\times\mathbf{B} = -\frac{\mathrm{e}\tau}{m^*}\mathbf{E} \,, \tag{2.2}$$

[a] Within the scope of this section, we restrict ourselves to positive magnetic field strengths $B > 0$.

which can be rewritten in terms of the charge current density $\mathbf{j}=-en\mathbf{v}$, the particle density n, and the cyclotron frequency $\omega_B=eB/m^*$:

$$\begin{pmatrix} 1 & \omega_B\tau \\ -\omega_B\tau & 1 \end{pmatrix}\mathbf{j} = \frac{e^2 n\tau}{m^*}\mathbf{E} \ . \tag{2.3}$$

This implies an associated conductivity tensor, which is implicitly defined by $\mathbf{j}=\sigma\mathbf{E}$:

$$\sigma = \frac{\sigma_{\text{Drude}}}{1+\omega_B^2\tau^2}\begin{pmatrix} 1 & -\omega_B\tau \\ \omega_B\tau & 1 \end{pmatrix}, \tag{2.4}$$

where $\sigma_{\text{Drude}}=e^2 n\tau/m^*$ is the Drude conductivity [98–100]. The inverse of this conductivity tensor defines the resistivity tensor

$$r=\sigma^{-1}=\frac{1}{\sigma_{\text{Drude}}}\begin{pmatrix} 1 & \omega_B\tau \\ -\omega_B\tau & 1 \end{pmatrix}=\begin{pmatrix} r_{\text{xx}} & r_{\text{xy}} \\ -r_{\text{xy}} & r_{\text{xx}} \end{pmatrix} \ . \tag{2.5}$$

Hence, we found the following values for the longitudinal and the off-diagonal resistivities

$$r_{\text{xx}}=\frac{m^*}{ne^2\tau} \quad \wedge \quad r_{\text{xy}}=\frac{B}{ne} \ . \tag{2.6}$$

Since experimentally one measures the resistance instead of the resistivity, let us calculate the corresponding values:

$$R_{\text{xx}}=\frac{V_{\text{x}}}{I_{\text{x}}}=\frac{\int_0^{L_{\text{x}}} E_{\text{x}}\,\mathrm{d}y}{\int_0^W J_{\text{x}}\,\mathrm{d}y}=\frac{L_{\text{x}}E_{\text{y}}}{WJ_{\text{x}}}=r_{\text{xx}}\frac{L_{\text{x}}}{W} \ , \tag{2.7}$$

$$R_{\text{xy}}=\frac{V_{\text{H}}}{I_{\text{x}}}=\frac{\int_0^W E_{\text{y}}\,\mathrm{d}y}{\int_0^W J_{\text{x}}\,\mathrm{d}y}=\frac{WE_{\text{y}}}{WJ_{\text{x}}}=r_{\text{yx}}=-r_{\text{xy}} \ . \tag{2.8}$$

where L_{x} and W define the length and the width of the Hall bar. R_{xx} is a constant function in terms of the magnetic field, but depends on the momentum relaxing scattering time τ as well as the particular geometry of the system. Instead, R_{xy} does not depend on these values but scales linearly in the magnetic field. This is schematically shown in Fig. 2.1(b). Here the solid lines correspond to a continuous Hall bar, whereas the dashed lines are associated to the so-called Swiss-Cheese model. In this model one cuts holes in the Hall bar, such that effectively L_{x} and W decrease[a]. However, this does not affect R_{xy}. This is the first indication that the Hall voltage is a topological response, meaning that it does not depend on the details of the geometry [99, 100]. In what follows, we are going to quantize the Hall effect, which makes this property even more apparent.

2.2 Quantum Hall Effect

The quantum version of the classical Hall effect, the so-called quantum Hall effect, was discovered by *Klaus von Klitzing* in 1980 [1]. Essentially, the quantum Hall effect fulfills the same relations as the classical Hall effect with one subtle difference: For a fixed chemical potential, the particle density n becomes a quantized value as a function of the magnetic field. This results from the formation of Landau levels, which are broadened δ-peaks in the density of states. The experimental consequence of this crucial property is shown in Fig. 2.2 [101]. The quantized values of the particle density lead to a step function in the off-diagonal

[a] In a usual Hall bar $L_{\text{x}} \gg W$.

resistivity, and to a vanishing longitudinal resistivity along the quantum Hall plateaus as a function of the magnetic field. In what follows, we will analytically derive the theory of the quantum Hall effect, which allows us to physically understand the experimental data shown in Fig. 2.2. Our line of reasoning will roughly follow the discussions within Refs. [100, 102].

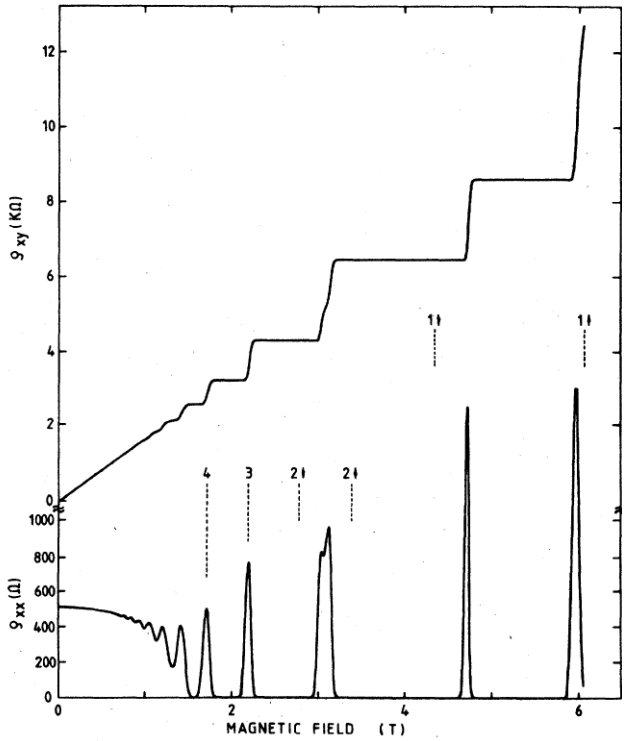

Figure 2.2: The quantum Hall effect [1, 101]. The longitudinal resistivity $r_{\mathrm{xx}}[\Omega]$ and the off-diagonal resistivity $r_{\mathrm{xy}}[\mathrm{k}\Omega]$ of a GaAs-$\mathrm{Al}_x\mathrm{Ga}_{1-x}$As hetero-structure are plotted as a function of the applied magnetic field $B[\mathrm{T}]$. The Landau level indices (including spin $\sigma = \uparrow, \downarrow$) are shown as an inset. The figure is reprinted from Ref. [101] with permission from the APS.

2.2.1 Landau Levels

The classical Lagrangian of a free, spinless electron of effective mass m^* and charge $-\mathrm{e} < 0$ which moves in a background magnetic field $\mathbf{B} = \epsilon^{ijk}\partial_j A_k \, \mathbf{e}_i$ is given by

$$L = \frac{1}{2} m^* \dot{\mathbf{x}}^2 - \mathrm{e}\dot{\mathbf{x}}\mathbf{A} \ . \tag{2.9}$$

Here, $\mathbf{A}$ defines the vector potential. With the canonical momentum $\mathbf{p} = \partial L / \partial \dot{\mathbf{x}} = m^* \dot{\mathbf{x}} - \mathrm{e}\mathbf{A}$ one obtains the corresponding Hamiltonian function via a Legendre transformation

$$H = \dot{\mathbf{x}}\mathbf{p} - L = \frac{1}{2m^*}(\mathbf{p} + \mathrm{e}\mathbf{A})^2 \ . \tag{2.10}$$

The conjugated variables x_i and p_j satisfy the Poisson brackets

$$\{x_i, p_j\}_+ = \delta_{ij} \quad \wedge \quad \{x_i, x_j\}_+ = \{p_i, p_j\}_+ = 0 \ , \tag{2.11}$$

where δ_{ij} is the Kronecker-delta. We quantize this theory by requiring that the corresponding quantum mechanical operators fulfill the canonical commutation relations [100]

$$[\hat{x}_i, \hat{p}_j] = \mathrm{i}\hbar\delta_{ij} \quad \wedge \quad [\hat{x}_i, \hat{x}_j] = [\hat{p}_i, \hat{p}_j] = 0 \ , \tag{2.12}$$

where $\hbar = \mathrm{h}/(2\pi)$ is the reduced Planck constant. As a next step, let us define the generalized momentum operator $\hat{\pi} = \hat{\mathbf{p}} + \mathrm{e}\hat{\mathbf{A}} = m^*\dot{\hat{\mathbf{x}}}$, which fulfills the commutation relation

$$[\hat{\pi}_\mathrm{x}, \hat{\pi}_\mathrm{y}] = -\mathrm{ie}\hbar B \ . \tag{2.13}$$

Moreover, we define the so-called ladder operators

$$\hat{a} \equiv \frac{1}{\sqrt{2\mathrm{e}\hbar B}} \left(\hat{\pi}_x - \mathrm{i}\hat{\pi}_y\right) \quad \wedge \quad \hat{a}^\dagger \equiv \frac{1}{\sqrt{2\mathrm{e}\hbar B}} \left(\hat{\pi}_x + \mathrm{i}\hat{\pi}_y\right) \tag{2.14}$$

with $[\hat{a}, \hat{a}^\dagger] = 1$. In terms of these operators, the classical Hamiltonian in Eq. (2.10) implies the quantum mechanical Hamilton operator

$$\hat{H} = \frac{\hat{\pi}^2}{2m^*} = \hbar\omega_B \left(\hat{a}^\dagger\hat{a} + \frac{1}{2}\right) \ . \tag{2.15}$$

Let us derive the spectrum of this operator. To this end, we define a ground-state $|0\rangle$ with $\hat{a}|0\rangle = 0$, and construct the rest of the Hilbert space by using the properties of the ladder operators

$$\hat{a}^\dagger|\lambda\rangle = \sqrt{\lambda+1}|\lambda+1\rangle \quad \wedge \quad \hat{a}|\lambda\rangle = \sqrt{\lambda}|\lambda-1\rangle \ . \tag{2.16}$$

This implies that the λ-th excitation, the state $|\lambda\rangle$, has a quantized energy

$$E_\lambda = \hbar\omega_B \left(\lambda + \frac{1}{2}\right) \quad \text{with} \quad \lambda \in \mathbb{N}_0 \ . \tag{2.17}$$

Hence, we found an equally spaced Landau level spectrum with groundstate energy $E_0 = \hbar\omega_B/2$, as it is exemplary shown in Fig. 2.3(a).

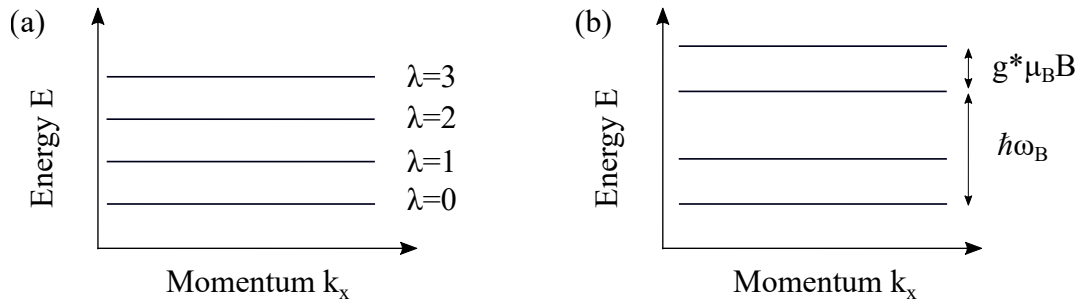

Figure 2.3: Landau level spectrum in momentum space. Here, $p_\mathrm{x} = \hbar k_\mathrm{x}$ defines the electron momentum in $\mathbf{e}_\mathrm{x}$-direction which remains to be well-defined in the Landau gauge $\hat{\mathbf{A}} = -\hat{y}B\mathbf{e}_\mathrm{x}$. Moreover, $\lambda \in \mathbb{N}$ defines the Landau level index and ω_B is the cyclotron frequency. Subfigure **(a)** shows the Landau level spectrum for a spinless system, whereas subfigure **(b)** takes into account the finite Zeeman splitting $g^*\mu_\mathrm{B}B$ resulting from the electron spin character. Further explanations are given in the text.

Next, we explicitly derive the eigen-states of the Hamiltonian in Eq. (2.15). Therefore, we

consider the so-called Landau gauge

$$\hat{\mathbf{A}} = -\hat{y}B\mathbf{e}_{\mathrm{x}} \ . \tag{2.18}$$

While this gauge breaks translation invariance in $\mathbf{e}_{\mathrm{y}}$-direction, it does not break this symmetry in $\mathbf{e}_{\mathrm{x}}$-direction. Hence, p_{x} remains a well-defined momentum in the Landau gauge, and Hamilton operator in Eq. (2.15) is given by [cf. Eq. (2.10)]

$$\hat{H} = \frac{1}{2m^*}\left((\hat{p}_{\mathrm{x}} - \mathrm{e}B\hat{y})^2 + \hat{p}_y^2\right) \ . \tag{2.19}$$

Due to the mentioned translation invariance in $\mathbf{e}_{\mathrm{x}}$-direction, the real space representation of the Hamiltonian's eigen-states $|\lambda\rangle$, namely $\psi_\lambda(x,y) = \langle r|\lambda\rangle$, can be characterized by plane waves of wave vector $k_{\mathrm{x}} = p_{\mathrm{x}}/\hbar$ in the $\mathbf{e}_{\mathrm{x}}$-direction (separation of variables)

$$\psi_{\lambda,k_{\mathrm{x}}}(x,y) = \mathrm{e}^{\mathrm{i}k_{\mathrm{x}}x} f_{\lambda,k_x}(y) \ . \tag{2.20}$$

In particular, we can replace $\hat{p}_{\mathrm{x}}$ in the Hamiltonian Eq. (2.19) by its eigenvalue $\hbar k_{\mathrm{x}}$, which implies [100]

$$H\psi_{\lambda,k_{\mathrm{x}}}(x,y) = H_{\lambda,k_{\mathrm{x}}}\psi_{\lambda,k_{\mathrm{x}}}(x,y) \quad \text{with} \quad H_{k_{\mathrm{x}}} = \frac{1}{2m^*}\hat{p}_{\mathrm{y}}^2 + \frac{m^*\omega_B^2}{2}(\hat{y} - \hat{k}_{\mathrm{x}}l_B^2)^2 \ . \tag{2.21}$$

Here, $l_B = \sqrt{\hbar/(\mathrm{e}B)}$ is the magnetic length. This Hamiltonian describes a displaced harmonic oscillator centered at $y_0 = k_{\mathrm{x}}l_B^2$. Consequently, its eigen-states are described by [102]

$$\psi_{\lambda,k_{\mathrm{x}}}(x,y) \propto \mathrm{e}^{\mathrm{i}k_{\mathrm{x}}x} H_\lambda(y - k_{\mathrm{x}}l_B^2)\mathrm{e}^{-(y-k_{\mathrm{x}}l_B^2)/(2l_B^2)}, \tag{2.22}$$

where the functions H_λ define the common Hermite polynomials of order $\lambda \in \mathbb{N}_0$ [103–105]. Using these wavefunctions enables us to determine the degeneracy of each Landau level. Our Hall bar has a finite length L_{x}, width W, and surface area $A = L_{\mathrm{x}}W$. Consequently, the momentum k_{x} is quantized in units of $2\pi/L_{\mathrm{x}}$ and the center of mass of each wave-function needs to fulfill $0 \leq y_0 \leq W$, implying $0 \leq k_{\mathrm{x}} \leq W/l_B^2$. Therefore, the degeneracy of each (spin polarized) Landau level is given by [100]

$$\mathbb{D} = \int_0^{W/l_B^2} \mathrm{d}k_{\mathrm{x}} \Big/ \frac{2\pi}{L_{\mathrm{x}}} = \frac{L_{\mathrm{x}}W}{2\pi l_B^2} = \frac{\mathrm{e}BA}{2\pi\hbar} \ . \tag{2.23}$$

The bulk particle density n in a quantum Hall sample is consequently quantized in terms of $\mathrm{e}B/\mathrm{h}$. Namely, for $N_{\mathrm{LL}} \in \mathbb{N}^+$ filled Landau levels, the associated density is given by

$$n = \frac{\mathrm{e}B}{2\pi\hbar}N_{\mathrm{LL}} \ . \tag{2.24}$$

Having determined the density, we can use Streda's formula [106] to obtain the quantized off-diagonal bulk conductivity

$$\sigma_{\mathrm{xy}} = \mathrm{e}\frac{\partial n}{\partial B} = N_{\mathrm{LL}}\frac{\mathrm{e}^2}{\mathrm{h}} \ . \tag{2.25}$$

If the chemical potential is placed in between two Landau levels, all bulk modes are confined to cyclotron orbits and the system is a bulk insulator and the diagonal conductivity vanishes, $\sigma_{\mathrm{xx}} = 0$. However, to entirely understand Fig. 2.2, we still need to include three more ingredients in our analysis: (*i*) Edge states, (*ii*) disorder, and (*iii*) spin-splitting.

2.2.2 Edge States

To derive the bulk Landau level spectrum in Fig. 2.3(a), we considered an infinite system with periodic boundary conditions. From an experimental point of view this is well justified for the longitudinal direction, since $L_\mathrm{x} \gg W$, and the current contacts are attached at the edges in $\mathbf{e}_\mathrm{x}$-direction [101]. However, to obtain the edge modes associated to the quantized Hall response in the Landau levels gaps, we need to add a confining potential $V_\mathrm{conf}(y)$ to the bulk Hamiltonian in Eq. (2.19). While this potential does not influence the bulk modes, it bends the Landau levels upwards at the sample's edges, as it is shown in Fig. 2.4(a) for a single Landau level. Notice, that due to the relation $y_0 = k_\mathrm{x} l_B^2$, which we derived in Eq. (2.21), there is a one-to-one correspondence between the momentum in $\mathbf{e}_\mathrm{x}$- and the real space in $\mathbf{e}_\mathrm{y}$-direction.

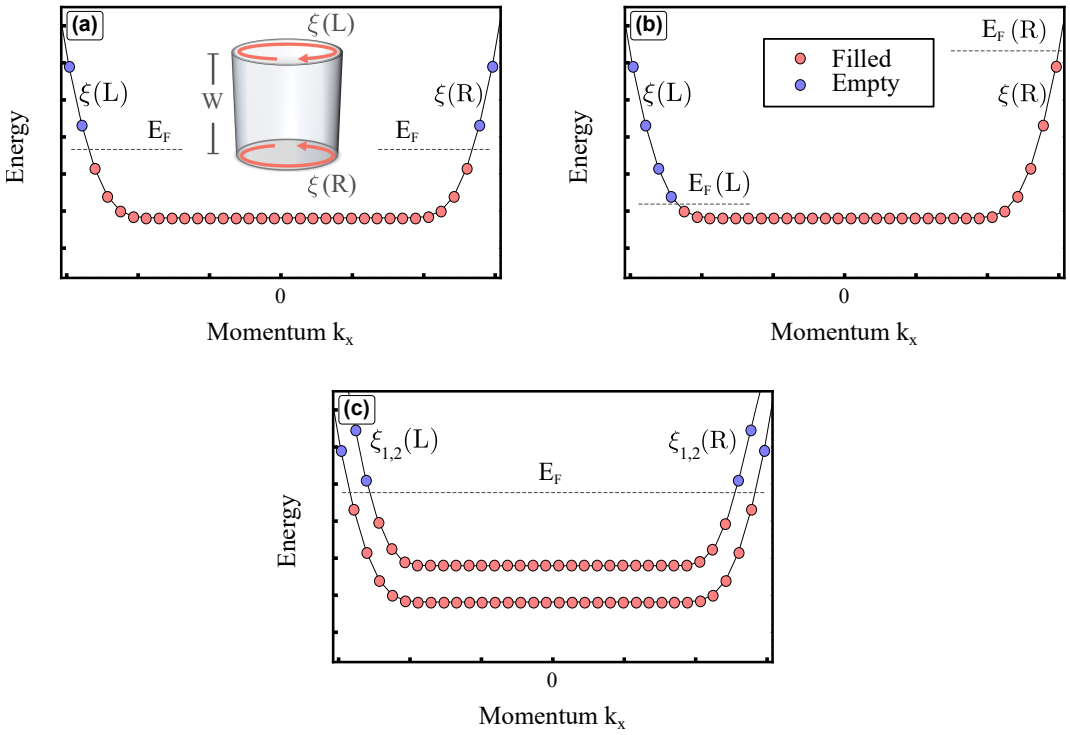

Figure 2.4: (a) Single Landau level under the influence of a confining potential $V_\mathrm{conf}(y)$. We consider an infinite system with periodic boundary conditions in $\mathbf{e}_\mathrm{x}$-direction and confine the electron system to a finite width W in $\mathbf{e}_\mathrm{y}$-direction. This defines the cylinder geometry which is shown as an inset. Notice, that due to the relation $y_0 = k_\mathrm{x} l_B^2$ [cf. Eq. (2.21)], there is an one-to-one correspondence between the momentum in $\mathbf{e}_\mathrm{x}$- and the real space in $\mathbf{e}_\mathrm{y}$-direction. At the sample's edges, the Landau level bends upwards, leading to the chiral edge modes $\xi(\mathrm{L},\mathrm{R})$ (left, right). **(b)** If one applies a potential gradient $\Delta\mu = E_\mathrm{F}(\mathrm{L}) - E_\mathrm{F}(\mathrm{R})$ at both edges, a net chiral edge current forms. **(c)** Two Landau level spectrum under the influence of the confining potential $V_\mathrm{conf}(y)$. Here, we assume a constant chemical potential for $N_\mathrm{LL} = 2$ filled Landau levels. Filled states are shown in red, empty states are depicted in blue.

In Fig. 2.4(a), all states up to the Fermi energy E_F are filled, which is encoded by red dots. Due to the curvature of the Landau level at the sample's boundaries, the chiral modes at each edge of the Hall bar have a finite drift velocity in $\mathbf{e}_\mathrm{x}$-direction [100]

$$v_\mathrm{x} = -\frac{1}{\mathrm{e}B}\frac{\partial V}{\partial y} \,. \tag{2.26}$$

Introducing a chemical potential difference $\Delta\mu$ in $\mathbf{e}_\mathrm{y}$-direction causes a net charge transport,

or equivalently a netto current I_x. The corresponding band-structure for a single Landau level in Fig. 2.4(b) gives rise to the charge current

$$I_x = -e \int \frac{dk_x}{2\pi} v_x(k_x) = \frac{e}{2\pi l_B^2} \int dy \frac{1}{eB} \frac{\partial V}{\partial y} = \frac{e}{2\pi\hbar} \Delta\mu \quad \Rightarrow \quad \sigma_{xy} = \frac{e^2}{h} \, . \tag{2.27}$$

So far, we have only analyzed the edge modes of a single Landau level. However, as long as we place the chemical potential in a Landau level gap, all our findings can be transferred to the edge physics of multiple filled Landau levels. This is shown in Fig. 2.4(c). For a chemical potential between N_{LL}- and $N_{LL}+1$- filled Landau levels, there are exactly N_{LL} chiral edge states at each boundary, corresponding to $\sigma_{xy} = N_{LL} e^2/h$ [100].

2.2.3 Disorder

As we have shown in Eq. (2.25), placing the chemical potential in between two Landau levels leads to a quantized value of the Hall conductivity. In contrast, the longitudinal conductivity vanishes in each Landau level gap, since each bulk mode is localized within its cyclotron orbit, defining a bulk insulator. However, these properties alone do not explain the extended Hall plateaus and peaks in the longitudinal resistance in Fig. 2.2. In a clean system one experimentally cannot place the chemical potential in a Landau level gap since there are no bulk modes to occupy. This changes as soon as one takes into account the effects of disorder, which can be modeled by adding a random disorder potential $V_{dis}(x, y)$ to the Hamiltonian Eq. (2.19). Effectively, the disorder potential broadens the Landau level energies from discrete values to a Gaussian distribution [100, 101]. In what follows, we assume the presence of a weak disorder potential which does not close the Landau level gaps. In particular, the Gaussian distributions corresponding to each Landau level do not overlap if the strength of the disorder potential is much smaller the Landau level spacing

$$|V_{dis}(x, y)| \ll \hbar\omega_B \, . \tag{2.28}$$

As shown in Fig. 2.5(a), a Gaussian distributed Landau level hosts two kind of bulk modes: Localized and extended states.

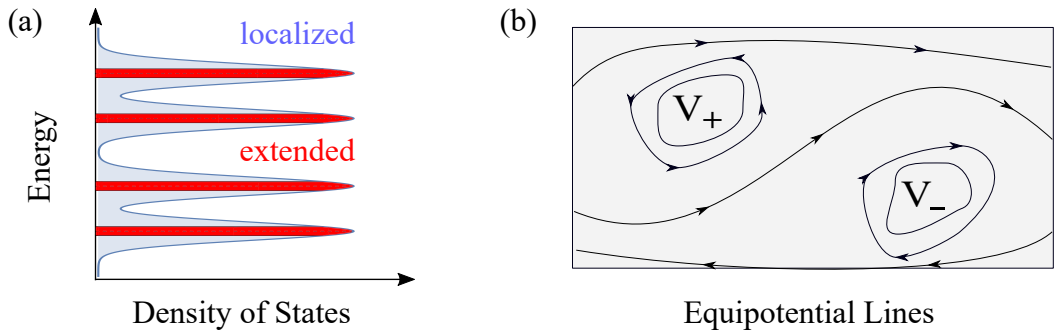

Figure 2.5: (a) Density of states of a quantum Hall system in the presence of a random disorder potential $V_{dis}(x, y)$. Each initially discrete Landau level (dashed lines) obtains a Gaussian broadening. The inner parts of the distributions correspond to extended modes, whereas the outer parts define localized states. **(b)** Equipotential lines corresponding to the random disorder potential $V_{dis}(x, y)$ with maximum V_+ and minimum V_-. Closed lines encode localized states, whereas open lines define extended modes. These figures are inspired by Figs. (18) and (19) in Ref. [100].

In Fig. 2.5(b), we illustrate the equipotential lines of a disorder potential with a maximum V_+ and a minimum V_-. Along these lines the cyclotron orbits of bulk modes can propagate. Next to the extreme values there are closed equipotential lines defining localized states. These modes correspond to the outer states in a disorder broadened Landau level [cf. Fig. 2.5(a)]. Open equipotential lines passing through the Hall bar define extended bulk states. These modes correspond to the inner states in a disorder broadened Landau level [cf. Fig. 2.5(a)]. While the extended modes contribute to electron transport, filling localized states does not change the conductivity. Consequently, the presence of disorder provides a regime in which the chemical potential can be varied without changing the Hall conductivity. This eventually explains the extended Hall plateaus in Fig. 2.2. Moreover, it also clarifies the peaks of the longitudinal resistance whenever the Hall plateau changes. In this case, the chemical potential passes the extended bulk states which contribute the charge transport [100].

2.2.4 Spin Splitting

To finally understand Fig. 2.2, we also need to take into account the electron's spin $\sigma = \uparrow, \downarrow$. As mentioned above, the bulk Landau level spectrum in Eq. (2.17) was derived for spinless modes. If one includes the spin character of the electrons in Eq. (2.17), one effectively needs to add a Zeeman energy to the bulk Landau level spectrum, which implies [100]

$$E_\lambda = \hbar\omega_B \left(\lambda + \frac{1}{2}\right) \pm \frac{1}{2} g^* \mu_\mathrm{B} B \quad \text{with} \quad \lambda \in \mathbb{N}_0 \ . \tag{2.29}$$

Here, $\pm$ defines the energy of spin-up $(-)$ and spin-down $(+)$ modes, $\mu_\mathrm{B} = \mathrm{e}\hbar/(2m_\mathrm{e})$ is the Bohr magneton, and g^* is the effective g-factor of the electrons in a certain solid state material. For instance in GaAs-Al_xGa_{1-x}As hetero-structures this factor is given by $g^* \approx 0.4$ [107]. Consequently, all Landau levels are splitted in energy by a finite Zeeman term, as it is schematically illustrated in Fig. 2.3(b).

2.2.5 Laughlin Argument

In Eq. (2.25), we derived the quantized off-diagonal conductivity of a quantum Hall sample via Streda's formula and the Landau level degeneracy $\mathbb{D}$ in Eq. (2.23). However, this derivation can be done in a more elegant fashion by virtue of the so-called Laughlin argument [108]. Since we will use the theoretical concepts of this argument several times throughout this thesis, let us review this famous argument in the following paragraphs based on the Refs. [100, 102, 108].

As discussed in Sec. 2.276, in the scope of our analysis we consider Hall bar geometries of length L_x and width W with periodic boundary conditions in $\mathbf{e}_\mathrm{x}$-, as well as hard wall boundary conditions in $\mathbf{e}_\mathrm{y}$-direction. The latter is realized via the confining potential $V_\mathrm{conf}(y)$ [cf. Fig. 2.4(a)]. Such geometries are defined by the surface of a cylinder, which is schematically illustrated in Fig. 2.6.

The out-of-plane magnetic field $\mathbf{B}$ is characterized by the magnetic flux Φ_B. Again, we are going to describe the magnetic field in terms of the Landau gauge $\mathbf{A} = -By\,\mathbf{e}_\mathrm{x}$. The cylinder geometry in Fig. 2.6 enables us to define an additional artificial magnetic Laughlin flux Φ_L parallel to the cylinder symmetry axis. According to Faraday's law [99], a time-dependent variation of this flux induces a longitudinal constant electric field

$$E_\mathrm{x} = -\partial_\mathrm{t}\Phi_\mathrm{L}/L_\mathrm{x} = -\partial_\mathrm{t} A_\mathrm{x} \ . \tag{2.30}$$

As a consequence of the Hall conductivity, such a field induces the current density $j_\mathrm{y} = \sigma_\mathrm{yx} E_\mathrm{x}$.

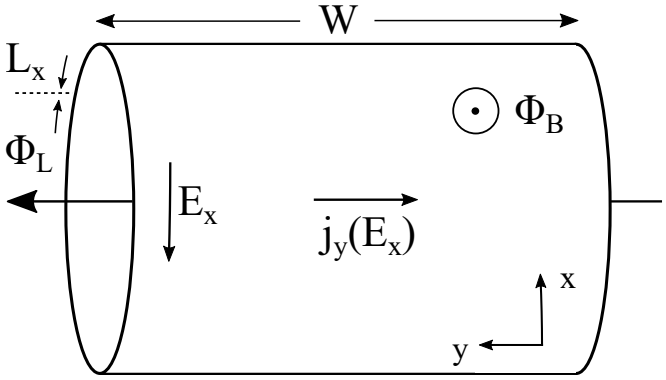

Figure 2.6: Cylinder geometry for the Laughlin argument [108]. We consider a Hall bar of length L_x and width W with periodic boundary conditions in $\mathbf{e}_\mathrm{x}$-, as well as hard wall boundary conditions in $\mathbf{e}_\mathrm{y}$-direction. The magnetic flux Φ_B defines the quantizing magnetic field which gives rise to the Landau level spectrum in Eq. (2.17). The Laughlin flux Φ_L will be tuned time-dependently which induces the longitudinal electric field $\mathbf{E} = E_\mathrm{x}\mathbf{e}_\mathrm{x}$. Due to the finite Hall conductivity σ_yx this generates a Hall current $\mathbf{j}_\mathrm{y}(E_\mathrm{x})$. Further explanations are given in the text.

In what follows, let us derive the quantized values of the Hall conductivity by using the Laughlin argument. According to Eq. (2.22), the center of mass of each eigenfunction is given by $y_0 = k_\mathrm{x} l_B^2$, and due to the finite length L_x the momentum k_x is integer quantized in units of $2\pi/L_\mathrm{x}$. Consequently, adjacent states in momentum- and real space are separated by $\Delta k_\mathrm{x} = 2\pi/L_\mathrm{x}$ and $\Delta y = 2\pi l_B^2/L_\mathrm{x}$, respectively. As mentioned above, a variation of the Laughlin flux changes the vector potential A_x by

$$\Delta A_\mathrm{x} = \Delta\Phi_\mathrm{L}/L_\mathrm{x} \ . \tag{2.31}$$

Thus, if we increase the Laughlin flux by one flux quantum $\Phi_0 = \mathrm{h/e}$, the vector potential evaluates to

$$A \to A + \left(\frac{\Phi_0}{L_\mathrm{x}}, 0\right) = A + B\Delta y\, \mathbf{e}_\mathrm{x} \ , \quad \text{since} \quad \frac{\Phi_0}{L_\mathrm{x}} = \frac{\mathrm{h}\Delta y}{\mathrm{e}2\pi l_B^2} = B\Delta y \ . \tag{2.32}$$

Effectively, this shifts the center of mass of each wavefunction by Δy in real-, or equivalently by Δk_x in momentum space. Increasing $\Phi_\mathrm{L} \to \Phi_\mathrm{L} + \Phi_0$ in a time T therefore effectively shifts one electron in each Landau level from the right ($y = 0$) to the left ($y = W$) boundary of the cylinder. For $N_\mathrm{LL} \in \mathbb{N}$ filled Landau levels, this implies

$$\mathrm{e}N_\mathrm{LL} = \int_0^T \mathrm{d}t\ j_\mathrm{y} L_\mathrm{x} = \sigma_\mathrm{yx} \int_0^T \mathrm{d}t\ E_\mathrm{x} L_\mathrm{x} = -\sigma_\mathrm{yx} \int_0^T \mathrm{d}t\ \partial_t \Phi = \sigma_\mathrm{xy} \Phi_0 \ , \tag{2.33}$$

which eventually leads to the quantized value of the Hall conductivity:

$$\sigma_\mathrm{xy} = N_\mathrm{LL} \frac{\mathrm{e}^2}{\mathrm{h}} \tag{2.34}$$

2.3 Minkowski Space-Time and Clifford Algebra

2.3.1 2+1 Space-Time Dimensions

In this work, we are considering Dirac spinors $\psi(x)$ and abelian U(1) gauge fields $A^\mu(x)$ in a flat 2+1 dimensional bulk space-time, which is described by the Minkowski metric [109]

$$g^{\mu\nu} = \begin{pmatrix} 1 & 0 & 0 \\ 0 & -1 & 0 \\ 0 & 0 & -1 \end{pmatrix} . \tag{2.35}$$

The associated set of irreducible 2+1 dimensional Dirac matrices $\gamma^{0,1,2}$ satisfies the Clifford algebra with the anti-commutation rule [56, 57]

$$\{\gamma^\mu, \gamma^\nu\}_+ = 2g^{\mu\nu}\mathbb{1}_2 , \tag{2.36}$$

where $\mathbb{1}_2$ is the 2×2 identity matrix. A common representation for these matrices via the Pauli matrices [109]

$$\sigma^1 = \begin{pmatrix} 0 & 1 \\ 1 & 0 \end{pmatrix}, \quad \sigma^2 = \begin{pmatrix} 0 & -\mathrm{i} \\ \mathrm{i} & 0 \end{pmatrix}, \quad \sigma^3 = \begin{pmatrix} 1 & 0 \\ 0 & -1 \end{pmatrix} \tag{2.37}$$

is the so-called Dirac representation [56, 57]

$$\gamma^0 = \sigma^3 = \begin{pmatrix} 1 & 0 \\ 0 & -1 \end{pmatrix} \quad \wedge \quad \gamma^1 = \mathrm{i}\sigma^1 = \begin{pmatrix} 0 & \mathrm{i} \\ \mathrm{i} & 0 \end{pmatrix} \quad \wedge \quad \gamma^2 = \mathrm{i}\sigma^2 = \begin{pmatrix} 0 & 1 \\ -1 & 0 \end{pmatrix} . \tag{2.38}$$

In particular, the Dirac matrices in 2+1 space-time dimensions satisfy the following trace identities, which will be used several times throughout this thesis [56, 57]:

$$\begin{aligned} \mathrm{Tr}\left[\gamma^\mu\right] &= 0 , \\ \mathrm{Tr}\left[\gamma^\mu\gamma^\nu\right] &= 2g^{\mu\nu} , \\ \mathrm{Tr}\left[\gamma^\mu\gamma^\nu\gamma^\lambda\right] &= -2\mathrm{i}\epsilon^{\mu\nu\lambda} , \\ \mathrm{Tr}\left[\gamma^\mu\gamma^\nu\gamma^\lambda\gamma^\rho\right] &= 2\left(g^{\mu\nu}g^{\lambda\rho} - g^{\mu\lambda}g^{\nu\rho} + g^{\mu\rho}g^{\nu\lambda}\right) , \end{aligned} \tag{2.39}$$

where $\epsilon^{\mu\nu\rho}$ is the anti-symmetric Levi-Civita symbol with $\epsilon^{012} = 1$. To prove the third identity, which is special in 2+1 space-time dimensions, we used that

$$\gamma^\mu\gamma^\nu = g^{\mu\nu}\mathbb{1}_2 - \mathrm{i}\epsilon^{\mu\nu\rho}\gamma_\rho , \tag{2.40}$$

which implies

$$\mathrm{Tr}\left[\gamma^\mu\gamma^\nu\gamma^\lambda\right] = \mathrm{Tr}\left[\left(g^{\mu\nu}\mathbb{1}_2 - \mathrm{i}\epsilon^{\mu\nu\rho}\gamma_\rho\right)\gamma^\lambda\right] = -\mathrm{i}\epsilon^{\mu\nu\rho}\mathrm{Tr}\left[\gamma_\rho\gamma^\lambda\right] = -2\mathrm{i}\epsilon^{\mu\nu\lambda} . \tag{2.41}$$

2.3.2 1+1 Space-Time Dimensions

The edge channels of our bulk theory are defined in a 1+1 dimensional Minkowski space-time with the reduced metric tensor

$$g^{\mu\nu} = \begin{pmatrix} 1 & 0 \\ 0 & -1 \end{pmatrix} . \tag{2.42}$$

In this space-time dimension we choose the following representation of the Dirac matrices [109]

$$\gamma^0 = \sigma^2 = \begin{pmatrix} 0 & -\mathrm{i} \\ \mathrm{i} & 0 \end{pmatrix} \quad \wedge \quad \gamma^1 = \mathrm{i}\sigma^1 = \begin{pmatrix} 0 & \mathrm{i} \\ \mathrm{i} & 0 \end{pmatrix} \quad \wedge \quad \gamma^5 = \gamma^0\gamma^1 = \sigma^3 = \begin{pmatrix} 1 & 0 \\ 0 & -1 \end{pmatrix} . \tag{2.43}$$

While there is no notion of chirality and thus no γ^5 matrix in 2+1 space-time dimensions, this concept is defined in 1+1 dimensions. In particular, γ^5 has the following properties

$$\gamma^5\gamma^5 = \mathbb{1}_2, \quad \gamma^5\gamma^\mu = -\gamma^\mu\gamma^5, \quad \gamma^\mu\gamma^\nu = g^{\mu\nu}\mathbb{1}_2 + \epsilon^{\mu\nu}\gamma^5 , \tag{2.44}$$

where $\epsilon^{\mu\nu}$ is the reduced anti-symmetric Levi-Civita symbol with $\epsilon^{01} = 1$. The eigenvalues of γ^5 are ± 1. These values define the chiralities of the associated left- and right handed Dirac spinors. In particular, the Dirac matrices have the following trace properties in 1+1 space-time dimensions

$$\begin{aligned} \mathrm{Tr}\left[\gamma^\mu\right] &= 0 , \qquad (2.45) \\ \mathrm{Tr}\left[\gamma^5\right] &= 0 , \\ \mathrm{Tr}\left[\gamma^\mu\gamma^\nu\right] &= 2g^{\mu\nu} , \\ \mathrm{Tr}\left[\gamma^\mu\gamma^\nu\gamma^5\right] &= 0 , \\ \mathrm{Tr}\left[\gamma^\mu\gamma^\nu\gamma^\lambda\gamma^\rho\right] &= 2\left(g^{\mu\nu}g^{\lambda\rho} + \epsilon^{\mu\nu}\epsilon^{\lambda\rho}\right) , \qquad (2.46) \\ \mathrm{tr}\left[\gamma^\mu\gamma^\nu\gamma^\lambda\gamma^\rho\gamma^5\right] &= 2\left(g^{\mu\nu}\epsilon^{\lambda\rho} + \epsilon^{\mu\nu}g^{\lambda\rho}\right) . \end{aligned}$$

2.3.3 Wick-Rotation

By a so-called Wick-rotation [109, 110], one can map every Minkowski metric to an Euclidean space-time, which is in particular defined by the (positive) metric tensor

$$\eta^{\mu\nu} = \mathbb{1}_3 . \tag{2.47}$$

Such a transformation rotates the time component of each space-time vector from the real- to the imaginary axis

$$x^0 \to \mathrm{i}x^0 \quad \wedge \quad x^i \to x^i . \tag{2.48}$$

This changes the Minkowski- to an (negative) Euclidean norm

$$|x|^2_{\mathrm{M}} = x_\mu x_\nu g^{\mu\nu} = x_0^2 - x_i^2 \quad \to \quad -|x|^2_{\mathrm{E}} = -x_\mu x_\nu \eta^{\mu\nu} = -x_0^2 - x_i^2 . \tag{2.49}$$

In solid state physics, this the Wick-rotation is frequently used in the framework of the Masubara theory [111].

2.4 Symmetries

It is the goal of the present subsection to introduce and to analyze different (symmetry) transformations in 2+1 space-time dimensions. In particular, we are going to discuss the parity $\mathcal{P}$-, the time-reversal $\mathcal{T}$-, the charge conjugation $\mathcal{C}$-, as well as the Lorentz transformation Λ. We will analyze in which way the Dirac spinor ψ as well as the U(1) gauge field A^μ behaves under such transformations, and will eventually derive the associated Noether currents.

2.4.1 Parity, Time-Reversal and Charge-Conjugation Transformations

Let us start our discussion by analyzing the concept of parity transformations $\mathcal{P}$. In 2+1 space-time dimensions a parity transformation changes just one of the spacial components, since it needs to have a determinant of -1. Here, we choose the x_1-direction. Thus, we define the parity transformation via

$$\mathcal{P}: \quad x_0 \to x_0 \quad \wedge \quad x_1 \to -x_1 \quad \wedge \quad x_2 \to x_2 \ . \tag{2.50}$$

This is fundamentally different to its definition in 3+1 space-time dimensions, where it satisfies $\mathbf{x} \to -\mathbf{x}$. In second quantization, a parity transformation is a linear and unitary operator which in the Dirac representation acts like [57]

$$\mathcal{P}\,\psi(x_0,x_1,x_2)\,\mathcal{P}^{-1} = \gamma^1\,\psi(x_0,-x_1,x_2) \ , \tag{2.51}$$
$$\mathcal{P}\,A_0(x_0,x_1,x_2)\,\mathcal{P}^{-1} = A_0(x_0,-x_1,x_2) \ , \tag{2.52}$$
$$\mathcal{P}\,A_1(x_0,x_1,x_2)\,\mathcal{P}^{-1} = -A_1(x_0,-x_1,x_2) \ , \tag{2.53}$$
$$\mathcal{P}\,A_2(x_0,x_1,x_2)\,\mathcal{P}^{-1} = A_2(x_0,-x_1,x_2) \ . \tag{2.54}$$

Instead, the time-reversal transformation $\mathcal{T}$ is an anti-linear and anti-unitary operator with $\mathcal{T}\mathrm{i}\mathcal{T}^{-1} = -\mathrm{i}$. It changes the direction of time in the Minkowski space

$$\mathcal{T}: \quad x_0 \to -x_0 \quad \wedge \quad x_1 \to x_1 \quad \wedge \quad x_2 \to x_2 \ . \tag{2.55}$$

In the Dirac representation, the time-reversal operator acts like [57]

$$\mathcal{T}\,\psi(x_0,x_1,x_2)\,\mathcal{T}^{-1} = \gamma^2\,\psi(-x_0,x_1,x_2) \ , \tag{2.56}$$
$$\mathcal{T}\,A_0(x_0,x_1,x_2)\,\mathcal{T}^{-1} = A_0(-x_0,x_1,x_2) \ , \tag{2.57}$$
$$\mathcal{T}\,\mathbf{A}(x_0,x_1,x_2)\,\mathcal{T}^{-1} = -\mathbf{A}(-x_0,x_1,x_2) \ . \tag{2.58}$$

The charge conjugation $\mathcal{C}$ is an unitary operator which converts particles ψ to anti-particles ψ_c. Requiring that ψ_c satisfies the charge conjugated Dirac equation implies a certain form for the charge conjugation matrix U_c:

$$\psi_\mathrm{c}(x_0,x_1,x_2) \equiv U_\mathrm{c}\gamma^0\psi^*(x_0,x_1,x_2) \quad \text{with} \quad (\gamma^\mu)^\mathrm{T} = -U_\mathrm{c}^{-1}\gamma^\mu U_\mathrm{c} \ . \tag{2.59}$$

In the Dirac representation, this condition can be fulfilled by choosing $U_\mathrm{c} = \gamma^2$ [57].

2.4.2 External Background Fields

So far, we have considered fluctuating U(1) gauge fields A_μ. Such fields for instance mediate the electron-electron (Coulomb) interactions in a solid state material. However, on a theoretical level, we can also solely couple the Dirac spinors ψ to external background fields A_μ^ext. Their transformation rules are fixed by the experimental setup. For instance, the back-

ground out-of-plane magnetic field B^{ext} in a quantum Hall system can be treated as such a field [cf. Sec. 2.2]. This leads to a subtlety. While the magnetic field B corresponding to a fluctuating gauge field is a pseudo-scalar under parity- and time-reversal transformations, an externally applied magnetic field B^{ext} is a scalar under these operations, as it does not change under internal (symmetry) transformations. In particular, we find

$$\begin{aligned}\mathcal{P}\, B(x_0,x_1,x_2)\,\mathcal{P}^{-1} &= \mathcal{P}\,\epsilon^{ij}\partial_i A_j(x_0,x_1,x_2)\,\mathcal{P}^{-1} \\ &= \epsilon^{12}(-\partial_1)A_2(x_0,-x_1,x_2)+\epsilon^{21}\partial_2(-A_1(x_0,-x_1,x_2)) \\ &= -\epsilon^{ij}\partial_i A_j(x_0,-x_1,x_2) = -B(x_0,-x_1,x_2)\ ,\end{aligned} \tag{2.60}$$

$$\begin{aligned}\mathcal{T}\, B(x_0,x_1,x_2)\,\mathcal{T}^{-1} &= \mathcal{T}\,\epsilon^{ij}\partial_i A_j(x_0,x_1,x_2)\,\mathcal{T}^{-1} \\ &= \epsilon^{12}\partial_1(-A_2(-x_0,x_1,x_2))+\epsilon^{21}\partial_2(-A_1(-x_0,x_1,x_2)) \\ &= -\epsilon^{ij}\partial_i A_j(-x_0,x_1,x_2) = -B(-x_0,x_1,x_2)\ ,\end{aligned} \tag{2.61}$$

whereas for an external magnetic background field we require

$$\begin{aligned}\mathcal{P}\, B^{\text{ext}}(x_0,x_1,x_2)\,\mathcal{P}^{-1} &= \mathcal{P}\,\epsilon^{ij}\partial_i A_j^{\text{ext}}(x_0,x_1,x_2)\,\mathcal{P}^{-1} \\ &= \epsilon^{12}(-\partial_1)\mathcal{P}A_2^{\text{ext}}(x_0,x_1,x_2)\mathcal{P}^{-1}+\epsilon^{21}\partial_2\mathcal{P}A_1^{\text{ext}}(x_0,x_1,x_2)\mathcal{P}^{-1} \\ &\stackrel{!}{=} B^{\text{ext}}(x_0,-x_1,x_2)\ ,\end{aligned} \tag{2.62}$$

$$\begin{aligned}\mathcal{T}\, B^{\text{ext}}(x_0,x_1,x_2)\,\mathcal{T}^{-1} &= \mathcal{T}\,\epsilon^{ij}\partial_i A_j^{\text{ext}}(x_0,x_1,x_2)\,\mathcal{T}^{-1} \\ &= \epsilon^{ij}\partial_i\mathcal{T}A_j^{\text{ext}}(x_0,x_1,x_2)\,\mathcal{T}^{-1} \stackrel{!}{=} B^{\text{ext}}(-x_0,x_1,x_2)\ .\end{aligned} \tag{2.63}$$

This implies the associated transformation rules

$$\mathcal{P}A_1^{\text{ext}}(x_0,x_1,x_2)\mathcal{P}^{-1} = A_1^{\text{ext}}(x_0,-x_1,x_2) \tag{2.64}$$

$$\mathcal{P}A_2^{\text{ext}}(x_0,x_1,x_2)\mathcal{P}^{-1} = -A_2^{\text{ext}}(x_0,-x_1,x_2) \tag{2.65}$$

$$\mathcal{T}\mathbf{A}^{\text{ext}}(x_0,x_1,x_2)\mathcal{T}^{-1} = \mathbf{A}^{\text{ext}}(-x_0,x_1,x_2)\ . \tag{2.66}$$

2.4.3 Lorentz and Galilean Symmetry

Beside the discrete transformations discussed above, there are several continuous symmetry transformations which a 2+1 space-time dimensional Dirac system should satisfy. One of these symmetries is the invariance under the Poincare group [38]. On the one hand, this group consists of the Lorentz transformations $\Lambda^{\mu}{}_{\nu}$, which map between different inertial systems via boosts and rotations of the relativistic coordinates [109, 110]:

$$x'_{\mu} = \Lambda_{\mu}{}^{\nu} x_{\nu}\ . \tag{2.67}$$

Since all inertial systems describe the same physics, Lorentz transformations do not change the metric tensor:

$$x^{\mu}x_{\mu} = x^{\mu}g_{\mu\nu}x^{\nu} \stackrel{!}{=} x'^{\mu}x'_{\mu} = x^{\beta}\Lambda_{\beta}{}^{\mu}g_{\mu\nu}\Lambda^{\nu}{}_{\alpha}x^{\alpha} \quad \Rightarrow \quad \Lambda^{\mathrm{T}}g\Lambda = g\ . \tag{2.68}$$

Consequently, with $g^{-1}=g$, the inverse Lorentz transformation Λ^{-1} is given by

$$g^{-1}\Lambda^{\mathrm{T}}g\Lambda\Lambda^{-1} = g^{-1}g\Lambda^{-1} \quad \Rightarrow \quad \Lambda^{-1} = g\Lambda^{\mathrm{T}}g\ . \tag{2.69}$$

Further, Eq. (2.68) implies $\det\Lambda = \pm 1$. Our convention $g_{00} = 1$ additionally requires

$$\Lambda_0{}^{\mu} g_{\mu\nu} \Lambda^{\nu}{}_0 = g_{00} = 1 \quad \Rightarrow \quad (\Lambda^0{}_0)^2 = 1 + \sum_{i=1}^{3} (\Lambda^i{}_0)^2 \geqslant 1 \ . \tag{2.70}$$

In general, one distinguishes between proper- and improper Lorentz transformations with $\det\Lambda = +1$ and $\det\Lambda = -1$, as well as between orthochronous and non-orthochronous Lorentz transformations with $\Lambda^0{}_0 \geqslant 1$ and $\Lambda^0{}_0 \leqslant -1$, respectively [109, 110]. Since boosts and rotations are continuously connected to the identity, we are only considering proper- and orthochronous Lorentz transformations with $\Lambda^{\mu}{}_{\nu} \in \mathrm{SO}(1,3)$. This group has several generators, which are implicitly defined via [109, 112]

$$\Lambda = \mathrm{e}^{-\mathrm{i}\alpha_i K^i - \mathrm{i}\beta_i L^i} = \mathrm{e}^{-\frac{\mathrm{i}}{2}\Omega_{\mu\nu} M^{\mu\nu}} \ . \tag{2.71}$$

Here K_i are the anti-hermitian generators for boosts along the $\mathbf{e}_i$-direction, and J_i generate rotations around the $\mathbf{e}_i$-axis. Together, they define the anti-symmetric tensor:

$$\mathcal{M}_{\mu\nu} = -\mathcal{M}_{\nu\mu} \quad \text{with} \quad \mathcal{M}_{i0} = K_i \quad \wedge \quad \mathcal{M}_{ij} = \epsilon_{ijk} J_k \ . \tag{2.72}$$

The coefficients which define the explicit Lorentz transformation in Eq. (2.71) are α_i and β_i, or analogously

$$\Omega_{\mu\nu} = -\Omega_{\nu\mu} \quad \text{with} \quad \Omega_{i0} = \alpha_i \quad \wedge \quad \Omega_{ij} = \frac{1}{2}\epsilon_{ijk}\beta_k \ . \tag{2.73}$$

The generators of rotations and boosts form a Lie-Algebra with the anti-commutation rules

$$[J_i, J_j] = \mathrm{i}\epsilon_{ijk} J_k \ , \tag{2.74}$$
$$[J_i, K_j] = \mathrm{i}\epsilon_{ijk} K_k \ , \tag{2.75}$$
$$[K_i, K_j] = -\mathrm{i}\epsilon_{ijk} J_k \ . \tag{2.76}$$

In 2+1 space-time dimensions these generators are defined by [112]

$$J_3 = \begin{pmatrix} 0 & 0 & 0 \\ 0 & 0 & -\mathrm{i} \\ 0 & \mathrm{i} & 0 \end{pmatrix}, \quad K_1 = \begin{pmatrix} 0 & -\mathrm{i} & 0 \\ -\mathrm{i} & 0 & 0 \\ 0 & 0 & 0 \end{pmatrix}, \quad K_2 = \begin{pmatrix} 0 & 0 & -\mathrm{i} \\ 0 & 0 & 0 \\ -\mathrm{i} & 0 & 0 \end{pmatrix} \ . \tag{2.77}$$

The entire Poincare group consists of the Lorentz transformations $\Lambda^{\mu}{}_{\nu}$ and, additionally, of the continuous space-time translations a_μ, in total giving rise to

$$x'_\mu = \Lambda_\mu{}^{\nu} x_\nu + a_\mu \ . \tag{2.78}$$

The generator of a continuous space-time translation a_μ is the three-momentum

$$P_\mu = \mathrm{i}\hbar\partial_\mu \ . \tag{2.79}$$

This operator allows us to construct the angular momentum operator

$$L_{\mu\nu} = x_\mu P_\nu - x_\nu P_\mu \quad \text{with} \quad J_i = \frac{1}{2}\epsilon_{ijk} L^{jk} \quad \wedge \quad K_i = L_{0i} \ . \tag{2.80}$$

Finally, the Lie Algebra of the entire Poincare group is given by [112]:

$$[P_0, J_i] = 0 \quad , \quad [P_i, J_j] = \mathrm{i}\epsilon_{ijk} P_k \quad , \quad [P_0, K_i] = \mathrm{i} P_i \ , \tag{2.81}$$
$$[P_\mu, P_\nu] = 0 \quad , \quad [P_i, K_j] = \mathrm{i}\delta_{ij} P_0 \quad , \quad [P_\mu, L_{\rho\sigma}] = \mathrm{i}(g_{\mu\rho} P_\sigma - g_{\mu\sigma} P_\rho) \ , \tag{2.82}$$

$$[L_{\mu\nu}, L_{\rho\sigma}] = -\mathrm{i}(g_{\mu\rho}L_{\nu\sigma} - g_{\mu\sigma}L_{\nu\rho} + g_{\nu\sigma}L_{\mu\rho} - g_{\nu\rho}L_{\mu\sigma}) \ . \tag{2.83}$$

For the Lorentz transformation rules of the spinor- and vector fields ψ and A_μ, one needs to derive the representation of the Lorentz group in their configuration space. While the vector fields have a trivial representation and transform like [109]

$$A^\mu(x) \to \Lambda^\mu{}_\nu A^\nu(\Lambda^{-1}x) \ , \tag{2.84}$$

the spinor fields transform as

$$\psi(x) \to S[\Lambda]\psi(\Lambda^{-1}x) \ . \tag{2.85}$$

Here, $S[\Lambda]$ is the spinor representation of the Dirac fields defined by [109]

$$S[\Lambda] = \mathrm{e}^{-\frac{\mathrm{i}}{2}\Omega_{\rho\sigma}S^{\rho\sigma}} \quad \text{with} \quad S^{\rho\sigma} = \mathrm{i}\left[\gamma^\rho, \gamma^\nu\right]/4 \ . \tag{2.86}$$

For a detailed derivation of these transformation rules we refer the interested reader to the References [109, 110, 112, 113].

2.4.4 Vector and Axial Gauge Symmetry

One of the most important symmetries of a physical system is the so-called U(1) gauge symmetry [109]. Let us clarify this concept for a single Dirac system in 2+1 space-time dimensions. Such a system is described by the Lagrangian

$$\mathcal{L}_0 = \bar{\psi}(\mathrm{i}\partial\!\!\!/ - m)\psi \ , \tag{2.87}$$

where $\bar{\psi} = \psi^\dagger\gamma^0$, $\partial\!\!\!/ = \partial_\mu\gamma^\mu$, and m is the electron mass. Experimentally it is only possible to measure the expectation value of the electron density operator $\langle\psi^\dagger\psi\rangle$, but not the individual phases of the Dirac spinors ψ and $\psi^\dagger$. Consequently, the underlying theory needs to be invariant under continuous U(1) phase transformations of the form

$$\psi(x) \to \mathrm{e}^{-\mathrm{i}\phi}\psi(x) \ , \tag{2.88}$$

$$\psi^\dagger(x) \to \mathrm{e}^{\mathrm{i}\phi}\psi^\dagger(x) \ . \tag{2.89}$$

Here, $\phi \in \mathbb{R}$ is an arbitrary space-time independent angle. This property is fulfilled by the Dirac Lagrangian in Eq. (2.87). To ensure that this feature also holds for a space-time dependent angle $\phi(x) \in \mathbb{R}$, we need to couple the Dirac system to a so-called vector gauge field A_μ. Technically, this is done by replacing the partial derivative ∂_μ by the covariant derivative

$$D_\mu = \partial_\mu + \mathrm{i}\mathrm{e}A_\mu \ . \tag{2.90}$$

In the solid state community this procedure is also known as minimal coupling [24, 111]. The resulting Lagrangian describes the theory of quantum electrodynamics (QED) in 2+1 space-time dimensions

$$\mathcal{L} = \bar{\psi}(\mathrm{i}D\!\!\!/ - m)\psi \ . \tag{2.91}$$

Under a local phase transformation vector gauge fields do only change by a total derivative [109]

$$A_\mu \to A_\mu + \frac{1}{\mathrm{e}}\partial_\mu\phi(x) \ . \tag{2.92}$$

Consequently, the measurable electric- and magnetic fields do not change under these transformations. This is essentially the origin of the name 'gauge transformations'. The transformation property in Eq. (2.92) is constructed such that the entire Lagrangian in Eq. (2.91) is locally gauge invariant, since

$$D_\mu\psi = \partial_\mu\psi + \mathrm{i}eA_\mu \to \partial_\mu(\mathrm{e}^{-\mathrm{i}\phi(x)}\psi) + \mathrm{i}e\left(A_\mu + \frac{1}{e}\partial_\mu\phi(x)\right)(\mathrm{e}^{-\mathrm{i}\phi(x)}\psi) = \mathrm{e}^{-\mathrm{i}\phi(x)}D_\mu\psi \ . \quad (2.93)$$

In even space-time dimensions we are able to develop another gauge symmetry, namely the invariance of the Lagrangian under chiral gauge transformations. To analyze this concept, let us for the moment consider a massless Dirac Lagrangian in 1+1 space-time dimensions

$$\mathcal{L}_0 = \bar{\psi}\mathrm{i}\partial\!\!\!/\psi \ . \quad (2.94)$$

Again, we can make the system invariant under local U(1) gauge transformations by coupling it to a vector gauge field A_μ. The presence of a γ^5 matrix in even space-time dimensions, with the properties [cf. Sec. 2.3.2]

$$\left(\gamma^5\right)^\dagger = \gamma^5 \quad \wedge \quad \left(\gamma^5\right)^2 = 1 \quad \wedge \quad \left\{\gamma^5, \gamma^\mu\right\} = 0 \ , \quad (2.95)$$

allows us to construct the additional axial or chiral gauge symmetry. The eigen-states of γ^5 define the left- and right handed spinors $\psi_{\mathrm{L/R}}$ with chiralities ± 1,

$$\psi_{\mathrm{L/R}} \equiv \psi_\pm = P_\pm\psi = \frac{\mathbb{1}_2 \pm \gamma^5}{2}\psi \quad \text{with} \quad \gamma^5\psi_\pm = \pm\psi_\pm \ . \quad (2.96)$$

Here, $P_\pm$ is the chiral projection operator with the properties

$$P_+ + P_- = \mathbb{1}_2, \quad P_\pm^2 = P_\pm, \quad P_+P_- = P_-P_+ = 0, \quad P_+\gamma^\mu = \gamma^\mu P_- \ . \quad (2.97)$$

Analogously to the vector gauge transformations in Eq. (2.90), we can make the Lagrangian in Eq. (2.94) invariant under both, local vector- and axial gauge transformations by introducing an additional axial gauge field in the covariant derivative [114]

$$\mathcal{L} = \bar{\psi}\mathrm{i}\not{D}\psi = \bar{\psi}\,\mathrm{i}\left(\partial\!\!\!/ + \mathrm{i}eA\!\!\!/ + \mathrm{i}eB\!\!\!/\gamma^5\right)\psi \ . \quad (2.98)$$

Tab. 2.1 summarizes the transformation rules of all spinor and gauge fields in Eq. (2.98) under these symmetry transformations.

Vector Gauge Transformations	**Axial Gauge Transformation**
$\psi \to \mathrm{e}^{-\mathrm{i}\phi(x)}\psi$	$\psi \to \mathrm{e}^{-\mathrm{i}\varphi(x)\gamma^5}\psi$
$\bar{\psi} \to \bar{\psi}\mathrm{e}^{\mathrm{i}\phi(x)}$	$\bar{\psi} \to \bar{\psi}\mathrm{e}^{-\mathrm{i}\varphi(x)\gamma^5}$
$A_\mu \to A_\mu + \frac{1}{e}\partial_\mu\phi(x)$	$B_\mu \to B_\mu + \frac{1}{e}\partial_\mu\varphi(x)$

Table 2.1: Transformation rules of spinors and gauge fields under the local vector- and axial gauge transformations $\phi(x)$ and $\varphi(x)$ [cf. Eq. (2.98)].

In a massless Dirac Lagrangian the left- and right handed chiralities due not mix, as a direct consequence of the properties of the projection operator $P_\pm$ in Eq. (4.13). We can therefore

decompose the Lagrangian in Eq. (2.98) into its chiral building blocks. Such a decomposition allows us to define the corresponding gauge transformations for left- and right handed spinors separately:

$$\mathcal{L} = (P_+ + P_-)\bar{\psi}\mathrm{i}\not{D}(P_+ + P_-)\psi = \bar{\psi}_\mathrm{L}\,\mathrm{i}\left(\not{\partial} + \mathrm{ie}\not{A}^\mathrm{L}\right)\psi_\mathrm{L} + \bar{\psi}_\mathrm{R}\,\mathrm{i}\left(\not{\partial} + \mathrm{ie}\not{A}^\mathrm{R}\right)\psi_\mathrm{R}\ , \tag{2.99}$$

where we defined

$$A^\mathrm{L}_\mu = A_\mu + B_\mu \quad \wedge \quad A^\mathrm{R}_\mu = A_\mu - B_\mu\ . \tag{2.100}$$

The two building blocks of the Lagrangian in Eq. (2.99) are separately invariant under the local U(1) gauge transformations which are shown in Tab. 2.2.

Left Handed	**Right Handed**
$\psi_\mathrm{L} \to \mathrm{e}^{-\mathrm{i}\theta_\mathrm{L}(x)}\psi_\mathrm{L}$	$\psi_\mathrm{R} \to \mathrm{e}^{-\mathrm{i}\theta_\mathrm{R}(x)}\psi_\mathrm{R}$
$\bar{\psi}_\mathrm{L} \to \bar{\psi}_\mathrm{L}\mathrm{e}^{\mathrm{i}\theta_\mathrm{L}(x)}$	$\bar{\psi}_\mathrm{R} \to \bar{\psi}_\mathrm{R}\mathrm{e}^{\mathrm{i}\theta_\mathrm{R}(x)}$
$A^\mathrm{L}_\mu \to A^\mathrm{L}_\mu + \frac{1}{\mathrm{e}}\partial_\mu\theta_\mathrm{L}(x)$	$A^\mathrm{R}_\mu \to A^\mathrm{R}_\mu + \frac{1}{\mathrm{e}}\partial_\mu\theta_\mathrm{R}(x)$

Table 2.2: Transformation rules of left- and right handed spinors and gauge fields under the local U(1) gauge transformations $\theta_{\mathrm{L/R}}(x)$ [cf. Eq.(2.99)].

The special case $\theta_\mathrm{L} = \theta_\mathrm{R}$ corresponds to the vector- gauge transformation, whereas the case $\theta_\mathrm{L} = -\theta_\mathrm{R}$ corresponds to the axial gauge transformation presented in Tab. 2.1 [114].

Having analyzed local vector- and local axial gauge transformations, let us discuss another crucial property of continuous gauge transformations, namely the difference between small- and large gauge transformations. For simplicity we will focus on vector gauge transformations and neglect the adjective 'vector' in the subsequent paragraphs.

As we discussed in Eq. (2.88), a gauge transformation only changes the phase of a Dirac spinor. By construction the phase-factor $\mathrm{e}^{-\mathrm{i}\phi(x)}$ is a single valued quantity. However, on a compact base manifold[a] this is not necessarily true for the phase $\phi(x)$ itself. Let us for simplicity consider a $0+1$ space-time dimensional QED system where the time is defined on a unit circle S^1_time. For consistency, the Dirac spinor and the gauge field need to satisfy anti-periodic as well as periodic boundary conditions, respectively [113, 115]:

$$\psi(x^0 + 2\pi) = -\psi(x^0) \tag{2.101}$$

$$A_\mu(x^0 + 2\pi) = A_\mu(x^0)\ . \tag{2.102}$$

Consequently, the gauge phase needs to satisfy

$$\phi(x^0 + 2\pi) - \phi(x^0) = 2\pi n \quad \text{with} \quad n \in \mathbb{Z}\ . \tag{2.103}$$

For instance, this can be achieved by choosing

$$\phi(x^0) = x^0 n\ . \tag{2.104}$$

As the time x^0 is defined on the unit circle S^1_time, the quantity ϕ is not single valued. For

[a] This statement does also hold for non-compact manifolds if the corresponding fields decay to zero at infinity.

instance, for $x_0^0 = \pi = 3\pi$, we find the deviating values

$$\phi(x_0^0 = \pi) = \pi n \quad \wedge \quad \phi(x_0^0 = 3\pi) = 3\pi n \ . \tag{2.105}$$

As required by Eq. (2.103), these values differ by a factor of $2\pi n$. The multi-valuedness of $\phi(x)$ is schematically shown in Fig. 2.7 for $n = 1, 2, 3$. Here, we confined $\phi(x)$ to a circle S^1_{phase} of circumference $2\pi n$.

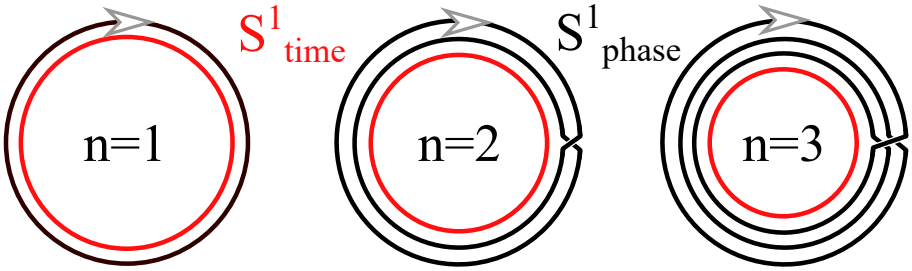

Figure 2.7: Schematic illustration of a large gauge transformation with winding $n \in \mathbb{Z}$. The circle S^1_{phase}, which defines the gauge phase $\phi(x^0)$, winds around the circle S^1_{time}, which defines the compact base manifold. The phase $\phi(x^0)$ is a multi-valued quantity, whereas the phase factor $\mathrm{e}^{-\mathrm{i}\phi(x^0)}$ remains single-valued. Further explanations are given in the text.

The winding $n \in \mathbb{Z}$ defines how often S^1_{phase} winds around S^1_{time}. Theoretically, this originates from the homotopy classification [6]

$$\pi_1(S^1) = \mathbb{Z} \ . \tag{2.106}$$

As a direct consequence of this property, the entire gauge group $U(1)_{\text{entire}}$ is not continuously connected on a compact manifold. Small gauge transformations, by definition, only connect gauge configurations which are defined by the same winding number n. Hence, the entire gauge group has several sub-sectors which are linked by topologically non-trivial so-called large gauge transformations $U(1)_{\text{entire}}/U(1)_{\text{small}} = \mathbb{Z}$ [116]. In particular, small and large gauge transformations have distinct physical consequences, which we are going to discuss within the scope of this thesis.

2.4.5 Noether Theorem

Suppose we have a system which is defined by fermionic and/or bosonic fields ϕ_a and their space-time derives $\partial_\mu \phi_a$. Its action in n space-time dimensions is thus given by [113, 115]

$$\mathcal{S}(\phi_a, \partial_\mu \phi_a) = \int \mathrm{d}^n x \, \mathcal{L}(\phi_a, \partial_\mu \phi_a) \ . \tag{2.107}$$

The equations of motion of each field ϕ_a can be derived by requiring that the action is stationary and therefore satisfies

$$\begin{aligned} \delta\mathcal{S}(\phi_a, \partial_\mu \phi_a) &= \int \mathrm{d}^n x \, \delta\mathcal{L}(\phi_a, \partial_\mu \phi_a) = \int \mathrm{d}^n x \left[\frac{\partial \mathcal{L}}{\partial \phi_a} \delta\phi_a + \frac{\partial \mathcal{L}}{\partial(\partial_\mu \phi_a)} \partial_\mu \delta\phi_a \right] \\ &= \int \mathrm{d}^n x \left[\frac{\partial \mathcal{L}}{\partial \phi_a} - \partial_\mu \frac{\partial \mathcal{L}}{\partial(\partial_\mu \phi_a)} \right] \delta\phi_a + \int \mathrm{d}^n x \, \partial_\mu \left[\frac{\partial \mathcal{L}}{\partial(\partial_\mu \phi_a)} \delta\phi_a \right] \overset{!}{=} 0 \ , \end{aligned} \tag{2.108}$$

where we partially integrated in the second line. Since the last term is the integral over a total space-time derivative, this term is a boundary term and can be neglected in an infinite system[a]. To fulfill, $\delta\mathcal{S} = 0$ for every variation $\delta\phi_a$, we need to require the so-called Euler Lagrange equations

$$\frac{\partial\mathcal{L}}{\partial\phi_a} - \partial_\mu \frac{\partial\mathcal{L}}{\partial(\partial_\mu\phi_a)} = 0\,. \tag{2.109}$$

These equations of motion can be used to prove the Noether theorem [117]:

Noether Theorem Every continuous symmetry transformation $\phi_a \to \phi_a + \delta\phi_a$ of an action $\mathcal{S}(\phi_a, \partial_\mu\phi_a)$, which changes the Lagrangian only by a total space-time derivative $\delta\mathcal{L}(\phi_a, \partial_\mu\phi_a) = \partial_\mu X^\mu(\phi_a, \partial_\mu\phi_a)$, gives rise to a locally conserved current density

$$j^\mu(x) = \frac{\partial\mathcal{L}}{\partial(\partial_\mu\phi_a)}\delta\phi_a - X^\mu(\phi_a, \partial_\mu\phi_a) \quad \text{with} \quad \partial_\mu j^\mu(x) = 0\ . \tag{2.110}$$

The proof of this theorem goes along the lines of the proof for the Euler-Lagrange equations:

$$\begin{aligned}\delta\mathcal{L}(\phi_a, \partial_\mu\phi_a) &= \left[\frac{\partial\mathcal{L}}{\partial\phi_a} - \partial_\mu\frac{\partial\mathcal{L}}{\partial(\partial_\mu\phi_a)}\delta\phi_a\right] + \partial_\mu\left[\frac{\partial\mathcal{L}}{\partial(\partial_\mu\phi_a)}\delta\phi_a\right] \\ &= \partial_\mu\left[\frac{\partial\mathcal{L}}{\partial(\partial_\mu\phi_a)}\delta\phi_a\right] \stackrel{!}{=} \partial_\mu X^\mu(\phi_a, \partial_\mu\phi_a)\ ,\end{aligned} \tag{2.111}$$

where we used the equations of motion in the second equality. Throughout this thesis we will make use of this theorem to determine the conserved currents of several Lagrangians. Table 2.3 already predicts which symmetries imply which conserved currents [113, 115].

Continuous Symmetry Transformation	**Conserved Current**
Translation in space-time	Energy-momentum current
Rotation in space	Angular momentum
U(1) gauge symmetry	Charge current
Chiral U(1) gauge symmetry	Chiral charge current

Table 2.3: Implications of the Noether theorem: Symmetries and conserved currents.

[a] This statement needs to be revised for topological field theories - like Chern-Simons forms - which will be discussed in Sec (2.6.4).

2.5 Quantum Anomalies

2.5.1 Definition

Having analyzed the possible symmetries of our system, we are now introducing the theoretical concept of quantum anomalies. It is mandatory to understand the definition of such an anomaly in detail, in order to grasp all of the results which are presented within the present thesis.

Definition 1 *If a symmetry of a classical system can not be maintained on the quantum level, the theory has a quantum anomaly. The breakdown of the parity symmetry on the quantum level is called parity anomaly. The breakdown of the chiral (gauge) symmetry on the quantum level is called chiral or axial anomaly.*

Before we derive the experimental consequences which result from such quantum anomalies, let us explain how the non-conservation of a classical symmetry on the quantum level arises in the Lagrangian formalism [114, 118–120].

2.5.2 Quantum Effective Action

Let us consider a classical system of Dirac spinors ψ and $\bar{\psi}$, as well as gauge fields A_μ, which is described by the Lagrangian

$$\mathcal{L}_{\mathrm{cl}} = \mathcal{L}_0(\psi, \bar{\psi}) + \mathcal{L}_0(A) + \mathcal{L}_{\mathrm{I}}(\psi, \bar{\psi}, A) \ . \tag{2.112}$$

Here, $\mathcal{L}_0(\psi, \bar{\psi})$ and $\mathcal{L}_0(A)$ define the Lagrangians of the free fermionic and bosonic systems, whereas $\mathcal{L}_{\mathrm{I}}(\psi, \bar{\psi}, A)$ encodes their interaction. Quantizing this theory can be done via the path integral formalism [109, 110]. In particular, any time ordered Green's function can be calculated via the generating functional $Z[\eta, \bar{\eta}, j_A]$, which plays the role of the partition function in a quantum field theory [121]:

$$\begin{aligned} &\langle 0|\mathrm{T}\left[\psi(x_1)\dots\bar{\psi}(y_1)...A_\mu(z_1)...A_\mu(z_n)\right]|0\rangle \\ &\qquad = \frac{\delta}{\mathrm{i}\,\delta\bar{\eta}(x_1)}\cdots\frac{\delta}{-\mathrm{i}\,\delta\eta(y_1)}\cdots\frac{\delta}{\mathrm{i}\,\delta j_A^\mu(z_1)}\cdots\frac{\delta}{\mathrm{i}\,\delta j_A^\mu(z_n)} Z[\eta,\bar{\eta},j_A]\Big|_{\eta,\bar{\eta},j_A=0} \ . \end{aligned} \tag{2.113}$$

Here, the Grassmann functions $\bar{\eta}$ and η are the source terms of ψ and $\bar{\psi}$, whereas the current j_A represents the source term of the vector gauge field A_μ. All of the source terms are set to zero after taking the functional derivatives. The generating functional itself is defined via the path integral over all field configurations:

$$Z[\eta, \bar{\eta}, j_A] = \frac{1}{\mathcal{N}} \int \mathrm{d}\psi\mathrm{d}\bar{\psi}\mathrm{d}A \, \exp\left[\mathrm{i}\int \mathrm{d}x \left(\mathcal{L}_{\mathrm{cl}} + \bar{\eta}\psi + \bar{\psi}\eta + A_\mu j_A^\mu\right)\right] \tag{2.114}$$

with its normalization

$$\mathcal{N} = \int \mathrm{d}\psi\mathrm{d}\bar{\psi}\mathrm{d}A \, \exp\left[\mathrm{i}\int \mathrm{d}x \, \mathcal{L}_{\mathrm{cl}}\right] \ . \tag{2.115}$$

To derive the non-interacting fermion propagator, let us calculate the free fermion Green's function $\langle 0|\mathrm{T}\left[\psi(x_1)\bar{\psi}(x_2)\right]|0\rangle$. Therefore, we set the vector field and its source term to zero, $A = j_A = 0$. Assuming that $\mathcal{L}_0(\bar{\psi}, \psi)$ is bilinear in $\bar{\psi}\psi$ allows us to define a matrix M, such that the fermionic part of the exponential in the generating functional becomes

$$\bar{\psi}M\psi + \bar{\eta}\psi + \bar{\psi}\eta = \left(\bar{\psi} + \bar{\eta}M^{-1}\right) M \left(\psi + M^{-1}\eta\right) - \bar{\eta}M^{-1}\eta \ . \tag{2.116}$$

This leads to (neglecting the space-time integral in the exponent for reasons of clarity)

$$Z_{\mathrm{F}}[\eta,\bar{\eta}] = \frac{1}{\mathcal{N}_{\mathrm{F}}}\int \mathrm{d}\psi\mathrm{d}\bar{\psi}\ \mathrm{e}^{\bar{\psi}M\psi+\bar{\eta}\psi+\bar{\psi}\eta} = \frac{1}{\mathcal{N}_{\mathrm{F}}}\mathrm{e}^{-\bar{\eta}M^{-1}\eta}\int \mathrm{d}\psi\mathrm{d}\bar{\psi}\ \mathrm{e}^{\left(\bar{\psi}+\bar{\eta}M^{-1}\right)M\left(\psi+M^{-1}\eta\right)} \tag{2.117}$$
$$= \frac{1}{\mathcal{N}_{\mathrm{F}}}\mathrm{e}^{-\bar{\eta}M^{-1}\eta}\int \mathrm{d}\psi'\mathrm{d}\bar{\psi}'\ \mathrm{e}^{\bar{\psi}'M\psi'} = \mathrm{e}^{-\bar{\eta}M^{-1}\eta}\ ,$$

where $\mathcal{N}_{\mathrm{F}} = Z_{\mathrm{F}}[0,0]$. Next, we define the inverse of the matrix M, which will turn out to be the free fermion propagator

$$MS_{\mathrm{F}}(x-y) = \delta(x-y) \Rightarrow Z[\eta,\bar{\eta},0] = \mathrm{e}^{-\mathrm{i}\int \mathrm{d}x\mathrm{d}y\bar{\eta}(x)S_{\mathrm{F}}(x-y)\eta(y)}\ . \tag{2.118}$$

According to Eq. (2.113), the time ordered two-point fermionic Green's function is given by

$$\langle 0|\mathrm{T}\left[\psi(x_1)\bar{\psi}(x_2)\right]|0\rangle = \frac{\delta^2 Z_{\mathrm{F}}[\eta,\bar{\eta}]}{\mathrm{i}\delta\bar{\eta}(x_1)(-\mathrm{i})\delta\eta(x_2)}\bigg|_{\eta=\bar{\eta}=0} \tag{2.119}$$
$$= \frac{\delta}{\mathrm{i}\delta\bar{\eta}(x_1)}(-)\int \mathrm{d}x\mathrm{d}y\ \bar{\eta}(x)S_{\mathrm{F}}(x-y)\delta(x_2-y)\mathrm{e}^{-\mathrm{i}\int \mathrm{d}x\mathrm{d}y\bar{\eta}(x)S_{\mathrm{F}}(x-y)\eta(y)}\bigg|_{\eta=\bar{\eta}=0}$$
$$= \frac{\delta}{\mathrm{i}\delta\bar{\eta}(x_1)}(-)\int \mathrm{d}x\ \bar{\eta}(x)S_{\mathrm{F}}(x-x_2)\mathrm{e}^{-\mathrm{i}\int \mathrm{d}x\mathrm{d}y\bar{\eta}(x)S_{\mathrm{F}}(x-y)\eta(y)}\bigg|_{\eta=\bar{\eta}=0}$$
$$= \mathrm{i}S_{\mathrm{F}}(x_1-x_2)\ .$$

After this brief pedagogical excursus, let us come back to our full interacting model in Eq. (2.114). The calculus of the generating functional allows us to totally get rid of the fermionic modes by deriving the so-called effective action S_{eff}. Technically, this is done by executing the Grassman integration for the fermionic fields [122]:

$$Z[0,0,j_A] = \frac{1}{\mathcal{N}}\int \mathrm{d}\psi\mathrm{d}\bar{\psi}\mathrm{d}A\ \exp\left[\mathrm{i}\int \mathrm{d}x\left(\mathcal{L}_0(A)+\mathcal{L}_0(\psi,\bar{\psi})+\mathcal{L}_{\mathrm{I}}(\psi,\bar{\psi},A)+A_\mu j_A^\mu\right)\right] \tag{2.120}$$
$$= \frac{1}{\mathcal{N}}\int \mathrm{d}A\ \exp\left[\mathrm{i}\int \mathrm{d}x\left(\mathcal{L}_0(A)+A_\mu j_A^\mu\right)\right]\int \mathrm{d}\psi\mathrm{d}\bar{\psi}\ \exp\left[\mathrm{i}\int \mathrm{d}x\ \bar{\psi}M[A]\psi\right]$$
$$= \frac{1}{\tilde{\mathcal{N}}}\int \mathrm{d}A\ \exp\left[\mathrm{i}\int \mathrm{d}x\left(\mathcal{L}_0(A)+\mathcal{L}_{\mathrm{eff}}(A)+A_\mu j_A^\mu\right)\right]\ ,$$

where we again assumed that the fermionic part of the full Lagrangian $\mathcal{L}_{\mathrm{cl}}(\bar{\psi},\psi,A)$ is bilinear in $\bar{\psi}\psi$ and revised the normalization $\tilde{\mathcal{N}} \equiv \int \mathrm{d}A\ \exp\left[\mathrm{i}\int \mathrm{d}x\,\mathcal{L}_0(A)+\mathcal{L}_{\mathrm{eff}}(A)\right]$. The effective action $S_{\mathrm{eff}}(A) = \int \mathrm{d}x\ \mathcal{L}_{\mathrm{eff}}(A)$ itself is implicitly defined by

$$\mathrm{e}^{\mathrm{i}S_{\mathrm{eff}}} \equiv \frac{\int \mathrm{d}\psi\mathrm{d}\bar{\psi}\ \exp\left[\mathrm{i}\int \mathrm{d}x\ \bar{\psi}M[A]\psi\right]}{\int \mathrm{d}\psi\mathrm{d}\bar{\psi}\ \exp\left[\mathrm{i}\int \mathrm{d}x\ \bar{\psi}M[0]\psi\right]} = \frac{\det\left(M[A]\right)}{\det\left(M[0]\right)}\ . \tag{2.121}$$

In the second equality we used the Grassmann integration (neglecting the space-time integral in the exponent for reasons of clarity):

$$\int \mathrm{d}\psi_1'\mathrm{d}\bar{\psi}_1'\ldots\mathrm{d}\psi_n'\mathrm{d}\bar{\psi}_n'\ \mathrm{e}^{\bar{\psi}_i'M^{ij}[A]\psi_j'} = \int \mathrm{d}\psi_1'\mathrm{d}\bar{\psi}_1'\ldots\mathrm{d}\psi_n'\mathrm{d}\bar{\psi}_n'\ \frac{1}{n!}\left(\bar{\psi}_i'M^{ij}[A]\psi_j'\right)^n$$
$$= \det(M[A])\ , \tag{2.122}$$

due to the basic properties of Grassman fields

$$\int \mathrm{d}\psi_i'(a+b\psi_j') = b\delta_{ij} \quad \wedge \quad \psi_i^2 = 0, \quad \psi_i\psi_j = -\psi_j\psi_i\ . \tag{2.123}$$

Within this thesis, we are going to describe Dirac systems coupled to electromagnetic U(1) gauge fields A_μ, which are experimentally applied. On the level of the generating functional this means that the bosonic path integral can be solved by a saddle-point integration around the electromagnetic field configuration. We are therefore interested in the partition function of these systems as a function of the gauge field configuration:

$$Z[A] = \frac{\det\left(M[A]\right)}{\det\left(M[0]\right)} = \mathrm{e}^{\mathrm{i}S_{\mathrm{eff}}(A)} \tag{2.124}$$

If we consider the 2+1 dimensional Dirac Lagrangian in Eq. (2.91) coupled to an abelian electromagnetic gauge field A^μ, we can further simplify the fermion determinant [122]:

$$\begin{aligned} Z[A] = \frac{\det\left[\mathrm{i}\not{D} - m + \mathrm{i}\epsilon\right]}{\det\left[\mathrm{i}\not{\partial} - m + \mathrm{i}\epsilon\right]} &= \det\left[1 - \mathrm{e}\frac{\not{A}}{i\not{\partial} - m + \mathrm{i}\epsilon}\right] \\ &= \exp\left(\mathrm{tr}\left[\log\left(1 - \mathrm{e}\frac{\not{A}}{i\not{\partial} - m + \mathrm{i}\epsilon}\right)\right]\right) \ . \end{aligned} \tag{2.125}$$

Thus, on the quantum level, such a system is described by the effective action

$$S_{\mathrm{eff}}[A] = -\int \mathrm{d}x \ \mathrm{i}\,\mathrm{tr}\left[\log\left(1 - \mathrm{e}\frac{\not{A}}{i\not{\partial} - m + \mathrm{i}\epsilon}\right)\right] \ . \tag{2.126}$$

To analyze the presence of a quantum anomaly, we need to evaluate the remaining expression of S_{eff} and analyze its symmetries in comparison to those of $\mathcal{L}_{\mathrm{cl}}$. This is the purpose of the next section.

2.6 Parity and Chiral Anomaly of Quantum Electrodynamics

2.6.1 Symmetries of the Classical Lagrangian

In what follows, we consider planar quantum electrodynamics, QED_{2+1}, which describes a single Dirac fermion in $2+1$ space-time dimensions coupled to an electromagnetic U(1) (vector) gauge field A_μ [cf. Eq. (2.91)]. On the classical level, such a system is described by the Lagrangian:

$$\mathcal{L}_{\mathrm{cl}}(x) = \bar{\psi}(x)\left(\mathrm{i}\not{D} - m\right)\psi(x) \ , \tag{2.127}$$

where $D_\mu = \partial_\mu + \mathrm{i}eA_\mu(x)$ is the covariant derivative [cf. Eq.(2.90)]. According to Sec. 2.4, this Lagrangian is invariant under local U(1) (vector) gauge- and Lorentz transformations:

$$\mathcal{L}_{\mathrm{cl}}(x) \overset{\phi(x)}{\to} \mathcal{L}'_{\mathrm{cl}}(x) = \mathrm{e}^{\mathrm{i}\phi(x)}\bar{\psi}(x)\left(\mathrm{e}^{-\mathrm{i}\phi(x)}\mathrm{i}\not{D}\psi(x) - \mathrm{e}^{-\mathrm{i}\phi(x)}m\psi(x)\right) = \mathcal{L}_{\mathrm{cl}}(x), \tag{2.128}$$

$$\begin{aligned} \mathcal{L}_{\mathrm{cl}}(x) \overset{\Lambda}{\to} \mathcal{L}'_{\mathrm{cl}}(x') &= S[\Lambda]^{-1}\bar{\psi}(\Lambda^{-1}x)\left(\mathrm{i}S[\Lambda]\not{D}\psi(\Lambda^{-1}x) - S[\Lambda]m\psi(\Lambda^{-1}x)\right) \\ &= \mathcal{L}_{\mathrm{cl}}(\Lambda^{-1}x) \ , \end{aligned} \tag{2.129}$$

where we used that $S[\Lambda]^{-1}\gamma^\mu S[\Lambda] = \Lambda^\mu{}_\nu\gamma^\nu$ [109]. The different building blocks of the QED_{2+1} Lagrangian in Eq. (2.127) have the following transformation rules:
According to Eq. (2.51), they transform under parity operations $\mathcal{P}$ as

$$\mathcal{P}\,\bar{\psi}(x_0, x_1, x_2)m\psi(x_0, x_1, x_2)\,\mathcal{P}^{-1} = -\bar{\psi}(x_0, -x_1, x_2)m\psi(x_0, -x_1, x_2) \ , \tag{2.130}$$

$$\mathcal{P}\,\bar{\psi}(x_0,x_1,x_2)\not{A}(x_0,x_1,x_2)\psi(x_0,x_1,x_2)\,\mathcal{P}^{-1} = \bar{\psi}(x_0,-x_1,x_2)\not{A}(x_0,-x_1,x_2)\psi(x_0,-x_1,x_2),$$
$$\mathcal{P}\,\bar{\psi}(x_0,x_1,x_2)\not{\partial}\psi(x_0,x_1,x_2)\,\mathcal{P}^{-1} = \bar{\psi}(x_0,-x_1,x_2)\not{\partial}\psi(x_0,-x_1,x_2)\ .$$

According to Eq. (2.56), they transform under time-reversal operations $\mathcal{T}$ as

$$\mathcal{T}\,\bar{\psi}(x_0,x_1,x_2)m\psi(x_0,x_1,x_2)\,\mathcal{T}^{-1} = -\bar{\psi}(-x_0,x_1,x_2)m\psi(-x_0,x_1,x_2)\ , \tag{2.131}$$
$$\mathcal{T}\,\bar{\psi}(x_0,x_1,x_2)\not{A}(x_0,x_1,x_2)\psi(x_0,x_1,x_2)\,\mathcal{T}^{-1} = \bar{\psi}(-x_0,x_1,x_2)\not{A}(-x_0,x_1,x_2)\psi(-x_0,x_1,x_2)\ ,$$
$$\mathcal{T}\,\bar{\psi}(x_0,x_1,x_2)\not{\partial}\psi(x_0,x_1,x_2)\,\mathcal{T}^{-1} = \bar{\psi}(-x_0,x_1,x_2)\not{\partial}\psi(-x_0,x_1,x_2)\ .$$

According to Eq. (2.59), they transform under charge conjugation operations $\mathcal{C}$ as

$$\mathcal{C}\,\bar{\psi}(x_0,x_1,x_2)m\psi(x_0,x_1,x_2)\,\mathcal{C}^{-1} = \bar{\psi}(x_0,x_1,x_2)m\psi(x_0,x_1,x_2)\ , \tag{2.132}$$
$$\mathcal{C}\,\bar{\psi}(x_0,x_1,x_2)\not{A}(x_0,x_1,x_2)\psi(x_0,x_1,x_2)\,\mathcal{C}^{-1} = \bar{\psi}(x_0,x_1,x_2)\not{A}(x_0,x_1,x_2)\psi(x_0,x_1,x_2)\ ,$$
$$\mathcal{C}\,\bar{\psi}(x_0,x_1,x_2)\not{\partial}\psi(x_0,x_1,x_2)\,\mathcal{C}^{-1} = \bar{\psi}(x_0,x_1,x_2)\not{\partial}\psi(x_0,x_1,x_2)\ .$$

Consequently, a massless QED_{2+1} system is parity-, time-reversal- and charge-conjugation symmetric on the classical level. In contrast, the first two symmetries are broken if the system has a finite Dirac mass term m.

These are the classical symmetries of a QED_{2+1} system. If one of these symmetries gets broken on the quantum level, a quantum anomaly is present [cf. Definition 1 in Sec. 2.5.1]. In what follows, we are going to show that a massless QED system in 2+1 space-time dimensions breaks the parity symmetry on the quantum level and, therefore, exhibits a parity anomaly.

2.6.2 Fermion Propagator and Gauge-Matter Vertex

In order to derive the parity anomaly of planar quantum electrodynamics, we need to calculate the associated effective action on the quantum level [cf. Sec. 2.5.2]. In particular, we need to evaluate the fermion determinant in Eq. (2.125), which includes the free fermion propagator and the gauge-matter vertex. From the non-interacting part of the QED_{2+1} Lagrangian in Eq. (2.127) we can read off the free fermion propagator [cf. Eq. (2.119)]. With

$$\not{k}\not{k} = k^\mu k^\nu \gamma_\mu\gamma_\nu = \frac{1}{2}k^\mu k^\nu\left(\gamma_\mu\gamma_\nu+\gamma_\nu\gamma_\mu\right) = g_{\mu\nu}k^\mu k^\nu = k^2\ , \tag{2.133}$$

and $k=\sqrt{k^2}$, the free fermion propagator in momentum space is given by

$$\mathrm{i}S_\mathrm{F}(k) = \frac{\mathrm{i}}{\not{k}-m} = \frac{\mathrm{i}(\not{k}+m)}{(\not{k}-m)(\not{k}+m)} = \frac{\mathrm{i}(\not{k}+m)}{k^2-m^2}\ . \tag{2.134}$$

Moreover, the interaction part in the Lagrangian Eq. (2.127) implies the associated gauge-matter vertex:

$$V^\mu = \mathrm{i}\frac{\delta\mathcal{S}_\mathrm{cl}}{\delta\bar{\psi}\delta A_\mu\delta\psi} = -\mathrm{ie}\gamma^\mu\ , \tag{2.135}$$

where $\mathcal{S}_\mathrm{cl}=\int \mathrm{d}x\,\mathcal{L}_\mathrm{cl}(x)$ is the classical action. Knowing the free fermion propagator and the gauge-matter coupling allows us to determine the fermion determinant in Eq. (2.125), and thus the quantum effective action. In what follows we are going to calculate this quantity.

2.6.3 Effective Action and Parity Anomaly in 2+1 Dimensions

According to Eq. (2.126), the effective action of quantum electrodynamics in 2+1 space-time dimensions for N_f fermion species is given by

$$S_\mathrm{eff}[A] = -N_\mathrm{f} \int \mathrm{d}x \; \mathrm{i}\,\mathrm{tr}\left[\log\left(1 - \mathrm{e}\frac{\not{A}}{i\not{\partial} - m + \mathrm{i}\epsilon}\right)\right] \; . \tag{2.136}$$

Since in QED the gauge-matter coupling is perturbatively small, let us Taylor expand the effective action in terms of the coupling constant e. Up to second order in the electric charge we obtain the expansion

$$\begin{aligned} S_\mathrm{eff}[A] &= -N_\mathrm{f} \int \mathrm{d}x \; \mathrm{i}\,\mathrm{tr}\left[-\mathrm{e}\left(\frac{\not{A}}{i\not{\partial} - m + \mathrm{i}\epsilon}\right) - \frac{\mathrm{e}^2}{2}\left(\frac{\not{A}}{i\not{\partial} - m + \mathrm{i}\epsilon}\frac{\not{A}}{i\not{\partial} - m + \mathrm{i}\epsilon}\right)\right] + \mathcal{O}(\mathrm{e}^3) \\ &= N_\mathrm{f} \int \mathrm{d}x \,\mathrm{tr}\left[\mathrm{ie}\left(\not{A}\frac{1}{i\not{\partial} - m + \mathrm{i}\epsilon}\right)\right] \qquad (2.137) \\ &\quad + N_\mathrm{f} \int \mathrm{d}x \;\mathrm{tr}\left[\frac{\mathrm{ie}^2}{2}\left(\not{A}\frac{1}{i\not{\partial} - m + \mathrm{i}\epsilon}\not{A}\frac{1}{i\not{\partial} - m + \mathrm{i}\epsilon}\right)\right] + \mathcal{O}(\mathrm{e}^3) \; , \qquad (2.138) \end{aligned}$$

where we used that $\log(1+z) = z - \frac{1}{2}z^2 + \mathcal{O}(z^3)$ for $|z| \ll 1$.
The first term, Eq. (2.137), is the contribution of the tadpole to the effective action and defines the system's charge density [109]. The second term, Eq. (2.138), encodes the vacuum polarization operator. It defines the system's conductivity and, in particular, leads to the parity anomaly. Let us therefore focus on this term in the following:

$$S^{(2)}_\mathrm{eff}[A] = \frac{N_\mathrm{f}}{2} \int \mathrm{d}x \; A^\mu \;\mathrm{tr}\left[\mathrm{ie}^2\left(\gamma_\mu \frac{1}{\mathrm{i}\not{\partial} - m + \mathrm{i}\epsilon}\gamma_\nu \frac{1}{\mathrm{i}\not{\partial} - m + \mathrm{i}\epsilon}\right)\right] A^\nu \; . \tag{2.139}$$

Fourier transforming Eq. (2.139) to momentum space implies

$$S^{(2)}_\mathrm{eff}[A] = \frac{N_\mathrm{f}}{2} \int \frac{\mathrm{d}^3 p}{(2\pi)^3} \left[A^\mu(-p)\Pi_{\mu\nu}(p)A^\nu(p)\right] \; , \tag{2.140}$$

which implicitly defines the vacuum polarization operator

$$\mathrm{i}\Pi_{\mu\nu}(p) = -(-\mathrm{ie})^2 \int \frac{\mathrm{d}^3 k}{(2\pi)^3} \frac{\mathrm{tr}[\gamma_\mu \mathrm{i}(\not{k} + m)\gamma_\nu \mathrm{i}(\not{k} + \not{p} + m)]}{(k^2 - m^2)[(k+p)^2 - m^2]} \; . \tag{2.141}$$

Diagrammatically, this fermion loop operator is visualized in Fig. 2.8.

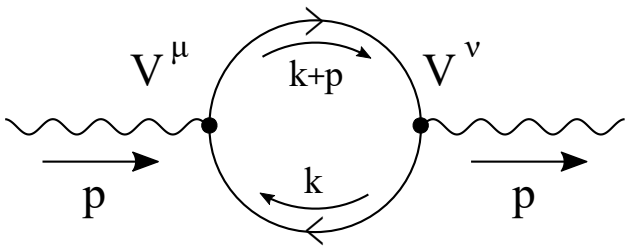

Figure 2.8: Feynman diagramm of the vacuum polarization operator in Eq. (2.141) with the internal loop momentum k, the external momentum p, and the gauge-matter vertices $V^{\mu,\nu}$.

In what follows, we are going to calculate the vacuum polarization operator explicitly. Let us first simplify the numerator in Eq. (2.141). Therefore, we use the trace-identities for 2+1

dimensional Dirac matrices, which we introduced in Eq. (2.39):

$$\begin{aligned}
\mathrm{tr}[\gamma_\mu\gamma_\lambda\gamma_\nu\gamma_\xi]k^\lambda k^\xi &= 4k_\mu k_\nu - 2g_{\mu\nu}k^2 \ , \\
\mathrm{tr}[\gamma_\mu\gamma_\lambda\gamma_\nu\gamma_\eta]k^\lambda p^\eta &= 2k_\mu p_\nu + 2k_\nu p_\mu - 2g_{\mu\nu}kp \ , \\
\mathrm{tr}[\gamma_\mu\gamma_\lambda\gamma_\nu]k^\lambda m &= -2\mathrm{i}\epsilon_{\mu\lambda\nu}k^\lambda m \ , \\
\mathrm{tr}[\gamma_\mu\gamma_\nu\gamma_\xi]k^\xi m &= -2\mathrm{i}\epsilon_{\mu\nu\xi}k^\xi m \ , \\
\mathrm{tr}[\gamma_\mu\gamma_\nu\gamma_\eta]p^\eta m &= -2\mathrm{i}\epsilon_{\mu\nu\eta}p^\eta m \ , \\
\mathrm{tr}[\gamma_\mu\gamma_\nu]m^2 &= 2g_{\mu\nu}m^2 \ .
\end{aligned} \tag{2.142}$$

With these identities we obtain the simplified expression

$$\mathrm{i}\Pi_{\mu\nu}(p) = -2\mathrm{e}^2\int\frac{\mathrm{d}^3k}{(2\pi)^3}\frac{2k_\mu k_\nu + k_\mu p_\nu + k_\nu p_\mu + g_{\mu\nu}(m^2-k^2-kp) - \mathrm{i}\epsilon_{\mu\nu\eta}p^\eta m}{(k^2-m^2)[(k+p)^2-m^2]} \ . \tag{2.143}$$

As a second step, we rewrite the denominator in Eq. (2.141) in terms of the Feynman parameter $x \in \mathbb{R}$ [109, 110]. This parameter is defined by the integral identity ($\{A, B\} \in \mathbb{C}$)

$$\frac{1}{AB} = \int_0^1 \mathrm{d}x \ \frac{1}{\left[A + (B-A)x\right]^2} \ . \tag{2.144}$$

With $A = k^2 - m^2$ and $B = (k+p)^2 - m^2$, the denominator of the polarization operator can be rewritten in terms of

$$\begin{aligned}
\frac{1}{(k^2-m^2)[(k+p)^2-m^2]} &= \int\limits_0^1 \mathrm{d}x \frac{1}{(k^2+2xkp+xp^2-m^2)^2} \\
&= \int\limits_0^1 \mathrm{d}x \frac{1}{(l^2+x(1-x)p^2-m^2)^2} \ ,
\end{aligned} \tag{2.145}$$

where in the last step we shifted the loop momentum by $k_\mu \to k_\mu + p_\mu x = l_\mu$ [109]. Under this shift, the numerator in Eq. (2.143) evaluates to

$$2l_\mu l_\nu - g_{\mu\nu}l^2 - 2x(1-x)p_\mu p_\nu + g_{\mu\nu}\left(m^2 + x(1-x)p^2\right) - \mathrm{i}\epsilon_{\mu\nu\eta}p^\eta m + \text{linear terms in } l \ . \tag{2.146}$$

Since the denominator is symmetric in l, the linear terms in the numerator do not contribute to the (symmetric) integration in Eq. (2.143). Next, we perform a Wick-rotation to an Euclidean space-time, $l \to l_\mathrm{E}$, as it was explained in Sec. 2.3.3:

$$\begin{aligned}
&\mathrm{i}\Pi_{\mu\nu}(p) = \\
&-2\mathrm{ie}^2\int\limits_0^1\mathrm{d}x\int\frac{\mathrm{d}^3l_\mathrm{E}}{(2\pi)^3}\frac{-\frac{2}{3}l_\mathrm{E}^2 g_{\mu\nu} + g_{\mu\nu}l_\mathrm{E}^2 - 2x(1-x)p_\mu p_\nu + g_{\mu\nu}\left(m^2+x(1-x)p^2\right) - \mathrm{i}\epsilon_{\mu\nu\eta}p^\eta m}{(l_\mathrm{E}^2 - x(1-x)p^2 + m^2)^2} .
\end{aligned} \tag{2.147}$$

Here, we used that due to the underlying Lorentz symmetry we can simplify $l_\mu l_\nu = \frac{1}{2+1}l^2 g_{\mu\nu}$ [110]. The remaining integration over the $n = 3$ dimensional Euclidean space-time can be performed explicitly by using the following identity [109]:

$$\int\frac{\mathrm{d}^n l_\mathrm{E}}{(2\pi)^n}\frac{1}{(l_\mathrm{E}^2+\Delta)^2} = \int\frac{\mathrm{d}\Omega_n}{(2\pi)^n}\cdot\int\limits_0^\infty \mathrm{d}l_\mathrm{E}\frac{l_\mathrm{E}^{n-1}}{(l_\mathrm{E}^2+\Delta)^2} \ . \tag{2.148}$$

Here, the first factor resembles the integral over an n-dimensional unit sphere, given by

$$\int \mathrm{d}\Omega_n = \frac{2\pi^{\frac{n}{2}}}{\Gamma\left(\frac{n}{2}\right)} \quad \text{with} \quad \Gamma\left(\frac{3}{2}\right) = \frac{\sqrt{\pi}}{2} \quad \Rightarrow \quad \int \mathrm{d}\Omega_3 = 4\pi \ . \tag{2.149}$$

By using Eqs. (2.148) and (2.149), we can simplify the expression for the vacuum polarization operator in Eq. (2.147). In particular, we obtain

$$\begin{aligned} &\mathrm{i}\Pi_{\mu\nu}(p) = \\ &-\frac{\mathrm{ie}^2}{\pi^2}\int_0^1 \mathrm{d}x \int_0^\infty \mathrm{d}l_\mathrm{E}\ l_\mathrm{E}^2 \frac{g_{\mu\nu}(\frac{1}{3}l_\mathrm{E}^2 - x(1-x)p^2 + m^2) + 2x(1-x)(g_{\mu\nu}p^2 - p_\mu p_\nu) - \mathrm{i}\epsilon_{\mu\nu\eta}p^\eta m}{(l_\mathrm{E}^2 - x(1-x)p^2 + m^2)^2} \ . \end{aligned} \tag{2.150}$$

Depending on their superficial degree of divergence and their tensor-structure, we distinguish three different contributions to Eq. (2.150):

First, there is a UV divergent term proportional to the metric tensor:

$$\begin{aligned} -\frac{\mathrm{ie}^2}{\pi^2}\int_0^1 \mathrm{d}x \int_0^\Lambda \mathrm{d}l_\mathrm{E}\ l_\mathrm{E}^2 \frac{g_{\mu\nu}(\frac{1}{3}l_\mathrm{E}^2 - x(1-x)p^2 + m^2)}{(l_\mathrm{E}^2 - x(1-x)p^2 + m^2)^2} \\ = -\frac{4\mathrm{ie}^2\Lambda^3 \mathrm{ArcCot}\left[\sqrt{\frac{4(\Lambda^2+m^2)}{p^2} - 1}\right]}{3\pi^2\sqrt{[(4(\Lambda^2+m^2) - p^2)\,p^2]}} g_{\mu\nu} \equiv g_{\mu\nu}\tilde{\Pi}^{(0)}(p,m) \ . \end{aligned} \tag{2.151}$$

Here we introduced the hard momentum cut-off Λ in order to regularize the UV divergence. Second, there is a convergent contribution proportional to the Levi-Civita symbol:

$$\begin{aligned} \frac{\mathrm{ie}^2}{\pi^2}\mathrm{i}\epsilon_{\mu\nu\eta}p^\eta m \int_0^1 \mathrm{d}x \int_0^\infty \mathrm{d}l_\mathrm{E} \frac{l_\mathrm{E}^2}{(l_\mathrm{E}^2 - x(1-x)p^2 + m^2)^2} \\ = -\frac{m\mathrm{e}^2}{2\pi\sqrt{p^2}}\epsilon_{\mu\nu\eta}p^\eta \mathrm{ArcCoth}\left(2\frac{\sqrt{m^2}}{\sqrt{p^2}}\right) \equiv -\epsilon_{\mu\nu\eta}p^\eta\tilde{\Pi}^{(2)}(p,m) \ . \end{aligned} \tag{2.152}$$

This term defines the system's off-diagonal (Hall) response.
Third, there is a convergent contribution proportional to $(g_{\mu\nu}p^2 - p_\mu p_\nu)$:

$$\begin{aligned} &-\frac{2\mathrm{ie}^2}{\pi^2}(g_{\mu\nu}p^2 - p_\mu p_\nu)\int_0^1 \mathrm{d}x \int_0^\infty \mathrm{d}l_\mathrm{E} \frac{x(1-x)l_\mathrm{E}^2}{(l_\mathrm{E}^2 - x(1-x)p^2 + m^2)^2} \\ &= -\frac{2\mathrm{ie}^2}{\pi^2}(g_{\mu\nu}p^2 - p_\mu p_\nu)\frac{\pi}{16\sqrt{p^2}^3}\left[-2\sqrt{m^2p^2} + \left(4m^2 + p^2\right)\mathrm{ArcCoth}\left(2\frac{\sqrt{m^2}}{\sqrt{p^2}}\right)\right] \\ &= -\frac{\mathrm{ie}^2}{8\pi\sqrt{p^2}^3}(g_{\mu\nu}p^2 - p_\mu p_\nu)\left[-2\sqrt{m^2p^2} + \left(4m^2 + p^2\right)\mathrm{ArcCoth}\left(2\frac{\sqrt{m^2}}{\sqrt{p^2}}\right)\right] \\ &\equiv -(g_{\mu\nu}p^2 - p_\mu p_\nu)\tilde{\Pi}^{(1)}(p^2,m) \ . \end{aligned} \tag{2.153}$$

Together these contributions specify the final form of the vacuum polarization operator:

$$\mathrm{i}\Pi_{\mu\nu}(p,m) \equiv g_{\mu\nu}\Pi^{(0)}(p,m) - (g_{\mu\nu}p^2 - p_\mu p_\nu)\Pi^{(1)}(p^2,m) - \epsilon_{\mu\nu\eta}p^\eta\Pi^{(2)}(p,m) \ . \tag{2.154}$$

To get rid of the divergent term $g_{\mu\nu}\Pi^{(0)}(p,m)$, we use a regularization/renormalization scheme

called Pauli-Villars regularization [109, 110]. We do not discuss this scheme in detail at this point. This will be the scope of Sec. 3.2.3. All we need to know for now is that in the Pauli-Villars approach, we introduce a second Dirac field of mass M with bosonic statistics. Hence, this field comes along with a relative '$-$' sign in the polarization operator (only fermion loops acquire a prefactor of -1). The response of this field needs to be added to Eq. (2.154). This removes the divergent term from the effective action, since

$$\lim_{\Lambda\to\infty} \left(\tilde{\Pi}^{(0)}(p,m) - \tilde{\Pi}^{(0)}(p,M)\right) = 0 \ . \tag{2.155}$$

Eventually, we take the limit $M \to \infty$ to decouple the Pauli-Villars fields from the theory. Since we are interested in the response of initially massive-, as well as massless Dirac fermions with $m = 0$, we are considering the following first order Taylor expansions:

$$\Pi^{(1)}(m^2 \gg p^2) = \frac{\mathrm{i}\mathrm{e}^2}{12\pi\sqrt{m^2}} \quad \wedge \quad \Pi^{(1)}(m^2 \ll p^2) = \frac{\mathrm{e}^2}{16\sqrt{p^2}} \ , \tag{2.156}$$

$$\Pi^{(2)}(m^2 \gg p^2) = \frac{\mathrm{e}^2}{4\pi}\mathrm{sign}(m) \quad \wedge \quad \Pi^{(2)}(m^2 \ll p^2) = -\frac{\mathrm{i}\mathrm{e}^2 m}{4\sqrt{p^2}} \ . \tag{2.157}$$

These identities imply the subsequent regularized contributions to the vacuum polarization operator of initially massless Dirac fermions with $m = 0$:

$$\Pi^{(1)}_{\mathrm{PV}}(p^2, m=0) = \Pi^{(1)}(p^2, m=0) - \Pi^{(1)}(p^2, M\to\infty) = \frac{\mathrm{e}^2}{16\sqrt{p^2}} \ , \tag{2.158}$$

$$\Pi^{(2)}_{\mathrm{PV}}(p^2, m=0) = \Pi^{(2)}(p^2, m=0) - \Pi^{(2)}(p^2, M\to\infty) = -\frac{\mathrm{e}^2}{4\pi}\mathrm{sign}(M) \ . \tag{2.159}$$

The corresponding contributions for initially massive Dirac fermions with $m \neq 0$ are instead given by:

$$\Pi^{(1)}_{\mathrm{PV}}(p^2, m) = \Pi^{(1)}(p^2, m) - \Pi^{(1)}(p^2, M\to\infty) = \Pi^{(1)}(p^2, m) \ , \tag{2.160}$$

$$\Pi^{(2)}_{\mathrm{PV}}(p^2, m) = \Pi^{(2)}(p^2, m) - \Pi^{(2)}(p^2, M\to\infty) = \Pi^{(2)}(p^2, m) - \frac{\mathrm{e}^2}{4\pi}\mathrm{sign}(M) \ . \tag{2.161}$$

For $p^2 \ll m^2$, these expressions simplify in first order to

$$\Pi^{(1)}_{\mathrm{PV}}(p^2 \ll m^2) = \Pi^{(1)}(p^2 \ll m^2) - \Pi^{(1)}(p^2, M\to\infty) = \frac{\mathrm{i}\mathrm{e}^2}{12\pi\sqrt{m^2}} \ , \tag{2.162}$$

$$\Pi^{(2)}_{\mathrm{PV}}(p^2 \ll m^2) = \Pi^{(2)}(p^2 \ll m^2) - \Pi^{(2)}(p^2, M\to\infty) = \frac{\mathrm{e}^2}{4\pi}\mathrm{sign}(m) - \frac{\mathrm{e}^2}{4\pi}\mathrm{sign}(M) \ . \tag{2.163}$$

According to the Eqs. (2.140) and (2.154), the off-diagonal part of the quadratic contribution to the effective action of a QED_{2+1} system is described by a parity-odd Chern-Simons term [56, 57]

$$S^{(2),\ \mathrm{odd}}_{\mathrm{eff}} \propto \epsilon^{\mu\nu\rho} A_\mu \partial_\nu A_\rho \ . \tag{2.164}$$

As is it was shown above, the proportionality constant depends on the details of the regularization scheme. In particular, this will be discussed in Sec. 3.2.3. Most remarkably, there exists no regularization scheme in 2+1 space-time dimensions which ensures at the same time gauge- as well as parity invariance. In the present calculation, we got rid of the non gauge invariant cut-off dependent term by introducing a parity-odd massive Pauli-Villars field. As a direct consequence, the quantum effective action of QED_{2+1} always contains a Chern-Simons

term which is a parity-odd but gauge invariant tensor structure. We will prove this statement in the beginning of the next section. Therefore, also a massless and hence classically parity symmetric QED system, breaks parity on the quantum level. Hence, such a system has a parity anomaly [cf. Sec. 2.5]. In what follows, we analyze the physics associated to Chern-Simons terms in detail.

2.6.4 Chern-Simons Field Theory

In this section, we discuss the physics associated to Chern-Simons field theories in 2+1 space-time dimensions. Our line of reasoning will roughly follow the corresponding discussions in the References [100, 115, 123–125]. In $2+1$ space-time dimensions, the Lagrangian of an abelian U(1) Chern-Simons theory is given by

$$\mathcal{L}_{\mathrm{CS}}(x) = \frac{\kappa}{2}\epsilon^{\mu\nu\rho}A_\mu(x)\partial_\nu A_\rho(x) \ , \tag{2.165}$$

where $\kappa \in \mathbb{R}$ is the so-called Chern-Simons level. In the subsequent sections we are going to show that κ matches the Hall conductivity σ_{xy} of two-dimensional Chern insulators.

Let us start our discussion by deriving the symmetries of the Chern-Simons Lagrangian in Eq. (2.165). Under Lorentz transformations Λ [cf. Sec. 2.4], this term evaluates to

$$\mathcal{L}_{\mathrm{CS}}(x) \overset{\Lambda}{\to} \mathcal{L}'_{\mathrm{CS}}(x') = \frac{\kappa}{2}\Lambda^\mu{}_\zeta\Lambda^\nu{}_\eta\Lambda^\rho{}_\xi\epsilon^{\zeta\eta\xi}\Lambda_\mu{}^\sigma A_\sigma(\Lambda^{-1}x)\Lambda_\nu{}^\lambda\partial_\lambda\Lambda_\rho{}^\phi A_\phi(\Lambda^{-1}x) = \mathcal{L}_{\mathrm{CS}}(\Lambda^{-1}x) \ , \tag{2.166}$$

where we used that the Levi-Civita symbol is a tensor of rank three. Hence, Eq. (2.165) is Lorentz invariant. In contrast, the Chern-Simons Lagrangian is odd under time-reversal as well as parity transformations [cf. Sec. 2.4.1]:

$$\mathcal{P}\,\epsilon^{\mu\nu\rho}A_\mu(x_0,x_1,x_2)\partial_\nu A_\rho(x_0,x_1,x_2)\,\mathcal{P}^{-1} = -\epsilon^{\mu\nu\rho}A_\mu(x_0,-x_1,x_2)\partial_\nu A_\rho(x_0,-x_1,x_2), \tag{2.167}$$

$$\mathcal{T}\,\epsilon^{\mu\nu\rho}A_\mu(x_0,x_1,x_2)\partial_\nu A_\rho(x_0,x_1,x_2)\,\mathcal{T}^{-1} = -\epsilon^{\mu\nu\rho}A_\mu(-x_0,x_1,x_2)\partial_\nu A_\rho(-x_0,x_1,x_2), \tag{2.168}$$

since either the x_1-derivative and A_1 change sign (parity-transformation), or the time derivative and both spacial gauge-field components A_i change sign (time-reversal). From this perspective, the Chern-Simons term exactly transforms as the Dirac fermion mass term in Sec. 2.6.1. It therefore shows up in the effective action of massive Dirac fermions in 2+1 space-time dimensions, as we have discussed in the last paragraph of the previous section.

Further, let us analyze the transformation rules of an abelian Chern-Simons term under U(1) vector gauge transformations. According to Sec. 2.4, we find that under $A_\mu \to A_\mu + \frac{1}{\mathrm{e}}\partial_\mu\varphi$ the Chern-Simons Lagrangian in Eq. (2.165) transforms like

$$\begin{aligned}\mathcal{L}_{\mathrm{CS}} &= \frac{\kappa}{2}\epsilon^{\mu\nu\rho}A_\mu\partial_\nu A_\rho \\ &\to \frac{\kappa}{2}\epsilon^{\mu\nu\rho}A_\mu\partial_\nu A_\rho + \frac{\kappa}{2\mathrm{e}}\epsilon^{\mu\nu\rho}\left(\partial_\mu\varphi\partial_\nu A_\rho + A_\mu\partial_\nu\partial_\rho\varphi + \frac{1}{\mathrm{e}}\partial_\mu\varphi\partial_\nu\partial_\rho\varphi\right) \\ &= \mathcal{L}_{\mathrm{CS}} + \delta\mathcal{L}_{\mathrm{CS}} \ ,\end{aligned} \tag{2.169}$$

with

$$\delta\mathcal{L}_{\mathrm{CS}} = \frac{\kappa}{2\mathrm{e}}\partial_\mu(\varphi\epsilon^{\mu\nu\rho}\partial_\nu A_\rho) \ . \tag{2.170}$$

In the last equality, we used that $\epsilon^{\mu\nu\rho}\partial_\nu\partial_\rho = \epsilon^{\mu\nu\rho}\partial_\mu\partial_\nu = 0$. Hence, a Chern-Simons Lagrangian is only gauge invariant up to a total space-time derivative. On the level of the action

$$\mathcal{S}_{\mathrm{CS}} = \int \mathrm{d}^3x \; \mathcal{L}_{\mathrm{CS}} \; , \tag{2.171}$$

Eq. (2.170) defines a boundary term which usually can be neglected. However, for topological field theories like the Chern-Simons action this is not the case. Even in the absence of a space-time boundary, the total derivative in Eq. (2.170) has highly non-trivial consequences [100, 115].

To see this, let us consider a compact space-time $S^1 \times S^2$, where the time is defined on a circle S^1 and the space manifold is defined on a compact two-sphere S^2. This system has no boundary by definition. Moreover, let us assume that one natural unit of magnetic flux $\phi_0 = \mathrm{h/e}$ threads the surface of the two-sphere:

$$\frac{1}{2\pi}\int_{S^2} \mathrm{d}^2x \, F_{12}(x) = \frac{\hbar}{\mathrm{e}} \; . \tag{2.172}$$

Here, we used that the magnetic field strength B is given by $B = F_{12}$ in terms of the field strength tensor $F_{\mu\nu} = \partial_\mu A_\nu - \partial_\nu A_\mu$. In what follows, we apply a large gauge transformation in time, which winds around the S^1 sphere with an integer winding number $n \in \mathbb{N}$ [cf. Fig. 2.7] such that

$$\int_{S^1} \mathrm{d}x_0 \, \partial_0\varphi(x_0) = 2\pi n \; . \tag{2.173}$$

Under such a gauge transformation the Chern-Simons action in Eq. (2.171) changes by

$$\begin{aligned} \delta S_{\mathrm{CS}} &= \frac{\kappa}{2\mathrm{e}}\epsilon^{\mu\nu\rho}\int_{S^2}\mathrm{d}^2x\int_{S^1}\mathrm{d}x_0\,\partial_\mu\left[\varphi(x_0)\partial_\nu A_\rho(x)\right] \\ &= \frac{\kappa}{\mathrm{e}}\epsilon^{0ij}\int_{S^2}\mathrm{d}^2x\,\partial_i A_j(x)\int_{S^1}\mathrm{d}x_0\,\partial_0\varphi(x_0) \\ &= \frac{\kappa}{\mathrm{e}}2\pi n\int_{S^2}\mathrm{d}^2x\,F_{12}(x) = \frac{\kappa}{\mathrm{e}}2\pi n\frac{\mathrm{h}}{\mathrm{e}} = 2\pi n\,\kappa\,\frac{\mathrm{h}}{\mathrm{e}^2} \; , \end{aligned} \tag{2.174}$$

where in the second line we integrated by parts [115]. The generating functional [cf. Eq. 2.114]

$$Z[A] = \mathrm{e}^{\mathrm{i}\mathcal{S}_{\mathrm{CS}}} \tag{2.175}$$

needs to be a gauge invariant object. This implies that the Chern-Simons level needs to be integer quantized in units of e^2/h [100, 115],

$$\kappa = \nu \times \frac{\mathrm{e}^2}{\mathrm{h}} \quad \text{with} \quad \nu \in \mathbb{Z} \; . \tag{2.176}$$

For small gauge transformations of zero winding, the Chern-Simons Lagrangian in Eq. (2.165) is invariant on compact manifolds. However, this changes if one considers manifolds with space-time boundaries. Before we mathematically analyze this case, let us briefly motivate the physical outcome. In Sec. 2.4, we discussed the Noether theorem, stating that any continuous symmetry transformation of our Lagrangian corresponds to a conserved current. It was shown that the U(1) gauge symmetry implies a conserved electric charge current. The corresponding current associated to the Chern-Simons action in Eq. (2.171) is given by

$$j^\mu_{\mathrm{CS}}(x) = -\frac{\delta\mathcal{S}_{\mathrm{CS}}}{\delta A_\mu(x)} = -\frac{\delta}{\delta A_\mu(x)}\left[\frac{\kappa}{2}\int \mathrm{d}^3x' \, \epsilon^{\lambda\xi\zeta}A_\lambda\partial_\xi A_\zeta\right] \tag{2.177}$$

$$= \frac{\kappa}{2} \int \mathrm{d}^3x' \, \epsilon^{\lambda\xi\zeta} \left[-\frac{\delta}{\delta A_\mu(x)} A_\lambda(x') \right] \partial_\xi A_\zeta - \frac{\kappa}{2} \int \mathrm{d}^3x' \, \partial_\xi \left[\epsilon^{\lambda\xi\zeta} A_\lambda \right] \left[-\frac{\delta}{\delta A_\mu(x)} A_\zeta(x') \right] .$$

Here, we made use of a partial integration with a vanishing boundary term in the third line, since for abelian U(1) gauge fields $\epsilon^{\xi\zeta} A_\xi A_\zeta = 0$. Executing the functional derivatives in Eq. (2.177) in particular yields

$$\begin{aligned} j^\mu_{\mathrm{CS}}(x) &= -\frac{\kappa}{2} \epsilon^{\mu\xi\zeta} \partial_\xi A_\zeta + \frac{\kappa}{2} \partial_\xi \left[\epsilon^{\lambda\xi\mu} A_\lambda \right] = -\frac{\kappa}{2} \epsilon^{\mu\xi\zeta} \partial_\xi A_\zeta + \frac{\kappa}{2} \epsilon^{\lambda\xi\mu} \partial_\xi A_\lambda \\ &= -\frac{\kappa}{2} \epsilon^{\mu\nu\rho} \partial_\nu A_\rho - \frac{\kappa}{2} \epsilon^{\mu\xi\lambda} \partial_\xi A_\lambda = -\kappa \epsilon^{\mu\nu\rho} \partial_\nu A_\rho \ . \end{aligned} \tag{2.178}$$

This current is locally conserved, as

$$\partial_\mu j^\mu_{\mathrm{CS}} = -\kappa \epsilon^{\mu\nu\rho} \partial_\mu \partial_\nu A_\rho = 0 \ . \tag{2.179}$$

If we naively confined our system in $\mathbf{e}_2$-direction via a Heaviside-Theta function $\Theta(x_2)$, we would instead obtain a non-conserved charge current

$$j^\mu_{\mathrm{CS}}(x) = -\Theta(x_2) \, \kappa \epsilon^{\mu\nu\rho} \partial_\nu A_\rho + \frac{\kappa}{2} \left[\partial_2 \Theta(x_2) \right] \epsilon^{2\mu\rho} A_\rho \tag{2.180}$$

with

$$\partial_\mu j^\mu_{\mathrm{CS}}(x) = \frac{\kappa}{2} \left[\partial_2 \Theta(x_2) \right] \epsilon^{2\mu\rho} \partial_\mu A_\rho \ . \tag{2.181}$$

We will rigorously derive Eqs. (2.180) and (2.181) in Sec. (2.6.7). The underlying reason for this current non-conservation is that we missed the source- or the sink- terms of the bulk Chern-Simons current at the boundary of the system. The bulk theory alone does not provide this information. For a consistent theory the bulk Chern-Simons action always comes along with chiral edge degrees of freedom, as we are going to show in the following paragraphs. Together both theories give rise to a locally conserved- and thus well-defined charge current.

In order to derive the existence of chiral edge modes living at the boundaries of a bulk Chern-Simons system, let us consider a semi-infinite 2+1 dimensional space-time with a 1+1 dimensional edge, located at $x_2 = 0$. For $x_2 < 0$ our system is defined by a bulk Chern-Simons action, whereas for $x_2 > 0$ we consider a trivial vacuum. Moreover, we choose periodic boundary conditions in $\mathbf{e}_1$-direction. Our subsequent discussion will go along the lines of Ref. [100]. Let us start our analysis by introducing a Chern-Simons action for a so-called statistical U(1) gauge field a_μ, which is coupled to the electromagnetic U(1) gauge field A_μ:

$$\mathcal{S}_{\mathrm{CS}}[a] = -\frac{\kappa}{2} \int \mathrm{d}^3x \, \epsilon^{\mu\nu\rho} a_\mu \partial_\nu a_\rho - \int \mathrm{d}^3x \, A_\lambda j^\lambda_a = \mathcal{S}^0_{\mathrm{CS}} + \mathcal{S}_{\mathrm{int}} \ , \tag{2.182}$$

with $j^\lambda_a = -\kappa \, \epsilon^{\lambda\eta\xi} \partial_\eta a_\xi$. In a nutshell, the statistical gauge field a_μ describes the quantum Hall response of either non-relativistic fermions in a strong magnetic field (Landau level physics [cf. Sec. 2.2]), or of massive Dirac fermions in 2+1 space-time dimensions [cf. Eq. (2.127)]. Integrating out the statistical gauge field a_μ via a bosonic path integral [cf. Eq. (2.120)] leads to the electromagnetic Chern-Simons action in Eq. (2.171). In the first part of our discussion we neglect the coupling to the electromagnetic gauge field A_μ and consider a free Chern-Simons theory defined by the statistical gauge field a_μ alone. A variation of the action in

Eq. (2.182) on our semi-infinite space manifold implies

$$\delta\mathcal{S}^0_{\mathrm{CS}} = -\frac{\kappa}{2}\int \mathrm{d}^3x\ \epsilon^{\mu\nu\rho}\left[\delta a_\mu \partial_\nu a_\rho + a_\mu \partial_\nu \delta a_\rho\right] = -\frac{\kappa}{2}\int \mathrm{d}^3x\ \epsilon^{\mu\nu\rho}\left[\delta a_\mu f_{\nu\rho} + \partial_\nu\left(a_\mu \delta a_\rho\right)\right]. \tag{2.183}$$

In the absence of boundaries, minimizing the action, $\delta\mathcal{S}^0_{\mathrm{CS}} = 0$, implies a flat gauge configuration $f_{\nu\rho} = 0$. Even in the presence of a boundary, this condition holds if we require that $a_0(x_2{=}0) = 0$, $a_1(x_2{=}0) = 0$, or that any linear combination [100]

$$\left(a_0 - v_{\mathrm{F}} a_1\right)\big|_{x_2=0} = 0\ . \tag{2.184}$$

Eventually, v_{F} will be the (Fermi) velocity of the chiral edge excitation. As we have show in Eq. (2.170), under a gauge transformation

$$a_\mu \to a_\mu + \frac{1}{\mathrm{e}}\partial_\mu \varphi \tag{2.185}$$

the Chern-Simons action in Eq. (2.182) changes by a boundary term

$$S^0_{\mathrm{CS}} \to S^0_{\mathrm{CS}} - \frac{\kappa}{2\mathrm{e}}\int \mathrm{d}^3x\, \partial_\mu(\varphi\epsilon^{\mu\nu\rho}\partial_\nu a_\rho) \tag{2.186}$$

$$= S^0_{\mathrm{CS}} - \frac{\kappa}{2\mathrm{e}}\int \mathrm{d}x_0\, \mathrm{d}x_1\ \varphi(\partial_0 a_1 - \partial_1 a_0)\big|_{x_2=0}\ . \tag{2.187}$$

We can make the Chern-Simons action gauge invariant if we only allow statistical gauge transformations that vanish at the system's boundary:

$$\varphi(x_2{=}0) = 0\ . \tag{2.188}$$

This set of gauge transformations does not alter the boundary condition in Eq. (2.184). In what follows, we choose a gauge in which Eq. (2.184) holds for the entire system,

$$a_0 - v_{\mathrm{F}}\, a_1 = 0\ . \tag{2.189}$$

The above statistical gauge-restriction is highly non-trivial. Gauge transformations do relate physically equivalent states. For instance, if two states $|\psi\rangle'$ and $|\psi\rangle$ are connected through a local U(1) gauge transformation characterized by $\alpha(x) \in \mathbb{R}$,

$$|\psi(x)\rangle = \mathrm{e}^{\mathrm{i}\alpha(x)}|\psi(x)\rangle\ , \tag{2.190}$$

these modes are physically equivalent. If one prohibits this kind of gauge transformations, these modes are not equivalent anymore. Thus a restriction onto an allowed subset of gauge transformations generates additional degrees of freedom. In the present case these degrees of freedom are chiral edge excitations. To derive this analytically, we need to insert the fixed boundary condition (2.189) into the Chern-Simons action Eq. (2.182). As a simplification, let us introduce the light-cone coordinates

$$x'_0 = x_0 \quad \wedge \quad x'_1 = x_1 + v_{\mathrm{F}} x_0 \quad \wedge \quad x'_2 = x_2\ . \tag{2.191}$$

The Chern-Simons action is invariant under such an coordinate transformation if we transform the statistical gauge fields accordingly [100]

$$a'_0 = a_0 - v_{\mathrm{F}} a_1 \quad \wedge \quad a'_1 = a_1 \quad \wedge \quad a'_2 = a_2\ . \tag{2.192}$$

Under this shift the boundary condition in Eq. (2.189) evaluates to:

$$a'_0 = 0 \ . \tag{2.193}$$

In particular, this condition implies solutions $f'_{12} = 0$, which can be constructed by introducing a scalar bosonic field ϕ via

$$a'_i = \partial'_i \phi \quad \text{with} \quad i = \{1, 2\} \ . \tag{2.194}$$

The effective edge theory can now be evaluated by inserting these solutions in the Chern-Simons action in Eq. (2.182):

$$\begin{aligned} \mathcal{S}^0_{\mathrm{CS}} &= -\frac{\kappa}{2} \int \mathrm{d}^3x' \ \epsilon^{i0j} a'_i \partial'_0 a'_j = \frac{\kappa}{2} \int \mathrm{d}^3x' \ \partial'_1 \phi \partial'_0 \partial'_2 \phi - \partial'_2 \phi \partial'_0 \partial'_1 \phi \\ &= \frac{\kappa}{2} \int \mathrm{d}^3x' \ \partial'_1 \left[\phi \partial'_0 \partial'_2 \phi\right] - \phi \partial'_1 \partial'_0 \partial'_2 \phi - \partial'_2 \left[\phi \partial'_0 \partial'_1 \phi\right] + \phi \partial'_2 \partial'_0 \partial'_1 \phi \\ &= -\frac{\kappa}{2} \int \mathrm{d}^3x' \ \partial'_2 \left[\phi \partial'_0 \partial'_1 \phi\right] = -\frac{\kappa}{2} \int_{x'_2 = 0} \mathrm{d}^2x' \ \phi \partial'_0 \partial'_1 \phi \\ &= \frac{\kappa}{2} \int_{x'_2 = 0} \mathrm{d}^2x' \ \partial'_1 \left[-\phi \partial'_0 \phi\right] + \partial'_1 \phi \partial'_0 \phi = \frac{\kappa}{2} \int_{x'_2 = 0} \mathrm{d}^2x' \ \partial'_1 \phi \partial'_0 \phi \ . \end{aligned} \tag{2.195}$$

Due to the periodic boundary conditions in $\mathbf{e}_1$-direction terms like $\int \mathrm{d}^3x' \ \partial'_1(\dots)$ vanish. In terms of the original coordinates, we eventually obtain the Chern-Simons edge theory

$$\begin{aligned} \mathcal{S}^0_{\mathrm{CS}} &= \frac{\kappa}{2} \int \mathrm{d}^2x \left(\partial_0 \phi - v_{\mathrm{F}} \partial_1 \phi\right) \partial_1 \phi = \frac{\kappa}{2} \int \mathrm{d}^2x \ \partial_0 \phi \partial_1 \phi - v_{\mathrm{F}} (\partial_1 \phi)^2 \\ &= -\frac{\kappa}{2} \int \mathrm{d}^2x \ \phi \left(\partial_0 \partial_1 \phi - v_{\mathrm{F}} \partial_1^2 \phi\right) \ . \end{aligned} \tag{2.196}$$

This is the so-called Floreanini-Jackiw action [100] with the associated Euler-Lagrange equation [cf. Eq. (2.109)]

$$\partial_0 \partial_1 \phi - v_{\mathrm{F}} \partial_1^2 \phi = 0 \ . \tag{2.197}$$

By defining an additional scalar field

$$\rho(x, t) = \kappa \, \partial_1 \phi \tag{2.198}$$

with SI units [C/m^2], this equation evaluates to

$$\partial_0 \rho - v_{\mathrm{F}} \partial_1 \rho = 0 \ . \tag{2.199}$$

Basically, Eq. (2.199) is the equation of motion of a chiral wave propagating in positive-, or in negative $\mathbf{e}_1$-direction with the (Fermi) velocity v_{F}. Hence, a U(1) gauge invariant Chern-Simons theory has a chiral scalar field living on its boundary. In particular, ρ should be interpreted as a charge density. In the remaining part of this section we are going to prove this statement [100]. The statistical gauge field a_μ, which characterizes the charge current in the system, couples to the electromagnetic gauge field A_μ via [cf. Eq. (2.182)]

$$S_{\mathrm{int}} = -\int \mathrm{d}^3x \ A_\mu j^\mu_a = \kappa \int \mathrm{d}^3x \ \epsilon^{\mu\nu\rho} A_\mu \partial_\nu a_\rho = \kappa \int \mathrm{d}^3x \ \epsilon^{\mu\nu\rho} a_\mu \partial_\nu A_\rho \ . \tag{2.200}$$

In the third equality, we integrated by parts and neglected the boundary term in order to obtain a gauge invariant coupling with respect to the electromagnetic gauge field A_μ [100]. Next, let us choose a gauge in which $A_2 = 0$ and $\partial_2 A_{0,1} = 0$. By using the gauge fixing

condition in Eq. (2.189) we obtain

$$\begin{aligned}\mathcal{S}_{\text{int}} &= \kappa \int \mathrm{d}^3x' \; a_2' \left(\partial_0' A_1' - \partial_1' A_0'\right) \\ &= \kappa \int \mathrm{d}^3x' \; \partial_2' \phi \left(\partial_0' A_1' - \partial_1' A_0'\right) = \kappa \int_{x_2=0} \mathrm{d}^2x' \; \phi \left(\partial_0' A_1' - \partial_1' A_0'\right) \\ &= \kappa \int_{x_2'=0} \mathrm{d}^2x' \; \left[-A_1' \partial_0' \phi + A_0' \partial_1' \phi + \partial_0'(\phi A_1') - \partial_1'(\phi A_0')\right] \\ &= \kappa \int_{x_2'=0} \mathrm{d}^2x' \; \left[A_0' \partial_1' \phi - A_1' \partial_0' \phi\right] \; .\end{aligned} \tag{2.201}$$

According to Eq. (2.197), we know that $\partial_0' \phi = \partial_0 \phi - v_{\text{F}} \partial_1 \phi$ is a constant. Setting this constant to zero, implies

$$\mathcal{S}_{\text{int}} = \kappa \int_{x_2=0} \mathrm{d}^2x \; \left(A_0 - v_{\text{F}} A_1\right) \partial_1 \phi = \int_{x_2=0} \mathrm{d}^2x \; \left(A_0 - v_{\text{F}} A_1\right) \rho \; . \tag{2.202}$$

Hence, ρ directly couples to A_0 and is thus a charge density. Due to the coupling of ρ to A_1, this density propagates in a certain direction, characterized by the (Fermi) velocity v_{F} [100]. In the following, we show that this chiral charge density is directly related to chiral Dirac modes located at the 1+1 dimensional boundary of the 2+1 dimensional bulk theory. These modes show a chiral anomaly which compensates the gauge anomaly of a 2+1 dimensional Chern-Simons term at the system's boundaries. To understand this statement in detail, we are going to analyze the chiral anomaly of 1+1 dimensional Dirac fermions in the next section.

2.6.5 Chiral Anomaly in 1+1 Dimension

In this section, we are going to discuss the concept of the chiral anomaly. Since this anomaly requires the notion of chirality, and thus a γ^5 matrix, it only occurs in even space-time dimensions. In what follows, we restrict ourselves to massless QED systems in $1+1$ space-time dimensions, defined by the classical Lagrangian [cf. Eq.(2.98)]

$$\mathcal{L}_{\text{cl}} = \bar{\psi}(\mathrm{i}\partial\!\!\!/ + \mathrm{e}A\!\!\!/)\psi \; . \tag{2.203}$$

According to Sec. 2.4, this Lagrangian is invariant under vector and axial vector (so-called chiral) gauge transformations. As a consequence, the Noether theorem [cf. Sec. 2.4.5] implies the existence of two classically conserved currents

$$\text{vector :} \quad j_\mu = \bar{\psi}\gamma_\mu\psi \; , \tag{2.204}$$

$$\text{axial vector :} \quad j_\mu^5 = \bar{\psi}\gamma_\mu\gamma^5\psi \; . \tag{2.205}$$

The classical conservation laws of these currents can be seen easily by conjugating the Dirac equation [114]

$$(\mathrm{i}\partial\!\!\!/ + \mathrm{e}A\!\!\!/)\psi = 0 \quad \wedge \quad \bar{\psi}(\mathrm{i}\overleftarrow{\partial\!\!\!/} - \mathrm{e}A\!\!\!/) = 0 \; , \tag{2.206}$$

which implies

$$\partial^\mu j_\mu = \bar{\psi}\overleftarrow{\partial\!\!\!/}\psi + \bar{\psi}\partial\!\!\!/\psi = \mathrm{i}\bar{\psi}(-\mathrm{e}A\!\!\!/)\psi + \mathrm{i}\bar{\psi}(\mathrm{e}A\!\!\!/)\psi = 0 \; , \tag{2.207}$$

$$\partial^\mu j_\mu^5 = \mathrm{i}\bar{\psi}(-\mathrm{e}A\!\!\!/)\gamma^5\psi - \mathrm{i}\bar{\psi}\gamma^5(\mathrm{e}A\!\!\!/)\psi = 0 \; . \tag{2.208}$$

Equation (2.208) will be violated on the quantum level, which implies the presence of a quantum anomaly [cf. Sec. 2.5]. We prove this statement in the following. We start our analysis with the definition of the left- and the right handed currents

$$j_\mu^{\mathrm{L}} = \frac{1}{2}\left(j_\mu + j_\mu^5\right) \quad \wedge \quad j_\mu^{\mathrm{R}} = \frac{1}{2}\left(j_\mu - j_\mu^5\right) \tag{2.209}$$

with

$$j_\mu = j_\mu^{\mathrm{L}} + j_\mu^{\mathrm{R}} \quad \wedge \quad j_\mu^5 = j_\mu^{\mathrm{L}} - j_\mu^{\mathrm{R}} \ . \tag{2.210}$$

By constructions, these currents are conserved classically

$$\partial^\mu j_\mu^{\mathrm{L}} = \partial^\mu j_\mu^{\mathrm{R}} = 0 \ . \tag{2.211}$$

In what follows, let us compactify our real-space dimension in $\mathbf{e}_1$-direction to a unit sphere S^1 of circumference L. In order to define a consistent theory, this compactification requires (anti-)periodic boundary conditions for the gauge- and for the Dirac fields, respectively:

$$\begin{aligned} A_\mu\left(x_0, x_1 = -L/2\right) &= A_\mu\left(x_0, x_1 = L/2\right) \ , \\ \psi\left(x_0, x_1 = -L/2\right) &= -\psi\left(x_0, x_1 = L/2\right) \ . \end{aligned} \tag{2.212}$$

Within the scope of the present analysis we are going to consider a gauge configuration which is only time-, but not space dependent. In particular, we choose $A_0 = 0$ and $A_1(x_0)$. Moreover, the local gauge invariance requires that $A_1 = 0$ is equivalent to $A_1 = 2\pi/(\mathrm{e}L)$ [cf. Eqs. (2.92) and (2.103)]. Specifically, the gauge field A_1 is defined on a circle S^1 of circumference $2\pi/(\mathrm{e}L)$. Due to the vector- and axial vector symmetry of the classial Lagrangian in Eq. (2.203), quantum electrodynamics in 1+1 space-time dimensions gives rise to two classically conserved charges: The vector-, as well as the axial charge [114]

$$Q(x_0) = \int \mathrm{d}x_1 \ j_0(x_0, x_1) \quad \wedge \quad Q^5(x_0) = \int \mathrm{d}x_1 \ j_0^5(x_0, x_1) \ . \tag{2.213}$$

As we have shown in Eq. (2.99), we can decompose the entire QED Lagrangian in Eq. (2.203) into its chiral building blocks

$$\mathcal{L} = \bar{\psi}_{\mathrm{L}} \mathrm{i} \not{D} \psi_{\mathrm{L}} + \bar{\psi}_{\mathrm{R}} \mathrm{i} \not{D} \psi_{\mathrm{R}} \ , \tag{2.214}$$

with the separately conserved chiral charges

$$Q_{\mathrm{L,R}}(x_0) = \int \mathrm{d}x_1 \ \bar{\psi}_{\mathrm{L,R}}(x_0, x_1) \gamma_0 \psi_{\mathrm{L,R}}(x_0, x_1) = \int \mathrm{d}x_1 \ \psi_{\mathrm{L,R}}^\dagger(x_0, x_1) \psi_{\mathrm{L,R}}(x_0, x_1) \ , \tag{2.215}$$

which satisfy

$$Q(x_0) = Q_{\mathrm{L}}(x_0) + Q_{\mathrm{R}}(x_0) \quad \wedge \quad Q^5 = Q_{\mathrm{L}}(x_0) - Q_{\mathrm{R}}(x_0) \ . \tag{2.216}$$

Via a Legendre transformation our system is described by the Hamiltonian

$$\begin{aligned} \mathcal{H} &= \psi^\dagger \mathrm{i} \partial_0 \psi - \mathcal{L} \\ &= -\mathrm{i} \psi_{\mathrm{L}}^\dagger \gamma^0 \gamma^1 D_1 \psi_{\mathrm{L}} - \mathrm{i} \psi_{\mathrm{R}}^\dagger \gamma^0 \gamma^1 D_1 \psi_{\mathrm{R}} \\ &= -\mathrm{i} \psi_{\mathrm{L}}^\dagger \gamma^5 D_1 \psi_{\mathrm{L}} - \mathrm{i} \psi_{\mathrm{R}}^\dagger \gamma^5 D_1 \psi_{\mathrm{R}} \\ &= -\mathrm{i} \psi_{\mathrm{L}}^\dagger D_1 \psi_{\mathrm{L}} + \mathrm{i} \psi_{\mathrm{R}}^\dagger D_1 \psi_{\mathrm{R}} \\ &= -\mathrm{i} \psi_{\mathrm{L}}^\dagger (\partial_1 + \mathrm{i}\mathrm{e} A_1) \psi_{\mathrm{L}} + \mathrm{i} \psi_{\mathrm{R}}^\dagger (\partial_1 + \mathrm{i}\mathrm{e} A_1) \psi_{\mathrm{R}} \end{aligned} \tag{2.217}$$

$$= \psi_{\mathrm{L}}^{\dagger}(-\mathrm{i}\partial_1 + \mathrm{e}A_1)\psi_{\mathrm{L}} - \psi_{\mathrm{R}}^{\dagger}(-\mathrm{i}\partial_1 + \mathrm{e}A_1)\psi_{\mathrm{R}} \ .$$

The eigen-states of this Hamiltonian are plane waves $\propto \mathrm{e}^{\mathrm{i}k_1^n x^1}$ with discretized momenta

$$k_1^n = \frac{2\pi n}{L} \quad \text{with} \quad n \in \mathbb{Z} \tag{2.218}$$

due to the compact space dimension S^1 [cf. Eq. (2.212)]. The system's eigen-energies are therefore given by [109]

$$\psi_{\mathrm{L}}: \quad E_n^{\mathrm{L}} = +(k_1^n + \mathrm{e}A_1) \ , \tag{2.219}$$

$$\psi_{\mathrm{R}}: \quad E_n^{\mathrm{R}} = -(k_1^n + \mathrm{e}A_1) \ . \tag{2.220}$$

Hence, on the quantum level each chiral fermion corresponds to an infinite set of equally spaced energy levels. Let us for the moment occupy all levels of negative energy with fermionic modes. We fill the so-called Dirac sea [109, 114]. If we now adiabatically change A_1 by $\Delta A_1 = \frac{2\pi}{\mathrm{e}L}$ in a period $x_0 \in [0, T]$, both spectra map into their initial form. However, every left-moving level E_n^{L} is increased by $\Delta n = 1$, whereas every right-moving level E_n^{R} is reduced by $\Delta n = -1$. Thus, one additional left-moving fermion enters the theory, whereas one right-moving fermion disappears (a hole enters). Hence $\Delta Q^5 = 2$, whereas $\Delta Q = 0$. This is the so-called Adler-Bell-Jackiw (ABJ) or chiral anomaly [126–128]. By calculating the quantum effective action one can explicitly show that in 1+1 space time dimensions one finds the (non-)conservation equation

$$\partial_\mu j^\mu = 0 \quad \wedge \quad \partial_\mu j^{\mu 5} = \frac{\mathrm{e}}{\pi}\epsilon^{\mu\nu}\partial_\mu A_\nu \ , \tag{2.221}$$

with

$$\int \mathrm{d}^2x \ \partial_\mu j^{\mu 5} = \int \mathrm{d}^2x \, \frac{\mathrm{e}}{\pi}\epsilon^{\mu\nu}\partial_\mu A_\nu = \int_0^T \int_{-L/2}^{L/2} \mathrm{d}x_0 \mathrm{d}x_1 \, \frac{\mathrm{e}}{\pi}\partial_0 A_1 = \frac{\mathrm{e}}{\pi} L \, \Delta A^1 = 2 = \Delta Q^5 \ . \tag{2.222}$$

The derivation of the quantum effective action will be the scope of the following section.

2.6.6 Effective Action of Chiral Edge Modes

In Sec. 2.6.4, we have shown that due to current-conservation, a bulk CS theory implies the existence of chiral edge modes. In this section, we derive the effective action of chiral Dirac fermions via their polarization operator in 1+1 space-time dimensions. We eventually incorporate the 2+1 dimensional bulk CS as well as the 1+1 dimensional chiral edge theory on a 2+1 dimensional space-time with boundaries. This leads to a well-defined system without gauge-anomalies.

We start our analysis with the derivation of the chiral gauge-matter coupling. The associated vertex structure can be read off from the massless QED_{1+1} Lagrangian in Eq. (2.203)

$$\mathcal{L}_{\mathrm{cl}} = \bar{\psi}\mathrm{i}\not{D}\psi = \bar{\psi}\mathrm{i}\gamma^\mu(\partial_\mu + \mathrm{i}\mathrm{e}A_\mu)\psi \ . \tag{2.223}$$

In Sec. 2.4.4, we identified the chiral building blocks of this Lagrangian [cf. Eq.(2.96)]

$$\psi_{\mathrm{L/R}} \equiv \psi_\pm = P_\pm\psi = \frac{\mathbb{1}_2 \pm \gamma^5}{2}\psi \quad \text{with} \quad \gamma^5\psi_\pm = \pm\psi_\pm \ , \tag{2.224}$$

which are γ^5 eigen-states of chirality ± 1. Moreover,

$$P_\pm = \frac{1}{2}\left(\mathbb{1}_2 \pm \gamma^5\right) \tag{2.225}$$

defines the chiral projection operator with the associated properties [cf. Eq. (4.13)]

$$P_+ + P_- = \mathbb{1}_2, \quad P_\pm^2 = P_\pm, \quad P_\pm^\dagger = P_\pm, \quad P_+P_- = P_-P_+ = 0, \quad P_+\gamma^\mu = \gamma^\mu P_- \ . \tag{2.226}$$

With these identities we can decompose Eq. (2.223) into its chiral building blocks

$$\begin{aligned}\mathcal{L} &= \bar\psi \mathrm{i}\not{D}\psi = \bar\psi\left(P_+ + P_-\right)\mathrm{i}\gamma^\mu D_\mu \left(P_+ + P_-\right)\psi \\ &= \bar\psi P_+ \mathrm{i}\gamma^\mu D_\mu P_-\psi + \bar\psi P_- \mathrm{i}\gamma^\mu D_\mu P_+\psi = \bar\psi_{\mathrm{R}}\mathrm{i}\not{D}\psi_{\mathrm{R}} + \bar\psi_{\mathrm{L}}\mathrm{i}\not{D}\psi_{\mathrm{L}} \ ,\end{aligned} \tag{2.227}$$

where we made use of the identities

$$\bar\psi P_- = \psi^\dagger\gamma^0 P_- = \psi^\dagger P_+\gamma^0 = \psi^\dagger P_+^\dagger\gamma^0 = \left(P_+\psi\right)^\dagger\gamma^0 = \psi_+^\dagger\gamma^0 = \bar\psi_+ = \psi_{\mathrm{L}} \ , \tag{2.228}$$

$$\bar\psi P_+ = \bar\psi_- = \psi_{\mathrm{R}} \quad \wedge \quad P_+\psi = \psi_+ = \psi_{\mathrm{L}} \quad \wedge \quad P_-\psi = \psi_- = \psi_{\mathrm{R}} \ . \tag{2.229}$$

Equation (2.227) encodes the chiral free fermion propagator and the associated gauge-matter coupling. However, in order to make use of the same techniques which we used for our calculation of the vacuum polarization operator in Eq. (2.141), we decompose Eq. (2.223) in a slightly different way:

$$\begin{aligned}\mathcal{L} &= \bar\psi\mathrm{i}\not{D}\psi = \bar\psi\left(P_+ + P_-\right)\mathrm{i}\gamma^\mu D_\mu\left(P_+ + P_-\right)\psi = \bar\psi\mathrm{i}\not{\partial}\psi - \mathrm{e}\left(\bar\psi P_+\not{A}P_-\psi + \bar\psi P_-\not{A}P_+\psi\right) \\ &= \bar\psi\mathrm{i}\not{\partial}\psi - \mathrm{e}\left(\bar\psi\not{A}P_-^2\psi + \bar\psi\not{A}P_+^2\psi\right) = \bar\psi\mathrm{i}\not{\partial}\psi - \mathrm{e}\left(\bar\psi\not{A}P_-\psi + \bar\psi\not{A}P_+\psi\right) \\ &= \bar\psi\mathrm{i}\not{\partial}\psi \ \underbrace{-\frac{\mathrm{e}}{2}\bar\psi\gamma^\mu\left(\mathbb{1}_2 - \gamma^5\right)A_\mu\psi}_{\text{right moving coupling}} \ \underbrace{-\frac{\mathrm{e}}{2}\bar\psi\gamma^\mu\left(\mathbb{1}_2 + \gamma^5\right)A_\mu\psi}_{\text{left moving coupling}} \ ,\end{aligned} \tag{2.230}$$

where $V_\pm^\mu$ encodes the chiral vertex structure

$$V_\pm^\mu = -\frac{\mathrm{ie}}{2}\left(\mathbb{1}_2 \pm \gamma^5\right) \ . \tag{2.231}$$

In terms of this vertex structure the chiral polarization operator $\Pi_\pm^{\mu\nu}$ for left- and right handed spinors of chirality $\gamma^5 = \pm 1$ is given by [cf. Eq. (2.141)]

$$\mathrm{i}\Pi_\pm^{\mu\nu}(p) = -\frac{(-\mathrm{ie})^2}{4}\int\frac{\mathrm{d}^2k}{(2\pi)^2}\frac{\mathrm{tr}\left[\gamma^\mu\left(\mathbb{1}_2 \pm \gamma^5\right)\gamma^\lambda\gamma^\nu\left(\mathbb{1}_2 \pm \gamma^5\right)\gamma^\zeta\right]\mathrm{i}k_\lambda\mathrm{i}(k+p)_\zeta}{k^2(k+p)^2} \ . \tag{2.232}$$

Diagrammatically, this fermion loop operator is visualized in Fig. 2.9.

To evaluate Eq. (2.232), we first simplify the Dirac trace according to the 1+1 dimensional trace identities in Eq. (2.45). In particular, these identities imply the relations:

$$(1): \quad \mathrm{tr}\left[\gamma^\mu\gamma^\lambda\gamma^\nu\gamma^\zeta\right] = 2\left(g^{\mu\lambda}g^{\zeta\nu} - \epsilon^{\mu\lambda}\epsilon^{\zeta\nu}\right) \ , \tag{2.233}$$

$$(2): \quad \mathrm{tr}\left[\gamma^\mu\gamma^5\gamma^\lambda\gamma^\nu\gamma^\zeta\right] = -\mathrm{tr}\left[\gamma^\mu\gamma^\lambda\gamma^\nu\gamma^\zeta\gamma^5\right] = 2\left(g^{\mu\lambda}\epsilon^{\zeta\nu} - \epsilon^{\mu\lambda}g^{\zeta\nu}\right) \ , \tag{2.234}$$

$$(3): \quad \mathrm{tr}\left[\gamma^\mu\gamma^\lambda\gamma^\nu\gamma^5\gamma^\zeta\right] = (2) \ , \tag{2.235}$$

$$(4): \quad \mathrm{tr}\left[\gamma^\mu\gamma^5\gamma^\lambda\gamma^\nu\gamma^5\gamma^\zeta\right] = (1) \ , \tag{2.236}$$

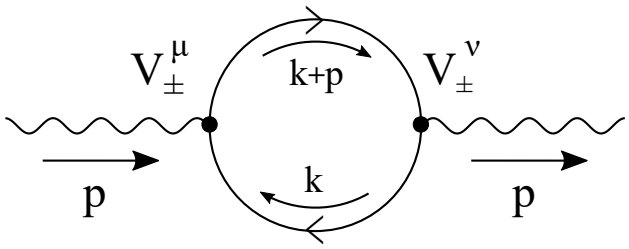

Figure 2.9: Feynman diagramm of the chiral vacuum polarization operator in Eq. (2.232) with the internal loop momentum k, the external momentum p, and the chiral gauge-matter vertices $V_{\pm}^{\mu,\nu}$ [cf. Eq.(2.231)].

where we used the cyclic properties of the Driac trace, as well as the anti-commutation rule of the γ^5 matrix [cf. Eq. (2.44)]. Consequently, the Dirac trace in the numerator of Eq. (2.232) evaluates to

$$\begin{aligned}\mathrm{tr}\left[\gamma^{\mu}\left(\mathbb{1}_2 \pm \gamma^5\right)\gamma^{\lambda}\gamma^{\nu}\left(\mathbb{1}_2 \pm \gamma^5\right)\gamma^{\zeta}\right] &= (1) \pm (2) \pm (3) + (4) = 2\left[(1) \pm (2)\right] \\ &= 4\left(g^{\mu\lambda} \mp \epsilon^{\mu\lambda}\right)\left(g^{\zeta\nu} \pm \epsilon^{\zeta\nu}\right) \equiv T_{\pm}^{\mu\nu\lambda\zeta} \ . \end{aligned} \tag{2.237}$$

To symmetrize the denominator with respect to the loop momentum, we use the Feynman parameterization introduced in Eq. (2.144) with $A = k^2$ and $B = (k+p)^2$. Moreover, we shift the loop momentum according to $k_\lambda \to k_\lambda + p_\lambda x = l_\lambda$ [109]. Altogether, this simplifies the form of the momentum integral in Eq. (2.232) [cf. Eq. (2.145)]

$$\mathrm{Int}_{\lambda\zeta} = \int \mathrm{d}^2k \ \frac{k_\lambda (k+p)_\zeta}{k^2(k+p)^2} = \int \mathrm{d}^2k \ \frac{k_\lambda k_\zeta + k_\lambda p_\zeta}{k^2(k+p)^2} = \int\limits_0^1 \mathrm{d}x \int \mathrm{d}^2l \ \frac{l_\lambda l_\zeta - x(1-x)p_\lambda p_\zeta}{(l^2 + x(1-x)p^2)^2} \ . \tag{2.238}$$

Here, we neglected all linear terms in l since they do not contribute to the (symmetric) integration. After performing a Wick-rotation to an Euclidean space-time, $l \to l_{\mathrm{E}}$ [cf. Sec. 2.3.3], this integral evaluates to

$$\mathrm{Int}_{\lambda\zeta} = \mathrm{i}\int\limits_0^1 \mathrm{d}x \int \mathrm{d}^2l_{\mathrm{E}} \frac{-\frac{1}{2}l_{\mathrm{E}}^2 g_{\lambda\zeta} - x(1-x)p_\lambda p_\zeta}{(l_{\mathrm{E}}^2 - x(1-x)p^2)^2} = \mathrm{Int}^1_{\lambda\zeta} + \mathrm{Int}^2_{\lambda\zeta} \ , \tag{2.239}$$

where we made use of $l_\lambda l_\zeta = \frac{1}{1+1} l^2 g_{\lambda\zeta}$, due to the underlying Lorentz symmetry [109]. Let us first calculate the convergent part $\mathrm{Int}^2_{\lambda\zeta}$. Therefore, we will use the following identities for the integration over an n-dimensional unit sphere in an Euclidean space-time [109]:

$$\int \frac{\mathrm{d}^n l_{\mathrm{E}}}{(2\pi)^n} \frac{1}{(l_{\mathrm{E}}^2 + \Delta)^2} = \int \frac{\mathrm{d}\Omega_n}{(2\pi)^n} \cdot \int\limits_0^\infty \mathrm{d}l_{\mathrm{E}} \frac{l_{\mathrm{E}}^{n-1}}{(l_{\mathrm{E}}^2 + \Delta)^2} \ , \tag{2.240}$$

$$\int \mathrm{d}\Omega_n = \frac{2\pi^{\frac{n}{2}}}{\Gamma\left(\frac{n}{2}\right)} \quad \text{with} \quad \Gamma(1) = 1 \ \Rightarrow \ \int \mathrm{d}\Omega_2 = 2\pi \ . \tag{2.241}$$

With these identities $\mathrm{Int}^2_{\lambda\zeta}$ evaluates to

$$\mathrm{Int}^2_{\lambda\zeta} = \mathrm{i}\int\limits_0^1 \mathrm{d}x \int \mathrm{d}^2l_{\mathrm{E}} \frac{-x(1-x)p_\lambda p_\zeta}{(l_{\mathrm{E}}^2 - x(1-x)p^2)^2} = 2\pi\mathrm{i}\int\limits_0^1 \mathrm{d}x \int\limits_0^\infty \mathrm{d}l_{\mathrm{E}} \ l_{\mathrm{E}} \frac{-x(1-x)p_\lambda p_\zeta}{(l_{\mathrm{E}}^2 - x(1-x)p^2)^2} \tag{2.242}$$

$$= -2\pi \mathrm{i} p_\lambda p_\zeta \int\limits_0^1 \mathrm{d}x \int\limits_0^\infty \mathrm{d}l_\mathrm{E}\; l_\mathrm{E} \frac{x(1-x)}{(l_\mathrm{E}^2 - x(1-x)p^2)^2} = \frac{-2\pi \mathrm{i} p_\lambda p_\zeta}{2p^2} \int\limits_0^1 \mathrm{d}x \frac{x(1-x)}{x(x-1)} = \mathrm{i}\pi \, \frac{p_\lambda p_\zeta}{p^2} \ .$$

Consequently, the convergent part of the chiral 1+1 dimensional polarization operator in Eq. (2.232) is given by

$$\begin{aligned} \mathrm{i}\Pi^{\mu\nu}_{\pm,\mathrm{conv}}(p) &= -\frac{\mathrm{e}^2}{4(2\pi)^2} T_\pm^{\mu\nu\lambda\zeta} \, \mathrm{Int}^2_{\lambda\zeta} = -\frac{\mathrm{e}^2}{4(2\pi)^2} T_\pm^{\mu\nu\lambda\zeta} \mathrm{i}\pi \, \frac{p_\lambda p_\zeta}{p^2} \\ &= -\frac{\mathrm{ie}^2}{4\pi} \left(g^{\mu\lambda} \mp \epsilon^{\mu\lambda} \right) \frac{p_\lambda p_\zeta}{p^2} \left(g^{\zeta\nu} \pm \epsilon^{\zeta\nu} \right) \ . \end{aligned} \tag{2.243}$$

We are still left with the calculation of the superficially divergent term in Eq. (2.239). In what follows, we calculate this term by using the concept of dimensional regularization [109, 110]. Applying this technique leads to the generalized n-dimensional integral

$$\begin{aligned} \mathrm{Int}^1_{\lambda\zeta} &= \mathrm{i}(2\pi)^2 \int\limits_0^1 \mathrm{d}x \int \frac{\mathrm{d}^2 l_\mathrm{E}}{(2\pi)^2} \frac{-\frac{1}{n} l_\mathrm{E}^2 g_{\lambda\zeta}}{(l_\mathrm{E}^2 - x(1-x)p^2)^2} \\ &= \mathrm{i}(2\pi)^2 \int\limits_0^1 \mathrm{d}x \int \frac{\mathrm{d}^n l_\mathrm{E}}{(2\pi)^n} \frac{-\frac{1}{n} l_\mathrm{E}^2 g_{\lambda\zeta}}{(l_\mathrm{E}^2 - x(1-x)p^2)^2} \ . \end{aligned} \tag{2.244}$$

Before we execute this integration, let us contract the tensor structure $T_\pm^{\mu\nu\lambda\zeta} \, \mathrm{Int}^1_{\lambda\zeta}$. This avoids the mathematical problem of a '$0 \times \infty$'. In n dimensions we find the contractions:

$$(0): \ \epsilon^{\mu\lambda}\epsilon^{\zeta\nu} = \left[g^{\mu\nu} g^{\lambda\zeta} - g^{\mu\zeta} g^{\lambda\nu} \right] \ , \tag{2.245}$$

$$(1): \ g^{\mu\lambda} g_{\lambda\zeta} g^{\zeta\nu} = g^\mu_\zeta g^{\zeta\nu} = g^{\mu\nu} \ , \tag{2.246}$$

$$(2): \ g^{\mu\lambda} g_{\lambda\zeta} \epsilon^{\zeta\nu} = \epsilon^{\mu\nu} \ , \tag{2.247}$$

$$(3): \ \epsilon^{\mu\lambda} g_{\lambda\zeta} g^{\zeta\nu} = \epsilon^{\mu\nu} \ , \tag{2.248}$$

$$(4): \ \epsilon^{\mu\lambda} g_{\lambda\zeta} \epsilon^{\zeta\nu} = \left[g^{\mu\nu} g^{\lambda\zeta} - g^{\mu\zeta} g^{\lambda\nu} \right] g_{\lambda\zeta} = [n-1] \, g^{\mu\nu} \ . \tag{2.249}$$

Consequently, one obtains

$$T_\pm^{\mu\nu\lambda\zeta} g_{\lambda\zeta} = 4 \left(g^{\mu\lambda} \mp \epsilon^{\mu\lambda} \right) \left(g^{\zeta\nu} \pm \epsilon^{\zeta\nu} \right) g_{\lambda\zeta} = 4 \left[(1) \pm (2) \mp (3) - (4) \right] = 4 \left[2 - n \right] g^{\mu\nu} \ . \tag{2.250}$$

Notice, that this expression vanishes for $n = 2$, which causes the '$0 \times \infty$' in Eq. (2.244). However, in combination we obtain the contribution

$$\begin{aligned} T_\pm^{\mu\nu\lambda\zeta} \, \mathrm{Int}^1_{\lambda\zeta} &= \mathrm{i}(2\pi)^2 \int\limits_0^1 \mathrm{d}x \int \frac{\mathrm{d}^n l_\mathrm{E}}{(2\pi)^n} \frac{-\frac{1}{n} l_\mathrm{E}^2 \, T_\pm^{\mu\nu\lambda\zeta} \, g_{\lambda\zeta}}{(l_\mathrm{E}^2 - x(1-x)p^2)^2} \\ &= \mathrm{i}(2\pi)^2 \int\limits_0^1 \mathrm{d}x \int \frac{\mathrm{d}^n l_\mathrm{E}}{(2\pi)^n} \frac{-\frac{1}{n} l_\mathrm{E}^2 4 \left[2 - n \right] g^{\mu\nu}}{(l_\mathrm{E}^2 - x(1-x)p^2)^2} \\ &= 4\mathrm{i}(2\pi)^2 \, g^{\mu\nu} \int\limits_0^1 \mathrm{d}x \int \frac{\mathrm{d}^n l_\mathrm{E}}{(2\pi)^n} \frac{\left(1 - \frac{2}{n} \right) l_\mathrm{E}^2}{(l_\mathrm{E}^2 - x(1-x)p^2)^2} \\ &= 4\mathrm{i}(2\pi)^2 \, g^{\mu\nu} \left(-\frac{1}{4\pi} \right) = -4\pi \mathrm{i} \, g^{\mu\nu} \ , \end{aligned} \tag{2.251}$$

where we made use $\Gamma(1) = 1$ and the n dimensional identity [109]

$$\int \frac{\mathrm{d}^n l_\mathrm{E}}{(2\pi)^n} \frac{\left(1-\frac{2}{n}\right) l_\mathrm{E}^2}{(l_\mathrm{E}^2+\Delta)^2} = \frac{1}{(4\pi)^{n/2}} \Gamma\left(2-\frac{n}{2}\right) \left(\frac{1}{\Delta}\right)^{2-n/2} (-\Delta) \overset{n=2}{\to} -\frac{1}{4\pi} \ . \tag{2.252}$$

Thus, after dimensional regularization the former divergent part in Eq. (2.239) yields

$$\mathrm{i}\Pi^{\mu\nu}_{\pm,\mathrm{div}}(p) = -\frac{\mathrm{e}^2}{4(2\pi)^2} T^{\mu\nu\lambda\zeta}_{\pm} \, \mathrm{Int}^1_{\lambda\zeta} = -\frac{\mathrm{e}^2}{4(2\pi)^2} \, (-4\pi\mathrm{i}) \, g^{\mu\nu} = \mathrm{i}\frac{\mathrm{e}^2}{4\pi} \, g^{\mu\nu} \ . \tag{2.253}$$

So in total, we found the following regularized chiral polarization operator

$$\mathrm{i}\Pi^{\mu\nu}_{\pm,\mathrm{reg}}(p) = \frac{\mathrm{i}}{4\pi}\mathrm{e}^2 \left[g^{\mu\nu} - \left(g^{\mu\lambda} \mp \epsilon^{\mu\lambda}\right) \frac{p_\lambda p_\zeta}{p^2} \left(g^{\zeta\nu} \pm \epsilon^{\zeta\nu}\right) \right] \ . \tag{2.254}$$

This operator defines the associated quadratic part of the effective action

$$\begin{aligned} S^{(2)}_{\mathrm{eff},\pm} &= \frac{1}{2} \int \frac{\mathrm{d}^2 p}{(2\pi)^2} \left[A_\mu(-p) \, \Pi^{\mu\nu}_{\pm,\mathrm{reg}}(p) \, A_\nu(p) \right] \\ &= \frac{\mathrm{e}^2}{8\pi} \int \frac{\mathrm{d}^2 p}{(2\pi)^2} \left[A_\mu(-p) \, \left(g^{\mu\nu} - \left(g^{\mu\lambda} \mp \epsilon^{\mu\lambda}\right) \frac{p_\lambda p_\zeta}{p^2} \left(g^{\zeta\nu} \pm \epsilon^{\zeta\nu}\right) \right) \, A_\nu(p) \right] \\ &= \frac{\mathrm{e}^2}{8\pi} \int \mathrm{d}^2 x \left[A_\mu \left(g^{\mu\nu} - \left(g^{\mu\lambda} \mp \epsilon^{\mu\lambda}\right) \frac{\partial_\lambda \partial_\zeta}{\Box} \left(g^{\zeta\nu} \pm \epsilon^{\zeta\nu}\right) \right) \, A_\nu \right] \ , \end{aligned} \tag{2.255}$$

where we made a Fourier transformation to the real space coordinates in the last equality and introduced the D'Alambert operator $\Box = \partial_\mu \partial^\mu$. The chiral current associated to this action is given by

$$j^\mu_\pm = -\frac{\delta S^{(2)}_{\mathrm{eff},\pm}}{\delta A_\mu} = -\frac{\mathrm{e}^2}{4\pi} \left[g^{\mu\nu} - \left(g^{\mu\lambda} \mp \epsilon^{\mu\lambda}\right) \frac{\partial_\lambda \partial_\zeta}{\Box} \left(g^{\zeta\nu} \pm \epsilon^{\zeta\nu}\right) \right] A_\nu \ . \tag{2.256}$$

Most remarkably, this current is not conserved

$$\partial_\mu j^\mu_\pm = -\frac{\mathrm{e}^2}{4\pi} \left[(1) - (2) \mp (3) \right] = \pm \frac{\mathrm{e}^2}{4\pi} \epsilon^{\zeta\nu} \partial_\zeta A_\nu \ . \tag{2.257}$$

Here, we made use of the following contraction rules

$$(1): \quad \partial_\mu g^{\mu\nu} A_\nu = \partial^\nu A_\nu \ , \tag{2.258}$$

$$(2): \quad \partial_\mu g^{\mu\lambda} \frac{\partial_\lambda \partial_\zeta}{\Box} g^{\zeta\nu} A_\nu = \partial^\nu A_\nu \ , \tag{2.259}$$

$$(3): \quad \partial_\mu g^{\mu\lambda} \frac{\partial_\lambda \partial_\zeta}{\Box} \epsilon^{\zeta\nu} A_\nu = \epsilon^{\zeta\nu} \partial_\zeta A_\nu \ , \tag{2.260}$$

$$(4): \quad \partial_\mu \epsilon^{\mu\lambda} \frac{\partial_\lambda \partial_\zeta}{\Box} g^{\zeta\nu} A_\nu = 0 \ , \tag{2.261}$$

$$(5): \quad \partial_\mu \epsilon^{\mu\lambda} \frac{\partial_\lambda \partial_\zeta}{\Box} \epsilon^{\zeta\nu} A_\nu = 0 \ , \tag{2.262}$$

where (4) and (5) vanish due to the contraction of a symmetric with an anti-symmetric tensor structure, $\epsilon^{\mu\lambda}\partial_\mu\partial_\lambda$.

Essentially, the (vector-)current non-conservation in Eq. (2.257) counts one fourth of the chiral anomaly equation which we have derived in Eq. (2.221). There are two reasons for

this. One factor of two originates from the fact that Eq. (2.257) defines the vector gauge-anomaly associated to each chiral left- or right moving mode separately [cf. Sec. 2.4.4]. In combination the entire vector current anomaly vanishes, whereas the chiral anomaly manifests itself:

$$\partial_\mu j^{\mu 5} = \partial_\mu \left(j^\mu_{\mathrm{L}} - j^\mu_{\mathrm{R}} \right) = \partial_\mu \left(j^\mu_{+} - j^\mu_{-} \right) = \frac{\mathrm{e}^2}{2\pi} \epsilon^{\mu\nu} \partial_\mu A_\nu \ . \tag{2.263}$$

If there is only a single chiral mode living on the 1+1 dimensional edge of a 2+1 dimensional bulk theory, the vector gauge anomaly in Eq. (2.257) gets compensated by the corresponding bulk Chern-Simons gauge non-invariance [cf. Sec. 2.6.4]. It is the goal of the following subsection to rigorously proof and to visualize this statement.
Still, Eq. (2.263) differs from Eq. (2.221) by a factor of two. This factor originates from the fact that in Eq. (2.263) we have derived the consistent anomaly, whereas Eq. (2.221) characterizes the covariant anomaly [129]. As we will show in the next section, the (vector) gauge non-invariance of a 2+1 dimensional Chern-Simons term on a manifold with 1+1 dimensional boundaries gets compensated by the consistent anomaly of the associated chiral edge theory. We are recommending Ref. [129] (especially section III) for a deeper discussion of the physical difference between consistent and covariant anomalies.

2.6.7 Callan-Harvey Mechanism

The derivation of the chiral fermion Lagrangian in Sec. 2.6.6 finally allows us to construct a consistent Chern-Simons theory on a 2+1 dimensional manifold with 1+1 dimensional boundaries. Such a geometry is exemplary shown in Fig. 2.10. Here, the 2+1 dimensional system is wrapped up on a cylinder, such that we have periodic boundary conditions in $\mathbf{e}_1$-direction and a finite system size W in $\mathbf{e}_2$-direction. Subfigures (a) and (b) show the current densities[a] in such a system as a response to two different electric field configuration: (a) A perpendicular electric field in $\mathbf{e}_2$-direction, as well as (b) a parallel electric field in $\mathbf{e}_1$-direction[b]. The currents originating from a single bulk Chern-Simons theory are encoded by $j^\mu_{\text{CS, bulk/edge}}$, whereas the currents associated to the chiral 1+1 dimensional edge degrees of freedom are described by j^μ_{1+1}. In what follows, we are going to derive the form of these currents analytically. The line of reasoning within this section will roughly follow Ref. [130].

As it was shown in Sec. 2.6.4, a single 2+1 dimensional Chern-Simons theory is described by the parity-odd action

$$\mathcal{S}_{\mathrm{CS}} = \frac{\sigma_{\mathrm{xy}}}{2} \int \mathrm{d}^3x \, \epsilon^{\mu\nu\rho} A_\mu \partial_\nu A_\rho \ . \tag{2.264}$$

In order to restrict this action to the finite-size geometry shown in Fig. 2.10, we introduce a spatial confining function f in $\mathbf{e}_2$-direction with

$$f(x_2) = \begin{cases} 1 & \text{for } -W/2 \leq x_2 \leq W/2 \ . \\ 0 & \text{otherwise} \ . \end{cases} \tag{2.265}$$

This allows us to confine Eq. (2.264) to the cylinder geometry in Fig. 2.10

$$\mathcal{S}_{\mathrm{CS}} = \frac{\sigma_{\mathrm{xy}}}{2} \int \mathrm{d}^3x \, f(x_2) \, \epsilon^{\mu\nu\rho} A_\mu \partial_\nu A_\rho \ . \tag{2.266}$$

[a] We neglect the description 'density' in the following.
[b] The nomenclature 'perpendicular' and 'parallel' defines the electric field direction with respect to the system's edges in $\mathbf{e}_1$-direction.

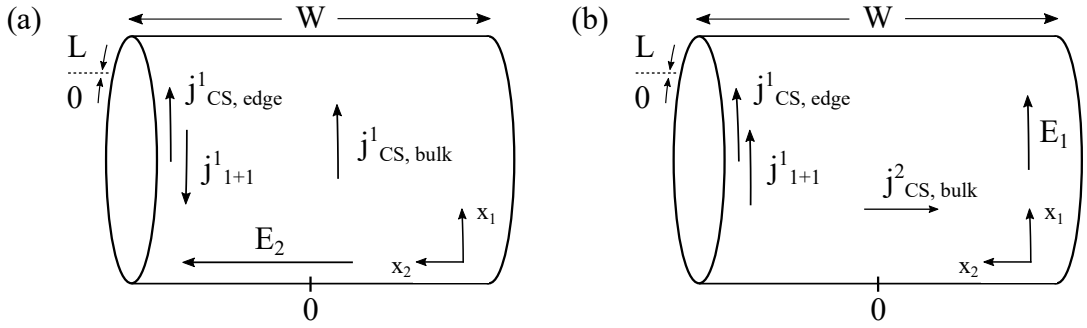

Figure 2.10: Cylinder geometry of a 2+1 dimensional bulk Chern-Simons theory including 1+1 dimensional chiral edge channels. The cylinder has a circumference L and a width W. Subfigures (a) and (b) correspond to different applied electric field configurations: **(a)** Perpendicular electric field, **(b)** Parallel electric field[b]. The assosiated bulk Chern-Simons currents are encoded by $j^\mu_{\text{CS, bulk/edge}}$, whereas the response of the chiral edge theory is described by the currents j^μ_{1+1}. Further explanations are given in the text.

The Chern-Simons current associated to this action is given by

$$\begin{aligned} j^\mu_{\text{CS}}(x) &= -\frac{\delta \mathcal{S}_{\text{CS}}}{\delta A_\mu(x)} = -\frac{\delta}{\delta A_\mu(x)} \left[\frac{\sigma_{\text{xy}}}{2} \int \mathrm{d}^3x'\, f(x'_2)\, \epsilon^{\lambda\kappa\zeta} A_\lambda \partial_\kappa A_\zeta \right] \\ &= \frac{\sigma_{\text{xy}}}{2} \int \mathrm{d}^3x'\, f(x'_2)\, \epsilon^{\lambda\kappa\zeta} \left[-\frac{\delta}{\delta A_\mu(x)} A_\lambda(x') \right] \partial_\kappa A_\zeta \\ &\quad - \frac{\sigma_{\text{xy}}}{2} \int \mathrm{d}^3x'\, \partial_\kappa \left[f(x'_2)\, \epsilon^{\lambda\kappa\zeta} A_\lambda \right] \left[-\frac{\delta}{\delta A_\mu(x)} A_\zeta(x') \right] . \end{aligned} \tag{2.267}$$

Here, we made use of a partial integration with a vanishing boundary term in the third line, since for abelian U(1) gauge fields $\epsilon^{\kappa\zeta} A_\kappa A_\zeta = 0$. Executing the functional derivatives in Eq. (2.267) in particular yields

$$\begin{aligned} j^\mu_{\text{CS}}(x) &= -\frac{\sigma_{\text{xy}}}{2} f(x_2)\, \epsilon^{\mu\kappa\zeta} \partial_\kappa A_\zeta + \frac{\sigma_{\text{xy}}}{2} \partial_\kappa \left[f(x_2)\, \epsilon^{\lambda\kappa\mu} A_\lambda \right] \\ &= -\frac{\sigma_{\text{xy}}}{2} f(x_2)\, \epsilon^{\mu\kappa\zeta} \partial_\kappa A_\zeta + \frac{\sigma_{\text{xy}}}{2} f(x_2)\, \epsilon^{\lambda\kappa\mu} \partial_\kappa A_\lambda + \frac{\sigma_{\text{xy}}}{2} \left[\partial_\kappa f(x_2) \right] \epsilon^{\lambda\kappa\mu} A_\lambda \\ &= -\frac{\sigma_{\text{xy}}}{2} f(x_2)\, \epsilon^{\mu\nu\rho} \partial_\nu A_\rho - \frac{\sigma_{\text{xy}}}{2} f(x_2)\, \epsilon^{\mu\kappa\lambda} \partial_\kappa A_\lambda + \frac{\sigma_{\text{xy}}}{2} \left[\partial_\kappa f(x_2) \right] \epsilon^{\kappa\mu\lambda} A_\lambda \\ &= -\sigma_{\text{xy}} f(x_2)\, \epsilon^{\mu\nu\rho} \partial_\nu A_\rho + \frac{\sigma_{\text{xy}}}{2} \left[\partial_2 f(x_2) \right] \epsilon^{2\mu\rho} A_\rho = j^\mu_{\text{CS, bulk}} + j^\mu_{\text{CS, edge}} \, . \end{aligned} \tag{2.268}$$

Notice that the edge current $\propto \partial_2 f(x_2)$ only arises in a Chern-Simons theory with boundaries. Since Eq. (2.266) is not (vector) gauge invariant due to the non-zero boundary contributions [cf. Eq. (2.170)], its electric current is locally not conserved at the edges of the sample:

$$\begin{aligned} \partial_\mu j^\mu_{\text{CS}} &= -\sigma_{\text{xy}} \left[\partial_\mu f(x_2) \right] \epsilon^{\mu\nu\rho} \partial_\nu A_\rho + \frac{\sigma_{\text{xy}}}{2} \left[\partial_2 f(x_2) \right] \epsilon^{2\mu\rho} \partial_\mu A_\rho \\ &= -\sigma_{\text{xy}} \left[\partial_2 f(x_2) \right] \epsilon^{2\nu\rho} \partial_\nu A_\rho + \frac{\sigma_{\text{xy}}}{2} \left[\partial_2 f(x_2) \right] \epsilon^{2\nu\rho} \partial_\nu A_\rho \\ &= -\frac{\sigma_{\text{xy}}}{2} \left[\partial_2 f(x_2) \right] \epsilon^{2\nu\rho} \partial_\nu A_\rho \, . \end{aligned} \tag{2.269}$$

In Sec. 2.6.4, we have shown that a bulk Chern-Simons term implies the existence of chiral

edge modes with chirality ± 1. Their effective action was derived in Sec. 2.6.6. In particular, we found [cf. Eq. (2.255)]

$$\mathcal{S}^{(2)}_{\text{eff},\pm} = \frac{\mathrm{e}^2}{8\pi} \int \mathrm{d}^2x \left[A_i \left(g^{il} - \left(g^{ik} \mp \epsilon^{ik} \right) \frac{\partial_k \partial_j}{\Box} \left(g^{jl} \pm \epsilon^{jl} \right) \right) A_l \right] . \tag{2.270}$$

Within this section roman indices do encode the 1+1 dimensional space-time coordinates, $\{i, j, k, l\} \in \{0, 1\}$, instead of the spatial coordinates of the underlying Minkowski metric.

A natural way to confine this action to the boundary of the 2+1 dimensional system considered is to generalize the chiral coupling in Eq. (2.270). The cylinder geometry in Fig. 2.10 defines two edge channels. In what follows, we are going to separately confine one chiral edge mode in Eq. (2.270) to each boundary of the cylinder. We are thus distinguishing between the left- and the right handed edge, without specifying their concrete localization. This confinement can be achieved mathematically by generalizing the chiral coupling in Eq. (2.270), such that

$$g^2_\pm(x_2) = \begin{cases} \mathrm{e}^2 \left| \partial_2 f_\mathrm{L}(x_2) \right| & \text{for left handed modes of chirality } +1 \\ \mathrm{e}^2 \left| \partial_2 f_\mathrm{R}(x_2) \right| & \text{for right handed modes of chirality } -1 \end{cases} . \tag{2.271}$$

The subscripts L and R define the left- and the right handed edges. The associated functions $f_{\mathrm{L,R}}$ are step functions which are constructed such that they match the system's confining function f [cf. Eq. (2.265)] at the left- and the right handed edge, respectively. Otherwise they remain constant, which gives rise to the definition

$$f_\mathrm{L} = f \;\big|_{\text{left handed edge}} \quad \wedge \quad f_\mathrm{L} = \text{const.} \;\big|_{\text{else}} , \tag{2.272}$$

$$f_\mathrm{R} = f \;\big|_{\text{right handed edge}} \quad \wedge \quad f_\mathrm{R} = \text{const.} \;\big|_{\text{else}} . \tag{2.273}$$

The concrete form of the confining function f in Eq. (2.265) in particular implies

$$\mathrm{sgn}\left[\partial_2 f_\mathrm{L}(x_2)\right] = -\mathrm{sgn}\left[\partial_2 f_\mathrm{R}(x_2)\right] , \tag{2.274}$$

$$\partial_2 f(x_2) = \partial_2 f_\mathrm{L}(x_2) + \partial_2 f_\mathrm{R}(x_2) . \tag{2.275}$$

As stated, the generalized chiral coupling in Eq. (2.271) allows us to attach modes of chirality $+1$ and -1 to the left- and to the right handed edge of our sample, respectively:

$$\mathcal{S}^{(2)}_{\text{eff},\pm} = \frac{1}{8\pi} \int \mathrm{d}^3x \, g^2_\pm(x_2) \left[A_i \left(g^{il} - \left(g^{ik} \mp \epsilon^{ik} \right) \frac{\partial_k \partial_j}{\Box} \left(g^{jl} \pm \epsilon^{jl} \right) \right) A_l \right] . \tag{2.276}$$

The associated edge currents are given by [cf. Eq. (2.256)]

$$j^i_\pm = -\frac{g^2_\pm(x_2)}{4\pi} \left[g^{il} - \left(g^{ik} \mp \epsilon^{ik} \right) \frac{\partial_k \partial_j}{\Box} \left(g^{jl} \pm \epsilon^{jl} \right) \right] A_l . \tag{2.277}$$

As we have shown in Eq. (2.257), these current are not conserved as they have a divergence of

$$\partial_i j^i_\pm = \pm \frac{g^2_\pm(x_2)}{4\pi} \epsilon^{kl} \partial_k A_l . \tag{2.278}$$

So neither the bulk Chern-Simons-, nor the chiral edge currents are locally conserved. In order to characterize a well-defined theory this property needs to be satisfied by the system's entire current:

$$j^\mu_\text{tot} = j^\mu_\text{CS} + j^\mu_\mathrm{L} + j^\mu_\mathrm{R} = 0 , \tag{2.279}$$

with $j^\mu_{\mathrm{L/R}} = \delta^\mu{}_i j^i_\pm$. In what follows, we assume that the bulk Chern-Simons theory is characterized by the Chern number $\mathcal{C} = \mathrm{sgn}(\partial_2 f_\mathrm{L}) = \pm 1$, which corresponds to ($\hbar = 1$)

$$\sigma_{\mathrm{xy}} = \mathrm{sgn}(\partial_2 f_\mathrm{L}) \frac{\mathrm{e}^2}{2\pi} = \mathrm{sgn}(\partial_2 f_\mathrm{L}) \frac{\mathrm{e}^2}{2\pi\hbar} = \mathrm{sgn}(\partial_2 f_\mathrm{L}) \frac{\mathrm{e}^2}{\mathrm{h}} \ . \tag{2.280}$$

This is for instance the conductivity of a single spin-polarized Landau level in a quantum Hall sample [cf. Eq. (2.34)], or the off-diagonal response of a QAH insulator in the system's bulk gap [cf. Eq. (1.1)]. The $\mathrm{sgn}(\partial_2 f_\mathrm{L})$ dependence is required for a consistent relation between the direction of the magnetic field and the associated chiralities at each spatial boundary of our system, which can be most easily understood by analyzing the corresponding cyclotron orbits. Therefore, we are in the following considering a system with a single filled 'Landau-level' in the bulk spectrum, as well as chiral edge movers at the boudaries of the sample. For such a system the divergence of the entire current is given by:

$$\begin{aligned}
\partial_\mu j^\mu_{\mathrm{tot}} &= \partial_\mu j^\mu_{\mathrm{CS}} + \partial_\mu j^\mu_\mathrm{L} + \partial_\mu j^\mu_\mathrm{R} \qquad (2.281)\\
&= -\frac{\sigma_{\mathrm{xy}}}{2} \left(\partial_2 f\right) \epsilon^{2\zeta\nu} \partial_\zeta A_\nu + \frac{\mathrm{e}^2}{4\pi} |\partial_2 f_\mathrm{L}| \epsilon^{kl} \partial_k A_l - \frac{\mathrm{e}^2}{4\pi} |\partial_2 f_\mathrm{R}| \epsilon^{kl} \partial_k A_l \\
&= -\frac{\sigma_{\mathrm{xy}}}{2} \left(\partial_2 f_\mathrm{L} + \partial_2 f_\mathrm{R}\right) \epsilon^{2\zeta\nu} \partial_\zeta A_\nu + \frac{\mathrm{e}^2}{4\pi} |\partial_2 f_\mathrm{L}| \epsilon^{kl} \partial_k A_l - \frac{\mathrm{e}^2}{4\pi} |\partial_2 f_\mathrm{R}| \epsilon^{kl} \partial_k A_l \\
&= -\frac{\mathrm{e}^2}{4\pi} \left(|\partial_2 f_\mathrm{L}| - |\partial_2 f_\mathrm{R}|\right) \epsilon^{2\zeta\nu} \partial_\zeta A_\nu + \frac{\mathrm{e}^2}{4\pi} |\partial_2 f_\mathrm{L}| \epsilon^{kl} \partial_k A_l - \frac{\mathrm{e}^2}{4\pi} |\partial_2 f_\mathrm{R}| \epsilon^{kl} \partial_k A_l = 0 \ ,
\end{aligned}$$

where we made use of the Eqs. (2.274) and (2.280) in the last line. Consequently, the system's entire current is a locally conserved and therefore a well-defined quantity.

Now that we have shown how the gauge anomaly of a bulk Chern-Simons theory gets canceled by the associated chiral edge modes, let us analyze the system's total electric charge current as a response to the two constant electric field configurations which are shown in Fig. 2.10:

$$\text{(a)}: \quad E_2 = -\partial_2 A_0(x_2) \quad \wedge \quad A_1 = A_2 = 0 \ , \tag{2.282}$$

$$\text{(b)}: \quad E_1 = -\partial_1 A_0(x_1) \quad \wedge \quad A_1 = A_2 = 0 \ . \tag{2.283}$$

Let us first calculate the Chern-Simons currents as a response to these field configurations. According to Eq. (2.268), this response is in general given by

$$j^\mu_{\mathrm{CS}} = -\sigma_{\mathrm{xy}} f(x_2)\, \epsilon^{\mu\nu\rho} \partial_\nu A_\rho + \frac{\sigma_{\mathrm{xy}}}{2} \left[\partial_2 f(x_2)\right] \epsilon^{2\mu\rho} A_\rho \ .$$

For $A_1 = A_2 = 0$, this expression implies the following Chern-Simons current in $\mathbf{e}_1$-direction

$$\begin{aligned}
j^1_{\mathrm{CS}} &= -\sigma_{\mathrm{xy}} f(x_2) \epsilon^{1\nu 0} \partial_\nu A_0 + \frac{\sigma_{\mathrm{xy}}}{2} \left[\partial_2 f(x_2)\right] \epsilon^{210} A_0 \qquad (2.284)\\
&= -\sigma_{\mathrm{xy}} f(x_2) \epsilon^{120} \partial_2 A_0 + \frac{\sigma_{\mathrm{xy}}}{2} \left[\partial_2 f(x_2)\right] \epsilon^{210} A_0 \\
&= -\sigma_{\mathrm{xy}} f(x_2) \partial_2 A_0 - \frac{\sigma_{\mathrm{xy}}}{2} \left[\partial_2 f(x_2)\right] A_0 \ .
\end{aligned}$$

We consequently found the subsequent expressions for the two field configurations (a) and (b):

$$\begin{aligned}
\text{(a)}: \quad j^1_{\mathrm{CS}} &= -\sigma_{\mathrm{xy}} f(x_2) \partial_2 A_0(x_2) - \frac{\sigma_{\mathrm{xy}}}{2} \left[\partial_2 f(x_2)\right] A_0(x_2) \qquad (2.285)\\
&= \sigma_{\mathrm{xy}} f(x_2) E_2 - \frac{\sigma_{\mathrm{xy}}}{2} \left[\partial_2 f(x_2)\right] A_0(x_2) \ ,
\end{aligned}$$

$$\text{(b)}: \quad j^1_{\mathrm{CS}} = -\sigma_{\mathrm{xy}} f(x_2) \partial_2 A_0(x_1) - \frac{\sigma_{\mathrm{xy}}}{2} \left[\partial_2 f(x_2)\right] A_0(x_1) \tag{2.286}$$

$$= -\frac{\sigma_{\rm xy}}{2} \left[\partial_2 f(x_2)\right] A_0(x_1) \ .$$

Analogously, for $A_1 = A_2 = 0$, one obtains the Chern-Simons current in $\mathbf{e}_2$-direction

$$j^2_{\rm CS} = -\sigma_{\rm xy} f(x_2) \epsilon^{210} \partial_1 A_0 + \frac{\sigma_{\rm xy}}{2} \left[\partial_2 f(x_2)\right] \epsilon^{220} A_0 = \sigma_{\rm xy} f(x_2) \partial_1 A_0 \ , \tag{2.287}$$

which implies to the corresponding dependencies:

$$\text{(a)}: \quad j^2_{\rm CS} = \sigma_{\rm xy} f(x_2) \partial_1 A_0(x_2) = 0 \ , \tag{2.288}$$

$$\text{(b)}: \quad j^2_{\rm CS} = \sigma_{\rm xy} f(x_2) \partial_1 A_0(x_1) = -\sigma_{\rm xy} f(x_2) E_1 \ . \tag{2.289}$$

In contrast, the time component of the Chern-Simons current in Eq. (2.284) vanishes for both field configurations, as

$$\text{(a)} \wedge \text{(b)}: \quad j^0_{\rm CS} = -\sigma_{\rm xy} f(x_2) \epsilon^{0\nu 0} \partial_\nu A_0 + \frac{\sigma_{\rm xy}}{2} \left[\partial_2 f(x_2)\right] \epsilon^{200} A_0 = 0 \ . \tag{2.290}$$

Above, we have calculated the Chern-Simons response to the two electric field configurations in Eq. (2.282). Let us now evaluate the corresponding response of the chiral 1+1 dimensional edge modes in Eq. (2.276). The particular form of the chiral edge current as a response to a general gauge configuration has been derived in Eq. (2.277). In order to circumvent the problem of how the inverse D'Alambert operator acts on the vector potential, we proceed with the corresponding edge current in momentum space

$$j^i_\pm = -\frac{g^2_\pm(x_2)}{4\pi} \left[g^{il} - \left(g^{ik} \mp \epsilon^{ik}\right) \frac{p_k p_j}{p^2} \left(g^{jl} \pm \epsilon^{jl}\right) \right] A_l \ . \tag{2.291}$$

First, we calculate the form of this current in $\mathbf{e}_1$- as well as in $\mathbf{e}_0$-direction:

$$\begin{aligned}
j^1_\pm &= -\frac{g^2_\pm(x_2)}{4\pi} \left[g^{10} - \left(g^{1k} \mp \epsilon^{1k}\right) \frac{p_k p_j}{p^2} \left(g^{j0} \pm \epsilon^{j0}\right) \right] A_0 \qquad (2.292)\\
&= \frac{g^2_\pm(x_2)}{4\pi} \left(g^{1k} \mp \epsilon^{1k}\right) \frac{1}{p^2} \left(p_k p^0 \mp p_k p_1\right) A_0 \\
&= \frac{g^2_\pm(x_2)}{4\pi p^2} \left(g^{1k} \mp \epsilon^{1k}\right) \left(p_k p^0 \mp p_k p_1\right) A_0 = \frac{g^2_\pm(x_2)}{4\pi p^2} \left(p^1 p^0 \mp p^1 p_1 \mp \epsilon^{1k} p_k p^0 + \epsilon^{1k} p_k p_1\right) A_0 \\
&= \frac{g^2_\pm(x_2)}{4\pi p^2} \left(p^1 p^0 \mp p^1 p_1 \pm p_0 p^0 - p_0 p_1\right) A_0 = \frac{g^2_\pm(x_2)}{4\pi p^2} \left(\pm p_0 p^0 \mp p^1 p_1 - p_0 p_1 + p^1 p^0\right) A_0 \\
&= \frac{g^2_\pm(x_2)}{4\pi p^2} \left(\pm \left(p_0 p^0 - p^1 p_1\right) - p_0 p_1 - p_1 p_0\right) A_0 = \frac{g^2_\pm(x_2)}{4\pi p^2} \left(\pm \left(p_0 p_0 + p_1 p_1\right) - 2 p_1 p_0\right) A_0 \\
&= \frac{g^2_\pm(x_2)}{4\pi p^2} \left(\pm \left(p_0 p_0 + p_1 p_1 \mp 2 p_1 p_0\right)\right) A_0 = \frac{g^2_\pm(x_2)}{4\pi p^2} \left(\pm \left(p_0 \mp p_1\right)^2\right) A_0 \\
&= \pm \frac{g^2_\pm(x_2)}{4\pi} \frac{\left(p_0 \mp p_1\right)^2}{p_0^2 - p_1^2} A_0 = \pm \frac{g^2_\pm(x_2)}{4\pi} \frac{\left(p_0 \mp p_1\right)^2}{\left(p_0 + p_1\right)\left(p_0 - p_1\right)} A_0 = \pm \frac{g^2_\pm(x_2)}{4\pi} \frac{p_0 \mp p_1}{p_0 \pm p_1} A_0 \ ,
\end{aligned}$$

$$\begin{aligned}
j^0_\pm &= -\frac{g^2_\pm(x_2)}{4\pi} \left[g^{00} - \left(g^{0k} \mp \epsilon^{0k}\right) \frac{p_k p_j}{p^2} \left(g^{j0} \pm \epsilon^{j0}\right) \right] A_0 \qquad (2.293)\\
&= -\frac{g^2_\pm(x_2)}{4\pi} \left[1 - \frac{1}{p^2} \left(p^0 p^0 - \epsilon^{0k} \epsilon^{j0} p_k p_j \mp 2 \epsilon^{0k} p_k p^0\right) \right] A_0 \\
&= -\frac{g^2_\pm(x_2)}{4\pi} \left[1 - \frac{1}{p^2} \left(p^0 p^0 + p^1 p^1 \mp 2 p_1 p^0\right) \right] A_0
\end{aligned}$$

$$= -\frac{g_\pm^2(x_2)}{4\pi}\left[1 - \frac{1}{p^2}\left(p_0p_0 + p_1p_1 \mp 2p_1p_0\right)\right] A_0$$
$$= -\frac{g_\pm^2(x_2)}{4\pi}\left[1 - \frac{p_0 \mp p_1}{p_0 \pm p_1}\right] A_0 \ .$$

As a next step in our calculation, let us derive the field configurations (a) and (b) in momentum space. Due to the non-interacting vacuum of our theory at $x_0 = \pm\infty$, we need to adiabatically turn the gauge potential A_0 on and off. Mathematically this can be realized by introducing a perturbatively small positive number $0 < a \ll 1$, which we eventually remove by executing the corresponding limit. This in particular leads to the Fourier transformed gauge field configurations:

$$\text{(a)}: \quad A_0(x_0,x_1,x_2) = -x^2\,\mathrm{e}^{-a|x^0|} \quad \rightarrow \quad A_0(p_0,p_1,p_2) = \frac{2\mathrm{i}a\sqrt{2\pi}\delta(p_1)\delta'(p_2)}{a^2+p_0^2} \ , \tag{2.294}$$

$$\text{(b)}: \quad A_0(x_0,x_1,x_2) = -x^1\,\mathrm{e}^{-a|x^0|} \quad \rightarrow \quad A_0(p_0,p_1,p_2) = \frac{2\mathrm{i}a\sqrt{2\pi}\delta(p_2)\delta'(p_1)}{a^2+p_0^2} \ . \tag{2.295}$$

In order to derive the real-space current contribution for configuration (a), we insert Eq. (2.294) into Eqs. (2.292) and (2.293), and inverse the Fourier transformation:

$$\text{(a)}: \quad j_\pm^1 = \pm\frac{g_\pm^2(x_2)}{4\pi}\int\frac{\mathrm{d}p_0}{\sqrt{2\pi}}\frac{\mathrm{d}p_1}{\sqrt{2\pi}}\frac{\mathrm{d}p_2}{\sqrt{2\pi}}\,\frac{p_0\mp p_1}{p_0\pm p_1}\frac{2\mathrm{i}a\sqrt{2\pi}\delta(p_1)\delta'(p_2)}{a^2+p_0^2}\mathrm{e}^{-\mathrm{i}(p_0x^0+p_1x^1+p_2x^2)} \tag{2.296}$$
$$= \pm\frac{g_\pm^2(x_2)}{4\pi}\int\frac{\mathrm{d}p_0}{\sqrt{2\pi}}\frac{\mathrm{d}p_1}{\sqrt{2\pi}}\,\frac{p_0\mp p_1}{p_0\pm p_1}\frac{-2ax^2\delta(p_1)}{a^2+p_0^2}\mathrm{e}^{-\mathrm{i}(p_0x^0+p_1x^1)}$$
$$= \pm\frac{g_\pm^2(x_2)}{4\pi}\int\frac{\mathrm{d}p_0}{\sqrt{2\pi}}\,\frac{p_0}{p_0}\left(-x^2\right)\sqrt{\frac{2}{\pi}}\frac{a}{a^2+p_0^2}\mathrm{e}^{-\mathrm{i}(p_0x^0)}$$
$$= \pm\frac{g_\pm^2(x_2)}{4\pi}\left(-x^2\right)\int\frac{\mathrm{d}p_0}{\sqrt{2\pi}}\,\sqrt{\frac{2}{\pi}}\frac{a}{a^2+p_0^2}\mathrm{e}^{-\mathrm{i}(p_0x^0)} = \pm\frac{g_\pm^2(x_2)}{4\pi}\left(-x^2\right)\mathrm{e}^{-a|x^0|}$$
$$= \pm\frac{g_\pm^2(x_2)}{4\pi}A_0(x_0,x_2) \ ,$$

$$j_\pm^0 = -\frac{g_\pm^2(x_2)}{4\pi}\left[1-1\right]A_0(x_0,x_2) = 0 \ . \tag{2.297}$$

In the last line we made use of the explicit relation between Eqs. (2.292) and (2.293). Finally, in the limit $a \rightarrow 0$, we find the contribution

$$j_+^1 + j_-^1 = \frac{\mathrm{e}^2}{4\pi}\left[|\partial_2 f_\mathrm{L}| - |\partial_2 f_\mathrm{R}|\right]A_0(x_2) \ . \tag{2.298}$$

To derive the real-space current contribution for configuration (b), we insert Eq. (2.295) into Eqs. (2.292) and (2.293), and subsequently inverse the Fourier transformation. For the current in $\mathbf{e}_1$-direction this implies

$$j_\pm^1 = \pm\frac{g_\pm^2(x_2)}{4\pi}\int\frac{\mathrm{d}p_2}{\sqrt{2\pi}}\frac{\mathrm{d}p_1}{\sqrt{2\pi}}\frac{\mathrm{d}p_0}{\sqrt{2\pi}}\,\frac{p_0\mp p_1}{p_0\pm p_1}\frac{2\mathrm{i}a\sqrt{2\pi}\delta(p_2)\delta'(p_1)}{a^2+p_0^2}\mathrm{e}^{-\mathrm{i}(p_0x^0+p_1x^1+p_2x^2)} \tag{2.299}$$
$$= \pm\frac{g_\pm^2(x_2)}{4\pi}\int\frac{\mathrm{d}p_1}{\sqrt{2\pi}}\frac{\mathrm{d}p_0}{\sqrt{2\pi}}\,\frac{p_0\mp p_1}{p_0\pm p_1}\frac{2\mathrm{i}a\delta'(p_1)}{a^2+p_0^2}\mathrm{e}^{-\mathrm{i}(p_0x^0+p_1x^1)}$$
$$= \pm\frac{g_\pm^2(x_2)}{4\pi}\left(-x^1\mathrm{e}^{-a|x^0|} \pm \frac{2}{a}\,\mathrm{sgn}(x^0)\left[1-\mathrm{e}^{-a|x^0|}\right]\right) \ .$$

In the limit $a \to 0$ this result should not have an explicit time dependence. However, this is not the case as

$$\lim_{a\to 0} \left(-x^1 \mathrm{e}^{-a|x^0|} \pm \frac{2}{a} \operatorname{sgn}(x^0) \left[1 - \mathrm{e}^{-a|x^0|} \right] \right) \quad = \pm 2x^0 - x^1 \ . \tag{2.300}$$

This property results from the ambiguity of our differential operator. If we find a function ϕ, satisfying the differential equation (Differential operator $\mathcal{D}$)

$$\mathcal{D}\phi = \varphi \ , \tag{2.301}$$

this function is ambiguous. We can always add zero modes ϕ_0 to ϕ, which does not change the outcome:

$$\mathcal{D}\phi_0 = 0 \quad \Rightarrow \quad \mathcal{D}(\phi + \phi_0) = \varphi \ . \tag{2.302}$$

Consequently, a differential operator which has zero modes cannot be inverted uniquely. A famous example is the D'Alambert operator, which leads to the retarded or advanced Green's function, depending on the boundary conditions chosen [109]. Here, our differential operator is given by $\mathcal{D} = \partial_0 \pm \partial_1$. Its zero modes are in particular given by ($c \in \mathbb{R}$)

$$\mathcal{D}\, c(x^0 \mp x^1) = c\,(\partial_0 x^0 \pm (\mp \partial_1 x^1)) = c\,(1-1) = 0 \ . \tag{2.303}$$

We can therefore get rid of the current's time dependence by adding the corresponding zero mode to our former result

$$\left(\pm 2x^0 - x^1 \right) \mp 2(x^0 \mp x^1) = x^1 \ . \tag{2.304}$$

The associated chiral edge currents for configuration (b) are thus given by

$$\begin{aligned} \text{(b)}: \quad j^1_\pm &= \pm \frac{g^2_\pm(x_2)}{4\pi} \left(x^1 \mathrm{e}^{-a|x^0|} \right) = \mp \frac{g^2_\pm(x_2)}{4\pi} (-x^1) \mathrm{e}^{-a|x^0|} \\ &= \mp \frac{g^2_\pm(x_2)}{4\pi} A_0(x_0, x_1) \ , \end{aligned} \tag{2.305}$$

$$j^0_\pm = -\frac{g^2_\pm(x_2)}{4\pi} \left[1 + 1 \right] A_0(x_0, x_1) \ . \tag{2.306}$$

In the last line we made use of the explicit relation between Eqs. (2.292) and (2.293). Finally, in the limit $a \to 0$, we find the current contributions

$$\text{(b)}: \quad j^1_+ + j^1_- = -\frac{\mathrm{e}^2}{4\pi} \left[|\partial_2 f_\mathrm{L}| - |\partial_2 f_\mathrm{R}| \right] A_0(x_1) \ , \tag{2.307}$$

$$j^0_+ + j^0_- = -\frac{\mathrm{e}^2}{2\pi} \left[|\partial_2 f_\mathrm{L}| + |\partial_2 f_\mathrm{R}| \right] A_0(x_1) \ . \tag{2.308}$$

Let us sum up all current contributions for the electric field configuration (a), which are given in Eqs. (2.285), (2.288), (2.290), (2.298), and (2.297):

$$\begin{aligned} j^1_\mathrm{tot} &= \sigma_\mathrm{xy} f(x_2) E_2 - \frac{\sigma_\mathrm{xy}}{2} \left[\partial_2 f \right] A_0(x_2) + \frac{\mathrm{e}^2}{4\pi} \left[|\partial_2 f_\mathrm{L}| - |\partial_2 f_\mathrm{R}| \right] A_0(x_2) \\ &= \sigma_\mathrm{xy} f(x_2) E_2 - \frac{\sigma_\mathrm{xy}}{2} \left[\partial_2 f_\mathrm{L} + \partial_2 f_\mathrm{R} \right] A_0(x_2) + \frac{\mathrm{e}^2}{4\pi} \left[|\partial_2 f_\mathrm{L}| - |\partial_2 f_\mathrm{R}| \right] A_0(x_2) \\ &= \sigma_\mathrm{xy} f(x_2) E_2 - \frac{\mathrm{e}^2}{4\pi} \left[|\partial_2 f_\mathrm{L}| - |\partial_2 f_\mathrm{R}| \right] A_0(x_2) + \frac{\mathrm{e}^2}{4\pi} \left[|\partial_2 f_\mathrm{L}| - |\partial_2 f_\mathrm{R}| \right] A_0(x_2) \\ &= \sigma_\mathrm{xy} f(x_2) E_2 \ . \end{aligned} \tag{2.309}$$

Here, we inserted Eq. (2.280) in the third line. The other two current contributions vanish in this field configuration

$$j^2_{\text{tot}} = 0 \quad \wedge \quad j^0_{\text{tot}} = 0 \ . \tag{2.310}$$

The corresponding current contributions for the electric field configuration (b) are given in Eqs. (2.286), (2.289), (2.290), (2.307), and (2.308). Together, these expressions give rise to the entire charge current

$$\begin{aligned} j^1_{\text{tot}} &= -\frac{\sigma_{\text{xy}}}{2} \left[\partial_2 f\right] A_0(x_1) - \frac{\text{e}^2}{4\pi} \left[|\partial_2 f_{\text{L}}| - |\partial_2 f_{\text{R}}|\right] A_0(x_1) \qquad (2.311) \\ &= -\frac{\text{e}^2}{4\pi} \left[|\partial_2 f_{\text{L}}| - |\partial_2 f_{\text{R}}|\right] A_0(x_1) - \frac{\text{e}^2}{4\pi} \left[|\partial_2 f_{\text{L}}| - |\partial_2 f_{\text{R}}|\right] A_0(x_1) \\ &= -\sigma_{\text{xy}} \left[\partial_2 f\right] A_0(x_1) \ , \\ j^2_{\text{tot}} &= -\sigma_{\text{xy}} f(x_2) E_1 \ , \qquad (2.312) \\ j^0_{\text{tot}} &= -\frac{\text{e}^2}{2\pi} \left[|\partial_2 f_{\text{L}}| + |\partial_2 f_{\text{R}}|\right] A_0(x_1) \ . \qquad (2.313) \end{aligned}$$

Here, we inserted Eq. (2.280) in the second and third line.

As expected, if we apply a constant electric field perpendicular to the boundaries of the system, we induce a parallel Chern-Simons bulk current as it is described by Eq. (2.309). In contrast, if we apply a constant electric field along the sample edges, we induce a parallel edge- [cf. Eq.(2.311)], as well as a perpendicular bulk Chern-Simons current [cf. Eq. (2.312)]. Notice, that the entire current is locally consevered, due to the Callan Harvey mechanism [131]:

$$\text{(a)} \quad \partial_\mu j^\mu_{\text{tot}} = \partial_0 j^0_{\text{tot}} + \partial_1 j^1_{\text{tot}} + \partial_2 j^2_{\text{tot}} = \partial_1 \left(\sigma_{\text{xy}} f(x_2) E_2\right) = 0 \ , \tag{2.314}$$

$$\begin{aligned} \text{(b)} \quad \partial_\mu j^\mu_{\text{tot}} &= \partial_1 \left(-\sigma_{\text{xy}} \left[\partial_2 f(x_2)\right] A_0(x_1)\right) + \partial_2 \left(-\sigma_{\text{xy}} f(x_2) E_1\right) \\ &= \sigma_{\text{xy}} \left[\partial_2 f(x_2)\right] E_1 - \sigma_{\text{xy}} \left[\partial_2 f(x_2)\right] E_1 = 0 \ . \qquad (2.315) \end{aligned}$$

The non-conservation of the Chern-Simons current is compensated by the non-conservation of the 1+1 dimensional edge theory. In Fig. 2.10, we schematically illustrated the single charge currents for both field configurations and showed how their edge contributions cancel-, or double each other.

We close this section by analyzing one more field configuration, which is in particular shown in Fig. 2.11.

The following discussion will be crucial to understand the main results in Sec. 3.3. It is the goal of the subsequent paragraphs to analyze the currents in our system as a response to an adiabatically increasing out-of-plane magnetic field $\mathbf{B}(x_0) = B(x_0)\mathbf{e}_3$ with field strength

$$B(x_0) = B_0 + b(x_0) \ . \tag{2.316}$$

Here, B_0 is a underlying static magnetic field which gives rise to a Landau level spectrum and $b(x_0)$ is a time-dependent contribution. In the Landau gauge [cf. Eq. (2.18)], this magnetic

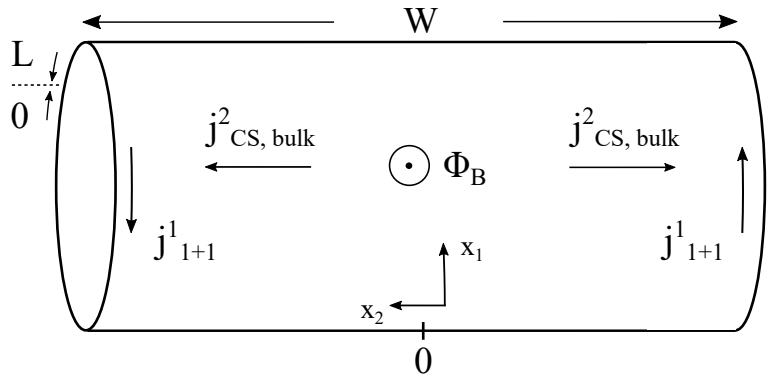

Figure 2.11: Cylinder geometry of a 2+1 dimensional bulk Chern-Simons theory including 1+1 dimensional chiral edge channels. The cylinder of circumference L and width W is penetrated by an adiabatically increasing out-of-plane magnetic flux Φ_B. The assosiated bulk Chern-Simons currents are encoded by $j^2_{\text{CS, bulk}}$, whereas the response of the chiral edge theory is described by the currents j^1_{1+1}. Further explanations are given in the text.

field can be described by the vector three-potential

$$A_\mu(x_0, x_2) = \begin{pmatrix} 0 \\ -x^2 B(x_0) \\ 0 \end{pmatrix} . \tag{2.317}$$

Due to Faraday's law, a time-dependent magnetic field comes along with an induced rotating electric field $\mathbf{E}$, as [99]

$$\nabla \times \mathbf{E} = -\frac{\partial \mathbf{B}}{\partial t} = -\frac{\partial \mathbf{b}}{\partial t} . \tag{2.318}$$

Together, electric- and magnetic fields are encoded by the system's field strength tensor

$$F_{\mu\nu} = \partial_\mu A_\nu - \partial_\nu A_\mu = \begin{pmatrix} 0 & E_1 & E_2 \\ -E_1 & 0 & B \\ -E_2 & -B & 0 \end{pmatrix} , \tag{2.319}$$

with c = 1 and

$$F_{01} = \partial_0 A_1 - \partial_1 A_0 = E_1 = -x^2 \partial_t B(x_0) = -x^2 \partial_t b(x_0) , \tag{2.320}$$
$$F_{02} = \partial_0 A_2 - \partial_2 A_0 = E_2 = 0 , \tag{2.321}$$
$$F_{12} = \partial_1 A_2 - \partial_2 A_1 = B(x_0) . \tag{2.322}$$

First let us calculate the bulk Chern-Simons currents according to Eq. (2.268)

$$\begin{aligned} j^0_{\text{CS, bulk}} &= -\sigma_{\text{xy}} f(x_2)\, \epsilon^{0\nu\rho} \partial_\nu A_\rho = -\sigma_{\text{xy}} f(x_2)\, \epsilon^{0ij} \partial_i A_j \\ &= -\sigma_{\text{xy}} f(x_2) F_{12} = -\sigma_{\text{xy}} f(x_2) B(x_0) , \end{aligned} \tag{2.323}$$
$$j^1_{\text{CS, bulk}} = -\sigma_{\text{xy}} f(x_2)\, \epsilon^{1\nu\rho} \partial_\nu A_\rho = +\sigma_{\text{xy}} f(x_2) F_{02} = 0 , \tag{2.324}$$
$$\begin{aligned} j^2_{\text{CS, bulk}} &= -\sigma_{\text{xy}} f(x_2)\, \epsilon^{2\nu\rho} \partial_\nu A_\rho = -\sigma_{\text{xy}} f(x_2) F_{01} \\ &= -\sigma_{\text{xy}} f(x_2) E_1 = \sigma_{\text{xy}} f(x_2) x^2 \partial_t b(x_0) . \end{aligned} \tag{2.325}$$

Moreover, according to Eq. (2.268) and $A_0 = A_2 = 0$, the edge Chern-Simons currents yield

$$j^0_{\text{CS, edge}} = +\frac{\sigma_{\text{xy}}}{2}\left[\partial_2 f(x_2)\right]\epsilon^{201}A_1 = -\frac{\sigma_{\text{xy}}}{2}\left[\partial_2 f(x_2)\right]x^2 B(x_0)\ , \tag{2.326}$$

$$j^1_{\text{CS, edge}} = +\frac{\sigma_{\text{xy}}}{2}\left[\partial_2 f(x_2)\right]\epsilon^{210}A_0 = 0\ , \tag{2.327}$$

$$j^2_{\text{CS, edge}} = +\frac{\sigma_{\text{xy}}}{2}\left[\partial_2 f(x_2)\right]\epsilon^{220}A_0 = 0\ . \tag{2.328}$$

The associated 1+1 dimensional edge currents, predicted by Eq. (2.291), are given by

$$j^i_{\pm} = -\frac{g^2_{\pm}(x_2)}{4\pi}\left[g^{i1} - \left(g^{ik} \mp \epsilon^{ik}\right)\frac{p_k p_j}{p^2}\left(g^{j1} \pm \epsilon^{j1}\right)\right]A_1\ . \tag{2.329}$$

This implies the following expressions in $\mathbf{e}_0$- as well as in $\mathbf{e}_1$-direction:

$$\begin{aligned} j^0_{\pm} &= -\frac{g^2_{\pm}(x_2)}{4\pi}\left[g^{01} - \left(g^{0k} \mp \epsilon^{0k}\right)\frac{p_k p_j}{p^2}\left(g^{j1} \pm \epsilon^{j1}\right)\right]A_1 \\ &= \frac{g^2_{\pm}(x_2)}{4\pi}\left(g^{0k} \mp \epsilon^{0k}\right)\frac{p_k p_j}{p^2}\left(g^{j1} \pm \epsilon^{j1}\right)A_1 \\ &= \frac{g^2_{\pm}(x_2)}{4\pi}\left(g^{1j} \mp \epsilon^{1j}\right)\frac{p_j p_k}{p^2}\left(g^{k0} \pm \epsilon^{k0}\right)A_1 \\ &= \frac{g^2_{\pm}(x_2)}{4\pi}\left(g^{1k} \mp \epsilon^{1k}\right)\frac{p_k p_j}{p^2}\left(g^{j0} \pm \epsilon^{j0}\right)A_1 = \pm\frac{g^2_{\pm}(x_2)}{4\pi}\frac{p_0 \mp p_1}{p_0 \pm p_1}A_1\ , \end{aligned} \tag{2.330}$$

$$\begin{aligned} j^1_{\pm} &= -\frac{g^2_{\pm}(x_2)}{4\pi}\left[g^{11} - \left(g^{1k} \mp \epsilon^{1k}\right)\frac{p_k p_j}{p^2}\left(g^{j1} \pm \epsilon^{j1}\right)\right]A_1 \\ &= \frac{g^2_{\pm}(x_2)}{4\pi}\left[1 + \frac{1}{p^2}\left(g^{1k} \mp \epsilon^{1k}\right)\left(p_k p^1 \pm p_k p_0\right)\right]A_1\ . \\ &= \frac{g^2_{\pm}(x_2)}{4\pi}\left[1 + \frac{1}{p^2}\left(p_k p^1 g^{1k} \mp p_k p^1 \epsilon^{1k} \pm p_k p_0 g^{1k} \mp \pm p_k p_0 \epsilon^{1k}\right)\right]A_1 \\ &= \frac{g^2_{\pm}(x_2)}{4\pi}\left[1 + \frac{1}{p^2}\left(p^1 p^1 \pm p_0 p^1 \pm p^1 p_0 + p_0 p_0\right)\right]A_1 \\ &= \frac{g^2_{\pm}(x_2)}{4\pi}\left[1 + \frac{1}{p^2}\left(p_1 p_1 \mp 2p_0 p_1 + p_0 p_0\right)\right]A_1\ . \\ &= \frac{g^2_{\pm}(x_2)}{4\pi}\left[1 + \frac{(p_0 \mp p_1)^2}{(p_0 + p_1)(p_0 - p_1)}\right]A_1 = \frac{g^2_{\pm}(x_2)}{4\pi}\left[1 + \frac{p_0 \mp p_1}{p_0 \pm p_1}\right]A_1\ , \end{aligned} \tag{2.331}$$

where we used Eq. (2.292) in the fifth equality. Analogously to the calculation in Eq. (2.296), we obtain the associated real-space expressions

$$j^0_{\pm} = \pm\frac{g^2_{\pm}(x_2)}{4\pi}A_1(x_0, x_2) \quad \wedge \quad j^1_{\pm} = \frac{g^2_{\pm}(x_2)}{4\pi}\left[1 + 1\right]A_1(x_0, x_2)\ , \tag{2.332}$$

and hence

$$j^0_+ + j^0_- = \frac{\mathrm{e}^2}{4\pi}\left(|\partial_2 f_{\text{L}}| - |\partial_2 f_{\text{R}}|\right)A_1\ , \tag{2.333}$$

$$j^1_+ + j^1_- = \frac{\mathrm{e}^2}{2\pi}\left(|\partial_2 f_{\text{L}}| + |\partial_2 f_{\text{R}}|\right)A_1\ . \tag{2.334}$$

We therefore found the following currents in our cylinder geometry as a response to an

adiabatically increasing out-of-plane magnetic field $\mathbf{B}(x_0)$:

$$j^1_{\text{tot}} = \frac{\mathrm{e}^2}{2\pi}\left[|\partial_2 f_{\text{L}}| + |\partial_2 f_{\text{R}}|\right] A_1 \ , \tag{2.335}$$

$$j^2_{\text{tot}} = -\sigma_{\text{xy}} f(x_2) E_1 = \sigma_{\text{xy}} f(x_2) x^2 \partial_t b(x_0) \ , \tag{2.336}$$

$$\begin{aligned} j^0_{\text{tot}} &= -\sigma_{\text{xy}} f(x_2) B(x_0) + \frac{\sigma_{\text{xy}}}{2}\left[\partial_2 f(x_2)\right] A_1 + \frac{\mathrm{e}^2}{4\pi}\left[|\partial_2 f_{\text{L}}| - |\partial_2 f_{\text{R}}|\right] A_1 \\ &= -\sigma_{\text{xy}} f(x_2) B(x_0) + \frac{\sigma_{\text{xy}}}{2}\left[\partial_2 f(x_2)\right] A_1 + \frac{\sigma_{\text{xy}}}{2}\left[\partial_2 f(x_2)\right] A_1 \\ &= -\sigma_{\text{xy}} f(x_2) B(x_0) + \sigma_{\text{xy}}\left[\partial_2 f(x_2)\right] A_1 \ , \end{aligned} \tag{2.337}$$

where we inserted Eq. (2.280) in the fourth equality. Let us make a few comments regarding Eqs. (2.335)-(2.337). First, the system's entire current is locally conserved as

$$\begin{aligned} \partial_\mu j^\mu_{\text{tot}} =& \partial_0\left(-\sigma_{\text{xy}} f(x_2) B(x_0) + \sigma_{\text{xy}}\left[\partial_2 f(x_2)\right] A_1\right) + \partial_2\left(-\sigma_{\text{xy}} f(x_2) E_1(x_2)\right) \\ =& -\sigma_{\text{xy}} f(x_2)\partial_0 B(x_0) + \sigma_{\text{xy}}\left[\partial_2 f(x_2)\right] E_1 \\ & - \sigma_{\text{xy}}\left[\partial_2 f(x_2)\right] E_1(x_2) - \sigma_{\text{xy}} f(x_2)\left[\partial_2 E_1(x_2)\right] \\ =& -\sigma_{\text{xy}} f(x_2)\partial_0 b(x_0) - \sigma_{\text{xy}} f(x_2)\left[-\partial_0 b(x_0)\right] = 0 \ . \end{aligned} \tag{2.338}$$

Second, Eq. (2.337) encodes an (anomalous) inflow/outflow of charge carriers from the bulk to the edges of the sample, or vice versa, dependent on $\text{sgn}(\sigma_{\text{xy}})$ and the direction of the applied magnetic field. Especially the U(1) vector gauge anomalies of the single bulk- and edge theories cancel each other. This procedure is known as the Callan-Harvey mechanism [131]. Moreover, let us emphasize that the bulk charge encoded in Eq. (2.337) is consistent with the well-known Streda formula [106]

$$j^0_{\text{bulk}} = -\sigma_{\text{xy}} B \ . \tag{2.339}$$

Third, we schematically visualized all real-space current contributions in Eqs. (2.335) and (2.336) in Fig. 2.11. We will in particular use this figure to supplement the discussion of our results in Sec. 3.3.

2.6.8 Field Theoretical Approach to the Quantum Hall Effect

In the previous sections we have introduced the mathematical framework of Chern-Simons field theories [cf. Sec. 2.6.4], as well as the concept of the parity- and the chiral anomaly [cf. Secs. 2.6.3 and 2.6.6] in 2+1 dimensional systems with 1+1 dimensional boundaries. Based on these concepts, we are now going to describe the quantum Hall effect, which we introduced in Sec. 2.2, from a quantum field theoretic perspective. While our discussion will roughly follow Ref.[132], we are recommending the Refs. [39, 133–136] for a more detailed discussion.

As we have explained in Sec. 2.2, a conventional quantum Hall system originates from two-dimensional electron gases which are confined to 2+1 space-time dimensions. As a function of the magnetic field those systems show quantized Hall plateaus in their off-diagonal conductivity σ_{xy} for low temperatures [cf. Fig. 2.2]. In general, the Lagrangian of a quantum Hall sample is defined via a Legendre transformation of the corresponding Pauli Hamiltonian $\mathcal{H}_{\text{P}}$ [cf. Eq (2.29)]:

$$\mathcal{L}_{\text{QH}} = \psi^\dagger\left(\mathrm{i}\partial_0 + \mu - \mathcal{H}_{\text{P}}[A]\right)\psi \ , \tag{2.340}$$

with $\psi = (\psi_\uparrow, \psi_\downarrow)^{\mathrm{T}}$, $B = \epsilon^{ij}\partial_i A_j$ and

$$\mathcal{H}_{\mathrm{P}}[A] = \frac{1}{2m^*}(\mathrm{i}\boldsymbol{\nabla} + \mathrm{e}\mathbf{A})^2 - g^*\mu_{\mathrm{B}}\frac{\sigma_3}{2}B \ . \tag{2.341}$$

Here, μ is the chemical potential, σ_3 is the third Pauli matrix, $\mu_{\mathrm{B}} = \mathrm{e}\hbar/(2m_{\mathrm{e}})$ is the Bohr magneton, and m^* as well as g^* are the system's effective mass parameter and g-factor. While the first term in Eq. (2.341) encodes the kinetic energy of the two-dimensional electron gas, the second term defines the corresponding Zeeman spin-splitting [cf. Sec. 2.2.4].

The eigenvalues of the Pauli Hamiltonian in Eq. (2.341) are the spin-splitted Landau levels which we have derived in Eq. (2.29). With $\lambda \in \mathbb{N}_0$ and $\sigma_\pm = \pm 1/2$, their energy values are given by

$$E_\lambda^\pm = \hbar\omega_B\left(\lambda + \frac{1}{2}\right) - g^*\mu_{\mathrm{B}}\frac{\sigma_\pm}{2}B \ , \tag{2.342}$$

where $\omega_B = |\mathrm{e}B|/m^*$ is the cyclotron frequency. In what follows, we are going to derive the effective action of the quantum Hall system considered. In the Secs. 2.6.3 and 2.6.6 we have achieved this goal by calculating the generating functional or, equivalently, the fermion determinant perturbatively [cf. Eq. (2.121)]

$$Z[A] = \frac{1}{Z[0]}\int \mathrm{d}\psi\mathrm{d}\psi^\dagger \ \exp\left[\mathrm{i}\int \mathrm{d}^3x \ \mathcal{L}_{\mathrm{QH}}\right] = \frac{\det\left(\mathrm{i}\partial_0 + \mu - H_{\mathrm{P}}[A]\right)}{\det\left(\mathrm{i}\partial_0 + \mu - H_{\mathrm{P}}[0]\right)} = \mathrm{e}^{\mathrm{i}S_{\mathrm{eff}}^{\mathrm{QH}}} \ . \tag{2.343}$$

$$\tag{2.344}$$

In the scope of the present section we make use of the results which we derived in Sec. 2.2 and evaluate the second order effective action by calculating the systems charge bubble instead of the vacuum polarization operator. In general, Landau levels of energy $E_\lambda^\pm$ are occupied by electronic states if $\mu > E_\lambda^\pm$ or, equivalently, if

$$\mu_\pm = \mu + g^*\mu_{\mathrm{B}}\frac{\sigma_\pm}{2}B > \hbar\omega_B\left(\lambda + \frac{1}{2}\right) \ . \tag{2.345}$$

The amount of occupied spin-up or spin-down Landau levels $N_{\mathrm{LL}}^\pm \in \mathbb{N}$ is therefore given by

$$N_{\mathrm{LL}}^\pm = \left[\frac{\mu_\pm}{\hbar\omega_B} + \frac{1}{2}\right]_{\mathrm{int}} \ , \tag{2.346}$$

where the bracket $[\ldots]_{\mathrm{int}}$ defines the integral part of its argument. In Eq. (2.23), we have further derived that every spin polarized Landau level has a degeneracy

$$\mathbb{D} = \frac{|\mathrm{e}B|A}{2\pi\hbar} \ , \tag{2.347}$$

where A is the system's area. The entire bulk charge density of a quantum Hall system is therefore given by (for $\hbar = 1$)

$$j^0 = -\mathrm{e}\frac{|\mathrm{e}B|}{2\pi}(N_{\mathrm{LL}}^+ + N_{\mathrm{LL}}^-) = -\mathrm{sgn}(\mathrm{e}B)\frac{\mathrm{e}^2}{2\pi}(N_{\mathrm{LL}}^+ + N_{\mathrm{LL}}^-)B = -\sigma_{\mathrm{xy}}B \ . \tag{2.348}$$

Adiabatically increasing the underlying magnetic field $B\mathbf{e}_3 \to (B + \delta B)\,\mathbf{e}_3$ for a fixed chemical potential μ consequently leads to an anomalous in- or outflow of charge carriers, which is described by Streda's fomula [106]

$$\delta j^0 = -\sigma_{\mathrm{xy}}\delta B \ . \tag{2.349}$$

We have already analyzed the physical mechanism behind this process in Eq. (2.339). In contrast, if we fix the magnetic field $\mathbf{B}$ and apply an electric probing field $\mathbf{E}$ in $\mathbf{e}_1$-direction, we obtain the charge current density j^2 by multiplying Eq. (2.348) with the drift velocity $v_{\text{Drift}} = E_1/B$:

$$j^2 = -\text{sgn}(\text{e}B)\frac{\text{e}^2}{2\pi}(N_{\text{LL}}^+ + N_{\text{LL}}^-)E_2 = -\sigma_{\text{xy}}E_1 \ . \tag{2.350}$$

The three-current density j^μ is a vector under Lorentz transformations [cf. Sec. 2.4.3]. The knowledge of the charge density in Eq. (2.348) or the current density in Eq. (2.350) as response to the vector potential is therefore sufficient to deduce the system's effective action:

$$j^\mu = -\sigma_{\text{xy}}\epsilon^{\mu\nu\rho}\partial_\nu A_\rho = -\frac{\delta\mathcal{S}_{\text{eff}}^{\text{QH}}}{\delta A_\mu} \ . \tag{2.351}$$

The second order effective action $\mathcal{S}_{\text{eff}}^{\text{QH}}$ in particular defines a topological Chern-Simons field theory [cf. Sec. 2.6.4]

$$\mathcal{S}_{\text{eff}}^{\text{QH}} = \int \text{d}^3x\, \mathcal{L}_{\text{eff}}^{\text{QH}} = \frac{\sigma_{\text{xy}}}{2}\int \text{d}^3x\, \epsilon^{\mu\nu\rho}A_\mu\partial_\nu A_\rho \ . \tag{2.352}$$

Due to the Callan-Harvey mechanism in Sec. 2.6.7, we can explicitly construct the 1+1 dimensional chiral edge theory of the 2+1 dimensional quantum Hall system. To ensure a locally conserved charge current everywhere, the non-gauge invariance of the Chern-Simons action at the system's boundaries needs to be compensated by the corresponding edge theory. If we consider the cylinder geometry shown in Fig. 2.11 with periodic boundary conditions in $\mathbf{e}_1$-direction and a finite system size in $\mathbf{e}_2$-direction, this defines the 1+1 dimensional edge theory [cf. Eq. (2.227)]

$$\mathcal{S}_{1+1} = \sum_{s=\pm,n=1}^{N_{\text{LL}}^s}\left[\int\limits_{\substack{\text{left handed}\\ \text{edge}}} \text{d}^2x\ \bar{\chi}_{n,\text{L}}^s \text{i}\not{\partial}\chi_{n,\text{L}}^s + \int\limits_{\substack{\text{right handed}\\ \text{edge}}} \text{d}^2x\ \bar{\chi}_{n,\text{R}}^s \text{i}\not{\partial}\chi_{n,\text{R}}^s\right] , \tag{2.353}$$

consisting of the left- and the right handed edges modes $\chi_{n,\text{L/R}}^s$ of the n-th Landau level with spin $s/2$. These modes are located at the left- or at the right boundary of the system, depending on the sign of the magnetic field chosen and the sign of the effective mass parameter[a] [cf. Fig. 2.4(c)].

[a] While $m^* > 0$ corresponds to conduction band Landau levels with a positive curvature at the system's edges, $m^* < 0$ defines valance band Landau levels with a negative curvature at the system's edges.

3

Consequences of the Parity Anomaly in Condensed Matter Systems

Contents

3.1 Quantum Anomalous Hall & Chern Insulators

3.1.1 QAH Phase from two-dimensional Topological Insulators

The path towards finding the first experimental realization of a quantum anomalous Hall (QAH) insulator started with the prediction of a directly related topological phase of matter, namely the prediction of two-dimensional topological insulators. Such systems are invariant under time-reversal transformations [cf. Sec. 2.4.1] and form the so-called quantum spin Hall (QSH) phase. Roughly speaking, a QSH phase is described by two copies of Chern insulators with different (pseudo-)spin polarization, which are related by a time-reversal transformation. Consequently, they are characterized by a vanishing Hall conductivity σ_{xy}. Instead, they have a finite spin Hall conductivity $\sigma^{\mathrm{s}}_{\mathrm{xy}}$:

$$\sigma_{\mathrm{xy}} = \sigma^{+}_{\mathrm{xy}} + \sigma^{-}_{\mathrm{xy}} = 0 \ , \tag{3.1}$$

$$\sigma^{\mathrm{s}}_{\mathrm{xy}} = \sigma^{+}_{\mathrm{xy}} - \sigma^{-}_{\mathrm{xy}} = \pm 2\frac{\mathrm{e}^2}{\mathrm{h}} \ , \tag{3.2}$$

where the $\pm$ index characterizes the (pseudo-)spin up- and down polarization, respectively. The first theoretical prediction of a QSH insulator in two spatial dimensions goes back to C. L. Kane and E. J. Mele, who predicted such a phase in the two-dimensional material graphene [7, 137]. In Sec. 4.1.5, we give a pedagogical introduction into graphene's band-structure and electronic properties. All we need to know for now is that in the presence of strong spin-orbit interactions the low-energy spectrum of graphene is described by two massive Dirac cones. These cones are located at the two high-symmetry points of graphene's honeycomb lattice structure, at the $\mathbf{K}$- and at the $\mathbf{K}'$-point, respectively [cf. Sec. 4.1.5]. Most remarkably, both of these Dirac cones are related by a time-reversal transformation, which in particular implies Eq. (3.1). However, it turned out that the mass gap in graphene is on the order off $\approx 10\mathrm{mK}$ [138], which makes an experimental observation of this predicted QSH phase exceptionally challenging.

Inspired by this idea, A. Bernevig, T. Hughes and S. Z. Zhang predicted another type of topological insulators in quantum wells made out of layered II-VI semiconductors [8]. In what follows, we discuss their theoretical predictions for (Hg,Cd)Te quantum wells. The subsequent analysis can also be transferred to different two-dimensional topological insulators like InAs/GaSb quantum wells [16], WTe_2 [139], and Bismuthene on a SiC substrate [140].

Fig. 3.1(A) shows the low-energy band-structure of HgTe and CdTe close to the Γ-point with $\mathbf{k} = 0$. As Hg is an extremely heavy element, it has a strong spin-orbit interaction and a large relativistic mass-velocity correction[a], which implies that the s-type Γ_6-band of HgTe is below its p-type Γ_8-band [141, 142]. For this reason HgTe shows a so-called inverted band-structure with a negative energy gap. In contrast, CdTe has a common band ordering as the Γ_8-band is energetically below the Γ_6-band. Figure 3.1(B) schematically shows the low-energy band-structure of a staggered (Hg,Cd)Te quantum well. In general, one distinguishes between two cases: (i) Below a critical quantum well thickness, for $d < d_{\mathrm{c}}$, the band-structure of CdTe mainly drives the band-structure of the quantum well. If we focus on the two lowest energy bands, the lowest electron-like band $|E_1\rangle$ is therefore energetically above the highest hole-like band $|H_1\rangle$. (ii) Above the critical value, for $d > d_{\mathrm{c}}$, the two lowest energy sub-bands invert

[a] The relativistic mass-velocity correction is defined as the first order correction to the conventional kinetic energy term $|\mathbf{p}|^2/(2m)$ in the non-relativistic limit of the Dirac dispersion:

$$\sqrt{|\mathbf{p}|^2\mathrm{c}_0^2 + m_{\mathrm{e}}^2\mathrm{c}_0^4} - m_{\mathrm{e}}\mathrm{c}_0^2 = |\mathbf{p}|^2/(2m) \underbrace{- |\mathbf{p}|^4/\left(8m^3\mathrm{c}_0^2\right)}_{\text{mass-velocity correction}} + \mathcal{O}\left(|\mathbf{p}|^6\right) \ . \tag{3.3}$$

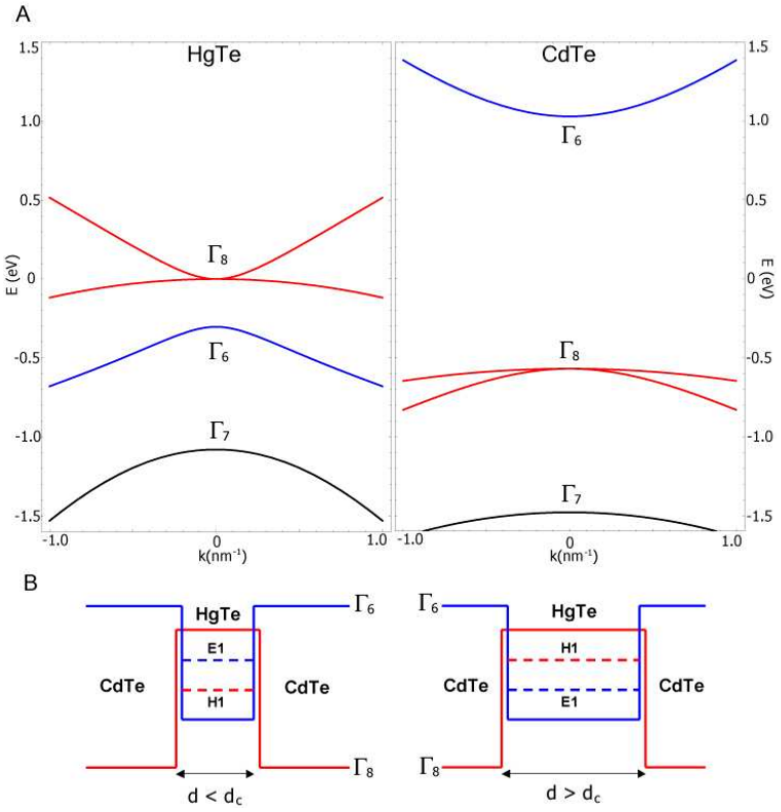

Figure 3.1: (**A**) Low-energy band-structure of HgTe and CdTe close to the Γ-point ($\mathbf{k} = 0$). (**B**) Schematic low-energy band-structure of a (Hg,Cd)Te quantum well in the trivial (left) and in the inverted (right) regime. The figure is reprinted from Ref. [8] with permission from the AAAS. Further explanations are given in the text.

and the QSH phase arises. For undoped (Hg,Cd)Te quantum wells, the critical thickness is given by $d_c = 6.3\,\mathrm{nm}$, as it is shown in Fig. 3.2 [8].

In the basis $(|E_1,+\rangle, |H_1,+\rangle, |E_1,-\rangle, |H_1,-\rangle)$, the low-energy physics of (Hg,Cd)Te quantum wells is described by the Bernevig-Hughes-Zhang (BHZ) Hamiltonian[a] [8]

$$\mathcal{H}_{\mathrm{BHZ}}(\mathbf{k}) = \begin{pmatrix} \mathcal{H}_+(\mathbf{k}) & 0 \\ 0 & \mathcal{H}_-(\mathbf{k}) \end{pmatrix} , \tag{3.4}$$

where $\mathcal{H}_-(\mathbf{k}) = \mathcal{H}_+^*(-\mathbf{k})$, and each (pseudo-)spin block is given by the Hamiltonian of a single Chern insulator

$$\mathcal{H}_+(\mathbf{k}) = \begin{pmatrix} \epsilon(\mathbf{k}) + M(\mathbf{k}) & Ak_+ \\ Ak_- & \epsilon(\mathbf{k}) - M(\mathbf{k}) \end{pmatrix} . \tag{3.5}$$

Here, $\epsilon(\mathbf{k}) = C - D|\mathbf{k}|^2$, $M(\mathbf{k}) = m - B|\mathbf{k}|^2$, $|\mathbf{k}|^2 = k_1^2 + k_2^2$, $k_\pm = k_1 \pm \mathrm{i}k_2$, and $A, B, C, D, m \in \mathbb{R}$ are material parameters characterizing the system's band-structure. Both Chern insulators, $\mathcal{H}_+(\mathbf{k})$ and $\mathcal{H}_-(\mathbf{k})$, are related by a time-reversal transformation [143]

$$U_{\mathcal{T}}^\dagger \mathcal{H}_+(\mathbf{k}) U_{\mathcal{T}} = \mathcal{H}_+^*(-\mathbf{k}) = \mathcal{H}_-(\mathbf{k}) , \tag{3.6}$$

[a] For the scope of this work, bulk inversion asymmetry terms are unimportant. Therefore, they are neglected throughout this thesis.

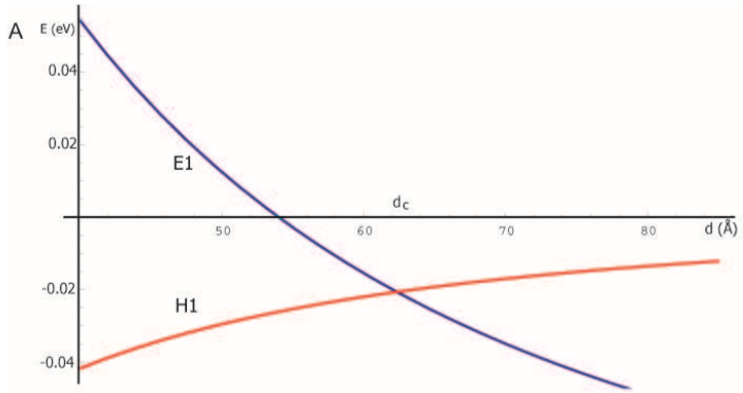

Figure 3.2: The energy of the lowest sub-bands in a pure (Hg,Cd)Te quantum well are shown as a function of the quantum well thickness d. For $d < d_c$ the lowest electron-like band $|E_1\rangle$ is energetically above the highest hole-like band $|H_1\rangle$. For $d > d_c$, the situation is vice versa. The latter phase characterizes the QSH regime. For pure (Hg,Cd)Te quantum wells, the critical quantum well thickness is given by $d_c = 6.3$nm. The figure is reprinted from Ref. [8] with permission from the AAAS.

where $U_{\mathcal{T}} = -\mathrm{i}\sigma_2\mathcal{K}$, and $\mathcal{K}$ is the operator of complex conjugation [143]. This makes the entire BHZ Hamiltonian in Eq. (3.4) time-reversal symmetric as

$$\tilde{U}_{\mathcal{T}}^{\dagger} H_{\mathrm{BHZ}}(\mathbf{k}) \tilde{U}_{\mathcal{T}} = \mathcal{H}_{\mathrm{BHZ}}(-\mathbf{k}) \ . \tag{3.7}$$

Here, the 4×4 time-reversal transformation associated to Eq. (3.4) is defined in terms of $\tilde{U}_{\mathcal{T}} = -\mathrm{i}\,(\tau_2 \otimes \sigma_0)\,\mathcal{K}$, where τ_2 is the second Pauli matrix acting on the (pseudo-)spin degree of freedom [143].
According to Eq. (3.4), two-dimensional topological insulators which are described by the BHZ Hamiltonian can be interpreted as two copies of Chern insulators. Each of those insulators comes along with a chiral edge state, as we have shown in Sec. 2.6.7. Hence, the BHZ Hamiltonian in Eq. (3.4) hosts helical edge modes which are protected from back-scattering by the underlying time-reversal symmetry in Eq. (3.7).

To construct a QAH from a QSH phase, one necessarily needs to break the time-reversal symmetry in order to obtain a finite Hall conductivity. In particular, one needs to invert the topological gap of one of the time-reversal-, so-called Kramer's partners [143]. Inspired by this idea, F. D. M. Haldane predicted the first QAH phase in graphene by using a special time-reversal odd mass term which opens the Dirac mass gaps at the **K**- and the **K′**-points in a parity-odd manner [25]. This induces a finite Chern number and thus a QAH phase. In Sec. 3.1.3, we further elaborate on the Haldane model and explain its relation to the parity anomaly. Up to date, the Haldane mass term has not yet been realized in crystalline structures. There exists however another theoretical prediction for a QAH phase which originates from two-dimensional topological insulators like (Hg,Cd)Te quantum wells. By magnetically doping such systems, one can invert the mass gap of one of the (pseudo)-spin polarized Chern insulators in Eq. (3.4) [42]. Additionally to the BHZ Hamilton, the magnetic dopants induce a finite energy splitting

$$\mathcal{H}_{\mathrm{g}} = \begin{pmatrix} g_{\mathrm{e}} & 0 & 0 & 0 \\ 0 & g_{\mathrm{h}} & 0 & 0 \\ 0 & 0 & -g_{\mathrm{e}} & 0 \\ 0 & 0 & 0 & -g_{\mathrm{h}} \end{pmatrix} , \tag{3.8}$$

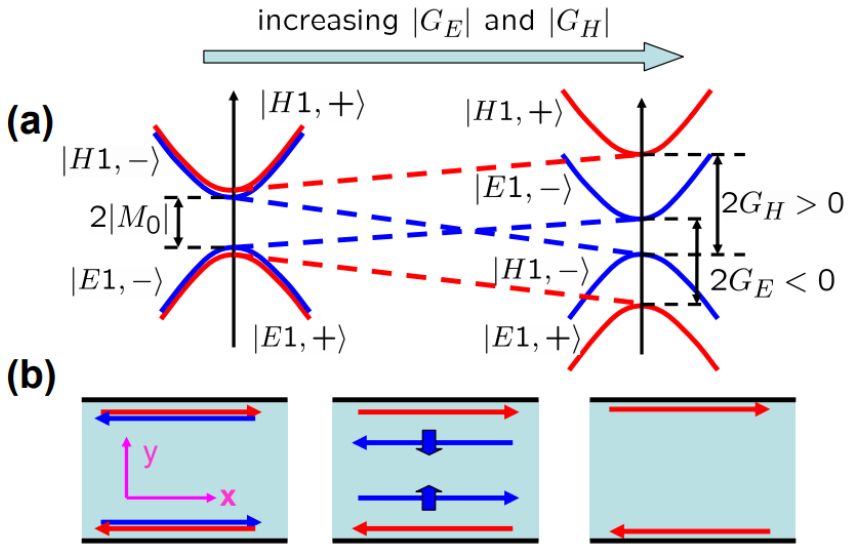

Figure 3.3: Schematic illustration of how to construct a QAH- from a QSH insulator by magnetically doping the system. The effective electron and hole g-factors $G_\mathrm{E} < 0$ and $G_\mathrm{H} > 0$ **(a)** invert the Dirac mass gap of one of the Chern insulators in the BHZ Hamiltonian (3.4) and, consequently, **(b)** fuse the associated chiral edge states. Thus, the system transforms from a QSH phase with helical edge states to a QAH phase with chiral edge modes. The figure is reprinted from Ref. [42] with permission from the APS.

where $g_{\mathrm{e,h}}$ are the effective electron and hole g-factors. As required, the entire Hamiltonian $\mathcal{H}_\mathrm{BHZ} + \mathcal{H}_\mathrm{g}$ breaks the time-reversal symmetry as

$$\tilde{U}_\mathcal{T}^\dagger \mathcal{H}_\mathrm{g} \tilde{U}_\mathcal{T} = -\mathcal{H}_\mathrm{g} \ . \tag{3.9}$$

Equation (3.8) most remarkably renormalizes the Dirac mass gap of the (pseudo-)spin polarized Chern insulators in Eq. (3.4) differently:

$$m_\pm = 2m \pm g_\mathrm{e} \mp g_\mathrm{h} \ . \tag{3.10}$$

Satisfying the conditions $g_\mathrm{e} g_\mathrm{h} < 0$ and

$$m_+ m_- < 0 \ , \tag{3.11}$$

leads to a mass gap inversion of only one of the Chern insulators, which drives the system into the QAH phase [42]. Schematically, this procedure is shown in Fig. 3.3. As one of the Chern insulators inverts its Dirac mass gap, the associated chiral edge state disappears. We mathematically describe the properties of such a system and further define its relation to the parity anomaly [cf. Sec. 2.5] in the subsequent sections.

Let us close this introduction to topological- and QAH insulators by giving one further remark. In (Hg,Cd)Te quantum wells the magnetic doping described by Eq. (3.8) is realized via Manganese dopants which are paramagnetic. As such, the QAH phase in these systems requires a small polarizing magnetic field. This directly raises the question: How does the topology of the magnetic field and the intrinsic band inversion interact in these systems. We answer this question in Sec. 3.3. Let us emphasize that this property is mainly related to QAH insulators based on (Hg,Cd)Te quantum wells. Hitherto, there are several predictions of the QAH phase in ferro-magnetically doped topological insulators, which do not require

a finite polarizing magnetic field. For instance, such phases where predicted and measured in Bi_2Te_3, Bi_2Se_3, and Sb_2Te_3 doped with Cr, Fe or Va [44–47]. The low-energy response of these systems can be described by the BHZ model, as well.

3.1.2 Hall Conductivity and Edge States of a Chern Insulator

In what follows, we are going to analyze a single (pseudo-)spin block of the BHZ Hamiltonian in Eq. (3.4). We have shown that each of these blocks is described by the Hamiltonian of a single 2+1 dimensional Chern insulator, which in the presence of magnetic doping [cf. Eq. (3.10)] can be written in three different forms

$$\mathcal{H}_\pm(\mathbf{k}) = \begin{pmatrix} \epsilon(\mathbf{k}) + M_\pm(\mathbf{k}) & \pm A k_\pm \\ \pm A k_\mp & \epsilon(\mathbf{k}) - M_\pm(\mathbf{k}) \end{pmatrix} = \epsilon(\mathbf{k})\sigma_0 \pm A(k_1\sigma_1 \mp k_2\sigma_2) + M_\pm(\mathbf{k})\sigma_3 \quad (3.12)$$

$$= \epsilon(\mathbf{k})\sigma_0 + \mathbf{d}_\pm \cdot \boldsymbol{\sigma} \ . \quad (3.13)$$

Here, $\epsilon(\mathbf{k}) = C - D|\mathbf{k}|^2$, $M_\pm(\mathbf{k}) = m_\pm - B|\mathbf{k}|^2$, $m_\pm = m \pm (g_\mathrm{e} - g_\mathrm{h})/2$, $|\mathbf{k}|^2 = k_1^2 + k_2^2$, $k_\pm = k_1 \pm \mathrm{i}k_2$, and $\mathbf{d}_\pm = (\pm A k_1, -A k_2, M_\pm(\mathbf{k}))^\mathrm{T}$. Moreover, $\boldsymbol{\sigma}$ is the vector of Pauli matrices. In the remaining part of this thesis, we set the diagonal and momentum independent term $C\sigma_0$ to zero as it only defines an energy off-set of the associated spectrum. It therefore does not influence any topological quantity.

Let us first compare the Chern insulator in Eq. (3.12) with the QED_{2+1} system which we have analyzed in Sec. 2.6. Analogously to the transformation rules of a massive QED_{2+1} system in Eq. (2.130), the Chern insulator in Eq. (3.12) breaks parity- and time-reversal symmetry for $m_\pm, B \neq 0$. With $U_\mathcal{P} = \sigma_2$ and $U_\mathcal{T} = -\mathrm{i}\sigma_2\mathcal{K}$ [143], one in particular obtains the transformation rules

$$U_\mathcal{P}^\dagger \mathcal{H}_\pm(k_1, k_2, m_\pm, B, D) U_\mathcal{P} = \mathcal{H}_\pm(-k_1, k_2, -m_\pm, -B, D) \ , \quad (3.14)$$

$$U_\mathcal{T}^\dagger \mathcal{H}_\pm(\mathbf{k}, m_\pm, B, D) U_\mathcal{T} = \mathcal{H}_\pm(-\mathbf{k}, -m_\pm, -B, D) \ . \quad (3.15)$$

Hence, both mass terms, the Dirac mass $m_\pm\sigma_3$ as well as the momentum dependent, so-called Newtonian mass $B|\mathbf{k}^2|\sigma_3$ are responsible for a broken parity- and time-reversal symmetry of a single Chern insulator. From this perspective, both terms should characterize the associated Hall conductivity. This will be shown in the following paragraphs.

The eigen-energies of the two-band model in Eq. (3.12) are given by

$$E_\pm^s(\mathbf{k}) = \epsilon(\mathbf{k}) + s\sqrt{A^2|\mathbf{k}|^2 + M_\pm^2(\mathbf{k})} \ , \quad (3.16)$$

where $s = \pm$ defines the valance and the conduction band, respectively. Moreover, the corresponding eigen-states are given by [50]

$$\phi_\pm^s(\mathbf{k}) = \begin{pmatrix} \dfrac{M_\pm(\mathbf{k}) + s\sqrt{A^2|\mathbf{k}|^2 + M_\pm(\mathbf{k})^2}}{\pm A k_\mp} \\ 1 \end{pmatrix} \ . \quad (3.17)$$

The Hall conductivity of the Chern insulator in Eq. (3.12) at a general chemical potential μ and a certain temperature T can be evaluated in terms of the Kubo Formula [50, 143]

$$\sigma_\mathrm{xy}^\pm(\mu, T) = \frac{\mathrm{e}^2}{2\hbar} \int \frac{\mathrm{d}^2\mathbf{k}}{(2\pi)^2} \frac{f_{k,\mathrm{c}}(\mu, T) - f_{k,\mathrm{v}}(\mu, T)}{d_\pm^3} \epsilon^{\alpha\beta\gamma} \left(\frac{\partial d_\alpha^\pm}{\partial k_1}\right) \left(\frac{\partial d_\beta^\pm}{\partial k_2}\right) d_\gamma^\pm \ , \quad (3.18)$$

where $d_\pm = |\mathbf{d}_\pm|$ is the norm of the $\mathbf{d}_\pm$-vector in Eq. (3.13) and $f_{k,\mathrm{c,v}}(\mu, T)$ encode the

Fermi-Dirac distribution functions in the conduction and in the valence band, respectively. Basically, Eq. (3.18) counts the winding of the mapping $\mathbf{d}_\pm(\mathbf{k}) : T^2 \to S^2$ from the periodic two-dimensional Brillouin zone, the torus T^2, to the two-sphere S^2. For zero temperatures and for chemical potentials in the Dirac mass gap the Fermi-Dirac distributions simplify to Heaviside-Theta functions and Eq. (3.18) evaluates to [43, 50]

$$\begin{aligned}\sigma_{\mathrm{xy}}^{\pm}(|\mu| < |m|, T = 0) &= \pm\frac{\mathrm{e}^2}{4\mathrm{h}} \int \mathrm{d}|\mathbf{k}|^2 \frac{A^2\left(\frac{m_\pm}{2} + B|\mathbf{k}|^2\right)}{\left(A^2|\mathbf{k}|^2 + \left(\frac{m_\pm}{2} - B|\mathbf{k}|^2\right)^2\right)^{3/2}} \\ &= \pm\frac{\mathrm{e}^2}{2\mathrm{h}}[\mathrm{sgn}(m_\pm) + \mathrm{sgn}(B)] \ . \end{aligned} \tag{3.19}$$

Notice, that the $D|\mathbf{k}|^2\sigma_0$ term in Eq. (3.12) does not influence the Hall conductivity as it is a diagonal contribution to the Hamiltonian. It is even under parity transformations [cf. Eq. (3.14)], but breaks the charge-conjugation symmetry of a single Chern insulator

$$U_{\mathcal{C}}^\dagger \mathcal{H}_\pm(\mathbf{k}, m_\pm, B, D) U_{\mathcal{C}} = -\mathcal{H}_\pm(-\mathbf{k}, m_\pm, B, -D) \ . \tag{3.20}$$

Here, we used that for the Hamiltonian in Eq. (3.12) $U_{\mathcal{C}} = \sigma_1 \mathcal{K}$ [143].

Let us make one more remark regarding the Dirac limit of Eq. (3.19). For $B = D = g_\mathrm{e} = g_\mathrm{h} = 0$, Eq. (3.12) defines a purely 2+1 dimensional Dirac Hamiltonian with Fermi velocity A and an energy offset C. In agreement with the quantum field theoretic calculations in Sec. 2.6.3, we obtain a half-quantized Hall conductivity for such a system in units of e^2/h:

$$\sigma_{\mathrm{xy}}(|\mu| < |m|, T = 0) = \pm\frac{\mathrm{e}^2}{2\mathrm{h}}\mathrm{sgn}(m) \ . \tag{3.21}$$

Hence, the $B|\mathbf{k}|^2$ term renormalizes the non-gauge invariant, half-quantized Hall conductivity of a single Dirac fermion [cf. Eq. (2.176)]. Most importantly, the $|\mathbf{k}|^2$ dependence implies that the $\mathbf{d}_\pm$-vector points in $-\mathrm{sgn}(B)\mathbf{e}_3$-direction for $|\mathbf{k}| \to \infty$. We can thus one-point compactify the $\mathbf{k}$-space at spatial infinity. For $\mathbf{k} = 0$ and $g_\mathrm{e} = g_\mathrm{h} = 0$ the $\mathbf{d}_\pm$-vector points in $\mathrm{sgn}(m)\mathbf{e}_3$-direction. Consequently, for $m/B > 0$ the $\mathbf{d}_\pm$-vector point in opposite $\mathbf{e}_3$-directions at $\mathbf{k} = 0$ and $|\mathbf{k}| \to \infty$. This implies a finite integer Hall conductivity in Eq. (3.19). In contrast, for $m/B < 0$ the $\mathbf{d}_\pm$-vector points in the same direction for $\mathbf{k} = 0$ and $|\mathbf{k}| \to \infty$, implying a vanishing Hall conductivity [49]. For a purely linear Dirac spectrum a compactification at $|\mathbf{k}| \to \infty$ is not possible. As a consequence, the Hall conductivity is half-quantized. In such a case both mass configurations $m \gtrless 0$ are topologically non-trivial as the winding of the $\mathbf{d}_\pm$-vector is not well-defined.

In the remaining part of this subsection, let us derive the edge theory of the Chern insulator in Eq. (3.12) from a solid state perspective. The subsequent analysis will go along the lines of the corresponding discussion in Ref. [49] and should serve as a complementary discussion regarding the quantum field theoretic considerations in Sec. 2.6.4. In what follows, we consider a semi-infinite two-dimensional space manifold with an one-dimensional edge at $x_1 = 0$. For $x_1 > 0$ the system is characterized by the Chern-insulator in Eq. (3.12), whereas for $x_1 < 0$ we consider a trivial vacuum.

In order to derive the topological edge states of such a geometry, we (partially) Fourier transform Eq. (3.12) to the real-space, as the momentum k_1 is not a well defined quantity anymore. The topological boundary along the $\mathbf{e}_2$-direction breaks the translation symmetry

in the $\mathbf{e}_1$-direction. For $k_1 \to -\mathrm{i}\partial_1$ this implies the Schrödinger equation [49]

$$\left[\mp \mathrm{i}A\partial_1\sigma_1 - Ak_2\sigma_2 + \left(m_\pm - Bk_2^2 + B\partial_1^2\right)\sigma_3\right]\phi(x_1,x_2) = E\phi(x_1,x_2) \ , \tag{3.22}$$

with the corresponding boundary conditions $\phi(x_1=0,x_2)=0$ and $\phi(x_1\to\infty,x_2)=0$. According to our analysis in Sec. 2.6.4, we know that the system under consideration has a chiral edge state with a linear dispersion in momentum k_2. Let us therefore first set $k_2=0$ and search for zero energy solutions of the second order differential Eq. (3.22). As the geometry under consideration is translation invariant in $\mathbf{e}_2$-direction, we are starting our calculation by evaluating the confinement of the edge modes in $\mathbf{e}_1$-direction by solving

$$\left[\mp \mathrm{i}A\partial_1\sigma_1 + \left(m_\pm + B\partial_1^2\right)\sigma_3\right]\psi_{\mathrm{edge}}^{k_2=0}(x_1) = 0 \ , \tag{3.23}$$

with the boundary conditions $\psi_{\mathrm{edge}}^{k_2=0}(x_1=0)=0$ and $\psi_{\mathrm{edge}}^{k_2=0}(x_1\to\infty)=0$. In order to find a normalizable eigen-state close to the topological boundary of our system, we make the ansatz:

$$\psi_{\mathrm{edge}}^{k_2=0}(x_1) \propto \mathrm{e}^{\lambda x_1}\xi \ , \tag{3.24}$$

where ξ is a two-component spinor and $\mathrm{Re}[\lambda]\in\mathbb{R}$ describes the decay of the wave-function with respect to the topological boundary. Inserting this ansatz into Eq. (3.23) and multiplying this equation with the third Pauli matrix σ_3 from the left, implies

$$\left[m_\pm + B\lambda^2\right]\xi \pm \left[A\lambda\sigma_2\right]\xi = 0 \ . \tag{3.25}$$

It is as such natural to define the spinor ξ as a σ_2 eigen-state with eigenvalue $\eta=\pm1$:

$$\sigma_2\xi_\eta = \eta\xi_\eta \ . \tag{3.26}$$

Inserting this definition into Eq. (3.25) eventually implies a conditional equation for λ:

$$B\lambda^2 \pm \eta A\lambda + m_\pm = 0 \quad \Rightarrow \quad \lambda_i(\eta) = \frac{1}{2B}\left(\mp\eta A - (-1)^i\sqrt{A^2-4Bm_\pm}\right) \ , \tag{3.27}$$

with $i\in\{1,2\}$, which satisfies the identity

$$\lambda_{1,2}(-1) = -\lambda_{2,1}(1) \ . \tag{3.28}$$

This eventually leads to the zero-energy edge-state solution of Eq. (3.23) [cf. Eq. (3.24)]

$$\psi_{\mathrm{edge}}^{k_2=0}(x_1) = \left[c_{+;1}\mathrm{e}^{\tilde{\lambda}_1x_1} + c_{+;2}\mathrm{e}^{\tilde{\lambda}_2x_1}\right]\xi_+ + \left[c_{-;1}\mathrm{e}^{-\tilde{\lambda}_1x_1} + c_{-;2}\mathrm{e}^{-\tilde{\lambda}_2x_1}\right]\xi_- \ , \tag{3.29}$$

where we introduced the prefactors $c_{\eta\,;\{1,2\}}\in\mathbb{C}$ and normalized the solutions for $\lambda_{1,2}(\eta)$ due to their symmetric property in Eq. (3.27)

$$\tilde{\lambda}_{1,2} = \lambda_{1,2}(1) \quad \wedge \quad -\tilde{\lambda}_{1,2} = \lambda_{2,1}(-1) \ . \tag{3.30}$$

We can further simplify Eq. (3.29) by making use of our specific boundary conditions. Since by definition ξ_+ and ξ_- are orthogonal spinors [cf. Eq. (3.29)], our first boundary condition $\psi_{\mathrm{edge}}^{k_2=0}(x_1=0)=0$ implies

$$c_{\eta\,;1} + c_{\eta\,;2} = 0 \ . \tag{3.31}$$

Under this condition Eq. (3.29) simplifies to

$$\begin{aligned}\psi_{\text{edge}}^{k_2=0}(x_1) &= c_{+;1}\left[\mathrm{e}^{\tilde{\lambda}_1 x_1} - \mathrm{e}^{\tilde{\lambda}_2 x_1}\right]\xi_+ + c_{-;1}\left[\mathrm{e}^{-\tilde{\lambda}_1 x_1} - \mathrm{e}^{-\tilde{\lambda}_2 x_1}\right]\xi_- \\ &= c_{+;1}\mathrm{e}^{\mp\frac{A}{2B}x_1}\left[\mathrm{e}^{\frac{\sqrt{A^2-4Bm_\pm}}{2B}x_1} - \mathrm{e}^{-\frac{\sqrt{A^2-4Bm_\pm}}{2B}x_1}\right]\xi_+ \\ &+ c_{-;1}\mathrm{e}^{\pm\frac{A}{2B}x_1}\left[\mathrm{e}^{-\frac{\sqrt{A^2-4Bm_\pm}}{2B}x_1} - \mathrm{e}^{\frac{\sqrt{A^2-4Bm_\pm}}{2B}x_1}\right]\xi_- \ .\end{aligned} \tag{3.32}$$

In combination with the orthogonality of ξ_+ and ξ_-, the second boundary condition at spatial infinity, $\psi_{\text{edge}}^{k_2=0}(x_1 \to \infty) = 0$, only allows two different cases: For the (pseudo)-spin up case we find

$$(i) \quad A/B > 0 \quad \wedge \quad c_{-;1} = 0 \ , \tag{3.33}$$

$$(ii) \quad A/B < 0 \quad \wedge \quad c_{+;1} = 0 \ , \tag{3.34}$$

whereas for the (pseudo)-spin up case we obtain

$$(i) \quad A/B < 0 \quad \wedge \quad c_{-;1} = 0 \ , \tag{3.35}$$

$$(ii) \quad A/B > 0 \quad \wedge \quad c_{+;1} = 0 \ . \tag{3.36}$$

However, all cases are accompanied by the topological criterion

$$\frac{m_\pm}{B} > 0 \ , \tag{3.37}$$

in order to ensure

$$\left|\sqrt{A^2 - 4Bm_\pm}\right| < |A| \ . \tag{3.38}$$

As a consequence, normalizable edge states do require a topologically non-trivial Chern insulator in Eq. (3.12) [cf. Eq. (3.19)]. For such a system, we eventually found the spin-polarized zero-energy edge states

$$(i) \quad \psi_{\text{edge}}^{k_2=0}(x_1) = c_{+;1}\left(\mathrm{e}^{\tilde{\lambda}_1 x_1} - \mathrm{e}^{\tilde{\lambda}_2 x_1}\right)\xi_+ \qquad \text{with} \quad A/B > 0 \ , \tag{3.39}$$

$$(ii) \quad \psi_{\text{edge}}^{k_2=0}(x_1) = c_{-;1}\left(\mathrm{e}^{-\tilde{\lambda}_1 x_1} - \mathrm{e}^{\tilde{\lambda}_2 x_1}\right)\xi_- \qquad \text{with} \quad A/B < 0 \ , \tag{3.40}$$

for the (pseudo-)spin up case, whereas we found

$$(i) \quad \psi_{\text{edge}}^{k_2=0}(x_1) = c_{+;1}\left(\mathrm{e}^{\tilde{\lambda}_1 x_1} - \mathrm{e}^{\tilde{\lambda}_2 x_1}\right)\xi_+ \qquad \text{with} \quad A/B < 0 \ , \tag{3.41}$$

$$(ii) \quad \psi_{\text{edge}}^{k_2=0}(x_1) = c_{-;1}\left(\mathrm{e}^{-\tilde{\lambda}_1 x_1} - \mathrm{e}^{\tilde{\lambda}_2 x_1}\right)\xi_- \qquad \text{with} \quad A/B > 0 \ , \tag{3.42}$$

for the (pseudo-)spin down case. Due to the fact that we considered an infinite manifold in $\mathbf{e}_2$-direction the momentum k_2 defines a good quantum number in the system considered. Under the assumption that $\psi_{\text{edge}}(x_1)$ itself does not depend on k_2 a natural finite energy extension of Eqs. (3.39)-Eq. (3.42) yields [49]

$$\phi_{\text{edge}}^{k_2}(x_1, x_2) = \psi_{\text{edge}}^{k_2=0}(x_1)\mathrm{e}^{\mathrm{i}k_2 x_2} \ , \tag{3.43}$$

with the associated spectra up to linear order in momentum k_2 [cf. Eq. (3.23)]:

$$E_+(k_2) = \begin{cases} -Ak_2 & \text{with} \quad A/B > 0 \\ Ak_2 & \text{with} \quad A/B < 0 \end{cases} \tag{3.44}$$

for the (pseudo-)spin up case and

$$E_-(k_2) = \begin{cases} -Ak_2 & \text{with} \quad A/B < 0 \\ Ak_2 & \text{with} \quad A/B > 0 \end{cases} \tag{3.45}$$

for the (pseudo-)spin down case. Hence, we derived the spectra of helical edge modes [49], whose velocities are determined by the parameter A, the (pseudo-)spin polarization, and the sign of the non-trivial Hall conductivity $\sigma_{\mathrm{xy}}^{\pm,\mathrm{QAH}}$

$$\mathrm{sgn(B)} \overset{\text{Eq. (3.37)}}{=} \frac{1}{2}\left[\mathrm{sgn}(m_\pm) + \mathrm{sgn}(B)\right] = \pm\mathrm{sgn}\left(\sigma_{\mathrm{xy}}^{\pm,\mathrm{QAH}}\right) \in \{-1, 1\} \ . \tag{3.46}$$

Let us close this subsection by giving one further remark regarding the connection between the two Chern insulators $\mathcal{H}_\pm(\mathbf{k})$ together defining the BHZ Hamiltonian in Eq. (3.4). As we have seen in the calculations for the Hall conductivity [cf. Eq. (3.19)], as well as for the edge state dispersion [cf. Eqs (3.44) and (3.45)], it is possible to deduce the physics of one of the (pseudo-)spin polarized Chern insulators from the other one, if one inverses the sign of the corresponding mass terms. This does not come as a surprise. By using the unitary transformation

$$U = \begin{pmatrix} \sigma_0 & 0 \\ 0 & \sigma_2 \end{pmatrix} \ , \tag{3.47}$$

we can rearrange the BHZ Hamiltonian in Eq. (3.4) such that it is described by the Hamiltonian of only one Chern insulator with oppositely signed mass terms in both (pseudo-)spin blocks of the BHZ Hamiltonian

$$U^\dagger \mathcal{H}_{\mathrm{BHZ}}(\mathbf{k}) U = \begin{pmatrix} \mathcal{H}_+(\mathbf{k}, A, m_+, B, D) & 0 \\ 0 & \mathcal{H}_+(\mathbf{k}, A, -m_-, -B, D) \end{pmatrix} \ . \tag{3.48}$$

We will make use of this property several time throughout this thesis in order to deduce the entire BHZ response from our calculations for a single (pseudo-)spin polarized Chern insulator.

3.1.3 Relation of the BHZ- and Haldane Model to the Parity Anomaly in 2+1 Space-Time Dimensions

In what follows, let us concretize in which way the BHZ model is related to the parity anomaly of massless QED_{2+1}. In order to clarify this point, we first study the Dirac- as well as the Newtonian mass terms of a single (pseudo-spin) polarized Chern insulator from a quantum field theoretic perspective by analyzing their contributions to the Chern-Simons effective action. As we have explained in Sec. 3.1.1, the BHZ model consists of two copies of (pseudo-spin) polarized Chern insulators. We already indicated that this property directly relates the QAH Hall phase of the BHZ model to Haldane's graphene model [25], which can be seen as the first solid state connection to the high-energy concept 'parity-anomaly'. In the second part of this section we elucidate this connection and specify in which sense the response of a QAH system like (Hg,Mn)Te can be interpreted as a measurement of the parity anomaly in 2+1 space-time dimensions.

Generating Functional and Fermion Determinant of a Chern Insulator

In what follows, we consider a single (pseudo-)spin polarized Chern insulator described by Eq. (3.12) coupled to an abelian U(1) gauge field $\mathcal{A}_\mu$. As we have shown in Sec. 2.5.2, such models can be quantized by calculating the partition function $\mathcal{Z}[\mathcal{A}]$, or analogously the effective action via integrating out the fermionic degrees of freedom [cf. Eq. (2.124)]

$$\mathcal{Z}[\mathcal{A}] = \frac{1}{\mathcal{Z}[0]} \int \mathrm{d}\bar{\psi}\, \mathrm{d}\psi\; \mathrm{e}^{\mathrm{i}\mathcal{S}[\bar{\psi},\psi,\mathcal{A}]} = \frac{1}{\mathcal{Z}[0]}\, \mathrm{e}^{\mathrm{i}S_{\mathrm{eff}}[\mathcal{A}]}\,. \tag{3.49}$$

Here, the bare and the effective action are defined by $\mathcal{S}[\bar{\psi},\psi,\mathcal{A}]$ and $\mathcal{S}_{\mathrm{eff}}[\mathcal{A}]$, respectively. If $\mathcal{S}_{\mathrm{eff}}[\mathcal{A}]$ has less symmetries than $S[\bar{\psi},\psi,\mathcal{A}]$, a quantum anomaly is present, as it was defined in Sec. 2.5.1. For instance, massless QED_{2+1} is described by the parity-symmetric bare action [cf. Eq. (2.127)]

$$\mathcal{S}[\bar{\psi},\psi,\mathcal{A}] = \int \mathrm{d}^3x\; \mathrm{i}\bar{\psi}\left(\partial\!\!\!/ + \mathrm{ie}\mathcal{A}\!\!\!/\right)\psi\,. \tag{3.50}$$

According to Eq. (2.126), the associated action is given by

$$\mathcal{S}_{\mathrm{eff}}[\mathcal{A}] = -\mathrm{i}\log\det\left[(\partial\!\!\!/ + \mathrm{ie}\mathcal{A}\!\!\!/)/\partial\!\!\!/\right]\;. \tag{3.51}$$

As it was shown initially in Ref. [52], the fermion determinant in Eq. (3.51) changes sign under large gauge transformations[a] of odd winding $\omega = 2n{+}1$ with $n \in \mathbb{Z}$ [cf. Fig. 2.7 in Sec. 2.4.4]

$$\det\left[(\partial\!\!\!/ + \mathrm{ie}\mathcal{A}\!\!\!/)/\partial\!\!\!/\right] \to (-1)^{|\omega|}\det\left[(\partial\!\!\!/ + \mathrm{ie}\mathcal{A}\!\!\!/)/\partial\!\!\!/\right] \quad \Rightarrow \quad \mathcal{S}_{\mathrm{eff}} \to \mathcal{S}_{\mathrm{eff}} \pm \pi|\omega|\;. \tag{3.52}$$

Hence, as it stands $\mathcal{S}_{\mathrm{eff}}[\mathcal{A}]$ is not a well-defined and physically meaningful object. This can also be seen by calculating the fermion determinant explicitly, which leads to a divergent expression, as we have seen in Eq. (2.151). Consequently, the theory requires a regularization scheme which needs to be chosen such that it ensures infinitesimal- as well as large gauge invariance of $\mathcal{Z}[\mathcal{A}]$ [cf. Sec. 2.4.4]. In particular, it was shown that each regularization scheme needs to break parity symmetry to ensure gauge invariance. This is known as the parity anomaly [33, 52]. The parity anomaly therefore results from the particular regularization of QED_{2+1}. Even though a massive QED_{2+1} system breaks parity on the classical level [cf. Eq. (2.130)], the fermion determinant still diverges and lacks gauge invariance, as we have shown in Eq. (2.151). Again, this requires a parity-breaking regularization scheme, which ensures an integer quantized DC Hall conductivity associated to a gauge invariant Chern-Simons term in the effective action. This property extends the peculiarities of the parity anomaly to the massive case [33, 52, 53, 57]. The non-invariance of a half-quantized Chern-Simons action [cf. Eq. (2.165)] in units of e^2/h has been derived in Eq. (2.174). In Eq. (3.19) we have shown that adding the Newtonian mass term to a massive QED_{2+1} Lagrangian leads to an integer quantized DC Hall conductivity, which is associated to a gauge invariant Chern-Simons term. From this perspective the Newtonian mass term, provided by the material, acts similar to a parity-breaking element of a mathematical regularization scheme[b]. Its contribution to the Hall conductivity does not vanish in the parity-symmetric limit $m_\pm, B \to 0$. Consequently, besides the Dirac mass also the Newtonian mass term is directly related to the parity anomaly. Inspired by this property, we compare in Sec. 3.2 the role of the Newtonian mass term for the calculation of the effective action of a Chern insulator to common parity-breaking regularization schemes of QED_{2+1}.

[a] For U(1) gauge fields such transformations only exist on compact non-trivial manifolds, such as $\mathcal{M} = T^2 \times S^1$.

[b] With 'similar' we mean that since the Newtonian mass is a real parameter of the theory, it does not vanish during renormalization. This latter requirement needs to be fulfilled by any mathematical regulator.

Relation of the BHZ Hamiltonian to the Haldane Model

Having discusses the role of the Dirac- and the Newtonian mass term of a Chern insulator in the context of the generating functional and fermion determinant, let us now specify the connection of the BHZ Hamiltonian to the Haldane model [25] and concretize the relation of these models to the parity anomaly of a single massless Dirac fermion in 2+1 space-time dimensions [cf. Sec. 2.6].

Even in the parity symmetric limit $m_\pm, B \to 0$, the Hall conductivity of a single Chern insulator in Eq. (3.19), does not vanish for $\mathrm{sgn}(m_\pm/B) > 0$. As we have discussed in the previous subsection, this effect is known as the parity anomaly of Dirac-like systems in odd space-time dimensions. Initially, the parity anomaly has been predicted for a pure Dirac spectrum in Ref. [52]. Due to the absence of a Newtonian mass term, the Chern number of a pure Dirac system is given by

$$\mathcal{C}_{\mathrm{QED}} = \sigma_{\mathrm{xy}}^{\mathrm{QED}} \frac{\mathrm{h}}{\mathrm{e}^2} = \pm\frac{1}{2}\mathrm{sgn}(m) \tag{3.53}$$

before regularization [cf. Eq. (2.157)]. Hence, it is half quantized and always non-zero. In contrast, the Hall conductivity in Eq. (3.19) is integer quantized in units of e^2/h and defines two different phases: For $m_\pm/B > 0$, the system is topologically nontrivial with Chern number $\mathcal{C}_{\mathrm{CI}} = \pm 1$, while for $m_\pm/B < 0$, the system is topologically trivial with $\mathcal{C}_{\mathrm{CI}} = 0$.

In a solid state system with a crystal lattice, Dirac fermions in 2+1 space-time dimensions always come in pairs[a]. The naive lattice discretization of a pure Dirac fermion leads to a phenomenon called fermion-doubling, which predicts the existence of a second Dirac fermion of opposite Chern number at the edge of the lattice Brillouin zone. Thus, the entire system has zero Hall conductivity and the parity anomaly of a single Dirac fermion cannot be measured. However, in his seminal work [25], Haldane found a way to circumvent this difficulty in a condensed matter system. He proposed a way of realizing a single gapless Dirac fermion in the bulk spectrum of graphene by separately manipulating the two Dirac gaps at the $\mathbf{K}$ and $\mathbf{K}'$ points of the hexagonal lattice structure via a complex hopping parameter. In Sec. 4.1.5, we give a pedagogical introduction into graphene's band-structure and electronic properties. All we need to know for now is that this complex hopping parameter allows to close only one of the Dirac gaps, whereas the other one remains open. Hence, his model suggests a way of constructing a solid state system which has a single gapless Dirac fermion in 2+1 dimensions but still a non-zero Hall conductivity proportional to the integer Chern number

$$\mathcal{C}_{\mathrm{HM}} = \left[\mathrm{sgn}(m_{\mathbf{K}}) - \mathrm{sgn}(m_{\mathbf{K}'})\right]/2 \ . \tag{3.54}$$

Here, $m_{\mathbf{K}}$ and $m_{\mathbf{K}'}$ are the Dirac mass terms at the $\mathbf{K}$ and $\mathbf{K}'$ points in graphene, respectively. While so far the Haldane model has not yet been realized in a solid state material, a closely related QAH effect has been predicted in two-dimensional QAH insulators like (Hg,Mn)Te quantum wells or magnetically doped (Bi,Sb)Te thin films, as we have discussed in Sec. 3.1.1. In the vicinity of the bulk gap, these systems can be described by the BHZ Hamiltonian in Eq. (3.4)[b], which consists of two copies of Chern insulators, explicitly defined in Eq. (3.12). The Dirac masses $m_\pm$ of each (pseudo-)spin polarized Chern insulator in Eq. (3.12) can be tuned by magnetically doping the system, as explained in Sec. 3.1.1. In particular, it is possible to drive one of the Chern insulators in the topologically trivial regime and to close,

[a] If the 2+1 dimensional manifold is the boundary theory of a 3+1 dimensional bulk, there could also be an odd number of Dirac fermions living at the boundary. For instance, this is the case at the boundary of 3+1 dimensional topological insulators. However, we are not considering such systems but focus our analysis on pure 2+1 dimensional bulk materials.

[b] For the scope of this work, off-diagonal bulk inversion asymmetry terms which couple the two Chern insulators are unimportant, we are therefore neglecting them throughout this thesis.

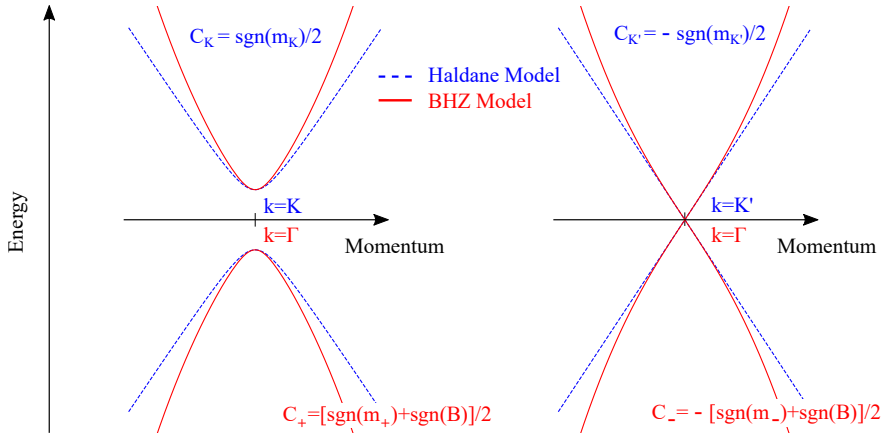

Figure 3.4: Schematic illustration of how a single Dirac fermion or Chern insulator realizes the parity anomaly in the Haldane (blue) or BHZ (red) model. In the Haldane model, both Dirac fermions at the **K** and **K′** points of the hexagonal lattice structure contribute $\pm 1/2$ to Chern number, whereas in the QAH phase of the BHZ model only one of the Chern insulators is topologically nontrivial and has a finite Chern number $\mathcal{C}_{\mathrm{CI}} = \pm 1$. More explanations are given in the text. The figure is reprinted from Ref. [P5] with permission from the APS.

at the same time, the gap of the second non-trivial Chern insulator. Analogously to the Haldane model, in this scenario the single gapless Chern insulator alone realizes the parity anomaly of a Dirac-like system in 2+1 dimensions. Schematically, this limit is illustrated in Fig. 3.4. However, while in the Haldane model both Dirac fermions contribute $\pm 1/2$ to the Chern number, in the QAH phase of the BHZ model only one of the Chern insulators has Chern number $\mathcal{C}_{\mathrm{CI}} = \pm 1$. The other one is topologically trivial with $C_{\mathrm{CI}} = 0$. Hence, studying a single Chern insulator in Eq. (3.12) is sufficient to analyze the consequences of the parity anomaly in experimentally realizable systems like (Hg,Mn)Te quantum wells or magnetically doped (Bi,Sb)Te thin films.

3.2 Anomaly Induced AC Hall Conductivity of QAH Insulators

In what follows, we are combining the theoretical principles which we have introduced in Chap. 2 and Sec. 3.1 in order

(*i*) to derive the AC response of QAH insulators which are described by the BHZ Hamiltonian [cf. Sec. 3.1.1], and

(*ii*) to relate this response to the parity anomaly of massless quantum electrodynamics in 2+1 space-time dimensions [cf. Secs. 2.6 and 3.1.3].

Within this section we are considering zero background magnetic fields, a particle-hole symmetric chemical potential at zero energy, as well as a vanishing temperature. While we are studying the influence of an out-of-plane magnetic field in Sec. 3.3, we are going to analyze the temperature and density dependence of our findings in Sec. 3.4. The subsequent discussion will mainly go along the lines of the manuscript '*Momentum-dependent mass and AC Hall conductivity of quantum anomalous Hall insulators and their relation to the parity anomaly*' (Phys. Rev. Research **2**, 033193), which I published in August 2020 [P4]. It is the goal of the

current section to discuss the theoretical findings associated to this work, which have been obtained in collaboration with Dr. Jan Böttcher[a]. While all analytic derivations have been obtained by myself, Dr. Jan Böttcher supported this work via fruitful discussions concerning the expected physical results.

In Sec. 3.1.1, we have shown that QAH insulators which are described by the BHZ model [cf. Eq.(3.4)] are characterized by the combined response of two (pseudo-)spin polarized Chern insulators, a topologically trivial as well as topologically non-trivial one [cf. Eq. (3.19)]. Each of these Chern insulators features Dirac-like physics in 2+1 space-time dimensions. Consequently, QAH insulators like (Hg,Mn)Te are directly related to the parity anomaly of planar quantum electrodynamics - a property which has been studied in Sec. 3.1.3. In what follows, we elaborate further on this statement.

According to Eq. (3.12), a Chern insulator is in general characterized by two different mass terms: A momentum independent Dirac mass $m_{\pm}$, as well as a momentum dependent Newtonian mass term $B|\mathbf{k}|^2$. The relation of the Dirac mass to the parity anomaly was been initially shown in Refs. [33, 52]. We discussed this relation in Secs. (2.6.3) and 3.1.3. However, up to date the connection of the Newtonian mass to the parity anomaly has not yet been analyzed. To bridge this gap, we derive in this section the effective action of a QAH insulator. In the corresponding calculation for a pure, massless QED_{2+1} system, the parity anomaly arises from the particular regularization of its infinite Dirac sea [cf. Sec 2.6.3]. As already indicated in Sec.3.1.3, we show that the Newtonian mass acts similar to a parity-breaking regulator in the calculation of the effective action. It is as such directly related to the parity anomaly. The non-quantized finite frequency corrections to the DC Hall conductivity of a single Chern insulator will be derived during our calculation of the effective action, as well. However, in order to understand our field theoretical analysis, let us start our discussion by briefly recapitulating the most important theoretical concepts which we have studied in the previous Secs. 2 and 3.1.

3.2.1 Band-Structure of a Chern Insulator: Topological Phase Transition

In Sec. 3.1.1, we have shown that the low-energy physics of two-dimensional QAH insulators like (Hg,Mn)Te quantum wells or magnetically doped (Bi,Sb)Te thin films can be described by means of the BHZ Hamiltonian in Eq. (3.4)[b]. We have in particular discussed that the BHZ model consists of two (pseudo-)spin polarized Chern insulators with Hamiltonian $\mathcal{H}_{\pm}(\mathbf{k})$ [cf. Eq. (3.12)], which in total give rise to [8]

$$\mathcal{H}_{\text{BHZ}}(\mathbf{k}) = \begin{pmatrix} \mathcal{H}_{+}(\mathbf{k}) & 0 \\ 0 & \mathcal{H}_{-}(\mathbf{k}) \end{pmatrix} . \tag{3.55}$$

In general, the basis of the BHZ Hamiltonian depends on the condensed matter system. For (Hg,Mn)Te quantum wells it is $(|E_1,+\rangle, |H_1,+\rangle, |E_1,-\rangle, |H_1,-\rangle)$, as we have explained above Eq. (3.4). The Hamiltonian of each of the two (pseudo-)spin polarized Chern insulators in Eq. (3.55) has been extensively studied in Sec. 3.1.2:

$$\mathcal{H}_{\pm}(\mathbf{k}) = -D|\mathbf{k}|^2\sigma_0 \pm A(k_1\sigma_1 \mp k_2\sigma_2) + \left(m_{\pm} - B|\mathbf{k}|^2\right)\sigma_3 . \tag{3.56}$$

[a] This publication has been supervised by Dr. René Meyer and by Prof. Dr. Ewelina M. Hankiewicz

[b] For the scope of this work, bulk inversion asymmetry terms are unimportant. Therefore, they are neglected throughout this thesis.

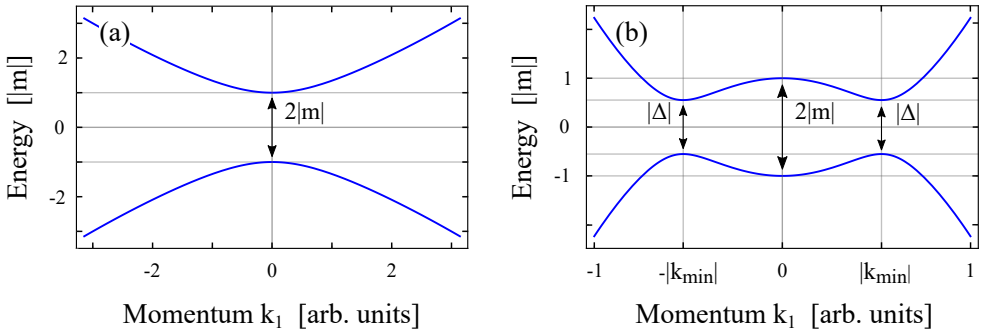

Figure 3.5: Band-structure corresponding to a single (pseudo-) spin block of the BHZ model for $k_2 = D = 0$ and for **(a)** a topologically non-trivial phase with $m = A = 1$ and $B = 0.1$. The minimal gap $2|m|$ is located at the Γ-point. **(b)** For a topologically non-trivial phase with $m = A = 1$ and $B = 3$. The minimal gap $|\Delta|$ is located at $|\mathbf{k}| = \pm|k_{\text{min}}|$. The figure is reprinted from Ref. [P4] with permission from the APS.

As each (pseudo-)spin block of the BHZ model is described by a single Chern insulator in 2+1 space-time dimensions, the physics originating from each of these blocks is directly related to the parity anomaly of QED_{2+1}. Let us briefly recapitulate that in Eq. (3.56), $m_\pm$ and $B|\mathbf{k}|^2$ are the parity-breaking mass terms [cf. Eq. (3.14)], and that the $D|\mathbf{k}|^2$ encodes a particle-hole (charge-conjugation) asymmetry [cf. Eq. (3.20)]. In the QSH phase, Eq. (3.55) is invariant under time reversal transformations, implying $m_+ = m_-$ and a total Chern number $\mathcal{C}_{\text{QSH}} = 0$ [cf. Eqs. (3.1) and (3.6)]. In the QAH phase, only one of the two (pseudo-)spin polarized Chern insulators is topologically non-trivial and has a finite Chern number [cf. Eq. (3.19)] [43, 50]

$$\mathcal{C}^i_{\text{CI}} = i\left[\text{sgn}(m_i) + \text{sgn}(B)\right]/2 \ , \quad i \in \{+,-\} \ . \tag{3.57}$$

The trivial (pseudo-)spin polarized Chern insulator has zero Chern number. Therefore, the entire topological response in the QAH phase is captured by a single Chern insulator in 2+1 space-time dimensions. If not stated otherwise, we focus on such a system in the remaining part of this section. We will in particular neglect the (pseudo-)spin index ± in the following analysis. Moreover, we will consider particle-hole symmetric Chern insulators, since the $D|\mathbf{k}|^2$ term in Eq. (3.56) is parity-even and thus does not contribute to the parity anomaly [cf. Eq. (3.20)]. The physics originating from the $D|\mathbf{k}|^2$ term has been studied explicitly by Dr. Jan Böttcher and myself in Reference [P3][a].

As we have shown in Eq. (3.16), the spectrum associated to Eq. (3.56) for $D = 0$ is given by

$$E^s(\mathbf{k}) = s\sqrt{A^2|\mathbf{k}|^2 + (m - B|\mathbf{k}|^2)^2} \ , \tag{3.58}$$

where $s = \pm$ encodes the conduction and the valence band, respectively. In Fig. 3.5, we show the influence of the mass parameters on the band-structure. While the Dirac mass m defines the mass gap at the $\Gamma-$point, the momentum dependent $B|\mathbf{k}|^2$ term acts like an effective mass of a non-relativistic fermion system. Depending on the values for m, B, and A, the band-structure significantly changes. For $m/B > 0$, the system is topologically non-trivial with $\mathcal{C}_{\text{CI}} = \pm 1$. However, depending on the absolute values of the input parameters, the minimal gap can either be located at the Γ-point [Fig. 3.5(a)], driven by the Dirac mass alone, or apart from $|\mathbf{k}| = 0$ [Fig. 3.5(b)] at $k_{\text{min}} = \pm\sqrt{2mB - A^2}/(\sqrt{2}B)$. The minimal gap

[a] This publication has been supervised by Dr. René Meyer and by Prof. Dr. Ewelina M. Hankiewicz

is therefore either defined by $2|m|$, or by the absolute value of

$$\Delta = A\sqrt{4mB - A^2}/B \ . \tag{3.59}$$

In contrast, for $m/B < 0$, the system is topologically trivial, characterized by $\mathcal{C}_{\mathrm{CI}} = 0$. In this case the minimal gap is always located at the Γ-point. At $m = 0$, the topological phase transition occurs, which comes along with a gap closing at $\mathbf{k}=0$. While in our plots we mostly consider positive mass terms, the inverted Dirac mass of an experimental QAH insulator is negative. Changing the overall sign of m and B alters the sign of the Chern number, but not the underlying physics. Notice, that according to Eq. (3.58) the Newtonian mass term does not make the spectrum bounded. It is from this perspective expected that the $B|\mathbf{k}|^2$ term does not render the effective action of a Chern insulator UV finite.

Having discussed the particular influence of the mass terms on the band-structure, let us emphasize one more time that both of them explicitly break the parity symmetry in 2+1 space-time dimensions, defined as invariance of the theory under $\mathcal{P} : (x_0, x_1, x_2) \to (x_0, -x_1, x_2)$ [cf. Eq. (2.50)]. Explicitly, this was shown in Sec. 3.1.2. Hence, the Dirac and the Newtonian mass term are both directly related to the parity anomaly of massless QED_{2+1}. To concretize this statement, let us briefly recapitulate the concept of quantum anomalies which we have detailedly discussed in Sec. 2.6.

3.2.2 Effective Action of a Chern Insulator

In what follows, we perturbatively evaluate the effective action corresponding to a single Chern insulator. The corresponding calculation for a pure QED_{2+1} system can be found in Sec. 2.6.3. First, let us Taylor expand the fermion determinant in Eq. (2.124) to second order in the U(1) gauge field $\mathcal{A}_\mu$. The free Lagrangian associated to Eq. (3.56)[a] can be obtained by a Legendre transformation. For $A = \hbar = 1$ and $D = 0$, this Lagragian is equivalent to a pure QED_{2+1} Lagrangian [cf. Eq. (2.127)] except for an additional correction, which is quadratic in spatial derivatives

$$\mathcal{L}_0 = \bar{\psi}\left(\mathrm{i}\not{\partial} - m\right)\psi - B\gamma^0(\partial_i\psi)^\dagger(\partial^i\psi) \ . \tag{3.60}$$

Here and in the following, we use the properties of the Dirac matrices given in Sec. 2.3.1. Coupling $\mathcal{L}_0$ covariantly to the U(1) gauge field $\mathcal{A}_\mu$, leads to the Lagrangian

$$\begin{aligned}\mathcal{L} &= \bar{\psi}\left(\mathrm{i}\not{D} - m\right)\psi - B\gamma^0(D_i\psi)^\dagger(D^i\psi) \\ &= \mathcal{L}_0 - \mathrm{e}\bar{\psi}(\not{\mathcal{A}}+\mathrm{e}B\mathcal{A}^i\mathcal{A}_i)\psi + \mathrm{ie}B\mathcal{A}^i\Big(\bar{\psi}(\partial_i\psi)-(\partial_i\bar{\psi})\psi\Big) \ ,\end{aligned} \tag{3.61}$$

where $D_\mu = \partial_\mu + \mathrm{ie}\mathcal{A}_\mu$ is the covariant derivative. From the interaction terms in $\mathcal{L}$, we can read off the vertex contributions. For an incoming electron of momentum k, incoming photons of momentum p, and an outgoing electron of momentum $k+p$, we find the vertices

$$V^\mu_{(1)}(2k+p) = -\mathrm{ie}(\gamma^\mu - B\,\delta^\mu{}_i\,(2k+p)^i) \ , \tag{3.62}$$

$$V^{\mu\nu}_{(2)}(k) = -2\mathrm{ie}^2 B\,\delta^\mu_i\delta^{i\nu} \ . \tag{3.63}$$

Here, the subscript defines the number of involved photons. In comparison to pure QED_{2+1}, the extra $B|\mathbf{k}|^2$ term in the Lagrangian renormalizes the gauge-matter coupling. The original QED vertex in Eq. (3.62) obtains a momentum dependent correction [cf. Eq. (2.135)]. Additionally, Eq. (3.63) defines a new vertex structure, which is of second order in gauge fields.

[a] As we have stated in Sec. 3.2.1, in our calculations we focus on a (pseudo-)spin up polarized Chern insulator and neglect the identifying subscript.

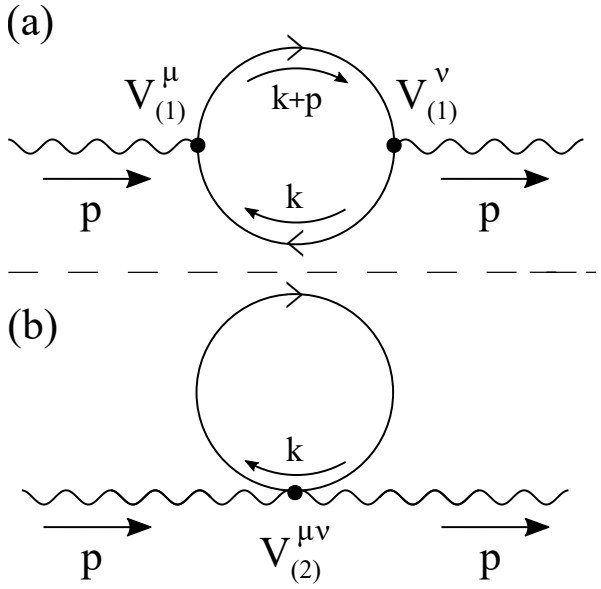

Figure 3.6: Feynman diagrams for the vacuum polarization operator of a single Chern insulator with vertices $V^{\mu,\nu}_{(1)}$ and $V^{\mu\nu}_{(2)}$. External momenta are denoted by p, loop momenta by k. The figure is reprinted from Ref. [P4] with permission from the APS.

This vertex encodes the diamagnetic response of the Chern insulator in Eq. (3.56) [99]. The fermion propagator associated to the Lagrangian $\mathcal{L}$ is given by

$$S(k) = \frac{\mathrm{i}}{\not{k} - (m - B|\mathbf{k}|^2) + \mathrm{i}\epsilon} = \mathrm{i}\frac{\not{k} + M(\mathbf{k})}{k^2 - M(\mathbf{k})^2 + \mathrm{i}\epsilon} \ . \tag{3.64}$$

Here, we defined the momentum dependent mass term $M(\mathbf{k}) = m - B|\mathbf{k}|^2$ as it has been done in Eq. (3.12) and used the Feynman prescription with $\epsilon \to 0^+$. To perturbatively obtain the second order effective action in gauge fields, we need to calculate the vacuum polarization operator $\Pi^{\mu\nu}(p)$ [a],

$$\mathcal{S}_{\text{eff}} = \frac{1}{2}\int \frac{\mathrm{d}^3 p}{(2\pi)^3}\ \mathcal{A}_\mu(-p)\Pi^{\mu\nu}(p)\mathcal{A}_\nu(p) \ . \tag{3.65}$$

Due to the vertex structure in Eqs. (3.62) and (3.63), the vacuum polarization operator is obtained by the sum of two one-loop Feynman integrals

$$\begin{aligned} \mathrm{i}\Pi^{\mu\nu}(p) &= \mathrm{i}\Pi^{\mu\nu}_{2\mathrm{a}}(p) + \mathrm{i}\Pi^{\mu\nu}_{2\mathrm{b}}(p) \\ &= -\int \frac{\mathrm{d}^3 k}{(2\pi)^3}\, \mathrm{Tr}\big[S(k)V^{\mu}_{(1)}(2k+p)S(k+p)V^{\nu}_{(1)}(2k+p) + S(k)V^{\mu\nu}_{(2)}(k)\big] \ , \end{aligned} \tag{3.66}$$

which are diagrammatically illustrated in Fig. 3.6. We start with the calculation of the first term in Eq. (3.66), $\mathrm{i}\Pi^{\mu\nu}_{2\mathrm{a}}(p)$, which is the usual QED_{2+1} vacuum polarization operator with renormalized vertex and propagator structure. As shown in Fig. 3.6(a), this tensor is given by

$$\mathrm{i}\Pi^{\mu\nu}_{2\mathrm{a}}(p) = \frac{\mathrm{e}^2}{(2\pi)^3}\int \mathrm{d}^3 k\ \frac{1}{(k^2 - M(\mathbf{k})^2 + \mathrm{i}\epsilon)((k+p)^2 - M(k+p)^2 + \mathrm{i}\epsilon)} \tag{3.67}$$

[a] Since we only consider zero chemical potential, the linear term in $\mathcal{A}_\mu$ needs to vanish. Physically, this term calculates the charge density, which is zero in the mass gap if there is no underlying magnetic field.

$$\times \operatorname{Tr}\Big([\gamma^\mu - B\,\delta^\mu_{\ i}(2k+p)^i\,\sigma_0]\mathrm{i}[\not{k}+M(\mathbf{k})][\gamma^\nu - B\,\delta^\nu_{\ j}(2k+p)^j\,\sigma_0]\mathrm{i}[(\not{k}+\not{p})+M(k+p)]\Big)\,.$$

There are four different contributions to the Dirac trace $\mathrm{Tr} = \mathrm{Tr}_{\gamma\gamma} + \mathrm{Tr}_{\gamma 0} + \mathrm{Tr}_{0\gamma} + \mathrm{Tr}_{00}$, where the subscript defines the Dirac and identity part of the vertex structure in Eq. (3.62). With the trace identities in Eq. (2.39) in Sec. 2.3.1 and with $C^\mu = -B\,\delta^\mu_{\ i}(2k+p)^i$, we obtain

$$\begin{aligned}
-\frac{1}{2}\mathrm{Tr}_{\gamma\gamma} &= 2k^\mu k^\nu + k^\mu p^\nu + k^\nu p^\mu + g^{\mu\nu}\Big(M(\mathbf{k})M(k+p) - k^2 - kp\Big)\,, \\
&\quad - \mathrm{i}\epsilon^{\mu\nu\lambda}\left([M(k+p) - M(k)]\,k_\lambda - M(\mathbf{k})p_\lambda\right)\,, \\
-\frac{1}{2}\mathrm{Tr}_{\gamma 0} &= C^\nu g^{\mu\lambda}\left[(M(\mathbf{k}) + M(k+p))\,k_\lambda + M(\mathbf{k})p_\lambda\right] + \mathrm{i}C^\nu\epsilon^{\mu\lambda\sigma}k_\lambda(k+p)_\sigma\,, \\
-\frac{1}{2}\mathrm{Tr}_{0\gamma} &= C^\mu g^{\nu\lambda}\left[(M(\mathbf{k}) + M(k+p))\,k_\lambda + M(\mathbf{k})p_\lambda\right] - \mathrm{i}C^\mu\epsilon^{\nu\lambda\sigma}k_\lambda(k+p)_\sigma\,, \\
-\frac{1}{2}\mathrm{Tr}_{00} &= C^\mu C^\nu\Big[g^{\lambda\sigma}k_\lambda\,(k+p)_\sigma + M(\mathbf{k})M(k+p)\Big]\,.
\end{aligned} \tag{3.68}$$

Since all physical response functions are given as functional derivatives of the effective action at zero external spatial momentum, from now on we focus on the calculation of $\mathrm{i}\Pi^{\mu\nu}(p_0, \mathbf{p}=0)$. With this assumption, $p^2 = p_0^2$, $\epsilon^{\mu\nu\lambda}p_\lambda = \epsilon^{\mu\nu 0}p_0$, and $M(k) = M(k+p)$. Next, we introduce the Feynman parameter $x \in [0,1]$ and shift the loop momentum according to $k = l - px$. As we have shown in Eq. (2.145), this gives the denominator in Eq. (3.67) a quadratic form, allowing us to drop all linear terms in l in the numerator, due to an anti-symmetric integration over symmetric boundaries [109]. With $\alpha = |\mathbf{l}|^2$, this leads to

$$\begin{aligned}
\mathrm{Tr} =& 2g^{\mu\nu}l^2 - 4l^\mu l^\nu - 2x(1-x)p_0^2 - 2g^{\mu\nu}\Big[M(\alpha)^2 + x(1-x)p_0^2\Big] - 2\mathrm{i}[M(\alpha) + 2B\alpha]\,\epsilon^{\mu\nu 0}p_0 \\
&+ 4B\alpha\delta^\nu_m\delta^\mu_m\Big[2M(\alpha) - B\Big[l_0^2 - \alpha - x(1-x)p_0^2 + M(\alpha)^2\Big]\Big].
\end{aligned} \tag{3.69}$$

In the QED_{2+1} limit $B \to 0$, the Dirac trace in Eq. (3.69) reduces to the well-known result

$$\mathrm{Tr} = 2g^{\mu\nu}l^2 - 4l^\mu l^\nu + 4x(1-x)p_0^2 - 2g^{\mu\nu}\Big(m^2 + x(1-x)p_0^2\Big) - 2\mathrm{i}m\epsilon^{\mu\nu 0}p_0\,, \tag{3.70}$$

which has been derived in Eq. (2.146) [109, 110, 144]. Notice, that the off-diagonal Chern-Simons contribution in Eq. (3.70) gets shifted by the renormalized vertex structure in Eq. (3.69). As argued above, this will lead to an integer quantized DC Hall conductivity associated to a gauge invariant Chern-Simons term.

Hall Response

To prove this statement, we evaluate the integral

$$\begin{aligned}
\mathrm{i}\Pi^{\mu\nu}_{\mathrm{CS}}(p_0, \mathbf{p}=0) &= \frac{\mathrm{e}^2}{(2\pi)^3}\int_0^1 \mathrm{d}x \int \mathrm{d}^3 l\, \frac{-2\mathrm{i}\epsilon^{\mu\nu 0}\,(M(\alpha) + 2B\alpha)\,p^0}{(l_0^2 - \alpha - M(\alpha)^2 + x(1-x)p_0^2 + \mathrm{i}\epsilon)^2} \\
&= \frac{\mathrm{e}^2}{8\pi}\epsilon^{\mu\nu 0}p_0 \int_0^1 \mathrm{d}x \int_0^\infty \mathrm{d}\alpha\, \frac{m + B\alpha}{(\alpha + M(\alpha)^2 - x(1-x)p_0^2 - \mathrm{i}\epsilon)^{3/2}}\,.
\end{aligned} \tag{3.71}$$

Here, we used the Feynman parametrization and solved the complex time-integration via the residue theorem. For Chern insulators, time and spatial momenta need to be integrated separately since the $B|\mathbf{k}|^2$ term breaks the Lorentz symmetry [cf. Sec. 2.4.3]. Hence, it is not possible to Wick-rotate and integrate over an Euclidean three-sphere as it was done in

Sec. 2.6.3. Integrating the Feynman parameter x implies

$$\int_0^1 \mathrm{d}x \, \frac{1}{(\alpha + M(\alpha)^2 - x(1-x)p_0^2 - \mathrm{i}\epsilon)^{3/2}} = \frac{4}{\sqrt{\alpha + M(\alpha)^2 - \mathrm{i}\epsilon}\,(4\alpha + 4M(\alpha)^2 - p_0^2 - 4\mathrm{i}\epsilon)} \,, \tag{3.72}$$

where we kept the $\mathrm{i}\epsilon$-prescription to circumvent the poles for $\alpha > 0$, appearing if p_0 exceeds the gap. Finally, we perform the remaining α-integration for an arbitrary driving frequency p_0 and subsequently set $\epsilon \to 0^+$. Due to its lengthy form, we present the general Chern-Simons contribution and its AC Hall conductivity $\sigma_{\mathrm{xy}}(p_0)$ later in Eq. (3.81),

$$\mathrm{i}\Pi^{\mu\nu}_{\mathrm{CS}}(p_0, \mathbf{p} = 0) = \sigma_{\mathrm{xy}}(p_0)\epsilon^{\mu\nu 0} p_0 \,. \tag{3.73}$$

Instead, we first analyze the Taylor expansion of the AC Hall conductivity in terms of the frequency p_0,

$$\sigma_{\mathrm{xy}}(p_0) = \sigma_{\mathrm{xy}}(0) + \frac{\sigma''_{\mathrm{xy}}(p_0)|_{p_0=0}}{2!} p_0^2 + \mathcal{O}(p_0^4) \tag{3.74}$$

with the coefficients (reintroducing A and $\hbar$)

$$\sigma_{\mathrm{xy}}(0) = \frac{\mathrm{e}^2}{2\mathrm{h}} \left[\mathrm{sgn}(m) + \mathrm{sgn}(B)\right] = \frac{\mathrm{e}^2}{\mathrm{h}} \mathcal{C}_{\mathrm{CI}} \,, \tag{3.75}$$

$$\sigma''_{\mathrm{xy}}(p_0)|_{p_0=0} = \frac{\mathrm{e}^2}{\mathrm{h}} \left[\frac{2\,\mathcal{C}_{\mathrm{CI}}}{3\Delta^2} - \frac{A^4}{\Delta^2 B^2} \frac{\mathrm{sgn}(m)}{24 m^2} \right] \,. \tag{3.76}$$

Equation (3.75) defines the DC Hall conductivity of the single Chern insulator given in Eq. (3.56), which we have also obtained in Eq. (3.19). In the QAH phase, this value matches the DC Hall conductivity of the entire system, as only one Chern insulator contributes to the topological response [43, 50]. In comparison to a pure QED_{2+1} system with a half-quantized $\sigma_{\mathrm{xy}}(0)$ [cf. Eq. (2.157)], the Newtonian mass term ensures an integer quantization. Hence, the associated Chern-Simons term is gauge invariant [a].

In contrast, Eq. (3.76) defines the leading order AC correction to $\sigma_{\mathrm{xy}}(0)$, which contains two terms of different origin. On the one hand, there is a term proportional to the Chern number $\mathcal{C}_{\mathrm{CI}}$. In the trivial phase $m/B < 0$, this term vanishes and the first order AC correction is solely given by the second term in Eq. (3.76). Instead, for $m/B > 0$, this term contributes to the first order AC correction. In experimental systems like (Hg,Mn)Te quantum wells with $m_+ = -10\mathrm{meV}$, $B = -1075\mathrm{meVnm}^2$, and $A = 365\mathrm{meVnm}$, the term proportional to $\mathcal{C}_{\mathrm{CI}}$ defines $\approx 10\%$ of the entire signal in Eq. (3.76). From a theoretical point of view, this term is induced by a finite Newtonian mass, which breaks the Lorentz symmetry in Eq. (3.175). Consequently, it vanishes in the QED limit $B \to 0$, since

$$\lim_{B\to 0} \frac{1}{\Delta^2} = 0 \quad \wedge \quad \lim_{B\to 0} \frac{A^4}{\Delta^2 B^2} = -1 \,. \tag{3.77}$$

In this limit, Eq. (3.76) reduces to the QED result

$$\lim_{B\to 0} \sigma''_{\mathrm{xy}}(p_0)|_{p_0=0} = \frac{\mathrm{e}^2}{\mathrm{h}} \frac{\mathrm{sgn}(m)}{24 m^2} \,. \tag{3.78}$$

Due to its unique relation to the Newtonian mass, the term proportional to the Chern number

[a] Notice, that the full renormalized effective action of QED_{2+1} is gauge invariant due to the presence of non-analytic terms which cannot be derived perturbatively [145]

in Eq. (3.76) is quadratically suppressed by the ratio of p_0 over the gap $|\Delta|$. In contrast, the second term in Eq. (3.76), which is the first order QED correction to the DC Hall conductivity, is quadratically suppressed by p_0 over the Dirac mass. According to the quadratic suppression of both terms, the AC signal in Eq. (3.76) stays close to quantized values and matches the AC Hall response of the entire QAH system for small driving frequencies p_0.

Let us briefly comment on how to experimentally disentangle the QED from the Newtonian part in the first order AC Hall correction. In QAH insulators like (Hg,Mn)Te quantum wells the topological phase transition originates from a sign change of the Dirac mass of one of the two Chern insulators [cf. Fig. 3.3]. In what follows, let us assume it is m_+, meaning that the topological phase transition takes place in the (pseudo-)spin up block of the BHZ model [cf. Eq. (3.55)]. Due to the parameters above, this transition is associated to an overall sign change of $\sigma''_{\mathrm{xy}}(p_0)|_{p_0=0}$, which is mainly driven by the QED correction in Eq. (3.76). Consequently, measuring the AC Hall signal at $\pm m_+$ [a], allows to substract the QED correction and, therefore, to isolate the contribution to Eq. (3.76) which is induced by the Newtonian mass. Moreover, $\sigma_{\mathrm{xy}}(p_0)$ is related to the Faraday and the Kerr angle of two-dimensional QAH insulators [146, 147]. The first term in Eq. (3.76) can be therefore resolved by magneto-optical experiments, as well. Let us consider a linearly polarized electric field, which incidents normally on the QAH system. For frequencies much smaller than the gap, which justify Eq. (3.74), one finds [147]

$$\Theta_{\mathrm{F}}(p_0) = \quad \mathrm{Arctan}\left[\frac{\pi\sigma_{\mathrm{xy}}(p_0)}{\epsilon_0 c_0}\right] , \tag{3.79}$$

$$\Theta_{\mathrm{K}}(p_0) = -\mathrm{Arctan}\left[\frac{\epsilon_0 c_0}{\pi\sigma_{\mathrm{xy}}(p_0)}\right] . \tag{3.80}$$

While these identities imply quantized values of the Faraday and Kerr angles in the DC limit, they carry the information of how these angles change due to the contribution of the first term in Eq. (3.76). To resolve this effect in one of these experiments, $|p_0| \ll \mathrm{Min}(2|m|, |\Delta|)$. For instance in inverted (Hg,Mn)Te/CdTe quantum wells, the gap is of the order of several meV [148], depending on the particular Manganese concentration. This corresponds to frequencies in the THz regime. For such frequencies, the first order correction to the DC Faraday and Kerr angles is on the order of milli-rad, which can be resolved by recent Faraday polarimeters [149].

Before we discuss the general solution of the AC Hall conductivity, note that the non-quantized value for $\sigma_{\mathrm{xy}}(p_0 \neq 0)$ makes the associated Chern-Simons term (large) gauge non-invariant. Since analogously to thermal effects, an AC driving field excites non-topological degrees of freedom, this effect corresponds to the non-gauge invariance of finite temperature Chern-Simons terms. For these theories, it was shown that the full effective action contains non-perturbative corrections in $\mathcal{A}_\mu$, absorbing this non-invariance [58, 67]. These terms cannot be found by the Taylor expansion of the fermion determinant Eq. (2.124). However, due to the fact that they are higher order in gauge fields, they do not contribute to the conductivity.

Let us now analyze the general solution of the AC Hall conductivity corresponding to a single Chern insulator.

$$\sigma_{\mathrm{xy}}(p_0) = -\frac{\mathrm{e}^2}{\mathrm{h}} \sum_{s=\pm 1} \left[\frac{(1-4mB-\Delta_{p_0})\,(\mathrm{Ln}_1 + \mathrm{Ln}_2)}{4B\Delta_{p_0}|p_0|} + \frac{(1-4mB+\Delta_{p_0})\,(\mathrm{Ln}_3 + \mathrm{Ln}_4)}{4B\Delta_{p_0}|p_0|} \right] , \tag{3.81}$$

[a] Throughout this experiment, m_- needs to be fixed in the topologically trivial region.

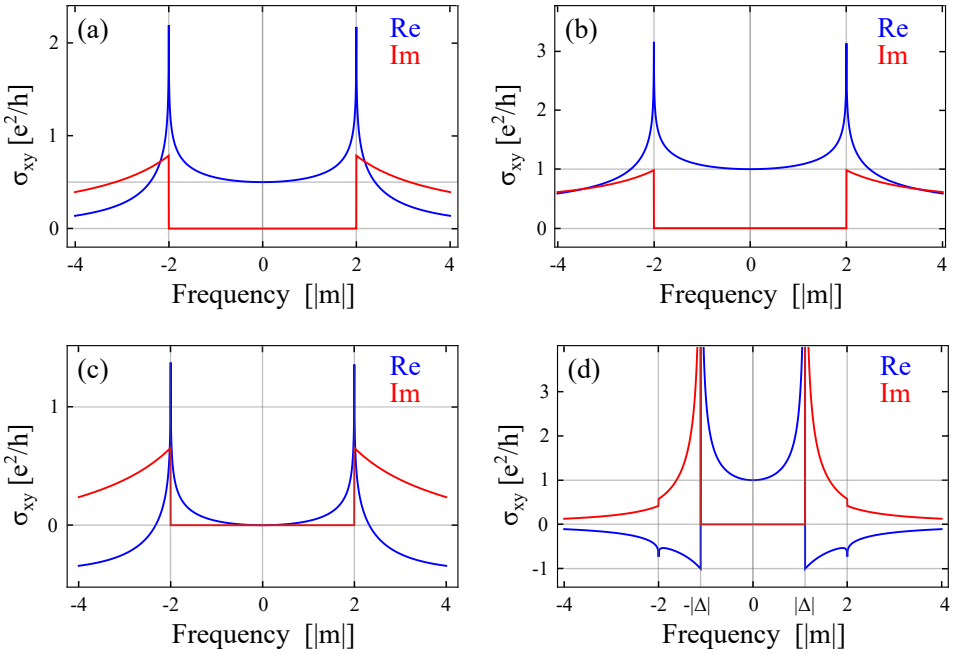

Figure 3.7: Hall conductivity $\sigma_{\mathrm{xy}}(p_0)$ for (**a**) a QED_{2+1} system with $m=A=1$ and $B=0$, (**b**) a non-trivial Chern insulator with $m=A=1$ and $B=0.1$, (**c**) a trivial Chern insulator with $m=A=1$ and $B=-0.1$ and (**d**) a non-trivial Chern insulator with $m=A=1$ and $B=3$. While the spectrum associated to (a)-(c) has the minimal gap $2|m|$ at the Γ-point, the spectrum related to (d) has the minimal gap $|\Delta|$ at k_{min} [cf. Sec. 3.2.1]. Notice that all discontinuities/singularities arise from the assumption of zero temperature and disorder. Taking into account these ingredients makes all curves continuous. The figure is reprinted from Ref. [P4] with permission from the APS.

where we defined $\Delta_{p_0}=s\sqrt{1-4mB+B^2p_0^2}$ and abbreviate the four logarithms

$$\begin{aligned}
\mathrm{Ln}_1 &= \mathrm{Ln}\left[-2sB^2\right] \ , \\
\mathrm{Ln}_2 &= \mathrm{Ln}\left[s\Big(1-4mB-2B^2|m||p_0|\Big)\Delta_{p_0}-s(1-2mB)\Delta_{p_0}^2\right] \ , \\
\mathrm{Ln}_3 &= \mathrm{Ln}\left[s\left(1-2mB+\Delta_{p_0}\right)\right] \ , \\
\mathrm{Ln}_4 &= \mathrm{Ln}\left[2sB^2\Big(\Delta_{p_0}^2-\Delta_{p_0}|B||p_0|\Big)\right] \ .
\end{aligned} \tag{3.82}$$

Notice, that exactly at $p_0=\Delta$, Δ_{p_0} evaluates to zero. Hence, this quantity encodes the physics originating from the mass gap apart from the Γ-point.

Figure 3.7 shows the real and the imaginary part of $\sigma_{\mathrm{xy}}(p_0)$ according to its general form in Eq. (3.81). To study the influence of the Newtonian mass term, Fig. 3.7(a) shows $\sigma_{\mathrm{xy}}(p_0)$ for a pure QED_{2+1} system [cf. Eq. (2.152)]. At $p_0=0$, one observes the characteristic half-quantization. Moreover, the real part of $\sigma_{\mathrm{xy}}(p_0)$ shows a resonance at $p_0=\pm 2|m|$ and tends to zero for larger frequencies. For $|p_0|\geq 2|m|$, the AC field excites particle-hole pairs which can propagate unhindered for $p_0=\pm 2|m|$. This is the origin of the resonance [150–152]. For large frequencies, the AC field dominates the gap which protects the topological phase. This leads to a vanishing AC Hall conductivity. The imaginary part of $\sigma_{\mathrm{xy}}(p_0)$ satisfies the Kramers-Kronig relation

$$\mathrm{Re}\,\sigma_{\mathrm{xy}}(p_0)=\frac{1}{\pi}\mathrm{P}\int \mathrm{d}p_0'\,\frac{\mathrm{Im}\,\sigma_{\mathrm{xy}}(p_0')}{p_0'-p_0} \ . \tag{3.83}$$

It is zero in the mass gap, becomes finite for $|p_0| \geq 2|m|$ and decreases afterwards. Since $\mathrm{Im}\,\sigma_{\mathrm{xy}}(p_0)$ results from interband absorptions [146, 150], it is only non-zero if the applied frequency is able to excite a finite density of states.

Figure 3.7(b) and 3.7(c) show the corresponding plots for a non-trivial and a trivial Chern insulator with minimal gap size $2|m|$. The AC Hall conductivity shows the same features as a pure Dirac system, except for the integer quantization of its DC Hall conductivity. However, for a minimal gap apart from the Γ-point, the situation differs, as shown in Fig. 3.7(d). Here, the first resonance of the real part occurs at $p_0 = \pm|\Delta|$. The $p_0 = \pm 2|m|$ resonance persists, but peaks in opposite direction since the density of states now decreases at $p_0 = \pm 2|m|$. This property can also be seen in $\mathrm{Im}\,\sigma_{\mathrm{xy}}(p_0)$, which resolves the Van Hove singularity at $p_0 = \pm|\Delta|$ and drops at $p_0 = \pm 2|m|$. Consequently, measuring the AC conductivity informs whether the minimal gap is defined by the Dirac mass at the Γ-point, or rather by an interplay between the Dirac and the Newtonian mass apart from $\mathbf{k} = 0$.

Above, we have discussed the AC Hall response of a single Chern insulator which is either in the topologically trivial phase with $m \equiv m_-$, or in the topologically non-trivial phase with $m \equiv m_+$. The entire QAH response of the two (pseudo-)spin blocks $\mathcal{H}_\pm(\mathbf{k})$ in the BHZ model [cf. Eq. (3.55)] corresponds to the superposition of both of these signals. In contrast to the DC Hall conductivity, the AC Hall conductivity contains corrections of non-topological origin. As such, also the topologically trivial (pseudo-)spin block of the BHZ model significantly contributes to the entire QAH response if the frequency $|p_0|$ is not much smaller than the trivial gap $2|m_-|$. As we have shown in Eq. (3.48), the physics of each (pseudo-)spin polarized Chern insulators can be deduced from the other one by inverting the sign of the corresponding mass terms.

Longitudinal Response

Having discussed the Hall response, we are still left with the calculation of the diagonal parts in Eq. (3.69). Since our system is a bulk insulator, we physically expect that these terms vanish for $p = 0$. The diagonal contributions can be calculated via the same techniques as used above. This leads to

$$\mathrm{i}\Pi^{\mu\nu}_{\mathrm{D,2a}}(p=0) = \frac{\mathrm{i}e^2\delta^\mu_i\delta^{i\nu}}{4\pi|B|}\left[1-2mB-2|m||B|-\mathrm{Ln}\left[\frac{4B^2\Lambda}{1-2Bm+2|m||B|}\right]\right] , \tag{3.84}$$

where Λ is a hard momentum cutoff in $\alpha = |\mathbf{l}|^2$ [cf. Eq. (2.151)] and we used [153]:

$$\int \mathrm{d}x\, \frac{1}{(ax^2+bx+c)^{3/2}} = -\frac{2(b+2ax)}{(b^2-4ac)\sqrt{c+x(b+ax)}} , \tag{3.85}$$

$$\int \mathrm{d}x\, \frac{x}{(ax^2+bx+c)^{3/2}} = \frac{4c+2bx}{(b^2-4ac)\sqrt{c+x(b+ax)}} . \tag{3.86}$$

So far, we focused on the contributions of the first Feynman diagram in Fig. (3.6). Using analogous techniques and the quadratic vertex in U(1) gauge fields, Eq. (3.63), the second Feynman diagram in Fig. (3.6) yields

$$\mathrm{i}\Pi^{\mu\nu}_{\mathrm{D,2b}}(p=0) = -\frac{\mathrm{i}e^2|B|\Lambda\delta^\mu_i\delta^{i\nu}}{2\pi} - \mathrm{i}\Pi^{\mu\nu}_{\mathrm{D,2a}}(p=0) , \tag{3.87}$$

where we used [153]

$$\int \mathrm{d}x \frac{x}{\sqrt{ax^2+bx+c}} = \frac{1}{a}\sqrt{ax^2+bx+c} - \frac{b}{2a}\int \mathrm{d}x \frac{1}{\sqrt{ax^2+bx+c}} , \tag{3.88}$$

$$\int \mathrm{d}x \frac{1}{\sqrt{ax^2+bx+c}} = \begin{cases} \frac{1}{\sqrt{a}} \mathrm{Ln}\left|2\sqrt{a(ax^2+bx+c)}+2ax+b\right| & \text{for } a>0 \\ -\frac{1}{\sqrt{-a}} \mathrm{Arcsin}\frac{2ax+b}{\sqrt{b^2-4ac}} & \text{for } a<0 \end{cases} . \tag{3.89}$$

This expression exactly cancels the finite and logarithmic divergent terms in Eq. (3.84). Nevertheless, the full effective action still contains a term proportional to the UV cutoff Λ which diverges during renormalization $\Lambda \to \infty$. However, as stated above, the diagonal contribution should be regularized/renormalized such that it vanishes for $p=0$. Physically, such a renormalization corresponds to a proper definition of the particle density. The second term in Eq. (3.66), which corresponds to the quadratic vertex in gauge fields Eq. (3.63), encodes the diamagnetic response of our system. This response is proportional to the particle density and as such needs to vanish in the gap. Due to the fact that we did not renormalize the Dirac sea contribution to the particle density, e.g. by anti-symmetrization, the divergence in Eq. (3.87) persists. As a consequence of the underlying parity- anomaly each regularization scheme for a single Chern insulator does either break parity or gauge symmetry. The naive introduction of the hard momentum cutoff Λ in Eq. (3.84) breaks the gauge symmetry. To preserve this symmetry, we should rather choose a parity-breaking regulator, such as a single Pauli-Villars field [cf. discussion above Eq. (2.155)] with mass terms M and B [a]. While this field by construction ensures

$$\mathrm{i}\Pi^{\mu\nu}_{\mathrm{D,2a}}(p=0) + \mathrm{i}\Pi^{\mu\nu}_{\mathrm{D,2b}}(p=0) = 0 \,, \tag{3.90}$$

it contributes to the AC Hall response, as it breaks parity. For the entire system, this can be resolved by introducing a second Pauli-Villars field for the regularization of the second (pseudo-)spin block of the BHZ model. If this field is constructed such that both Pauli-Villars fields are Kramers (time-reversal) partners [8], their combined contribution to the AC Hall conductivity of the entire QAH system vanishes.

3.2.3 Newtonian Mass in the Context of Regularization

Albeit the Newtonian mass term in the Hamilton of a single Chern insulator [cf. Eq. (3.56)] is a physical parameter provided by the material, before renormalization it acts similar to a parity-breaking regulator of a pure QED_{2+1} system in the calculation of the effective action[b]. In what follows, let us concretize this statement.

In the context of quantum field theories there are plenty of different regularization schemes, each breaking different symmetries. As discussed in Sec. 3.1.3, the regularization scheme associated to an odd number of 2+1 dimensional Dirac fermions[c] needs to break the parity symmetry in order to ensure the gauge invariance of the effective action. Manifestly parity breaking regularization schemes are for example Pauli-Villars regularization, lattice regularization with Wilson fermions, and the ζ-function regularization. In what follows, we briefly review these schemes [53, 57, 69, 145].

Lattice Regularization. A common way to regularize a quantum field theory is the introduction

[a] To decouple the Pauli-Villars field during renormalization we eventually tune its mass gap to infinity, $M \to \infty$.

[b] During renormalization each mathematical regulator needs to be removed from the theory. This is in strong contrast to the Newtonian mass term which is a real parameter of the system. Therefore, any comparison between the $B|\mathbf{k}|^2$ term and a regulator needs to be done before renormalization.

[c] Another way to regularize the theory would be to add a second (staggered) Dirac fermion in total respecting all symmetries. Since this is not the physical situation we are interested in, we do not consider this case [37, 52].

of a space-time lattice. In this method, the finite lattice spacing a introduces a momentum cut-off $\Lambda_{\text{lattice}} \propto a^{-1}$. Lattice regularization explicitly breaks the parity symmetry of classical QED_{2+1} [cf. Eq. (2.130)]. This is not a property of the lattice itself, but happens due the mandatory introduction of additional terms in the Lagrangian which prevent artificial gap closings at the high symmetry points of the lattice Brillouin zone. In particular, the Euclidean lattice action $\mathcal{S}_{\text{latt}}(\bar{\psi}, \psi, A)$ is given by [51, 154, 155]

$$S_{\text{latt}}(\bar{\psi}, \psi, A) = -a^3 \sum_x \bar{\psi}(x)(D - m)\psi(x) \ , \tag{3.91}$$

where $x = (an_1, an_2, an_3)$ with $n_\mu \in \mathbb{Z}$. Moreover,

$$D = \frac{1}{2}\gamma_\mu^{\text{E}}(\nabla_\mu^* + \nabla_\mu) + \frac{1}{2}wa\nabla_\mu^*\nabla_\mu \tag{3.92}$$

is the massless 3 dimensional lattice Dirac operator, ∇_μ is the lattice covariant derivative, and $\gamma_\mu^{\text{E}} = \sigma_\mu$ are the Euclidean Dirac matrices. In comparison to continuum QED_{2+1}, $S_{\text{latt}}(\bar{\psi}, \psi, A)$ includes the so-called Wilson term, proportional to the Wilson parameter $w = \pm 1$. This term acts like a momentum dependent fermion mass and therefore explicitly breaks the parity symmetry of the system. As a consequence, it induces a Chern-Simons term in the effective action, proportional to $\text{sgn}(w)$. Hence, this term acts very similar to the Newtonian $B|\mathbf{k}|^2$ term in Eq. (3.56). However, there are two significant differences. One the one hand, the Wilson mass is Lorentz covariant, while the Newtonian mass breaks this symmetry [cf. Sec. 2.4.3]. On the other hand, the Wilson mass vanishes as $a \to 0$, which is not the case for the Newtonian mass term as it is a real parameter of the system.

Higher Derivative Regularization. The Lagrangian associated to the higher derivative regularization of QED_{2+1} is given by [55, 128]:

$$\mathcal{L}_{\text{HD}} = \bar{\psi}\left(\mathrm{i}\gamma^\mu\partial_\mu - m\right)\left(1 + \frac{\partial^2}{M^2}\right)\psi + \mathrm{e}\,\bar{\psi}\gamma^\mu\mathcal{A}_\mu\psi \ , \tag{3.93}$$

where M is a parameter, allowing to remove the higher derivative correction during the renormalization process, $M \to \infty$. Notice, that by construction, the higher derivative term breaks local gauge invariance [cf. Sec. 2.4.4]. However, this property is fixed during renormalization [54]. If the higher derivative correction would come with covariant derivatives, it would not reduce the superficial degree of divergence. Hence, the higher derivative regulator differs significantly form the Newtonian mass in Eq. (3.56). While the Newtonian mass term is parity-odd, breaks Lorentz symmetry and renormalizes the Dirac mass in a gauge invariant fashion, the higher derivative term is Lorenz invariant, breaks local gauge symmetry and multiplies the full non-interacting QED_{2+1} part [cf. Sec. 2.4]. As such, it contains a parity even as well as a parity odd contribution. Moreover, it vanishes during renormalization as $M \to \infty$.

Pauli-Villars Regularization. In contrast to the two schemes above, the Pauli-Villars regularization adds additional bosonic particles χ to the classic QED_{2+1} Lagrangian:

$$\mathcal{L}_{\text{PV}} = \bar{\psi}\left(\mathrm{i}\gamma^\mu D_\mu - m\right)\psi + \bar{\chi}\left(\mathrm{i}\gamma^\mu D_\mu - M\right)\chi \ . \tag{3.94}$$

Their mass term M breaks the parity symmetry and therefore induces a Chern-Simons term in the effective action, proportional to $\text{sgn}(M)$. During renormalization the Pauli-Villars field decouples from the theory, $M \to \infty$. However, it still leaves its trace in the Chern number as we have seen in Eq. (2.159) [37, 52]. Since this regularization scheme includes an additional particle to ensure an integer quantized DC conductivity, it significantly differs from the New-

tonian mass term in Eq. (3.56).

Zeta-Function Regularization. The ζ-function regularization completely differs from the schemes introduced above [53]. It regularizes the generating functional via a certain calculation scheme for the fermion determinant:

$$Z[\mathcal{A}]_{\text{reg}} = \det D[\mathcal{A}]\Big|_{\text{reg}} = \mathrm{e}^{-\frac{d}{ds}\zeta(D[\mathcal{A}],s)}\Big|_{s=0} . \tag{3.95}$$

Here, the Euclidean Dirac operator with $\gamma_\mu^{\text{E}} = \sigma_\mu$ and the ζ-function are defined via

$$\zeta(D[\mathcal{A}],s) = \text{Tr}\left(D^{-s}[\mathcal{A}]\right) \quad \text{with} \quad D[\mathcal{A}] = \gamma_\mu^{\text{E}}(\mathrm{i}\partial^\mu + \mathrm{e}\mathcal{A}^\mu) + \mathrm{i}m . \tag{3.96}$$

By construction, this scheme is gauge invariant, but breaks the parity symmetry, which is related to peculiarities during the associated contour integration (explicit path). It therefore also leads to an integer quantized DC conductivity where one part comes from $\text{sgn}(m)$ and an additional contribution (± 1) stems from the choice of the integration contour [53].

All the schemes introduced above induce a parity odd Chern-Simons term in the effective action of a QED_{2+1} system, directly proportional to the sign of the regularization parameter which breaks the parity symmetry. For the schemes considered, this is the Pauli-Villars mass, the Wilson parameter, as well as the integration contour in the ζ-function regularization. Together with the Chern-Simons contribution induced by the finite Dirac mass m, this leads to an integer quantized DC Hall conductivity [51, 53]. For the Pauli-Villars scheme this can be seen for instance in Eq. (2.163).

Adding the Newtonian mass term to a pure QED_{2+1} system also ensures this property [cf. Eq. (3.75)]. Even if one would remove the physical parameter $B \to 0$ in the end of the calculation, its contribution to the DC Hall conductivity persists and the Chern number remains integer quantized. From this perspective the $B|\mathbf{k}|^2$ term acts similar to a parity breaking element of a certain regularization scheme. To concretize what we mean with 'similar', let us compare the role of the Newtonian mass term in the calculation of the effective action to common parity-breaking regulators before renormalization[a]. Since the $B|\mathbf{k}|^2$ term provides a momentum dependent Dirac mass correction, it is natural to compare its role in the calculation of the effective action to regularization schemes which add terms of higher order derivatives to the bare Lagrangian. As discussed above, such approaches are for example the lattice regularization with Wilson fermions [51] and the higher derivative regularization [54]. However, except for the property that these schemes also yield an integer quantized Chern number, there are several key differences to the $B|\mathbf{k}|^2$ term. By construction, each regularization needs to render the effective action finite [109]. As shown in Eq. (3.87), adding the Newtonian mass to a massive Dirac Lagrangian does not exhibit this property.

To reduce the superficial degree of divergence, the higher derivative regularization multiplies the entire non-interacting Dirac Lagrangian by $(1 + \partial^2/M^2)$. This has two implications. In contrast to the $B|\mathbf{k}|^2$ term, it circumvents the vertex renormalizations in Eqs. (3.62) and (3.63), but as a price manifestly breaks local gauge invariance[b] [cf. Sec. 2.4.4]. Moreover, by construction this approach also regularizes the kinetic part of the Lagrangian.

In a lattice approach, the inverse lattice spacing a^{-1} makes the theory finite. To avoid fermion

[a] During renormalization each mathematical regulator needs to be removed from the theory. This is in strong contrast to the Newtonian mass term which is a real parameter of the system. Therefore, any comparison between the $B|\mathbf{k}|^2$ term and a regulator needs to be done before renormalization.

[b] This property is reestablished during renormalization.

doubling and to break the parity, the lattice QED_{2+1} Lagrangian comes along with an additional Wilson mass term $\propto wak^2$. Here, $w = \pm 1$ is the Wilson parameter and k is the lattice three-momentum [51, 156, 157]. The Wilson mass is clearly related to the $B|\mathbf{k}|^2$ term. However, by construction the Wilson mass is Lorentz invariant, while the Newtonian mass breaks this symmetry [cf. Sec. 2.4.3]. Further, the Wilson mass vanishes during renormalization, $a \to 0$, which is not the case for the $B|\mathbf{k}|^2$ term since it is a material parameter.

Let us end this section by emphasizing that an extensive summary of the results which we have obtained within the scope of this section can be found in Sec. 5.

3.3 Signatures of the Parity Anomaly in Out-Of-Plane Magnetic fields

In Sec. 2.6.3, we have sown that in 2+1 space-time dimensions the parity anomaly results from the incompatibility of parity- and U(1) gauge symmetry after quantization. We calculated the polarization operator of a massive QED_{2+1} system, illustrated how a parity-odd Chern-Simons term arises in the system's effective action, and discussed the peculiarities of regularization schemes for the associated Hall conductivity. Further, in Sec. 3.1.3, we explained in which sense both, the Dirac as well as the Newtonian mass term of a QAH insulator, which is described by the BHZ model, are related to the parity anomaly of planar quantum electrodynamics. We concretized this relation in Sec. 3.2.2 by analyzing the role of the Newtonian mass term in the calculation of the quantum effective action, and, subsequently, discussed this peculiar mass term of a QAH insulator in the context of common high-energy regularization schemes in Sec. 3.2.3. In a nutshell, we performed all of these analyses in order to understand the zero-field Chern number [cf. Eq. (3.19)]

$$\mathcal{C}_{\mathrm{CI}} = [\mathrm{sgn}(m) + \mathrm{sgn}(B)]/2 \tag{3.97}$$

of a single (pseudo-)spin polarized Chern insulator of the BHZ model in the context of the parity anomaly of QED_{2+1}. More precisely, it was the goal of the aforementioned studies to shed light on possible signatures of the parity anomaly in QAH insulators like (Hg,Mn)Te quantum wells or magnetically doped (Bi,Sb)Te thin films. In the present section, we extend our considerations to finite out-of-plane magnetic fields. Especially in QAH insulators like (Hg,Mn)Te quantum wells the application of such a field is mandatory to polarize the paramagnetic Mn dopants, which drives the transition from the QSH to the QAH phase, as it has been explained in Sec. 3.1.1.

In Sec. 2.2, we have elucidated the physics behind the conventional QH effect of two-dimensional electron gases in quantizing out-of-plane magnetic fields. We in particular discussed in Sec. 2.4.2 that such background fields classically break the parity symmetry in 2+1 space-time dimensions and, therefore, give rise to a finite Chern number. Hence, by definition, the parity anomaly is a zero magnetic field effect. This gives rise to the two fundamental questions:

(*i*) Is it possible to measure signatures of the parity anomaly in quantizing out-of-plane magnetic fields?

(*ii*) In which way does the magnetic field topology affect the intrinsic band-inversion of a Chern insulator, Eq. (3.97). As we have shown in our previous analyses, this quantity is directly related to the parity anomaly at zero magnetic fields.

We answered these seminal questions in our recent publication *Survival of the quantum anomalous Hall effect in out-of-plane magnetic magnetic fields as a consequence of the par-*

ity anomaly (Phys. Rev. Lett. **123**, 226602) in November 2019 [P1]. In what follows, we are elucidating the theoretical findings presented in this work, which have been obtained in strong collaboration with Dr. Jan Böttcher[a]. Both of us contributed equally to this publication. While the spectral asymmetry and the Landauer-Büttiker calculations have been mainly developed by Dr. Jan Böttcher, I calculated the LL response for zero-, as well as finite temperatures, derived the corresponding edge state theory including the anomaly inflow, and supported our field theoretical results by determining the Hall conductivity of a single Chern insulator in quantzing out-of-plane magnetic fields by a conventional solid-state Kubo formula [158]. In order to make our field theoretic calculations more comprehensible for an interdisciplinary community, this calculation is, due to its lengthy and sophisticated form, presented in App. 6.1. To simulate the experimental signatures of a Chern insulator under the influence of an adiabatically increasing out-of-plane magnetic field, we solved the associated Schrödinger equation numerically, by using a finite difference approach [159, 160]. The development of the corresponding time-evolution code has been obtained in strong collaboration.

Before we start our discussion, let us briefly elaborate on an intuitive picture regarding the answer to the aforementioned questions (*i*) and (*ii*). As is was explained in Sec. 2.2.1, an out-of-plane magnetic field H adds a parabolic confinement to each wave-function of the system [cf. Eq. (2.22)] and, for this reason, increases/decreases the energy of electron and hole-like states, respectively. This property is in particular independent on the sign of the applied magnetic field. Consequently, an out-of-plane magnetic field counteracts the intrinsic band-inversion of a QAH insulator. As this band-inversion is protected by the system's mass gap, a critical out-of-plane magnetic field is needed in order to remove this inversion completely. In what follows, we are going to show that this critical field is given by

$$H_{\text{crit}} = \text{sgn}(\text{e}H)\,\frac{\hbar m}{\text{e}B}\ . \tag{3.98}$$

Up to this field strength the QAH phase survives in materials like (Hg,Mn)Te quantum wells or magnetically doped (Bi,Sb)Te thin films.

3.3.1 Eigen-System of a Chern-Insulator: Magnetic Field Analysis

Zero Field Dispersion and Finite Difference Method

We start our analysis with the Hamiltonian of the (pseudo-)spin up block of the BHZ model in Eq. (3.4). As explained in Sec. 3.1.1, this Hamiltonian corresponds to a single (pseudo-)spin up polarized Chern insulator in 2+1 space-time dimensions, defined by [cf. Eq. (3.12)]

$$\mathcal{H}_+(\mathbf{k}) = -D|\mathbf{k}|^2\sigma_0 + A\left(k_1\sigma_1 - k_2\sigma_2\right) + \left(m_+ - B|\mathbf{k}|^2\right)\sigma_3\ . \tag{3.99}$$

If it is not stated otherwise, we are neglecting the (pseudo-)spin index $\pm$ for simplification. In what follows, we support our analytic calculations by numerical simulations via a standard finite difference method [159, 160]. This allows us, for instance, to evaluate the energy eigenvalues corresponding to Eq. (3.99) numerically, by mapping the Hamiltonian on a stripe geometry with finite length L_2 in the $\mathbf{e}_2$-direction and periodic boundary conditions along the $\mathbf{e}_1$-direction [161]. In Fig. 3.8(a), the associated band-structure is shown in the topologically non-trivial regime with Chern number $\mathcal{C} = -1$. The bulk bands which are analytically given by [cf. Eq. (3.16)]

$$E^s\left(\mathbf{k}\right) = -D|\mathbf{k}|^2 + s\sqrt{A^2|\mathbf{k}|^2 + \left(m - B|\mathbf{k}|^2\right)^2}\ , \tag{3.100}$$

[a] This work has been supervised by Laurens W. Molenkamp and by Prof. Dr. Ewelina M. Hankiewicz.

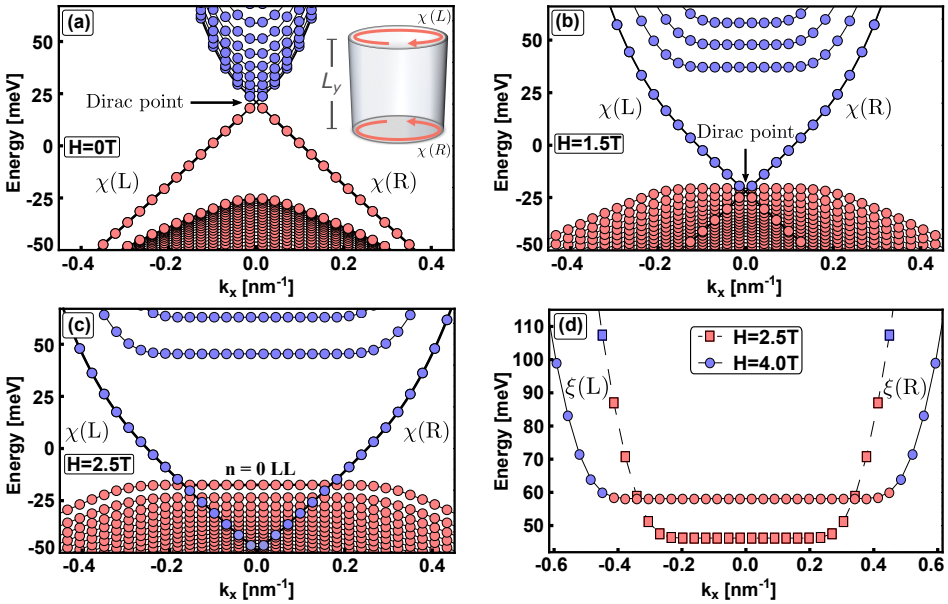

Figure 3.8: Dispersion of a single Chern insulator, $k_1 = k_\mathrm{x}$, in an out-of-plane magnetic field $\mathbf{H} = H\mathbf{e}_3$ (black lines) for $m = -25\,\mathrm{meV}$, $B = -1075\,\mathrm{meVnm}^2$, $D = -900\,\mathrm{meVnm}^2$, and $A = 365\,\mathrm{meVnm}$. χ(L/R) and ξ(L/R) depict QAH and QH edge states at the left- and at the right edge of our system, respectively. (**a**) Spectrum for $H = 0$ at half filling with chiral QAH edge states traversing the bulk gap. The inset illustrates the sample geometry with a finite system size in $\mathbf{e}_2$-direction, $L_2 = L_\mathrm{y}$, and periodic boundary conditions in $\mathbf{e}_1$-direction. (**a**)-(**c**) Evolution of the spectrum and its filling with increasing H. Unoccupied and occupied states are marked in blue and red, respectively. (**d**) Analogous analysis for an initially filled conduction band LL. The figure is reprinted from Ref. [P1] with permission from the APS.

split into multiple subbands due to the finite system size. Again, $s = \pm$ defines the valance- and the conduction band, respectively. Moreover, one observes chiral QAH edge states[a], which traverse the Dirac mass gap. Since we are considering a finite particle-hole asymmetry $D \neq 0$, the Dirac point is located close to the conduction band edge [162].

Next, we implement an out-of-plane magnetic field $\mathbf{H} = H\mathbf{e}_3$ in the Landau gauge via

$$\mathbf{A} = -x_2 H \mathbf{e}_1 \ . \tag{3.101}$$

This has two main effects which are illustrated in Figs. 3.8(b)-(c). We separately analyze these features in the two following subsections.

Bulk Landau Level Spectrum vs. Band Inversion

As a first effect, all bulk subbands evolve into LLs for $l_H \ll L_2$. This causes an asymmetric spectrum which can be understood by analyzing the continuum model. Following the same procedure which we have performed in Sec. 2.2.1, allows us to derive the continuum Landau level spectrum. To this end, we perform a Peierls substitution, insert the gauge-independent momentum operators $\pi_i = k_i + \mathrm{e}A_i/\hbar$ in Eq. (3.99), and replace these operators by the ladder

[a] Since the chiral edge sates of a topologically non-trivial Chern insulator represent the chiral edge states of the associated QAH insulator in the BHZ model (3.4), we label the edge states of a non-trivial Chern insulator 'QAH edge states' within this thesis.

operators a and $a^\dagger$ [cf. Eq. (2.14)]. Depending on the magnetic field, we therefore insert

$$\pi_+ \to \frac{\sqrt{2}}{l_H}\begin{cases} a^\dagger \text{ for } \mathrm{sgn}(\mathrm{e}H) > 0 \\ -a \text{ for } \mathrm{sgn}(\mathrm{e}H) < 0 \end{cases} \quad \wedge \quad \pi_- \to \frac{\sqrt{2}}{l_H}\begin{cases} a \text{ for } \mathrm{sgn}(\mathrm{e}H) > 0 \\ -a^\dagger \text{ for } \mathrm{sgn}(\mathrm{e}H) < 0 \end{cases} \tag{3.102}$$

in the zero-field Hamiltonian Eq. (3.99), where $l_H = \sqrt{\hbar/|\mathrm{e}H|}$ defines the magnetic length. This gives rise to the Hamiltonian of a (pseudo-)spin polarized Chern insualtor in quantizing out-of-plane magentic fields $\mathbf{H} = H\mathbf{e}_\mathrm{z}$. For $\mathrm{sgn}(\mathrm{e}H) = 1$, we find

$$\mathcal{H}(a, a^\dagger) = \begin{pmatrix} m - \omega_+\left(a^\dagger a + \frac{1}{2}\right) & \alpha\, a^\dagger \\ \alpha\, a & -m - \omega_-\left(a^\dagger a + \frac{1}{2}\right) \end{pmatrix}, \tag{3.103}$$

where we defined the abbreviations

$$\alpha = \sqrt{2}A/l_H, \quad \omega_\pm = \delta \pm \beta, \quad \beta = 2B/l_H^2, \quad \delta = 2D/l_H^2\ . \tag{3.104}$$

An appropriate ansatz to solve the corresponding Schrödinger equation for a general magnetic field configuration is given by

$$\psi^s_{n,k_1}(x_2) \propto \begin{cases} \begin{pmatrix} \left(m - \beta n - \frac{\mathrm{sgn}(\mathrm{e}H)\delta}{2} + s\,\epsilon_n\right)\langle x_2|n, k_1\rangle \\ \mathrm{sgn}(\mathrm{e}H)\alpha\sqrt{n}\langle x_2|n-1, k_1\rangle \end{pmatrix} & \text{for } \mathrm{sgn}(\mathrm{e}H) > 0 \\ \begin{pmatrix} \left(m - \beta n - \frac{\mathrm{sgn}(\mathrm{e}H)\delta}{2} + s\,\epsilon_n\right)\langle x_2|n-1, k_1\rangle \\ \mathrm{sgn}(\mathrm{e}H)\alpha\sqrt{n}\langle x_2|n, k_1\rangle \end{pmatrix} & \text{for } \mathrm{sgn}(\mathrm{e}H) < 0\ , \end{cases} \tag{3.105}$$

and

$$\psi_{0,k_1}(x_2) \propto \begin{cases} \begin{pmatrix} \langle x_2|0, k_1\rangle \\ 0 \end{pmatrix} & \text{for } \mathrm{sgn}(\mathrm{e}H) > 0 \\ \begin{pmatrix} 0 \\ \langle x_2|0, k_1\rangle \end{pmatrix} & \text{for } \mathrm{sgn}(\mathrm{e}H) < 0\ , \end{cases} \tag{3.106}$$

where $\epsilon_n = \sqrt{\alpha^2 n + (m - n\beta - \mathrm{sgn}(\mathrm{e}H)\delta/2)^2}$. In the expressions above, we have neglected the normalization constants for simplicity. The corresponding LL eigen-energies for an arbitrary magnetic field configuration are given by [163]

$$E^s_{n\neq 0} = -\mathrm{sgn}(\mathrm{e}H)\beta/2 - n\delta + s\,\epsilon_n\ , \tag{3.107}$$

$$E_0 = \mathrm{sgn}(\mathrm{e}H)\,(m - \beta/2) - \delta/2\ . \tag{3.108}$$

A hallmark of the Dirac-like Hamiltonian in Eq. (3.103) is the relativistic structure of its LL spinors, Eqs. (3.105) and (3.106). This structure follows from the off-diagonal contributions $\propto a$ and $a^\dagger$ in Eq. (3.103), which couple the two conventional, diagonal pseudospin polarized harmonic oscillators in the $\{|E1, +\rangle, |H1, +\rangle\}$-basis. Without hybridization, for $A = 0$, the system would define two independent LL spectra with two decoupled $n = 0$ LLs. This is exemplary shown in Fig. 3.9(a). For $A \neq 0$, the n-th $E1$ and the $(n-1)$-th $H1$ LLs hybridize [163]. It is this asymmetric coupling in out-of-plane magnetic fields which gives rise to the asymmetric LL spectrum in Eqs. (3.107) and (3.108) [33, 39]. However, beside the asymmetry in Eq. (3.107), all LLs with $n \in \mathbb{N}$ come in pairs, meaning that for each

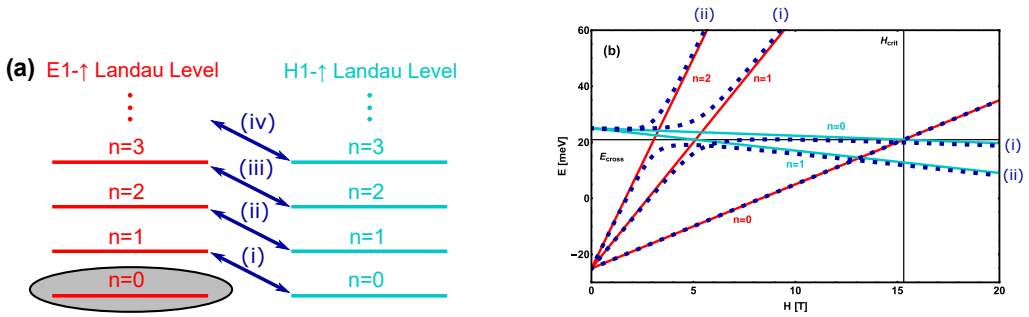

Figure 3.9: Hybridization process and Dirac mass gap closing in the LL spectrum of a single Chern insulator in quantizing out-of-plane magnetic fields. Except for A, all system parameters are defined in the caption of Fig. 3.8. The hybridization between the $E1$- and the $H1$ LLs in out-of-plane magnetic fields is schematically illustrated in subfigure (**a**), where red and cyan lines indicate the $E1$ and $H1$ pseudospin character, respectively. In subfigure (**b**), the LL energies without coupling, meaning for $A = 0$, are depicted by solid lines and are labeled by LL indices. Blue dotted lines illustrate the evolution of LLs in the presence of an hybridization with $A = 45$ meVnm. The figure is reprinted from Ref. [P1] with permission from the APS.

LL in the conduction band with E_n^+, there exists a LL in the valence band with E_n^-. In contrast, the zeroth LL completely decouples from the hybridization process, as it is shown in Fig. 3.9(a). Consequently, its energy eigenvalue in Eq. (3.108) lacks a partner, and its LL spinor in Eq. (3.106) is pseudospin polarized in the $\{|E1,+\rangle, |H1,+\rangle\}$-basis.

Having analyzed the asymmetry of the Landau level spectrum and the form of the corresponding spinors, let us elaborate on the band ordering in out-of-plane magnetic fields. More precisely, let us clarify in which sense the band inversion of a topologically non-trivial Chern insulator, which has been extensively discussed in Sec. 3.1.1, persists in quantizing out-of-plane magnetic fields.
For $H = 0$, the diagonal, parity-odd mass terms in Eq. (3.100) define the band ordering in momentum space. Most remarkably, these elements characterize the band ordering of the Chern insulator in out-of-plane magnetic fields, as well. To understand this statement in detail, let us first study the evolution of the $E1$ and $H1$ LLs without hybridization, separately. To this end, we first study the academic limit $A = 0$, implying that the system is driven by its diagonal contributions. This illustrative model is illustrated by the solid lines in Fig. 3.9(b). Here, we in particular find that each pair of LLs with opposite pseudospin polarization, but with the same LL index n, crosses at the very same energy $E_{\text{cross}} = -mD/B$. This LL crossing is a signature of an inverted band-structure. The higher the LL index, the earlier a pair of states crosses each other with respect to the corresponding out-of-plane magnetic field strength. Without hybridization, the latest crossing would occur between the two $n = 0$ LLs, exactly at the critical field given by Eq. (3.98), $H_{\text{crit}} = \text{sign}(\text{e}H)\hbar m/(\text{e}B)$. This transition defines the critical field at which all $E1$ LLs are above $H1$ LLs. Hence for $H > H_{\text{crit}}$, the band-structure becomes normally ordered. For a finite coupling parameter A, however, this crossing is hidden, due to the hybridization between the $n=1-$ E1 LL and the $n=0-$ H1 LL. This is explicitly shown by the blue dashed line in Fig. 3.9(b)[a]. According to our discussion at zero magnetic fields, the band ordering in finite out-of-plane magnetic fields

[a]Here, we have chosen here a smaller value for the A-parameter than in Fig. 3.8, in order to make the hybridization between adjacent LLs more evident.

should still be solely determined by the parity-odd diagonal mass terms of the Hamiltonian. The coupling parameter A only hides the critical magnetic field at which the band-structure becomes normally ordered. We therefore deduce from our illustrative model that H_{crit} defines the critical magnetic field strength at which the magnetic field topology removes the intrinsic band inversion.
In order to avoid any misunderstanding, let us emphasize once more that the argumentation above has been given for a single (pseudo-)spin polarized Chern insulator in the BHZ model Eq. (3.4). The derived crossing should not be mixed up with the one occurring in the full BHZ model Eq. (3.4), where one would instead observe a crossing between two pseudospin polarized $n = 0$ LLs [163], where each level belongs to a distinct (pseudo-)spin block.

QAH Edge States: Scattering and Hybridization

The second effect of an increasing out-of-plane magnetic field is that it gradually lowers the energy of the Dirac point so that it enters the valence band at $H = H_{\mathrm{scat}}$, as it is illustrated in Figs. 3.8(a,c). The evolution of the QAH edge states as a function of H has been determined by Zhou et al. in Ref. [162]:

$$E^{\pm}_{\mathrm{edge}}\left(k_1, H\right) = E_{\mathrm{D}}(0) - \mu_{\mathrm{B}} g_{\mathrm{eff}}\left(L_2\right) H \pm \hbar v_1 k_1 \ , \tag{3.109}$$

where v_1 is the edge state velocity, $E_{\mathrm{D}}(0)$ is the Dirac point energy at $H = 0$ and the effective g-factor is given by

$$g_{\mathrm{eff}}(L_2) = \mathrm{m}_0\, v_1 \hbar^{-1} \left[L_2 - \lambda_1^{-1} - \lambda_2^{-1} - 2(\lambda_1 + \lambda_2)^{-1}\right] . \tag{3.110}$$

In this expression, $\lambda_{1,2}$ are the decay length scales of the edge states. For $L_2 \gg \lambda_{1,2}^{-1}$, we can further simplify $g_{\mathrm{eff}}(L_2) \approx \mathrm{m}_0 v_1 \hbar^{-1} L_2$. This approximately defines the evolution of the Dirac point with increasing H at $k_1 = 0$:

$$E_{\mathrm{D}}(H) \approx E_{\mathrm{D}}(0) - g_{\mathrm{eff}} \mu_{\mathrm{B}} H \ . \tag{3.111}$$

As it is shown in Figs. 3.8(a,c), the QAH edge states survive (up to finite size gaps) even for large magnetic field strength. This results from the property that these states are protected from hybridization with bulk LL modes by their wave function localization. Let us analyze this feature in detail:

For $\mathrm{sgn}(\mathrm{e}H) > 0$, the QAH edge states are successively lowered in energy with increasing magnetic field strength H. Figure 3.10 simplifies this scenario by only taking into account the flat bulk $n = 0$ LL, as well as the QAH edge states. We are going to use this proof-of-principle model in order to estimate an upper limit until which the QAH edge states can survive in finite out-of-plane magnetic fields. More precisely, with the nomenclature 'survival' we mean that even for $H \neq 0$ the QAH edge states and bulk LLs remain decoupled up to finite size gaps, which are exponentially suppressed in the limit $L_2 \to \infty$. We start our analysis by studying the properties of the zeroth LL in greater detail. While the energy of this level is given by Eq. (3.108), its degeneracy, and therefore its width in the momentum space, increases linearly with the magnetic field strength:

$$k_{\mathrm{max}} = \frac{\mathrm{e}\, H\, L_2}{2\hbar} \ . \tag{3.112}$$

Here, $2\, k_{\mathrm{max}}$ is the full width of the zeroth LL, explicitely depicted in Fig. 3.10. The associated wave functions, $\psi_{0,k_1}(x_2)$, are centered at $x_2(k_1) = l_H^2 k_1$ and their spatial width decreases

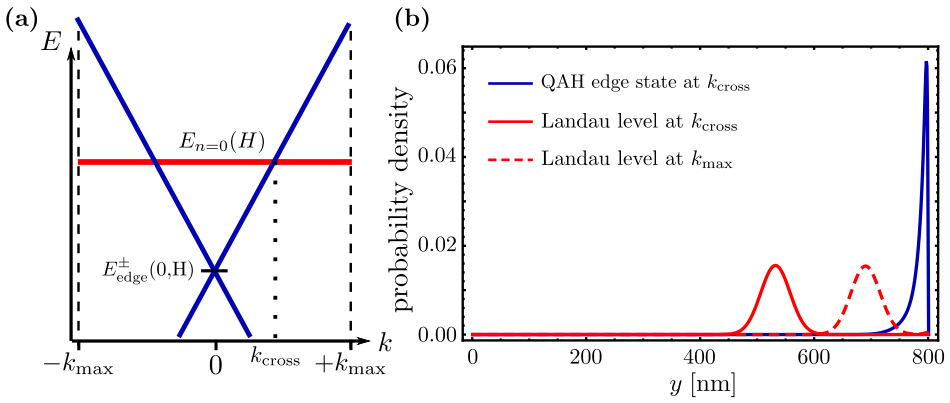

Figure 3.10: Energy gaps between a QAH edge state (blue) and the $n = 0$ LL (red). (**a**) The QAH edge state is successively shifted down in energy with increasing out-of-plane magnetic field strength H, and crosses the flat $n = 0$ bulk LL at $k = k_{\rm cross}$. (**b**) If $k_{\rm cross} \ll k_{\rm max}$, the wave functions of the $n = 0$ bulk LL, depicted as a solid red line, and of the QAH edge state, depicted as a solid blue line, have an exponentially small overlap. The associated hybridization gaps are therefore finite size gaps. Only if the crossing of the QAH edge state and the $n = 0$ LL occur close to $k = k_{\rm max}$, they would significantly start to hybridize causing a finite gap in the spectrum. The associated QAH wave-function is indicated by a red dashed line. The figure is reprinted from Ref. [P1] with permission from the APS.

linearly as we increase H. In Eq. (3.109), we have already approximated the evolution of the QAH edge states in increasing out-of-plane magnetic fields. The crossing between the zeroth LL and the QAH edge states in momentum space, as shown in Fig. 3.10 (a), is denoted by $k_{\rm cross}$. It shifts to larger momenta with increasing magnetic fields. This originates from the fact that the QAH edge states are pushed down in energy, while the $n = 0$ LL is pushed up in energy as a function of H. Most remarkably, Fig. 3.10(b) (solid lines) schematically illustrates that the wave functions of the QAH edge states and the bulk LL are protected from hybridization due to their strong spatial localization. For momenta $k_{\rm cross} \ll k_{\rm max}$, their overlap is exponentially small such that their hybridization gap defines a finite size gap. If the crossing between these states however occurs close to the maximal width of the LL, the bulk wave functions start to strongly overlap with the QAH edge states and energy gaps larger than finite size gaps emerge. As an estimate, the maximal momentum above which the QAH edge states significantly start to hybridize with bulk LLs is, for this reason, determined by $k_{\rm cross} = k_{\rm max}$. Let us clarify at which magnetic field strength this is happening. Therefore, we solve the equation

$$E_{\rm edge}(k_{\rm max}, H) = E_{n=0}(H) \tag{3.113}$$

for H. Due to our discussion above, it is no surprise that the critical magnetic field strength, above which the QAH edge states start to hybridize strongly with bulk LLs, is again given by Eq. (3.98). Hence, our analysis shows that in general the QAH edge states can therefore survive as long as the band inversion 'survives' in quantizing out-of-plane magnetic fields. Nevertheless, let us remark that hybridization gaps larger than finite size gaps might already form for $H < H_{\rm crit}$ as the given proof-of-principle only implies to an upper limit[a].

Let us end this section by computing the critical magnetic field $H_{\rm scat}$ at which the Dirac point enters the valence band. Above this field scattering processes between counterpropagating

[a] This might happen if, for instance, higher order terms in k_1 or H in Eq. (3.109) become of significant relevance.

QH and QAH edges states [cf. Fig. 3.8(c)] become possible, as we will explain in Sec. 3.3.4 in detail. In order to derive an analytic expression for this field, we solve

$$E^{+}_{\text{edge}}(0, H_{\text{scat}}) = E_{n=0}(H_{\text{scat}}) \tag{3.114}$$

for H_{scat}, which implies

$$H_{\text{scat}} = \frac{m\,(B+D)}{B\,(B+D)\,\frac{\mathrm{e}}{\hbar} - \frac{\mathrm{e}}{2}Bv_1\hbar L_2} \propto \frac{1}{L_2}\ . \tag{3.115}$$

3.3.2 Effective Action of a Chern Insulator in Magnetic Fields

To deeply understand the interplay between the parity anomaly and the magnetic field topology from a field theoretic perspective, we derive in this section the low-energy effective bulk Lagrangian $\mathcal{L}^{\text{bulk}}_{\text{eff}}$ of a single Chern insulator in quantizing out-of-plane magnetic fields. Within the scope of our analysis, we derive the system's bulk particle number, relate this value to the so-called spectral asymmetry, which turns out to be a measure of the parity anomaly in magnetic fields, and, eventually, derive from these quantities the system's bulk effective action by using the Lorentz symmetry of the relativistic three current. Hitherto, similar calculations in the literature have been solely performed for pure QED_{2+1} systems [33, 34, 36, 38, 39], meaning for two-dimensional Dirac systems without a $B|\mathbf{k}|^2$ mass term.

Bulk Particle Number and Spectral Asymmetry

As the Chern insulator in Eq. (3.99) is a Dirac-like system it has an infinite Dirac sea. We have already seen several times throughout this thesis that this property causes infinite expressions for many physical observables. For this reason, it requires an appropriate regularization- as well as renormalization scheme, as it has been discussed in Sec. 3.2.3. For zero magnetic fields, this can be achieved by the physical requirement that the fermion number needs to vanish if the chemical potential is placed at the charge neutrality point $E_{\text{z}} = -mD/B$. For a particle-hole symmetric Chern insulator with $D = 0$ the charge neutrality point is located in the middle of the system's bulk gap at $E_{\text{z}} = 0$. One possibility to satisfy the physical constraint above, is to choose antisymmetrization as the appropriate operator ordering for the bulk fermion number operator [36]:

$$N = \frac{1}{2}\int_V \mathrm{d}\mathbf{x}\ \sum_{\alpha}\left[\psi^{\dagger}_{\alpha}(\mathbf{x}), \psi_{\alpha}(\mathbf{x})\right]\ , \tag{3.116}$$

where $\psi(\mathbf{x})$ is a two-component fermionic field operator. In order to calculate the bulk fermion number in finite out-of-plane magnetic fields, the renormalization scheme given by Eq. (3.116) needs to be maintained for $H \neq 0$. In this case, the fermionic field operators can be expanded in terms of the normalized LL spinors of the conduction band $u_{n,k_1}(\mathbf{x}) = \mathrm{e}^{ik_1x}\psi^{+}_{n,k_1}(x_2)$, as well as the valence band $v_{n,k_1}(\mathbf{x}) = \mathrm{e}^{ik_1x}\psi^{-}_{n,k_1}(x_2)$, which we have introduced in Eq. (3.105). In particular, we define:

$$\psi\,(\mathbf{x}) = \sum_{k_1,n} b_{n,k_1}u_{n,k_1}(\mathbf{x}) + \sum_{k_1,n} d^{\dagger}_{n,k_1}v_{n,k_1}(\mathbf{x})\ . \tag{3.117}$$

In this expression b_{n,k_1} destroys an electron in the n-th conduction band LL with momentum k_1, and $d^{\dagger}_{n,k_1}$ creates a hole in the n-th valence band LL with momentum k_1. The associated LL energies are determined by Eqs. (3.107) and (3.108). As we have discussed above, the zeroth LL is special in the sense that it is either part of the valence- or of the conduction

band, depending on its energy. As a result, for $E_{n=0} > E_z$ the first sum in Eq. (3.117) runs from $n = 0 \dots \infty$ and the second sum from $n = 1 \dots \infty$. The situation is vice versa, if the zeroth LL is located at an energy $E_{n=0} < E_z$. In general, all fermionic operators fulfill the conventional anti-commutation relations

$$\left\{b_{n,k_1}, b^\dagger_{m,q_1}\right\} = \delta_{n,m}\delta_{k_1,q_1} \quad \wedge \quad \left\{d_{n,k_1}, d^\dagger_{m,q_1}\right\} = \delta_{n,m}\delta_{k_1,q_1} \,. \tag{3.118}$$

Inserting Eq. (3.117) into Eq. (3.116) implies

$$N = \frac{1}{2}\left(\sum_{k_1,n}[b^\dagger_{n,k_1}, b_{n,k_1}] + \sum_{k_1,n}[d_{n,k_1}, d^\dagger_{n,k_1}]\right) = N_0 - \eta_H/2 \,, \tag{3.119}$$

where we explicitly made use of Eq. (3.118). In Eq. (3.119), N_0 and the so-called spectral asymmetry η_H are given by [36]

$$N_0 = \sum_{k_1,n} b^\dagger_{n,k_1} b_{n,k_1} - \sum_{k_1,n} d^\dagger_{n,k_1} d_{n,k_1}, \tag{3.120}$$

$$\eta_H = \sum_{E>E_z} 1 - \sum_{E<E_z} 1 = \sum_E \mathrm{sgn}\,(E - E_z)\,. \tag{3.121}$$

Let us make some remarks on the spectral asymmetry η_H, as this peculiar quantity will be of significant importance throughout the remaining part of this thesis. By definition, the spectral asymmetry η_H quantifies the asymmetry of the entire eigenvalue spectrum. It counts the difference in the amount of states in the valence and in the conduction band, respectively. As this value is invariant under small, local perturbations, η_H is a topological quantity [36]. While we have explicitly shown in Ref. [P3] that the spectral asymmetry does not depend on the particle-hole asymmetry parameter D, we consider, for simplicity, in the subsequent calculation for η_H a particle-hole symmetric Chern insulator with $D = 0$.

The spectral asymmetry η_H vanishes at $H = 0$, as the amount of states contributing to both individual sums in Eq. (3.121) is symmetric. This line of reasoning breaks down at $H \neq 0$, where this symmetry is violated. In this case every summand in Eq. (3.121) contributes to η_H, as there is no symmetry argument which allows us to cancel summands from the first with the second sum. Due to the fact that η_H consists of two infinite sums which are separately divergent, a regularization scheme has to be introduced. In the scope of the present analysis we are using a heat-kernel approach [6],

$$\forall n \in \mathbb{N}_0 : \quad 1 \to \mathrm{e}^{-\kappa|E_n|}\,, \tag{3.122}$$

where the regularization parameter $\kappa > 0$ ensures the absolute convergence of both sums. At the end of our calculation, during the renormalization procedure, we will perform the limit $\kappa \to 0^+$. Let us make use of Eq. (3.122) in order to rewrite Eq. (3.121):

$$\begin{aligned}\eta_H(\kappa) &= \sum_{k_1,n=1} \mathrm{e}^{-\kappa E^+_n} - \sum_{k_1,n=1} \mathrm{e}^{\kappa E^-_n} + \sum_{k_1} c\mathrm{e}^{-\kappa|E_0|} \\ &= \mathbb{D}\left(\sum_{n=1} \mathrm{e}^{-\kappa E^+_n} - \sum_{n=1} \mathrm{e}^{\kappa E^-_n} + c\,\mathrm{e}^{-\kappa|E_0|}\right) \,,\end{aligned} \tag{3.123}$$

where $c = \mathrm{sgn}\,(\mathrm{e}H)\,\mathrm{sgn}\,(m - \beta/2)$. The last term marks the contribution of the zeroth LL and, in the second equality, we made use of the momentum independence of the eigenvalue spectrum to extract the LL degeneracy $\mathbb{D} = \sum_{k_1} 1 = V/(2\pi l_H^2)$. Here, V is the area of the system. To further simplify Eq. (3.123), we Taylor expand the eigen-energies for large

n:

$$E_n^{\pm} = -s\frac{\beta}{2} \pm n|\beta|\sqrt{1+\frac{\alpha^2 n + m^2 - 2m\beta n}{n^2\beta^2}} \approx -s\frac{\beta}{2} \pm \left[n|\beta| + \mathrm{sgn}(\beta)\left(\frac{\alpha^2}{2\beta} - m\right)\right] . \quad (3.124)$$

Next, we insert this approximation in Eq. (3.123). While this step is only justified for small values of κ, it becomes exact in the limit $\kappa \to 0^+$ for which the heat-kernel regulator affects solely large energy solutions[a]. If we additionally use the geometric series, we are able to recast Eq. (3.123) in the form

$$\eta_{\mathrm{H}}(\kappa)/\mathbb{D} \approx 2s\, \mathrm{e}^{-\kappa \mathrm{sign}(\beta)\left(\frac{\alpha^2}{2\beta} - m\right)} \sinh\left(\kappa\beta/2\right)\left[\frac{1}{1-\mathrm{e}^{-\kappa|\beta|}} - 1\right] + c\,\mathrm{e}^{-\kappa|E_0|} . \quad (3.125)$$

The spectral asymmetry is defined as the analytic continuation of Eq. (3.125) for $\kappa \to 0^+$. This eventually implies

$$\eta_{\mathrm{H}} = \lim_{\kappa\to 0^+} \eta_{\mathrm{H}}(\kappa) = \mathbb{D}\,\mathrm{sgn}\left(\mathrm{e}H\right)\left[\mathrm{sgn}\left(m - \beta/2\right) + \mathrm{sgn}\left(B\right)\right] . \quad (3.126)$$

Equations (3.120) and (3.126) finally enable us to calculate the bulk charge density $j^0_{\mathrm{bulk}}(\mu, H)$. Let us first focus on the ground state with the chemical potential located at charge neutrality $\mu = E_{\mathrm{z}}$. In this case, according to Eq. (3.119), the bulk charge density is given by

$$j^0_{\mathrm{bulk}}(\mu = E_{\mathrm{z}}, H) = -\mathrm{e}\langle \mathrm{vac}|N|\mathrm{vac}\rangle/V , \quad (3.127)$$

where we defined $|\mathrm{vac}\rangle = \Pi_{n,k_1} d_{n,k_1}|0\rangle$. Since in Eq. (3.120) the operators are normally ordered with respect to E_{z}, $N_0|\mathrm{vac}\rangle = 0$. Thus in the ground state, at $\mu = E_{\mathrm{z}}$, the bulk charge carrier density is solely given by the spectral asymmetry

$$j^0_{\mathrm{bulk}}(\mu = E_{\mathrm{z}}, H) = \frac{\mathrm{e}}{2V}\eta_{\mathrm{H}} = \frac{\mathrm{e}^2 H}{2\mathrm{h}}\left[\mathrm{sgn}\left(m - \beta/2\right) + \mathrm{sgn}\left(B\right)\right] . \quad (3.128)$$

This crucial feature is a hallmark of the parity anomaly in quantizing out-of-plane magnetic fields [33, 38]. In contrast to the half-quantized Hall conductivity [cf. Eq. (3.21)] obtained for a massive two-dimensional Dirac fermion [33, 39], we find that the effective mass parameter $B|\mathbf{k}|^2$ acts similar than a high-energy regulator for the calculation of the bulk charge density, resulting in the required integer quantization of the Hall conductivity [25]. In Sec. 3.2.2, we have clarified this relation in detail for zero magnetic fields. The present analysis generalizes our conclusions to quantizing out-of-plane magnetic fields.

Let us make some more remarks regarding our result in Eq. (4.114). The asymmetry of the entire LL spectrum which originates from the Newtonian mass term acts as if effectively a partner of the zeroth LL exists at large energies. Most remarkably, Eq. (3.126) implies that the spectral asymmetry vanishes when the $n = 0$ LL crosses charge neutrality at $E_{\mathrm{n=0}} = E_{\mathrm{z}}$. This corresponds to the critical magnetic field H_{crit} in Eq. (3.98) at which the LL spectrum loses all its information about the band inversion. Last but not least let us emphasize that Eq. (4.114) does not change if we include a finite particle-hole asymmetry in the calculation above. We have rigorously proven this statement in Ref. [P3]. Basically, this property originates from the fact that the $D|\mathbf{k}|^2$-term is not related to the parity anomaly [cf. Secs. 3.1.2 and 3.2], as it is a parity-even contribution to the zero-field Hamiltonian.

Now that we have determined j^0_{bulk} at charge neutrality, $\mu = E_{\mathrm{z}}$, let us proceed by calculating the bulk charge density for arbitrary chemical potentials. As this response is in general dependent on the particle-hole asymmetry, we will from now on again incorporate a finite D-

[a] To proof this statement, we use the identity $\lim_{\kappa\to 0^+}\left[\sum_{n=1}^{\infty}(\kappa n^{-1})^m \mathrm{e}^{-\kappa c n}\right] = 0$ for $m = 1, 2, 3, \ldots$

parameter. With Eq. (3.119) the entire bulk charge density at an arbitrary chemical potential μ is given by

$$j^0_{\text{bulk}}(\mu, H) = = -\frac{\mathrm{e}}{V}\langle\Phi(\mu)|N_0|\Phi(\mu)\rangle + j^0_{\text{bulk}}(\mu = E_{\text{z}}, H) \ , \tag{3.129}$$

where $|\Phi(\mu)\rangle$ defines a general many-particle state for which all states are filled up to μ. The vacuum expectation value of the ordinary particle number operator N_0 at a finite thermal energy $\mathrm{k_B}T = \beta_{\text{th}}^{-1}$ and a chemical potential μ, is given by [36]

$$\langle N_0\rangle = \sum_{n\in\mathbb{N}_0} \mathrm{sgn}(E_n - E_{\text{z}}) \left(\frac{\Theta(E_n - E_{\text{z}})}{\mathrm{e}^{\beta_{\text{th}}(E_n-\mu)}+1} + \frac{\Theta(E_{\text{z}} - E_n)}{\mathrm{e}^{-\beta_{\text{th}}(E_n-\mu)}+1} \right) \ , \tag{3.130}$$

where $\mathrm{k_B}$ is the Boltzmann constant and the sum over E_n runs over all eigen-energies in Eqs. (3.107) and (3.108). Here, we are considering the zero temperature limit

$$\lim_{\beta_{\text{th}}\to\infty} \frac{1}{\mathrm{e}^{-\beta_{\text{th}}(E_n-\mu)}+1} = \Theta(E_n - \mu) \ . \tag{3.131}$$

An extension incorporating thermal effects will be discussed in Sec.3.4. First, let us calculate the $n \neq 0$ LL contributions to Eq. (3.130). With the LL degeneracy $|\mathrm{e}H|/(2\pi)$ these contributions are given by

$$\begin{aligned} &\sum_{n\neq 0} \mathrm{sgn}(E_n - E_{\text{z}}) \left(\Theta[E_n - E_{\text{z}}]\Theta[\mu - E_n] + \Theta[-E_n + E_{\text{z}}]\Theta[E_n - \mu]\right) \qquad (3.132)\\ &= \frac{|\mathrm{e}H|}{2\pi} \sum_{n\neq 0} \Theta[\mu - E_n^+] + \sum_{n\neq 0} (-1)\Theta[-(\mu - E_n^-)] = \frac{|\mathrm{e}H|}{2\pi} \sum_{n\neq 0, s=\pm} s\,\Theta[s(\mu - E_n^s)] \ , \end{aligned}$$

where $E_n^{\pm}$ are the conduction and valence band energy solutions in Eq. (3.107). Next, we are performing the same analysis for the $n = 0$ LL. The energy of this level is given by [cf. Eq. (3.108)]

$$E_0 = \mathrm{sgn}(\mathrm{e}H)(m - \beta/2) - \delta/2 \equiv \tilde{E}_0 - \delta/2 \ . \tag{3.133}$$

Here, $\tilde{E}_0$ is the energy of the zeroth LL at zero particle-hole asymmetry, meaning for $D = \delta = 0$. Taking the zero temperature limit of Eq. (3.130) for the zeroth LL implies:

$$\begin{aligned} &\frac{|\mathrm{e}H|}{2\pi} \mathrm{sgn}(E_0 - E_{\text{z}}) \left[\Theta(E_0 - E_{\text{z}})\Theta(\mu - E_0) + \Theta(-E_0 + E_{\text{z}})\Theta(E_0 - \mu)\right] \qquad (3.134)\\ &= \frac{|\mathrm{e}H|}{2\pi} \mathrm{sgn}(E_0 - E_{\text{z}}) \left[\Theta(E_0 - E_{\text{z}})\Theta(\bar{\mu} - \tilde{E}_0) + \Theta(-E_0 + E_{\text{z}})\Theta(\tilde{E}_0 - \bar{\mu})\right] \ , \qquad (3.135) \end{aligned}$$

where we introduced $\bar{\mu} = \mu + \delta/2$. As we have shown in Sec. 3.3.1, the magnetic field at which the zeroth LL crosses charge neutrality, namely H_{crit}, exactly corresponds to the magnetic field at which the band-inversion vanishes and the system becomes trivial [cf. Eq. (4.114)]. Consequently,

$$\mathrm{sgn}(E_0 - E_{\text{z}}) = \mathrm{sgn}(\tilde{E}_0) \ . \tag{3.136}$$

While for $D = 0$ this identity is trivially satisfied, it needs to be proven for $D \neq 0$. On the one hand, for $E_{\text{z}} = -mD/B$, both arguments in Eq. (3.136) change sign at the same magnetic field strength as

$$\tilde{E}_0 = 0 \quad \Rightarrow \quad H_{\text{crit}} = \mathrm{sgn}(\mathrm{e}H)\frac{m}{B} \qquad \wedge \qquad E_0 = E_{\text{z}} \quad \Rightarrow H_{\text{crit}} = \mathrm{sgn}(\mathrm{e}H)\frac{m}{B} \ . \tag{3.137}$$

On the other hand, they have the same sign for small magnetic fields, assuming that $D/B < 1$, which means that the Dirac point, and hence charge neutrality, is located in the system's mass gap:

$$\begin{aligned}\operatorname{sgn}(E_0 - E_\mathrm{z}) &\overset{\text{small field}}{=} \operatorname{sgn}\left[\operatorname{sgn}(\mathrm{e}H)m - (-mD/B)\right] \\ &= \operatorname{sgn}\left[m(\operatorname{sgn}(\mathrm{e}H) + D/B)\right) = \operatorname{sgn}(\mathrm{e}Hm)\ ,\end{aligned} \tag{3.138}$$

$$\operatorname{sgn}(\tilde{E}_0) \overset{\text{small field}}{=} \operatorname{sgn}[\mathrm{e}Hm]\ . \tag{3.139}$$

Using the identity in Eq. (3.136) implies the zeroth LL charge contribution

$$\begin{aligned}&\frac{|\mathrm{e}H|}{2\pi}\operatorname{sgn}(\tilde{E}_0)\left[\Theta(\tilde{E}_0)\Theta(\bar{\mu}-\tilde{E}_0) + \Theta(-\tilde{E}_0)\Theta(\tilde{E}_0-\bar{\mu})\right] \\ &= \frac{|\mathrm{e}H|}{2\pi}\operatorname{sgn}(\tilde{E}_0)\left[\Theta(\tilde{E}_0)\Theta(\bar{\mu}-|\tilde{E}_0|) + \Theta(-\tilde{E}_0)\Theta(-|\tilde{E}_0|-\bar{\mu})\right] \\ &= \frac{|\mathrm{e}H|}{2\pi}\operatorname{sgn}(\tilde{E}_0)\left[\Theta(\tilde{E}_0)\Theta(\bar{\mu})\Theta(|\bar{\mu}|-|\tilde{E}_0|) + \Theta(-\tilde{E}_0)\Theta(-\bar{\mu})\Theta(|\bar{\mu}|-|\tilde{E}_0|)\right] \\ &= \frac{|\mathrm{e}H|}{2\pi}\operatorname{sgn}(\tilde{E}_0)\left[\Theta(\tilde{E}_0)\Theta(\bar{\mu}) + \Theta(-\tilde{E}_0)\Theta(-\bar{\mu})\right]\Theta(|\bar{\mu}|-|\tilde{E}_0|) \\ &= \frac{|\mathrm{e}H|}{2\pi}\,\frac{1}{2}\left(\operatorname{sgn}(\bar{\mu}) + \operatorname{sgn}(\tilde{E}_0)\right)\Theta(|\bar{\mu}|-|\tilde{E}_0|)\ .\end{aligned} \tag{3.140}$$

Consequently, we found that the entire bulk charge density in our system is given by

$$\begin{aligned}j^0_\mathrm{bulk}(\mu,H) = \frac{\mathrm{e}^2 H}{2\mathrm{h}}\left[\operatorname{sgn}(m-\beta/2) + \operatorname{sgn}(B)\right] - \frac{\mathrm{e}|\mathrm{e}H|}{2\mathrm{h}}\left(\operatorname{sgn}(\bar{\mu}) + \operatorname{sgn}(\tilde{E}_0)\right)\Theta(|\bar{\mu}|-|\tilde{E}_0|) \\ - \frac{\mathrm{e}|\mathrm{e}H|}{\mathrm{h}}\sum_{n\neq 0, s=\pm} s\,\Theta[s(\mu - E^s_n)]\ .\end{aligned} \tag{3.141}$$

Bulk Effective Action: A Chern-Simons Analysis

Having determined the bulk charge density allows us to derive the effective bulk Lagrangian $\mathcal{L}^\mathrm{bulk}_\mathrm{eff}(\mu,H)$ of a single Chern insulator in quantizing out-of-plane magnetic fields, which characterizes the response of our system to a small perturbing field a_μ on top of the underlying background field H. This small perturbation induces an additional bulk charge density $j^0_\mathrm{ind} = \sigma_\mathrm{xy}\,\nabla\times\mathbf{a}$ on top of j^0_bulk. From this expression we can deduce the entire induced three current j^μ_ind by the requirement of Lorentz covariance [33]:

$$j^\mu_\mathrm{ind}(\mu) = \sigma_\mathrm{xy}(\mu,H)\epsilon^{\mu\nu\rho}\partial_\nu a_\rho\ . \tag{3.142}$$

From this expression we can derive the effective bulk Lagrangian using the property

$$j^\mu_\mathrm{ind}(\mu) = \frac{\delta\mathcal{S}^\mathrm{bulk}_\mathrm{eff}(\mu,H)}{\delta a_\mu} \quad \text{with} \quad \mathcal{S}^\mathrm{bulk}_\mathrm{eff} = \int \mathrm{d}^3x\,\mathcal{L}^\mathrm{bulk}_\mathrm{eff}\ . \tag{3.143}$$

In particular, this implies the topological Chern-Simons Lagrangian [164]

$$\mathcal{L}^\mathrm{bulk}_\mathrm{eff}(\mu,H) = \frac{\sigma_\mathrm{xy}(\mu,H)}{2}\,\epsilon^{\mu\nu\rho}a_\mu\partial_\nu a_\rho\,, \tag{3.144}$$

with the quantized Hall conductivity

$$\sigma_{\mathrm{xy}} = \kappa_{\mathrm{QAH}} - \kappa^0_{\mathrm{QH}}\Theta\left(|\mu + D/l_H^2| - \left|m - B/l_H^2\right|\right) - \sum_{s=\pm,\, n=1}^{\infty} s\kappa_{\mathrm{QH}}\Theta\left[s(\mu - E_n^s)\right] \ . \tag{3.145}$$

The peculiarities of Chern-Simons field theories have been extensively discussed in Sec. 2.6.4. According to their physical origin, we separated σ_{xy} into three parts:

$$\kappa_{\mathrm{QAH}} = \frac{\mathrm{e}^2}{2\mathrm{h}}\left[\mathrm{sgn}(m - B/l_H^2) + \mathrm{sgn}(B)\right] \ , \tag{3.146a}$$

$$\kappa^0_{\mathrm{QH}} = \frac{\mathrm{e}^2}{2\mathrm{h}}\left[\mathrm{sgn}(\mathrm{e}H)\,\mathrm{sgn}(\mu + D/l_H^2) + \mathrm{sgn}(m - B/l_H^2)\right] \ , \tag{3.146b}$$

$$\kappa_{\mathrm{QH}} = \frac{\mathrm{e}^2}{\mathrm{h}}\mathrm{sgn}(\mathrm{e}H) \ . \tag{3.146c}$$

Let us remark that in order to make our field theoretic calculations more comprehensible for an interdisciplinary community, we also determined the Hall conductivity in the system's Dirac mass gap, Eq. (3.146a), via a conventional solid-state Kubo formula [158]. This calculation is, due to its lengthy and sophisticated form, presented in App. 6.1.

As we have discussed in Secs. 2.6 and 3.2, CS terms arise in the effective action of 2+1 dimensional Dirac-like systems as a consequence of a broken parity as well as time-reversal symmetry [37, 164]. In our case, Eq. (3.146) originates from the parity-odd mass terms m and $B|\mathbf{k}|^2$, as well as from the parity breaking magnetic field H [cf. Sec. 2.4.2]. In general, we distinguish two types of CS terms in Eq. (3.146):

The first type, Eq. (3.146a), is defined by its exclusive relation to m and $B|\mathbf{k}|^2$, implying a violation of the Onsager relation, $\sigma_{\mathrm{xy}}(-H) \neq -\sigma_{\mathrm{xy}}(H)$[a]. This term is a signature of the parity anomaly at $H = 0$, which requires that a single, parity invariant Chern insulator cannot exist in 2+1 space-time dimensions [37], as it has been elucidated in the Secs. 2.6.3 and 3.1.3. This special origin of the first CS term is reflected by the fact that Eq. (3.146a) is solely determined by the spectral asymmetry

$$\eta_{\mathrm{H}} = \frac{2\mathbb{D}\mathrm{h}}{\mathrm{e}^2}\mathrm{sgn}(\mathrm{e}H)\kappa_{\mathrm{QAH}} \ , \tag{3.147}$$

as we have proven in Eq. (4.114). Consequently, this CS contribution is a property of the entire eigenvalue spectrum and, hence, does not come along with an Heaviside function.

The second type of CS terms, Eqs. (3.146b) and (3.146c), describes conventional QH physics generated by a quantizing out-of-plane magnetic field, as it is indicated by their $\mathrm{sgn}(\mathrm{e}H)$-dependence, implying the Onsager relation $\sigma_{\mathrm{xy}}(-H) = -\sigma_{\mathrm{xy}}(H)$. In contrast to the first type, each of these CS terms is related to a single LL, which is reflected by the fact that they come along with cut-off Heaviside Theta functions. As such, these terms can only contribute to the entire Hall conductivity for chemical potential satisfying $|\mu + D/l_H^2| > |m - B/l_H^2|$.

Fig. 3.11 visualizes these statements by analyzing the Landau fan of our Chern insulator in increasing out-of-plane magnetic fields H. Here, we assumed $D = 0$ for simplicity.

Let us first discuss our findings for the topologically trivial case with $m/B < 0$. In this case only κ^0_{QH} and κ_{QH} contribute to the entire Hall conductivity σ_{xy} as $\kappa_{\mathrm{QAH}} = 0$. The corresponding evolution of the LL energies in Eqs. (3.107) and (3.108) as a function of the magnetic field strength H is shown in the Figs. 3.11 (a) and (b) for positive as well as for

[a] More precisely, in the present thesis we define the Onsager relation as $\sigma_{\mathrm{xy}}(-H, m, B) = -\sigma_{\mathrm{xy}}(H, m, B)$. This property does not hold in the Dirac mass gap of a Chern insulator where Eq. (3.146a) describes the system's response. We call this feature a 'violation' of the Onsager relation. Instead, a Chern insulator fulfills the generalized definition $\sigma_{\mathrm{xy}}(-H, -m, -B) = -\sigma_{\mathrm{xy}}(H, m, B)$.

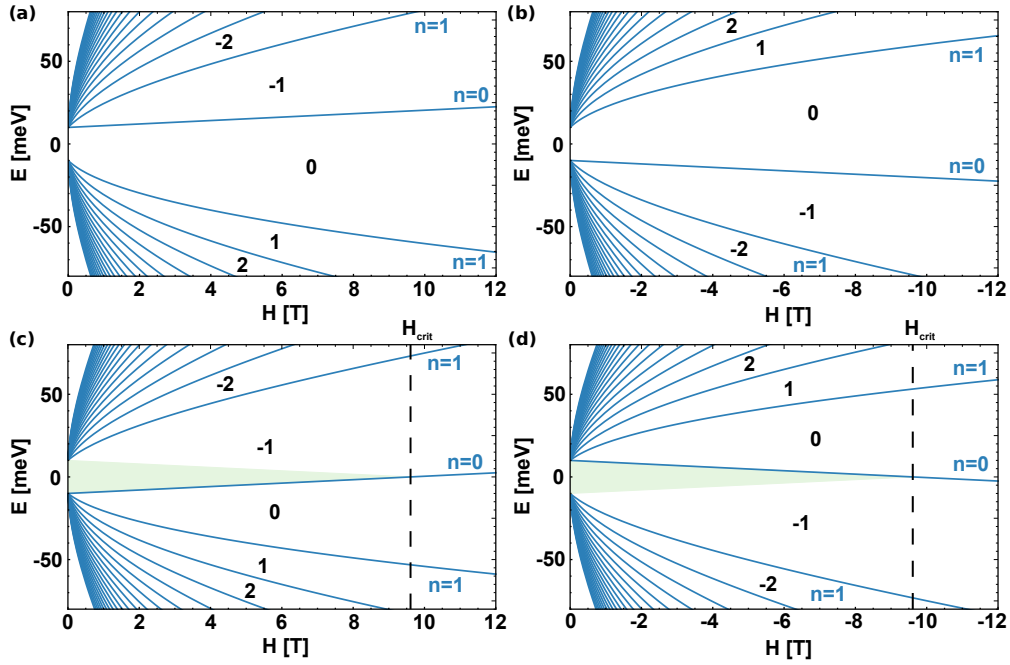

Figure 3.11: The evolution of the bulk LL energies (3.107) and (3.108), the so-called LL-fan, is depicted as a function of the out-of-plane magnetic field strength H. For (**a**) and (**c**) $H > 0$, whereas for (**b**) and (**d**) $H < 0$. Black numbers indicate the entire Hall conductivity σ_{xy} [e^2/h] in the corresponding region. The Hall conductivity only changes if a LL (blue line) is crossed. For (a) and (b) we use $m = +10\,\mathrm{meV}$, $B = -685\,\mathrm{meVnm}^2$, $D = 0\,\mathrm{meVnm}^2$, and $A = 365\,\mathrm{meVnm}$, implying that $\kappa_{\mathrm{QAH}} = 0$. For (c) and (d) the same parameters as in (a) and (b) are used except for $m = -10\,\mathrm{meV}$, implying $\kappa_{\mathrm{QAH}} = -\mathrm{e}^2/\mathrm{h}$ for $H < H_{\mathrm{crit}}$. If the chemical potential is placed such that $|\mu| < |E_0|$ which is depicted by the green shaded areas, the Hall conductivity remains invariant for $H \to -H$ below this critical field. For clarity, the $n = 0$ LL and the first pair of LLs with $n = 1$ are labeled in all subfigures. The figure is reprinted from Ref. [P1] with permission from the APS.

negative magnetic fields, respectively. For $n \geq 1$, all LLs come in pairs $E^{\pm}_{n\neq 0}$, indicating that every conduction band LL has a partner in the valence band. According to Eq. (3.146c), each of these valence (conduction) band LL contributes $\sigma_{\mathrm{xy}} = +\mathrm{e}^2/\mathrm{h}$ ($\sigma_{\mathrm{xy}} = -\mathrm{e}^2/\mathrm{h}$) to the entire Hall conductivity for $H > 0$. For $H < 0$, they contribute with the opposite sign. This characteristic $\mathrm{sgn}(\mathrm{e}H)$-dependence is a feature of a conventional LL response. Let us emphasize that the $\mathrm{sgn}(\mathrm{e}H)$-dependence does also hold for the $n = 0$ LL. However, as pointed out before, the zeroth LL lacks a partner [25]. This implies that there is only one $n = 0$ LL which is either part of the valence or of the conduction band, as can be seen by comparing Fig. 3.11 (a) with (b). This asymmetry is reflected by Eq. (3.146b). One the one hand, it shows the characteristic $\mathrm{sgn}(\mathrm{e}H)$-dependence, whereas on the other hand it contains the information about the absence of a zeroth LL partner. Finally, let us remark that one would need to shift the chemical potential from the conduction into the valence band ($\mu \to -\mu$) in order to observe for $H > 0$ and $H < 0$ the same sign of the Hall conductivity.

Having discussed the trivial topology, let us now focus on the topologically non-trivial case with $m/B > 0$. In this situation, all statements made for κ_{QH} and κ^0_{QH} remain valid but, in contrast to the trivial case, κ_{QAH} now contributes to the entire Hall conductivity. This case is shown in Figs. 3.11 (c) and (d). Since $\kappa_{\mathrm{QAH}} \neq 0$ for $H < H_{\mathrm{crit}}$, there is a range of chemical potentials for which the Hall conductivity does not change its sign for $H \to -H$. To be precise, this regime is given by $|\mu| < |E_0|$, meaning that the chemical potential must

be placed in the Dirac mass gap, which is indicated by the green shaded area in Fig. 3.11. Physically, this implies that the conventional Landau level physics, described by κ_{QH} and κ^0_{QH}, comes on top of an overall underlying contribution κ_{QAH}. According to Eq. (3.126), this contribution is related to the spectral asymmetry and shifts the Hall conductivity such that it becomes $\sigma_{\mathrm{xy}} = -\mathrm{e}^2/\mathrm{h}$ (for $m, B < 0$) in the Dirac mass gap. We identify this signature as a hallmark of the QAH response which remains encoded even in quantizing out-of-plane magnetic fields. This property is in accordance with Streda's formula but implies that the Onsager relation, $\sigma_{\mathrm{xy}}(-H) = -\sigma_{\mathrm{xy}}(H)$, is violated in the Dirac mass gap due to the parity anomaly.

Effective Edge Theory and The Callan-Harvey Mechanism

In order to derive the corresponding edge theory of our bulk CS Lagrangian in Eq. (3.144), we have to add a new degree of freedom to $\mathcal{L}^{\mathrm{bulk}}_{\mathrm{eff}}$. This can be inferred from the fact that any CS term changes by a total derivative under a local gauge transformation, $\mathcal{L}^{\mathrm{bulk}}_{\mathrm{eff}} \to \mathcal{L}^{\mathrm{bulk}}_{\mathrm{eff}} + \delta\mathcal{L}^{\mathrm{bulk}}_{\mathrm{eff}}$, causing a violation of the charge conservation, $\partial_\mu j^\mu_{\mathrm{ind}} \neq 0 \,|_{\partial\Omega}$, at the boundary $\partial\Omega$ [164, 165]. We have extensively studied this property in the Secs. 2.165, 2.6.7, and 2.6.6. It was shown that in order to cancel this U(1)-anomaly, we need to enlarge our description by an effective edge Lagrangian $\mathcal{L}^{\partial\Omega}_{\mathrm{eff}}$, which restores gauge invariance via anomaly cancellation between the edge- and the bulk theory, respectively [102, 131, 165, 166]:

$$\begin{aligned} \partial_\mu j^\mu_{\mathrm{tot}} &= \partial_\mu \left(j^\mu_{\mathrm{ind}} + j^\mu_{\mathrm{L}} + j^\mu_{\mathrm{R}}\right) = 0 \\ \Rightarrow \partial_\mu j^\mu_{\mathrm{L/R}} &= \frac{\sigma_{\mathrm{xy}}}{2}\, \delta\Big(x_2 - x_2^{\mathrm{L/R}}\Big)\, \epsilon^{2\nu\lambda}\partial_\nu a_\lambda = -\partial_\mu j^\mu_{\mathrm{ind}}\,, \end{aligned} \tag{3.148}$$

where $j^\mu_{\mathrm{L/R}}$ characterizes the induced currents at the left/right edge of our stripe geometry [cf. Sec. 2.6.6]. This procedure, known as the Callan-Harvey mechanism [cf. Sec. 2.6.7], is the field-theoretical analog to the bulk-boundary correspondence [121].

As it has already been shown in Fig. 2.11, Eq. (3.148) implies that an increasing out-of-plane magnetic field induces a charge accumulation in the system's bulk, which is compensated by a charge depletion at its edges, if one assumes a fixed integrated charge density [38, 130, 167]. The amount of the induced bulk charge density is given by $j^0_{\mathrm{ind}} = \sigma_{\mathrm{xy}} \nabla \times \mathbf{a}$. From Eq. (3.148), one can deduce the effective edge theory [cf. Secs. 2.6.5 and 2.6.6]:

$$\mathcal{L}^{\partial\Omega}_{\mathrm{eff}} = \mathcal{L}^{\mathrm{L}}_{\mathrm{eff}}\, \delta\left(x_2 - x_2^{\mathrm{L}}\right) + \mathcal{L}^{\mathrm{R}}_{\mathrm{eff}}\, \delta\left(x_2 - x_2^{\mathrm{R}}\right),$$

$$\mathcal{L}^{\frac{\mathrm{L}}{\mathrm{R}}}_{\mathrm{eff}} = \chi^\dagger\, \mathrm{i}\left(\partial_t \mp \frac{\mathrm{h}}{\mathrm{e}^2}\kappa_{\mathrm{QAH}}\, D_1\right)\chi \tag{3.149a}$$

$$+\ \xi_0^\dagger\, \mathrm{i}\left(\partial_t \mp \frac{\mathrm{h}}{\mathrm{e}^2}\kappa^{n=0}_{\mathrm{QH}}\, D_1\right)\xi_0\, \Theta\left(|\mu + \frac{D}{l_H^2}| - |m - \frac{B}{l_H^2}|\right) \tag{3.149b}$$

$$+\ \sum_{n=1\,,\,s=\pm}^{\infty} s\, \xi_n^\dagger\, \mathrm{i}\left(\partial_t \mp \frac{\mathrm{h}}{\mathrm{e}^2}\kappa^n_{\mathrm{QH}}\, D_1\right)\xi_n \Theta\left[s(\mu - E^s_n)\right], \tag{3.149c}$$

where χ (ξ_n) defines QAH (QH) edge states and $D_1 = \partial_1 + \mathrm{i}\mathrm{e}\, a_\mu/\hbar$. Equation (3.149a) is linked to Eq. (3.146a) and characterizes QAH edge states, persisting in quantizing out-of-plane magnetic fields. The QAH edge states do not come along with an Heaviside Theta function and are therefore not bound to a specific LL . In contrast, they bridge the gap between the valence- and the conduction band. This finding is in accordance with our band-structure calculations, shown in Fig. 3.8. Since Eq. (3.149a) is connected to the spectral asymmetry η_{H}, charge pumping via anomaly cancellation can occur from the QAH edge states into any LL. This pumping mechanism is therefore a signature of the parity anomaly and can, in

general, exist until the Dirac mass gap is eventually closed at the critical field

$$H_{\mathrm{crit}} = (\mathrm{e}H)\,\frac{\hbar}{\mathrm{e}}\frac{m}{B}\ . \tag{3.150}$$

Equations (3.149b) and (3.149c) are related to Eqs. (3.146b) and (3.146c) and define conventional QH edge states. These states are bound by single LLs, which is indicated by their Theta functions. Therefore, the corresponding charge flow only appears between the individual edge states and their associated LL.

3.3.3 Anomaly Induced Charge Pumping: QAH vs. QH Phase

In the present section, we are going to highlight the differences in the charge pumping between QAH- and QH phases. Therefore, we simulate the associated time-dependent charge distributions as a function of an increasing out-of-plane magnetic field strength $H(t)$ by solving the time-dependent Schrödinger equation numerically. Within the scope of this section, we consider an impurity-free system. We will comment on effects originating from (in)elastic scattering processes in the next section. As in typical experiments [168–170], we keep the system's integrated particle density instead of the chemical potential constant throughout our simulations.

Time Evolution and Anomaly Inflow

In what follows, we elucidate the response of our system originating from an applied vector potential $\mathbf{A}(t) = \mathbf{A}(t_{\mathrm{i}}) + \mathbf{a}(t)$ with $t \in [t_{\mathrm{i}} = 0, t_{\mathrm{f}}]$, where $\mathbf{A}(t_{\mathrm{i}})$ is a time-independent gauge field and $\mathbf{a}(t) = -x_2 H(t)\mathbf{e}_1$ is a time-dependent perturbation. Since we apply the Peierls substitution in the Landau gauge [cf. Eq. (3.101)], k_1 remains a well-defined momentum in the system considered. This enables us to write the time-dependent Hamiltonian and its corresponding Hilbert space in terms of a direct sum:

$$\mathcal{H}(t) = \bigoplus_{k_1} \mathcal{H}_{k_1}(t)\ . \tag{3.151}$$

Consequently, our numerical simulations can be performed on each Hilbert subspace separately. At the initial time t_{i}, the system's eigen-states are solutions of the time-independent Schrödinger equation:

$$\mathcal{H}(t_{\mathrm{i}})|\psi_{j,k_1}(t_{\mathrm{i}})\rangle = E_{j,k_1}(t_{\mathrm{i}})|\psi_{j,k_1}(t_{\mathrm{i}})\rangle\ , \tag{3.152}$$

where j labels the j-th lattice subband on our discretized space-time. Starting from this initial configuration, the out-of-plane magnetic field is now increased as a function of the time, and we trace the evolution of all eigen-states via the time-dependent Schrödinger equation,

$$\mathrm{i}\hbar\partial_t|\psi_{j,k_1}(t)\rangle = \mathcal{H}(t)|\psi_{j,k_1}(t)\rangle\ . \tag{3.153}$$

We compute the time-evolution of each eigen-state on our discretized time-line numerically, by using an iterative approach [171]:

$$|\psi_{j,k_1}(t+\Delta t)\rangle = \mathrm{e}^{-\mathrm{i}\mathcal{H}(t)\Delta t/\hbar}|\psi_{j,k_1}(t)\rangle = U(t+\Delta t, t)|\psi_{j,k_1}(t)\rangle\ , \tag{3.154}$$

where $U(t_2, t_1)$ denotes the unitary time evolution operator which mediates each state from $t_1 \to t_2$, and we choose the time discretization Δt small enough to ensure the convergence of

our simulations. After the period t, one obtains

$$|\psi_{j,k_1}(t)\rangle = U(t,t_\mathrm{i})|\psi_{j,k_1}(t_\mathrm{i})\rangle \ . \tag{3.155}$$

We perform the above described iterative procedure in order to analyze the evolution of the following non-interacting many-particle state in our field configuration:

$$|\Phi(\mu, t=t_\mathrm{i})\rangle = \prod_{\substack{j\leq j_\mathrm{max}\\ k_1\leq k_\mathrm{max}}} |\psi_{j,k_1}(t_\mathrm{i})\rangle \, . \tag{3.156}$$

Here, all single-particle states satisfying $j \leq j_\mathrm{max}$ and $k_1 \leq k_\mathrm{max}$ are filled by the (initial) chemical potential μ. Tracing Eq. (3.156) via Eq. (3.155) enables us to determine two characteristic, time-dependent quantities. On the one hand, we can compute the induced charge density distribution in order to study the charge current in our Chern insulator:

$$j^0_\mathrm{ind}(\mathbf{x},t) = -\mathrm{e}\sum_{\substack{k_1\leq k_\mathrm{max}\\ j\leq j_\mathrm{max}}} \psi^\dagger_{j,k_1}(\mathbf{x},t)\ \psi_{j,k_1}(\mathbf{x},t) - j^0_\mathrm{back} \, , \tag{3.157}$$

where j^0_back ensures $j^0_\mathrm{ind}(\mathbf{x},t_i)=0$. On the other hand, we can identify the states which are responsible for this peculiar charge flow. To this end, we trace the filling probabilities of each instantaneous eigen-state at time t of the time-independent Schrödinger equation

$$\mathcal{H}(t)|\phi_{i,k_1}(t)\rangle = \ E_{i,k_1}(t)|\phi_{i,k_1}(t)\rangle \ . \tag{3.158}$$

Notice that here t is not a dynamical variable defining the time evolution of states, as in Eq. (3.155), but rather parametrizes the eigen-system of the Hamiltonian at time t. In particular, the occupation probability of an eigen-state $|\phi_{i,k_1}(t)\rangle$ is given by:

$$P_{i,k_1}(t) = \sum_{j\leq j_\mathrm{max}} |\langle\psi_{j,k_1}(t)|\phi_{i,k_1}(t)\rangle|^2 \, . \tag{3.159}$$

This quantity can be used to rewrite Eq. (3.157) in the form

$$j^0_\mathrm{ind}(\mathbf{x},t) = -\mathrm{e}\sum_{i,k_1} P_{i,k_1}(t)|\phi_{i,k_1}(\mathbf{x},t)|^2 - j^0_\mathrm{back} \ . \tag{3.160}$$

In the following analysis we are going to distinguish two different cases: At initial time t_i, the ground state for

- (I) the QAH phase is determined by $\mathbf{A}(t_\mathrm{i})=0$ with a chemical potential μ which is placed at the Dirac point E_z [cf. Fig. 3.8(a)], whereas for
- (II) the QH phase we consider a finite background field $\mathbf{A}(t_\mathrm{i}) = -x_2 H_0 \mathbf{e}_1$ and place the chemical potential μ above the first LL [cf. Fig. 3.8(d)].

Let us start our discussion by analyzing the numerical results for the QAH phase under initial condition (I). The occupation of the eigen-states and the evolution of the induced charge density $j^0_\mathrm{ind}(\mathbf{x},t) = -\mathrm{e}\, n_\mathrm{ind}(\mathbf{x},t)$ with an increasing out-of-plane magnetic field strength $H(t)$ are shown in Figs. 3.8(a)-(c) and Fig. 3.12 with $n_\mathrm{ind}(\mathbf{x},t) = \sum_{i,k_1} P_{i,k_1}(t)|\phi_{i,k_1}(\mathbf{x},t)|^2 - n_\mathrm{back}$. Here, n_back ensures that $n_\mathrm{ind}(\mathbf{x},t_i)=0$. At $t=t_i$, the charge distribution is flat (zero). An increase of $H(t)$ essentially induces a net charge flow from the QAH edge states into all valence band LLs. This causes a charge depletion at the system's edge, whereas it induces a charge accumulation in the system's bulk. Since our system is a bulk insulator, this charge redistribution is driven by polarization effects. As a function of the magnetic field strength $H(t)$ all occupied wave functions shift their spectral weight towards the middle of the sample.

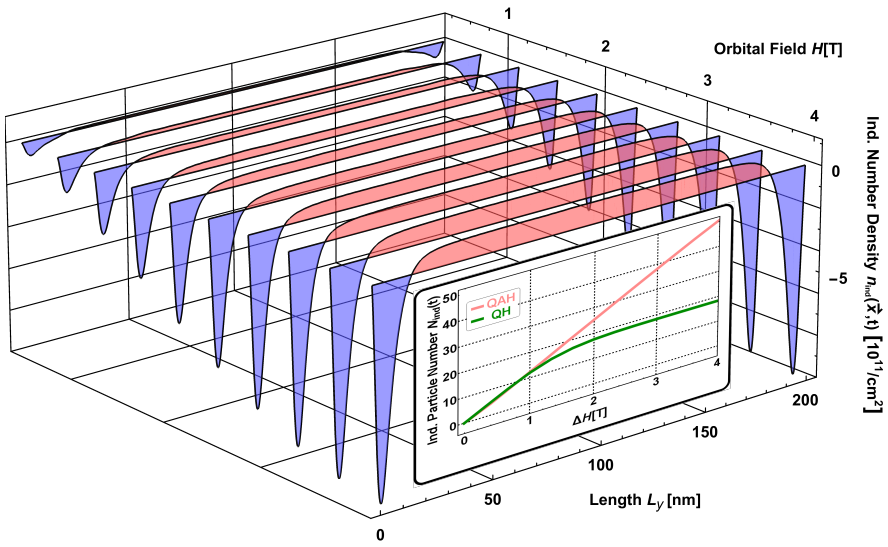

Figure 3.12: Evolution of $n_{\mathrm{ind}}(\mathbf{x},t)$ in an increasing out-of-plane magnetic field $H(t)$, corresponding to Figs. 3.8(a)-(c). An adiabatic increase of the magnetic field strength causes a charge depletion (blue) at the system's edges and a charge accumulation (red) in the system's bulk. The inset compares the induced bulk particle number $N_{\mathrm{ind}}(t) = \int \mathrm{d}\mathbf{x}\; n_{\mathrm{ind}}(\mathbf{x},t)$ between the QAH (red) and the QH phase (green). Further explanations are given in the text. The figure is reprinted from Ref. [P1] with permission from the APS.

This effectively gives rise to the charge redistribution which is shown in Fig. 3.12. Notice, that during this process, all valence band LLs, including the $n = 0$ LL, remain filled. As it is illustrated in the inset of Fig. 3.12, this causes a linear increase of the integrated bulk charge density

$$\int \mathrm{d}^2x\, j^0_{\mathrm{ind}} = \int \mathrm{d}^2x\, \sigma_{\mathrm{xy}} \nabla \times \mathbf{a} = \int \mathrm{d}^2x\, \kappa_{\mathrm{QAH}} H(t)\ . \tag{3.161}$$

Since this type of charge pumping is restricted to the existence of QAH edge states, it can only exist for $H < H_{\mathrm{crit}}$ [cf. Eq. (3.150)]. Let us emphasize that these results are consistent with our field theoretic calculations based on the Callan-Harvey mechanism which we have briefly discussed around Eq. (3.148) and extensively studied in Sec. 2.6.7.

The results for the QH phase under initial condition (II) are shown in Fig. 3.8(d) and in the inset of Fig. 3.12, respectively. In agreement with our field-theoretical approach, we find that the bulk charge originates purely from the associated QH edge states in Eq. (3.149), implying a saturation of the charge accumulation already for small magnetic fields. Therefore, our numerical studies provide further evidence that the QAH edge states are related to a distinct CS term which is connected to the spectral asymmetry η_{H} and not to a single LL.

Time Scales and Finite Size Gaps

Let us give one further remark regarding the time-scales for our charge pumping procedure. In the numerical approach presented above, we increase $H(t)$ within the finite time interval $[t_{\mathrm{i}} = 0, t_{\mathrm{f}}]$, which corresponds to a certain ramping speed

$$v_{\mathrm{ramp}} = \frac{H_{\mathrm{max}}}{t_{\mathrm{f}}} \quad \text{with} \quad H_{\mathrm{max}} = H\left(t_{\mathrm{f}}\right)\ . \tag{3.162}$$

For a fixed value of $H_{\max}$, we are able to simulate different ramping speeds by varying t_{f}. In general, the results which have been presented in the Figs. 3.8 and 3.12, fulfill the two following requirements: On the one hand, the ramping time t_{f} and, therefore, the ramping speed v_{ramp} have to be chosen such that

$$t_{\mathrm{f}}^{\min} \overset{(i)}{\ll} t_{\mathrm{f}} \overset{(ii)}{\ll} t_{\mathrm{f}}^{\max} \ , \tag{3.163}$$

where (ii) only needs to be fulfilled for $H > H_{\mathrm{scat}}$ [cf. Fig.1 (c)]. (i) The lower (upper) bound on t_{f} (v_{ramp}) results from the fact that states should not be excited between different bulk bands. As a consequence, $H(t)$ has to be increased on a time scale which is adiabatic with respect to any bulk energy gap E_{g}. This, in particular, implies that $t_{\mathrm{f}}^{\min} \ll t_{\mathrm{f}}$ with

$$t_{\mathrm{f}}^{\min} = \frac{\hbar}{E_{\mathrm{g}}} \ . \tag{3.164}$$

In general, E_{g} can be on the order of a few tenth of meV. In order to overcome such a value for E_{g}, we would need to ramp up $H_{\max}$ (a few Tesla) on a very small time scale $t_{\mathrm{f}} \ll 10^{-13}$s. (ii) The upper (lower) bound on t_{f} (v_{ramp}) is caused by the fact that, for $H > H_{\mathrm{scat}}$, unoccupied QAH edge states and occupied bulk LLs form finite hybridization gaps Δ_{Hyb} as the QAH edge states are lowered in energy with increasing $H(t)$ [cf. Fig. 1(c)]. In order to ensure that the QAH edge states and all bulk LLs separately maintain their initial filling probabilities throughout our simulation process, we need to choose t_{f}, for $H > H_{\mathrm{scat}}$, such that we diabatically overcome Δ_{Hyb}. The nomenclature 'diabatically' is meant in the sense that neither the filling probabilities, nor the local densities of the QAH edge states and the bulk LL wave functions change, if they pass each other with increasing magnetic field strength. Analogous to Eq. (3.164), this implies that $t_{\mathrm{f}} \ll t_{\mathrm{f}}^{\max}$ with

$$t_{\mathrm{f}}^{\max} = \frac{\hbar}{\Delta_{\mathrm{Hyb}}} \ . \tag{3.165}$$

If the hybridization gaps Δ_{Hyb} are finite size gaps, which by definition satisfy

$$\Delta_{\mathrm{Hyb}}(L_2) \ = \Delta_0 \ \mathrm{e}^{-\lambda L_2} \quad \text{with} \quad \lambda > 0 \ , \tag{3.166}$$

time-scales which are possible to reach experimentally become accessible, as $t_{\mathrm{f}}^{\max}$ increases exponentially. As shown in Fig. 3.13, we find that for $H_{\mathrm{scat}} < H < H_{\mathrm{crit}}$ and $k_1 = 0$ [a], the energy gaps between the QAH edge states and the $n=0$ LL are exponentially suppressed. In a typical macroscopic Hall bar the system length can be on the order of $L_2 \approx 100\,\mu$m [172]. This implies that $t_{\mathrm{f}}^{\max}$ can be approximately infinite in comparison to all other experimental time scales. From this perspective, even for $H > H_{\mathrm{scat}}$ the QAH charge pumping could, in principle, be experimentally observable in macroscopically large systems, if it would be possible to strongly suppress scattering processes between QAH and QH edge states. It is, however, expected that in a conventional device elastic- and inelastic scattering processes between the QAH and the QH edge states eventually cause a relaxation of our simulated charge redistribution. In the following section, we are going to study those experimental signatures of our system which persist even after such a charge relaxation.

[a] The same conclusions do also hold for $k_1 \neq 0$.

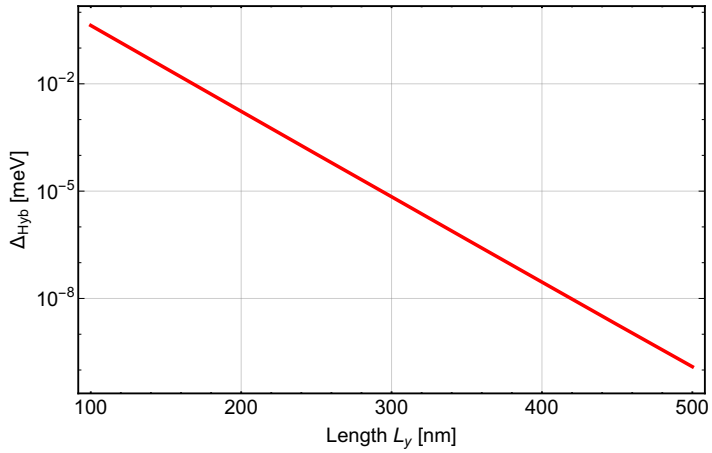

Figure 3.13: Finite size gap $\Delta_{\mathrm{Hyb}}(L_2)$ for $k_1 = 0$ and $H_{\mathrm{scat}} < H < H_{\mathrm{crit}}$, forming between QAH edge states and the $n = 0$ LL, as a function of the system length L_2. The figure is depicted in Log-Lin fashion. The system parameters are given in the caption of Fig. 3.8. The linear behavior of $\log(\Delta_{\mathrm{Hyb}})(L_2)$ shows that Δ_{Hyb} exponentially decreases with $L_2 = L_{\mathrm{y}}$, as it is described by Eq. (3.166). For the fit-parameters in this equation, we found that here $\Delta_0 = 100\,\mathrm{meV}$ and $\lambda = 0.05\,\mathrm{nm}^{-1}$. We obtain analogous results for $k_1 \neq 0$. The figure is reprinted from Ref. [P1] with permission from the APS.

3.3.4 Experimental Signatures & the Entire BHZ Response

So far our analysis has been restricted to an impurity-free system. As a natural extension we are going to take into account a finite disorder in this section. In particular, we are going to study the experimental consequences of (in)elastic scattering processes on the theoretical prediction which we have derived above.

QAH-QH Edge State Scattering: A Landauer-Büttiker Approach

As long as the Dirac point is above the $n=0$ LL, for $H < H_{\mathrm{scat}}$, there is no charge inversion in spectrum and the system is in its energetic ground state. As such, scattering processes cannot cause a relaxation of the induced bulk charge density. The presence of disorder can therefore not affect the results which we have presented in the Figs. 3.8(b) and 3.12. As a hallmark of the QAH phase in the Dirac mass gap we find a quantized Hall plateau with $\sigma_{\mathrm{xy}} = \kappa_{\mathrm{QAH}}$ starting at $H(t_i) = 0$. The length of this plateau scales with $H_{\mathrm{scat}} \sim L_2^{-1}$, as it has been derived in Eq. (3.115). This feature is encoded by region **I** in Fig. 3.14 and results from $g_{\mathrm{eff}} \sim L_2$ [cf. Eq. (3.110)].

Experimentally realistic systems are imperfect in the sense that they have a finite disorder and impurity mean free path. From this perspective, it is expected that in(elastic) scattering processes between occupied QH and unoccupied QAH edge states cause a momentum and an energy relaxation for $H > H_{\mathrm{scat}}$, as it is indicated by region **II** in Fig. 3.14. For this reason, it is expected that eventually any charge inversion in the system's spectrum relaxes, until a common chemical potential has set in. In such a ground state, counterpropagating QAH and QH edge states coexist at a single boundary. This is exemplary shown in the inset of region **II**, where for instance at the right edge, due to the slope of the dispersion, the QAH edge state has a positive velocity, whereas the QH edge state has a negative velocity. Similarly to Ref. [173], which uses the Landauer-Büttiker formalism [174, 175], we expect deviations

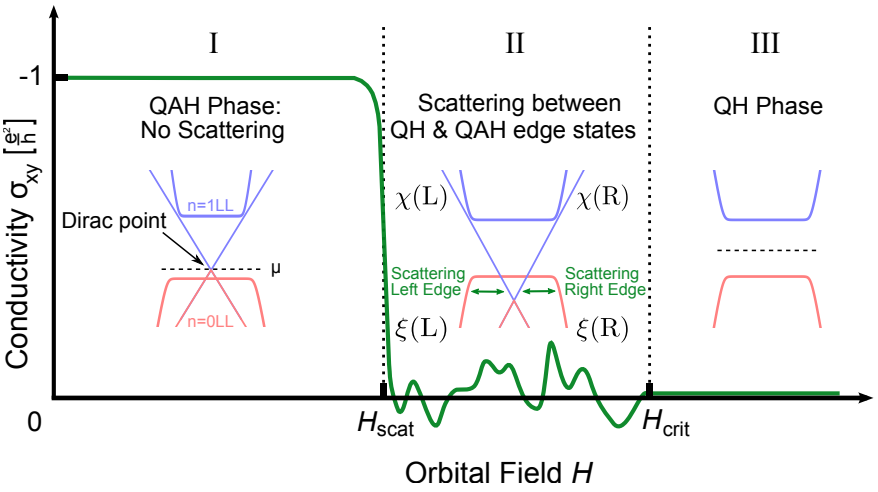

Figure 3.14: Schematic evolution of σ_{xy} for a Chern insulator in an out-of-plane (orbital) magnetic field in the presence of elastic- and inelastic scattering. The insets schematically illustrate the underlying band-structure according to Fig. 3.8(a)-(c), using the same color code. In region **II**, scattering processes between counterpropagating QH $\xi(L/R)$ (red) and QAH $\chi(L/R)$ (blue) edge states allow for a momentum- and an energy relaxation. Further explanations are given in the text. The figure is reprinted from Ref. [P1] with permission from the APS.

from a perfectly quantized Hall plateau arising from scattering between QH and QAH edge states, as explained in the next paragraph. When the transmission probability $T_{i,j}$ between the contacts i and j on a typical Hall bar is symmetric, meaning for $T_{i,i+1} = T_{i+1,i}$, it is expected that $\sigma_{\mathrm{xy}} = 0$. However, in the case that scattering processes between the coexisting edge states microscopically differ on both edges of the Hall bar, we expect deviations from a perfectly quantized Hall plateau. This is indicated by the wiggly line in region **II** of Fig. 3.14 and will be shown in the next paragraph by developing a simplistic model. Most remarkably, for $T_{i,i+1} \neq T_{i+1,i}$, the average value of this Hall plateau can significantly deviate from zero. In large (Hg,Mn)Te Hall bars, such direction-dependent transmission probabilities can arise from a large charge puddle [176–178] density, as we will show in the scope of the subsequent analysis.

In region **III** of Fig. 3.14, for $H > H_{\mathrm{crit}}$, the Dirac mass gap has been closed. This eventually implies a perfectly vanishing $\sigma_{\mathrm{xy}} = 0$ plateau.

In what follows, we are substantiating the above statements by an analytic derivation. In the Landauer-Büttiker formalism [173, 175], the current in the i-th contact is given by

$$I_i = -\frac{\mathrm{e}}{\mathrm{h}} \sum_{j=1}^{N} \left[T_{ij}\mu_j - T_{ji}\mu_i \right] \ , \tag{3.167}$$

where T_{ij} defines the transmission probability from contact j to contact i, $N \in \mathbb{N}$ is the entire number of contacts, and μ_i defines the local chemical potential in the i-th probe. The inset in Fig. 3.15(a) schematically illustrates a typical Hall bar with $N = 6$ contacts. In such a setup, contact I and IV act as source and drain of currents with $I_1 = -I_4$, and the four remaining contacts are voltage probes satisfying $I_j = 0$. In general, we distinguish two resistance contributions, namely the Hall resistance $R_{\mathrm{H}} = R_{26}/I_1$, as well as the longitudinal resistance $R_{\mathrm{L}} = R_{23}/I_1$.

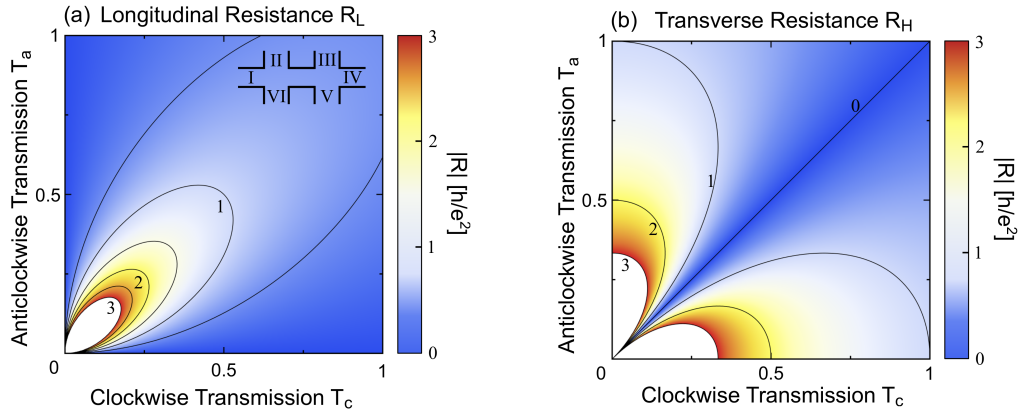

Figure 3.15: Illustration of the entire phase space for (**a**) the longitudinal and (**b**) the Hall resistance predicted by Eq. (3.168) for $T_{12}, T_{21} \leq 1$. The conventional six-terminal Hall bar is schematically depicted in the inset of (a). The current flows between contacts I and IV. The particular color code highlights the absolute value of the resistance. White areas indicate that the resistance is out of scale. For clarity, we plotted the contour lines (a) $R_{\mathrm{L}} = 0.5, 1, 1.5, 2, 2.5, 3$ and (b) $R_{\mathrm{H}} = 0, 1, 2, 3$ in units of $\mathrm{h/e^2}$. The figure is reprinted from Ref. [P1] with permission from the APS.

In what follows, let us analyze the transport signatures of our system defining the transmission probabilities in clockwise- and in anticlockwise direction as $T_{i+1,i} = T_{\mathrm{c}}$ and $T_{i,i+1} = T_{\mathrm{a}}$, respectively. Solving the linear system of equations in Eq. (3.167), yields the following analytic expressions for the Hall and the longitudinal resistance,

$$R_{\mathrm{H}} = \frac{\mathrm{h}}{\mathrm{e}^2} \frac{T_{\mathrm{c}} - T_{\mathrm{a}}}{T_{\mathrm{c}}^2 - T_{\mathrm{a}} T_{\mathrm{c}} + T_{\mathrm{a}}^2} \quad \wedge \quad R_{\mathrm{L}} = \frac{\mathrm{h}}{\mathrm{e}^2} \frac{T_{\mathrm{c}} T_{\mathrm{a}}}{T_{\mathrm{c}}^3 + T_{\mathrm{a}}^3} \,. \tag{3.168}$$

In Fig. 3.15, we illustrate the full parameter space for the Hall- and for the longitudinal resistance, considering $T_{\mathrm{c}}, T_{\mathrm{a}} \leq 1$. If $T_{\mathrm{c}} = T_{\mathrm{a}} = 1$, we find the characteristic values of a QSH phase, $R_{\mathrm{H}} = 0$ and $R_{\mathrm{L}} = \mathrm{h/2e^2}$ [163]. If $T_{\mathrm{c}} = 1$ and $T_{\mathrm{a}} = 0$, or analogously $T_{\mathrm{c}} = 0$ and $T_{\mathrm{a}} = 1$, we find the transport signatures of a single chiral edge mode. As explained, our system can contain counterpropagating QH and QAH edge states which are, most remarkably, not protected by symmetry [a]. Therefore, the associated transmission probabilities of these states can deviate from the limiting cases $T_{\mathrm{a,c}} = 1$ in realistic experiments. Nevertheless, as it is shown by Fig. 3.15, in the vicinity of the contour lines the resistance values can be still close to quantized values for a wide range of parameters. Most remarkably, Fig. 3.15(b) demonstrates that small deviations from the symmetric case $T_{\mathrm{c}} = T_{\mathrm{a}}$ can cause large deviations from $R_{\mathrm{H}} = 0$, if $T_{\mathrm{c}}, T_{\mathrm{a}} \ll 1$. Inspired by this property, let us investigate the peculiarities of QH - QAH edge state scattering processes at the same edge of the sample in more detail. As these counterpropagating modes are not protected by symmetry, point-like impurities can already give rise to backscattering. Due to the unitarity of the S-matrix, we find that for these kind of processes the scattering probabilities are symmetric, $T_{\mathrm{c}} = T_{\mathrm{a}}$, both tending to zero in the large system limit. However, let us highlight a peculiarity: Any small difference in the scattering processes between the two edges of the Hall bar can cause slight deviations from a perfectly quantized Hall plateau. This is schematically illustrated by the wiggly line in regime **II** of Fig. 3.14.

[a] This is for instance the case for counterpropagating QSH edge states, as discussed in Sec. 3.1.1.

Backscattering through Charge Puddles

So-called charge puddles are another prominent source for backscattering [176]. Especially in HgTe based two-dimensional topological insulators these charged islands represent a major, if not the dominant, source for backscattering [177]. The characteristic value of $R_\mathrm{L} = \mathrm{h}/2\mathrm{e}^2$ in QSH insulators, therefore, has been solely measured in micro-structured Hall bars. In the present analysis, we instead want to focus on large samples with $L_1 > n_\mathrm{p}^{-1/2}$, where n_p is the charge puddle density [176]. In this limit it was shown that the bulk conductivity cannot be neglected if the system size exceeds the leakage length $L_1^* = 1/\sigma_\mathrm{B}\rho_\mathrm{e}$ [176]. In this expression, σ_B is the bulk conductivity and ρ_e is the edge resistivity. If $L_1 > L_1^*$, the top and the bottom edge can be connected via a puddle-to-puddle hopping. To elaborate on a better understanding of this feature, let us study a toy model by using the Landauer-Büttiker approach once more. For simplicity, we assume that the top and the bottom edge are connected by a single charge puddle[a]. Schematically, this situation is depicted in Fig. 3.16(a). On a theoretical level, the scattering from the edge states onto the considered charge puddle can be described by the following S-matrix:

$$S = \begin{pmatrix} r_{11} & t_{12} & t_{13} \\ t_{21} & r_{22} & t_{23} \\ t_{31} & t_{32} & r_{33} \end{pmatrix} , \tag{3.169}$$

where t_{ij} and r_{ij} define the transmission and reflection amplitudes from the j-th incoming to the i-th outgoing scattering state, respectively. For the top edge, scattering states are labeled according to Fig. 3.16(a). For the bottom edge, we assume the same type of scatterer but both, QH and QAH edge states switch their propagation direction, as it is shown in regime **II** of Fig. 3.14. This model describes partially coherent transmission [174] of QH and QAH edge states (t_{12} and t_{21}), where only a fraction of the current is transmitted onto the charge puddle (t_{31} and t_{32}). Since charge puddles act like inelastic scatterers, they cause dephasing and, consequently, can be modeled as fictious voltage probes [175]. Let us emphasize that QH and QAH edge states have different spin character and wave function localization. For this reason, the QH-to-puddle tunneling probability $|t_{31}|^2$ can be significantly different than the QAH-to-puddle tunneling probability $|t_{32}|^2$.

Let us study a proof-of-principle model in order to derive asymmetric transmission probabilities T_{ij}. If we choose $r_{11} = r_{22} = t_{32} = t_{13} = 0$, the unitarity of the S-matrix requires that

$$T_\mathrm{QH} = 1 \ , \qquad T_\mathrm{QAH} + T_\mathrm{p} = 1 \ , \qquad R_\mathrm{p} + T_\mathrm{p} = 1 \ , \tag{3.170}$$

where $T_\mathrm{QAH} = |t_{21}|^2$, $T_\mathrm{QH} = |t_{12}|^2$, $T_\mathrm{p} = |t_{31}|^2 = |t_{23}|^2$, and $R_\mathrm{p} = |r_{33}|^2$. Most importantly, T_p denotes the transmission probability from the chiral QH edge state to the charge puddle. Without loss of generality, we take $\mu_1 > \mu_2$ and $\mu_2 = 0$. The current into the charge puddle is for this reason given by

$$I_\mathrm{p} = -\frac{\mathrm{e}}{\mathrm{h}} \left[(2 - 2R_\mathrm{p})\, \mu_\mathrm{p} - T_\mathrm{p}\, \mu_1 \right] \ . \tag{3.171}$$

With $I_\mathrm{p} = 0$, Eq. (3.171) implies that $\mu_\mathrm{p} = \mu_1/2$. The current which flows along the top edge into contact II is instead given by

$$I_2 = -\frac{\mathrm{e}}{\mathrm{h}} \left(T_\mathrm{QAH}\, \mu_1 + T_\mathrm{p}\, \mu_\mathrm{p} \right) = -\frac{\mathrm{e}}{\mathrm{h}} \left(1 - T_\mathrm{p}/2 \right) \mu_1 \ . \tag{3.172}$$

[a] Instead, in a realistic situation, an electron needs to hop several times between adjacent puddles in order to reach the other edge of the sample

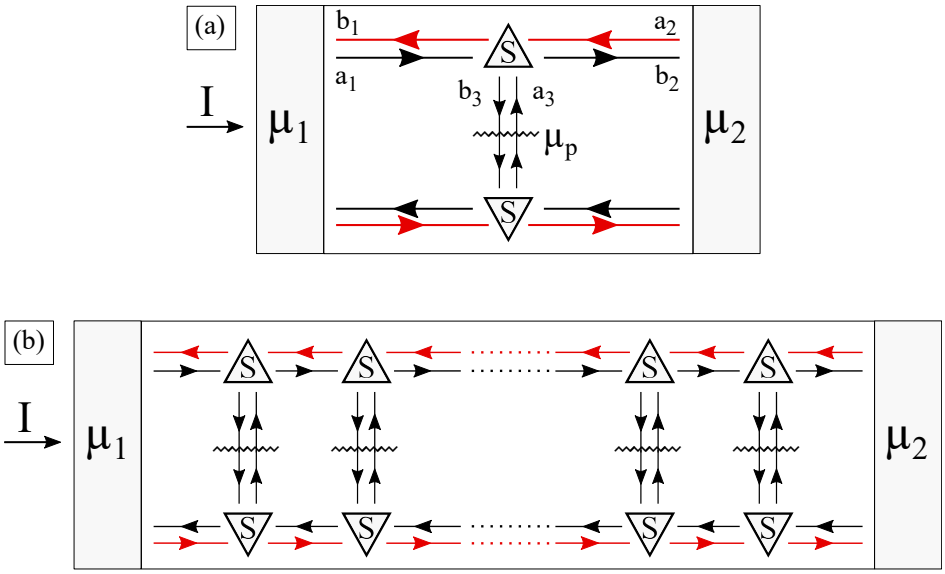

Figure 3.16: Schematic illustration of a two-terminal channel, where counterpropagating QH and QAH edge states are encoded by red and black arrows at the top and the bottom edge, respectively. Triangles indicate scattering events with charge puddles which are described by the scattering matrix S. They partially transmit states coherently and partially scatter states into a fictitious contact with chemical potential μ_p, which is indicated by a wiggly line. The fictitious contacts model inelastisc scattering events which connect the top with the bottom edge of the channel. In (**a**), we consider a proof-of-principle model with a single charge puddle, whereas in (**b**) we generalize our approach including $N \in \mathbb{N}$ charge puddles. In (a), incoming a_i and outgoing b_i scattering states are labeled for clarity at the top edge. The figure is reprinted from Ref. [P1] with permission from the APS.

Consequently, we can interpret $1 - T_\mathrm{p}/2$ as the effective transmission coefficient between contact I and II, namely T_{21}. Since $T_{12} = T_\mathrm{QH} = 1$ and $T_{21} < 1$ for $T_\mathrm{p} \neq 0$, the presented model proves the possibility of having asymmetric transmission coefficients when the top and bottom edge states are connected via a puddle-to-puddle hopping.

As T_p is in general a small number, it is interesting to look at the case of multiple charge puddles, a situation which is schematically depicted in Fig. 3.16(b). Following an analogous calculation as the one presented above, it is straightforward to generalize Eq. (3.172) to the situation of $N \in \mathbb{N}$ puddles:

$$I_2 = -\frac{\mathrm{e}}{\mathrm{h}} \frac{2 - T_\mathrm{p}}{2 + (N-1)T_\mathrm{p}} \mu_1 \ . \tag{3.173}$$

In a nutshell this model shows that for $L_1 > L_1^*$ a system which contains counterpropagating QH and QAH edge states can still have a finite Hall conductivity which deviates from zero, and, in principle, can even approximate values of $\sigma_\mathrm{xy} \approx \mathrm{e}^2/\mathrm{h}$. Let us again emphasize that the above presented toy model serves as a proof-of-principle. The experimental scaling behavior in realistic QAH insulators can deviate from the analytic form shown in Eq. (3.173). The derivation of an appropriate microscopic model is subject of future studies.

Entire BHZ Response

In the discussion above, we have explained the experimental signatures originating from a single non-trivial Chern insulator. As such a system only defines one (pseudo-)spin block of the entire BHZ model, we also need to incorporate the response of the second Chern insulator to make reliable predictions for typical materials such as (Hg,Mn)Te/CdTe quantum wells [8, 42, 179].

So far, we considered the (pseudo-)spin up block of the BHZ model and assumed that the (pseudo-)spin down block is in the topologically trivial phase in order to describe the physics of a QAH insulator. As we have shown in Eq. (3.48) of Sec. 3.1.2, our previous analysis can be easily transferred to the (pseudo-)spin down block by replacing $(m_+, B) \to (-m_-, -B)$ in all our formulas. We have explained in Sec. 3.1.1 that due to the paramagnetic doping of (Hg,Mn)Te/CdTe quantum wells [180], a finite magnetic field is required to close the Dirac mass gap of the (pseudo-)spin down block of the BHZ model and, equivalently, to drive the system from the QSH to the QAH phase. For this reason, we are expecting that the (pseudo-) spin down block of the BHZ model causes an additional transition from the QSH phase with $\sigma_{\mathrm{xy}} = 0$ to region **I** with $\sigma_{\mathrm{xy}} = -\mathrm{e}^2/\mathrm{h}$ in Fig 3.14.

Let us end this section by emphasizing that in Bi-based QAH insulators, one should be able to observe similar transitions as the ones shown in Fig. 3.14. However, we expect two significant differences in comparison to (Hg,Mn)Te/CdTe quantum wells. On the one hand, due to the ferromagnetic doping of Bi-based systems, there is no QSH to QAH phase transition expected with increasing $H(t)$. On the other hand, measuring conventional QH physics in these systems is challenging due to a short impurity mean free path [45–48].

Finally, let us emphasize that an extensive summary of the results which we have obtained within the scope of this section can be found in Sec. 5.

3.4 Temperature and Density Dependence of the Parity Anomaly

In Sec. 3.2, we have analyzed the relation of the Dirac- as well the Newtonian mass of a QAH insulator to the parity of planar electrodynamics. Further, in Sec. 3.3, we have shown that even in quantizing magnetic fields the signatures of the parity anomaly persist in QAH insulators like (Hg,Mn)Te quantum wells or magnetically doped (Bi,Sb)Te thin films. It has been shown that the associated features in particular remain encoded in the spectral asymmetry η_{H} [cf. Eq. (3.121)] [34]. However, all these findings do not incorporate thermal effects. So far, finite temperature signatures in parity anomaly driven systems are restricted to pure Dirac models. Calculating the quantum effective action of these systems induces a temperature dependent and thus large gauge non-invariant Chern-Simons term originating from the parity anomaly [36, 57–61]. While it was shown that this non-invariance is absorbed by higher order non-perturbative corrections to the effective action [62–69], this feature still gives rise to a fundamental question:

Does the parity anomaly get renormalized by thermal effects? (3.174)

We answered this basic question within the manuscript *Temperature and chemical potential dependence of the parity anomaly in quantum anomalous Hall insulators* (Phys. Rev. B **102**, 205407), which has been published in November 2020 [P5]. It is the goal of the present section to discuss the theoretical findings associated to this work, which have been obtained

in collaboration with Dr. Flavio S. Nogueira and Dr. Christian Northe[a]. While all analytic derivations have been obtained by myself, Dr. Flavio S. Nogueira supported this work with several fruitful discussions and remarks regarding the influence of a finite temperature on the parity anomaly in 2+1 space-time dimensions. Dr. Christian Northe contributed to this work with critical questions rendering the associated results accessible for a broad- and interdisciplinary community.

Before we start our analysis, let us emphasize that answering the question (3.174) is in particular not only relevant for the QAH effect in the aforementioned materials. It is especially important in the case of interfaces between ferromagnetic insulators and three-dimensional topological insulators, where a proximity-induced interface magnetization has been experimentally observed at high temperatures [70, 71]. In this case the out-of-plane magnetization causes a gap opening in the interface Dirac spectrum, which induces a parity anomaly on the TI surface and a concomitant magnetoelectric torque in the Landau-Lifshitz equation [72–74]. A similar effect is expected to occur on the surface of the recently discovered antiferromagnetic TI $MnBi_2Te_4$ [75, 76], where the gap in the surface Dirac spectrum is an intrinsic feature of the system.

By definition [cf. Sec. 2.5.1], the parity anomaly only implies the breakdown of the parity symmetry at the quantum level. This dictates a certain form of the band-structure, which is temperature independent [b]. Hence, the parity anomaly cannot obtain any finite temperature correction. In contrast, the prefactor of the anomaly induced Chern-Simons term in the effective action corresponds to the finite temperature Hall conductivity. In what follows, we are going to calculate this non-dissipative transport coefficient for single (pseudo-)spin polarized Chern insulators including both, a Dirac- as well as a momentum-dependent mass term [cf. Sec. 3.1.2]. We will study these systems in the absence and presence of an out-of-plane magnetic field, as well as with and without particle-hole symmetry. In a nutshell, this will lead us to the following results:

(*i*) The parity anomaly induces a topological part in the Hall conductivity of a QAH insulator which is temperature as well as chemical potential independent and solely described by the system's Chern number.

(*ii*) The non-quantized finite temperature and chemical potential corrections to the Hall conductivity also originate from the parity anomaly, since they also depend on the band-structure. However, they do not depend on its topology, being rather related to the temperature-dependent filling of the valence and conduction bands. As expected, an increasing Dirac mass counteracts finite temperature effects. On the other hand, we show that in the nontrivial phase an increasing Newtonian mass enhances the finite temperature corrections.

(*iii*) In quantizing out-of-plane magnetic fields, the thermal LL response renormalizes the parity anomalous part of the Hall conductivity. In the Dirac mass gap it adds to the otherwise quantized parity anomaly related contribution which has been rigorously derived in Eq. (3.146a).

In order to understand the finite temperature analysis in this section, we start our discussion by briefly recapitulating the most important theoretical concepts which we have studied in the previous Secs. 3.1, (3.2.1), and (3.3).

[a] This work has been supervised by Prof. Dr. Jeroen van den Brink and by Prof. Dr. Ewelina M. Hankiewicz

[b] Rigorously, this statement is only true for small temperatures. For very large temperatures the system can deform, which essentially changes the band-structure. However, this scenario is beyond the scope of our analysis.

3.4.1 Band-Structure of a Chern Insulator: Camel-Back Gap

In what follows, we describe the anomaly related finite temperature and density response of QAH insulators in the presence and in the absence of quantizing out-of-plane magnetic fields. As we have explained in Sec. 3.1, we are therefore analyzing (pseudo-)spin polarized 2+1 dimensional Chern insulators which are defined by two different mass terms: A momentum independent Dirac mass $m_\pm$, as well as a momentum dependent Newtonian mass term $B|\mathbf{k}|^2$ [cf. Eq. (3.12)]. The free Lagrangian of a single particle-hole symmetric Chern insulator in 2+1 space-time dimensions has been derived in Eq. (3.60):

$$\mathcal{L}_0 = \bar{\psi}\left(A\not{k} - m_\pm + Bk_ik^i\right)\psi \ . \tag{3.175}$$

In comparison to a pure Dirac Lagrangian, the additional Newtonian mass term in Eq. (3.175) breaks the Lorentz symmetry as it only involves spatial momenta [cf. Sec. 2.4.3]. Let us remark at this point that a similar Lagrangian can also be used for the description of 2+1 dimensional superfluid Fermi liquids, as it is for instance described in Ref. [181]. The first-quantized Hamiltonian associated to Eq. (3.175) can be derived by a Legendre transformation. Within the upcoming analysis we are considering the (pseudo-)spin up block of the BHZ Hamiltonian in Eq. (3.4) and neglect the characterizing subindex. We are therefore considering the Hamilonian in Eq. (3.12)

$$\mathcal{H}(\mathbf{k}) = -D\alpha\sigma_0 + A(k_1\sigma_1 - k_2\sigma_2) + (m - B\alpha)\,\sigma_3 \ , \tag{3.176}$$

where we introduced the abbreviation $\alpha = k_1^2 + k_2^2$ and reintroduced the particle-hole asymmetry term $D\alpha\sigma_0$. As we have already emphasized several times throughout this thesis, both of the mass terms in Eq. (3.176), m and $B\alpha$, break the parity symmetry of the Hamilton [cf. Eq. (3.14)]. Consequently, the Dirac-, as well as the Newtonian mass contribute to the integer Chern number [cf. Eq.(3.19)] [5, 50]

$$\mathcal{C}_{\mathrm{CI}} = \left[\mathrm{sgn}(m) + \mathrm{sgn}(B)\right]/2 \ . \tag{3.177}$$

Notice, that adding higher-order momentum dependent mass corrections to the Hamiltonian of a Chern insulator affects the analytic form of its Chern number. To respect the Galilean invariance of the system, any additional mass correction needs to be of even order in momentum. Essentially, the prefactor of the highest order mass correction replaces the Newtonian mass parameter B in the Chern number Eq. (3.177). Since higher order mass corrections do change the band-curvature, they will also alter the nonquantized Hall response at finite temperatures and chemical potentials. However, they will only change this response quantitatively. In particular, they do not prevent the possible gap closing apart from the Γ-point which drives the low-energy response studied in this section [cf. Eq. (3.192)].

As we have shown in Eq. (3.16), the spectrum associated to Eq. (3.176) for $D=0$ is given by

$$E^s(\alpha) = s\sqrt{A^2\alpha + (m - B\alpha)^2} \ , \tag{3.178}$$

where $s = \pm$ encodes the conduction and the valence band, respectively. In Fig. 3.17, we show the influence of the mass parameters on the band-structure. Depending on the values for m, B, and A, the band-structure changes significantly. For $m/B > 0$, the system is topologically nontrivial with $\mathcal{C}_{\mathrm{CI}} = \pm 1$. The minimal gap can be either located at the Γ-point or at $\alpha_{\mathrm{min}} = (2mB - A^2)/(2B^2)$, corresponding to a camel-back structure. Thus, it is defined by $2|m|$ or by the absolute value of

$$\Delta = A\sqrt{4mB - A^2}/B \ . \tag{3.179}$$

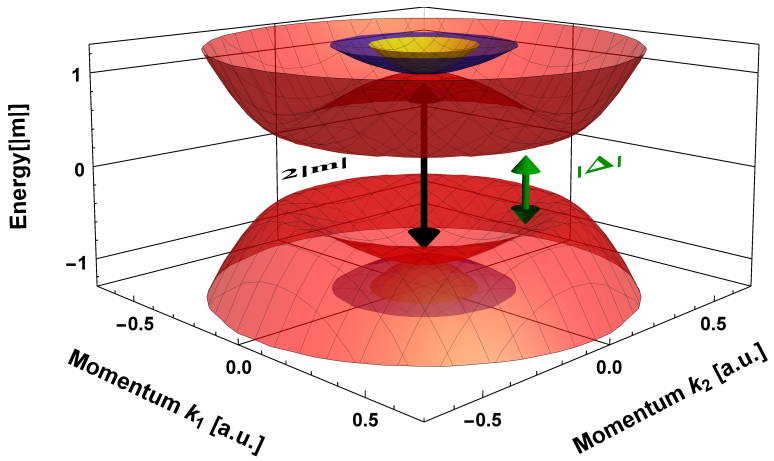

Figure 3.17: Band-structure of a Chern insulator for zero magnetic field and $D=0$. Red and blue curves encode topologically non-trivial phases with $m=A=1$, and $B=5$ (red, camel-back), or $m=1$, $A=3$, and $B=0.1$ (blue). The yellow curve corresponds to a topologically trivial phase with $m=1$, $A=5$, and $B=-0.1$. The minimal gap is either defined by $2|m|$ at the Γ-point or by $|\Delta|$ at $\alpha=\alpha_{\rm min}$, indicated by the black or green arrow, respectively. The figure is reprinted from Ref. [P5] with permission from the APS.

Increasing $|m|$ or $|B|$ in the nontrivial phase leads to a camel-back structure if $2mB>A^2$, associated to $\alpha_{\rm min}>0$. This property has partially also been analyzed in Sec. 3.2.1. The camel-back gap $|\Delta|$ increases with m but decreases with B. For $4mB=A^2$, Δ vanishes and the spectrum simplifies to,

$$E^{\rm s}(\alpha)=s|(m+B\alpha)|\ . \tag{3.180}$$

For $m/B<0$, the system is topologically trivial. In this case the minimal gap is always located at the Γ-point.

If we include an out-of-plane magnetic field H, a LL spectrum forms if the magnetic length $l_H=\sqrt{\hbar/|{\rm e}H|}$ is smaller than the system size [163]. As we have shown in Sec. 3.3.1, for a finite particle-hole asymmetry D, one obtains

$$E^s_{n\neq0}=-{\rm sgn}({\rm e}H)\beta/2-n\delta+s\,\epsilon_n\ , \tag{3.181}$$
$$E_0={\rm sgn}({\rm e}H)\,(m-\beta/2)-\delta/2\ . \tag{3.182}$$

Here, we defined $\tilde{\alpha}=\sqrt{2}A/l_H$, $\beta=2B/l_H^2$, $\delta=2D/l_H^2$, and

$$\epsilon_n=\sqrt{\tilde{\alpha}^2n+(m-n\beta-{\rm sgn}({\rm e}H)\delta/2)^2}\quad\text{with}\quad n\in\mathbb{N}^+. \tag{3.183}$$

As shown in Eq. (3.146a), H renormalizes the zero-field Chern number $\mathcal{C}_{\rm CI}$ in Eq. (3.177) to

$$\mathcal{C}_{\rm CI}(H)=\left[{\rm sgn}\left(m-B/l_H^2\right)+{\rm sgn}\,(B)\right]/2\ . \tag{3.184}$$

Hence, a magnetic field counteracts the parity anomaly related contribution to the Chern number, Eq. (3.184), which survives the parity symmetric limit $m,B,H\to0$. In particular, the magnetic field closes the Dirac mass gap at $H_{\rm crit}={\rm sgn}({\rm e}H)m/B$ [cf. Eq. (3.98)]. Beyond

this critical magnetic field the parity anomaly vanishes. The parity anomaly of a single Chern insulator is a zero magnetic field effect. It is directly related to the parity breaking elements of the zero-field Hamiltonian in Eq. (3.176) and its band-structure in Fig. 3.17. In quantizing magnetic fields, the Chern number of each LL only results from the magnetic field as it only depends on the magnetic length l_H. Nevertheless, the parity anomaly still has significant consequences in magnetic fields. Namely, it defines the Chern number in the Dirac mass gap, Eq. (3.184), resulting from the spectral asymmetry of the entire LL spectrum. In particular this has been shown and discussed in Sec. 3.3. Since for $|H| > |H_{\mathrm{crit}}|$, the spectral asymmetry vanishes, there are no measurable consequences of the parity anomaly beyond this value. In what follows, we are going to study finite temperature and density effects on the parity anomaly induced transport by calculating the Hall conductivity in zero, as well as in finite out-of-plane magnetic fields.

3.4.2 Zero Magnetic Field

In what follows, we calculate the finite temperature Hall conductivity σ_{xy} corresponding to a particle-hole symmetric Chern insulator at zero magnetic field. As we have extensively discussed in Sec. 3.4.1, this parity-odd and non-dissipative transport coefficient is directly related to the parity anomaly in 2+1 space-time dimensions as it does not vanish in the parity symmetric limit $m, B \to 0^{\pm}$. In our calculation, we disentangle topological from non-topological contributions to σ_{xy}, the latter originating from thermal effects. For $D=0$, the finite temperature Hall conductivity of the Chern insulator in Eq. (3.176) is given by [cf. Eqs. (3.19) and (3.71)]

$$\sigma_{\mathrm{xy}}(T,\mu) = \frac{\mathrm{e}^2}{\mathrm{h}} \int_0^\infty \mathrm{d}\alpha \, \frac{A^2(m+B\alpha)\left[f_{\mathrm{v}}(T,\mu) - f_{\mathrm{c}}(T,\mu)\right]}{4(A^2\alpha + (m-B\alpha)^2)^{3/2}} \,, \tag{3.185}$$

where $f_{\mathrm{c,v}}(T,\mu) = [\mathrm{e}^{(E^{s=\pm}(\alpha)-\mu)/(\mathrm{k_B}T)} + 1]^{-1}$ are the conduction and valence band Fermi functions [60]. This result is obtained by calculating the vacuum polarization operator or, analogously, the current-current correlation function, as it has been done in Sec. 3.2.2. In the language of quantum field theory, this corresponds to the evaluation of the one-loop Feynman diagram in Fig. 3.6(a), whereas in the solid-state community Eq. (3.185) results from the Kubo-formalism. In order to disentangle topological from thermal contributions to σ_{xy}, we use that

$$f_{\mathrm{v}}(T,\mu) = 1 - \frac{\Theta(-E)\,\mathrm{e}^{(E-\mu)/(\mathrm{k_B}T)}}{\mathrm{e}^{(E-\mu)/(\mathrm{k_B}T)} + 1} \,, \tag{3.186}$$

where $E(\alpha)$ encodes the entire spectrum and Θ is the Heaviside step function. With this identity, Eq. (3.185) decomposes into two building blocks,

$$\sigma_{\mathrm{xy}}(T,\mu) = \sigma^0_{xy} - \sigma^1_{\mathrm{xy}}(T,\mu) \,, \tag{3.187}$$

with

$$\sigma^0_{\mathrm{xy}} = \frac{\mathrm{e}^2}{2\mathrm{h}} \left[\mathrm{sgn}(m) + \mathrm{sgn(B)}\right] \,, \tag{3.188}$$

and

$$\sigma^1_{\mathrm{xy}}(T,\mu) = \frac{\mathrm{e}^2}{\mathrm{h}} \int \mathrm{d}\alpha \, \frac{A^2(m+B\alpha)\,\mathrm{sgn}(E)}{4\pi E^3} \left(\frac{\Theta(E)}{\mathrm{e}^{(E-\mu)/(\mathrm{k_B}T)} + 1} + \frac{\Theta(-E)}{\mathrm{e}^{-(E-\mu)/(\mathrm{k_B}T)} + 1} \right). \tag{3.189}$$

Notice, that due to the parity anomaly, neither Eq. (3.188) nor Eq. (3.189) necessarily vanishes in the parity-symmetric limit $m, B \to 0$. Equation (3.188) encodes the topological part of the Hall conductivity. In Eq. (3.19), we have shown that this contribution can be interpreted as a winding number. In contrast, Eq. (3.189) defines the corrections originating from a finite temperature and chemical potential. These non-topological and thus non-quantized corrections are based on particle-hole excitations in the conduction and in the valence band, respectively. To solve Eq. (3.189), we use the assumption of a particle-hole symmetric Chern insulator with $D=0$. In particular, this implies

$$\sigma_{\mathrm{xy}}^{1}(T,\mu) = \sigma_{\mathrm{xy}}^{\mathrm{corr}}(T,\mu) + \sigma_{\mathrm{xy}}^{\mathrm{corr}}(T,-\mu) \ . \tag{3.190}$$

In order to determine $\sigma_{\mathrm{xy}}^{\mathrm{corr}}(T,\mu)$ in the energy space, we need to solve Eq. (3.178) for α. Due to the possible camel-back structure, this leads to the two solutions

$$\alpha_{\pm} = \alpha_{\mathrm{min}} \pm \frac{\sqrt{E^2-\Delta^2}}{|B|} \quad \text{with} \quad \frac{\mathrm{d}\alpha_{\pm}}{\mathrm{d}E} = \pm \frac{E}{|B|\sqrt{E^2-\Delta^2}} \ . \tag{3.191}$$

With these identities, we in particular find the correction

$$\sigma_{\mathrm{xy}}^{\mathrm{corr}}(T,\mu) = \frac{\mathrm{e}^2}{2\mathrm{h}}\Theta[\alpha_{\mathrm{min}}] \int\limits_{|\Delta|}^{\sqrt{m^2}} \frac{A^2 + \dfrac{2|B|\Delta^2}{\sqrt{E^2-\Delta^2}}}{BE^2\left(\mathrm{e}^{(E-\mu)/T}+1\right)} \,\mathrm{d}E + \frac{\mathrm{e}^2}{4\mathrm{h}} \int\limits_{\sqrt{m^2}}^{\infty} \frac{A^2 + \dfrac{2|B|\Delta^2}{\sqrt{E^2-\Delta^2}}}{BE^2\left(\mathrm{e}^{(E-\mu)/T}+1\right)} \,\mathrm{d}E \ . \tag{3.192}$$

While in Eq. (3.192) the second term captures the correction from a monotonic band-structure, the first term encodes a possible camel-back correction. For $4mB = A^2$ with $\Delta=0$, $\sigma_{\mathrm{xy}}^{\mathrm{corr}}(T,\mu)$ reduces to

$$\sigma_{\mathrm{xy}}^{\mathrm{corr}}(T,\mu) = \frac{m\mathrm{e}^2}{\mathrm{h}} \int\limits_{\sqrt{m^2}}^{\infty} \frac{A^2}{E^2\left(\mathrm{e}^{(E-\mu)/(\mathrm{k_B}T)}+1\right)} \,\mathrm{d}E \ , \tag{3.193}$$

which is twice the QED_{2+1} result with $B=0$. Analogously to Eq. (3.188), the Newtonian mass provides a factor of two to the thermal corrections of the QED_{2+1} conductivity. For the solution in Eq. (3.193), we can define the corrections in terms of the Gamma function $\Gamma(x)$ and the reduced Fermi-Dirac integral

$$F_j(x,b) = \frac{1}{\Gamma(j+1)} \int\limits_{b}^{\infty} \mathrm{d}t \, \frac{t^j}{\mathrm{e}^{t-x}+1} \ . \tag{3.194}$$

In total, this leads to

$$\sigma_{\mathrm{xy}}^{1}(T,\mu) = \frac{\mathrm{e}^2}{\mathrm{h}} \sum_{s=\pm} \frac{A^2\,\Gamma(-1)F_{-2}\left(\frac{s\mu}{\mathrm{k_B}T}, \frac{|m|}{\mathrm{k_B}T}\right)}{\mathrm{k_B}T} \overset{\mathrm{k_B}T \ll |m|}{=} \frac{\mathrm{e}^2}{\mathrm{h}} \frac{A^2\,\Gamma\left(-1, \frac{|m|}{\mathrm{k_B}T}\right)}{\mathrm{k_B}T} \ . \tag{3.195}$$

In Eq. (3.195), we approximate the result for low temperatures in comparison to the gap and for a vanishing chemical potential. Moreover, $\Gamma(s,b)$ is the incomplete Gamma function

$$\Gamma(s,b) = \int_{b}^{\infty} \mathrm{d}t \, t^{s-1} e^{-t} \ . \tag{3.196}$$

The general correction in Eq. (3.192) cannot be expressed via the integral functions above

since $\Delta \neq 0$. In Fig. 3.18, we plot the functional dependence of $\sigma_{xy}(T, \mu)$ for different choices of m and B. While increasing the Dirac mass always counteracts the temperature, increasing B enhances temperature effects in the topologically nontrivial phase. As discussed below Eq. (3.179), this originates from the property that B decreases the camel-back gap. Thus, both masses contribute equally to the topological part of the Hall conductivity in Eq. (3.188), while they counteract each other in the thermal corrections, Eq. (3.189), for $m/B > 0$. Notice, that even in the topologically trivial phase $m/B < 0$ the system has a finite Hall conductivity in the Dirac mass gap [cf. Figs. 3.18(c) and (d)]. This is also directly related to the parity anomaly since it arises from the broken parity symmetry of the band-structure, which is independent of $\mathrm{sgn}(m/B)$. However, in the topologically trivial phase the Newtonian mass cannot generate a camel-back structure. In this case both, the Dirac and the Newtonian mass term counteract the finite temperature broadening of the Fermi-Dirac distribution.

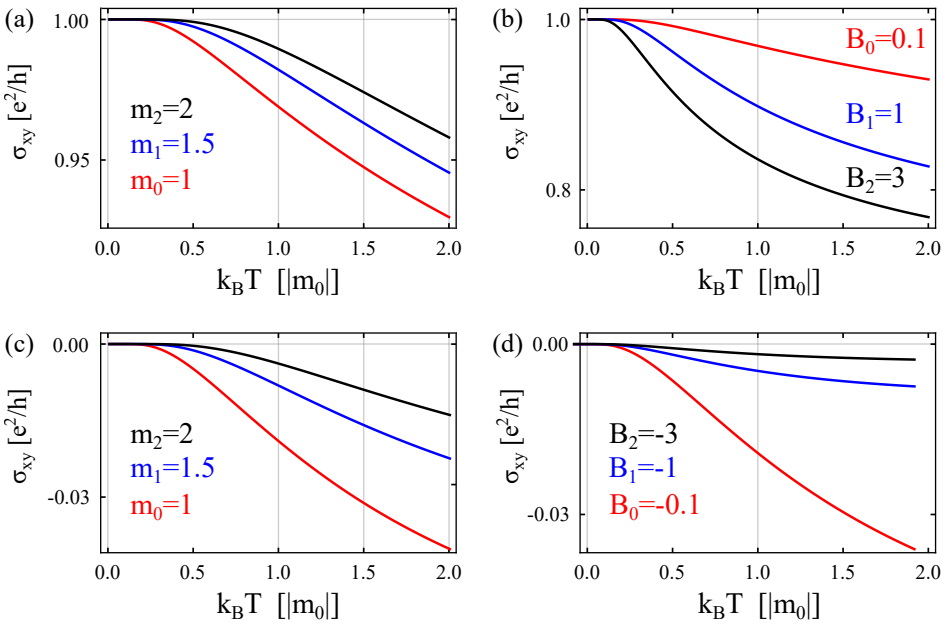

Figure 3.18: Finite temperature Hall conductivity of a Chern insulator with $A = 1$ and $D = 0$. In **(a)** and **(c)**, we vary the Dirac mass while $B = \pm 0.1$, respectively. In **(b)** and **(d)**, we vary the Newtonian mass for $m = 1$. In all sub-figures we consider zero chemical potential. Sub-figures **(a)** and **(b)** correspond to the topologically non-trivial regime, while sub-figures **(c)** and **(d)** correspond to the topologically trivial regime. The figure is reprinted from Ref. [P5] with permission from the APS.

3.4.3 Finite Magnetic Fields

Having analyzed a particle-hole symmetric Chern insulator at zero magnetic field, we now include a particle-hole asymmetry and an out-of-plane magnetic field H, where the latter gives rise to the LL spectrum in Eq. (3.181). As we have shown in Sec. 3.3.2, the Hall conductivity can be calculated by means of Streda's formula via the expectation value of the charge operator $\langle N \rangle_{T,\mu}$ [36, 106]. In terms of N_0 [cf. Eq. (3.120)] and the spectral asymmetry η_{H} [cf. Eq. (3.121)] Eq. (3.119) in particular implies

$$\sigma_{xy}(T, \mu) = -\frac{\partial \langle \mathrm{e}N \rangle_{T,\mu}}{\partial H} = \frac{\mathrm{e}}{2} \frac{\partial \eta_{\mathrm{H}}}{\partial H} - \frac{\partial \langle \mathrm{e}N_0 \rangle}{\partial H} \,. \tag{3.197}$$

Here, $E_\mathrm{z} = -mD/B$ is the charge neutrality point, and, according to Eq. (3.126), one obtains

$$\eta_\mathrm{H} = \sum_n \mathrm{sgn}(E_n - E_\mathrm{z}) = -\frac{\mathrm{e}H}{\mathrm{h}} \left[\mathrm{sgn}(m-\beta/2) + \mathrm{sgn}(B)\right] \ , \tag{3.198}$$

$$\langle N_0 \rangle = \sum_n \mathrm{sgn}(E_n - E_\mathrm{z}) \left[\frac{\Theta(E_n - E_\mathrm{z})}{\mathrm{e}^{\frac{E_n-\mu}{\mathrm{k_B}T}}+1} + \frac{\Theta(E_\mathrm{z} - E_n)}{\mathrm{e}^{-\frac{E_n-\mu}{\mathrm{k_B}T}}+1} \right] \ .$$

By definition, the spectral asymmetry counts the difference in the number of conduction and valence band states. Therefore, as long as the band-structure is not changed, it is temperature and chemical potential independent and solely carries the information of the topological contribution of the parity anomaly to σ_xy in magnetic fields. This enables the connection between the Hall conductivity and the parity anomaly even at finite magnetic fields, as discussed in Sec. 3.3. In contrast, $\langle N_0 \rangle$ encodes the thermal LL response, as it defines the thermal occupation of the valence and the conduction band. Due to the associated flat dispersion relation, this response entirely originates from the magnetic field topology and no more from the parity anomaly. All LLs with $n \in \mathbb{N}^+$ come in pairs. With the degeneracy $|\mathrm{e}H|/\mathrm{h}$, their contribution to the charge operator is given by

$$\langle N_0 \rangle_{n\neq 0} = \frac{|\mathrm{e}H|}{\mathrm{h}} \sum_{n\neq 0, s=\pm} \frac{s}{\mathrm{e}^{\frac{s(E_n^s-\mu)}{\mathrm{k_B}T}}+1} \ . \tag{3.199}$$

Additionally to this conventional LL response for finite μ and T, the zero LL also needs to compensate its contribution to η_H outside of the Dirac mass gap. In particular, it needs to cancel the term $\propto \mathrm{sgn}(m-\beta/2)$ in Eq. (3.198) for $|\mu+\delta/2| > |m-\beta/2|$ [cf. Eq. (3.145)]. Since the zero LL can either be part of the conduction or of the valence band, we can simplify its contribution to $\langle N_0 \rangle$. By using the properties of the hyperbolic tangent, we find for the zero LL with $n = 0$

$$\langle N_0 \rangle_0 = -\frac{|\mathrm{e}H|\mathrm{sgn}(E_0 - E_\mathrm{z})}{2\mathrm{h}} \left[\Theta(E_0 - E_\mathrm{z}) \left[\tanh\left(\frac{E_0-\mu}{2\mathrm{k_B}T}\right) - 1 \right] \Theta(E_\mathrm{z} - E_0) \left[\tanh\left(\frac{E_0-\mu}{2\mathrm{k_B}T}\right) + 1 \right] \right] . \tag{3.200}$$

This expression can be simplified further via the identities

$$\mathrm{sgn}(E_0 - E_\mathrm{z}) = \mathrm{sgn}(E_0 + \delta/2) = \mathrm{sgn}(\mathrm{e}H)\,\mathrm{sgn}(m-\beta/2) \ , \tag{3.201}$$

$$\Theta(E_0 - E_\mathrm{z}) - \Theta(-E_0 + E_\mathrm{z}) = \mathrm{sgn}(E_0 - E_\mathrm{z}) \ , \tag{3.202}$$

$$\Theta(E_0 - E_\mathrm{z}) + \Theta(-E_0 + E_\mathrm{z}) = 1 \ . \tag{3.203}$$

Eventually, this implies the zero LL contribution

$$\langle N_0 \rangle_0 = \frac{|\mathrm{e}H|}{2\mathrm{h}} \left[\mathrm{sgn}(\mathrm{e}H)\,\mathrm{sgn}(m-\beta/2) - \tanh\left(\frac{E_0-\mu}{2\mathrm{k_B}T}\right) \right] , \tag{3.204}$$

which reduces for $T \to 0$ and $\bar{\mu} = \mu + D/l_H^2$ to Eq. (3.146b)

$$\langle N_0 \rangle_0 = \frac{|\mathrm{e}H|}{2\mathrm{h}}\, \Theta(|\bar{\mu}| - |m-\beta/2|) \left[\mathrm{sgn}(\mathrm{e}H)\,\mathrm{sgn}(\mathrm{m}-\beta/2) + \mathrm{sgn}(\bar{\mu}) \right] \ . \tag{3.205}$$

For $T = 0$, the zero LL contribution to η_H clearly gets compensated outside of the Dirac mass gap. As expected, finite temperature effects soften this property. Let us briefly comment on how to derive Eq. (3.205) from Eq. (3.204). In the zero temperature limit, the hyperbolic tangent in Eq. (3.205) becomes a sign-function, $\lim_{T\to 0} \tanh(x/T) = \mathrm{sgn}(x)$. Due to this

property, we need to distinguish two cases. The chemical potential is either located (i) inside or (ii) outside of the Dirac mass gap:

$$(i) \quad |\mu + \delta/2| < |m - \beta/2| \ , \tag{3.206}$$

$$(ii) \quad |\mu + \delta/2| > |m - \beta/2| \ . \tag{3.207}$$

For case (i), the hyperbolic tangent in Eq. (3.205) reduces to $\mathrm{sgn}(\mathrm{e}H)\mathrm{sgn}(m-\beta/2)$ and consequently leads to $\langle N_0 \rangle_0 = 0$. Instead, for case (ii), it reduces to $\mathrm{sgn}(\mu + \delta/2)$, eventually implying Eq. (3.205). While the first, temperature independent term in Eq. (3.205) describes the asymmetry of the zero LL with respect to zero energy, the second term encodes its temperature-dependent response. This term ensures that at $T = 0$ the zero LL only contributes outside of the Dirac mass gap, exactly compensating its contribution to the spectral asymmetry. As expected, this property becomes softened by finite temperature effects.

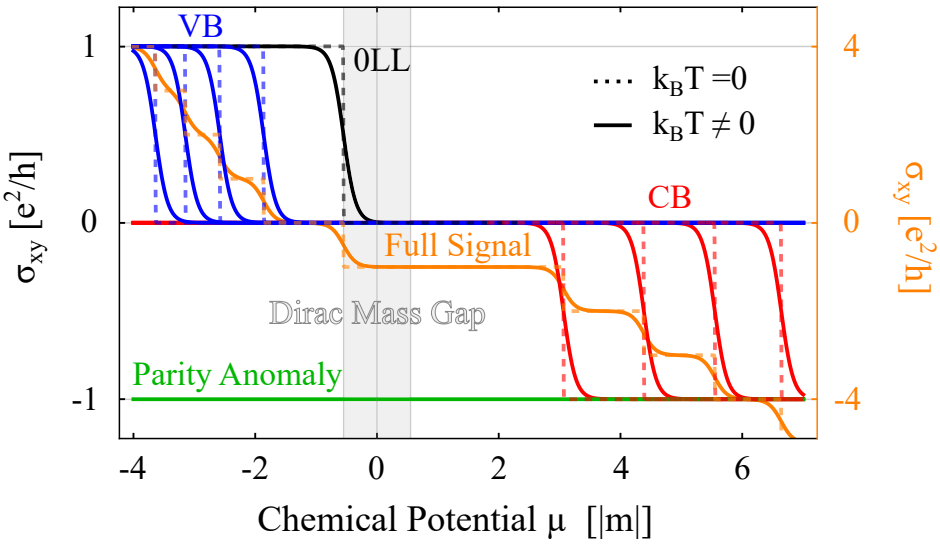

Figure 3.19: Finite temperature Hall conductivity of a Chern insulator in a magnetic field $H = 3\mathrm{T}$ with: $A = 1$, $m = -1$, $B = -0.1$, and $D = -0.05$. The response of each valence (blue) and conduction band (red) LL is shown separately. The zero LL response is illustrated in black, the parity anomaly related contribution is depicted in green. The combined signal is shown in orange. Dashed lines correspond to $\mathrm{k_B}T = 0$, solid lines are associated to $\mathrm{k_B}T = 0.01$. The Dirac mass gap is shown in grey. The figure is reprinted from Ref. [P5] with permission from the APS.

In Fig. 3.19, we used Eq. (3.197) to connect the charge operator to σ_{xy} and plotted the Hall conductivity corresponding to the parity anomaly and to each LL, separately. Moreover, we show the entire signal as a function of the chemical potential. While the Hall conductivity contribution related to the parity anomaly is T and μ independent, each LL comes along with an exponentially suppressed temperature broadening. Consequently, all LLs contribute to the Hall conductivity in the Dirac mass gap. This renormalizes the zero temperature violation of the Onsager relation[a], as it has been discussed below Eq. (3.146). Let us emphasize that the Hall plateau originating from the parity anomaly is much more robust than LL plateaus

[a] At $T = 0$, the only contribution to the Hall conductivity in the Dirac mass gap is given by the parity anomaly in terms of the spectral asymmetry η_{H} [cf. Eq. (3.197)]. Due to Eq. (3.198) this contribution clearly violates the Onsager relation defined as $\sigma_{\mathrm{xy}}(-H) = -\sigma_{\mathrm{xy}}(H)$. In contrast, this identity is fulfilled by any (thermal) LL contribution.

with respect to finite temperature effects. In the Dirac mass gap all LL contributions to the Hall conductivity are exponentially suppressed. Due to the lack of a zero-LL partner, the parity anomaly response is approximately unaltered even beyond this gap, until the chemical potential comes close to the $n=1$ conduction or valence band LL, depending on the sign of the magnetic field. Quantitatively, this means

$$|E_1^+ - E_0| > |E_{n+1}^{\pm} - E_n^{\pm}| \qquad \forall n \in \mathbb{N}^+ \ , \tag{3.208}$$

assuming that the zero-LL is part of the valence band [cf. Fig. 3.19]. Therefore, finite temperature effects firstly smear out the LL steps before they eventually prevent any quantization of the finite temperature Hall conductivity.

Let us end this section by emphasizing that an extensive summary of the results which we have obtained within the scope of this section can be found in Sec. 5.

4

Hydrodynamic Transport in Solid State Materials

Contents

4.1 Hydrodynamic Electron Transport

Hydrodynamic transport is a macroscopic theory which crucially relies on the conservation laws for the particle density, the energy-, as well as the momentum flow. It is applicable to any fluid in which the momentum conserving scattering length in between its microscopic constituents defines the shortest length scale present[a]. For instance, it can be used to describe the flow of water through a pipe, as the H_2O molecules mostly collide with each other and only rarely interact with the boundaries of the pipe. Due to its general assumptions, the theory of hydrodynamics is also applicable to condensed matter systems. If the electron-electron scattering length is the shortest length scale present, the hydrodynamic transport theory can be used to derive the charge current in response to an applied perturbation which only varies slowly in space and time [81]. Essentially, the hydrodynamic transport theory is applicable to both, weakly- as well as strongly interacting solid state systems, as long as electron-electron scattering processes dominate [182].

4.1.1 Characteristic Length Scales

In what follows, we discuss the hydrodynamic regime in a solid state material by analyzing the different length scales present. Let us consider a two-dimensional electron liquid which is confined to a rectangular channel geometry of width W and length $L \gg W$. Since collisions with impurities as well as with thermally excited phonons are momentum non-conserving, the impurity and phonon mean free path l_{imp} and l_{ph} together define the bulk momentum relaxing length scale

$$l_{\mathrm{mr}} \equiv (l_{\mathrm{imp}}^{-1} + l_{\mathrm{ph}}^{-1})^{-1} \ . \tag{4.1}$$

In the hydrodynamic regime, this length scale needs to be much larger than the momentum conserving electron-electron mean free path $l_{\mathrm{ee}} \ll l_{\mathrm{mr}}$. The hydrodynamic transport theory assumes the existence of a local thermal equilibrium. Since the length scale of thermalization is defined by l_{ee}, another requirement for the applicability of hydrodynamics is that the electron-electron mean free path is much shorter than the thermal fluctuations of any thermodynamic state variable $\mathcal{V}$. Quantitatively, this means that

$$l_{\mathrm{ee}} \ll l_{\mathrm{tfl}} \equiv \left(\frac{\partial_\mu \mathcal{V}}{|\mathcal{V}|} \right)^{-1} \quad \text{with} \quad \partial_\mu = (\partial_{\mathrm{t}}/v_{\mathrm{F}}, \partial_i) \ . \tag{4.2}$$

Here, v_{F} is the Fermi velocity of the electron liquid. In general, the interplay between l_{ee}, l_{mr} and W defines the three different transport regimes which are listed in Tab. 4.1 [183].

Condition	Dominating Scattering Process	Transport Regime
$l_{\mathrm{mr}} \ll W, l_{\mathrm{ee}}$	Impurity or Phonon	Ohmic
$W \ll l_{\mathrm{ee}}, l_{\mathrm{mr}}$	Boundary/Wall	Ballistic
$l_{\mathrm{ee}} \ll W \ll l_{\mathrm{mr}}$	Electron-Electron	Hydrodynamic

Table 4.1: Transport regimes for a different order of scattering length scales [86].

In the ohmic regime, the most prominent scattering process is scattering from impurities or phonons. Electron-electron and boundary scattering processes can be neglected and the

[a] While this statement is rigorously true for a continuous theory, in a solid-state system the underlying lattice spacing defines a consistent lower bound for the momentum conserving scattering length.

velocity profile of the fluid is approximately flat. Instead, in the ballistic regime electrons mainly scatter at the channel boundaries. However, if the electron-electron mean free path is the shortest length scale present the fluid behaves hydrodynamically, and it is characterized by a Poiseuille-like velocity profile [80].

If one applies an out-of-plane magnetic field to the channel geometry another characteristic length scale enters our analysis, namely the cyclotron radius r_c. As long as the electron-electron mean free path defines the shortest length scale present - in particular satisfying $l_{ee} \ll r_c$ -, the electron liquid remains in the hydrodynamic regime. Hence, a hydrodynamic description of a condensed matter system is only justified for weak out-of-plane magnetic fields. Roughly speaking, it is required that electrons collide several times with each other before they would have completed their corresponding non-interacting cyclotron orbit [184, 185].

4.1.2 Constitutive Relation and Conservation Equations

As stated above, hydrodynamic transport is a macroscopic long-wavelength and small frequency theory, which only relies on the conservation of mass, energy and momentum. In a relativistic notation, these conserved quantities can be encoded in the particle number current density N^μ, as well as in the energy-momentum tensor $T^{\mu\nu}$. Here and in the following, Greek indices correspond to the 2+1 dimensional space-time coordinates $\mu = \{0, 1, 2\}$, whereas Roman indices solely correspond to the two-dimensional space indices $i = \{1, 2\}$. Moreover, we work in a flat 2+1 dimensional Minkowski space, characterized by the metric tensor $g^{\mu\nu} = \mathrm{diag}(-1, 1, 1)$. In a relativistic notation, the conservation of mass, energy, and momentum is given by the two conservation equations (in the absence of electromagnetic fields):

$$\partial_\mu N^\mu = 0 \quad \text{and} \quad \partial_\mu T^{\mu\nu} = 0 \ . \tag{4.3}$$

In what follows, we derive explicit forms of the particle number current density as well as for the energy-momentum tensor, and derive from these expressions the relativistic and non-relativistic hydrodynamic equations of motion. Our subsequent discussion will roughly follow the references [186], [80] and [187]

The Ideal Non-Dissipative Fluid

Let us consider for the moment an ideal rotational- and parity invariant fluid, characterized by the fluid velocity

$$u^\mu = \Gamma(v_F, \mathbf{v}) \quad \text{with} \quad \Gamma = \frac{1}{\sqrt{1 - \mathbf{v}^2/v_F^2}} \ , \tag{4.4}$$

which is a time-like vector of norm $u_\mu u^\mu = -v_F^2$. As a relativistic three-vector in 2+1 space-time dimensions, the particle current density is in general given by ($[N^\mu]_{SI} = \mathrm{m}^{-1}\mathrm{s}^{-1}$)

$$N^\mu = (N^0, \mathbf{N}) = (v_F n, \mathbf{N}) \ , \tag{4.5}$$

where $\mathbf{N}$ is the spatial particle current density and n is the particle density. In the local rest frame of an ideal or analogously non-dissipitive fluid, defined by $\mathbf{v}|_{LR} = 0$ and thus by $u^\mu|_{LR} = (v_F, 0)$, the particle current density is given by

$$N^\mu|_{LR} = (v_F n, 0) = n u^\mu|_{LR} \ . \tag{4.6}$$

In any reference frame related by a Lorentz transformation, the particle current density is in general given by

$$N^\mu = n u^\mu \ . \tag{4.7}$$

The energy-momentum tensor $T^{\mu\nu}$ encodes the densities and currents of energy and momentum. In particular, T^{00} defines the energy density ϵ, $v_\mathrm{F} T^{0i}$ defines the i-th component of the energy flux density $\mathbf{j}_\mathrm{E}$, $v_\mathrm{F}^{-1} T^{i0}$ defines the i-th component of the momentum density $\mathbf{n_p}$ and T^{ij} is the stress or analogously momentum flux-density tensor. More precisely, T^{ij} encodes how much momentum in the $\mathbf{e}_i$-direction threats through a two-dimensional surface with a normal vector which points in $\mathbf{e}_j$-direction. In general, one defines [187]

$$T^{\mu\nu} = \begin{pmatrix} \epsilon & v_\mathrm{F}^{-1}\mathbf{j}_\mathrm{E} \\ v_\mathrm{F}\mathbf{n}_\mathrm{p} & \Pi^{ij} \end{pmatrix} \tag{4.8}$$

with SI units

$$[T^{\mu\nu}]_\mathrm{SI} = \frac{\mathrm{J}}{\mathrm{m}^2} = \frac{\mathrm{kg\,m}^2}{\mathrm{s}^2\,\mathrm{m}^2} = \frac{\mathrm{kg}}{\mathrm{s}^2} \ . \tag{4.9}$$

For isotropic space-times the energy-momentum tensor is symmetric

$$T^{\mu\nu} = T^{\nu\mu} \ , \tag{4.10}$$

which implies that $v_\mathrm{F}^{-1}\mathbf{j}_\mathrm{E} = v_\mathrm{F}\mathbf{n_p}$[a]. In the local rest frame of an ideal fluid, the energy current density vanishes and the energy-momentum tensor becomes diagonal:

$$T^{\mu\nu}|_\mathrm{LR} = \begin{pmatrix} \epsilon & 0 \\ 0 & P\delta^{ij} \end{pmatrix} = \frac{\epsilon + P}{v_\mathrm{F}^2} u^\mu u^\nu|_\mathrm{LR} + P g^{\mu\nu} \ . \tag{4.11}$$

Here, P is the (isotropic) pressure. Analogously to the particle current, one can Lorentz transform this expression to any reference frame, obtaining the general expression

$$T^{\mu\nu} = \frac{\epsilon}{v_\mathrm{F}^2} u^\mu u^\nu + P\Delta^{\mu\nu} \ , \tag{4.12}$$

where we defined the projection operator

$$\Delta^{\mu\nu} = g^{\mu\nu} + \frac{u^\mu u^\nu}{v_\mathrm{F}^2} \ . \tag{4.13}$$

In particular, this operator projects to the space orthogonal to the fluid velocity u^μ, implying the identities

$$u_\mu \Delta^{\mu\nu} = 0 \quad \wedge \quad \Delta^\mu_\rho \Delta^\rho_\nu = \Delta^{\mu\nu} \ . \tag{4.14}$$

The Dissipative Fluid - First Order Gradient Expansion

So far, we assumed an ideal non-dissipative fluid. Beyond this academic limit, the particle current density as well as the energy momentum tensor acquire dissipative corrections. For

[a] We agree with the presented form of the energy-momentum tensor in Eq. (4.8) for isotropic systems. If the energy-momentum tensor is not symmetric the off-diagonal entries in Eq. (4.8) should be interchanged in order to consistently interpret the energy-momentum conservation equation. In the remaining part of this thesis we stick to the definition in Eq. (4.8) to enable an easy comparison of our results to the recent literature.

small thermal fluctuations it is in general possible to expand the particle current density as well as the energy-momentum tensor in terms of a small parameter κ which characterizes the deviation from an ideal fluid. Since thermalization is driven by l_{ee}, and since thermal fluctuations are encoded by l_{tfl} [cf. Eq.(4.2)], this small expansion parameter can be naturally defined via

$$\kappa \equiv l_{\mathrm{ee}}/l_{\mathrm{tfl}} \ll 1 \ . \tag{4.15}$$

In what follows, we expand the particle current density as well as the energy-momentum tensor up to first order in κ, which introduces the corrections δN^μ and $\delta T^{\mu\nu}$:

$$N^\mu = N_0^\mu + \delta N^\mu, \qquad T^{\mu\nu} = T_0^{\mu\nu} + \delta T^{\mu\nu} \ . \tag{4.16}$$

For an ideal fluid, the particle current density and the energy density always move in the same direction. This property changes as soon as one includes dissipative effects, which makes the fluid velocity u^μ an ambiguous quantity. On the one hand, u^μ can be chosen such that it describes the flow of the total energy flux throughout the system. This choice is the so-called Landau frame with $T^{\mu\nu}u_{\nu,\mathrm{Landau}} = T_0^{\mu\nu}u_{\nu,\mathrm{Landau}} = -\epsilon_{\mathrm{Landau}}u^\mu$. On the other hand, u^μ can be chosen such that it describes the total particle flow throughout the system, defining the so-called Eckart frame via $N^\mu_{\mathrm{Eckart}}u_{\mu,\mathrm{Eckart}} = -v_{\mathrm{F}}^2 n_{\mathrm{Eckart}}$. These frames essentially can be realized by choosing [186]

$$u^\mu_{\mathrm{Eckart}} = \frac{N^\mu}{\sqrt{-N_\nu N^\nu}} \qquad \text{or} \qquad u^\mu_{\mathrm{Landau}} = \frac{T^\mu{}_\nu u^\nu_{\mathrm{Landau}}}{\sqrt{-u^\lambda_{\mathrm{Landau}} T_\lambda{}^\rho \ T_{\rho\sigma} u^\sigma_{\mathrm{Landau}}}} \ . \tag{4.17}$$

Since both of these frames are physically equivalent we solely consider the Landau frame within this work and neglect the corresponding subscript in the following. One crucial property of the Landau frame is that within this frame-choice the heat current vanishes, which implies that

$$u_\mu \delta T^{\mu\nu} = 0 \ . \tag{4.18}$$

Moreover, we assume that N^0 is proportional to the particle density in the lab-frame of our system, n, which implies $u_\mu \delta N^\mu = 0$. The hydrodynamic assumption of a local thermodynamic equilibrium implies the existence of a local entropy current density s^μ whose divergence is non-zero (second law of thermodynamics),

$$\partial_\mu s^\mu \geq 0 \ . \tag{4.19}$$

This property can be used to derive the most general forms of δN^μ and $\delta T^{\mu\nu}$ in the first order gradient expansion of the constitutive relations in Eq. (4.16) [80]. In order to calculate these tensor combinations, we will make use of the energy-momentum conservation equation in Eq. (4.3), which implies

$$0 = u_\mu \partial_\nu T^{\mu\nu} = -u^\mu \partial_\mu \epsilon - (\epsilon + P)\partial_\mu u^\mu + u_\mu \partial_\nu \delta T^{\mu\nu} \tag{4.20}$$

$$= -u^\mu \partial_\mu \epsilon - (\epsilon + P)\partial_\mu u^\mu - \delta T^{\mu\nu}\partial_\mu u_\nu \ , \tag{4.21}$$

where we made use of

$$u_\nu \partial_\mu \delta T^{\mu\nu} = \partial_\mu \underbrace{(u_\nu \delta T^{\mu\nu})}_{=0 \text{ cf. Eq. (4.18)}} - \delta T^{\mu\nu}\partial_\mu u_\nu = -\delta T^{\mu\nu}\partial_\mu u_\nu \ . \tag{4.22}$$

As a next step in our calculation we make use of the Gibbs-Duhem relation for a fixed area $\mathrm{d}V = 0$

$$\epsilon + P = \mu n + Ts \quad \wedge \quad \mathrm{d}\epsilon = T\mathrm{d}s + \mu \mathrm{d}n \ , \tag{4.23}$$

where $\mu(\mathbf{r})$ is the local chemical potential and $T(\mathbf{r})$ is the local temperature. Inserting this identity in Eq. (4.21) implies the equality

$$\begin{aligned} 0 &= -u^\mu \partial_\mu \epsilon - (\epsilon + P)\partial_\mu u^\mu - \delta T^{\mu\nu}\partial_\mu u_\nu = -\mu u^\mu \partial_\mu n - T u^\mu \partial_\mu s - (\mu n + Ts)\partial_\mu u^\mu - \delta T^{\mu\nu}\partial_\mu u_\nu \\ &= -\mu \underbrace{\partial_\mu (n u^\mu)}_{=-\partial_\mu \delta N^\mu \text{ cf. Eq. (4.3)}} - T\partial_\mu (s u^\mu) - \delta T^{\mu\nu}\partial_\mu u_\nu \\ &= \mu \partial_\mu \delta N^\mu - T\partial_\mu (s u^\mu) - \delta T^{\mu\nu}\partial_\mu u_\nu \ . \end{aligned} \tag{4.24}$$

This identity can be rewritten in the intuitive form

$$\partial_\mu s^\mu \equiv \partial_\mu \left(s u^\mu - \frac{\mu}{T}\delta N^\mu \right) = -\frac{1}{T}\delta T^{\mu\nu}\partial_\mu u_\nu - \delta N^\mu \partial_\mu \frac{\mu}{T} \ . \tag{4.25}$$

The left hand side of this equation defines the divergence of the entropy current density s^μ up to first order in the hydrodynamic derivative expansion. It consists of the ideal convective term $s u^\mu$ and a dissipative particle current density correction $\propto \delta N^\mu$ [80, 186]. In order to ensure that the entropy current density has a positive divergence, the first order corrections to N_0^μ and $T_0^{\mu\nu}$ in general need to satisfy the following functional dependencies [188, 189]

$$\delta N^\mu = -\frac{\sigma_\mathrm{Q}}{\mathrm{e}^2} T \Delta^{\mu\nu}\partial_\nu \frac{\mu}{T} \quad \wedge \quad \delta T^{\mu\nu} = -\eta \Sigma^{\mu\nu} - \zeta \partial_\alpha u^\alpha \Delta^{\mu\nu} \ , \tag{4.26}$$

where we introduced the traceless disspiative shear stress tensor

$$\Sigma^{\mu\nu} = \Delta^{\mu\rho}\Delta^{\nu\sigma}\left(\partial_\rho u_\sigma + \partial_\sigma u_\rho - g_{\rho\sigma}\partial_\alpha u^\alpha\right) \ . \tag{4.27}$$

Here, the positive constants $\sigma_\mathrm{Q} \geq 0$, $\eta \geq 0$, and $\zeta \geq 0$ define the quantum-critical conductivity, the shear viscosity and the bulk viscosity, respectively.

Coupling the hydrodynamic system to an electromagnetic field A^μ mainly has two effects. On the one hand, the electromagnetic field modifies the conservation equation of the energy-momentum tensor

$$\partial_\nu T^{\mu\nu} = \mathrm{e}\, F^{\mu\nu} N_\nu \ , \tag{4.28}$$

where ($[F^{\mu\nu}]_\mathrm{SI} = \mathrm{kg/(Cs)}$)

$$\begin{aligned} F^{\mu\nu} = \partial^\mu A^\nu - \partial^\nu A^\mu &= \begin{pmatrix} 0 & (\mathrm{c}/v_\mathrm{F})E_\mathrm{x}/\mathrm{c} & (\mathrm{c}/v_\mathrm{F})E_\mathrm{y}/\mathrm{c} \\ -(\mathrm{c}/v_\mathrm{F})E_\mathrm{x}/\mathrm{c} & 0 & B \\ -(\mathrm{c}/v_\mathrm{F})E_\mathrm{y}/\mathrm{c} & -B & 0 \end{pmatrix} \\ &= \begin{pmatrix} 0 & E_\mathrm{x}/v_\mathrm{F} & E_\mathrm{y}/v_\mathrm{F} \\ -E_\mathrm{x}/v_\mathrm{F} & 0 & B \\ -E_\mathrm{y}/v_\mathrm{F} & -B & 0 \end{pmatrix} \end{aligned} \tag{4.29}$$

is the anti-symmetric 'improved' field-strength tensor [187, 188], consisting of the electric field components E_i and the out-of-plane magnetic field strength B. The prefactor $(\mathrm{c}/v_\mathrm{F})$, where c is the speed of light in the medium, originates from the redefinition of the space-time coordinates in terms of the 'causal' (Fermi) velocity v_F [cf. Eq.(4.2)].

On the other hand, the electromagnetic field enters the dissipative particle current density correction in the first order gradient expansion [189]

$$\delta N^{\mu} = \frac{\sigma_{\mathrm{Q}}}{\mathrm{e}} \left(F^{\mu\nu} u_{\nu} - \frac{1}{\mathrm{e}} T \Delta^{\mu\nu} \partial_{\nu} \frac{\mu}{T} \right) \equiv \frac{\sigma_{\mathrm{Q}}}{\mathrm{e}} V^{\mu} \ , \tag{4.30}$$

with the electric field $\mathcal{E}^{\mu} = F^{\mu\nu} u_{\nu}$ and magentic field $\mathcal{B} = -\frac{1}{2} \epsilon^{\mu\nu\rho} u_{\mu} F_{\nu\rho} / v_{\mathrm{F}}$ in the fluid frame. Before we also allow for parity breaking terms in the first order gradient expansion, let us emphasize that one can naturally include impurity scattering in our analysis by adding a phenomenological correction to the right hand side of the energy-momentum conservation equation (4.28) [187]:

$$\partial_{\nu} T^{\mu\nu} = \mathrm{e}\, F^{\mu\nu} N_{\nu} + \frac{1}{l_{\mathrm{imp}}} \left(\delta^{\mu}{}_{\nu} + \frac{u^{\mu} u_{\nu}}{v_{\mathrm{F}}^2} \right) T^{\nu\gamma} \frac{u_{\gamma}}{v_{\mathrm{F}}} \ , \tag{4.31}$$

where l_{imp} is the impurity mean free path. The phenomenological scattering term in Eq. (4.31) is constructed such that in the laboratory frame impurity scattering only relaxes the momentum density $v_{\mathrm{F}}^{-1} T^{i0}$ [188].

The Breakdown of Parity Symmetry

Next, let us analyze the concept of parity breaking hydrodynamics in 2+1 space-time dimensions. The parity can be broken extrinsically for instance by an applied out-of-plane magnetic field, or intrinsically by adding a parity-odd (mass) term to the Hamiltonian which describes the electron fluid. Within the scope of this thesis we are mainly interested in two different parity-breaking transport coefficients:

(*i*) The quantum anomalous Hall conductivity $\sigma_{\mathrm{QAH}} \in \mathbb{R}$, which we already studied in the previous chapter from a quantum field theoretic perspective, and

(*ii*) the Hall viscosity $\eta_{\mathrm{H}} \in \mathbb{R}$ [84] which is the analogon of the electrical Hall conductivity in the scope of (transverse) momentum transport [190].

Both of these non-dissipative transport coefficients arise in the constitutive relations for parity-breaking hydrodynamics in 2+1 space-time dimensions[a] [189]

$$N^{\mu} = n u^{\mu} + \frac{\sigma_{\mathrm{Q}}}{\mathrm{e}} V^{\mu} + \frac{\sigma_{\mathrm{QAH}}}{\mathrm{e}} \bar{V}^{\mu} \tag{4.32}$$

$$T^{\mu\nu} = \frac{\epsilon}{v_{\mathrm{F}}^2} u^{\mu} u^{\nu} + (P - \zeta\, \partial_{\alpha} u^{\alpha})\, \Delta^{\mu\nu} - \eta \Sigma^{\mu\nu} - \eta_{\mathrm{H}} \bar{\Sigma}^{\mu\nu} \ . \tag{4.33}$$

Here, we included the dual forms

$$\bar{V}^{\mu} = \epsilon^{\mu\nu\rho} \frac{u_{\nu}}{v_{\mathrm{F}}} V_{\rho} \qquad \wedge \qquad \bar{\Sigma}^{\mu\nu} = \frac{1}{2 v_{\mathrm{F}}} \left(\epsilon^{\mu\alpha\rho} u_{\alpha} \Sigma_{\rho}{}^{\nu} + \epsilon^{\nu\alpha\rho} u_{\alpha} \Sigma_{\rho}{}^{\mu} \right) \ . \tag{4.34}$$

The Kubo formulas for the bulk-, shear-, and Hall viscosity, as well as for the quantum critical- and quantum anomalous Hall conductivity are in particular given by the following relations [189]

$$\zeta = \lim_{\omega \to 0} \frac{1}{4\omega} \delta_{ij} \delta_{kl}\, \mathrm{Im}\, G_{\mathrm{R}}^{ij,kl}(\omega, \mathbf{p}{=}0) \ , \tag{4.35}$$

$$\eta = \lim_{\omega \to 0} \frac{1}{8\omega} \left(\delta_{ik} \delta_{jl} - \epsilon_{ik} \epsilon_{jl} \right)\, \mathrm{Im}\, G_{\mathrm{R}}^{ij,kl}(\omega, \mathbf{p}{=}0) \ , \tag{4.36}$$

[a] In the scope of our analysis we neglect contributions from parity-odd thermodynamic transport coefficients. Their origin and physical implications are in particular discussed within the references [189] and [191].

$$\eta_{\mathrm{H}} = \lim_{\omega\to 0} \frac{1}{4\omega}\delta_{ik}\epsilon_{jl}\,\mathrm{Im}\,G_{\mathrm{R}}^{ij,kl}(\omega,\mathbf{p}=0)\ , \tag{4.37}$$

$$\sigma_{\mathrm{Q}} = \lim_{\omega\to 0} \frac{1}{2\omega}\delta_{ij}\,\mathrm{Im}\,G_{\mathrm{R}}^{i,j}(\omega,\mathbf{p}=0)\ , \tag{4.38}$$

$$\sigma_{\mathrm{QAH}} = \lim_{\omega\to 0} \frac{1}{2\omega}\epsilon_{ij}\,\mathrm{Im}\,G_{\mathrm{R}}^{i,j}(\omega,\mathbf{p}=0)\ . \tag{4.39}$$

Here, $\epsilon^{\mu\nu\rho}$ defines the three-dimensional Levi-Civita symbol with $\epsilon^{012}=1$, $\epsilon^{ij}=\epsilon^{0ij}$ defines the two-dimensional Levi-Civita symbol, and $G_{\mathrm{R}}(\omega,\mathbf{p})$ denotes the frequency ω and spatial momentum $\mathbf{p}$ dependent retarded current - current, or energy momentum - energy momentum correlation function in thermal equilibrium

$$G_{\mathrm{R}}^{\mu,\nu} = \mathrm{e}^2\,\langle N^\mu N^\nu\rangle_{\mathrm{R}}, \qquad G_{\mathrm{R}}^{\mu\nu,\rho\sigma} = \langle T^{\mu\nu}T^{\rho\sigma}\rangle_{\mathrm{R}}\ . \tag{4.40}$$

The Non-Relativistic Limit

In the previous subsection we have derived general expressions of the energy-momentum tensor and the particle current density in the context of relativistic hydrodynamics. If the fluid velocity v of the hydrodynamic system considered is much smaller than its 'causal' (Fermi) velocity v_{F}, the constitutive relations (4.32), as well as the conservation equations (4.3) and (4.28) approximate their non-relativistic expressions. It is the goal of the present subsection to derive the hydrodynamic constitutive relations and conservation equations in the non-relativistic limit

$$v = |\mathbf{v}| \ll v_{\mathrm{F}}\ . \tag{4.41}$$

We start our calculation by separating the non-relativistic part from the rest energy contribution to the entire energy density

$$\epsilon = nmv_{\mathrm{F}}^2 + \epsilon_{\mathrm{nr}}\ . \tag{4.42}$$

Moreover, we boost the rest-energy density via a Lorentz transformation in order to derive hydrodynamic expressions in terms of the (co-)moving rest-energy density

$$\rho v_{\mathrm{F}}^2 = \Gamma nmv_{\mathrm{F}}^2\ . \tag{4.43}$$

In order to obtain the non-relativistic particle number conservation and Navier-Stokes equations, we need to Taylor expand the energy-momentum tensor as well as the particle current density in the constitutive relations Eq. (4.32) in terms of the small expansion parameter $v/v_{\mathrm{F}} \ll 1$. Therefore, we particularly need the following Taylor expansions of the space-time dependent Lorentz factor Γ, which we introduced in Eq. (4.4):

$$\Gamma = 1 + \frac{1}{2}\left(\frac{v}{v_{\mathrm{F}}}\right)^2 + \frac{3}{8}\left(\frac{v}{v_{\mathrm{F}}}\right)^4 + \mathcal{O}\left[\left(\frac{v}{v_{\mathrm{F}}}\right)^6\right]\ , \tag{4.44}$$

$$\Gamma^{-1} = 1 - \frac{1}{2}\left(\frac{v}{v_{\mathrm{F}}}\right)^2 - \frac{1}{8}\left(\frac{v}{v_{\mathrm{F}}}\right)^4 + \mathcal{O}\left[\left(\frac{v}{v_{\mathrm{F}}}\right)^6\right]\ , \tag{4.45}$$

$$\Gamma^2 = 1 + \quad\left(\frac{v}{v_{\mathrm{F}}}\right)^2 + \quad\left(\frac{v}{v_{\mathrm{F}}}\right)^4 + \mathcal{O}\left[\left(\frac{v}{v_{\mathrm{F}}}\right)^6\right]\ , \tag{4.46}$$

$$\Gamma^3 = 1 + \frac{3}{2}\left(\frac{v}{v_{\mathrm{F}}}\right)^2 + \frac{15}{8}\left(\frac{v}{v_{\mathrm{F}}}\right)^4 + \mathcal{O}\left[\left(\frac{v}{v_{\mathrm{F}}}\right)^6\right]\ , \tag{4.47}$$

$$\partial_\mu\Gamma = \Gamma^3\ \frac{v^k\,\partial_\mu v_k}{v_{\mathrm{F}}^2}\ =\ \left(\frac{v}{v_{\mathrm{F}}}\right)^2\ \frac{\partial_\mu v}{v} + \mathcal{O}\left[\left(\frac{v}{v_{\mathrm{F}}}\right)^4\right] = \mathcal{O}\left[\left(\frac{v}{v_{\mathrm{F}}}\right)^2\right]\ . \tag{4.48}$$

For the corresponding Taylor expansions of the dimensionless fluid velocity $\tilde{u}^\mu \equiv u^\mu/v_\mathrm{F}$ [cf. Eq. (4.4)], these identities imply:

$$\tilde{u}^0\tilde{u}^0 = \Gamma^2 = 1 + \left(\frac{v}{v_\mathrm{F}}\right)^2 + \mathcal{O}\left[\left(\frac{v}{v_\mathrm{F}}\right)^4\right], \qquad \tilde{u}^0\tilde{u}^i = \Gamma^2\frac{v^i}{v_\mathrm{F}} = \frac{v^i}{v_\mathrm{F}} + \frac{v^2 v^i}{v_\mathrm{F}^3} + \mathcal{O}\left[\left(\frac{v}{v_\mathrm{F}}\right)^5\right],$$

$$\tilde{u}^i\tilde{u}^j = \Gamma^2\,\frac{v^i v^j}{v_\mathrm{F}^2} = \frac{v^i v^j}{v_\mathrm{F}^2} + \mathcal{O}\left[\left(\frac{v}{v_\mathrm{F}}\right)^4\right], \qquad \partial_0\tilde{u}_0 = \frac{1}{v_\mathrm{F}}\partial_\mathrm{t}\Gamma = \mathcal{O}\left[\left(\frac{v}{v_\mathrm{F}}\right)^3\right], \tag{4.49}$$

$$\partial_i\tilde{u}_0 = \partial_i\Gamma = \frac{v^k\partial_i v_k}{v_\mathrm{F}^2} + \mathcal{O}\left[\left(\frac{v}{v_\mathrm{F}}\right)^4\right], \tag{4.50}$$

$$\partial_0\tilde{u}_i = \frac{1}{v_\mathrm{F}^2}\partial_\mathrm{t}(\Gamma v_i) = \frac{1}{v_\mathrm{F}^2}(v_i\partial_\mathrm{t}\Gamma + \Gamma\partial_\mathrm{t}v_i) = \frac{\partial_\mathrm{t}v_i}{v_\mathrm{F}^2} + \mathcal{O}\left[\left(\frac{v}{v_\mathrm{F}}\right)^4\right], \tag{4.51}$$

$$\partial_i\tilde{u}_j = \frac{1}{v_\mathrm{F}}\partial_i(\Gamma v_j) = \frac{1}{v_\mathrm{F}}(v_j\partial_i\Gamma + \Gamma\partial_i v_j) = \frac{\partial_i v_j}{v_\mathrm{F}} + \mathcal{O}\left[\left(\frac{v}{v_\mathrm{F}}\right)^3\right], \tag{4.52}$$

$$\partial_\mu\tilde{u}^\mu = \partial_0\tilde{u}^0 + \partial_i\tilde{u}^i = \frac{\partial_i v^i}{v_\mathrm{F}} + \mathcal{O}\left[\left(\frac{v}{v_\mathrm{F}}\right)^3\right]. \tag{4.53}$$

Moreover, with the metric tensor $g^{\mu\nu} = \mathrm{diag}(-1,1,1)$, the Taylor expansion of the projection operator $\Delta^{\mu\nu}$, which we defined in Eq. (4.13), yields

$$\Delta^{00} = \tilde{u}^0\tilde{u}^0 + g^{00} = 1 + \left(\frac{v}{v_\mathrm{F}}\right)^2 + \mathcal{O}\left[\left(\frac{v}{v_\mathrm{F}}\right)^4\right] - 1 = \left(\frac{v}{v_\mathrm{F}}\right)^2 + \mathcal{O}\left[\left(\frac{v}{v_\mathrm{F}}\right)^4\right], \tag{4.54}$$

$$\Delta^{0i} = \tilde{u}^0\tilde{u}^i = \frac{v^i}{v_\mathrm{F}} + \mathcal{O}\left[\left(\frac{v}{v_\mathrm{F}}\right)^3\right], \tag{4.55}$$

$$\Delta^{ij} = \tilde{u}^i\tilde{u}^j + g^{ij} = \frac{v^i v^j}{v_\mathrm{F}^2} + \delta^{ij} + \mathcal{O}\left[\left(\frac{v}{v_\mathrm{F}}\right)^4\right]. \tag{4.56}$$

With these identities we can Taylor expand the bulk viscosity term in the first order dissipative correction to the energy-momentum tensor in Eq. (4.26). In particular, we find that

$$-\zeta\partial_\alpha u^\alpha = -v_\mathrm{F}\zeta\partial_\alpha\tilde{u}^\alpha = -v_\mathrm{F}\zeta\left(\frac{\partial_i v^i}{v_\mathrm{F}} + \mathcal{O}\left[\left(\frac{v}{v_\mathrm{F}}\right)^3\right]\right) = -\zeta\partial_i v^i + \mathcal{O}\left[\left(\frac{v}{v_\mathrm{F}}\right)^2\right], \tag{4.57}$$

which implies the following bulk viscous contributions to Eq. (4.26)

$$-\zeta\partial_\alpha u^\alpha\Delta^{00} = \mathcal{O}\left[\left(\frac{v}{v_\mathrm{F}}\right)^2\right], \tag{4.58}$$

$$-\zeta\partial_\alpha u^\alpha\Delta^{i0} = -\zeta\partial_\alpha u^\alpha\Delta^{0i} = -\frac{\zeta}{v_\mathrm{F}}v^i\partial_k v^k + \mathcal{O}\left[\left(\frac{v}{v_\mathrm{F}}\right)^3\right], \tag{4.59}$$

$$-\zeta\partial_\alpha u^\alpha\Delta^{ij} = -\zeta\delta^{ij}\partial_k v^k + \mathcal{O}\left[\left(\frac{v}{v_\mathrm{F}}\right)^2\right]. \tag{4.60}$$

Next, let us Taylor expand the dissipative shear stress tensor $\Sigma^{\mu\nu}$, which we defined in Eq. (4.27). We start our calculation by analyzing its spatial components normalized to the Fermi velocity v_F

$$\Sigma^{ij}/v_\mathrm{F} = \Delta^{i\rho}\Delta^{j\sigma}\left(\partial_\rho\tilde{u}_\sigma + \partial_\sigma\tilde{u}_\rho - g_{\rho\sigma}\partial_\alpha\tilde{u}^\alpha\right). \tag{4.61}$$

In particular, we need to distinguish several cases:

$$\begin{aligned}
\rho=\sigma=0: &\quad \mathcal{O}\left[\left(\frac{v}{v_{\mathrm{F}}}\right)^2\right]\left(\mathcal{O}\left[\left(\frac{v}{v_{\mathrm{F}}}\right)^3\right]+\mathcal{O}\left[\left(\frac{v}{v_{\mathrm{F}}}\right)^3\right]+\mathcal{O}\left[\left(\frac{v}{v_{\mathrm{F}}}\right)\right]\right)=\mathcal{O}\left[\left(\frac{v}{v_{\mathrm{F}}}\right)^3\right],\\
\rho=0\wedge\sigma=j: &\quad \mathcal{O}\left[\left(\frac{v}{v_{\mathrm{F}}}\right)\right]\left(\mathcal{O}\left[\left(\frac{v}{v_{\mathrm{F}}}\right)^2\right]+\mathcal{O}\left[\left(\frac{v}{v_{\mathrm{F}}}\right)^2\right]+\ 0\ \right)=\mathcal{O}\left[\left(\frac{v}{v_{\mathrm{F}}}\right)^3\right],\\
\rho=0\wedge\sigma=l\neq j: &\quad \mathcal{O}\left[\left(\frac{v}{v_{\mathrm{F}}}\right)^3\right]\left(\mathcal{O}\left[\left(\frac{v}{v_{\mathrm{F}}}\right)^2\right]+\mathcal{O}\left[\left(\frac{v}{v_{\mathrm{F}}}\right)^2\right]+\ 0\ \right)=\mathcal{O}\left[\left(\frac{v}{v_{\mathrm{F}}}\right)^5\right],\\
\rho=i\wedge\sigma=0: &\quad \mathcal{O}\left[\left(\frac{v}{v_{\mathrm{F}}}\right)\right]\left(\mathcal{O}\left[\left(\frac{v}{v_{\mathrm{F}}}\right)^2\right]+\mathcal{O}\left[\left(\frac{v}{v_{\mathrm{F}}}\right)^2\right]+\ 0\ \right)=\mathcal{O}\left[\left(\frac{v}{v_{\mathrm{F}}}\right)^3\right],\\
\rho=k\neq i\wedge\sigma=0: &\quad \mathcal{O}\left[\left(\frac{v}{v_{\mathrm{F}}}\right)^3\right]\left(\mathcal{O}\left[\left(\frac{v}{v_{\mathrm{F}}}\right)^2\right]+\mathcal{O}\left[\left(\frac{v}{v_{\mathrm{F}}}\right)^2\right]+\ 0\ \right)=\mathcal{O}\left[\left(\frac{v}{v_{\mathrm{F}}}\right)^5\right],\\
\rho=i\wedge\sigma=l\neq j: &\quad \mathcal{O}\left[\left(\frac{v}{v_{\mathrm{F}}}\right)^2\right]\left(\mathcal{O}\left[\left(\frac{v}{v_{\mathrm{F}}}\right)\right]+\left[\left(\frac{v}{v_{\mathrm{F}}}\right)\right]+\left[\left(\frac{v}{v_{\mathrm{F}}}\right)\right]\right)=\mathcal{O}\left[\left(\frac{v}{v_{\mathrm{F}}}\right)^3\right],\\
\rho=k\neq i\wedge\sigma=j: &\quad \mathcal{O}\left[\left(\frac{v}{v_{\mathrm{F}}}\right)^2\right]\left(\mathcal{O}\left[\left(\frac{v}{v_{\mathrm{F}}}\right)\right]+\left[\left(\frac{v}{v_{\mathrm{F}}}\right)\right]+\left[\left(\frac{v}{v_{\mathrm{F}}}\right)\right]\right)=\mathcal{O}\left[\left(\frac{v}{v_{\mathrm{F}}}\right)^3\right],\\
\rho=k\neq i\wedge\sigma=l\neq j: &\quad \mathcal{O}\left[\left(\frac{v}{v_{\mathrm{F}}}\right)^4\right]\left(\mathcal{O}\left[\left(\frac{v}{v_{\mathrm{F}}}\right)\right]+\left[\left(\frac{v}{v_{\mathrm{F}}}\right)\right]+\left[\left(\frac{v}{v_{\mathrm{F}}}\right)\right]\right)=\mathcal{O}\left[\left(\frac{v}{v_{\mathrm{F}}}\right)^5\right].
\end{aligned}$$

The only case which significantly contributes to Σ^{ij} is given by $\rho=i$ and $\sigma=j$, implying

$$\Sigma^{ij}/v_{\mathrm{F}}=\frac{1}{v_{\mathrm{F}}}\left(\partial^i v^j+\partial^j v^i-\delta^{ij}\partial_k v^k\right)+\mathcal{O}\left[\left(\frac{v}{v_{\mathrm{F}}}\right)^3\right]. \tag{4.62}$$

Let us further understand the scaling of

$$\Sigma^{i0}/v_{\mathrm{F}}=\Delta^{i\rho}\Delta^{0\sigma}\left(\partial_\rho\tilde{u}_\sigma+\partial_\sigma\tilde{u}_\rho-g_{\rho\sigma}\partial_\alpha\tilde{u}^\alpha\right) \tag{4.63}$$

in terms of the small Taylor expansion parameter v/v_{F}. In order to derive this scaling, we need to analyze the different cases

$$\begin{aligned}
\rho=\sigma=0: &\quad \mathcal{O}\left[\left(\frac{v}{v_{\mathrm{F}}}\right)^3\right]\left(\mathcal{O}\left[\left(\frac{v}{v_{\mathrm{F}}}\right)^3\right]+\mathcal{O}\left[\left(\frac{v}{v_{\mathrm{F}}}\right)^3\right]+\mathcal{O}\left[\left(\frac{v}{v_{\mathrm{F}}}\right)\right]\right)=\mathcal{O}\left[\left(\frac{v}{v_{\mathrm{F}}}\right)^4\right],\\
\rho=i\wedge\sigma=0: &\quad \mathcal{O}\left[\left(\frac{v}{v_{\mathrm{F}}}\right)^2\right]\left(\mathcal{O}\left[\left(\frac{v}{v_{\mathrm{F}}}\right)^2\right]+\mathcal{O}\left[\left(\frac{v}{v_{\mathrm{F}}}\right)^2\right]+0\right)=\mathcal{O}\left[\left(\frac{v}{v_{\mathrm{F}}}\right)^4\right],\\
\rho=l\neq i\wedge\sigma=0: &\quad \mathcal{O}\left[\left(\frac{v}{v_{\mathrm{F}}}\right)^4\right]\left(\mathcal{O}\left[\left(\frac{v}{v_{\mathrm{F}}}\right)^2\right]+\mathcal{O}\left[\left(\frac{v}{v_{\mathrm{F}}}\right)^2\right]+0\right)=\mathcal{O}\left[\left(\frac{v}{v_{\mathrm{F}}}\right)^6\right],\\
\rho=0\wedge\sigma=k: &\quad \mathcal{O}\left[\left(\frac{v}{v_{\mathrm{F}}}\right)^2\right]\left(\mathcal{O}\left[\left(\frac{v}{v_{\mathrm{F}}}\right)^2\right]+\mathcal{O}\left[\left(\frac{v}{v_{\mathrm{F}}}\right)^2\right]+0\right)=\mathcal{O}\left[\left(\frac{v}{v_{\mathrm{F}}}\right)^4\right],\\
\rho=l\neq i\wedge\sigma=k: &\quad \mathcal{O}\left[\left(\frac{v}{v_{\mathrm{F}}}\right)^3\right]\left(\mathcal{O}\left[\left(\frac{v}{v_{\mathrm{F}}}\right)\right]+\mathcal{O}\left[\left(\frac{v}{v_{\mathrm{F}}}\right)\right]+\mathcal{O}\left[\left(\frac{v}{v_{\mathrm{F}}}\right)\right]\right)=\mathcal{O}\left[\left(\frac{v}{v_{\mathrm{F}}}\right)^4\right].
\end{aligned}$$

The only case which significantly contributes to Σ^{i0} is given by $\rho=i$ and $\sigma=k$, implying

$$\Sigma^{i0}/v_{\mathrm{F}}=\frac{v^k}{v_{\mathrm{F}}^2}\left(\partial^i v_k+\partial_k v^i-\delta^i_k\partial_n v^n\right)+\mathcal{O}\left[\left(\frac{v}{v_{\mathrm{F}}}\right)^4\right]. \tag{4.64}$$

Last but not least, let us understand the scaling behavior of

$$\Sigma^{00}/v_{\mathrm{F}} = \Delta^{0\rho}\Delta^{0\sigma}\left(\partial_\rho \tilde{u}_\sigma + \partial_\sigma \tilde{u}_\rho - g_{\rho\sigma}\partial_\alpha \tilde{u}^\alpha\right) \tag{4.65}$$

in terms of the small Taylor expansion parameter v/v_{F}. In order to derive this scaling, we again need to analyze different cases

$$\begin{aligned}
\rho=\sigma=0: &\quad \mathcal{O}\left[\left(\frac{v}{v_{\mathrm{F}}}\right)^4\right]\left(\mathcal{O}\left[\left(\frac{v}{v_{\mathrm{F}}}\right)^3\right]+\mathcal{O}\left[\left(\frac{v}{v_{\mathrm{F}}}\right)^3\right]+\mathcal{O}\left[\left(\frac{v}{v_{\mathrm{F}}}\right)\right]\right)=\mathcal{O}\left[\left(\frac{v}{v_{\mathrm{F}}}\right)^5\right]\,,\\
\rho=0\wedge\sigma=j: &\quad \mathcal{O}\left[\left(\frac{v}{v_{\mathrm{F}}}\right)^3\right]\left(\mathcal{O}\left[\left(\frac{v}{v_{\mathrm{F}}}\right)^2\right]+\mathcal{O}\left[\left(\frac{v}{v_{\mathrm{F}}}\right)^2\right]+0\right)=\mathcal{O}\left[\left(\frac{v}{v_{\mathrm{F}}}\right)^5\right]\,,\\
\rho=i\wedge\sigma=0: &\quad \mathcal{O}\left[\left(\frac{v}{v_{\mathrm{F}}}\right)^3\right]\left(\mathcal{O}\left[\left(\frac{v}{v_{\mathrm{F}}}\right)^2\right]+\mathcal{O}\left[\left(\frac{v}{v_{\mathrm{F}}}\right)^2\right]+0\right)=\mathcal{O}\left[\left(\frac{v}{v_{\mathrm{F}}}\right)^5\right]\,,\\
\rho=i\wedge\sigma=j: &\quad \mathcal{O}\left[\left(\frac{v}{v_{\mathrm{F}}}\right)^2\right]\left(\mathcal{O}\left[\left(\frac{v}{v_{\mathrm{F}}}\right)\right]+\mathcal{O}\left[\left(\frac{v}{v_{\mathrm{F}}}\right)\right]+\mathcal{O}\left[\left(\frac{v}{v_{\mathrm{F}}}\right)\right]\right)=\mathcal{O}\left[\left(\frac{v}{v_{\mathrm{F}}}\right)^3\right]\,.
\end{aligned}$$

Hence, we found that

$$\Sigma^{00}/v_{\mathrm{F}} = \mathcal{O}\left[\left(\frac{v}{v_{\mathrm{F}}}\right)^3\right]\,. \tag{4.66}$$

With the scalings in Eqs. (4.62), (4.64) and (4.66), we finally can calculate the overall contributions to the dissipative part of the energy momentum tensor in Eq. (4.26):

$$-\eta\Sigma^{ij} = -\eta\left(\partial^i v^j + \partial^j v^i - \delta^{ij}\partial_k v^k\right) + \mathcal{O}\left[\left(\frac{v}{v_{\mathrm{F}}}\right)^2\right]\,, \tag{4.67}$$

$$-\eta\Sigma^{i0} = -\eta\Sigma^{0i} = -\eta\frac{v^k}{v_{\mathrm{F}}}\left(\partial^i v_k + \partial_k v^i - \delta^i_k\partial_n v^n\right) + \mathcal{O}\left[\left(\frac{v}{v_{\mathrm{F}}}\right)^3\right]\,, \tag{4.68}$$

$$-\eta\Sigma^{00} = -v_{\mathrm{F}}\,\eta\,\mathcal{O}\left[\left(\frac{v}{v_{\mathrm{F}}}\right)^3\right] = \mathcal{O}\left[\left(\frac{v}{v_{\mathrm{F}}}\right)^2\right]\,. \tag{4.69}$$

In particular, these identities directly imply the scaling of the Hall viscous contribution to the first order correction of the energy-momentum tensor in terms of the expansion parameter v/v_{F} [cf. Eq. (4.34)]:

$$\begin{aligned}
-\eta_{\mathrm{H}}\bar{\Sigma}^{ij} &= -\frac{\eta_{\mathrm{H}}}{2}\left(\epsilon^{i\alpha\rho}\tilde{u}_\alpha\Sigma_\rho{}^j + \epsilon^{j\alpha\rho}\tilde{u}_\alpha\Sigma_\rho{}^i\right) \;=\; -\frac{\eta_{\mathrm{H}}}{2}\left(\epsilon^{i0k}\tilde{u}_0\Sigma_k{}^j + \epsilon^{j0k}\tilde{u}_0\Sigma_k{}^i\right) \;+\; \mathcal{O}\left[\left(\frac{v}{v_{\mathrm{F}}}\right)^2\right]\\
&= \frac{\eta_{\mathrm{H}}}{2}\left(\epsilon^{i0k}\Sigma_k{}^j + i\leftrightarrow j\right) + \mathcal{O}\left[\left(\frac{v}{v_{\mathrm{F}}}\right)^2\right] = -\eta_{\mathrm{H}}\left(\epsilon^{ik}\delta^{jm} + i\leftrightarrow j\right)v_{km} + \mathcal{O}\left[\left(\frac{v}{v_{\mathrm{F}}}\right)^2\right]\,,
\end{aligned}$$

$$\begin{aligned}
-\eta_{\mathrm{H}}\bar{\Sigma}^{i0} &= -\frac{\eta_{\mathrm{H}}}{2}\left(\epsilon^{i\alpha\rho}\tilde{u}_\alpha\Sigma_\rho{}^0 + \epsilon^{0\alpha\rho}\tilde{u}_\alpha\Sigma_\rho{}^i\right) = -\frac{\eta_{\mathrm{H}}}{2}\left(\epsilon^{i0k}\tilde{u}_0\Sigma_k{}^0 + \epsilon^{0jk}\tilde{u}_j\Sigma_k{}^i\right) + \mathcal{O}\left[\left(\frac{v}{v_{\mathrm{F}}}\right)^2\right]\\
&= -\frac{\eta_{\mathrm{H}}}{2}\left(\epsilon^{ik}\frac{v_j}{v_{\mathrm{F}}}\Sigma_k{}^j + \epsilon^{jk}\frac{v_j}{v_{\mathrm{F}}}\Sigma_k{}^i\right) + \mathcal{O}\left[\left(\frac{v}{v_{\mathrm{F}}}\right)^2\right]\\
&= -\frac{\eta_{\mathrm{H}}}{2v_{\mathrm{F}}}v_j\left(\epsilon^{ik}\Sigma_k{}^j + \epsilon^{jk}\Sigma_k{}^i\right) + \mathcal{O}\left[\left(\frac{v}{v_{\mathrm{F}}}\right)^3\right]
\end{aligned}$$

$$= -\frac{\eta_{\mathrm{H}}}{v_{\mathrm{F}}} v_j \left(\epsilon^{ik}\delta^{jm} + i \leftrightarrow j\right) v_{km} + \mathcal{O}\left[\left(\frac{v}{v_{\mathrm{F}}}\right)^3\right] ,$$

$$-\eta_{\mathrm{H}}\bar{\Sigma}^{00} = -\frac{\eta_{\mathrm{H}}}{2}\left(\epsilon^{0\alpha\rho}\tilde{u}_\alpha \Sigma_\rho{}^0 + \epsilon^{0\alpha\rho}\tilde{u}_\alpha \Sigma_\rho{}^0\right) = -\eta_{\mathrm{H}}\epsilon^{0\alpha\rho}\tilde{u}_\alpha \Sigma_\rho{}^0 = -\eta_{\mathrm{H}}\epsilon^{0ij}\tilde{u}_i \Sigma_j{}^0 = \mathcal{O}\left[\left(\frac{v}{v_{\mathrm{F}}}\right)^2\right].$$

where we introduced the symmetrized velocity derivative

$$v^{mn} = \frac{1}{2}\left(\partial^m v^n + \partial^n v^m\right) . \tag{4.70}$$

Equipped with the scalings of the bulk, shear, and Hall viscous contributions to the energy momentum tensor in terms of v/v_{F}, we are able to perform the Taylor expansion for this operator. In what follows, we separately expand the different components of the energy momentum tensor, starting with the calculation of T^{00}:

$$\begin{aligned} T_0^{00} &= \frac{\epsilon}{v_{\mathrm{F}}^2} u^0 u^0 + P\Delta^{00} \\ &= \left(nmv_{\mathrm{F}}^2 + \epsilon_{\mathrm{nr}}\right)\left(1 + \left(\frac{v}{v_{\mathrm{F}}}\right)^2 + \mathcal{O}\left[\left(\frac{v}{v_{\mathrm{F}}}\right)^4\right]\right) + P\left(\left(\frac{v}{v_{\mathrm{F}}}\right)^2 + \mathcal{O}\left[\left(\frac{v}{v_{\mathrm{F}}}\right)^4\right]\right) \\ &= nmv_{\mathrm{F}}^2\left(1 + \left(\frac{v}{v_{\mathrm{F}}}\right)^2\right) + \epsilon_{\mathrm{nr}} + \mathcal{O}\left[\left(\frac{v}{v_{\mathrm{F}}}\right)^2\right] = \Gamma^{-1}\rho v_{\mathrm{F}}^2 + \Gamma^{-1}\rho v^2 + \epsilon_{\mathrm{nr}} + \mathcal{O}\left[\left(\frac{v}{v_{\mathrm{F}}}\right)^2\right] \\ &= \rho v_{\mathrm{F}}^2 - \frac{\rho}{2}v^2 + \rho v^2 + \epsilon_{\mathrm{nr}} + \mathcal{O}\left[\left(\frac{v}{v_{\mathrm{F}}}\right)^2\right] = \rho v_{\mathrm{F}}^2 + \left[\epsilon_{\mathrm{nr}} + \frac{1}{2}\rho v^2\right] + \mathcal{O}\left[\left(\frac{v}{v_{\mathrm{F}}}\right)^2\right] , \end{aligned} \tag{4.71}$$

$$\delta T^{00} = -\zeta\partial_\alpha u^\alpha \Delta^{00} - \eta\Sigma^{00} - \eta_{\mathrm{H}}\bar{\Sigma}^{00} = \mathcal{O}\left[\left(\frac{v}{v_{\mathrm{F}}}\right)^2\right] , \tag{4.72}$$

$$T^{00} = T_0^{00} + \delta T^{00} = \rho v_{\mathrm{F}}^2 + \left[\epsilon_{\mathrm{nr}} + \frac{1}{2}\rho v^2\right] + \mathcal{O}\left[\left(\frac{v}{v_{\mathrm{F}}}\right)^2\right] . \tag{4.73}$$

We are proceeding with the calculation of T^{i0}:

$$\begin{aligned} T_0^{i0} &= \frac{\epsilon}{v_{\mathrm{F}}^2} u^0 u^i + P\Delta^{0i} = \left(nmv_{\mathrm{F}}^2 + \epsilon_{\mathrm{nr}}\right)\left(\frac{v^i}{v_{\mathrm{F}}} + \frac{v^2 v^i}{v_{\mathrm{F}}^3} + \mathcal{O}\left[\left(\frac{v}{v_{\mathrm{F}}}\right)^5\right]\right) + P\frac{v^i}{v_{\mathrm{F}}} + \mathcal{O}\left[\left(\frac{v}{v_{\mathrm{F}}}\right)^3\right] \\ &= \Gamma^{-1}\rho v_{\mathrm{F}}^2\left(\frac{v^i}{v_{\mathrm{F}}} + \frac{v^2 v^i}{v_{\mathrm{F}}^3}\right) + \left(\epsilon_{\mathrm{nr}} + P\right)\frac{v^i}{v_{\mathrm{F}}} + \mathcal{O}\left[\left(\frac{v}{v_{\mathrm{F}}}\right)^3\right] \\ &= \rho v_{\mathrm{F}} v^i + \frac{1}{v_{\mathrm{F}}}\left(\left(\epsilon_{\mathrm{nr}} + P\right) + \frac{1}{2}\rho v^2\right) v^i + \mathcal{O}\left[\left(\frac{v}{v_{\mathrm{F}}}\right)^3\right] \\ &= \rho v_{\mathrm{F}} v^i + \frac{1}{v_{\mathrm{F}}}\left(w_{\mathrm{nr}} + \frac{1}{2}\rho v^2\right) v^i + \mathcal{O}\left[\left(\frac{v}{v_{\mathrm{F}}}\right)^3\right] , \end{aligned} \tag{4.74}$$

$$\begin{aligned} \delta T^{i0} &= -\zeta\partial_\alpha u^\alpha \Delta^{i0} - \eta\Sigma^{i0} - \eta_{\mathrm{H}}\bar{\Sigma}^{i0} \\ &= -\frac{\zeta}{v_{\mathrm{F}}} v^i \partial_k u^k - \frac{\eta}{v_{\mathrm{F}}} v_j\left(\partial^i v^j + \partial^j v^i - \delta^{ij}\partial_k v^k\right) \\ &\quad - \frac{\eta_{\mathrm{H}}}{v_{\mathrm{F}}} v_j\left(\epsilon^{ik}\delta^{jm} + i \leftrightarrow j\right) v_{km} + \mathcal{O}\left[\left(\frac{v}{v_{\mathrm{F}}}\right)^3\right] \end{aligned} \tag{4.75}$$

$$= -\frac{v_j}{v_\mathrm{F}}\delta T^{ij}_\mathrm{nr} + \mathcal{O}\left[\left(\frac{v}{v_\mathrm{F}}\right)^3\right] , \tag{4.76}$$

$$T^{i0} = T^{i0}_0 + \delta T^{i0} = \rho v_\mathrm{F} v^i + \frac{1}{v_\mathrm{F}}\left[\left(w_\mathrm{nr} + \frac{1}{2}\rho v^2\right) v^i - \delta T^{ij}_\mathrm{nr} v_j\right] + \mathcal{O}\left[\left(\frac{v}{v_\mathrm{F}}\right)^3\right] , \tag{4.77}$$

where $w_\mathrm{nr} = \epsilon_\mathrm{nr} + P$ is the non-relativistic enthalpy density and we defined the non-relativistic viscosity tensor

$$\delta T^{ij}_\mathrm{nr} = \eta(\partial^i v^j + \partial^j v^i - \delta^{ij}\partial_k v^k) - \eta_\mathrm{H}\left(\epsilon^{ik}\delta^{jm} + i \leftrightarrow j\right) v_{km} + \zeta\delta^{ij}\partial_k v^k . \tag{4.78}$$

Last but not least, let us calculate the spatial components T^{ij}:

$$\begin{aligned} T^{ij}_0 &= \frac{\epsilon}{v_\mathrm{F}^2} u^i u^j + P\Delta^{ij} = \frac{(nmv_\mathrm{F}^2 + \epsilon_\mathrm{nr})}{v_\mathrm{F}^2}\left(v^i v^j + \mathcal{O}\left[\left(\frac{v}{v_\mathrm{F}}\right)^2\right]\right) + P\delta^{ij} + \mathcal{O}\left[\left(\frac{v}{v_\mathrm{F}}\right)^2\right] \\ &= \Gamma^{-1}\rho v_\mathrm{F}^2 \frac{v^i v^j}{v_\mathrm{F}^2} + P\delta^{ij} + \mathcal{O}\left[\left(\frac{v}{v_\mathrm{F}}\right)^2\right] = \rho v^i v^j + P\delta^{ij} + \mathcal{O}\left[\left(\frac{v}{v_\mathrm{F}}\right)^2\right] , \end{aligned} \tag{4.79}$$

$$\begin{aligned} \delta T^{ij} &= -\zeta\delta^{ij}\partial_k v^k - \eta\left(\partial^i v^j + \partial^j v^i - \delta^{ij}\partial_k v^k\right) - \eta_\mathrm{H}\left(\epsilon^{ik}\delta^{jm} + i \leftrightarrow j\right) v_{km} + \mathcal{O}\left[\left(\frac{v}{v_\mathrm{F}}\right)^2\right] \\ &= -\delta T^{ij}_\mathrm{nr} + \mathcal{O}\left[\left(\frac{v}{v_\mathrm{F}}\right)^2\right] , \end{aligned} \tag{4.80}$$

$$T^{ij} = T^{ij}_0 + \delta T^{ij} = \rho v^i v^j + P\delta^{ij} - \delta T^{ij}_\mathrm{nr} + \mathcal{O}\left[\left(\frac{v}{v_\mathrm{F}}\right)^2\right] . \tag{4.81}$$

In order to derive the non-relativistic equations of motion, we also need to Taylor expand the particle current density N^μ in Eq. (4.32). Therefore, we first need to evaluate the following identities [cf. Eq. (4.29)]:

$$F^{0\nu}u_\nu = F^{00}u_0 + F^{0i}u_i = E^i\frac{1}{v_\mathrm{F}}\Gamma v_i = \frac{1}{v_\mathrm{F}}E^i v_i + \mathcal{O}\left[\left(\frac{v}{v_\mathrm{F}}\right)^3\right] , \tag{4.82}$$

$$F^{i\nu}u_\nu = F^{i0}u_0 + F^{ij}u_j = E^i\frac{1}{v_\mathrm{F}}\Gamma v_\mathrm{F} + B\epsilon^{ij}\Gamma v_j = E^i + B\epsilon^{ij}v_j + \mathcal{O}\left[\left(\frac{v}{v_\mathrm{F}}\right)^2\right] , \tag{4.83}$$

$$\Delta^{0\nu}\partial_\nu = \Delta^{00}\partial_0 + \Delta^{0i}\partial_i = \frac{v^i}{v_\mathrm{F}}\partial_i + \mathcal{O}\left[\left(\frac{v}{v_\mathrm{F}}\right)^3\right] , \tag{4.84}$$

$$\Delta^{i\nu}\partial_\nu = \Delta^{i0}\partial_0 + \Delta^{ij}\partial_j = \delta^{ij}\partial_j + \mathcal{O}\left[\left(\frac{v}{v_\mathrm{F}}\right)^2\right] . \tag{4.85}$$

In particular, these scalings imply the following contributions to the particle current density correction δN^μ:

$$\frac{\sigma_\mathrm{Q}}{\mathrm{e}}V^0 = \frac{\sigma_\mathrm{Q}}{\mathrm{e}}\left(F^{0\nu}u_\nu - \frac{T}{\mathrm{e}}\Delta^{0\nu}\partial_\nu\frac{\mu}{T}\right) = \frac{\sigma_\mathrm{Q}}{\mathrm{e}}\frac{v^i}{v_\mathrm{F}}\left(E_i - \frac{T}{\mathrm{e}}\partial_i\frac{\mu}{T}\right) + \mathcal{O}\left[\left(\frac{v}{v_\mathrm{F}}\right)^3\right] , \tag{4.86}$$

$$\frac{\sigma_\mathrm{Q}}{\mathrm{e}}V^i = \frac{\sigma_\mathrm{Q}}{\mathrm{e}}\left(F^{i\nu}u_\nu - \frac{T}{\mathrm{e}}\Delta^{i\nu}\partial_\nu\frac{\mu}{T}\right) = \frac{\sigma_\mathrm{Q}}{\mathrm{e}}\left(E^i + B\epsilon^{ij}v_j - \frac{T}{\mathrm{e}}\delta^{ij}\partial_j\frac{\mu}{T}\right) + \mathcal{O}\left[\left(\frac{v}{v_\mathrm{F}}\right)^2\right] , \tag{4.87}$$

$$\frac{\sigma_{\mathrm{QAH}}}{\mathrm{e}}\bar{V}^0 = \frac{\sigma_{\mathrm{QAH}}}{\mathrm{e}}\epsilon^{0ij}\frac{u_i}{v_{\mathrm{F}}}V_j = \frac{\sigma_{\mathrm{QAH}}}{\mathrm{e}}\epsilon^{0ij}\frac{v_i}{v_{\mathrm{F}}}\left(E_j + B\epsilon_{jk}v^k - \frac{T}{\mathrm{e}}\delta_{jk}\partial^k\frac{\mu}{T}\right) + \mathcal{O}\left[\left(\frac{v}{v_{\mathrm{F}}}\right)^2\right], \tag{4.88}$$

$$\begin{aligned}\frac{\sigma_{\mathrm{QAH}}}{\mathrm{e}}\bar{V}^i &= \frac{\sigma_{\mathrm{QAH}}}{\mathrm{e}}\epsilon^{i\nu\rho}\frac{u_\nu}{v_{\mathrm{F}}}V_\rho = \frac{\sigma_{\mathrm{QAH}}}{\mathrm{e}}\left(\epsilon^{i0m}\frac{u_0}{v_{\mathrm{F}}}V_m + \epsilon^{im0}\frac{u_m}{v_{\mathrm{F}}}V_0\right) \\ &= \frac{\sigma_{\mathrm{QAH}}}{\mathrm{e}}\epsilon^{ij}\left(E_j + B\epsilon_{jk}v^k - \frac{T}{\mathrm{e}}\delta_{jk}\partial^k\frac{\mu}{T}\right) + \mathcal{O}\left[\left(\frac{v}{v_{\mathrm{F}}}\right)^2\right].\end{aligned} \tag{4.89}$$

Thus, the Taylor expansion for the entire particle current density N^μ is given by

$$\begin{aligned}N^0 &= nu^0 + \frac{\sigma_{\mathrm{Q}}}{\mathrm{e}}V^0 + \frac{\sigma_{\mathrm{QAH}}}{\mathrm{e}}\bar{V}^0 \\ &= \frac{\rho}{m}\Gamma^{-1}\Gamma v_{\mathrm{F}} + \frac{\sigma_{\mathrm{Q}}}{\mathrm{e}}\frac{v^i}{v_{\mathrm{F}}}\left(E_i - \frac{T}{\mathrm{e}}\partial_i\frac{\mu}{T}\right) \\ &\qquad + \frac{\sigma_{\mathrm{QAH}}}{\mathrm{e}}\epsilon^{0ij}\frac{v_i}{v_{\mathrm{F}}}\left(E_j + B\epsilon_{jk}v^k - \frac{T}{\mathrm{e}}\delta_{jk}\partial^k\frac{\mu}{T}\right) + \mathcal{O}\left[\left(\frac{v}{v_{\mathrm{F}}}\right)^2\right] \\ &= \frac{\rho}{m}v_{\mathrm{F}} + \frac{v_i}{\mathrm{e}v_{\mathrm{F}}}\Bigg[\sigma_{\mathrm{Q}}\delta^{ij}\left(E_j - \frac{T}{\mathrm{e}}\partial_j\frac{\mu}{T}\right) \\ &\qquad + \sigma_{\mathrm{QAH}}\epsilon^{ij}\left(E_j + B\epsilon_{jk}v^k - \frac{T}{\mathrm{e}}\delta_{jk}\partial^k\frac{\mu}{T}\right)\Bigg] + \mathcal{O}\left[\left(\frac{v}{v_{\mathrm{F}}}\right)^2\right],\end{aligned} \tag{4.90}$$

$$\begin{aligned}N^i &= nu^i + \frac{\sigma_{\mathrm{Q}}}{\mathrm{e}}V^i + \frac{\sigma_{\mathrm{QAH}}}{\mathrm{e}}\bar{V}^i \\ &= \frac{\rho}{m}v^i + \frac{\sigma_{\mathrm{Q}}}{\mathrm{e}}\left(E^i + B\epsilon^{ij}v_j - \frac{T}{\mathrm{e}}\delta^{ij}\partial_j\frac{\mu}{T}\right) \\ &\qquad + \frac{\sigma_{\mathrm{QAH}}}{\mathrm{e}}\epsilon^{ij}\left(E_j + B\epsilon_{jk}v^k - \frac{T}{\mathrm{e}}\delta_{jk}\partial^k\frac{\mu}{T}\right) + \mathcal{O}\left[\left(\frac{v}{v_{\mathrm{F}}}\right)^2\right] \\ &= \frac{\rho}{m}v^i + \frac{1}{\mathrm{e}}\left(\sigma_{\mathrm{Q}}\delta^{ij} + \sigma_{\mathrm{QAH}}\epsilon^{ij}\right)\left(E_j + B\epsilon_{jk}v^k - \frac{T}{\mathrm{e}}\delta_{jk}\partial^k\frac{\mu}{T}\right) + \mathcal{O}\left[\left(\frac{v}{v_{\mathrm{F}}}\right)^2\right].\end{aligned} \tag{4.91}$$

Since the above calculations have been very long, let us summarize our findings:

$$T^{00} = v_{\mathrm{F}}^2\rho + \left[\epsilon_{\mathrm{nr}} + \frac{1}{2}\rho v^2\right] + \mathcal{O}\left[\left(\frac{v}{v_{\mathrm{F}}}\right)^2\right], \tag{4.92}$$

$$T^{0i} = \rho v_{\mathrm{F}}v^i + \frac{1}{v_{\mathrm{F}}}\left[\left(w_{\mathrm{nr}} + \frac{1}{2}\rho v^2\right)v^i - \delta T^{ij}_{\mathrm{nr}}v_j\right] + \mathcal{O}\left[\left(\frac{v}{v_{\mathrm{F}}}\right)^3\right], \tag{4.93}$$

$$T^{ij} = \rho v^i v^j + P\delta^{ij} - \delta T^{ij}_{\mathrm{nr}} + \mathcal{O}\left[\left(\frac{v}{v_{\mathrm{F}}}\right)^2\right] \equiv \Pi^{ij}_{\mathrm{nr}} + \mathcal{O}\left[\left(\frac{v}{v_{\mathrm{F}}}\right)^2\right], \tag{4.94}$$

$$\begin{aligned}N^0 = \frac{\rho v_{\mathrm{F}}}{m} + \frac{v_i}{\mathrm{e}v_{\mathrm{F}}}\Bigg[&\sigma_{\mathrm{Q}}\delta^{ij}\left(E_j - \frac{T}{\mathrm{e}}\partial_j\frac{\mu}{T}\right) \\ &+ \sigma_{\mathrm{QAH}}\epsilon^{ij}\left(E_j + B\epsilon_{jk}v^k - \frac{T}{\mathrm{e}}\delta_{jk}\partial^k\frac{\mu}{T}\right)\Bigg] + \mathcal{O}\left[\left(\frac{v}{v_{\mathrm{F}}}\right)^2\right],\end{aligned} \tag{4.95}$$

$$N^i = \frac{\rho}{m}v^i + \frac{1}{\mathrm{e}}\left(\sigma_{\mathrm{Q}}\delta^{ij} + \sigma_{\mathrm{QAH}}\epsilon^{ij}\right)\left(E_j + B\epsilon_{jk}v^k - \frac{T}{\mathrm{e}}\delta_{jk}\partial^k\frac{\mu}{T}\right) + \mathcal{O}\left[\left(\frac{v}{v_{\mathrm{F}}}\right)^2\right], \tag{4.96}$$

where Π^{ij}_{nr} is the non-relativistic stress tensor [cf. Eq. (4.8)]. With these identities, the relativistic particle current conservation $\partial_\mu N^\mu = 0$ in the non-relativistic limit $v/v_{\mathrm{F}} \to 0$

reduces to

$$\partial_{\mathrm{t}}\left(\frac{\rho}{m}\right)+\partial_i\left(\frac{\rho}{m}v^i+\frac{1}{\mathrm{e}}\left(\sigma_{\mathrm{Q}}\delta^{ij}+\sigma_{\mathrm{QAH}}\epsilon^{ij}\right)\left(E_j+B\epsilon_{jk}v^k-\frac{T}{\mathrm{e}}\delta_{jk}\partial^k\frac{\mu}{T}\right)\right)=0\ , \tag{4.97}$$

and the energy-momentum conservation $\partial_\nu T^{\mu\nu}=\mathrm{e}F^{\mu\nu}N_\nu$ in Eq. (4.28) implies the non-relativistic Navier-Stokes equations [187, 191]

$$\begin{aligned}\partial_{\mathrm{t}}\left(\epsilon_{\mathrm{nr}}+\frac{1}{2}\rho v^2\right)+\partial_i j^i_{\mathrm{E}}=&\\ \frac{\mathrm{e}\rho}{m}E^i v_i+\left[E^i+\frac{mv_{\mathrm{F}}^2}{\mathrm{e}}\partial^i\right]&\left[\left(\sigma_{\mathrm{Q}}\delta_{ij}+\sigma_{\mathrm{QAH}}\epsilon_{ij}\right)\left(E^j+B\epsilon^{jk}v_k-\frac{T}{\mathrm{e}}\delta^{jk}\partial_k\frac{\mu}{T}\right)\right],\end{aligned} \tag{4.98}$$

$$\partial_{\mathrm{t}}(\rho v^i)+\partial_j\Pi^{ij}_{\mathrm{nr}}=\frac{\mathrm{e}\rho}{m}\left(E^i+B\epsilon^{ij}v_j\right)+B\epsilon^{ij}\left(\sigma_{\mathrm{Q}}\delta_{jk}+\sigma_{\mathrm{QAH}}\epsilon_{jk}\right)\left(E^k+B\epsilon^{kl}v_l-\frac{T}{\mathrm{e}}\delta^{kl}\partial_l\frac{\mu}{T}\right), \tag{4.99}$$

with the i-th component of the energy flux density [cf. Eq.(4.8)]

$$j^i_{\mathrm{E}}=\left(\left[\epsilon_{\mathrm{nr}}+\frac{1}{2}\rho v^2\right]v^i-\delta T^{ij}_{\mathrm{nr}}v_j\right)\ . \tag{4.100}$$

For this result, we also performed the non-relativistic limit $v/v_{\mathrm{F}}\to 0$, and used the subsequent expressions for the right-hand side of the energy-momentum conservation equation [cf. Eq. (4.29)]:

$$\begin{aligned}\mathrm{e}F^{0\nu}N_\nu&=\mathrm{e}F^{00}N_0+\mathrm{e}F^{0i}N_i \\ &=\frac{\mathrm{e}}{v_{\mathrm{F}}}E^i\left[\frac{\rho}{m}v_i+\frac{1}{\mathrm{e}}\left(\sigma_{\mathrm{Q}}\delta_{ij}+\sigma_{\mathrm{QAH}}\epsilon_{ij}\right)\left(E^j+B\epsilon^{jk}v_k-\frac{T}{\mathrm{e}}\delta^{jk}\partial_k\frac{\mu}{T}\right)\right]\ ,\end{aligned} \tag{4.101}$$

$$\begin{aligned}\mathrm{e}F^{i\nu}N_\nu&=\mathrm{e}F^{i0}N_0+\mathrm{e}F^{ij}N_j \\ &=\mathrm{e}\frac{E^i}{v_{\mathrm{F}}}\frac{\rho}{m}v_{\mathrm{F}}+\mathrm{e}B\epsilon^{ij}\left[\frac{\rho}{m}v_j+\frac{1}{\mathrm{e}}\left(\sigma_{\mathrm{Q}}\delta_{jk}+\sigma_{\mathrm{QAH}}\epsilon_{jk}\right)\left(E^k+B\epsilon^{kl}v_l-\frac{T}{\mathrm{e}}\delta^{kl}\partial_l\frac{\mu}{T}\right)\right] \\ &=\frac{\mathrm{e}\rho}{m}E^i+\mathrm{e}B\epsilon^{ij}\left[\frac{\rho}{m}v_j+\frac{1}{\mathrm{e}}\left(\sigma_{\mathrm{Q}}\delta_{jk}+\sigma_{\mathrm{QAH}}\epsilon_{jk}\right)\left(E^k+B\epsilon^{kl}v_l-\frac{T}{\mathrm{e}}\delta^{kl}\partial_l\frac{\mu}{T}\right)\right] \\ &=\frac{\mathrm{e}\rho}{m}\left(E^i+B\epsilon^{ij}v_j\right)+B\epsilon^{ij}\left(\sigma_{\mathrm{Q}}\delta_{jk}+\sigma_{\mathrm{QAH}}\epsilon_{jk}\right)\left(E^k+B\epsilon^{kl}v_l-\frac{T}{\mathrm{e}}\delta^{kl}\partial_l\frac{\mu}{T}\right).\end{aligned} \tag{4.102}$$

Moreover, we used the following identities for the space-time derivatives of the energy-momentum tensor:

$$\begin{aligned}\partial_\nu T^{0\nu}=\partial_0 T^{00}+\partial_i T^{0i}&=v_{\mathrm{F}}\left(\partial_{\mathrm{t}}\rho+\partial_i(\rho v^i)\right) \\ &+\frac{1}{v_{\mathrm{F}}}\left[\partial_{\mathrm{t}}\left[\epsilon_{\mathrm{nr}}+\frac{1}{2}\rho v^2\right]+\partial_i\left(\left[\epsilon_{\mathrm{nr}}+\frac{1}{2}\rho v^2\right]v^i-\delta T^{ij}_{\mathrm{nr}}v_j\right)\right]+\mathcal{O}\left[\left(\frac{v}{v_{\mathrm{F}}}\right)^2\right], \\ &=-\frac{mv_{\mathrm{F}}}{\mathrm{e}}\partial_i\left[\left(\sigma_{\mathrm{Q}}\delta^{ij}+\sigma_{\mathrm{QAH}}\epsilon^{ij}\right)\left(E_j+B\epsilon_{jk}v^k-\frac{T}{\mathrm{e}}\delta_{jk}\partial^k\frac{\mu}{T}\right)\right] \\ &+\frac{1}{v_{\mathrm{F}}}\left[\partial_{\mathrm{t}}\left[\epsilon_{\mathrm{nr}}+\frac{1}{2}\rho v^2\right]+\partial_i\left(\left[\epsilon_{\mathrm{nr}}+\frac{1}{2}\rho v^2\right]v^i-\delta T^{ij}_{\mathrm{nr}}v_j\right)\right]+\mathcal{O}\left[\left(\frac{v}{v_{\mathrm{F}}}\right)^2\right],\end{aligned} \tag{4.103}$$

$$\partial_\nu T^{i\nu}=\partial_0 T^{i0}+\partial_j T^{ij}=\partial_{\mathrm{t}}(\rho v^i)+\partial_j\Pi^{ij}_{\mathrm{nr}}+\mathcal{O}\left[\left(\frac{v}{v_{\mathrm{F}}}\right)\right]\ , \tag{4.104}$$

where we used Eq. (4.97) in the second equality.

4.1.3 Transport Coefficients

The Quantum Critical Conductivity σ_{Q}

The quantum critical conductivity σ_{Q}, which was introduced in Eq. (4.26), contributes to the longitudinal part of the electrical conductivity tensor $\hat{\sigma}$.

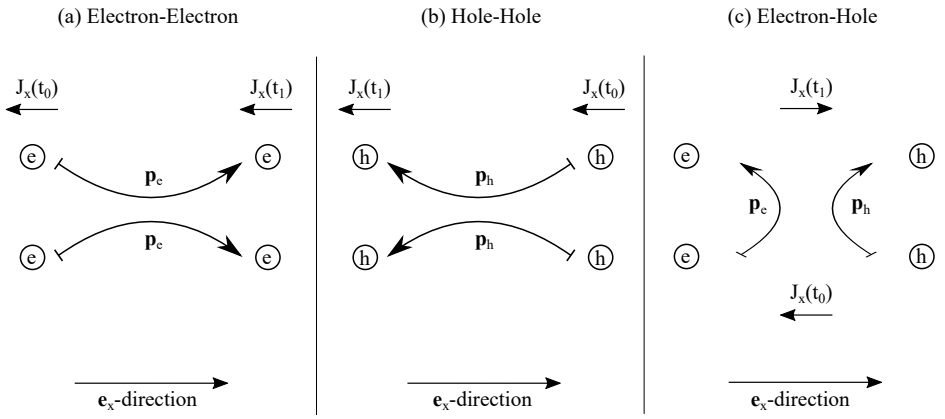

Figure 4.1: Schematic illustration of electron-electron, hole-hole, and electron-hole scattering processes. While electron-electron and hole-hole scattering processes are charge current conserving, electron-hole collisions can drastically change their combined current contribution. Electron- and hole momenta are encoded by $p_{\mathrm{e,h}}$ and the charge currents at time t_i are denoted by $\mathbf{J}(t_i)$. This figure is inspired by Fig. 2 of Ref. [192].

In terms of a Kubo formula, this conductivity is given by a retarded charge current-current correlation function [cf. Eq. (4.35)]

$$\sigma_{\mathrm{Q}} = \lim_{\omega\to 0} \frac{1}{2\omega}\delta_{ij}\,\mathrm{Im}\,G_{\mathrm{R}}^{i,j}(\omega,\mathbf{p}=0) \qquad \text{with} \qquad G_{\mathrm{R}}^{i,j} = \mathrm{e}^2\,\langle N^i N^j\rangle_{\mathrm{R}}\ . \tag{4.105}$$

The quantum critical conductivity is a dissipative transport coefficient and arises from electron-hole scattering processes [193]. As it is schematically shown in Fig. 4.1, electron-electron as well as hole-hole scattering processes do not change the associated charge current and therefore do not contribute to the electrical conductivity tensor. In contrast, electron-hole scattering can change the charge current drastically. This originates from the fact that an electron-hole pair can carry a finite charge current even without transporting a finite momentum. Consequently, the charge current related to an electron-hole pair is even able to reverse under electron-hole scattering processes.

The Bulk Viscosity ζ

In Eq. (4.27), we introduced the so-called bulk viscosity ζ, which encodes the dissipation of energy under an isotropic fluid expansion or compression. This mechanism is schematically illustrated in Fig. 4.2.

According to Eq. (4.35), the bulk viscosity is defined by the retarded correlation function of two energy momentum tensors

$$\zeta = \lim_{\omega\to 0} \frac{1}{4\omega}\delta_{ij}\delta_{kl}\,\mathrm{Im}\,G_{\mathrm{R}}^{ij,kl}(\omega,\mathbf{p}=0) \qquad \text{with} \qquad G_{\mathrm{R}}^{ij,kl} = \langle T^{ij}T^{kl}\rangle_{\mathrm{R}}\ . \tag{4.106}$$

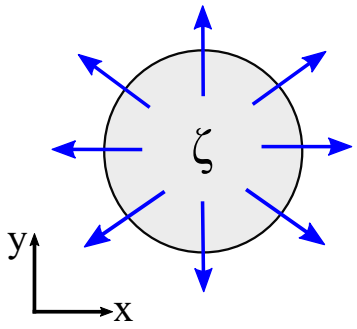

Figure 4.2: Schematic illustration of the bulk viscosity ζ, which encodes the dissipation of energy under an isotropic fluid expansion or compression. Further explanations are given in the text.

For an isotropic system with $T^{\mathrm{xx}} = T^{\mathrm{yy}}$ this expression significantly simplifies to

$$\zeta = \lim_{\omega \to 0} \frac{1}{\omega} \mathrm{Im}\; G_{\mathrm{R}}^{\mathrm{xx,xx}}(\omega, \mathbf{p} = 0) \; . \tag{4.107}$$

In the scope of this thesis we are solely considering incompressible hydrodynamic fluids which are associated to a vanishing bulk viscosity term [84].

The Shear Viscosity η

In Eq. (4.27), we have also introduced the shear viscosity η, which defines the required force to generate a certain velocity gradient transverse to the fluid flow. Let us consider for the moment a translationally invariant velocity profile $\mathbf{v}(y)$ in $\mathbf{e}_{\mathrm{x}}$-direction through a rectangular channel of width W. To obtain a certain velocity gradient $\mathbf{G}_{\perp} \equiv \partial \mathbf{v} / \partial y$, the upper (or lower) plate which confines the two-dimensional channel needs to be accelerated by the force

$$\mathbf{F} = \eta \, \mathbf{G}_{\perp} \, W \; . \tag{4.108}$$

This process is schematically shown in Fig. 4.3. Notice, that the shear viscosity of a strongly interacting fluid is smaller than the one of a weakly interacting system. By definition, η is a measure for the efficiency of momentum transfer transverse to the flow direction. It is therefore directly related to the fluid's internal friction. The stronger the interactions, the smaller is the unhindered transverse momentum transfer in the fluid, and thus the shear viscosity itself. According to Eq. (4.108), this means that in a strongly interacting system, a smaller force is required to generate the same velocity gradient than in a weakly interacting system [194].

According to Eq. (4.35), the shear viscosity is, analogously to the bulk viscosity, given by the retarded correlation function of two energy momentum tensors

$$\eta = \lim_{\omega \to 0} \frac{1}{8\omega} \left(\delta_{ik} \delta_{jl} - \epsilon_{ik} \epsilon_{jl} \right) \mathrm{Im}\; G_{\mathrm{R}}^{ij,kl}(\omega, \mathbf{p} = 0) \qquad \text{with} \qquad G_{\mathrm{R}}^{ij,kl} = \langle T^{ij} T^{kl} \rangle_{\mathrm{R}} \; . \tag{4.109}$$

For an isotropic system with $T^{\mathrm{xx}} = T^{\mathrm{yy}}$, the symmetry of the energy momentum tensor, $T^{\mu\nu} = T^{\nu\mu}$, further implies

$$\eta = \lim_{\omega \to 0} \frac{1}{2\omega} \mathrm{Im}\; G_{\mathrm{R}}^{xy,xy}(\omega, \mathbf{p} = 0) \; . \tag{4.110}$$

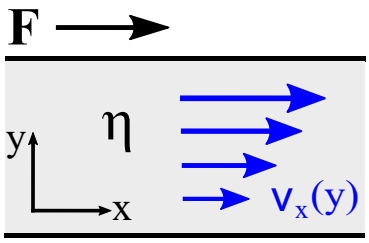

Figure 4.3: Schematic illustration of the shear viscosity η, which encodes the transverse gradient of the fluid's velocity profile, $\partial_y \mathbf{v}$, as a response to a force $\mathbf{F}$, which accelerates the upper plate of the rectangular channel geometry considered. We assumed a translation invariant fluid flow along the $\mathbf{e}_x$-direction, which is associated to a shear viscosity induced velocity gradient along the $\mathbf{e}_y$-direction. More explanations are given in the text.

In 2+1 space-time dimensions the shear viscosity η, which appears in the first order gradient expansion of $T^{\mu\nu}$, has SI units

$$[\eta]_{\mathrm{SI}} = \frac{\mathrm{kg}}{\mathrm{s}} \,. \tag{4.111}$$

More specifically, η defines the so-called dynamical or absolute shear viscosity. If one normalizes this viscosity to the system's mass density $m^* n$, one obtains the so-called kinematic shear viscosity

$$\nu = \frac{\eta}{m^* n} \quad \text{with SI units} \quad \frac{\mathrm{kg}}{\mathrm{s}} \cdot \frac{\mathrm{m}^2}{\mathrm{kg}} = \frac{\mathrm{m}^2}{\mathrm{s}} \,. \tag{4.112}$$

Within the scope of this thesis we are also studying the hydrodynamic behavior of massless Dirac systems like graphene, which do not posses a conventional mass density [cf. Sec. 4.1.5]. In such systems it is common to normalize the dynamic shear viscosity to the enthalpy density $w = \epsilon + P$ in order to define an analogous kinematic shear viscosity [187]

$$\nu = \frac{\eta\, v_{\mathrm{F}}^2}{\epsilon + P} \quad \text{with SI units} \quad \frac{\mathrm{kg}}{\mathrm{s}} \cdot \frac{\mathrm{m}^2}{\mathrm{s}^2} \cdot \frac{\mathrm{s}^2}{\mathrm{kg}} = \frac{\mathrm{m}^2}{\mathrm{s}} \,. \tag{4.113}$$

Here, we used that $[\epsilon + P]_{\mathrm{SI}} = \mathrm{kg/s}^2$.

The Hall Viscosity η_{H}

In Eq. (4.35), we additionally introduced the Hall viscosity η_{H} via the retarded correlator of two energy momentum tensors

$$\eta_{\mathrm{H}} = \lim_{\omega \to 0} \frac{1}{4\omega} \delta_{ik} \epsilon_{jl} \mathrm{Im}\, G_{\mathrm{R}}^{ij,kl}(\omega, \mathbf{p} = 0) \qquad \text{with} \qquad G_{\mathrm{R}}^{ij,kl} = \langle T^{ij} T^{kl} \rangle_{\mathrm{R}} \,. \tag{4.114}$$

For an isotropic system with $T^{\mathrm{xx}} = T^{\mathrm{yy}}$, the symmetry of the energy momentum tensor, $T^{\mu\nu} = T^{\nu\mu}$, in particular implies

$$\eta_{\mathrm{H}} = \lim_{\omega \to 0} \frac{1}{\omega} \mathrm{Im}\, G_{\mathrm{R}}^{\mathrm{xx,xy}}(\omega, \mathbf{p} = 0) \,. \tag{4.115}$$

As the Hall viscosity is a non-dissipative, parity- and time-reversal odd transport coefficient, these discrete symmetries are required to be broken in order to allow for an non-zero value of η_{H} [189]. This can for instance be realized by applying an out-of-plane magnetic field to

the system considered.

The physical interpretation of the Hall viscosity can be most intuitively read off from the Navier-Stokes equations (4.98). According to these equations, the Hall viscosity gives rise to a Hall viscous force acting transverse to the fluid flow if parity- and time reversal symmetry are broken [195]

$$\mathbf{F}_{\eta_\mathrm{H}} = \eta_\mathrm{H} \nabla^2 \mathbf{v} \times \mathbf{e}_\mathrm{z} \ . \tag{4.116}$$

Consequently, the Hall viscosity defines the amount of transverse momentum pumped across a channel of width W as a response to a certain curvature of the velocity profile [84, 196].

The Slip Length l_s

Solving the hydrodynamic conservation equations for the charge-, energy-, and momentum flow, which are given in Eqs. (4.3) and (4.28), implies a certain form of the velocity profile. A hydrodynamic flow in the absence of impurities or defects through a two-dimensional channel of width W corresponds to a Poiseuille-like velocity profile which is translationally invariant along the flow direction. Such a velocity profile is exemplary shown in Fig. 4.4.

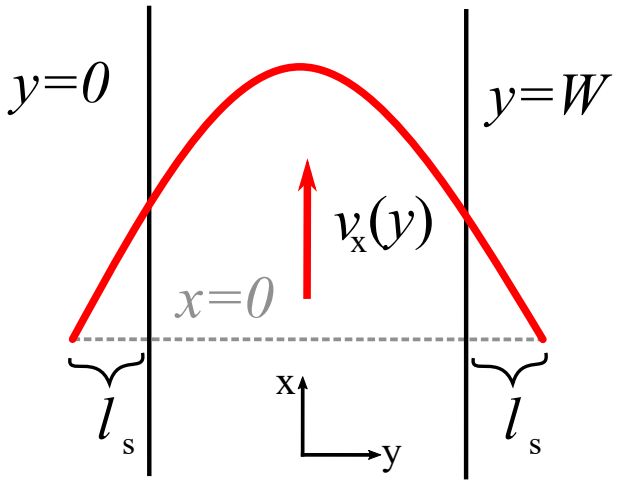

Figure 4.4: Schematic illustration of a hydrodynamic fluid flow through a two-dimensional channel of width W. The velocity profile is translationally invariant in longitudinal-, whereas it is characterized by a Poiseuille-like curvature in transverse direction. Here, we allowed for a finite slip length l_s, which characterizes the fluid velocity at the system's edges [197].

Since the velocity profile arises from the differential equations in Eqs. (4.3) and (4.28), it requires certain boundary conditions to fix its value at the edges of the system. These boundary conditions are encoded by the so-called slip length l_s via

$$v_\mathrm{x}(-l_\mathrm{s}) = v_\mathrm{x}(W + l_\mathrm{s}) = 0 \ . \tag{4.117}$$

For no-slip boundary conditions, characterized by $l_\mathrm{s} = 0$, the velocity profile vanishes at the system's edges. In contrast, for no-stress boundary conditions, characterized by $l_\mathrm{s} \to \infty$, the velocity profile becomes flat, even though the flow is still hydrodynamic [90, 197].

4.1.4 Two-Dimensional Electron Gases

In this section, we are going to introduce the microscopic theory of two-dimensional electron gases and derive their corresponding macroscopic quantities, which are entering the hydrodynamic derivative expansion in Eq. (4.32).

The transport properties of conventional two-dimensional semiconductors in vicinity to the insulating gap can be described by the parabolic Hamiltonian of a two-dimensional electrons gas

$$\hat{H} = \frac{|\hat{\mathbf{p}}|^2}{2m^*} = \frac{\hbar^2 \hat{\mathbf{k}}^2}{2m^*} \ . \tag{4.118}$$

Here, $\hat{\mathbf{p}} = \hbar\hat{\mathbf{k}}$ is the two-dimensional momentum operator with $|\hat{\mathbf{p}}|^2 = \hat{p}^2 = \hat{p}_\mathrm{x}^2 + \hat{p}_\mathrm{y}^2$, $\hat{\mathbf{k}}$ is the assosiated wave-vector, and m^* is the effective mass parameter defining the curvature of the parabolic dispersion

$$E(k) = \frac{p^2}{2m^*} = \frac{\hbar^2 k^2}{2m^*} \ . \tag{4.119}$$

In particular, $m^* < 0$ characterizes the valence-, whereas $m^* > 0$ characterizes the conduction band.

Charge-, Energy, and Pressure Densities

In general, the density of states $g(E)$ in D-space dimensions encodes the amount of available states per unit volume and energy. Assuming a two-dimensional isotropic material with periodic boundary conditions quantizes the allowed momenta in both space directions, since the solutions of the Schrödinger equation are required to be periodic at the boundaries of the system:

$$k_\mathrm{x} = \frac{n_1\,\pi}{L_\mathrm{x}} \ , \quad k_\mathrm{y} = \frac{n_2\,\pi}{L_\mathrm{y}} \quad \text{with} \quad n_1, n_2 \in \mathbb{Z} \ . \tag{4.120}$$

Here, L_x and L_y are the length and the width of the material, together defining its area $A = L_\mathrm{x} L_\mathrm{y}$. In the corresponding two-dimensional $\mathbf{k}$-space, this defines a discrete amount of grid points per unit area

$$\left(\frac{L_\mathrm{x}}{2\pi}\right)\left(\frac{L_\mathrm{y}}{2\pi}\right) = \frac{A}{4\pi^2} \ . \tag{4.121}$$

The equilibrium occupation of states in the $\mathbf{k}$-space is in general encoded by the equilibrium Fermi-Dirac distribution:

$$f_0(k, \mu, T) = \frac{1}{1 + \mathrm{e}^{(E(\vec{k}) - \mu)/(\mathrm{k_B} T)}} \ , \tag{4.122}$$

where μ is the chemical potential. In the scope of this analysis, we are considering two-dimensional electron gases with a positive effective mass parameter m^*, and thus a positive dispersion relation [cf. Eq. (4.119)]. Therefore, if it is not stated otherwise, we also assume positive chemical potentials $\mu > 0$ in the following. At zero temperatures, the chemical potential equals the Fermi energy $E_\mathrm{F} = \mu(T = 0)$, which defines the largest energy of an electron with respect to the bottom edge of the (conduction) band $E_\mathrm{c} = 0$. At $T = 0$ the

equilibrium Fermi-Dirac distribution reduces to a Heaviside-Theta function:

$$f_0(k, E_\mathrm{F}, T=0) = \Theta\left[E_\mathrm{F} - E(k)\right] \ , \tag{4.123}$$

which implies that all momenta up to the Fermi-surface are occupied. In two space dimensions, the Fermi surface at $T = 0$ is given by a circle of radius k_F, which defines the Fermi momentum. For a two-dimensional electron gas this momentum is given by

$$E_\mathrm{F} = \frac{\hbar^2 k_\mathrm{F}^2}{2m^*} \quad \Rightarrow \quad k_\mathrm{F} = \frac{\sqrt{2m^* E_\mathrm{F}}}{\hbar} \ . \tag{4.124}$$

This implies the following relation for the corresponding Fermi velocity

$$v_\mathrm{F} = \left.\frac{\partial E(p)}{\partial p}\right|_{p=p_\mathrm{F}} = \frac{p_\mathrm{F}}{m^*} = \frac{\hbar k_\mathrm{F}}{m^*} = \sqrt{\frac{2E_\mathrm{F}}{m^*}} \ . \tag{4.125}$$

The number of (occupied) states per area which is enclosed by the Fermi circle at $T = 0$ defines the zero temperature electron density ($[n] = \mathrm{m}^{-2}$)

$$n(T{=}0) = N_\mathrm{f} \frac{A}{4\pi^2} \frac{\pi k_\mathrm{F}^2}{A} = N_\mathrm{f} \frac{k_\mathrm{F}^2}{4\pi} \ , \tag{4.126}$$

where N_f encodes the fermion species in the system. For a two-dimensional electron gas, $N_\mathrm{f} = 2$ takes into account the underlying spin degeneracy. At finite temperatures the (equilibrium) charge density n needs to be evaluated by solving the integral over the Fermi-Dirac distribution either in momentum-, or in energy space

$$n = N_\mathrm{f} \int \frac{\mathrm{d}^2 k}{(2\pi)^2} \, f_0(k, \mu, T) = \int \mathrm{d}E \, g(E) \, f_0(E, \mu, T) \ . \tag{4.127}$$

The latter equality implicitly defines the two-dimensional density of states $g(E)$. Together, our assumption of an isotropic and thus rotational invariant system, as well as the mathematical identity

$$\int \frac{\mathrm{d}^2 k}{(2\pi)^2} = \int_0^\infty \frac{k \mathrm{d}k}{2\pi} = \int_0^\infty \frac{k(E)}{2\pi} \frac{\mathrm{d}k}{\mathrm{d}E} \mathrm{d}E, \tag{4.128}$$

imply a general expression for the two-dimensional density of states

$$g(E) = N_\mathrm{f} \frac{k(E)}{2\pi} \frac{\mathrm{d}k}{\mathrm{d}E} \ . \tag{4.129}$$

In the case of a two-dimensional electron gas with $\mathrm{d}E/\mathrm{d}k = \hbar^2 k / m^*$ [cf. Eq. (4.119)], one obtains

$$g(E) = \frac{m^*}{\pi \hbar^2} \ . \tag{4.130}$$

This functional dependency gives rise to the following form of the system's Thomas-Fermi screening wave-vector [198]

$$q_\mathrm{TF} = \frac{2\pi \mathrm{e}^2}{4\pi \epsilon_0 \epsilon_\mathrm{r}} g(E_\mathrm{F}) = \frac{m^* \mathrm{e}^2}{2\pi \epsilon_\mathrm{r} \epsilon_0 \hbar^2} \ . \tag{4.131}$$

Moreover, inserting Eq. (4.130) into Eq. (4.127) implies the corresponding temperature and chemical potential dependent equilibrium charge density

$$n = \int_{E_\mathrm{c}=0}^{\infty} \mathrm{d}E\, g(E)\, f_0(E,\mu,T) = \frac{m^*}{\pi\hbar^2} \mathrm{k_B} T \ln\left(1 + \mathrm{e}^{\frac{\mu}{\mathrm{k_B}T}}\right) \,. \tag{4.132}$$

In consistency with the Eqs. (4.124) and (4.126), this expression reduces to

$$n(T=0) = \frac{m^*}{\pi\hbar^2}\mu(T=0) = \frac{m^*}{\pi\hbar^2} E_\mathrm{F} \tag{4.133}$$

in the zero temperature limit. Here, we used that for $\mu > 0$,

$$\lim_{T\to 0} \frac{\mathrm{k_B}T}{\mu} \ln\left(1 + \mathrm{e}^{\frac{\mu}{\mathrm{k_B}T}}\right) = 1 \,. \tag{4.134}$$

Experimentally, the charge density does not change by only varying the temperature of the system. To ensure this property, the chemical potential has to change with the temperature, as it is implicitly described by Eq. (4.132). In order to derive the functional dependence of this scaling, we fix the density in Eq. (4.132) at its zero temperature value, which is given by Eq. (4.202). In particular, this implies

$$\frac{m^*}{\pi\hbar^2} E_\mathrm{F} = \frac{m^*}{\pi\hbar^2} \mathrm{k_B} T \ln\left(1 + \mathrm{e}^{\frac{\mu}{\mathrm{k_B}T}}\right) \quad \Rightarrow \quad \mu = \mathrm{k_B} T \ln\left(\mathrm{e}^{\frac{E_\mathrm{F}}{\mathrm{k_B}T}} - 1\right) \,. \tag{4.135}$$

Hence, for a fixed density the chemical potential decreases as a function of an increasing temperature. If one would instead fix the chemical potential $\mu = \mu_0$ under an increasing temperature, one would induce a thermal density. According to Eq. (4.132), this density is given by

$$\begin{aligned} n_\mathrm{th}(\mu_0, T) &= n(\mu_0, T) - n(\mu_0, 0) = \frac{m^*}{\pi\hbar^2} \mathrm{k_B} T \ln\left(1 + \mathrm{e}^{\frac{\mu_0}{\mathrm{k_B}T}}\right) - \frac{m^*}{\pi\hbar^2}\mu_0 \\ &= \frac{m^*}{\pi\hbar^2} \mathrm{k_B} T \left[\ln\left(1 + \mathrm{e}^{\frac{\mu_0}{\mathrm{k_B}T}}\right) - \ln\left(\mathrm{e}^{\frac{\mu_0}{\mathrm{k_B}T}}\right)\right] = \frac{m^*}{\pi\hbar^2} \mathrm{k_B} T \ln\left(1 + \mathrm{e}^{-\frac{\mu_0}{\mathrm{k_B}T}}\right) \,. \end{aligned} \tag{4.136}$$

For chemical potentials much larger than the thermal energy, the thermally induces density approximately yields

$$n_\mathrm{th}(\mu_0, T) = \frac{m^*}{\pi\hbar^2} \mathrm{k_B} T \ln\left(1 + \mathrm{e}^{-\frac{\mu_0}{\mathrm{k_B}T}}\right) \approx \frac{m^*}{\pi\hbar^2} \mathrm{k_B} T\, \mathrm{e}^{-\frac{\mu_0}{\mathrm{k_B}T}} \,. \tag{4.137}$$

Here, we used that $\ln(1+x) \approx x + \mathcal{O}(x^2)$ for $0 < x \ll 1$.

Analogously to the charge density, the density of states in Eq. (4.130) allows us to calculate the system's energy density. In a local equilibrium this quantity is given by

$$\epsilon = \int_{E_\mathrm{c}=0}^{\infty} \mathrm{d}E\, E\, g(E) f_0(E,\mu,T) = \frac{m^*}{\pi\hbar^2} \int_{E_\mathrm{c}=0}^{\infty} \mathrm{d}E\, E\, \frac{1}{1 + \mathrm{e}^{(E-\mu)/(\mathrm{k_B}T)}} \tag{4.138}$$

$$= -\frac{m^*}{\pi\hbar^2} (\mathrm{k_B}T)^2\, \mathrm{Li}_2\left(-\mathrm{e}^{\frac{\mu}{\mathrm{k_B}T}}\right) \,. \tag{4.139}$$

Here, $\mathrm{Li}_2(z) = \sum_{k=1}^{\infty} z^k/k^2$ encodes the poly-logarithm of order two. In the zero temperature

limit the equilibrium energy density is in particular given by [cf. Eq. (4.123)]

$$\epsilon_0 = \int_{E_\mathrm{c}=0}^{\infty} \mathrm{d}E\, E\, \frac{m^*}{\pi\hbar^2}\Theta(E_\mathrm{F}-E) = \frac{m^*}{\pi\hbar^2}\int_{E_\mathrm{c}=0}^{E_\mathrm{F}} \mathrm{d}E\, E = \frac{m^* E_\mathrm{F}^2}{2\pi\hbar^2} = \frac{\pi\hbar^2 n^2}{2m^*}\ . \tag{4.140}$$

Hence, the average kinetic energy per charge carrier at small temperatures approximately yields

$$\bar{E}^{\mathrm{2DEG}}_{\mathrm{kinetic}} = \frac{\epsilon_0 A}{nA} = \frac{\pi\hbar^2}{2m^*}n\ . \tag{4.141}$$

We close this section by calculating the pressure P of a two-dimensional electron gas, which is defined as the average momentum flux through a perpendicular unit surface. For an isotropic two-dimensional electron gas this definition implies (with $D = 2$)

$$P = \frac{1}{D}\int_{E_\mathrm{c}=0}^{\infty} \mathrm{d}E\, v(E)p(E)\, g(E)f(E,\mu,T) = \frac{1}{2}\int_{E_\mathrm{c}=0}^{\infty} \mathrm{d}E\, \frac{\partial E}{\partial p}p(E)\, g(E)f(E,\mu,T) \tag{4.142}$$

$$= \int_{E_\mathrm{c}=0}^{\infty} \mathrm{d}E\, \frac{p^2(E)}{2m^*}\, g(E)f(E,\mu,T) = \int_{E_\mathrm{c}=0}^{\infty} \mathrm{d}E\, E\, g(E)f(E,\mu,T) = \epsilon\ . \tag{4.143}$$

Hence, the pressure matches the energy density in two-dimensional electron gases. With this identity we can approximate the enthalpy density w. For chemical potentials much larger than the thermal energy, this quantity is approximately given by:

$$w = \epsilon + P = 2\epsilon \overset{\mu\gg \mathrm{k_B}T}{\approx} 2\epsilon_0 = 2\frac{m^* E_\mathrm{F}^2}{2\pi\hbar^2} = nE_\mathrm{F} = \frac{1}{2}nm^*\left(\sqrt{\frac{2E_\mathrm{F}}{m^*}}\right)^2 = \frac{1}{2}nm^* v_\mathrm{F}^2\ , \tag{4.144}$$

For this estimate we used Eqs. (4.140), (4.202) and (4.125), respectively.

Electron-Electron Scattering Time τ_{ee}

As we have discussed in Sec.4.1.1, the most relevant criterion to observe hydrodynamic charge transport in a two-dimensional electron system is that the electron-electron mean free path $l_{\mathrm{ee}} = v_\mathrm{F}\tau_{\mathrm{ee}}$ is the shortest length scale present. In what follows, we will elaborate on an intuitive picture which demonstrates the phase-space scaling of the electron-electron scattering rate in a two-dimensional electron liquid.

Figure 4.5 schematically shows the zero temperature relaxation process of a single electron state due to interactions with the filled Fermi two-sphere. At $T = 0$, the equilibrium Fermi-Dirac distribution is described by a Heaviside-Theta function [cf.Eq. (4.123)] and all electron states up to the (circular) Fermi surface are filled. If one adds an additional electron of energy $\xi_1 > E_\mathrm{F}$ above the Fermi surface, this electron needs to scatter with a second electron of energy $\xi_2 < E_\mathrm{F}$ in order to relax its energy. However, the phase space for this scattering process is strongly suppressed as a consequence of the energy conservation equation and the Pauli principle. While energy conservation predicts that that the overall scattering mechanisms needs to satisfy

$$\xi_1 + \xi_2 = \xi_1' + \xi_2'\ , \tag{4.145}$$

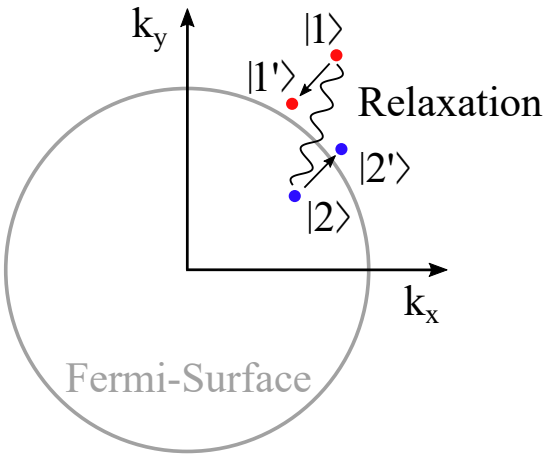

Figure 4.5: Schematic electron-electron relaxation process. An excited state $|1\rangle$ with energy ξ_1 relaxes its energy and momentum via scattering with another state $|2\rangle$ of energy ξ_2, which is initially located in the Fermi two-sphere. The scattering process is indicated by a curly line, the final states are encoded by $|1'\rangle$ and $|2'\rangle$. Further explanations are given in the text.

the Pauli principle additionally requires

$$\xi_2 < E_\mathrm{F}, \quad \xi_1' > E_\mathrm{F} \quad \wedge \quad \xi_2' > E_\mathrm{F} \ , \tag{4.146}$$

as only states above the Fermi surface are initially unoccupied. Equations (4.145) and (4.146) in particular imply that ξ_1' and ξ_2 are only allowed to vary within the distance $|\xi_1 - E_\mathrm{F}|$ around the Fermi surface. Quantitatively this means that

$$|\xi_2 - E_\mathrm{F}| < |\xi_1 - E_\mathrm{F}| \ , \tag{4.147}$$
$$|\xi_1' - E_\mathrm{F}| < |\xi_1 - E_\mathrm{F}| \ . \tag{4.148}$$

In contrast, the third energy ξ_2' is fixed by energy conservation once the other energies have been chosen. Consequently, the phase space for all allowed scattering processes scales as $|\xi_1 - E_\mathrm{F}|^2$, which implies that the corresponding relaxation time scales as

$$\tau_\mathrm{ee} \propto |\xi_1 - E_\mathrm{F}|^{-2} \ . \tag{4.149}$$

Notice, that for $\xi_1 \to E_\mathrm{F}$ the scattering time diverges, which corresponds to the existence of long-lived excitations.
This divergence disappears as soon as we turn on a finite temperature $T \neq 0$ which softens the Fermi-Dirac distribution around the Fermi surface [cf. Eq. (4.122)]. Crucially, this also allows electron-electron relaxation process for $\xi_1 = E_\mathrm{F}$, since it provides a temperature dependent phase-space volume of the order $\mathcal{O}[(\mathrm{k_B}T)^2]$. Hence, the electron-electron relaxation time for $\xi_1 = E_\mathrm{F}$ is given by

$$\tau_\mathrm{ee} \propto (\mathrm{k_B}T)^{-2} \ . \tag{4.150}$$

For $\xi_1 > E_\mathrm{F}$ both of these effects are present and a dimensional analysis implies that the overall electron-electron scattering rate is approximately given by

$$\tau_\mathrm{ee}^{-1} = a\frac{|\xi_1 - E_\mathrm{F}|^2}{\hbar E_\mathrm{F}} + b\frac{(\mathrm{k_B}T)^2}{\hbar E_\mathrm{F}} \ , \tag{4.151}$$

where a and b are some dimensionless constants [198].

A more sophisticated calculation of the electron-electron relaxation rate based on a rigorous evaluation of Fermi's Golden rule for interacting electron liquids can be found in the References [199] and [200]. According to these references, the two-dimensional relaxation rate of excitations close to the Fermi surface ($\xi_1 \approx E_\mathrm{F}$), is given by

$$\tau_\mathrm{ee}^{-1} = \frac{(\pi \mathrm{k_B} T)^2}{32\pi\hbar E_\mathrm{F}} \left(3 - 4\frac{r_\mathrm{s}}{\sqrt{2}(r_\mathrm{s}+\sqrt{2})^2}\right) \ln\left[\frac{2E_\mathrm{F}}{\mathrm{k_B}T}\right] \ , \tag{4.152}$$

where the Wigner-Seitz radius

$$r_\mathrm{s} = (\pi n)^{-1/2} \tag{4.153}$$

takes into account finite screening effects of the free charge carrier density n.

Transport Coefficients

As explained in Sec. 4.1.3, the quantum critical conductivity σ_Q is a part of the longitudinal conductivity tensor. In particular, it arises from electron-hole scattering processes which can reverse the charge current, even though they conserve the overall momentum. Therefore, the quantum critical conductivity can only be of significant relevance if the electron- and hole-densities are comparable in the system considered. Since in a two-dimensional electron gas, the majority of charge carriers is either defined by electrons ($m^* > 0$) or by holes ($m^* < 0$), the contribution of the quantum critical conductivity to the entire conductivity tensor can be neglected [80],

$$\sigma_\mathrm{Q} \approx 0 \ . \tag{4.154}$$

The Bulk viscosity, introduced in Sec. 4.1.3 defines the dissipation of energy under an isotropic fluid expansion or compression. In the scope of the this thesis we are considering incompressible electron liquids, which are by definition characterized by a vanishing bulk viscosity term [84]

$$\zeta = 0 \ . \tag{4.155}$$

In Sec. 4.1.3, we have conceptually introduced the shear viscosity η. As we have seen, the shear viscosity is a measure of the fluid's layer interaction and thus significantly depends on its internal 'friction' τ_ee. In particular, it encodes the efficiency of the momentum transfer transverse to the fluid flow. The stronger the fluid layers interact, the more transversal momentum can be relaxed and the shear viscosity decreases. One source of transversal momentum relaxation is impurity and/or phonon scattering, together giving rise to the bulk momentum relaxation time scale τ_mr [cf. Eq. (4.1)]. Even though electron-electron scattering processes conserve the overall momentum, they might transfer transverse- to longitudinal momentum, dependent on the explicit scattering geometry. According to Matthiessen's rule [198], the shear viscosity is thus given by [86, 201]

$$\eta_0 = \frac{1}{4} n m^* v_\mathrm{F}^2 \tau_{2,\mathrm{ee}} \ , \tag{4.156}$$

where $\tau_{2,\mathrm{ee}}$ is the transverse moment relaxation time

$$\tau_{2,ee}^{-1} = A_{\mathrm{ee}}^{\mathrm{FL}} \frac{(\mathrm{k_B}T)^2}{\hbar E_{\mathrm{F}}} \left(\ln \left[\frac{E_{\mathrm{F}}}{\mathrm{k_B}T} \right] \right)^{-2} + \tau_{2,0}^{-1} \ . \tag{4.157}$$

Here, the coefficient $A_{\mathrm{ee}}^{\mathrm{FL}}$ is a cumbersome function of Landau interaction parameters. Since its explicit form does not contribute to the physical understanding of the transverse momentum relaxation time, we only refer the interested reader to Ref. [201], where its closed analytic form in a kinetic theory approach can be found explicitly. Instead, let us detailedly discuss the physical origin of the two terms together giving rise to $1/\tau_{2,\mathrm{ee}}$.
On the one hand, the term $1/\tau_{2,0}$ defines the transverse momentum relaxation time originating from electron interactions with phonons or static defects. Within the scope of our analysis we only consider the latter, temperature independent source term for $1/\tau_{2,0}$, as we are solely interested in the hydrodynamic low-temperature transport theory of two-dimensional electron liquids. In this regime phonon contributions to $1/\tau_{2,0}$ are strongly suppressed.
On the other hand, the first term in Eq. (4.157) measures the transverse momentum relaxation originating from electron-electron scattering processes. As such, this term is directly related to the total electron-electron scattering rate $1/\tau_{\mathrm{ee}}$, which we derived in Eq. (4.152). However, in comparison to $1/\tau_{\mathrm{ee}}$ the first term in Eq. (4.157) is logarithmically suppressed, as not all electron-electron collisions do satisfy the constraint of transverse momentum relaxation [201].

In order to compare the (shear) viscosities of different materials, it is common to normalize this values to the system's (effective) mass density [cf. Eq.(4.112)]. In particular, this gives rise to the so-called kinematic shear viscosity

$$\nu_0 = \frac{\eta}{nm^*} = \frac{1}{4} v_{\mathrm{F}} l_{2,\mathrm{ee}} \ . \tag{4.158}$$

To get an intuition for experimental values of the transverse momentum relaxation time, the kinematic shear viscosity, as well as the impurity mean free path of two-dimensional electron liquids, Tab. 4.2 shows these quantities in a GaAs channel of width $W = 5\mu$m [90–92]. The authors of the cited references executed magneto-electrical transport measurements in mesoscopic GaAs quantum wells of thickness ≈14.2nm. In particular, they measured the temperature dependent local- and non-local (Hall) resistivity in Hall-bar shaped geometries. The values in Tab. 4.2 have been obtained by fitting the experimental data with the theoretical predictions presented above.

E_{F} [meV]	T [K]	$\tau_{2,0}$ [s]	$A_{\mathrm{ee}}^{\mathrm{FL}}$	v_{F} [m/s]	$l_{2,\mathrm{ee}}$ [μm]	l_{mr} [μm]	ν_0 [m^2/s]
32.5	1.4	6.90×10^{-12}	2.6	4.1×10^5	2.8	40	0.3

Table 4.2: Experimentally measured and theoretically fitted system parameters of a GaAs channel of width $W = 5\mu$m and effective mass $m^* = 0.067\mathrm{m_e}$ [90–92]. Further explanations are given in the text.

As we have discussed in Sec. 4.1.3, the Hall viscosity is a parity- and time-reversal odd transport coefficient. As such, both of these symmetries are required to be broken in order to allow for $\eta_{\mathrm{H}} \neq 0$. In two space dimensions this can be done for instance by applying an out-of-plane magnetic field B with cyclotron radius $r_{\mathrm{c}} = m^* v_{\mathrm{F}}/|\mathrm{e}B|$ and cyclotron frequency $\omega_{\mathrm{c}} = |\mathrm{e}B|/m^*$.

With increasing magnetic field, r_c localizes the electron orbits and consequently reduces the layer-layer interaction in the two-dimensional electron liquids considered. The cyclotron radius in particular provides an additionally relaxation length scale for the transverse momentum transfer. Therefore, the shear viscosity η is expected to decrease monotonically as a function of the magnetic field.
The Hall viscosity defines the amount of momentum transfer transverse to the fluid flow as a response to a certain curvature of the velocity profile [cf. Eq. (4.116)]. For zero magnetic fields, such an effect is prohibited by parity- as well as time reversal symmetry. In finite out-of-plane magnetic fields these symmetries are broken, which implies an initial increase of the Hall viscosity η_H as a function of B. However, since the transverse momentum transfer is hindered by the same mechanisms which contribute to the shear viscosity, the Hall viscosity should exhibit a maximum and eventually decrease in the large magnetic field limit.
The particular scaling of the dynamical shear- and Hall viscosities in an external magnetic field can be calculated by using the mathematical framework of the kinetic Boltzmann theory. Initially, this has been done in Ref. [86], which predicts the following dependencies

$$\eta = \frac{\eta_0}{1+\left(2\tau_{2,\mathrm{ee}}\omega_c\right)^2} = \frac{\eta_0}{1+\left(\dfrac{2l_{2,\mathrm{ee}}}{r_c}\right)^2} \,, \tag{4.159}$$

$$\eta_H = \frac{\left(2\tau_{2,\mathrm{ee}}\omega_c\right)\eta_0}{1+\left(2\tau_{2,\mathrm{ee}}\omega_c\right)^2} = \frac{\left(\dfrac{2l_{2,\mathrm{ee}}}{r_c}\right)\eta_0}{1+\left(\dfrac{2l_{2,\mathrm{ee}}}{r_c}\right)^2} \,,$$

where $l_{2,\mathrm{ee}} = v_F\tau_{2,\mathrm{ee}}$ is the transverse momentum relaxation length introduced in Eq. (4.157).

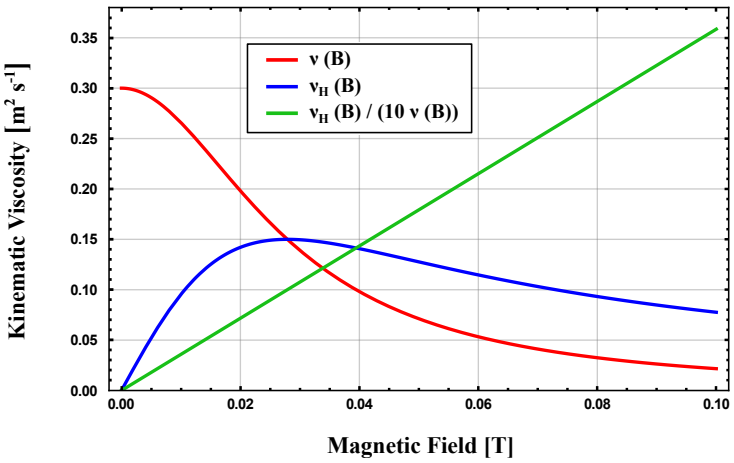

Figure 4.6: The kinematic shear- and Hall viscosities ν (red) and ν_H (blue), as well as their rescaled ratio $\nu_H/(10\nu)$ (green) are shown as a function of the magnetic field B in a GaAs sample. While the shear viscosity monotonically decreases as a function of B, the Hall viscosity initially increases, reaches a maximum at $B_{\max} = m^* v_F/(2el_{2,\mathrm{ee}})$, and eventually decreases as a function of the magnetic field. The ratio ν_H/ν linearly depends on the magnetic field. The GaAs parameters for this plot are taken from Tab. 4.2. Further explanations are given in the text.

In Fig. 4.6, we plot the corresponding kinematic shear- and Hall viscosities

$$\nu = \frac{\eta}{nm^*} \quad \wedge \quad \nu_H = \frac{\eta_H}{nm^*} \tag{4.160}$$

as a function of the magnetic field B for the GaAs sample considered above [cf. Tab. 4.2]. As expected from physical grounds, the (kinematic) shear viscosity decreases monotonically as a function of the magnetic field. In contrast, the (kinematic) Hall viscosity initially increases with the magnetic field before it reaches a maximum at

$$B_{\max} = \frac{m^* v_{\mathrm{F}}}{2\mathrm{e}\, l_{2,\mathrm{ee}}} \quad \text{where} \quad r_{\mathrm{c}} = 2l_{2,\mathrm{ee}} \tag{4.161}$$

and eventually decreases again. While both viscosities vanish in the large magnetic field limit

$$\lim_{B\to\infty} \nu(B) = 0 \quad \wedge \quad \lim_{B\to\infty} \nu_{\mathrm{H}}(B) = 0 \ , \tag{4.162}$$

their ratio ν_{H}/ν linearly increases as a function of B, since

$$\frac{\nu_{\mathrm{H}}}{\nu} = \frac{\eta_{\mathrm{H}}}{\eta} = \frac{2l_{2,\mathrm{ee}}}{r_{\mathrm{c}}} = \frac{2l_{2,\mathrm{ee}}|\mathrm{e}B|}{m^* v_{\mathrm{F}}} \ . \tag{4.163}$$

This ratio will be of significant importance in Sec. 4.2, where we derive the hydrodynamic response of two-dimensional electron liquids. Hence, we will frequently refer to Eq. (4.163) in the subsequent sections of our analysis.

In the scope of this thesis we are mostly interested in small magnetic fields which justify the condition $l_{2,\mathrm{ee}} \ll r_{\mathrm{c}}$. However, let us close this section by explicitly discussing the strong magnetic field limit of Eq. (4.159), since it encodes an interesting feature. In this limit, the kinematic Hall viscosity approximates

$$\begin{aligned} \nu_{\mathrm{H}} &\overset{r_{\mathrm{c}}\ll l_{2,\mathrm{ee}}}{=} \frac{r_{\mathrm{c}}}{2l_{2,\mathrm{ee}}}\nu_0 = \frac{r_{\mathrm{c}}}{2l_{2,\mathrm{ee}}}\frac{v_{\mathrm{F}} l_{2,\mathrm{ee}}}{4} = \frac{1}{8} v_{\mathrm{F}} r_{\mathrm{c}} \\ &= \frac{1}{8}\frac{m^* v_{\mathrm{F}}^2}{|eB|} = \frac{1}{8}\frac{\hbar^2 k_{\mathrm{F}}^2}{m^*|eB|} = \frac{1}{8}\frac{\hbar\, 4\pi n\, l_B^2}{N_{\mathrm{f}} m^*} = \frac{1}{4}\frac{\hbar N_{\mathrm{LL}}}{m^*} \ , \end{aligned} \tag{4.164}$$

where we (re-)introduced (spin-)degeneracy N_{f}, the magnetic length $l_B^2 = \hbar/|eB|$, and rewrote the density n in terms of the Landau level filling factor [cf. Eq. (2.23)]

$$N_{\mathrm{LL}} = \frac{2\pi\hbar n}{N_{\mathrm{f}}|eB|} = \frac{\pi n l_B^2}{N_{\mathrm{f}}} \Rightarrow n = N_{\mathrm{f}}\frac{N_{\mathrm{LL}}}{2\pi l_B^2} \ . \tag{4.165}$$

Equation (4.164) makes two interesting predictions: On the one hand, the kinematic Hall viscosity becomes independent of $l_{2,\mathrm{ee}}$ as the cyclotron orbits prohibit the layer-layer interactions in strong magnetic fields. On the other hand, Eq. (4.164) shows that in the large magnetic field limit the dynamical Hall viscosity approximates

$$\eta_{\mathrm{H}} = n m^* \nu_{\mathrm{H}} = \frac{1}{4} n\hbar N_{\mathrm{LL}} = \frac{N_{\mathrm{f}}}{8\pi}\frac{\hbar N_{\mathrm{LL}}^2}{l_B^2} \ , \tag{4.166}$$

which is exactly the Hall viscosity related to N_{LL} filled Landau levels of (spin-)degeneracy N_{f} [85, 183, 190].

Experimental Evidence of Hydrodynamic Transport

Back in the 1990s, the authors of Refs. [77], [78], and [79] observed the first hydrodynamic electron flow in (Ga,Al)As hetero-structures. In these systems, they measured the so-called Gurzhi effect. The Gurzhi effect is an electron transport phenomenon which is observable in clean systems with an adjustable electron-electron mean free path. In what follows, we briefly review their experimental findings. Let us therefore consider two-dimensional channels of width $W \ll l_{\mathrm{imp}}$, which are characterized by diffusive boundary conditions. If $l_{\mathrm{ee}} \gg W$, electron transport is ballistic and particles mostly collide with the diffusive channel walls [cf. Tab. 4.1]. With decreasing l_{ee} the electron-electron scattering probability increases. As a result, more and more particles are deviated towards the diffusive walls of the system, where they partially relax their longitudinal momentum. This leads to an increasing differential resistivity $\mathrm{d}V/\mathrm{d}I$ with decreasing l_{ee}. Further reducing l_{ee} drives the system eventually in the hydrodynamic regime, associated to a Poiseuille-like fluid profile. In this regime, particles mostly collide with each other and only rarely interact with the channel walls. The enhanced electron-electron collision rate with decreasing l_{ee} reduces the electron-boundary scattering rate and therefore leads to a decreasing differential resistivity. The transition from the ballistic, so-called Knudsen transport regime to the hydrodynamic Poiseuille flow regime as a function of the electron mean free path (or the density) is known as the Gurzhi effect [202].

Channel	Length L [μm]	Width W [μm]	Density n [$10^{11}\mathrm{cm}^{-2}$]	l_{imp} [μm]
I	20.2	3.5	2.2	12.4
II	63.7	3.6	2.7	19.7
III	127.3	3.6	2.7	19.7

Table 4.3: System parameters of the GaAs channels which are studied in the Refs. [77], [78] and [79].

The system parameters of the different channels which are studied in the experiments mentioned above, are listed in Tab. 4.3. Within these channels, the electron-electron mean-free path is adjustable by applying a longitudinal heat current. While the lattice temperature T_{latt} is fixed by an external cryostat, applying the heat current I allows to vary the electron temperature T_{e} (nearly) independently from the lattice temperature. For $I < 40\mu\mathrm{A}$ and $T_{\mathrm{latt}} < 2\mathrm{K}$, one obtains

$$T_{\mathrm{e}} = T_{\mathrm{latt}} + \frac{C\, I^2}{\sigma^{11}\, W^2} \ , \tag{4.167}$$

where σ^{11} is the longitudinal channel conductivity and $C \approx 0.05\,\mathrm{m^2K/W}$ is a material specific constant. As mentioned, a variation of the electron temperature via the heating current can be used to vary the electron-electron mean free path $l_{\mathrm{ee}} = v_{\mathrm{F}}\tau_{\mathrm{ee}}$. Here, $\tau_{\mathrm{ee}}(T_{\mathrm{e}}, n)$ is the temperature and density dependent electron-electron scattering time which we defined in Eq. (4.152). In Fig. 4.7, the differential (longitudinal) resistances of the channels I, II, and III are shown as a function of the heating current I. In Fig. 4.7(a), this value is measured for several lattice temperatures in channel I. T_{latt} decreases from the top to the bottom curve. The top curve shows a nearly quadratic increase of the $\mathrm{d}V/\mathrm{d}I$ characteristic as a consequence of strong electron-phonon scattering. Lowering the lattice temperature allows to observe the Gurzhi (decreasing $\mathrm{d}V/\mathrm{d}I$) regime, as well as the Knudsen (increasing $\mathrm{d}V/\mathrm{d}I$) regime for small heating currents. The ballistic Knudsen regime requires a large phonon

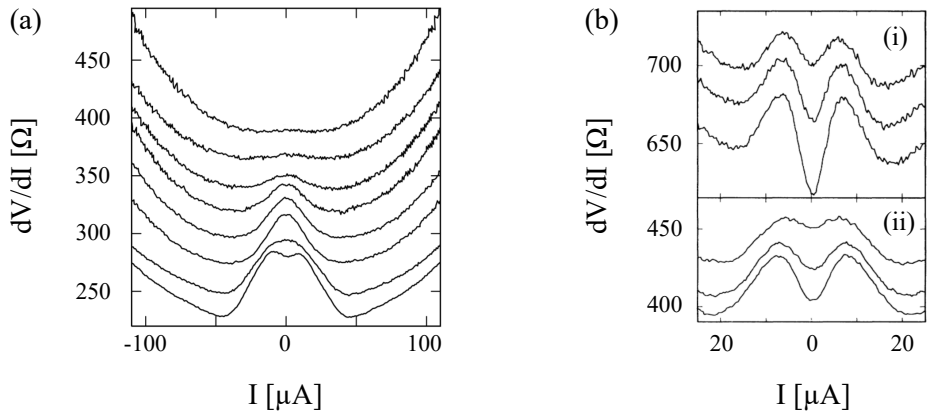

Figure 4.7: (a) Differential resistance dV/dI of the GaAs channel I [cf. Tab. 4.3] as a function of the heating current I for lattice temperatures (from top to bottom) 24.7, 20.4, 17.3, 13.6, 10.4, 8.7, 4.4, and 1.5 K. **(b)** dV/dI as a function of I for (**i**) the GaAs channel II and (**ii**) the GaAs channel III, for lattice temperatures (from top to bottom) 4.5, 3.1, and 1.8 K. With decreasing lattice temperature and increasing impurity mean free path the Gurzhi-effect becomes apparent. Further explanations are given in the text. The figures are adapted from Ref. [78] with permission from the APS.

and impurity mean free path. Consequently, it can be only observed in the very low lattice temperature regime. Heating the lattice increases the electron-phonon coupling, but reduces l_{ee} at the same time. This makes the Gurzhi regime much more robust than the Knudsen regime. Since the channels II and III are characterized by a smaller value of W/l_{imp}, the Gurzhi effect is much clearer to observe in these systems. In particular, the absolute Gurzhi effect in channel III is twice as strong than it is in channel II. The measured effect is thus directly proportional to the system length and does not rely on the contact resistance [77–79].

4.1.5 The Fermi Liquid- and The Dirac Fluid Phase in Graphene

In the previous subsection, we have analyzed the hydrodynamic properties and transport coefficients of weakly interacting electron- or hole liquids in 2+1 space-time dimensions. In particular, these systems are characterized by a large Fermi surface in comparison to $k_B T$, which reduces the available phase-space for electron-electron scattering processes [cf. Fig. 4.5]. In the absence of a large Fermi surface, the physics of interacting electron- or hole liquids significantly changes. Such a phase is for instance realized in graphene close to the charge neutrality point, where the total charge density vanishes [203]. Quantitatively, this happens for $|\mu| \ll k_B T$. Adjusting the chemical potential such that this requirement is fulfilled leads to the formation of a so-called Dirac fluid phase. A Dirac fluid is a strongly coupled material consisting of electrons and holes with a relativistic (linear) dispersion. In what follows, we introduce the band-structure of graphene [204–206], analyze its Fermi liquid- as well as Dirac fluid phase [80, 184, 207], and discuss different signatures of these regimes in recent thermoelectric experiments [97, 208].

Lattice Structure, Brillouin Zone and Dispersion Relation

Monolayer graphene is a purely two-dimensional material made out of carbon atoms which are bounded in a hexagonal honeycomb lattice. The electronic configuration of an isolated carbon atom is given by $1s^2 2s^2 2p^2$. While the 1s-electrons are approximately inert, the 2s- and 2p-orbitals hybridize in condensed matter systems. In graphene monolayers, the 2s- and $2p_{x,y}$-orbitals hybridize into three sp^2-orbitals, which arrange themselves in-plane at angles of 120°. This gives rise to the two-dimensional honeycomb lattice which is shown in Fig. 4.8. In addition to these orbitals which define the so-called chemical σ-bonding, each carbon atom hosts a free out-of-plane p_z-orbital, which allows for π-bonds and can be used for electron- or hole transport.

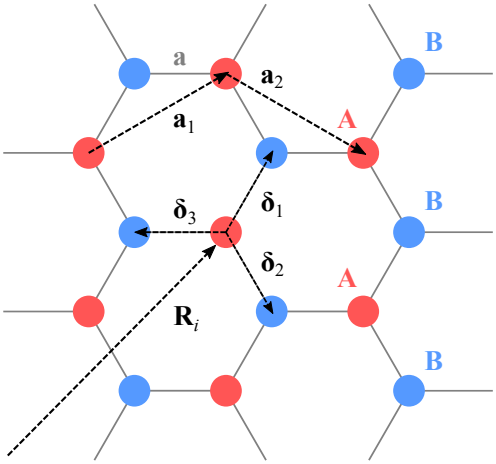

Figure 4.8: Hexagonal real space lattice structure of graphene. A (red) and B (blue) indicate the two inequivalent sublattices, the lattice constant $a \approx 14.2\,\text{nm}$ defines the carbon atom spacing, $\mathbf{a}_{1,2}$ encode the primitive lattice vectors, and $\boldsymbol{\delta}_{1,2,3}$ are the nearest-neighbor hopping vectors with respect to $\mathbf{R}_i$, which characterizes the i-th unit cells in the A sublattice.

Figure 4.8 shows the real space hexagonal lattice structure of graphene. The lattice constant $a \approx 14.2\,\text{nm}$ defines the carbon atom spacing, and blue as well as red dots indicate the two inequivalent sublattices A and B. We choose our Bravais lattice such that it has the primitive

lattice vectors

$$\mathbf{a}_1 = \frac{\mathrm{a}}{2}\left(3, \sqrt{3}\right) \quad \wedge \quad \mathbf{a}_2 = \frac{\mathrm{a}}{2}\left(3, -\sqrt{3}\right) \ . \tag{4.168}$$

The associated reciprocal lattice vectors, defined by $\mathbf{a}_i \mathbf{b}_j = 2\pi\delta_{ij}$, are given by

$$\mathbf{b}_1 = \frac{2\pi}{3\mathrm{a}}\left(1, \sqrt{3}\right) \quad \wedge \quad \mathbf{b}_2 = \frac{2\pi}{3\mathrm{a}}\left(1, -\sqrt{3}\right) \ . \tag{4.169}$$

For our subsequent notation in real space, we use the relative coordinates $\boldsymbol{\delta}_{1,2,3}$, defined via $\mathbf{r}_i = \mathbf{R}_i + \boldsymbol{\delta}_i$. Here, $\mathbf{R}_i$ characterizes the i-th unit cell with respect to the A sublattice. The three nearest-neighbor vectors $\boldsymbol{\delta}_{1,2,3}$ are given by

$$\boldsymbol{\delta}_1 = \frac{\mathrm{a}}{2}\left(1, \sqrt{3}\right), \quad \boldsymbol{\delta}_2 = \frac{\mathrm{a}}{2}\left(1, -\sqrt{3}\right), \quad \boldsymbol{\delta}_3 = -\mathrm{a}(1, 0) \ . \tag{4.170}$$

For the sake of completeness, all these vectors are illustrated in Fig. 4.8. Fourier transforming the real space lattice to momentum space leads to a honeycomb structure which is rotated by an angle of $\pi/6$, as it is shown in Fig. 4.9.

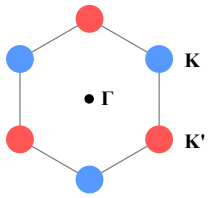

Figure 4.9: Graphene's first Brillouin zone. The **K**- and **K′**-points, as well as the **Γ**-point are highlighted in blue, red, and black, respectively. Further explanations are given in the text.

Due to the underlying C_3-symmetry, the six corners of the first Brillouin zone can be devided into two groups of three equivalent points. The two nonequivalent corners are commonly labeled by

$$\mathbf{K} = \frac{2\pi}{3\mathrm{a}}\left(1, \frac{1}{\sqrt{3}}\right) \quad \wedge \quad \mathbf{K}' = \frac{2\pi}{3\mathrm{a}}\left(1, -\frac{1}{\sqrt{3}}\right) \ . \tag{4.171}$$

Having analyzed the real- and the momentum space lattice structures, let us now derive graphene's eigen-spectrum. As mentioned above, transport in graphene is mediated via the non-hybridized out-of-plane $\mathrm{p_z}$-orbitals. Due to their spin degree of freedom $\sigma = \uparrow, \downarrow$, this gives rise to the nearest neighbor (**NN**) hopping Hamiltonian

$$\hat{H}_{\mathrm{NN}} = -t \sum_{i,j=\mathrm{NN},\sigma} \left(a^\dagger_{i\sigma} b_{j\sigma} + \mathrm{h.c.}\right) \ . \tag{4.172}$$

Here, $t \approx 2.8\,\mathrm{eV}$ is the hopping energy and $a^\dagger_{i\sigma}$ as well as $b^\dagger_{i\sigma}$ are electron creation operators of spin σ in the A and B sublattices of the unit cell i. The eigenfunctions of the NN Hamiltonian in Eq. (4.172) can be written in terms of [a]

$$\begin{pmatrix} \alpha_{\mathbf{k}} \\ \beta_{\mathbf{k}} \end{pmatrix} = \sum_i \mathrm{e}^{\mathrm{i}\mathbf{k}\cdot\mathbf{R}_i} \begin{pmatrix} a^\dagger_i \mathrm{e}^{-\mathrm{i}\mathbf{k}\cdot\boldsymbol{\delta}_1/2} \\ b^\dagger_i \mathrm{e}^{\mathrm{i}\mathbf{k}\cdot\boldsymbol{\delta}_1/2} \end{pmatrix} \ . \tag{4.173}$$

[a] Here, we neglect the real spin degree of freedom $\sigma = \uparrow, \downarrow$, which is considered as a degeneracy in the following.

In this basis, the corresponding **k**-space Hamiltonian becomes purely off-diagonal

$$\hat{H}_{\mathbf{k}} = \begin{pmatrix} 0 & \Delta_{\mathbf{k}} \\ \Delta_{\mathbf{k}}^* & 0 \end{pmatrix} \quad \text{with} \quad \Delta_{\mathbf{k}} = -t \sum_{l=1}^{3} \mathrm{e}^{\mathrm{i}\mathbf{k}\cdot\boldsymbol{\delta}_l} = -t\,\mathrm{e}^{-\mathrm{i}k_\mathrm{x}\mathrm{a}} \left(1 + 2\mathrm{e}^{3\mathrm{i}k_\mathrm{x}\mathrm{a}/2} \cos\left(\sqrt{3}k_\mathrm{y}\mathrm{a}/2\right)\right) . \tag{4.174}$$

The eigen-spectrum of this Hamiltonian is given by [209]

$$E_{\mathbf{k}} = \pm|\Delta_{\mathbf{k}}| = \pm t \left(1 + 4\cos(3k_\mathrm{x}\mathrm{a}/2)\cos\left(\sqrt{3}k_\mathrm{y}\mathrm{a}/2\right) + 4\cos^2\left(\sqrt{3}k_\mathrm{y}\mathrm{a}/2\right)\right)^{1/2} . \tag{4.175}$$

In Fig. 4.10, we show this dispersion relation in the first lattice Brillouin zone. While the spectrum is gapped at the **Γ**-point, it becomes gapless at the **K**- and **K′**-points.

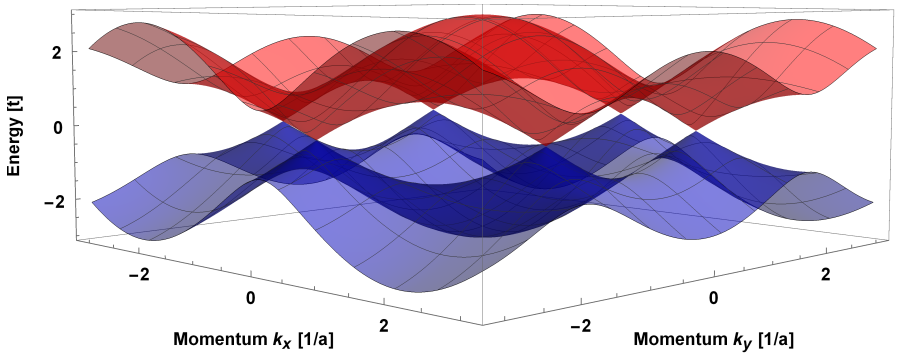

Figure 4.10: Dispersion relation of graphene in the first lattice Brillouin zone. The spectrum is gapped at the **Γ**-point, whereas it is gapless at the C_3 high-symmetry points **K** and **K′**. The valence band is shown in blue, the conduction band is depicted in red.

In order to derive the low-energy physics of graphene, we need to Taylor expand the spectrum around the **K**- and the **K′**-point, respectively. We start with the expansion around the **K**-point. In particular, let us define the relative coordinate $\mathbf{q} = \mathbf{k} - \mathbf{K}$ and expand $\Delta_{\mathbf{k}}$ up to first order in the momentum $\mathbf{q}$ around the expansion point $\mathbf{q}_0 = 0$:

$$\Delta_{\mathbf{K}}(\mathbf{q}) \approx 2t\mathrm{e}^{-\mathrm{i}K_\mathrm{x}\mathrm{a}}\mathbf{q}\cdot\boldsymbol{\nabla}_{\mathbf{k}} \left(\mathrm{e}^{3\mathrm{i}k_\mathrm{x}\mathrm{a}/2}\cos\left(\sqrt{3}k_\mathrm{y}\mathrm{a}/2\right)\right)_{\mathbf{k}=\mathbf{K}} = -\frac{3t\mathrm{a}}{2}\mathrm{e}^{-\mathrm{i}K_\mathrm{x}a}(\mathrm{i}q_\mathrm{x} - q_\mathrm{y}) . \tag{4.176}$$

Since overall phase-factors do not change the underlying physics, we are allowed to drop the exponential prefactor $-\mathrm{i}\mathrm{e}^{-\mathrm{i}K_\mathrm{x}a}$ in Eq. (4.176). In particular, this implies

$$\Delta_{\mathbf{K}}(\mathbf{q}) \approx \hbar v_\mathrm{F}(q_\mathrm{x} + \mathrm{i}q_\mathrm{y}) \quad \text{with} \quad v_\mathrm{F} = 3t\mathrm{a}/(2\hbar) \approx \mathrm{c}_0/300 \approx 10^6\,\mathrm{m/s} . \tag{4.177}$$

Here, we introduced the (bare) Fermi velocity in graphene, v_F, which is approximately 300 times smaller than the speed of light in vacuum. According to Eq. (4.177), graphene's low-energy spectrum close to the **K**-point is effectively described by a relativistic Dirac Hamiltonian with a causal Fermi velocity v_F:

$$\hat{H}_{\mathbf{K}} = \hbar v_\mathrm{F} \begin{pmatrix} 0 & q_\mathrm{x} + \mathrm{i}q_\mathrm{y} \\ q_\mathrm{x} - \mathrm{i}q_\mathrm{y} & 0 \end{pmatrix} = \hbar v_\mathrm{F}\,\hat{\boldsymbol{\sigma}}\cdot\mathbf{q} \quad \text{with} \quad \boldsymbol{\sigma} = (\sigma_\mathrm{x}, \sigma_\mathrm{y}) \ , \quad E_{\mathbf{K}} = \lambda\hbar v_\mathrm{F} q \ , \tag{4.178}$$

$\lambda = \pm 1$, and $q = |\mathbf{q}|$. The eigenfunctions of the Dirac Hamiltonian in Eq. (4.178) are given

by

$$\psi^{\lambda}_{\mathbf{K}}(\mathbf{q}) = \frac{1}{\sqrt{2}} \begin{pmatrix} \mathrm{e}^{-\mathrm{i}\theta_{\mathbf{q}}/2} \\ \lambda\, \mathrm{e}^{\mathrm{i}\theta_{\mathbf{q}}/2} \end{pmatrix} \quad \text{with} \quad \theta_{\mathbf{q}} = \arctan(q_{\mathrm{x}}/q_{\mathrm{y}}) \ . \tag{4.179}$$

Performing the same (linear) Taylor expansion around the $\mathbf{K}'$-point with $K'_{\mathrm{x}} = K_{\mathrm{x}}$, $K'_{\mathrm{y}} = -K_{\mathrm{y}}$, and $\mathbf{q} = \mathbf{k} - \mathbf{K}'$ yields

$$\Delta_{\mathbf{K}'}(\mathbf{q}) = \Delta^{*}_{\mathbf{K}}(\mathbf{q}) \approx \hbar v_{\mathrm{F}}(q_{\mathrm{x}} - \mathrm{i}q_{\mathrm{y}}) \ , \tag{4.180}$$

which implies the associated Dirac Hamiltonian

$$\hat{H}_{\mathbf{K}'} = \hbar v_{\mathrm{F}} \begin{pmatrix} 0 & q_{\mathrm{x}} - \mathrm{i}q_{\mathrm{y}} \\ q_{\mathrm{x}} + \mathrm{i}q_{\mathrm{y}} & 0 \end{pmatrix} = \hbar v_{\mathrm{F}} \hat{\boldsymbol{\sigma}}^{*} \cdot \mathbf{q} \quad \text{with} \quad E_{\mathbf{K}'} = E_{\mathbf{K}} = \lambda \hbar v_{\mathrm{F}} q \tag{4.181}$$

and the corresponding eigenfunctions

$$\psi^{\lambda}_{\mathbf{K}'}(\mathbf{q}) = \frac{1}{\sqrt{2}} \begin{pmatrix} \mathrm{e}^{\mathrm{i}\theta_{\mathbf{q}}/2} \\ \lambda\, \mathrm{e}^{-\mathrm{i}\theta_{\mathbf{q}}/2} \end{pmatrix} \ . \tag{4.182}$$

Hence, the entire low-energy physics of graphene is described by the superposition of two Dirac spectra, one at the $\mathbf{K}$- and one at the $\mathbf{K}'$-point. These two Dirac Hamiltonians are in particular related by a time-reversal- $[\hat{H}_{\mathbf{K}'}(q_{\mathrm{x}}, q_{\mathrm{y}}) = \hat{H}^{*}_{\mathbf{K}}(q_{\mathrm{x}}, q_{\mathrm{y}})]$, or by a parity transformation $[\hat{H}_{\mathbf{K}'}(q_{\mathrm{x}}, q_{\mathrm{y}}) = \hat{H}_{\mathbf{K}}(q_{\mathrm{x}}, -q_{\mathrm{y}})]$ in 2+1 space-time dimensions [cf. Eq. (2.51)]. As a consequence, the low-energy theory of graphene is time-reversal- as well as parity invariant [204–206]. In what follows, we are going to study the physics originating from the low-energy Dirac spectra in graphene.

Charge-, Imbalance-, Energy- and Pressure Density

As discussed in the previous subsection, the amount of fermion species in graphene is given by $N_{\mathrm{f}} = 2 \times 2 = 4$, resulting from the two (real) spin- and the two valley degrees of freedom ($\mathbf{K}$ and $\mathbf{K}'$). With the linear dispersion relation $\mathrm{d}E/\mathrm{d}k = \lambda \hbar v_{\mathrm{F}}$, the low-energy two-dimensional density of states in graphene is given by [cf. Eq. (4.129)]:

$$g(E) = N_{\mathrm{f}} \frac{k(E)}{2\pi} \frac{\mathrm{d}k}{\mathrm{d}E} = \frac{2|E|}{\pi \hbar^2 v_{\mathrm{F}}^2} \ . \tag{4.183}$$

Moreover, the Fermi momentum and -energy, as well as the Thomas-Fermi screening wave-vector [205] are given by [cf. Eq. (4.126)]:

$$k_{\mathrm{F}} = \sqrt{\frac{4\pi|n|}{N_{\mathrm{f}}}} = \sqrt{\pi|n|} \ , \tag{4.184}$$

$$E_{\mathrm{F}} = \mathrm{sgn}(n) \hbar v_{\mathrm{F}} k_{\mathrm{F}} = \mathrm{sgn}(n) \hbar v_{\mathrm{F}} \sqrt{\pi|n|} \ , \tag{4.185}$$

$$q_{\mathrm{TF}} = \frac{2\pi \mathrm{e}^2}{4\pi\epsilon_0\epsilon_{\mathrm{r}}} g(E_{\mathrm{F}}) = \frac{\mathrm{e}^2}{4\pi\epsilon_0\epsilon_{\mathrm{r}}} \frac{4|E_{\mathrm{F}}|}{\hbar^2 v_{\mathrm{F}}^2} = 4\alpha_0 k_{\mathrm{F}} \quad \text{with} \quad \alpha_0 = \frac{\mathrm{e}^2}{4\pi\epsilon_0\epsilon_{\mathrm{r}}\hbar v_{\mathrm{F}}} \ . \tag{4.186}$$

Here, n is the system's charge carrier density ($[n] = \mathrm{m}^{-2}$) relative to the charge neutrality point with $n_{\mathrm{CP}} = 0$ and $\epsilon_{\mathrm{r}} = (\epsilon_{\mathrm{r}}^{\mathrm{above}} + \epsilon_{\mathrm{r}}^{\mathrm{below}})/2$ defines the average relative dielectric constant of the materials above and below the two-dimensional graphene monolayer.

Having calculated the density of states allows us to derive the macroscopic quantities ap-

pearing in the hydrodynamic derivative expansion (4.32) as a function of the chemical potential and the temperature. The low-energy Dirac dispersion in graphene is a two-band model with $\lambda = \pm 1$. It is common to define the (quasi-)particle densities associated to each band separately. Under the assumption of a local equilibrium, these densities are given by [187, 207]

$$n_+ = \int_0^\infty \mathrm{d}E\, n_+(E) = \int_0^\infty \mathrm{d}E\, g(E) f_+^0(E, \mu_+, T) = -\frac{2\mathrm{k}_\mathrm{B}^2 T^2}{\pi\hbar^2 v_\mathrm{F}^2}\, \mathrm{Li}_2\left[-\mathrm{e}^{\frac{\mu_+}{\mathrm{k}_\mathrm{B}T}}\right] , \tag{4.187}$$

$$n_- = \int_{-\infty}^0 \mathrm{d}E\, n_-(E) = \int_{-\infty}^0 \mathrm{d}E\, g(E)\left[1 - f_-^0(E, \mu_-, T)\right] = -\frac{2\mathrm{k}_\mathrm{B}^2 T^2}{\pi\hbar^2 v_\mathrm{F}^2}\, \mathrm{Li}_2\left[-\mathrm{e}^{-\frac{-\mu_-}{\mathrm{k}_\mathrm{B}T}}\right] . \tag{4.188}$$

Here, $\mu_\pm$ is the local chemical potential of (quasi-)particles in the conduction- and valence band, associated to the local equilibrium Fermi-Dirac distribution[a]

$$f_\lambda^0(E, \mu_\lambda, T) = \left[1 + \exp\left(\frac{E(\mathbf{r}) - \mu_\lambda(\mathbf{r})}{\mathrm{k}_\mathrm{B}T(\mathbf{r})}\right)\right]^{-1} . \tag{4.189}$$

Moreover, $\mathrm{Li}_m[z] = \sum_{k=1}^\infty z^k/k^m$ defines the poly-logarithm of order m, which satisfies the limit

$$\lim_{x\to\infty} \mathrm{Li}_m(-\mathrm{e}^{-x}) = 0 \qquad \forall m \in \mathbb{N} . \tag{4.190}$$

The two different linear combinations of the (quasi-)particle densities $n_\pm$ give rise to the charge density n, as well as the imbalance density n_imb, which defines the entire particle density:

$$n = n_+ - n_- = -\frac{2\mathrm{k}_\mathrm{B}^2 T^2}{\hbar^2\pi v_\mathrm{F}^2}\left(\mathrm{Li}_2\left[-\mathrm{e}^{\frac{\mu_+}{\mathrm{k}_\mathrm{B}T}}\right] - \mathrm{Li}_2\left[-\mathrm{e}^{-\frac{\mu_-}{\mathrm{k}_\mathrm{B}T}}\right]\right) , \tag{4.191}$$

$$n_\mathrm{imb} = n_+ + n_- = -\frac{2\mathrm{k}_\mathrm{B}^2 T^2}{\hbar^2\pi v_\mathrm{F}^2}\left(\mathrm{Li}_2\left[-\mathrm{e}^{\frac{\mu_+}{\mathrm{k}_\mathrm{B}T}}\right] + \mathrm{Li}_2\left[-\mathrm{e}^{-\frac{\mu_-}{\mathrm{k}_\mathrm{B}T}}\right]\right) . \tag{4.192}$$

In Fig. 4.11, we illustrated $n_\pm(E)$ for different values of $\mu/(\mathrm{k}_\mathrm{B}T)$ in the equilibrium situation $\mu_\pm = \mu$. In the Fermi liquid regime mainly one band contributes to the entire charge and imbalance density. Hence, these two densities become degenerated [cf. Eq. (4.190)] and it is possible to approximate them by Taylor expanding Eq. (4.191) in terms of the small expansion parameter $\mathrm{k}_\mathrm{B}T/\mu$:

$$n(|\mu| \gg \mathrm{k}_\mathrm{B}T) = n_\mathrm{imb}(|\mu| \gg \mathrm{k}_\mathrm{B}T) = \frac{\mu^2}{\pi\hbar^2 v_\mathrm{F}^2} + \frac{2\pi(\mathrm{k}_\mathrm{B}T)^2}{3\hbar^2 v_\mathrm{F}^2} + \mathcal{O}\left[\left(\frac{\mathrm{k}_\mathrm{B}T}{\mu}\right)^3\right] . \tag{4.193}$$

Here, we used that

$$\mathrm{Li}_2\left[-\mathrm{e}^{\frac{\mu}{\mathrm{k}_\mathrm{B}T}}\right] \pm \mathrm{Li}_2\left[-\mathrm{e}^{-\frac{\mu}{\mathrm{k}_\mathrm{B}T}}\right] = -\frac{\mu^2}{2(\mathrm{k}_\mathrm{B}T)^2} - \frac{\pi^2}{6} + \mathcal{O}\left[\frac{(\mathrm{k}_\mathrm{B}T)^2}{\mu^2}\right] . \tag{4.194}$$

In the Dirac fluid phase both bands significantly contribute to the charge density, implying

[a] In the scope of this thesis, we are only interested in small hydrodynamic fluid velocities in comparison to the Fermi velocity v_F. Therefore, we neglect the background contribution $\mathbf{v}\cdot\mathbf{k}/(\mathrm{k}_\mathrm{B}T)$ to the exponential function in Eq. (4.189).

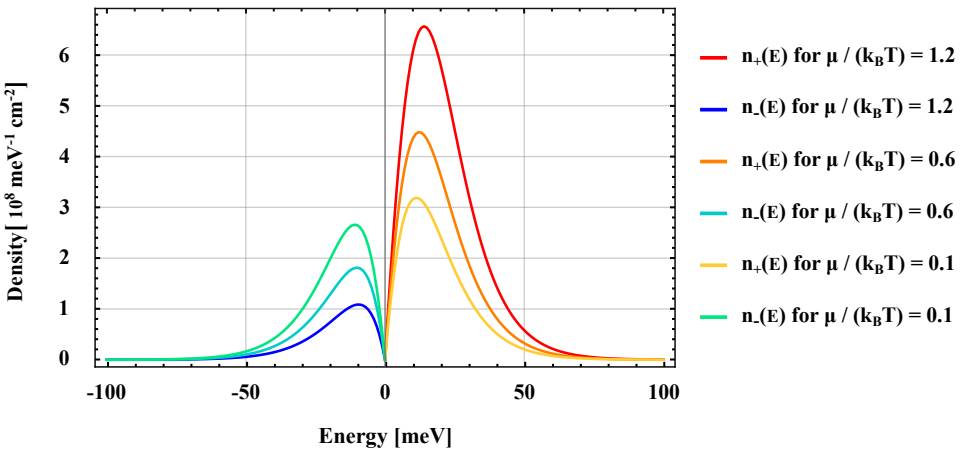

Figure 4.11: The (quasi-)particle densities $n_\lambda(E)$ in the conduction- ($\lambda = +$, reddish) and the valence band ($\lambda = -$, bluish) are shown as a function of the energy E for $\mu_\pm = \mu$. While all curves are calculated at $T = 100\,\mathrm{K}$, they correspond to different chemical potentials. The ratios $\mu/(\mathrm{k_B}T) = 0.1$, $\mu/(\mathrm{k_B}T) = 0.6$ and $\mu/(\mathrm{k_B}T) = 1.2$ are visualized from yellow to red in the conduction- and from green to blue in the valence band, respectively. In the Fermi liquid regime mainly one band contributes to the overall charge density, whereas in the Dirac fluid phase both bands are of equal relevance.

that $n \neq n_{\mathrm{imb}}$. Exactly at charge neutrality, for $\mu = 0$, one finds

$$n(\mu = 0, T) = 0 \tag{4.195}$$

$$n_{\mathrm{imb}}(\mu = 0, T) = \frac{2(\mathrm{k_B}T)^2}{\pi\hbar^2 v_{\mathrm{F}}^2}\frac{\pi^2}{6} = \frac{\pi}{3}\frac{(\mathrm{k_B}T)^2}{\hbar^2 v_{\mathrm{F}}^2}\ , \tag{4.196}$$

where we made use of the limiting cases

$$\lim_{\mu\to 0}\left(\mathrm{Li}_2\left[-\mathrm{e}^{\frac{\mu}{\mathrm{k_B}T}}\right] - \mathrm{Li}_2\left[-\mathrm{e}^{-\frac{\mu}{\mathrm{k_B}T}}\right]\right) = 0 \tag{4.197}$$

$$\lim_{\mu\to 0}\left(\mathrm{Li}_2\left[-\mathrm{e}^{\frac{\mu}{\mathrm{k_B}T}}\right] + \mathrm{Li}_2\left[-\mathrm{e}^{-\frac{\mu}{\mathrm{k_B}T}}\right]\right) = -\frac{\pi^2}{6}\ . \tag{4.198}$$

Usually the hydrodynamic equations are given by the conservation of the charge current as well as the energy-momentum flow. However, in graphene n_+ and n_- are assumed to be separately conserved, which leads to another (quasi-)conservation equation. Beside the charge density, it is also the imbalance density which is (approximately) conserved

$$\partial_{\mathrm{t}} n + \partial_{\mathbf{r}} \cdot \mathbf{j} = 0 \tag{4.199}$$

$$\partial_{\mathrm{t}} n_{\mathrm{imb}} + \partial_{\mathbf{r}} \cdot \mathbf{j}_{\mathrm{imb}} = -\frac{n_{\mathrm{imb}} - n_{\mathrm{imb}}^0}{\tau_{\mathrm{imb}}}\ . \tag{4.200}$$

Here, n_{imb}^0 is the equilibrium imbalance density, τ_{imb} is the (long) imbalance relaxation time, and the charge and imbalance currents are defined via

$$\mathbf{j} = \mathbf{j}_+ - \mathbf{j}_- \quad \wedge \quad \mathbf{j}_{\mathrm{imb}} = \mathbf{j}_+ + \mathbf{j}_-\ . \tag{4.201}$$

According to Reference [210], $\tau_{\mathrm{imb}} \gg \tau_{\mathrm{ee}}$ for small temperatures, since in this regime Auger processes, three-particle collisions and electron-phonon interactions are sub-leading [207].

Fixing the charge density n and changing at the same time the temperature T alters the corresponding chemical potential. In order to derive the functional dependence of this scaling, let us fix the charge density in the equilibrium situation $\mu_\pm = \mu$ and express it in terms of the Fermi energy. Therefore, we perform the zero temperature limit of Eq. (4.191)

$$\lim_{T\to 0} n(T) = \mathrm{sgn}[\mu(T=0)]\,\frac{\mu^2(T=0)}{\pi\hbar^2 v_\mathrm{F}^2} = \mathrm{sgn}(\mathrm{E_F})\frac{E_\mathrm{F}^2}{\pi\hbar^2 v_\mathrm{F}^2}\ . \tag{4.202}$$

Notice, that this result is consistent with Eq. (4.185). Inserting Eq. (4.202) in the left hand side of Eq. (4.191) implicitly defines the scaling of the chemical potential as a function of the temperature for $\mu_\pm = \mu$ if the charge density is fixed:

$$-\frac{\mathrm{sgn}(\mathrm{E_F})}{2}\left(\frac{E_\mathrm{F}}{\mathrm{k_B}T}\right)^2 = \mathrm{Li}_2\left[-\mathrm{e}^{\frac{\mu}{\mathrm{k_B}T}}\right] - \mathrm{Li}_2\left[-\mathrm{e}^{-\frac{\mu}{\mathrm{k_B}T}}\right]\ . \tag{4.203}$$

Analogously to the charge- and imbalance densities, the two-dimensional density of states in Eq. (4.183) allows us to calculate the (low-)energy density ϵ and the pressure P in the local equilibrium of a graphene monolayer [187, 207]:

$$\begin{aligned}\epsilon &= \int_0^\infty \mathrm{d}E\, E\, g(E)\, f_+^0(E,\mu_+,T) + \int_{-\infty}^0 \mathrm{d}E\, E\, g(E)\, \left[1 - f_-^0(E,\mu_-,T)\right] \\ &= -\frac{4\mathrm{k_B}^3 T^3}{\pi\hbar^2 v_\mathrm{F}^2}\left(\mathrm{Li}_3\left[-\mathrm{e}^{\frac{\mu_+}{\mathrm{k_B}T}}\right] + \mathrm{Li}_3\left[-\mathrm{e}^{-\frac{\mu_-}{\mathrm{k_B}T}}\right]\right)\ .\end{aligned} \tag{4.204}$$

Again, in the Fermi liquid regime mainly one band contributes to the overall energy density as a direct consequence of Eq. (4.190). The associated Taylor expansion in terms of the small expansion parameter $\mathrm{k_B}T/\mu$ is given by

$$\epsilon = \frac{2\mu^3}{3\pi\hbar^2 v_\mathrm{F}^2} + \frac{2\pi\mu(\mathrm{k_B}T)^2}{3\hbar^2 v_\mathrm{F}^2} + \mathcal{O}\left[\left(\frac{\mathrm{k_B}T}{\mu}\right)^3\right]\ , \tag{4.205}$$

where we made use of

$$\mathrm{Li}_3\left[-\mathrm{e}^{\frac{\mu}{\mathrm{k_B}T}}\right] + \mathrm{Li}_3\left[-\mathrm{e}^{-\frac{\mu}{\mathrm{k_B}T}}\right] = -\frac{\mu^3}{6(\mathrm{k_B}T)^3} - \frac{\pi^2\mu}{6T} + \mathcal{O}\left[\frac{(\mathrm{k_B}T)^2}{\mu^2}\right]\ . \tag{4.206}$$

In particular, the zero temperature limit of Eq. (4.204) implies

$$\epsilon_0 = \lim_{T\to 0}\epsilon = \frac{2}{3\pi\hbar^2 v_\mathrm{F}^2}E_\mathrm{F}^3 = \frac{2\left(\pi\hbar^2 v_\mathrm{F}^2 n\right)^{3/2}}{3\pi\hbar^2 v_\mathrm{F}^2} = \frac{2\sqrt{\pi}\hbar v_\mathrm{F} n\sqrt{\pi|n|}}{3}\ . \tag{4.207}$$

Hence, the average kinetic energy per charge carrier at small temperatures is given by

$$\bar{E}_\mathrm{kinetic}^\mathrm{Graphene} = \frac{\epsilon_0 A}{nA} = \frac{2\hbar v_\mathrm{F}\sqrt{\pi|n|}}{3} = \frac{2}{3}E_\mathrm{F}\ , \tag{4.208}$$

where A defines the area of the graphene monolayer. Moreover, in a linear spectrum the pressure P is directly proportional to the energy density ϵ. Since pressure is defined as the amount of momentum flux through a perpendicular unit surface, one obtains for an isotropic two-band system in D space dimensions

$$P = \frac{1}{D}\int_0^\infty \mathrm{d}E\, v(E)\, p(E)\, g(E) f_+(E,\mu_+,T) + \frac{1}{D}\int_{-\infty}^0 \mathrm{d}E\, v(E)\, p(E)\, g(E) f_-(E,\mu_-,T)\ . \tag{4.209}$$

For graphene in $D = 2$ space dimensions with an energy and momentum independent single particle velocity $v(E) = v_\mathrm{F}$, this formula implies

$$P = \frac{1}{2}\left(\int_0^\infty \mathrm{d}E\,\hbar v_\mathrm{F}\,k(E)\,g(E) f_+(E,\mu_+,T) + \int_{-\infty}^0 \mathrm{d}E\,\hbar v_\mathrm{F}\,k(E)\,g(E) f_-(E,\mu_+,T)\right) = \frac{\epsilon}{2}\,. \tag{4.210}$$

Hence, due to graphene's low-energy Dirac spectra, the energy density ϵ and pressure P only differ by a factor of two. This property enables us to derive enlightening expressions for the enthalpy density in the Fermi liquid ($|\mu| \gg \mathrm{k_B}T$) as well as in the Dirac fluid regime ($|\mu| \ll \mathrm{k_B}T$):

$$(\epsilon + P)_\mathrm{FL} \approx \frac{3}{2}\frac{4(\mathrm{k_B}T)^3}{\pi\hbar^2 v_\mathrm{F}^2}\frac{\mu^3}{6(\mathrm{k_B}T)^3} \approx \frac{E_\mathrm{F}^3}{\pi\hbar^2 v_\mathrm{F}^2} = \frac{\hbar^3 v_\mathrm{F}^3 k_\mathrm{F}^3}{\pi\hbar^2 v_\mathrm{F}^2} = \frac{\hbar v_\mathrm{F} k_\mathrm{F} k_\mathrm{F}^2}{\pi} \approx \mu|n| \tag{4.211}$$

$$(\epsilon + P)_\mathrm{DF} \approx \frac{3}{2}\frac{4(\mathrm{k_B}T)^3}{\pi\hbar^2 v_\mathrm{F}^2}\frac{3\zeta(3)}{2} = \frac{9\zeta(3)}{\pi^2}\frac{\pi(\mathrm{k_B}T)^2}{\hbar^2 v_\mathrm{F}^2}\mathrm{k_B}T = \frac{27\zeta(3)}{\pi^2} n_\mathrm{imb}\mathrm{k_B}T \approx \pi \mathrm{k_B}T n_\mathrm{imb}\,. \tag{4.212}$$

Here, we made use of the Fermi liquid Taylor expansion in Eq. (4.193), as well as the Dirac liquid limits Eq. (4.196) and

$$\lim_{\mu\to 0}\left(\mathrm{Li}_3\left[-\mathrm{e}^{\frac{\mu}{\mathrm{k_B}T}}\right] + \mathrm{Li}_3\left[-\mathrm{e}^{-\frac{\mu}{\mathrm{k_B}T}}\right]\right) = -\frac{3\,\zeta(3)}{2}\,. \tag{4.213}$$

In this expression, $\zeta(x)$ is the Riemann zeta function with $\zeta(3) \approx 1.2$.

We close this section by emphasizing that in the Fermi liquid regime it is common to rewrite the low-energy Dirac dispersion around each Dirac point in graphene via an effective quadratic dispersion in momentum. In contrast to conventional two-dimensional electron systems with a quadratic spectrum, the effective mass parameter in graphene is by definition density dependent:

$$E_\mathrm{F} = \mathrm{sgn}(n)\hbar v_\mathrm{F} k_\mathrm{F} \stackrel{!}{=} \frac{\hbar^2 k_\mathrm{F}^2}{2m^*} \quad \Rightarrow \quad m^* = \mathrm{sgn}(n)\,\frac{\hbar k_\mathrm{F}}{2v_\mathrm{F}} = \mathrm{sgn}(n)\,\frac{\hbar\sqrt{\pi|n|}}{2v_\mathrm{F}}\,. \tag{4.214}$$

Fermi Liquid vs. Dirac Fluid Regime

In the previous two subsections we have analyzed the band-structure of graphene and derived its equilibrium charge-, imbalance-, energy- and pressure densities. In what follows, we discuss the Fermi liquid- as well as the Dirac fluid phase within this two-dimensional material. The line of reasoning in the present subsection roughly follows the discussions within the References [80, 184, 207, 211].

In Sec. 4.1.5, we have shown that the low-energy physics of graphene is captured by the superposition of two Dirac Hamiltonians located at $\mathbf{k} = \mathbf{K}$ and $\mathbf{k} = \mathbf{K'}$, respectively. So far, our analysis did not take into account electron-electron (Coulomb) interactions. An naive approach to estimate the relevance of electron-electron interactions in graphene is to analyze the ratio of the average unscreened potential- and kinetic energy per charge carrier. This dimensionless quantity is commonly known as the system's bare interaction parameter or 'fine-structure' constant α_0. In a two-dimensional electron- or hole system with a quadratic dispersion in momentum and an effective mass parameter m^* [cf. Sec. 4.1.4], this ratio is

density dependent and tends to zero in the high density limit

$$\alpha_0^{\mathrm{2DEG}} = \frac{\bar{E}^{\mathrm{2D}}_{\mathrm{Coulomb}}}{\bar{E}^{\mathrm{2DEG}}_{\mathrm{kinetic}}} = \frac{\mathrm{e}^2\sqrt{|n|}}{4\pi\epsilon_0\epsilon_{\mathrm{r}}} \Big/ \frac{\hbar^2\pi n}{2m^*} = \frac{\mathrm{e}^2|m^*|}{2\pi^2\hbar^2\epsilon_0\epsilon_{\mathrm{r}}\sqrt{|n|}} \,. \tag{4.215}$$

Here, we inserted the average unscreened potential energy as a function of the charge carrier density $|n| = 1/\bar{r}^2$, where $\bar{r}$ is the average distance between charge carriers:

$$\bar{E}^{\mathrm{2D}}_{\mathrm{Coulomb}} = \frac{\mathrm{e}^2}{4\pi\epsilon_0\epsilon_{\mathrm{r}}\bar{r}} = \frac{\mathrm{e}^2\sqrt{|n|}}{4\pi\epsilon_0\epsilon_{\mathrm{r}}} \,. \tag{4.216}$$

Moreover, we used the density-dependent form of the average kinetic energy per charge carrier $\bar{E}^{\mathrm{2DEG}}_{\mathrm{kinetic}}$ which was derived in Eq. (4.141) of Sec. 4.1.4. Even though Eq. (4.215) neglects the effect of screening and renormalization, it already predicts the existence of a weakly coupled electron liquid at high densities.

In two-dimensional Dirac materials with a linear dispersion in momentum the bare 'fine-structure' constant is instead density independent. Let us derive this quantity for the Dirac dispersion in graphene

$$\alpha_0^{\mathrm{Graphene}} = \frac{\bar{E}^{\mathrm{2D}}_{\mathrm{Coulomb}}}{\bar{E}^{\mathrm{Graphene}}_{\mathrm{kinetic}}} = \frac{\mathrm{e}^2\sqrt{|n|}}{4\pi\epsilon_0\epsilon_{\mathrm{r}}} \Big/ \frac{2\hbar v_{\mathrm{F}}\sqrt{\pi|n|}}{3} = \frac{\mathrm{e}^2}{4\pi\epsilon_0\epsilon_{\mathrm{r}}\hbar v_{\mathrm{F}}}\frac{3}{2\sqrt{\pi}} \approx \frac{1.85}{\epsilon_{\mathrm{r}}} \,. \tag{4.217}$$

Here, we used the average kinetic energy per charge carrier $\bar{E}^{\mathrm{Graphene}}_{\mathrm{kinetic}}$ which was derived in Eq. (4.208). For the last approximation in Eq. (4.217), we used that $v_{\mathrm{F}} \approx \mathrm{c}_0/300$ [cf. Eq. (4.177)]. Dependent on the substrate, the relative dielectric constant in Eq. (4.217) is in between $1 < \epsilon_{\mathrm{r}} < 5$. For instance, it is $\epsilon_{\mathrm{r}} \approx 1$ for suspended graphene, whereas it is $\epsilon_{\mathrm{r}} \approx 4$ for graphene sandwiched between two hexagonal Boron Nitrid (**hBN**) layers [93]. In comparison to a free QED_{2+1} system with

$$\alpha_0^{\mathrm{QED}_{2+1}} = \frac{\bar{E}^{\mathrm{2D}}_{\mathrm{Coulomb}}}{\bar{E}^{\mathrm{QED}_{2+1}}_{\mathrm{kinetic}}} = \frac{\mathrm{e}^2\sqrt{|n|}}{4\pi\epsilon_0} \Big/ \frac{2\hbar \mathrm{c}_0\sqrt{\pi|n|}}{3} = \frac{\mathrm{e}^2}{4\pi\epsilon_0\hbar \mathrm{c}_0}\frac{3}{2\sqrt{\pi}} \approx 6.17\times10^{-3} \,, \tag{4.218}$$

the relative dielectric constant ϵ_{r} slightly reduces the ratio

$$\frac{\alpha_0^{\mathrm{Graphene}}}{\alpha_0^{\mathrm{QED}_{2+1}}} = \frac{\mathrm{c}_0}{v_{\mathrm{F}}}\frac{1}{\epsilon_{\mathrm{r}}} \,. \tag{4.219}$$

However, since the causal (Fermi-) velocity in graphene is much slower than the speed of light in vacuum, $v_{\mathrm{F}} \approx \mathrm{c}_0/300$, unlike in QED_{2+1} the bare electron-electron interactions are not perturbatively small. In particular, one obtains

$$\alpha_0^{\mathrm{Graphene}} \approx 1.85 \quad \text{for suspended graphene}\,, \tag{4.220}$$

$$\alpha_0^{\mathrm{Graphene}} \approx 0.46 \quad \text{for graphene encapsulated by hBN}\,. \tag{4.221}$$

In summary, the density independence and the large value of $\alpha_0^{\mathrm{Graphene}}$ in comparison to $\alpha_0^{\mathrm{QED}_{2+1}}$ makes graphene a promising candidate to observe strong interacting electron-hole dynamics. However, so far our analysis did not take into account the screening of Coulomb interactions by free charge carriers in the system, as well as the running of the 'fine-structure' constant with respect to energy. These two effects will be studied in the following paragraphs. In order to directly relate our analysis to the recent literature on graphene [80, 207] and to the actual definition of the fine-structure constant α, we will subsequently use the following

definition of graphene's bare 'fine-structure' constant:

$$\alpha_0 = \frac{\mathrm{e}^2}{4\pi\epsilon_0\epsilon_\mathrm{r}\hbar v_\mathrm{F}} \ . \tag{4.222}$$

In comparison to the estimate in Eq. (4.217) this definition only differs by a factor of $3/\left(2\sqrt{\pi}\right) \approx 0.85$.

The Fermi Liquid Phase As estimated in Eq. (4.217), the bare electron interactions in graphene are strong. However, for large values of $|\mu|/(\mathrm{k_B}T)$, these interactions are screened by a large Fermi surface in comparison to the thermal energy. This effect can be incorporated by shifting the unscreened Coulomb potential in momentum space by the Thomas-Fermi screening wave-vector q_TF, which we defined in Eq. (4.186) [184]:

$$V^\mathrm{Coloumb}_\mathrm{unscreened}(q) = -\frac{\mathrm{e}}{2\epsilon_\mathrm{r}\epsilon_0 q} \quad \overset{\text{screening}}{\rightarrow} \quad V^\mathrm{Coloumb}_\mathrm{screened}(q) = -\frac{\mathrm{e}}{2\epsilon_\mathrm{r}\epsilon_0\left(q+q_\mathrm{TF}\right)} = -\frac{\mathrm{e}}{2\epsilon_\mathrm{r}\epsilon(q)q} \ . \tag{4.223}$$

For the concrete form of the Coulomb potential in momentum space used above, we performed a Fourier transformation in two space dimensions. In particular, we made us of

$$\int \mathrm{d}^2 r \ \frac{1}{r}\,\mathrm{e}^{-\mathrm{i}qr} = \frac{2\pi}{q} \ . \tag{4.224}$$

Moreover, in Eq. (4.223) we introduced the generalized momentum dependent dielectric function

$$\epsilon(q) = \left(1 + \frac{q_\mathrm{TF}}{q}\right)\epsilon_0 \ . \tag{4.225}$$

Adding the Thomas-Fermi screening vector to the unscreened Coulomb energy in Eq. (4.217) reduces the value of α_0 with increasing density. However, the Fermi liquid regime in graphene becomes most apparent when calculating the quasi-particle life time τ_ee for $|\mu|/(\mathrm{k_B}T) \gg 1$. In this parameter regime, the large Fermi surface in comparison to the thermal energy $\mathrm{k_B}T$ reduces the phase space available for electron-electron scattering processes drastically [cf. Fig. 4.5]. As a consequence, long-lived quasi-particles arise and the Fermi liquid theory applies. According to Refs. [212–214], the quasi-particle life time in a random phase approximation for $|\mu|/(\mathrm{k_B}T) \gg 1$ is on the order of

$$\tau_\mathrm{ee,FL} \approx -\frac{N_\mathrm{f}}{\pi}\frac{\hbar\mu}{(\mathrm{k_B}T)^2}\ln\left(\chi\frac{\mathrm{k_B}T}{|\mu|}\right)^{-1} \ . \tag{4.226}$$

with $\chi = 3/\sqrt{5}$. In what follows, we calculate an exemplary value of the electron-electron scattering time for a typical chemical potential and temperature in the Fermi liquid regime. We choose $\mu = 100\mathrm{meV}$ and $T = 60\mathrm{K}$, which corresponds to a ratio of $|\mu|/(\mathrm{k_B}T) \approx 19$. For these values one obtains

$$\tau_\mathrm{ee,FL} \approx 1.2 \times 10^{-12}\,\mathrm{s} \ . \tag{4.227}$$

This result is in particular independent on the substrate which encapsulates the graphene monolayer [212–214].

The Dirac Fluid Phase In order to obtain a reliable estimate for graphene's electron-electron scattering time in the Dirac fluid regime, we need to calculate the so-called running of α with respect to the chemical potential and the temperature. As it is shown in Ref. [184, 207], a sophisticated renormalization-group (**RG**) analysis implies that graphene's effective 'fine-structure' constant for general μ and T is given by

$$\alpha(\mu,T) = \alpha_0/R_\Lambda(\mu,T) \quad \text{with} \quad R_\Lambda(\mu,T) = 1 + \frac{\alpha_0}{4}\ln\left(\frac{\mathrm{k_B}T_\Lambda}{\max\left(|\mu|,\mathrm{k_B}T\right)}\right) \ . \tag{4.228}$$

Here, $T_\Lambda \approx 8.34\times10^4\,\mathrm{K}$ is the energy scale at which deviations from the linear spectrum become significant. The running of α originates from the renormalization of the Fermi velocity, since neither the spinor fields nor the electric charge become renormalized in the RG flow of graphene's effective action [80]. In particular, the running of the Fermi velocity is given by

$$v_\mathrm{F}(\mu,T) = v_\mathrm{F}^0 R_\Lambda(\mu,T) \ , \tag{4.229}$$

where $v_\mathrm{F}^0 \approx 10^6\,\mathrm{m/s}$ is the high-density Fermi velocity derived in Eq. (4.177). This theoretical prediction has in particular been measured in Ref. [215]. The renormalization function R_Λ has its highest relevance in the Dirac fluid regime $|\mu| \ll k_\mathrm{B}T$. In particular, Eq. (4.228) implies that at charge neutrality the coupling strength α becomes marginally irrelevant as one lowers the temperature

$$\alpha(\mu=0,T) = \frac{\alpha_0}{1+\dfrac{\alpha_0}{4}\ln\left[\dfrac{T_\Lambda}{T}\right]} \quad \text{with} \quad \lim_{T\to0}\alpha(\mu=0,T) = 0 \ . \tag{4.230}$$

At reasonable temperatures graphene nevertheless forms a strongly coupled Dirac fluid close to the charge neutrality point, as the logarithmic running is very slow. The Dirac fluid regime becomes most apparent when calculating the quasi-particle life time τ_ee for $|\mu|/(\mathrm{k_B}T) \ll 1$. In this limit the Fermi surface effectively vanishes in comparison to the thermal energy, and there is no effective screening of the Coulomb interactions. As a direct consequence, the quasi-particle life time in graphene for $|\mu|/(\mathrm{k_B}T) \ll 1$ is approximately given by [184]

$$\tau_\mathrm{ee,DF} \approx 0.274\frac{1}{\alpha(0,T)^2}\frac{\hbar}{\mathrm{k_B}T} \ . \tag{4.231}$$

As an exemplary value let us calculate this time scale for a typical temperature in the Dirac fluid regime [208]. For $T = 60\mathrm{K}$, Eqs. (4.230) and (4.231) yield the values

$$R_\Lambda(0,60\mathrm{K}) = 6.2, \qquad \alpha(0,60\mathrm{K}) = 0.35, \qquad \tau_\mathrm{ee,DF} \approx 2.8\times10^{-13}\,\mathrm{s} \ , \tag{4.232}$$

for suspended graphene, and

$$R_\Lambda(0,60\mathrm{K}) = 2.3, \qquad \alpha(0,60\mathrm{K}) = 0.24, \qquad \tau_\mathrm{ee,DF} \approx 6.2\times10^{-13}\,\mathrm{s} \tag{4.233}$$

for graphene encapsulated by hBN.

In summary, Fig. 4.12 schematically illustrates the formation of Fermi liquid- and Dirac fluid phases in graphene dependent on the ratio $|\mu|/(\mathrm{k_B}T)$.

We close this paragraph by emphasizing that even in the Fermi liquid regime RG effects are of significant relevance if $\mathrm{k_B}T \ll |\mu| \ll \mathrm{k_B}T_\Lambda$. In agreement with the findings in Ref. [207], we obtain the following values for the renormalization function R_Λ at $\mu = 100\mathrm{meV}$ and

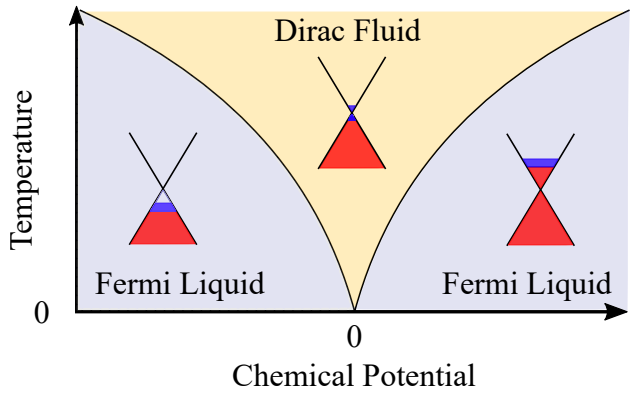

Figure 4.12: The formation of Fermi liquid- and Dirac fluid phases in graphene is schematically illustrated as a function of the chemical potential μ and the temperature T. For simplicity the spectrum of only one of the Dirac cones at $\mathbf{k} = \mathbf{K}$ (or $\mathbf{k} = \mathbf{K}'$) is depicted. If $|\mu|/(\mathrm{k_B}T) \gg 1$ (grey shaded region) the large Fermi surface provides a strong screening mechanism. In this case, the system forms an electron- or hole-like Fermi liquid. Instead, if $|\mu|/(\mathrm{k_B}T) \ll 1$ (sandy shaded region) the Fermi surface approximately vanishes and an unscreened Dirac fluid arises. While the temperature independent part of the carrier density is schematically encoded in red, thermally excited states are highlighted in blue [cf. Fermi-Dirac distribution in Eq. (4.189)]. This figure is inspired by Fig. 5 in Ref. [80].

$T = 60\mathrm{K}$:

$$R_\square(100\mathrm{meV}, 60\mathrm{K}) = 4.6 \qquad \text{for suspended graphene ,} \tag{4.234}$$

$$R_\square(100\mathrm{meV}, 60\mathrm{K}) = 1.9 \qquad \text{for graphene encapsulated by hBN .} \tag{4.235}$$

Hydrodynamic Transport Above, we have discussed the formation of Fermi liquid- and Dirac fluid phases in graphene as a function of $|\mu|/(\mathrm{k_B}T)$. To realize hydrodynamic transport within these regimes, the electron-electron mean free path $l_{\mathrm{ee}} = v_{\mathrm{F}}\tau_{\mathrm{ee}}$ needs to be the shortest length scale present. In particular, the electron-electron scattering time τ_{ee} needs to be short in comparison to the impurity- and phonon scattering time, or, if a magnetic field is applied, in comparison to the typical cyclotron frequency $\omega_{\mathrm{c}}^{\mathrm{th}}$ of thermally excited states [185].

At temperatures below $T \approx 100\mathrm{K}$, electron-phonon scattering in graphene does not play an essential role [80]. The dominant mechanism for bulk momentum relaxing scattering processes originates from (charged) impurity scattering. Even though the hexagonal lattice structure of graphene can be realized approximately 'defect-less', charged impurities in the substrate induce local density fluctuations in the graphene monolayer. The interactions of electrons with these so-called charge puddles define the bulk momentum relaxing scattering time τ_{mr}. The higher the chemical potential (density) or temperature, these scattering processes become less important, since underlying density fluctuations become less relevant. For weak disorder, the scattering time associated to charged impurities in the substrate of charge $q = Z\mathrm{e}$ and density n_{imp} is to leading order given by [184]

$$\tau_{\mathrm{imp}} = \frac{\hbar}{n_{\mathrm{imp}}} \left(\frac{\pi Z \mathrm{e}^2}{\epsilon_{\mathrm{r}}}\right)^{-2} \frac{\epsilon + P}{n_{\mathrm{imb}}} \approx \frac{\hbar}{n_{\mathrm{imp}}} \left(\frac{\pi Z \mathrm{e}^2}{\epsilon_{\mathrm{r}}}\right)^{-2} \max[\pi \mathrm{k_B}T, |\mu|] \ , \tag{4.236}$$

which incorporates all of the effects mentioned above. Here, we used the Fermi liquid- as well

as the Dirac fluid approximation of the enthalpy density which we derived in Eq. (4.211) and Eq. (4.212), respectively. In Tab. 4.4 we listed recently measured values of τ_{mr} at different densities and temperatures [97, 208].

τ_{mr} [10^{-12}s]	l_{mr} [μm]	n [-$10^{11}\,\mathrm{cm}^{-2}$]	T [K]
6.3	12	2	7.5
12.6	23	6	7.5
3.7	7	2	75
4.4	8	6	75
2.1	4	2	150
2.2	4	6	150
1.5	1.5	0.1	60

Table 4.4: Experimental values of the bulk momentum relaxing scattering time τ_{mr} and mean free path $l_{\mathrm{mr}} = v_{\mathrm{F}}\tau_{\mathrm{mr}}$ for different graphene monolayers encapsulated in hexagonal boron nitride. These values are shown for different charge densities n and temperatures T [97, 208].

As mentioned above, for low temperatures phonon scattering can be neglected and impurity scattering is the dominant source of bulk momentum relaxation. According to Eq. (4.236), τ_{imp} is a density dependent quantity in the Fermi liquid regime as $\mu \propto k_{\mathrm{F}} \propto \sqrt{|n|}$. For $T = 7.5$K the density dependence of τ_{imp} can be seen in Tab. 4.4. For higher temperatures phonon scattering becomes relevant and suppresses the density dependence of τ_{mr}. Notice, that especially at small densities in the Dirac fluid regime (here at $T = 60$K) hydrodynamic transport can be realized as τ_{mr} is an order of magnitude larger than the typical electron-electron scattering time, which we estimated in Eq. (4.233).

Last but not least, in an external magnetic field B, the electron-electron scattering rate also needs to exceed the typical cyclotron frequency of thermally excited states [184, 185]

$$\omega_{\mathrm{c}}^{\mathrm{th}} = \frac{n\mathrm{e}Bv_{\mathrm{F}}^2}{\epsilon + P} \ . \tag{4.237}$$

Even though charge carriers are confined to cyclotron orbits in magnetic fields, this requirement ensures the existence of a local thermal equilibrium in each fluid cell. In the Fermi liquid- as well as in the Dirac Fluid regime, we can approximate Eq. (4.237) by using the corresponding expressions for the enthalpy density, which we derived in Eq. (4.211) and Eq. (4.212), respectively:

$$\omega_{\mathrm{c,FL}}^{\mathrm{th}} \approx \frac{\mathrm{e}B\,v_{\mathrm{F}}^2}{|\mu|} \ , \tag{4.238}$$

$$\omega_{\mathrm{c,DF}}^{\mathrm{th}} \approx \frac{n}{n_{\mathrm{imb}}}\frac{\mathrm{e}B\,v_{\mathrm{F}}^2}{\pi \mathrm{k_B} T} \ . \tag{4.239}$$

In order to give exemplary values of these time scales in graphene encapsulated by hBN, let

us assume a small magnetic field $B \approx 10\text{mT}$. For such a field, Eq. (4.237) predicts

$$1/\omega_{\text{c}}^{\text{th}}(100\text{meV}, 60\text{K}) \approx 2.8 \times 10^{-12}\,\text{s} \tag{4.240}$$

in the Fermi liquid regime with $\mu/(\text{k}_\text{B}T) = 19$, and

$$1/\omega_{\text{c}}^{\text{th}}(1\text{meV}, 60\text{K}) \quad \approx 2.0 \times 10^{-12}\,\text{s} \tag{4.241}$$

in the Dirac fluid regime with $\mu/(\text{k}_\text{B}T) = 0.19$.

Transport Coefficients

As we have discussed in the previous subsections, adjusting the temperature and chemical potential in graphene such that l_{ee} is the shortest length scale present gives rise to hydrodynamic transport within this two-dimensional material. For $|\mu| \gg \text{k}_\text{B}T$, this transport is very similar to the hydrodynamic transport of common Fermi liquids with a quadratic dispersion in momentum. Instead, for $|\mu| \ll \text{k}_\text{B}T$, a hydrodynamic Dirac fluid phase has been predicted to arise in clean graphene samples [184]. It is the goal of the following (sub-)sections to apply the hydrodynamic framework introduced in Secs. 4.1.2 and 4.1.3 to graphene, and to analyze its hydrodynamic transport analytically, as well as numerically. We start our analysis with the discussion of graphene's different transport coefficients. These quantities will be used as input parameters for our subsequent hydrodynamic simulations. Recently, the authors of Refs. [184, 207, 216] derived the dissipative transport coefficients of graphene by using a kinetic Boltzmann approach. Strictly speaking, this mathematical framework is only valid for weakly coupled systems with $\alpha \ll 1$. As we have seen in the previous section the 'bare' interaction parameter α_0 in graphene does not necessarily have this property. However, in equation Eq. (4.230), we have shown that the effective coupling strength in graphene is marginally irrelevant. Hence, taking into account graphene's characteristic RG flow, the (large) relative dielectric constant of its encapsulating material, as well as finite screening effects for $\mu \neq 0$, significantly increases the reliability of the kinetic theory approach mentioned above. In what follows, we are going to review the particular results for graphene's dissipative transport coefficients, which were initially derived in Refs. [184, 207, 216].

The Quantum Critical Conductivity σ_Q One of the transport coefficients which is left undetermined by hydrodynamics is the quantum critical conductivity σ_Q, which was introduced and discussed in Sec. 4.1.3. A general derivation of this quantity can be found in Ref. [184]. Based on a kinetic Boltzmann approach and a random phase approximation, the authors of this reference predict the following functional dependence of the quantum critical conductivity and the electron-electron scattering time:

$$\sigma_\text{Q}(\mu,\omega) = \frac{1}{\alpha^2}\frac{4\pi}{\hat{g}_1(\mu,T)}\left(\tau_{\text{ee}}(\mu,T)\frac{\alpha^2\text{k}_\text{B}T}{\hbar}\right)^2 \frac{1}{1-\text{i}\omega\tau_{\text{ee}}}\frac{\text{e}^2}{\text{h}}\,, \tag{4.242}$$

$$\tau_{\text{ee}}(\mu,T) = \frac{1}{\alpha^2}\frac{\hat{g}_1(\mu,T)}{2}\left(\frac{2\ln\left(2\cosh[\mu/(2\text{k}_\text{B}T)]\right)}{\pi} - \frac{n^2(\hbar v_\text{F})^2}{(\epsilon+P)\text{k}_\text{B}T}\right)\frac{\hbar}{\text{k}_\text{B}T}\,. \tag{4.243}$$

Here, ω encodes the AC frequency of an applied electric field and $\hat{g}_1(\mu,T)$ is a complicated α-independent scattering function which needs to be evaluated numerically via the inversion of a scattering matrix. In the scope of our analysis, we are mainly interested in the DC limiting values of these quantities. In the Dirac fluid phase $|\mu| \ll \text{k}_\text{B}T$, the Fermi surface vanishes and screening effects become negligible. This implies the following DC values at

charge neutrality

$$\sigma_{\mathrm{Q}}\left(0,0\right)=\frac{4\pi}{\alpha^{2}}\hat{g}_{1}\left(0,T\right)\left(\frac{\ln(2)}{\pi}\right)^{2}\frac{\mathrm{e}^{2}}{\mathrm{h}}=\frac{0.760}{\alpha^{2}}\frac{\mathrm{e}^{2}}{\mathrm{h}}\ , \tag{4.244}$$

$$\tau_{\mathrm{ee}}(0,0)=\frac{1}{\alpha^{2}}\frac{\hbar}{\mathrm{k_{B}}T}\frac{\hat{g}_{1}(0,T)\ln(2)}{\pi}=0.274\frac{\hbar}{\alpha^{2}\mathrm{k_{B}}T}\ , \tag{4.245}$$

with $\hat{g}_1(0,T)\approx 1.24$. In the Fermi liquid regime only one kind of (majority) charge carriers, either electrons or holes, significantly contributes to the electric transport [cf. Fig. 4.11]. As such, the quantum critical conductivity is negligible within this regime [184].

To get an intuition of how the quantum critical conductivity effects the thermo-electric response in graphene, let us briefly discuss the longitudinal thermo-electric conductivities in the presence of an AC driving field and a weak charged impurity density n_{imp} [cf. Eq.(4.236)], which will be encoded in the dimensionless parameter

$$\Delta=\pi^{2}\left(\frac{Z\mathrm{e}^{2}}{\mathrm{k_{B}}T\epsilon_{\mathrm{r}}}\right)^{2}n_{\mathrm{imp}}\ . \tag{4.246}$$

In general, the relation between the two-dimensional heat- $\mathbf{Q}$ and charge current $\mathbf{J}$ as a response to an applied electric field $\mathbf{E}$ and a thermal gradient $\boldsymbol{\nabla}T$ is given by

$$\begin{pmatrix}\mathbf{J}\\ \mathbf{Q}\end{pmatrix}=\begin{pmatrix}\hat{\sigma} & \hat{\alpha}\\ T\hat{\alpha} & \hat{\bar{\kappa}}\end{pmatrix}\begin{pmatrix}\mathbf{E}\\ -\boldsymbol{\nabla}T\end{pmatrix}\ , \tag{4.247}$$

where $\hat{\sigma}$ defines the electrical conductivity tensor, $\hat{\bar{\kappa}}$ is the thermal conductivity tensor, and $\hat{\alpha}$ encodes the thermopower as well as the Peltier coefficient [184]. For $k=0$, the hydrodynamic conservation equations for the charge-, energy- and momentum flow [cf. Eqs. (4.3) and (4.28)], imply the local response functions [80, 184]

$$\sigma^{ij}(\omega;\mu,\Delta)=\delta^{ij}\left[\frac{\mathrm{e}^{2}}{\tau_{\mathrm{imp}}^{-1}-\mathrm{i}\omega}\frac{nv_{\mathrm{F}}^{2}}{\epsilon+P}+\sigma_{\mathrm{Q}}+\delta\sigma\left(\Delta,\omega,\mu\right)\right]\ , \tag{4.248}$$

$$\alpha^{ij}(\omega;\mu,\Delta)=\delta^{ij}\left[\frac{\mathrm{e}}{\tau_{\mathrm{imp}}^{-1}-\mathrm{i}\omega}\frac{snv_{\mathrm{F}}^{2}}{\epsilon+P}-\frac{\sigma_{\mathrm{Q}}}{\mathrm{e}}\frac{\mu}{T}+\delta\alpha\left(\Delta,\omega,\mu\right)\right]\ ,$$

$$\bar{\kappa}^{ij}(\omega;\mu,\Delta)=\delta^{ij}\left[\frac{1}{\tau_{\mathrm{imp}}^{-1}-\mathrm{i}\omega}\frac{s^{2}Tv_{\mathrm{F}}^{2}}{\epsilon+P}+\frac{\sigma_{\mathrm{Q}}}{\mathrm{e}^{2}}\frac{\mu^{2}}{T}+\delta\kappa\left(\Delta,\omega,\mu\right)\right]\ ,$$

where $\delta\sigma,\delta\alpha,\delta\kappa=\mathcal{O}(\Delta/\alpha^{2})$. The first terms in all these formulas represent the so-called Drude peak which is proportional to the charge- or entropy density. In the DC limit $\omega\to 0$, its upper bound is set by the impurity mean free path. The second terms originate from the quantum critical conductivity and dominate the zero density response. With an increasing charge density n or impurity scattering time τ_{imp} these terms become less and less relevant, as they are associated to relativistic physics.

Equation (4.248) in particular allows us to derive graphene's so-called Lorenz ratio $\mathcal{L}$ in the hydrodynamic regime

$$\mathcal{L}\equiv\frac{\kappa^{11}(\omega=0)}{T\sigma^{11}(\omega=0)},\quad\text{where}\quad\kappa^{ij}=\bar{\kappa}^{ij}-T\alpha^{ik}\sigma_{kl}^{-1}\alpha^{lj} \tag{4.249}$$

is the electric contribution to the thermal conductivity. The latter tensor is defined as the proportionality between the heat current and the thermal gradient at zero charge current,

$$\mathbf{Q} = -\hat{\kappa}\boldsymbol{\nabla}T\big|_{\mathbf{J}=0} \,. \tag{4.250}$$

The particular form of $\hat{\kappa}$ is determined by Eq. (4.248). In the DC limit, one finds

$$\kappa^{ij}(\omega=0) = \delta^{ij}\frac{v_{\mathrm{F}}^2(\epsilon+P)\tau_{\mathrm{imp}}}{T}\frac{\sigma_{\mathrm{Q}}(\omega=0)}{\sigma^{11}(\omega=0)} \,, \tag{4.251}$$

which implies the hydrodynamic Lorentz ratio

$$\mathcal{L} = \frac{\mathcal{L}_{\mathrm{DF}}}{\left[1+\left(\dfrac{n}{n_0}\right)^2\right]^2} \quad \text{with} \quad \mathcal{L}_{\mathrm{DF}} = \frac{v_{\mathrm{F}}^2(\epsilon+P)\tau_{\mathrm{imp}}}{T^2\sigma_{\mathrm{Q}}} \quad \text{and} \quad n_0^2 = \frac{(\epsilon+P)\sigma_{\mathrm{Q}}}{\mathrm{e}^2 v_{\mathrm{F}}^2\tau_{\mathrm{imp}}} \,. \tag{4.252}$$

In weakly interacting electron systems in which impurity or phonon scattering dominates, e.g. in non-hydrodynamic Fermi liquid transport, this ratio is predicted to satisfy the Wiedemann-Franz law [98, 217–219]:

$$\mathcal{L} = \mathcal{L}_{\mathrm{WF}} = \frac{\pi^2}{3}\left(\frac{\mathrm{k_B}}{\mathrm{e}}\right)^2 = 2.44\times10^{-8}\ \mathrm{W\Omega K^{-2}} \,. \tag{4.253}$$

The Wiedemann-Franz law predicts that the electric contribution to the longitudinal thermal conductivity is directly proportional to the longitudinal electrical conductivity. This originates from the fact that in such systems the charge- and thermal relaxation times are directly proportional to each other, since electron-electron scattering processes are subleading in these materials. However, once these interactions become relevant, they differently effect the charge- and thermal relaxation time, such that the Wiedemann-Franz law gets violated [213]. By definition, this effect is expected to be large in the hydrodynamic regime in which τ_{ee} is the most relevant time-scale. Equation (4.252) clearly encodes this breakdown. In the zero density limit, the Lorentz ratio diverges as $\tau_{\mathrm{imp}} \to \infty$. This property originates from the fact that the longitudinal conductivity approximates a finite value at charge neutrality, $\sigma^{11} \to \sigma_{\mathrm{Q}}$, whereas κ^{11} diverges as $\tau_{\mathrm{imp}} \to \infty$ and $n \to 0$. In the large density limit, the Lorentz ratio tends to zero. This results from the fact that for $n \to \infty$ charge as well as heat transport are both mediated via local momentum densities [80]. Initially, the experimental evidence of both of these effects has been observed in Reference [208].

For the sake of completeness, we briefly review these experimental findings in the following. The authors of Ref. [208] measured the normalized Lorentz ration $\mathcal{R} \equiv \mathcal{L}/\mathcal{L}_{\mathrm{WF}}$ as a function of the induced charge density n and the temperature T in the three different graphene monolayers which are characterized in Tab. 4.5. The residual density at charge neutrality, $n_{\mathrm{min}}(T)$, originates from spatial fluctuations of the chemical potential caused by charged impurities in the hexagonal boron nitride substrate [cf. Eq. (4.236)]. The presence of these charge puddles sets an lower temperature boundary for measuring characteristics of the hydrodynamic Dirac fluid regime, as it will be explained in the following.

Figure 4.13 illustrates the experimental result for the graphene monolayer ML1. While dark blue values encode $\mathcal{R} \lesssim 2$, close to the charge neutrality point for charge densities $|n| < n_{\mathrm{min}}(T)$ and for moderate temperatures $T_{\mathrm{dis}} < T < T_{\mathrm{ph}}$, one can observe an order of magnitude deviation from the Wiedemann-Franz law.
For temperatures smaller than the disorder temperature T_{dis} the underlying charge puddles

Graphene Layer	L [μm]	W [μm]	μ_{mobility} [$10^5\text{cm}^2\text{V}^{-1}\text{s}^{-1}$]	$n_{\text{min}}(T=0)$ [10^9cm^{-2}]
ML1	3	9	3	5
ML2	3	9	2.5	8
ML3	4	10.5	0.8	10

Table 4.5: Length L, width W, mobility μ_{mobility}, and residual density $n_{\text{min}}(T=0)$ of the three graphene monolayers which are studied in the Reference [208].

prohibit the formation of a Dirac fluid phase. In particular, the local chemical potential fluctuations $\mu_{\text{dis}}(\mathbf{r})$ do not satisfy $|\mu_{\text{dis}}(\mathbf{r})|/(\text{k}_\text{B}T) \ll 1$ for $T < T_{\text{dis}}$, which sets a lower temperature boundary for the observation of Dirac fluid physics. For the graphene monolayer ML1, the disorder temperature $T_{\text{dis}} \approx 40\text{K}$. For temperatures above the phonon temperature T_{ph} the electron-phonon mean free path becomes comparable to the electron-electron scattering length. In this case, momentum-relaxing phonon scattering processes lead to a breakdown of the hydrodynamic regime. In the graphene monolayer ML1, the phonon temperature $T_{\text{ph}} \approx 80\text{K}$.

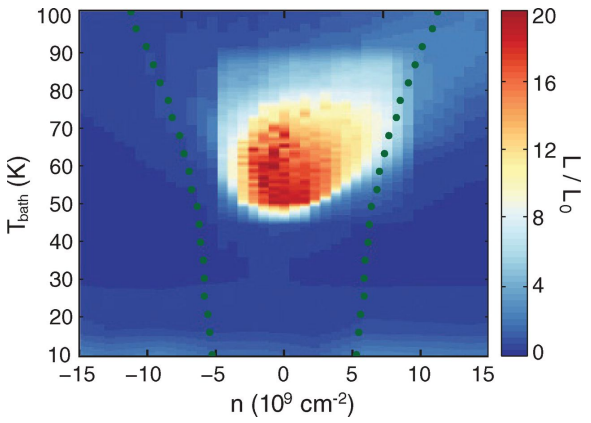

Figure 4.13: Breakdown of the Wiedemann-Franz law in a graphene monolayer [ML1, cf. Tab. 4.5]. The Lorentz ratio $\mathcal{L}$ is measured as a function of the temperature $T = T_{\text{bath}}$ and the charge density n. The data are normalized to the expected Wiedemann-Franz value $\mathcal{L}_{\text{WF}} = \mathcal{L}_0$ in the Fermi liquid regime. Close to the charge neutrality point for $|n| < n_{\text{min}}(T)$ (green dots) and for intermediate temperatures $T_{\text{dis}} < T < T_{\text{ph}}$, the Wiedemann-Franz law is violated by an order of magnitude due to the formation of a hydrodynamic Dirac fluid [cf. Eq. (4.252)]. Further explanations are given in the text. The figure is reprinted from Ref. [208] with permission from the AAAS.

The largest deviation from the Wiedemann-Franz value $\mathcal{R}_{\text{WF}} = 1$ in the graphene monolayer ML1 is measured at $n = 0$ and $T \approx 55\text{K}$, namely $\mathcal{R} = 22$. With increasing charge density $|n|$ the Lorentz ratio decreases as it is predicted by Eq. (4.252). This scaling becomes even more apparent in Fig. 4.14, which illustrates $\mathcal{R}$ as a function of n at $T = 60\text{K}$ for the three graphene monolayers ML1 (blue), ML2 (red), and ML3 (green). While dots indicate measured values, the dashed lines correspond to theoretical fits, which are based on Eq. (4.252). Within the hydrodynamic Dirac fluid regime, the theoretical curves perfectly match the experimental data. Since ML1 has the highest mobility [cf. Tab. 4.5] it manifests the strongest deviation from the Wiedemann-Franz law. However, for large $|n|$ the theoretical fits strongly differ from the

experimental data. Equation (4.252) predicts that in the hydrodynamic Fermi liquid regime $\mathcal{R} \to 0$, whereas the experimental data approximate the Wiedemann-Franz value $\mathcal{R}_{\mathrm{WF}} = 1$. This difference results from the fact that the hydrodynamic assumptions break down with increasing density. However, in the cleanest sample ML1 one can clearly observe that the normalized Lorentz ratio approximates $\mathcal{R} = 0$ with increasing density, before it eventually raises again and approximates $\mathcal{R}_{\mathrm{WF}} = 1$ in the non-hydrodynamic regime.

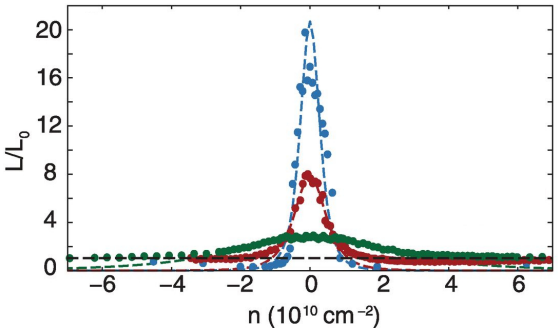

Figure 4.14: Scaling of the Lorentz ratio $\mathcal{L}$ as a function of the charge density n at $T = 60$K for the three graphene monolayers ML1 (blue), ML2 (red), and ML3 (green) [cf. Tab. 4.5]. All values are normalized to the expected Wiedemann-Franz value in the Fermi liquid regime $\mathcal{L}_{\mathrm{WF}} = \mathcal{L}_0$. Dots indicate measured data, dashed curves correspond to theoretical fits, which are based on Eq. (4.252). While in the Dirac fluid regime close to charge neutrality the hydrodynamic theory applies, it strongly deviates in the non-hydrodynamic large density limit. Further explanations are given in the text. The figure is reprinted from Ref. [208] with permission from the AAAS.

As we have mentioned, Eq. (4.248) only encodes the local thermo-electric transport functions at $k = 0$ and neglects $\mathcal{O}(k^2)$ corrections, originating from the viscous transport coefficients in the hydrodynamic expansion [85, 195, 220]. In what follows, we are going to analyze these coefficients in the context of kinetic theory.

Shear-, Bulk-, and Hall Viscosities We start our discussion of the viscous transport coefficients with the shear viscosity η, conceptually introduced in Sec. 4.1.3. In the framework of a kinetic Boltzmann theory and a random phase approximation, this dissipative transport coefficient in the screened Fermi liquid regime is predicted to have the following form [207, 216]:

$$\eta_{\mathrm{FL}} \approx \frac{n\mu}{4}\tau_{2,\mathrm{ee}} = \frac{3}{128\pi^2\hbar v_{\mathrm{F}}^2\,\alpha^2\,(\ln[\alpha^{-1}] - \delta_2)}\frac{\mu^4}{(\mathrm{k_B}T)^2}\ , \tag{4.254}$$

where $\tau_{2,\mathrm{ee}}$ is graphene's transverse momentum relaxation time in the Fermi liquid regime [cf. Sec. 4.1.3]

$$\tau_{2,\mathrm{ee}} = \frac{3\hbar\mu}{32\pi(\mathrm{k_B}T)^2\alpha^2(\ln[\alpha^{-1}] - \delta_2)} \tag{4.255}$$

and $\delta_2 \approx 2.44$. In the Dirac fluid phase where screening effects effectively vanish, the shear viscosity is instead given by [207, 221]

$$\eta_{\mathrm{DF}} \approx 0.45 \times \frac{(\mathrm{k_B}T)^2}{\hbar v_{\mathrm{F}}^2\alpha^2}\ . \tag{4.256}$$

In contrast to the shear viscosity, the bulk viscosity [cf. Sec. 4.1.3] in graphene vanishes at low energies as a consequence of the scale invariance of the relativistic massless Dirac spectrum [216]

$$\zeta = 0 \ . \tag{4.257}$$

Last but not least, the parity-odd Hall viscosity which we introduced in Sec. 4.1.3 vanishes in low-energy graphene due to its parity-even gapless Dirac dispersion. This effect is in particular independent of the chemical potential and the temperature. As an out-of-plane magnetic field B breaks the parity symmetry, applying such a field allows for a non-zero Hall viscosity. In particular, in the Fermi liquid regime, the shear- and Hall viscosities [cf. Eq. (4.254)] renormalize to [207]

$$\eta_{\mathrm{FL}}(B) = \frac{\eta_{\mathrm{FL}}(B=0)}{1+\Gamma_B^2} \quad \wedge \quad \eta_{\mathrm{H,FL}}(B) = \frac{\Gamma_B}{1+\Gamma_B^2}\,\eta_{\mathrm{FL}}(B=0) \ , \tag{4.258}$$

where

$$\Gamma_B = 2\omega_{B,\mathrm{FL}}\tau_{2,\mathrm{ee}} \qquad \wedge \qquad \omega_{B,\mathrm{FL}} = \frac{\mathrm{e}v_{\mathrm{F}}^2 B}{|\mu|} \ . \tag{4.259}$$

Notice that these formulas have the same form than the ones which apply for two-dimensional electron gases in Eq. (4.159). The only difference is that the classical cyclotron frequency of quasi-free massive particles is replaced by its corresponding value in graphene, Eq. (4.238), which takes into account the massless Dirac dispersion. Since in the Fermi liquid regime graphene is essentially described by semi-classical single band physics [cf. Fig. 4.11], the correspondence to Eq. (4.159) does not come as a surprise. This analogy does not hold it the Dirac fluid regime, in which the relativistic effects of the linear dispersion in low-energy graphene become most relevant. Exactly at the charge neutrality point, the electron-hole symmetry implies two unique features: (*i*) Even in external out-of-plane magnetic fields the Hall viscosity $\eta_{\mathrm{H}} \propto \mathrm{sgn}(\mathrm{e}B)$ remains zero, as the Hall viscous force in magnetic fields accelerates the thermally excited electrons and holes in different directions [cf. Eq.(4.116)]. Due to the electron-hole symmetry at $n = 0$ there is no net Hall viscous effect. (*ii*) The same symmetry implies that the shear viscosity approximates a non-zero constant value in strong classical magnetic fields B_{CS}, after initially decreasing. In particular, one obtains

$$\eta(B, \mu = 0) = \frac{(\mathrm{k_B}T)^2}{\hbar v_{\mathrm{F}}^2 \alpha^2} \frac{\mathcal{B} + \mathcal{B}_1 \omega_{B,\mathrm{DF}}^2}{1 + \mathcal{B}_2 \omega_{B,\mathrm{DF}}^2} \quad \wedge \quad \omega_{B,\mathrm{DF}} = \frac{\mathrm{e}v_{\mathrm{F}}^2 B}{\alpha^2 (\mathrm{k_B}T)^2} \tag{4.260}$$

with $\mathcal{B} \approx 0.45$, $\mathcal{B}_1 \approx 0.0037$, $\mathcal{B}_2 \approx 0.0274$ and

$$\lim_{B \to B_{\mathrm{CS}}} \eta(B, \mu = 0) = \frac{\mathcal{B}_1}{\mathcal{B}\mathcal{B}_2} \eta(B = 0, \mu = 0) \approx 0.31\, \eta(B = 0, \mu = 0) \ . \tag{4.261}$$

For chemical potentials above $\mu = 0$ but below the Fermi liquid regime, the shear- as well as the Hall viscosity can not be derived in a closed analytic form. Instead, these quantities need to be calculated numerically by solving the corresponding expressions (B1a) and (B1b) in Ref. [207].

In Eq. (4.229), we have shown that as a consequence of the RG flow in graphene, the Fermi velocity v_{F} is a chemical potential and temperature dependent quantity. In all of the expressions above, this scaling is implicitly included.

4.2 Hall Voltage in Two-Dimensional Fermi Liquids

In Sec. 4.1 we have discussed the theory of hydrodynamic charge transport in 2+1 space-time dimensions. Based on these principles, I published the manuscript *Functional dependence of Hall viscosity induced transverse voltage in two-dimensional Fermi liquids* (Phys. Rev. B **101**, 045423) in January 2020 [P2]. It is the goal of the present section to discuss the theoretical findings associated to this work, which have been obtained in strong collaboration with Ioannis Matthaiakakis and Dr. David Rodríguez Fernández (shared first-authorship)[a]. While all analytic derivations have been obtained by Ioannis Matthaiakakis and myself, Dr. David Rodríguez Fernández provided numerical results to supplement our theoretical findings and to extend our results beyond the weak magnetic field regime where a closed analytic consideration can not be derived in the framework of perturbation theory.

As we have discussed in Sec. 4.1.4, the idea of describing electrons in solid state systems via hydrodynamics goes back to the discovery of the Gurzhi effect in (Al)GaAs quantum wires [77–79]. Recently, hydrodynamic transport has received renewed attention due to the accessibility of the hydrodynamic regime in modern materials [80–83]. In Sec. 4.1.5, we have for instance discussed graphene's hydrodynamic transport theory in both, the Fermi liquid as well as the Dirac fluid regime [90–92]. In particular, two-dimensional systems that violate parity invariance are of special interest, since they exhibit novel non-dissipative hydrodynamic transport coefficients, such as the Hall viscosity η_{H} introduced in Sec. 4.1.3 [84–89]. Recent experiments in graphene have shown that η_{H} may be of the same order of magnitude as the shear viscosity η and therefore is expected to significantly affect the fluid transport [93]. However, current theoretical and experimental works [94–97] do not provide a quantitative answer to the functional dependency of Hall viscous effects on all parameters describing the system, including a finite slip length l_{s} [cf. Sec 4.1.3] and impurity length l_{imp} [cf. Sec 4.1.1].

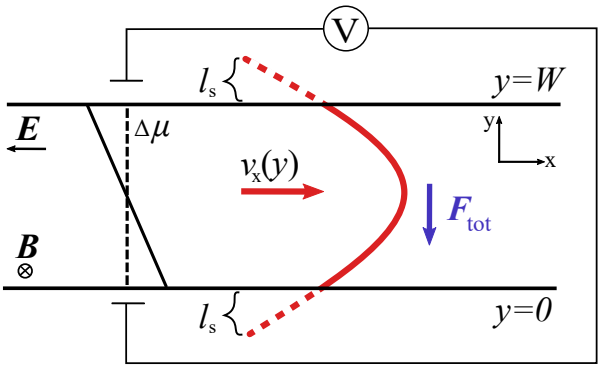

Figure 4.15: Setup to distinguish Hall viscous from Lorentz force contributions to the total Hall voltage. The red curve shows the hydrodynamic velocity profile $v_{\mathrm{x}}(y)$ in a channel of length L and width $W \ll L$ in presence of an electric field $\mathbf{E}$ and an out-of-plane magnetic field $\mathbf{B}$. Momentum transfer to the boundaries, captured by the slip length l_{s}, is shown by the red dashed curve. The total Hall force $\mathbf{F}_{\mathrm{tot}}$ induces a transverse pressure gradient, giving rise to a gradient in the chemical potential $\Delta\mu$, illustrated (initially) by the (dashed) black line. The figure is reprinted from Ref. [P2] with permission from the APS.

To address this open issue, we derived the Hall viscous contribution $\Delta V_{\eta_{\mathrm{H}}}$ to the total Hall voltage $\Delta V_{\mathrm{tot}} = \Delta V_{\eta_{\mathrm{H}}} + \Delta V_B$ measured across the two-dimensional channel shown in Fig. 4.15,

[a] This work has been supervised by Prof. Dr. Ewelina M. Hankiewicz, Prof. Dr. Johanna Erdmenger, and Dr. René Meyer.

in the hydrodynamic regime. Here, ΔV_B is the Lorentz force contribution. Up to first order in the electric field, we calculate the complete functional dependency of $\Delta V_{\eta_\mathrm{H}}$ and ΔV_B on all external parameters as a function of the transverse channel coordinate. In particular, we evaluate the dependence of both voltage contributions on l_imp, l_s, the wire width W, the equilibrium carrier density n_0 as well as on the magnetic field B. This allows to distinguish $\Delta V_{\eta_\mathrm{H}}$ from ΔV_B via measurements on two-dimensional Hall setups with varying W and n_0.

Most remarkably, we derive that the two voltage contributions differ in sign and that the ratio $|\Delta V_{\eta_\mathrm{H}}|/|\Delta V_B|$ decreases with increasing $|B|$. Hence, the total Hall voltage cancels at a certain critical magnetic field B_c, which is a smoking gun feature of Hall viscous transport. Additionally, we show that local measurements of the Hall voltage are suitable to identify the Hall viscosity. In particular, we analytically derive the parabolic form in the transverse channel coordinate of the total Hall electric field, as was recently measured in Ref. [97]. While the curvature of this parabola is mainly defined by the Lorentz contribution, its offset is explicitly characterized by $\Delta V_{\eta_\mathrm{H}}$ and hence by the Hall viscosity. For both, weak and strong magnetic fields as well as for clean systems our approach is analytical, whereas for intermediate field regimes we numerically solve the non-relativistic Navier-Stokes equations, derived in Eq. (4.98)[a]. In particular, we demonstrate that ΔV_B is proportional to the velocity profile integrated over the channel width, and therefore proportional to the total fluid momentum. In contrast, $\Delta V_{\eta_\mathrm{H}}$ exclusively depends on the gradient of the velocity profile at the boundaries of the system. Based on this, we analytically prove that for small fields and clean systems with Poiseuille-like (parabolic) velocity profile the ratio $\Delta V_{\eta_\mathrm{H}}/\Delta V_B$ is determined completely by the interplay of length scales defining the system [cf. Sec. 4.1.1]. While the modulus of this ratio increases with the transverse electron-electron mean free path l_ee, it decreases with W, l_s and l_imp. Since l_ee and l_imp are density dependent, the ratio acquires a density dependence, as well. In the absence of impurities $\Delta V_{\eta_\mathrm{H}}/\Delta V_B = \mathcal{O}(n_0^3)$, whereas for weak impurity strength there exists an additional $\mathcal{O}(n_0^2)$ contribution. Hence, it is possible to achieve $|\Delta V_{\eta_\mathrm{H}}|/|\Delta V_B| > 1$ by tuning the width and density of the sample. For $n_0 = 9.1\times10^{11}\mathrm{cm}^{-1}$ and $W = 3\mu\mathrm{m}$, such a regime is for instance realized in GaAs for $|B| \leq 20\mathrm{mT}$. Beyond the weak field limit, we show that increasing $|B|$ strongly reduces $|\Delta V_{\eta_\mathrm{H}}|/|\Delta V_B|$, due to the suppression of η and η_H by the magnetic field, which we have shown in Sec. 4.1.4. For large magnetic fields, for example in GaAs for $|B| \gtrsim 0.5\mathrm{T}$, impurities dominate the transport, which causes an Ohmic (flat) fluid profile with vanishing $\Delta V_{\eta_\mathrm{H}}/\Delta V_B$. The critical field $|B_\mathrm{c}|$, at which $\Delta V_{\eta_\mathrm{H}}/\Delta V_B = -1$ and the total Hall voltage $\Delta V_\mathrm{tot} = 0$, increases with decreasing $W, l_\mathrm{s}, l_\mathrm{imp}$ and l_ee^{-1}. In particular, for GaAs we find $|B_\mathrm{c}| \simeq \mathcal{O}(10\mathrm{mT})$, which makes our predictions experimentally verifiable.

4.2.1 Model & Equations of Motion

We are going to derive these predictions in the following. Therefore, we analyze the hydrodynamic flow of non-relativistic electrons along the two-dimensional channel geometry in Fig. 4.15 under the combined influence of a DC electric field $\mathbf{E} = -E_\mathrm{x}\mathbf{e}_\mathrm{x}$ and an out-of-plane magnetic field $\mathbf{B} = -B\mathbf{e}_\mathrm{z}$[b]. To justify our hydrodynamic approach, we assume that l_ee is the shortest length scale in our system [182]. In particular, it is smaller than the cyclotron radius $r_\mathrm{c} = m^* v_\mathrm{F}/|\mathrm{e}B|$ [cf. Sec. 4.1.1], which is defined in terms of the effective electron mass m^*, the electron charge $\mathrm{e} < 0$ and the Fermi velocity v_F [cf. Sec. 4.1.4]. Additionally, we assume that our system is incompressible and has translational invariance in longitudinal, as well as vanishing current in transversal direction.

[a] The definition of weak, intermediate and strong magnetic fields in terms of the Gurzhi length is given below.

[b] In what follows, we assume that the screening length in our material is much shorter than the width of our channel. Hence, the electric field sourced by the redistribution of charge carriers can be neglected.

For this ansatz, the equations of motion are defined by the non-relativistic Navier-Stokes equations which we derived in Eq. (4.98). For incompressible two-dimensional Fermi liquids with $\sigma_{\mathrm{Q}} = \sigma_{\mathrm{QAH}} = 0$, these equations are, in the presence of impurity scattering [cf. Eq. (4.31)], in particular given by[a] [222–224]

$$(\partial_{\mathrm{t}} + \mathbf{v}\cdot\nabla)\, n = -n\nabla\cdot\mathbf{v}, \tag{4.262}$$

$$\begin{aligned} m^* n\,(\partial_{\mathrm{t}} + \mathbf{v}\cdot\nabla)\,\mathbf{v} &= -\nabla p + \eta\nabla^2\mathbf{v} + \eta_{\mathrm{H}}\nabla^2(\mathbf{v}\times\mathbf{e}_{\mathrm{z}}) \\ &\quad + en(\mathbf{E} + \mathbf{v}\times\mathbf{B}) - \frac{n_0 v_{\mathrm{F}} m^*}{l_{\mathrm{imp}}}\mathbf{v}, \end{aligned} \tag{4.263}$$

in the framework of linear response theory. In our analysis, we consider a steady, hydrodynamic flow of electrons, which is translationally invariant along the $\mathbf{e}_{\mathrm{x}}$-direction [cf. Fig. 4.15]. Moreover, we assume a vanishing current in the $\mathbf{e}_{\mathrm{y}}$-direction, implying that the velocity profile takes the form $\mathbf{v} = v_{\mathrm{x}}(y)\mathbf{e}_{\mathrm{x}}$. To obtain an inhomogeneous, non-trivial velocity profile, our system needs to deviate from global thermal equilibrium. In order to be able to linearize Eqs. (4.262) and (4.263), we assume that variations of the chemical potential and the temperature are small compared to their global equilibrium values

$$\begin{aligned} \mu(y) &= \mu_0 + \Delta\mu(y) \quad \text{with} \quad \Delta\mu(y) \ll \mu_0\ , \\ T(y) &= T_0 + \Delta T(y) \quad \text{with} \quad \Delta T(y) \ll T_0\ . \end{aligned} \tag{4.264}$$

For typical Fermi liquids, such as GaAs, $\mu_0 = \mathcal{O}(50\mathrm{meV})$ whereas $T_0 = \mathcal{O}(1\mathrm{K})$. Notice, that due to time- and translational invariance in $\mathbf{e}_{\mathrm{x}}$-direction, $\Delta\mu$ and ΔT solely vary in the $\mathbf{e}_{\mathrm{y}}$-direction. In addition, for $T_0 = \mathcal{O}(1\mathrm{K})$ the pressure and density fluctuations in our system are given in terms of $\mu(y)$ and $T(y)$ by

$$\begin{aligned} n(y) &= n_0 + \frac{\partial n_0}{\partial\mu_0}\Delta\mu + \frac{\partial n_0}{\partial T_0}\Delta T\,, \\ p(y) &= p_0 + \frac{\partial p_0}{\partial\mu_0}\Delta\mu + \frac{\partial p_0}{\partial T}\Delta T = p_0 + n_0\Delta\mu + s_0\Delta T\,, \end{aligned} \tag{4.265}$$

where s_0 is the equilibrium entropy of our fluid. Under the assumption of a steady and unidirectional fluid flow with $v_{\mathrm{y}} = 0$, Eq. (4.262) reduces to $\partial_{\mathrm{x}} n = 0$. This enforces a constant density along the fluid flow, whereas it allows for density fluctuations in $\mathbf{e}_{\mathrm{y}}$-direction. Explicitly, that is compatible with our incompressibility condition $\nabla\cdot\mathbf{v} = 0$. Together, Eqs. (4.262)-(4.265) dictate the dynamics of $v_{\mathrm{x}}(y)$, $\Delta\mu(y)$ and $\Delta T(y)$. For our system the gradient of the temperature is negligible compared to the gradient of the chemical potential. To see this explicitly, we write

$$\partial_{\mathrm{y}} p = n_0\mu_0\partial_{\mathrm{y}}\left(\frac{\Delta\mu}{\mu_0}\right) + s_0 T_0\partial_{\mathrm{y}}\left(\frac{\Delta T}{T_0}\right)\ . \tag{4.266}$$

Due to the assumptions in Eq. (4.264), the dimensionless gradients $\partial_{\mathrm{y}}(\Delta\mu/\mu_0)$ and $\partial_{\mathrm{y}}(\Delta T/T_0)$ are of the same order of magnitude. As a consequence, the relative strength of the chemical potential contribution to the temperature contribution in Eq. (4.266) is given by $\mathcal{U} = n_0\mu_0/s_0T_0$. If $\mathcal{U} \gg 1$, the chemical potential gradient dominates over temperature fluctuations and vice versa. For typical Fermi liquids at $T = \mathcal{O}(1\mathrm{K})$, such as GaAs, we find $\mathcal{U} \simeq 10^{16}$. Hence, in those samples the gradient of temperature is clearly negligible. Thus, we assume $T(y) = T_0$

[a] The charge conservation equation $\partial_{\mathrm{t}} n + \nabla\cdot(n\mathbf{v}) = 0$, derived in Eq. (4.97), is trivially satisfied due to our assumption of a steady and translational invariant flow $\mathbf{v} = v_{\mathrm{x}}(y)\mathbf{e}_{\mathrm{x}}$. In addition, since we restrict ourselves to $T = \mathcal{O}(1\mathrm{K})$, phonons are negligible in our approach [77–79].

and define

$$n(y) = n_0 + \frac{\partial n_0}{\partial \mu_0}\Delta\mu(y) \ \wedge \ p(y) = p_0 + n_0\Delta\mu(y) \ . \tag{4.267}$$

Substituting this into Eq. (4.263), leads to

$$\eta\partial_{\mathrm{y}}^2 v_{\mathrm{x}}(y) = \left(n_0 + \frac{\partial n_0}{\partial \mu}\Delta\mu\right)\left(\mathrm{e}E_{\mathrm{x}} + \frac{v_{\mathrm{F}}m^*}{l_{\mathrm{imp}}}v_{\mathrm{x}}(y)\right), \tag{4.268}$$

$$\partial_{\mathrm{y}} p = \left[\mathrm{e}B\left(n_0 + \frac{\partial n_0}{\partial \mu}\Delta\mu\right) - \eta_{\mathrm{H}}\partial_{\mathrm{y}}^2\right] v_{\mathrm{x}}(y) \ . \tag{4.269}$$

Notice, that Eqs. (4.268) and (4.269) contain terms which are proportional to $\Delta\mu(y)v_{\mathrm{x}}(y)$. These terms induce non-linear corrections to our observables in terms of the electric field E_{x}. In the framework of linear response theory, we are therefore allowed to drop them without loss of generality. In particular, this leads to

$$\eta\,\partial_{\mathrm{y}}^2\, v_{\mathrm{x}} = \mathrm{e}\left(n_0 + \frac{\partial n_0}{\partial \mu}\Delta\mu\right)E_{\mathrm{x}} + \frac{n_0 v_{\mathrm{F}}m^*}{l_{\mathrm{imp}}}v_{\mathrm{x}}(y) \ , \tag{4.270}$$

$$\partial_{\mathrm{y}}\, p \ = n_0\,\partial_{\mathrm{y}}\Delta\mu = \left(\mathrm{e}Bn_0 - \eta_{\mathrm{H}}\partial_{\mathrm{y}}^2\right) v_{\mathrm{x}}(y) \ . \tag{4.271}$$

Let us make some remarks concerning Eqs. (4.270) and (4.271).

First, we emphasize one more time that the incompressibility condition for our unidirectional fluid flow, $\nabla\cdot\mathbf{v} = 0$, solely implies a constant density along the $\mathbf{e}_{\mathrm{x}}$-direction. In particular, $v_{\mathrm{y}} = 0$ allows for density fluctuations satisfying $\partial_{\mathrm{y}} n \propto \partial_{\mathrm{y}}\Delta\mu \neq 0$.

Second, Eq. (4.270) contains a term $\propto \Delta\mu E_{\mathrm{x}}$, which in particular is higher order in the electromagnetic fields E_{x} as well as B. Therefore, it does not affect our linear response results, which we present in the following. However, we kept this term because we want to explicitly check that the Lorentz and the Hall-viscosity induced force influences the velocity profile in the expected way. Namely, we expect $v_{\mathrm{x}}(y)$ to deviate from its symmetric Poiseuille form, corresponding to a fluid flow which concentrates towards one of the sides of the channel, depending on the sign of the magnetic field. The simplest way to see this deviation is to take into account the $\Delta\mu E_{\mathrm{x}}$ term since it only couples to the first order correction of the velocity profile and decouples from the equations for $v_{\mathrm{x}}^0(y)$. We will rigorously prove this statement in Eqs. (4.279) and (4.292).

Third, we did not include the electric field sourced by the inhomogeneous density distribution resulting from Eqs. (4.270) and (4.271). This is justified, since the Thomas-Fermi screening length of our system is $\lambda_{\mathrm{TF}} \propto n_0^{-1/2} \simeq 0.01\ \mu$m [cf. Eq. (4.131)], which is about 100 times smaller than the width of our channel ($W \simeq 1\mu$m). Therefore, we expect the corresponding electric field to be effectively screened, and hence to be much smaller than E_{x} or $\partial_{\mathrm{y}}\Delta\mu/e$. This will be derived in the following.

In order to solve Eqs. (4.270) and (4.271) for the hydrodynamic variables, we supplement these differential equations with the general boundary conditions

$$v_{\mathrm{x}}(-l_{\mathrm{s}}) = v_{\mathrm{x}}(W+l_{\mathrm{s}}) = 0, \quad \Delta\mu\big|_{y=0} = -\Delta\mu\big|_{y=W} \ . \tag{4.272}$$

As it was discussed in Sec. 4.1.3, the slip length l_{s} characterizes the velocity profile at the boundaries of the system. This property is exemplary shown in Fig. 4.15. For $l_{\mathrm{s}} = 0$ the fluid flow is Poiseuille-like (parabolic), whereas $l_{\mathrm{s}} \to \infty$ defines the diffusive regime with a flat velocity profile $v_{\mathrm{x}}(y)$. Notice that we do not use standard Robin type boundary conditions to define the slip length in our system [197]. This relies on the fact that our set of boundary

conditions naturally describes the case of a finite drift velocity. However, in our channel geometry, Robin-type boundary conditions [197] are equivalent with our choice of boundary conditions, Eq. (4.272), as we will show in Sec. 4.2.4.

Let us close this section by emphasizing that in two space dimensions the dynamics of incompressible, non-relativistic fluids is entirely captured by the magnetic field dependent shear and Hall viscosities η and η_{H}, which have been introduced and discussed in Eq. (4.159) [86, 183]

$$\eta = \frac{\eta_0}{1+(2\,l_{\mathrm{ee}}/r_{\mathrm{c}})^2} \quad \wedge \quad \eta_{\mathrm{H}} = \frac{2\,\mathrm{sgn}(B)\,\eta_0\,l_{\mathrm{ee}}/r_{\mathrm{c}}}{1+(2\,l_{\mathrm{ee}}/r_{\mathrm{c}})^2}\,. \tag{4.273}$$

Here $\eta_0 = m^* n_0 v_{\mathrm{F}} l_{\mathrm{ee}}/4$ is the dynamic shear viscosity at zero magnetic field [cf. Eq. (4.156)]. The main goal of the following sections is to derive the total Hall voltage

$$\Delta V_{\mathrm{tot}} = -\int_0^W dy\; \partial_{\mathrm{y}} \Delta\mu/e = -\left(\Delta\mu(W) - \Delta\mu(0)\right)/\mathrm{e} \tag{4.274}$$

up to first order in E_{x}, and to separate Hall viscous from Lorentz force contributions therein.

4.2.2 The Global Hall Voltage

The total Hall voltage $\Delta V_{\mathrm{tot}} = \Delta V_{\eta_{\mathrm{H}}} + \Delta V_B$ consists of two different terms, namely the Hall viscous- and the Lorentz force contributions. To analytically derive the functional dependence of these building blocks, we first restrict ourselves to weak magnetic fields, defined by $l_{\mathrm{G}}/r_{\mathrm{c}} \ll 1$. The Gurzhi length $l_{\mathrm{G}} = \sqrt{l_{\mathrm{imp}}\eta/(n_0 m^* v_{\mathrm{F}})}$ quantifies the relative strength of impurity to shear effects. While the flow is Poiseuille-like for $l_{\mathrm{G}}/W \gg 1$, it becomes Ohmic for $l_{\mathrm{G}}/W \ll 1$.

Analytic Solutions in the Weak Magnetic Field Regime In what follows, we provide an explicit solution of the Navier-Stokes Eqs. (4.270)-(4.271) under the boundary condition (4.272) in the weak magnetic field limit $r_{\mathrm{c}} \gg l_{\mathrm{G}}$. The assumption of weak magnetic fields allows us to expand the velocity profile and hence the Navier-Stokes equations in powers of B. Technically, this expansion is achieved by introducing the dimensionless parameter ϵ, satisfying

$$B \to \epsilon B,\; \eta_{\mathrm{H}} \to \epsilon\eta_{\mathrm{H}},\; \Delta\mu \to \epsilon\Delta\mu\,,\; v_{\mathrm{x}} = v_{\mathrm{x}}^0 + \epsilon v_{\mathrm{x}}^1. \tag{4.275}$$

In particular, this assumes that to first order the system responds linearly in terms of the magnetic field. With this ansatz the Navier-Stokes Eqs. (4.270)-(4.271) reduce to[a]

$$\eta\partial_{\mathrm{y}}^2 v_{\mathrm{x}}^0(y) - \frac{m^* v_{\mathrm{F}} n_0}{l_{\mathrm{imp}}} v_{\mathrm{x}}^0(y) = \mathrm{e}n_0 E_{\mathrm{x}}\,, \tag{4.276}$$

$$\left(\mathrm{e}Bn_0 - \eta_{\mathrm{H}}\partial_{\mathrm{y}}^2\right) v_{\mathrm{x}}^0(y) = n_0 \partial_{\mathrm{y}}\Delta\mu(y)\,, \tag{4.277}$$

$$\eta\partial_{\mathrm{y}}^2 v_{\mathrm{x}}^1(y) - \frac{m^* v_{\mathrm{F}} n_0}{l_{\mathrm{imp}}} v_{\mathrm{x}}^1(y) = \mathrm{e}E_{\mathrm{x}} \frac{\partial n_0}{\partial\mu}\Delta\mu(y)\,. \tag{4.278}$$

To find an explicit solution of this set of equations we first determine $v_{\mathrm{x}}^0(y)$ by solving Eq. (4.276), which is the zero-field Poiseuille flow equation in the presence of impurities. Once we have obtained $v_{\mathrm{x}}^0(y)$, we calculate $\Delta\mu(y)$ by integrating Eq. (4.277). Substituting

[a] Here, we assumed that the Hall viscosity is approximately constant for small fluctuations of the magnetic field.

this quantity in Eq. (4.278) finally allows us to derive the first order velocity correction $v_{\mathrm{x}}^{1}(y)$. Explicitly, we find

$$v_{\mathrm{x}}^{0}(y) = -\frac{\mathrm{e}E_{\mathrm{x}}l_{\mathrm{imp}}}{m^{*}v_{\mathrm{F}}}\Big(A_1\cosh\Big[yl_{\mathrm{G}}^{-1}\Big]+A_2\sinh\Big[yl_{\mathrm{G}}^{-1}\Big]+1\Big) \tag{4.279}$$

$$\begin{aligned}\Delta\mu(y) = \frac{\mathrm{e}\,l_{\mathrm{imp}}\,E_{\mathrm{x}}}{m^{*}v_{\mathrm{F}}}\Big[l_{\mathrm{G}}\Big(\frac{m^{*}v_{\mathrm{F}}\eta_{\mathrm{H}}}{\eta l_{\mathrm{imp}}}-\mathrm{e}B\Big) \\ \times\Big(A_1\sinh\Big[yl_{\mathrm{G}}^{-1}\Big]+A_2\cosh\Big[yl_{\mathrm{G}}^{-1}\Big]\Big)-\mathrm{e}By\Big]+\Gamma,\end{aligned} \tag{4.280}$$

where for clarity we defined

$$A_1 = -\cosh\left[\frac{W}{2l_{\mathrm{G}}}\right]\operatorname{sech}\left[\frac{2l_{\mathrm{s}}+W}{2l_{\mathrm{G}}}\right], \tag{4.281}$$

$$A_2 = \sinh\left[\frac{W}{2l_{\mathrm{G}}}\right]\operatorname{sech}\left[\frac{2l_{\mathrm{s}}+W}{2l_{\mathrm{G}}}\right].$$

$$\Gamma = -\frac{\mathrm{e}\,l_{\mathrm{imp}}E_{\mathrm{x}}}{2m^{*}v_{\mathrm{F}}}\Big[l_{\mathrm{G}}\Big(\frac{m^{*}v_{\mathrm{F}}\eta_{\mathrm{H}}}{\eta l_{\mathrm{imp}}}-\mathrm{e}B\Big)\Big(A_1\sinh\Big[Wl_{\mathrm{G}}^{-1}\Big]+A_2\Big[\cosh\Big[Wl_{\mathrm{G}}^{-1}\Big]+1\Big]\Big)-\mathrm{e}BW\Big]\,.$$

Before we explicitly present our result for $v_{\mathrm{x}}^{1}(y)$, let us emphasize that Eq. (4.280) predicts the total Hall voltage ΔV_{tot}, measured across the sample

$$\begin{aligned}\Delta V_{\mathrm{tot}} &= -\frac{\Delta\mu(W)-\Delta\mu(0)}{\mathrm{e}} \\ &= \frac{\mathrm{e}l_{\mathrm{imp}}E_{\mathrm{x}}}{m^{*}v_{\mathrm{F}}}\Big[l_{\mathrm{G}}\Big(\frac{m^{*}v_{\mathrm{F}}\eta_{\mathrm{H}}}{\mathrm{e}\eta l_{\mathrm{imp}}}-B\Big)\Big(A_1\sinh\Big(Wl_{\mathrm{G}}^{-1}\Big)+A_2\Big[\cosh\Big(Wl_{\mathrm{G}}^{-1}\Big)-1\Big]\Big)-BW\Big]\,.\end{aligned} \tag{4.282}$$

In the scope of our analysis, we are mainly interested in Poiseuille like velocity profiles which are dominanted by shear effects. Since such fluid flows correspond to $W/l_{\mathrm{G}} \ll 1$, we further Taylor expand the hyperbolic functions in Eq. (4.281) in terms of W/l_{G}. As a result, we find

$$\Delta V_{\eta_{\mathrm{H}}} = \frac{\eta_{\mathrm{H}}}{\eta}E_{\mathrm{x}}\left[W-\frac{1}{12l_{\mathrm{G}}^{2}}\left(W^{3}+6l_{\mathrm{s}}W^{2}+6l_{\mathrm{s}}^{2}W\right)\right], \tag{4.283}$$

$$\Delta V_{B} = -\frac{\mathrm{sgn}(B)\,E_{\mathrm{x}}}{3r_{\mathrm{c}}l_{\mathrm{ee}}}\left(W^{3}+6l_{\mathrm{s}}W^{2}+6l_{\mathrm{s}}^{2}W\right)\,. \tag{4.284}$$

For weak magnetic fields, this functional dependence implies the scaling

$$\frac{|\Delta V_{\eta_{\mathrm{H}}}|}{|\Delta V_{B}|} = \frac{l_{\mathrm{ee}}^{2}}{\frac{1}{6}W^{2}+l_{\mathrm{s}}W+l_{\mathrm{s}}^{2}}+2\frac{l_{\mathrm{ee}}}{l_{\mathrm{imp}}}\,. \tag{4.285}$$

Hence, for $l_{\mathrm{G}}/r_{\mathrm{c}} \ll 1$ and $W/l_{\mathrm{G}} \ll 1$, this ratio is completely determined by the characteristic length scales of the system. Its modulus decreases as a function of W, l_{s} and l_{imp}, whereas it increases with l_{ee}. While the hydrodynamic assumption $l_{\mathrm{ee}} \ll l_{\mathrm{imp}}$ strongly suppresses the second term in Eq. (4.285) [a], the first term experimentally can be much larger than one [90–92]. For very small l_{s} and W in comparison to l_{ee}, engineered e.g. in Ref. [225], the Hall viscous contribution can strongly dominate the Lorentz signal.

In addition, Eq. (4.283) provides the density dependence of each voltage contribution. For temperatures much smaller than the Fermi energy, we obtain the dependence [99, 226]

$$\Delta V_{\eta_{\mathrm{H}}} = f_1\,n_0 + f_2(n_{\mathrm{imp}}) \quad \wedge \quad \Delta V_{B} = f_3\,n_0^{-2}\,, \tag{4.286}$$

[a] In this limit, according to Eq. (4.283), $\Delta V_{\eta_{\mathrm{H}}}$ becomes insensitive to the form of the boundary conditions.

where n_{imp} is the impurity concentration and $f_{1,2,3}$ are density independent functions which will be derived in the next paragraph. Explicitly, Eq. (4.286) predicts

$$\frac{\Delta V_{\eta_{\mathrm{H}}}}{\Delta V_B} = \mathcal{O}_{\mathrm{clean}}(n_0^3) + \mathcal{O}_{\mathrm{imp}}(n_0^2) \ . \tag{4.287}$$

Hence, in the weak field limit and for $W/l_{\mathrm{G}} \ll 1$, the Hall viscous contribution becomes strongly enhanced in comparison to the Lorentz force signal as the carrier density increases.

So far, we did not specify the functions $f_{1,2,3}$. This will be the purpose of the following paragraph. The linear, impurity independent scaling of $\Delta V_{\eta_{\mathrm{H}}}$ is defined as the $l_{\mathrm{imp}} \to \infty$ limit of Eq. (4.283). The density dependence of this term is given by [cf. Eq. (4.273)]

$$\begin{aligned} \Delta V^0_{\eta_{\mathrm{H}}} &= \frac{\eta_{\mathrm{H}}}{\eta} E_{\mathrm{x}} W = \frac{2 l_{\mathrm{ee}} E_{\mathrm{x}} W}{\mathrm{sgn}(B) r_{\mathrm{c}}} = \frac{2 \tau_{\mathrm{ee}} E_{\mathrm{x}} W |\mathrm{e}| B}{m^*} \\ &= \frac{12 \hbar^3 E_{\mathrm{x}} W |\mathrm{e}| B}{F_\pi^2 (m^*)^2 k_{\mathrm{B}}^2 T^2} \ln^2\left(\frac{\hbar^2 \pi n_0}{m^* k_{\mathrm{B}} T}\right) n_0 = f_1 n_0 \ . \end{aligned} \tag{4.288}$$

Here, $\tau_{2,\mathrm{ee}}$ is the transverse momentum relaxation time which has been introduced and discussed in Eq. (4.157) [86, 199, 201, 226]

$$\tau_{\mathrm{ee}} = \frac{l_{\mathrm{ee}}}{v_{\mathrm{F}}} = \frac{6\hbar^3}{F_\pi^2 m^* k_{\mathrm{B}}^2 T^2} \ln^2\left(\frac{\hbar^2 \pi n_0}{m^* k_{\mathrm{B}} T}\right) n_0 \ , \tag{4.289}$$

where $\mathrm{k_B}$ is the Boltzmann constant and F_π is a geometric factor, characterizing electron-electron scattering amplitudes. Notice, that in comparison to Eq. (4.157) we neglected in Eq. (4.289) density independent contributions to $\tau_{2,\mathrm{ee}}$ which originate from static impurities or defects as we are considering the $l_{\mathrm{imp}} \to \infty$ limit in Eq. (4.288). Moreover, since density variations do not significantly change the $\ln^2(\mu/k_{\mathrm{B}}T)$ terms in the Fermi liquid regime $\mu \gg \mathrm{k_B}T$, we treat f_1 as a density independent function.

The dominant impurity contribution to $\Delta V_{\eta_{\mathrm{H}}}$ is given by

$$\begin{aligned} \Delta V^{\mathrm{imp}}_{\eta_{\mathrm{H}}} &= -\frac{\eta_{\mathrm{H}}}{\eta} E_{\mathrm{x}} \frac{1}{12 l_{\mathrm{G}}^2} \left(W^3 + 6 l_{\mathrm{s}} W^2 + 6 l_{\mathrm{s}}^2 W\right) \\ &= -\frac{|\mathrm{e}| B (m^*)^2 \nu_0^2 n_{\mathrm{imp}} E_{\mathrm{x}}}{3\hbar^5 \pi} \left(W^3 + 6 l_{\mathrm{s}} W^2 + 6 l_{\mathrm{s}}^2 W\right) = f_2 . \end{aligned} \tag{4.290}$$

Here, we considered point like impurities with concentration n_{imp}, scattering strength ν_0 and inverse momentum relaxation time $\tau_{\mathrm{imp}}^{-1} = v_{\mathrm{F}} l_{\mathrm{imp}}^{-1} = m^* \nu_0^2 \hbar^{-3} n_0 n_{\mathrm{imp}}$ [99]. In the same manner, Eq. (4.284) evolves to

$$\begin{aligned} \Delta V_B &= -\frac{\mathrm{sgn}(B) E_{\mathrm{x}}}{3 r_{\mathrm{c}} l_{\mathrm{ee}}} \left(W^3 + 6 l_{\mathrm{s}} W^2 + 6 l_{\mathrm{s}}^2 W\right) \\ &= -\frac{|\mathrm{e}| m^* B E_{\mathrm{x}}}{6\pi\hbar^2 n_0 \tau_{\mathrm{ee}}} \left(W^3 + 6 l_{\mathrm{s}} W^2 + 6 l_{\mathrm{s}}^2 W\right) = f_3 n_0^{-2} \ . \end{aligned} \tag{4.291}$$

After having clarified how to disentangle $\Delta V_{\eta_{\mathrm{H}}}$ and ΔV_B in terms of their width and density dependence, let us proceed in presenting our solution for $v_{\mathrm{x}}^1(y)$. Therefore, we substitute Eq. (4.280) into Eq. (4.278), which leads to the first order velocity correction

$$v_{\mathrm{x}}^1(y) = (C_1 + \lambda_1 y) \cosh\left[y l_{\mathrm{G}}^{-1}\right] + (C_2 + \lambda_2 y) \sinh\left[y l_{\mathrm{G}}^{-1}\right] - A_3 + A_4 y \ . \tag{4.292}$$

Here, for clarity, we defined the following functions

$$\lambda_{1,2} = \frac{\mathrm{e}^2 l_{\mathrm{imp}} E_{\mathrm{x}}^2 \frac{\partial n_0}{\partial \mu}}{2 m^* v_{\mathrm{F}}} \left(\mathrm{e}B - \frac{m^* v_{\mathrm{F}} \eta_{\mathrm{H}}}{l_{\mathrm{imp}}} \right) A_{2,1} \quad , \quad A_3 = \frac{\mathrm{e}\, l_{\mathrm{imp}} E_{\mathrm{x}} \frac{\partial n_0}{\partial \mu}}{m^* v_{\mathrm{F}} n_0} \Gamma \quad , \quad A_4 = \frac{\mathrm{e}^2 l_{\mathrm{imp}}^2 E_{\mathrm{x}} B}{(m^*)^2 v_{\mathrm{F}}^2 n_0} \ ,$$

$$\begin{aligned} C_1 = & \operatorname{csch}[(2l_{\mathrm{s}}+W) l_{\mathrm{G}}^{-1}] \Big(\sinh[(l_{\mathrm{s}}+W) l_{\mathrm{G}}^{-1}] \left[A_3 - l_{\mathrm{s}} \left(\lambda_2 \sinh[l_{\mathrm{s}} l_{\mathrm{G}}^{-1}] - \lambda_1 \cosh[l_{\mathrm{s}} l_{\mathrm{G}}^{-1}] - A_4 \right) \right] \\ & - \sinh[l_{\mathrm{s}} l_{\mathrm{G}}^{-1}] [(\lambda_2 l_{\mathrm{s}} - A_3 + W) \sinh[(l_{\mathrm{s}}+W) l_{\mathrm{G}}^{-1}] \\ & + \lambda_1 (l_{\mathrm{s}}+W) \cosh[(l_{\mathrm{s}}+W) l_{\mathrm{G}}^{-1}] + A_4 (l_{\mathrm{s}}+W)] \Big), \end{aligned} \tag{4.293}$$

$$\begin{aligned} C_2 = & - \operatorname{csch}[(2l_{\mathrm{s}}+W) l_{\mathrm{G}}^{-1}] \Big(2(A_4 W - A_3) \cosh[l_{\mathrm{s}} l_{\mathrm{G}}^{-1}] + 2A_3 \cosh[(l_{\mathrm{s}}+W) l_{\mathrm{G}}^{-1}] \\ & + \lambda_2 W \sinh[(2l_{\mathrm{s}}+W) l_{\mathrm{G}}^{-1}] + \sinh[W l_{\mathrm{G}}^{-1}] + \lambda_1 W \left[\cosh[(2l_{\mathrm{s}}+W) l_{\mathrm{G}}^{-1}] + \cosh[W l_{\mathrm{G}}^{-1}] \right] \\ & + 2l_{\mathrm{s}} \Big[\lambda_1 \left[\cosh[(2l_{\mathrm{s}}+W) l_{\mathrm{G}}^{-1}] + \cosh[W l_{\mathrm{G}}^{-1}] \right] \\ & + A_4 \left[\cosh[(l_{\mathrm{s}}+W) l_{\mathrm{G}}^{-1}] + \cosh[l_{\mathrm{s}} l_{\mathrm{G}}^{-1}] \right] + \lambda_2 \sinh[W l_{\mathrm{G}}^{-1}] \Big] \Big) / 2 \ . \end{aligned}$$

Notice, that for $\eta_{\mathrm{H}} \neq 0$, the first order correction $v_{\mathrm{x}}^1(y)$ breaks the reflection symmetry of the entire velocity profile with respect to $y = W/2$, as expected. Explicitly this is caused by the linear terms in powers of y within Eq. (4.292). Moreover, since $C_{1,2}$, $\lambda_{1,2}$ and $A_{1,2,3,4}$ are non-linear in E_{x} and l_{imp}, Eq. (4.292) implies that the first order correction $v_{\mathrm{x}}^1 \ll v_{\mathrm{x}}^0$ in the linear response regime.

Analytic Solutions in the Strong Magnetic Field Regime We now move on to the discussion of strong magnetic fields, implicitly defined by $r_{\mathrm{c}} \ll l_{\mathrm{G}}$. In this limit, η and η_{H} tend to zero [cf. Eq. (4.273)], which strongly simplifies Eqs. (4.270) and (4.271). In particular, these equations yield

$$v_{\mathrm{x}} = -\frac{\mathrm{e}\, l_{\mathrm{imp}} E_{\mathrm{x}}}{m^* v_{\mathrm{F}}} \quad \wedge \quad \partial_{\mathrm{y}} \Delta\mu = \mathrm{e}B v_{\mathrm{x}} \ . \tag{4.294}$$

Here, we dropped the term $\propto \Delta\mu\, E_{\mathrm{x}}$ to make explicit predictions for our linear response theory. In particular, the solution of Eq. (4.294) reads:

$$\Delta V_{\mathrm{tot}} = -\mathrm{sgn}(B) E_{\mathrm{x}} W l_{\mathrm{imp}} / r_{\mathrm{c}} \ . \tag{4.295}$$

Hence, the Hall voltage solely depends on l_{imp} and W in the strong magnetic field limit.

Numerical Solutions in the Intermediate Field Regime Above, we have analytically shown that in the limit of weak magnetic fields and clean systems the distinct dependence of $\Delta V_{\eta_{\mathrm{H}}}$ and ΔV_B on $n_0, W, l_{\mathrm{s}}, l_{\mathrm{imp}}$ and l_{ee} allows to experimentally distinguish these two contributions. Beyond the weak magnetic field limit, the Hall viscous and Lorentz force contributions to ΔV_{tot} need to be evaluated numerically. By solving Eqs. (4.270) and (4.271) for the velocity profile, we obtain

$$\begin{aligned} \Delta V_B &= -B \int_0^W \mathrm{d}y\, v_{\mathrm{x}}(y) \ , \\ \Delta V_{\eta_{\mathrm{H}}} &= \frac{\eta_{\mathrm{H}}}{\mathrm{e} n_0} \int_0^W \mathrm{d}y\, \partial_{\mathrm{y}}^2 v_{\mathrm{x}}(y) = \frac{\eta_{\mathrm{H}}}{\mathrm{e} n_0} [\partial_{\mathrm{y}} v_{\mathrm{x}}(y)]_{y=0}^W \ . \end{aligned} \tag{4.296}$$

In what follows, we numerically investigate the dependence of these voltage contributions on B, W, l_s, l_{imp} and l_{ee}. Notice, that while ΔV_B is proportional to the integrated value of $v_x(y)$, which characterizes the overall fluid momentum, ΔV_{η_H} is totally determined by the gradient of the velocity profile at the boundaries of the channel.

In Fig. 4.16, we plot the velocity profile of a general Fermi liquid for different magnetic fields in the context of our linear response theory. As a direct consequence, these profiles are in particular symmetric with respect to reflections around $y = W/2$. Notice, that in Eq. (4.292) we have explicitly evaluated their anti-symmetric correction beyond the linear response regime, which is sourced by the $\Delta\mu E_x$ term in Eq. (4.270). In particular, we have shown that this anti-symmetric correction is dictated by the direction of the Lorentz as well as Hall-viscosity induced force and is at least five orders of magnitude smaller than the leading contribution, depending on the magnetic field strength.

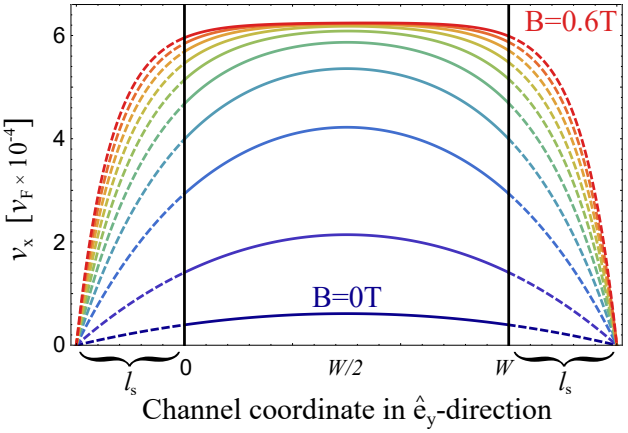

Figure 4.16: Velocity profile $v_x(y)$ of a general Fermi liquid with $n_0 = 9.1 \times 10^{11}\text{cm}^{-2}$, $\eta_0 = 1.7 \times 10^{-16}\text{Js/m}^2$ and $l_{imp} = 40\mu\text{m}$[90], derived up to first order in electromagnetic fields. From the bottom up, the magnetic field is raised from $B = 0\text{T}$ (blue) to $B = 0.6\text{T}$ (red), associated with an increase of the fluid velocity. The asymptotic flat velocity profile is caused by impurities, since for large magnetic fields these provide the only mechanism for attaining a steady fluid flow. The figure is reprinted from Ref. [P2] with permission from the APS.

Returning now to Fig. 4.16, we observe that with increasing $|B|$, the fluid is accelerated due to the corresponding suppression of η [cf. Eq. (4.273)]. According to Eq. (4.296), this leads to an enhancement of $|\Delta V_B|$. For large fields, η vanishes and solely impurity scattering is responsible for momentum relaxation, leading to an Ohmic velocity profile [cf. Eq. (4.279)].

The dependence of ΔV_{η_H} on the magnetic field is more subtle. Figure 4.16 shows that for weak magnetic fields, the gradient $|\partial_y v_x(y)|_{y=0,W}|$ increases as a function of $|B|$. According to Eq. (4.296), this corresponds to an enhancement of $|\Delta V_{\eta_H}|$. As discussed above, impurity scattering causes an Ohmic (flat) velocity profile for large magnetic fields. This decreases $|\partial_y v_x(y)|_{y=0,W}$ and therefore reduces $|\Delta V_{\eta_H}|$. Altogether, this implies that systems in which Hall viscous effects dominate the weak magnetic field regime, are eventually always driven to $|\Delta V_{\eta_H}|/|\Delta V_B| \ll 1$. The transition from Hall viscous to Lorentz force dominated transport occurs for $\Delta V_{\eta_H}/\Delta V_B = -1$, where $\Delta V_{tot} = 0$. This happens at a certain critical magnetic field B_c, which strongly depends on W, l_s and l_{ee}. This is shown in Fig. 4.17, which displays $|\Delta V_{\eta_H}|/|\Delta V_B|$ as a function of W, l_s, l_{ee} and l_{imp} [a].

[a] Note that the system lies within the range of validity of the hydrodynamic regime, even though $l_{ee} \lesssim W$ [97].

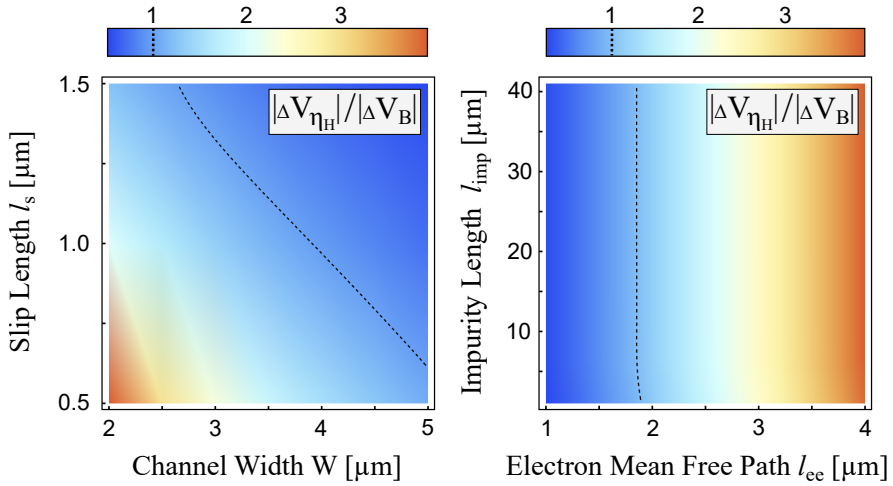

Figure 4.17: $|\Delta V_{\eta_H}|/|\Delta V_B|$ for different fluids at $B = 10$mT. In the left (right) panel, this ratio is shown as a function of W vs. l_s (l_{ee} vs. l_{imp}). For those parameters that are not altered, we choose $l_s = 0.5\mu$m, $W = 3\mu$m, $n_0 = 9.1 \times 10^{11}$cm^{-2}, $T = 1.4K$, $\eta_0 = 1.7\times10^{-16}$Js/m^2 and $l_{imp} = 40\mu$m [90]. While $|\Delta V_{\eta_H}|/|\Delta V_B|$ strongly decreases with W and l_s, the ratio is rather unaffected by l_{imp} and increases as a function of l_{ee}. The black dashed curve, for which $\Delta V_{\eta_H}/\Delta V_B = -1$, shows the range of parameters where the total Hall voltage vanishes. The figure is reprinted from Ref. [P2] with permission from the APS.

According to Eq. (4.296), the dependence of this ratio on these parameters can be explained by analyzing the corresponding velocity profiles, depicted in Fig. 4.16. As l_s increases, the gradient $|\partial_y v_x(y)|_{y=0,W}|$ decreases, leading to a reduction of $|\Delta V_{\eta_H}|$. In contrast, since the overall fluid momentum is enhanced, $|\Delta V_B|$ increases as a function of the slip length. Therefore, $|\Delta V_{\eta_H}|/|\Delta V_B|$ decreases with l_s, as illustrated in Fig. 4.17. Increasing the channel width leads to the same result, since it also increases the overall fluid momentum and at the same time decreases $|\partial_y v_x(y)|_{y=0,W}|$. In contrast, $|\Delta V_{\eta_H}|/|\Delta V_B|$ increases with the electron-electron mean free path. According to Eq. (4.273), the viscosities η, $|\eta_H|$ as well as the ratio $|\eta_H|/\eta$ increase as a function of l_{ee} as long as $l_{ee} \ll r_c$, implied by the hydrodynamic assumption. This reduces the overall fluid momentum but increases $|\Delta V_{\eta_H}|$. Last but not least, Fig. 4.17 shows that since $l_{ee} \ll l_{imp}$, the impurity length does not significantly change the ratio $\Delta V_{\eta_H}/\Delta V_B$ for weak magnetic fields.

To demonstrate the experimental relevance of our predictions, Fig. 4.18 finally shows $|\Delta V_{\eta_H}|$, $|\Delta V_B|$ and $|\Delta V_{tot}|$ in GaAs as a function of the magnetic field [90, 91][a]. Since in this material the slip length is highly dependent on the etching technique, we plot the corresponding curves for $l_s = 0, 0.5, 1.0\mu$m [b]. For $|B| \ll |B_c|$, the ratio $|\Delta V_{\eta_H}|/|\Delta V_B| \gg 1$, giving rise to a Hall viscosity dominated transport regime. As indicated by Eq. (4.285) and confirmed by Fig. 4.17, this property is strongly pronounced if the slip length decreases. With the exception of l_{ee}, it is possible to evaluate all parameters in Eqs. (4.270)-(4.273) precisely. Therefore, measuring ΔV_{η_H} and ΔV_B with increasing $|B|$, enables us to determine the electron-electron mean free path in this sample by fitting theoretical and experimental data. In general, this procedure works for any Fermi liquid and therefore is a powerful tool to evaluate the electron interaction strength. For $B = B_c$, the two voltage contributions are equal in magnitude but

[a] Note that the system lies within the range of validity of the hydrodynamic regime, even though $l_{ee} \lesssim W$ [97].

[b] Private communication with Prof. Laurens Molenkamp, University of Wuerzburg

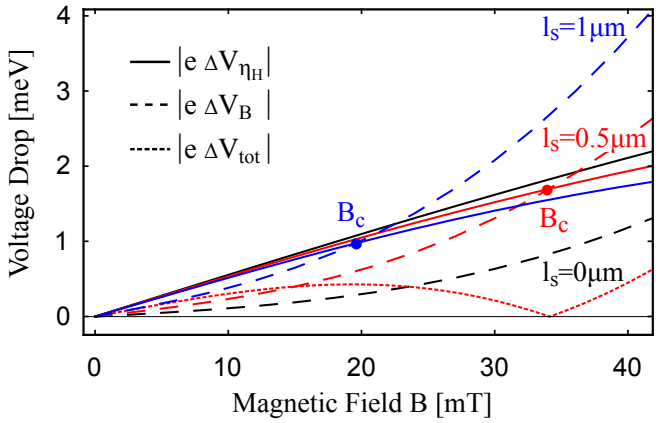

Figure 4.18: Absolute values of the Lorentz ΔV_B and Hall viscous contribution $\Delta V_{\eta_{\rm H}}$ to the total Hall voltage $\Delta V_{\rm tot}$ in GaAs are shown as functions of the magnetic field B for $l_{\rm s} = 0, 0.5, 1.0\mu$m. Parameters for this calculation are given in the caption of Fig. 4.17. For $B < B_{\rm c}$, we find $|\Delta V_{\eta_{\rm H}}|/|\Delta V_B| > 1$, whereas otherwise $|\Delta V_{\eta_{\rm H}}|/|\Delta V_B| < 1$. At $B = B_{\rm c}$, the ratio $\Delta V_{\eta_{\rm H}}/\Delta V_B = -1$, which implies a vanishing Hall voltage $\Delta V_{\rm tot} = 0$. The figure is reprinted from Ref. [P2] with permission from the APS.

opposite in sign, leading to $\Delta V_{\rm tot} = 0$. Experimentally, this smoking gun feature can be used to prove our Hall viscous magnetotransport theory. For $|B| \gg |B_{\rm c}|$, Fig. 4.18 shows that transport is dominated by the Lorentz signal. Eventually, this leads to an Ohmic, impurity driven velocity profile as we have shown in Eq. (4.294). Our present approach does not incorporate the formation of Landau levels which in GaAs occurs beyond the applicability of hydrodynamics for $|B| \gtrsim 1$T. Finally, we remark that the Hall voltage we predict depends non-linearly on the magnetic field strength. Since ballistic transport predicts $\Delta V_B \propto B$, this non-linear behavior is a direct consequence of the hydrodynamic regime.

4.2.3 The Local Hall Voltage

So far, we have focused on global voltage measurements across the entire channel. In addition, Eq. (4.296) predicts the local voltage contributions:

$$\begin{aligned}\Delta V_{\eta_{\rm H}} &= \frac{\eta_{\rm H}}{\eta} E_{\rm x} \left[y - \frac{1}{12 l_{\rm G}^2} \left[6 l_{\rm s}(l_{\rm s}+W) + y(3W-2y) \right] y \right] \\ \Delta V_B &= -\frac{{\rm sgn}(B) E_{\rm x}}{3 r_{\rm c} l_{\rm ee}} \left[6 l_{\rm s}(l_{\rm s}+W) + y(3W-2y) \right] y \ . \end{aligned} \tag{4.297}$$

Hence, the total Hall voltage $\Delta V_{\rm tot}$ scales as y^3, whereas the Hall field $E_{\rm y} = -{\rm d}\Delta V_{\rm tot}/{\rm d}y$ has parabolic structure. For large $l_{\rm imp}$, the curvature of this parabola,

$$\kappa = -4 E_{\rm x} \left[{\rm sgn}(B)/r_{\rm c} + \eta_{\rm H}/(\eta l_{\rm imp}) \right]/l_{\rm ee} \ , \tag{4.298}$$

is mainly characterized by the Lorentz contribution. In contrast, the Hall viscous signal significantly defines the offset of this parabola,

$$E_{\rm y}(0) = E_{\rm x} \left[\frac{2 l_{\rm s}(l_{\rm s}+W)}{{\rm sgn}(B) r_{\rm c} l_{\rm ee}} - \left(1 - \frac{2 l_{\rm s}(l_{\rm s}+W)}{l_{\rm ee} l_{\rm imp}} \right) \frac{\eta_{\rm H}}{\eta} \right] . \tag{4.299}$$

For $l_{\rm s} \ll l_{\rm ee} \ll l_{\rm imp}$, this relation becomes $E_{\rm y}(0) \simeq E_{\rm x} \eta_{\rm H}/\eta$.

Recently, the authors of Ref. [97] measured the local Hall voltage in the hydrodynamic regime of graphene, particularly satisfying $l_\mathrm{s} \simeq l_\mathrm{ee} \ll W$. They explicitly reproduced the parabolic form of the Hall field, as well as that $|\kappa|$ decreases with increasing l_ee.

4.2.4 Discussion of Boundary Conditions

Below Eq. (4.272) we have already mentioned that our set of boundary conditions, which supplements the Navier-Stokes equations (4.262) and (4.263), differs from conventional Robin type boundary conditions. In particular, our definition of the slip length l_s differs from the one given in Ref. [197]. However, it is the purpose of this subsection to prove that in the two-dimensional channel geometry considered [cf. Fig. 4.15], our set of boundary conditions in Eq. (4.272) is equivalent to the standard Robin type boundary conditions

$$u_\mathrm{x}^0(0) - l_\mathrm{R}\partial_\mathrm{y} u_\mathrm{x}(0) = u_\mathrm{x}(W) + l_\mathrm{R}\partial_\mathrm{y} u_\mathrm{x}(W) = 0 \ . \tag{4.300}$$

Here $u_\mathrm{x}^0(y)$ defines the Robin velocity profile and l_R is the corresponding slip length. As a solution of the weak magnetic field Navier-Stokes Eqs. (4.276)-(4.278), $u_\mathrm{x}^0(y)$ is given by

$$u_\mathrm{x}^0(y) = -\frac{\mathrm{e}E_\mathrm{x} l_\mathrm{imp}}{m^* v_\mathrm{F}}\Big(C_1 \cosh\Big[y l_\mathrm{G}^{-1}\Big] + C_2 \sinh\Big[y l_\mathrm{G}^{-1}\Big] + 1\Big) \ . \tag{4.301}$$

Here, we define the amplitudes C_1 and C_2 via

$$C_1 = -l_\mathrm{G}\left[l_\mathrm{G} + l_\mathrm{R}\tanh\left[W/(2l_\mathrm{G})\right]\right]^{-1} \ , \tag{4.302}$$

$$C_2 = \ \ l_\mathrm{G}\left[l_\mathrm{R} + l_\mathrm{G}\coth\left[W/(2l_\mathrm{G})\right]\right]^{-1} \ . \tag{4.303}$$

In order to prove the equivalence between the two types of boundary conditions, it is sufficient to show that the velocity profiles $u_\mathrm{x}^0(y)$ and $v_\mathrm{x}^0(y)$ match each other. According to Eq. (4.301), the Robin slip length is defined to be the normalized value of the inverse first derivative of the velocity profile at the boundaries. Hence, let us define the effective Robin slip length for our velocity profile

$$l_\mathrm{R}^\mathrm{eff} \equiv \frac{v^0(0)}{\partial_\mathrm{y} v_\mathrm{x}^0(0)} = -\frac{v^0(W)}{\partial_\mathrm{y} v_\mathrm{x}^0(W)} \ . \tag{4.304}$$

This quantity allows us to derive the equivalence of the two types of boundary conditions if we are able to prove that

$$u_\mathrm{x}^0(y; l_\mathrm{R} = l_\mathrm{R}^\mathrm{eff}) = v_\mathrm{x}^0(y; l_\mathrm{s}) \ . \tag{4.305}$$

For weak magnetic fields, satisfying $l_\mathrm{G}/r_\mathrm{c} \ll 1$, Eq. (4.279) defines $v_\mathrm{x}^0(y)$ analytically. In this limit, Eq. (4.304) implies that for $l_\mathrm{R} = l_\mathrm{R}^\mathrm{eff}$

$$\begin{aligned} l_\mathrm{R} &= l_\mathrm{G}\ \mathrm{csch}[W/l_\mathrm{G}](\cosh[(2l_\mathrm{s}+W)/l_\mathrm{G}] - \cosh[W/(2l_\mathrm{G})]) \ , \\ l_\mathrm{s} &= l_\mathrm{G}\mathrm{arcosh}[\sinh[W/(2l_\mathrm{G})]\,(l_\mathrm{G}\coth[W/(2l_\mathrm{G})] + l_\mathrm{R})/l_\mathrm{G}] - W/2 \ . \end{aligned} \tag{4.306}$$

This mapping identifies the velocity profiles $u_\mathrm{x}^0(y)$ and $v_\mathrm{x}^0(y)$, since it maps Eq. (4.301) onto Eq. (4.279). In particular, the Robin type equivalents to the Hall viscous- and the Lorentz force contribution to the total Hall voltage in Eqs. (4.283) and (4.284) are given by

$$\Delta V_{\eta_\mathrm{H}}^R = \frac{\eta_\mathrm{H}}{\eta} E_\mathrm{x}\left[W - \frac{1}{12 l_\mathrm{G}^2}\left(W^3 + 6 l_\mathrm{R} W^2\right)\right],$$

$$\Delta V_B^R = -\frac{\mathrm{sgn}(B) E_\mathrm{x}}{3 r_\mathrm{c} l_\mathrm{ee}} \left(W^3 + 6 l_\mathrm{R} W^2 \right) \ . \tag{4.307}$$

Since Eq. (4.283) and Eq.(4.284) are derived under the assumption $W/l_\mathrm{G} \ll 1$, Eq. (4.307) is obtained by inserting the Robin slip length, given by Eq. (4.306) in the same limit, $l_\mathrm{R} \simeq l_\mathrm{s} + l_\mathrm{s}^2/W$. Beyond the weak magnetic field regime Eq. (4.305) is still justified. Since in this limit $l_\mathrm{G}/r_\mathrm{c} \gtrsim 1$, this can not be proven analytically. Instead, we confirmed the validity of Eq. (4.305) by numerically evaluating the Robin slip length in Eq. (4.304). As soon as the cyclotron radius $r_\mathrm{c} \ll W$, one enters the strong magnetic field regime. While in this limit the Robin slip length diverges, our slip length remains constant by definition. Therefore, we can not justify Eq. (4.305) for strong magnetic fields. However, in this limit the equivalence of both types of boundary conditions is given trivially. Since the fluid layer interaction decreases as function of r_c, all our results become slip length and therefore boundary condition independent for $r_\mathrm{c} \ll W$ [cf. Eq. (4.295)].

4.2.5 Work in Progress & Future Research Directions

In the above analysis we have shed light on the Hall viscous transport of two-dimensional, non-relativistic electron fluids in external out-of-plane magnetic fields. In particular, we have presented a setup that allowed us to distinguish between the Hall viscous- and the Lorentz force contributions to the entire Hall voltage of conventional Fermi liquids such as GaAs. An extensive summary of our results can be found in Sec. 5.

Based on our theoretical considerations in Sec. 4.1.5, we are currently extending our analysis to two-dimensional Dirac systems such as graphene. More precisely, we are including graphene's linear Dirac dispersion in our analytic approach and, at the same time, develop realistic numerical simulations for this material. In the Fermi liquid regime of graphene, for $\mu/(\mathrm{k_B} T) \gg 1$, the expected results should only quantitatively, but not qualitatively differ from our results for conventional Fermi liquids with a quadratic dispersion in momentum [97]. This is in stark contrast to the expected signatures in graphene's Dirac fluid phase $\mu/(\mathrm{k_B} T) \ll 1$. It will we very interesting to understand in which way quantum critical effects like $\sigma_\mathrm{Q} \neq 0$ enter the functional dependencies presented in the previous sections. Within the scope of this thesis, the corresponding Navier-Stokes equations have been derived in Eq. (4.98). Moreover, in Sec. 4.1.5, we elaborated on graphene's transport coefficients in both, the Fermi liquid as well as the Dirac fluid regime. In order to experimentally confirm our theoretical findings we are currently closely collaborating with the group of Prof. Dr. Amir Yacoby at the Harvard University.

Another extremely interesting extension of our work is to study massive Dirac systems in which parity- and time-reversal symmetry are already broken in the absence of external magnetic fields. Such systems are in particular characterized by a finite quantum anomalous Hall conductivity $\sigma_\mathrm{QAH} \neq 0$ [P1], as well as a finite torsional Hall viscosity $\eta_\mathrm{H}^\mathrm{t} \neq 0$ [85, 227]. Analyzing the Hall response of such systems in particular sheds light on the role of the parity anomaly [37, 52] in $2+1$ dimensional hydrodynamic fluid flows. While Eq. (4.98) already includes the contribution of the quantum anomalous Hall conductivity σ_QAH, a remaining task is to include torsional effects to the non-relativistic Navier-Stokes equations. In order to prepare these calculations, we will derive the torsional Hall viscosity of a single Chern insulator in the remaining section of this thesis.

4.3 Torsional Hall Viscosity in Dirac-Like Systems

4.3.1 Scientific Context

In what follows, we are going to calculate the so-called torsional Hall viscosity $\eta_{\mathrm{H}}^{\mathrm{t}}$ of a massive Dirac fermion in 2+1 space-time dimensions. Initially, the calculation of this non-dissipative, parity-odd transport coefficient has been performed by T. L. Hughes, R. G. Leigh, O. Parrikar, and E. Fradkin in Refs. [227–230]. In the subsequent sections, we are mainly following the line of reasoning in these publications. Similar to the analysis of the QED_{2+1} polarization operator in Sec. 2.6.3, and its generalization towards QAH insulators in Sec. 3.2.2, the present considerations should serve as a starting point in order to transfer pure Dirac physics to QAH insulators at finite temperatures, densities, and in quantizing out-of-plane magnetic fields. In contrast to the Hall conductivity, the torsional Hall viscosity of a Dirac-like system cannot be a quantized value in terms of the Dirac mass m, due to its mass dimension. Based on this mass dimension and the relation of the Hall viscosity to the Hall conductivity [190], which we has been studied in Sec. 3.1.2, we are expecting that $\eta_{\mathrm{H}}^{\mathrm{t}} \propto m^2 \mathrm{sgn}(m)$ for a pure Dirac fermion after proper renormalization. The latter statement originates from the fact that in contrast to the Hall conductivity, the bare torsional Hall viscosity is expected to be a divergent quantity, as it can be most easily seen by a power counting argument. The authors of the aforementioned references renormalize their results by using a Pauli-Villars approach [cf. Sec. 3.2.3]. They discretize their space manifold on an artificial lattice and add up the different Dirac contributions originating from the fermion doubling at the high-symmetry points of the lattice Brillouin zone. Also having in mind the derivation of the torsional Hall viscosity of the BHZ model [cf. Sec. 3.1.1], each of the fermion doublers has a different mass term, as it will be discussed in the subsequent analysis. In our follow-up calculation, which is currently in progress, we are going to derive the torsional Hall viscosity of a planar Dirac-like system in a fundamentally different way. Analogously to Sec. 3.2, our goal is it to derive the stress-stress correlator for a single Chern insulator including both, a Dirac- as well as a Newtonian mass term $B|\mathbf{k}|^2$. It is a future task to include finite density and temperature effects. Based on our analysis in Sec. 3.3, we are expecting that for out-of-plane magnetic field strengths $H < H_{\mathrm{crit}}$, due to the parity anomaly the zero field torsional Hall viscosity adds a contribution to the entire LL response. Our calculations will significantly differ from the aforementioned references. As it was explained in Sec. 3.1.1, the BHZ model is a low-energy model close to the Γ-point of a QSH- or QAH insulator, respectively. Consequently, a regularization scheme which relies on fermion doublers appearing at the edges of an artificial lattice Brillouin-zone needs to be treated with caution. Our calculation should, in addition, shed light into the low-energy AC response of QAH insulators in the continuum model. To this end, it seems reasonable to incorporate the Newtonian mass term already at the level of a Lorentz non-invariant action [cf. Eq. (3.60)]. In order to understand all of our extensions, it is, however, inevitable to first understand the simplified calculation of a pure Dirac fermion in 2+1 space-time dimensions. As a consequence, we are presenting this analysis in the following paragraphs. Again, let us emphasize that this calculation is crucially related to the aforementioned references [227–230].

As a generalization of the conventional Hall viscosity

$$\eta_{\mathrm{H}} = \lim_{\omega\to 0} \frac{1}{4\omega} \delta_{ik}\epsilon_{jl}\, \mathrm{Im}\, G_{\mathrm{R}}^{ij,kl}(\omega, \mathbf{p}=0) \quad \text{with} \quad G_{\mathrm{R}}^{\mu\nu,\rho\sigma} = \langle T^{\mu\nu} T^{\rho\sigma} \rangle_{\mathrm{R}} \ , \tag{4.308}$$

which we have introduced in Eq. (4.35), the torsional Hall viscosity is given by [85, 228]

$$\eta_{\mathrm{H}}^{\mathrm{t}} = \lim_{p_0\to 0} \frac{1}{4p_0} \delta_{ik}\epsilon_{jl}\, \mathrm{Im}\, \tilde{G}_{\mathrm{R}}^{ij,kl}(p_0, \mathbf{p}=0) \ , \tag{4.309}$$

where we defined $p_0 = \omega$ in order to use a covariant notation for the three momentum. The only difference between the conventional Hall viscosity in Eq. (4.308) and the torsional Hall viscosity in Eq. (4.309) is that in the latter definition we have used the canonical instead of the symmetric energy-momentum tensor for the retarded correlator

$$\tilde{G}_{\mathrm{R}}^{\mu\nu,\rho\sigma} = \langle T^{\mu\nu}_{\mathrm{canonical}} T^{\rho\sigma}_{\mathrm{canonical}} \rangle_{\mathrm{R}} \ . \tag{4.310}$$

For a detailed discussion of this generalization we are referring the interested reader to Ref. [85]. In what follows, we are going to derive the canonical energy-momentum tensor of free Dirac fermion coupled to a general 2+1 dimensional space-time manifold. Within the scope of this analysis we are neglecting effects originating form the spin connection as the torsional Hall viscosity is a purely geometrical response, which corresponds to a quadratic Chern-Simons form [cf. Sec. 2.6.4] in terms of the frame fields $e_a{}^\mu$ on the level of the effective action [227, 228]. We are in particular working in the framework of a linear-response theory with respect to the frame fields. Their fluctuations are encoded in the Chern-Simons form of the system's effective action. The transport coefficients, however, need to be calculated on a flat background in order to neglect higher order contributions of the torsional Hall response in terms of $e_a{}^\mu$. Moreover, for reasons of clarity, we are neglecting the identifying subscript 'canonical' in the subsequent calculations.

4.3.2 The Continuum Dirac Model

We start our analysis with the Lagrangian of a massive Dirac fermion coupled to a curved 2+1 dimensional space-time with non-zero torsion, which is described by the general metric tensor $g^{\mu\nu}$. In order to use the Clifford algebra of 2+1 dimensional Dirac matrices with respect to a flat Minkowski space-time $\eta^{\mu\nu}$, as it is described in Sec. 2.3.1, we introduce the so-called frame fields $e_a{}^\mu$ which locally map between the 'curved' and the 'flat' metric. In particular, we are considering the Lagrangian [227, 228]

$$\mathcal{L}(x) = e\, \bar{\psi}(x) \left(\mathrm{i}\gamma^a e_a{}^\mu \partial_\mu - m \right) \psi(x) \quad \text{with} \quad \{\mu, a\} \in \{0, 1, 2\} \ . \tag{4.311}$$

The factor $e = \det(e_\mu{}^m) = \sqrt{\det(g_{\mu\nu})}$ makes the space-time volume covariant under general coordinate transformations[a]. In the above notation, we have used latin subscripts to encode 'flat' space-time indicies in the non-holonomic frame basis, whereas we have used 'curved' greek subscripts to indicate the holonomic coordinate basis [231]. Be aware, that we are using latin subscripts to indicate the spatial part of each space-time, as well. The concrete relation clearly arises from the scientific context.

The canonical energy momentum tensor of a system which is invariant under space-time translations can be calculated by means of the Noether theorem, which we have analyzed in Sec. 2.4.5 in-depth [109]:

$$T^\mu{}_\nu(x) = \frac{\delta \mathcal{L}}{\delta[\partial_\mu \psi(x)]} \partial_\nu \psi(x) + \frac{\delta \mathcal{L}}{\delta[\partial_\mu \bar{\psi}(x)]} \partial_\nu \bar{\psi}(x) - \mathcal{L}(x)\, \delta^\mu{}_\nu \ . \tag{4.312}$$

In order to derive the torsional Hall viscosity in Eq. (4.309), we only need to consider the spatial part of this tensor, the so-called canonical stress tensor [cf. Eq. (4.8)]. To this end,

[a] The indices are written for clarity even though we do not want to specify the entries of the associated tensors.

we separate the Einstein convention in Eq. (4.311), which implies

$$\mathcal{L} = e\,\bar{\psi}(x)\left[\mathrm{i}\,e^0{}_a\gamma^a\partial_0 - m + \mathrm{i}\sum_{i,a=1,2} e^i{}_a\gamma^a\partial_i\right]\psi(x) \tag{4.313}$$

$$= e\,\bar{\psi}(x)\left[\mathrm{i}\,e^0{}_a\gamma^a\partial_0 - m + \mathrm{i}\sum_{i,a,c=1,2}\eta_{ac}e^c{}_i\gamma^a\partial^i\right]\psi(x)\ . \tag{4.314}$$

With the definition in Eq. (4.312), the Lagrangian in Eq. (4.313) implies the following expression for the canonical stress tensor [227]

$$T_{ij}(x) = \bar{\psi}(x)\mathrm{i}\left[\eta_{ac}e^c_{(j}\partial_{i)}\gamma^a\right]\psi(x) + \delta_{ij}\mathcal{L} \quad \text{with} \quad \{i,j\} = \{1,2\}\ . \tag{4.315}$$

Here, and in the following, we are using the abbreviated notation:

$$A_{(\mu}B_{\nu)} = \frac{1}{2}\left(A_\mu B_\nu + A_\nu B_\mu\right)\ . \tag{4.316}$$

Off-Diagonal Contributions

Let us first neglect those contributions to Eq. (4.309) which originate from the diagonal terms $\propto \delta_{ij}\mathcal{L}$. Due to the tensor contraction in Eq. (4.309), these terms do not contribute to $\eta_{\mathrm{H}}^{\mathrm{t}}$, as we will prove in Sec. 4.3.2. According to Eq. (4.315), we are therefore calculating the retarded stress-stress correlator [227]

$$\langle T_{ij}(x)T_{kl}(0,\mathbf{0})\rangle = -4\mathrm{Tr}\left(\left[\frac{1}{2}\eta_{ac}e^c_{(j}\mathrm{i}\partial_{i)}\gamma^a\right]\mathrm{i}S_{\mathrm{F}}(x)\left[\frac{1}{2}\eta_{bd}e^d_{(l}\mathrm{i}\partial_{k)}\gamma^b\right]\mathrm{i}S_{\mathrm{F}}(-x)\right)\ . \tag{4.317}$$

As we have shown in Eq. (2.134), the free propagator of a massive Dirac fermion is given by

$$\mathrm{i}S_{\mathrm{F}} = \left(\mathrm{i}\not{\partial} - m\right)^{-1}\ , \tag{4.318}$$

where $\not{\partial} = \gamma^\mu\partial_\mu$ defines the Feynman slash notation. As we have mentioned above, we are working in the framework of a linear-response theory with respect to the frame fields $e_a{}^\mu$. Their fluctuation is encoded in the Chern-Simons form of the system's effective action. The transport coefficients, however, need to be calculated on a flat background in order to neglect higher order contributions of the torsional Hall response in terms of $e_a{}^\mu$. For this reason, we are considering $e_j{}^c = \delta_j{}^c$ in the following, which implies

$$\eta_{ac}e^c_{(j}\partial_{i)}\gamma^a = \eta_{ac}\delta^c_{(j}\partial_{i)}\gamma^a = \delta_{a(j}\partial_{i)}\gamma^a = \gamma_{(j}\partial_{i)} = \partial_{(i}\gamma_{j)}\ . \tag{4.319}$$

With this identity, we find the following expression for Eq. (4.317) in momentum space [227]

$$\langle T_{ij}T_{kl}\rangle(p) = -4\mathrm{i}^4\mathrm{Tr}\int\frac{\mathrm{d}^3q}{(2\pi)^3}\frac{\left[\frac{1}{2}q_{(i}\gamma_{j)}\right]\left(\not{q}+m\right)\left[\frac{1}{2}r_{(k}\gamma_{l)}\right]\left(\not{r}+m\right)}{(q^2-m^2)(r^2-m^2)}\ , \tag{4.320}$$

where $r^\mu = p^\mu + q^\mu$. As we have mentioned above, within the scope of this analysis we are only interested in the parity-odd part of this integral. This contribution is proportional to the Levi-Civita symbol, and, therefore, proportional to the trace of three Dirac matrices. The

relevant terms are therefore given by

$$\langle T_{ij}T_{kl}\rangle_{\text{odd}}(p) = -\int \frac{\mathrm{d}^3q}{(2\pi)^3}\frac{m}{(q^2-m^2)(r^2-m^2)}\; q_{(i}r_{(k}\mathrm{Tr}\,\gamma_{j)}\not{q}\gamma_{l)} - \int \frac{\mathrm{d}^3q}{(2\pi)^3}\frac{m}{(q^2-m^2)(r^2-m^2)}\; q_{(i}r_{(k}\mathrm{Tr}\,\gamma_{j)}\gamma_{l)}\not{r}\ .$$

This expression can be simplified significantly as the spatial indices $j,l \in \{1,2\}$. Consequently, the only non-zero contributions to Eq. (4.321) are given by the terms proportional to p_0 and r_0, respectively. With the identity $\mathrm{Tr}(\gamma_0\gamma_i\gamma_j) = -2\mathrm{i}\epsilon_{0ij}$ we find the two non-zero contributions

$$\begin{aligned}(1) &= -\int \frac{\mathrm{d}^3q}{(2\pi)^3}\frac{m}{(q^2-m^2)(r^2-m^2)}\; q_{(i}r_{(k}q_0\mathrm{Tr}\,\gamma_{j)}\gamma^0\gamma_{l)} \\ &= -\int \frac{\mathrm{d}^3q}{(2\pi)^3}\frac{m}{(q^2-m^2)(r^2-m^2)}\; q_{(i}r_{(k}q_0\mathrm{Tr}\,\gamma^0\gamma_{l)}\gamma_{j)} \\ &= -\int \frac{\mathrm{d}^3q}{(2\pi)^3}\frac{m}{(q^2-m^2)(r^2-m^2)}\; q_{(i}r_{(k}q_0(-2\mathrm{i}\epsilon_{l)j)}) = 2\mathrm{i}\epsilon_{(l(j}\int \frac{\mathrm{d}^3q}{(2\pi)^3}\frac{m\,q_{i)}r_{k)}q_0}{(q^2-m^2)(r^2-m^2)},\end{aligned} \tag{4.321}$$

and

$$\begin{aligned}(2) &= -\int \frac{\mathrm{d}^3q}{(2\pi)^3}\frac{m}{(q^2-m^2)(r^2-m^2)}\; q_{(i}r_{(k}\mathrm{Tr}\,\gamma_{j)}\gamma_{l)}\not{r} \\ &= -\int \frac{\mathrm{d}^3q}{(2\pi)^3}\frac{m}{(q^2-m^2)(r^2-m^2)}\; q_{(i}r_{(k}r_0\mathrm{Tr}\,\gamma_{j)}\gamma_{l)}\gamma^0 \\ &= -\int \frac{\mathrm{d}^3q}{(2\pi)^3}\frac{m}{(q^2-m^2)(r^2-m^2)}\; q_{(i}r_{(k}r_0(-2\mathrm{i}\epsilon_{j)l)}) = -2\mathrm{i}\epsilon_{(l(j}\int \frac{\mathrm{d}^3q}{(2\pi)^3}\frac{m\,q_{i)}r_{k)}r_0}{(q^2-m^2)(r^2-m^2)}.\end{aligned} \tag{4.322}$$

In combination, these contributions give rise to the entire parity-odd stress-stress correlation

$$\begin{aligned}\langle T_{ij}T_{kl}\rangle_{\text{odd}}(p) &= (1)+(2) \\ &= 2\mathrm{i}\epsilon_{(l(j}\int \frac{\mathrm{d}^3q}{(2\pi)^3}\frac{m\,q_{i)}r_{k)}q_0}{(q^2-m^2)(r^2-m^2)} - 2\mathrm{i}\epsilon_{(l(j}\int \frac{\mathrm{d}^3q}{(2\pi)^3}\frac{m\,q_{i)}r_{k)}r_0}{(q^2-m^2)(r^2-m^2)} \\ &= 2\mathrm{i}\epsilon_{(l(j}\int \frac{\mathrm{d}^3q}{(2\pi)^3}\frac{m\,q_{i)}r_{k)}(q_0-r_0)}{(q^2-m^2)(r^2-m^2)} = -2\mathrm{i}\epsilon_{(l(j}\int \frac{\mathrm{d}^3q}{(2\pi)^3}\frac{m\,q_{i)}r_{k)}p_0}{(q^2-m^2)(r^2-m^2)}.\end{aligned} \tag{4.323}$$

As a next step in our calculation we perform the limit $\mathbf{p}\to\mathbf{0}$, as it is required by Eq. (4.309). In this limit, one obtains the correlator

$$\lim_{\mathbf{p}\to\mathbf{0}}\left[\langle T_{ij}T_{kl}\rangle_{\text{odd}}(p_0,\mathbf{p})\right] = -2\mathrm{i}\epsilon_{(l(j}\int \frac{\mathrm{d}^3q}{(2\pi)^3}\frac{m\,q_{i)}q_{k)}p_0}{(q^2-m^2)(r_0^2-|\mathbf{q}|^2-m^2)}\ . \tag{4.324}$$

In the scope of this section, we are interested in the low-frequency response originating from the torsional Hall viscosity. As a consequence, we are evaluating the integral in Eq. (4.324) under the assumption $p_0 \ll m^2+|\mathbf{q}|^2$, by using the residuum theorem. In particular, we will make use of the identity [a]

$$\int \mathrm{d}q_0\,\frac{1}{(q^2-m^2)(r_0^2-|\mathbf{q}|^2-m^2)} \overset{p_0\ll m^2+|\mathbf{q}|^2}{=} -\frac{\mathrm{i}\pi}{2(|\mathbf{q}|^2+m^2)^{3/2}}\ . \tag{4.325}$$

[a] The overall minus sign in Eq. (4.325) results from the retarded integration contour.

With this identity we can substantially simplify Eq. (4.324):

$$\begin{aligned}\langle T_{ij}T_{kl}\rangle^{\mathrm{exp}}_{\mathrm{odd}}(p) &= \frac{p_0}{2}\int\frac{\mathrm{d}^2q}{(2\pi)^2}\frac{m\,\epsilon_{(l(j}q_{i)}q_{k)}}{(|\mathbf{q}|^2+m^2)^{3/2}} \overset{(*)}{=} \frac{p_0}{4}\epsilon_{(l(j}\delta_{i)k)}\int\frac{\mathrm{d}^2q}{(2\pi)^2}\frac{m\,|\mathbf{q}|^2}{(|\mathbf{q}|^2+m^2)^{3/2}}\\ &\overset{(**)}{=} \pi\frac{p_0}{4}\epsilon_{(l(j}\delta_{i)k)}\int\frac{\mathrm{d}|\mathbf{q}|^2}{(2\pi)^2}\frac{m\,|\mathbf{q}|^2}{(|\mathbf{q}|^2+m^2)^{3/2}}\\ &\overset{(***)}{=} \frac{p_0}{16\pi}\epsilon_{(l(j}\delta_{i)k)}\int_0^\infty\mathrm{d}y\,\frac{m\,y}{(m^2+y)^{3/2}}\\ &\overset{(****)}{\equiv} -\frac{p_0}{8\pi}\epsilon_{(l(j}\delta_{i)k)}I_{\mathrm{T}}(m)\ .\end{aligned} \tag{4.326}$$

In the second equality, which is indicated by $(*)$, we used that the integration over q_i and q_j vanishes if $i\neq j$ due to symmetry reasons. In the third equality, which is indicated by $(**)$, we introduced polar coordinates in order to use the identity

$$\int d^2q = \iint|\mathbf{q}|\mathrm{d}|\mathbf{q}|\mathrm{d}\varphi = 2\pi\int\frac{\mathrm{d}|\mathbf{q}|^2}{2} = \pi\int\mathrm{d}|\mathbf{q}|^2\ . \tag{4.327}$$

In the fourth equality, which is indicated by $(***)$, we substituted $|\mathbf{q}|^2=y$. Eventually, the fifth equality, which is indicated by $(****)$, introduces the divergent integral [227, 228]

$$I_{\mathrm{T}}(m) = -\frac{m}{2}\int_0^\infty\mathrm{d}y\,\frac{y}{(m^2+y)^{3/2}}\ . \tag{4.328}$$

In order to regularize the divergence we introduce a hard momentum cut-off $\Lambda=|\mathbf{q}_{\mathrm{max}}|$, as it has been done in Eqs. (2.151) and (3.84), as well. With the upper limit $y_{\mathrm{max}}=|\mathbf{q}_{\mathrm{max}}|^2=\Lambda^2$, this procedure implies

$$I_{\mathrm{T}}(m) = -\frac{m}{2}\int_0^{\Lambda^2}\mathrm{d}y\,\frac{y}{(m^2+y)^{3/2}} = -\frac{m}{2}\left[\frac{2(2m^2+y)}{\sqrt{m^2+y}}\right]_0^{\Lambda^2} \tag{4.329}$$

$$= -\frac{m}{2}\left(\frac{2(2m^2+\Lambda^2)}{\sqrt{m^2+\Lambda^2}}-\frac{4m^2}{\sqrt{m^2}}\right)\overset{\Lambda\gg m}{=} -\frac{m\Lambda^2}{\sqrt{\Lambda^2}}+\frac{2m^3}{|m|} = -m\Lambda+2\,\mathrm{sgn}(m)m^2\ . \tag{4.330}$$

Inserting this identity into Eq. (4.326) implies the regularized parity-odd stress-stress correlation

$$\langle T_{ij}T_{kl}\rangle^{\mathrm{reg}}_{\mathrm{odd}}(p) = -\frac{p_0}{8\pi}\epsilon_{(l(j}\delta_{i)k)}\left(-m\Lambda+2\,\mathrm{sgn}(m)m^2\right)\ . \tag{4.331}$$

In order to calculate the entire torsional Hall viscosity as it is defined in Eq. (4.309),

$$\eta^{\mathrm{t}}_{\mathrm{H}} = \lim_{p_0\to0}\frac{1}{4p_0}\delta_{ik}\epsilon_{jl}\,\mathrm{Im}\,\tilde{G}^{ij,kl}_{\mathrm{R}}(p_0,\mathbf{p}=0)\ , \tag{4.332}$$

we first contract the corresponding tensor structure

$$\begin{aligned}\delta^{ik}\epsilon^{jl}\epsilon_{(l(j}\delta_{i)k)} &= \frac{1}{2}\left(\delta^{ik}\epsilon^{jl}\epsilon_{(lj}\delta_{ik)}\right)+\left(\delta^{ik}\epsilon^{jl}\epsilon_{(li}\delta_{jk)}\right)\\ &= \frac{1}{4}\left(\delta^{ik}\epsilon^{jl}\left[\epsilon_{lj}\delta_{ik}+\epsilon_{kj}\delta_{il}\right]\right)+\left(\delta^{ik}\epsilon^{jl}\left[\epsilon_{li}\delta_{jk}+\epsilon_{ki}\delta_{jl}\right]\right)\\ &= \frac{1}{4}\left(\epsilon^{jl}\left[2\epsilon_{lj}+\epsilon_{lj}\right]\right)+\left(\epsilon^{jl}\left[\epsilon_{lj}+0\right]\right) = -2\ .\end{aligned} \tag{4.333}$$

Here, we used that $\delta^{ik}\delta_{ik} = 2$ and $\epsilon^{lj}\epsilon_{lj} = 2$. Eventually, this implies the regularized torsional Hall viscosity of single massive Dirac fermion in 2+1 space-time dimensions [227, 228]

$$\eta_{\mathrm{H}}^{\mathrm{t}} = \frac{1}{16\pi} I_{\mathrm{T}}(m) = \frac{1}{16\pi}\left(-m\Lambda + 2\,\mathrm{sgn}(m)m^2\right) \ . \tag{4.334}$$

As this result is infinite if one removes the cutoff $\Lambda \to \infty$, it requires a suitable renormalization scheme [cf. discussion in Sec. 3.2.3]. This will be the scope of Sec. 4.3.3. However, let us first check that we were allowed to neglect the diagonal parts in Eq. (4.315).

Diagonal Contributions

In Sec. 4.3.2 we have neglected all contributions to the torsional Hall viscosity in Eq. (4.309) originating form the diagonal parts of the canonical stress tensor in Eq. (4.315) $\propto \delta_{ij}\mathcal{L}$. We have claimed that these terms do not contribute to $\eta_{\mathrm{H}}^{\mathrm{t}}$. Let us prove this statement in the following. For our line of reasoning, we will use the two following properties:

$$(1): \qquad \delta^{ik}\epsilon^{jl}\delta_{ij}\delta_{kl} = \delta^{ik}\delta_{ij}\epsilon^{jl}\delta_{lk} = \delta^{ik}\epsilon_{ik} = \epsilon^{i}{}_{i} = 0 \ , \tag{4.335}$$

$$(2): \qquad \mathcal{L}(q)\mathrm{i}S_{\mathrm{F}}(q) = \left(\not{q} - m\right)\left(\not{q} - m\right)^{-1} = 1 \ . \tag{4.336}$$

Structurally, there are three possible contributions from the diagonal terms of the canonical stress tensor to the general stress-stress correlation: First, there is a term proportional to

$$\begin{aligned}\delta^{ik}\epsilon^{jl}\,\mathrm{Tr}\left(\left[\delta_{ij}\mathcal{L}(q)\right]\mathrm{i}S_{\mathrm{F}}(q)\left[\delta_{kl}\mathcal{L}(r)\right]\mathrm{i}S_{\mathrm{F}}(r)\right) \\ = \delta^{ik}\epsilon^{jl}\delta_{ij}\delta_{kl}\,\mathrm{Tr}\left(\left[\mathcal{L}(q)\right]\mathrm{i}S_{\mathrm{F}}(q)\left[\mathcal{L}(r)\right]\mathrm{i}S_{\mathrm{F}}(r)\right) = 0 \ ,\end{aligned} \tag{4.337}$$

where in the last equality we used Eq. (4.335). Second, there is a contribution proportional to

$$\begin{aligned}\delta^{ik}\epsilon^{jl}\,\mathrm{Tr}\left(\left[\delta_{ij}\mathcal{L}(q)\right]\mathrm{i}S_{\mathrm{F}}(q)\left[\frac{1}{2}\eta_{bd}e^{d}_{(l}\mathrm{i}r_{k)}\gamma^{b}\right]\mathrm{i}S_{\mathrm{F}}(r)\right) \\ = \delta^{ik}\epsilon^{jl}\delta_{ij}\,\mathrm{Tr}\left(\left[\frac{1}{2}\eta_{bd}e^{d}_{(l}\mathrm{i}r_{k)}\gamma^{b}\right]\mathrm{i}S_{\mathrm{F}}(r)\right) \propto \delta^{ik}\epsilon^{jl}\delta_{ij}\delta_{kl} = 0 \ .\end{aligned} \tag{4.338}$$

Here, we use $\mathrm{Tr}(\gamma^{\mu}) = 0$, $\mathrm{Tr}(\gamma^{\mu}\gamma^{\nu}) \propto \eta^{\mu\nu}$, and Eq. (4.335) in the last equality. Last but not least, there is a contribution proportional to

$$\delta^{ik}\epsilon^{jl}\,\mathrm{Tr}\left(\left[\frac{1}{2}\eta_{ac}e^{c}_{(j}\mathrm{i}q_{i)}\gamma^{a}\right]\mathrm{i}S_{\mathrm{F}}(q)\left[\delta_{kl}\mathcal{L}(r)\right]\mathrm{i}S_{\mathrm{F}}(r)\right) = 0 \ , \tag{4.339}$$

which vanishes with an analog line of reasoning as the one which we have used in Eq. (4.338).

4.3.3 Pauli-Villars Approach for a Chern Insulator

In order to regularize Eq. (4.334) for a QAH insulator which is described by the BHZ model, the authors of Ref. [227–230] made use of a finite difference method. In particular, they add up the pure Dirac contributions of each Dirac cone in the lattice Brillouin zone of a Dirac-like system, arising from the fermion doubling at its high-symmetry points [8]. By having in mind an application for a QAH system, they performed their calculations for a Chern insulator [single (pseudo-)spin block of the BHZ model, cf. Sec. 3.1.2] including a Dirac- as well as a Newtonian mass term. As it was explained in Sec. 3.1.1, the BHZ model is a low-energy model close to the Γ-point of a QSH- or QAH insulator, respectively. Consequently, a regularization scheme which relies on fermion doublers appearing at the edges of an artificial lattice Brillouin-zone needs to be treated with caution. In Sec. 4.3.1, we motivated our scientific road-map

of how to circumvent this debatable issue. Nevertheless, in order to understand the results derived in the aforementioned references, let us comment on the torsional Hall viscosity of a Chern insulator on an artificial lattice Brillouin zone.

We start our calculation by discretizing the Hamiltonian of a single 2+1 dimensional Chern insulator, defined in Eq. (3.12). Within the scope of this analysis we are restricting ourselves to the (pseudo-)spin up block of the BHZ model and neglect the identifying subscript [cf. Sec. 3.1.1]. In order to perform our finite difference method, we replace the momenta according to

$$k_i \to \frac{1}{a}\sin\left(k_i a\right) \quad \wedge \quad k_i^2 \to \frac{2}{a^2}\left[1-\cos\left(k_i a\right)\right] \ , \tag{4.340}$$

where a is the artificial lattice constant. For simplicity, we assume $a = 1$ in the following. This implies the lattice Hamiltonian of a single Chern insulator

$$H_{\text{latt}} = \boldsymbol{\sigma}\cdot\mathbf{d}_{\text{latt}} \quad \text{with} \quad \mathbf{d}_{\text{latt}} = \begin{pmatrix} A\sin(k_1) \\ A\sin(k_2) \\ m - 2B\left(2-\cos(k_1)-\cos(k_2)\right) \end{pmatrix} \ . \tag{4.341}$$

Similar to Eq. (3.18), let us calculate the lattice Chern number of this Hamiltonian in terms of the Kubo Formula [190]. For zero temperature and zero chemical potential this Chern number is given by [50, 143]

$$\mathcal{C} = \frac{1}{4\pi}\int \mathrm{d}^2k\ \hat{\mathbf{d}}\cdot\left(\partial_{k_1}\hat{\mathbf{d}}\times\partial_{k_2}\hat{\mathbf{d}}\right) \quad \text{with} \quad \hat{\mathbf{d}} \equiv \frac{\mathbf{d}}{|\mathbf{d}|} \ , \tag{4.342}$$

which implies

$$\mathcal{C} = \frac{1}{4\pi}\int_{\text{BZ}} \mathrm{d}^2k\ \frac{A^2\left(2B\cos(k_2)+\cos(k_1)\left[2B+(-4B+m)\cos(k_2)\right]\right)}{\left(\left[-4B+m+2B(\cos(k_1)+\cos(k_2))\right]^2+A^2\left[\sin(k_1)^2+\sin(k_2)^2\right]\right)^{3/2}} \ . \tag{4.343}$$

Figure 4.19 shows the corresponding topological phases.

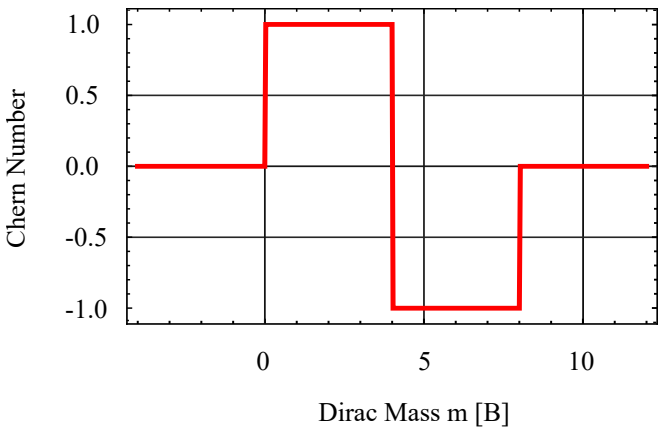

Figure 4.19: Lattice Chern number of a single Chern insulator as a function of the Dirac mass m for $A = B = a = 1$. We observe three topologically different phases: (i) $m/B < 0$ and $m/B > 8$ with Chern number $\mathcal{C} = 0$, (ii) $0 < m/B < 4$ with Chern number $\mathcal{C} = 1$, (iii) $4 < m/B < 8$ with Chern number $\mathcal{C} = -1$. Further explanations are given in the text.

In general, one identifies three topological phase transitions, which can be most easily understood by analyzing the corresponding spectra at the phase transition points. These are shown in Fig. 4.20. Effectively, a lattice Chern insulator consists of four pure Dirac fermions at the high symmetry points of the lattice Brillouin zone. The first order Taylor expansions in the momenta k_i of the lattice Hamiltonian in Eq. (4.341) around these points imply the four Dirac Hamiltonians [8]

$$H_{(0,0)} = +Ak_1\sigma_1 + Ak_2\sigma_2 + m\sigma_3 \ , \tag{4.344}$$

$$H_{(\pm\pi,0)} = -Ak_1\sigma_1 + Ak_2\sigma_2 + (m-4B)\sigma_3 \ , \tag{4.345}$$

$$H_{(0,\pm\pi)} = +Ak_1\sigma_1 - Ak_2\sigma_2 + (m-4B)\sigma_3 \ , \tag{4.346}$$

$$H_{(\pm\pi,\pm\pi)} = -Ak_1\sigma_1 - Ak_2\sigma_2 + (m-8B)\sigma_3 \ . \tag{4.347}$$

Here, the subscript corresponds to the k_1 and k_2 values, respectively [$a = 1$]. All of these pure Dirac Hamiltonians contribute $\pm 1/2$ to the Chern number, as we have discussed in Sec. 3.1.2. However, due to the $B|\mathbf{k}|^2$ mass term in the continuum model, each Dirac Hamiltonian at the high-symmetry points of the artificial lattice closes at different values of m/B. The original Dirac Hamiltonian of the continuum theory is located at the Γ-point. The additional Dirac fermions located at the edge of the Brillouin zone result from fermion-doubling, as it was explained above. They are a direct consequence of the artificial lattice.

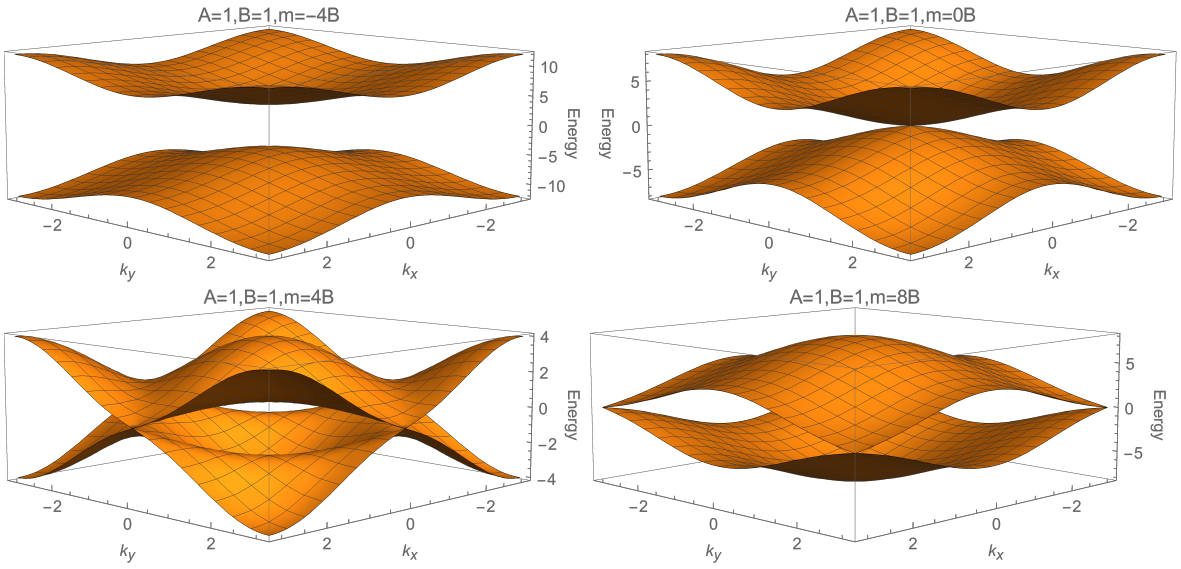

Figure 4.20: Dispersion of the lattice Chern insulator in Eq. (4.341) with $A = B = a = 1$ at the topological phase transition points $m/B \in \{0, 4, 8\}$ and in the topologically trivial phase $m/B = -4$. The spectra in momentum space are visualized in the first lattice Brillouin zone from $[-\pi/a, \pi/a]$. More explanations are given in the text.

The continuum model of a single Chern insulator only has one topological phase transition when m/B changes sign [cf. Eq. (3.19)],

$$\mathcal{C}^{\text{cont}} = \left[\text{sgn}(m) + \text{sgn}(B)\right]/2 \ . \tag{4.348}$$

This transition originates from the band inversion of a single Dirac-like fermion located at the Γ-point in the continuum Brillouin zone. Instead, on the artificial lattice, there are four sources of Berry potential at all high symmetry points of the Brillouin zone [cf. Eqs.(4.344)-(4.347)], each contributing $\pm 1/2$ to the entire Chern number. In the trivial phase, the $\pm 1/2$

coming from the Dirac fermion at the Γ-point is compensated by the other Dirac fermions. While their contribution to the entire Chern number does not change when m/B changes sign, the contribution at the Γ-point flips its sign, leading to an integer Chern number for $m/B > 0$. The same scenario happens at the remaining phase transitions at $m/B = 4$ and $m/B = 8$. These transitions are pure lattice artifacts and do not occur in the continuum model. At these points, either Eqs. (4.345) and (4.346) change their contribution to the entire Chern number [$m/B = 4$], or Eq. (4.347) changes its contribution [$m/B = 8$]. Since all these artificial transitions arise from the lattice discretization, they need to disappear as one approximates the continuum. If we would have not assumed $a = 1$, these phase transitions would occur at $m/B = 4/a^2$ and $m/B = 8/a^2$. Thus, in the continuum limit $a \to 0$, these artificial transitions are shifted towards an infinitely large Dirac mass. Summarizing, the lattice discretization of a Chern insulator needs to be treated with caution. While it gives the same Chern number and also the correct spectrum up to first order in momentum close to the Γ-point if one assumes $|m/B| \ll 1$, it has several artificial effects far from the Γ-point and for $m/B > 1$, which need to be analyzed and interpreted very carefully.

Based on Eqs. (4.344)-(4.347), it seems natural to regularize the torsional Hall viscosity in Eq. (4.334) by superimposing the Dirac responses of all sources of Berry potential on the artificial lattice Brillouin zone described above. Technically, this implies [227, 228]

$$\eta_{\mathrm{H}}^{\mathrm{t}} = \frac{1}{16\pi} \sum_{i=0}^{3} c_i I_{\mathrm{T}}(M_i) \quad \wedge \quad I_{\mathrm{T}}(M_i) = -M_i \Lambda + 2\,\mathrm{sgn}(M_i) M_i^2 \ , \tag{4.349}$$

with $c_i = \{+, -, -, +\}$ and

$$M_0 = m, \qquad M_1 = m - 4B, \qquad M_2 = m - 4B, \qquad M_3 = m - 8B \ , \tag{4.350}$$

describing the Chern number of the single Dirac cones in Eqs. (4.344)-(4.347). If we calculate the torsional Hall viscosity via Eq. (4.349), we obtain

$$\eta_{\mathrm{H}}^{\mathrm{t}} = \frac{-m|m| + (8B - m)\,|-8\,B + m| + 2\,(-4B + m)\,|-4\,B + m|}{16\pi A^2} \ . \tag{4.351}$$

Let us emphasize that this ansatz is not equivalent to a usual Pauli-Villars approach which, commonly, adds fields of opposite statistics to the bare Lagrangian [cf. Sec. 3.2.3]. The aforementioned procedure does not have this property. Nevertheless, as it is required for any reliable renormalization, the ansatz considered cures the divergence in Eq. (4.334), since [227, 228]

$$\sum_{i=0}^{3} c_i M_i = 0 \ . \tag{4.352}$$

Let us now simplify Eq. (4.351) close to the phase transition points.

Phase Transition at $\mathbf{m = 0}$

First, we focus on the phase transition at $m = 0$ where the sign of m/B changes if we do not change the sign of B. As we have mentioned above, this is the physical topological phase transition in the sense that it describes the phase transition of the continuum model of a Chern insulator [cf. Eq. (3.1.1)]. To analyze this transition, we need to consider Eq. (4.351) in the limit $|m| \ll |4B|$, which implies

$$\eta_{\mathrm{H}}^{\mathrm{t}}(m \approx 0) = \frac{-\mathrm{sgn}(m)\, m^2 + \mathrm{sgn}(B)\,(m - 8B)^2 - 2\ \mathrm{sgn}(B)\,(m - 4B)^2}{16\pi A^2} \tag{4.353}$$

$$= \frac{\left(32B^2 - m^2\right)\,\mathrm{sgn}(B) - m^2\,\mathrm{sgn}(m)}{16\pi A^2}\,.$$

In order to derive the change of the torsional Hall viscosity throughout this phase transition, we subtract the non-trivial phase with $\mathrm{sgn}(m) = \mathrm{sgn}(B)$ from the trivial phase with $\mathrm{sgn}(m) = -\mathrm{sgn}(B)$. This in particular implies

$$\Delta\eta_{\mathrm{H}}^{\mathrm{t}}(m \approx 0) = \eta_{\mathrm{H}}^{\mathrm{t,triv}}(m \approx 0) - \eta_{\mathrm{H}}^{\mathrm{t,non-triv}}(m \approx 0) = \frac{m^2\,[\mathrm{sgn}(m) + \mathrm{sgn}(B)]}{16\pi A^2}\,. \tag{4.354}$$

Let us make two remarks regarding Eq. (4.354). First, the change of the torsional Hall viscosity is propotional to the Chern number of the system, which is defined by both, the Dirac- as well as the Newtonian mass term. Due to the relation between the Hall viscosity and the Hall conductivity [190] studied in Sec. 4.1, this does not come as a surprise. Second, Eq. (4.354) is only proportional to a quantized number, as expected due to its mass dimension. This property has been elucidated in Sec. 4.3.1.

Even though the artificial topological phase transitions on the lattice Brillouin zone at $m/B = 4$ and $m/B = 8$ do not describe the continuum model, it is enlightening to study the change of the torsional Hall viscosity throughout these transition points, as we will show in the following.

Phase Transition at m = 8B

In order to analyze this phase transition, we need to consider Eq. (4.351) in the limit $|m| \gg |4B|$:

$$\eta_{\mathrm{H}}^{\mathrm{t}}(m \approx 8B) = \frac{-\mathrm{sgn}(m)\,m^2 + (8B - m)\,|-8\,B + m| + 2\,\mathrm{sgn}(m)\,(m - 4B)^2}{16\pi A^2}\,. \tag{4.355}$$

Throughout this topological phase transition, we subtract the non-trivial phase with from the trivial phase, implying

$$\begin{aligned}\Delta\eta_{\mathrm{H}}^{\mathrm{t}}(m \approx 8B) &= \eta_{\mathrm{H}}^{\mathrm{t,triv}}(m \approx 8B) - \eta_{\mathrm{H}}^{\mathrm{t,non-triv}}(m \approx 8B) \\ &= -\frac{(m - 8\,B)^2\,[\mathrm{sgn}(m) + \mathrm{sgn}(B)]}{16\pi A^2}\,.\end{aligned} \tag{4.356}$$

Phase Transition at m = 4B

Last but not least, in order to analyze the phase transition at $m = 4B$, we need to consider Eq. (4.351) in the limit $0 \ll |m| \ll |8B|$, which implies

$$\eta_{\mathrm{H}}^{\mathrm{t}}(m \approx 4B) = \frac{-\mathrm{sgn}(m)\,m^2 + \mathrm{sgn}(B)\,(m - 8B)^2 + 2\,(-4B + m)\,|-4\,B + m|}{16\pi A^2}\,. \tag{4.357}$$

Throughout this phase transition, we subtract the non-trivial phase with Chern number $\mathcal{C} = -1$ from the non-trivial phase with Chern number $\mathcal{C} = 1$, implying

$$\begin{aligned}\Delta\eta_{\mathrm{H}}^{\mathrm{t}}(m \approx 4B) &= \eta_{\mathrm{H}}^{\mathrm{t},\mathcal{C}=1}(m \approx 4B) - \eta_{\mathrm{H}}^{\mathrm{t},\mathcal{C}=-1}(m \approx 4B) \\ &= -\frac{2(m - 4\,B)^2\,[\mathrm{sgn}(m) + \mathrm{sgn}(B)]}{16\pi A^2}\,.\end{aligned} \tag{4.358}$$

Notice, that essentially Eqs. (4.356) and (4.358) show the same features as Eq. (4.354). The change of the torsional Hall viscosity is proportional to the system's Chern number and, in particular, proportional to the squared Dirac mass term of those Hamiltonians which close their mass gap at the corresponding phase transition points.

4.3.4 Finite Difference Result for a Chern Insulator

In the above calculation we have used a Pauli-Villars approach in the sense that we superimposed all Dirac responses of a discretized Chern insulator on an artificial lattice. This allowed us to derive a well defined change of the torsional Hall viscosity throughout the corresponding topological phase transitions. In order to obtain the entire response of a Chern insulator on a discretized space lattice, one needs to calculate the stress-stress correlator by using a finite difference method form the start. This calculation has been explicitly done in Ref. [232], or, with a slight discrepancy[a], in Ref. [233]. Starting with the discretized lattice Hamiltonian in Eq. (4.341), it is straightforward to show that one obtains for the lattice stress tensor [232]

$$T_{11} = -\sin(k_1)\left[A\cos(k_1)\sigma_1 - 2B\sin(k_1)\sigma_3\right] \ , \tag{4.359}$$
$$T_{12} = -\sin(k_1)\left[A\cos(k_2)\sigma_2 - 2B\sin(k_2)\sigma_3\right] \ , \tag{4.360}$$
$$T_{21} = -\sin(k_2)\left[A\cos(k_1)\sigma_1 - 2B\sin(k_1)\sigma_3\right] \ , \tag{4.361}$$
$$T_{22} = -\sin(k_2)\left[A\cos(k_2)\sigma_2 - 2B\sin(k_2)\sigma_3\right] \ . \tag{4.362}$$

Again, for reasons of simplicity, we have chosen a lattice spacing of $a = 1$.

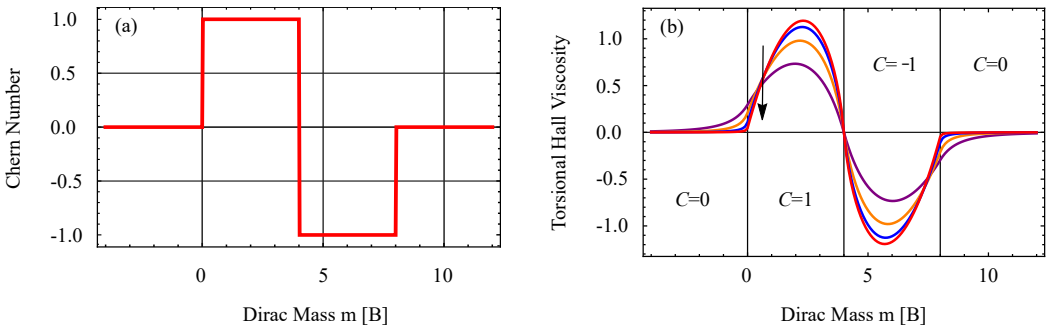

Figure 4.21: (a) Lattice Chern number of a Chern insulator as a function of the Dirac mass m for $A = B = a = 1$. This subfigure has already been shown in Fig. 4.19. Here, it should support the understanding of subfigure **(b)**: Torsional Hall viscosity of a Chern insulator on a discretized space lattice in units $\hbar/a^2$ as a function of the Dirac mass m with $B = a = 1$. The black arrow indicates an increasing A parameter, $A \in \{0.25, 0.5, 1, 2\}$. Subfigure (b) has been inspired by Fig. 6 of Ref. [232]. More explanations are given in the text.

With the eigen-vectors and eigen-energies of Eq. (4.341), the torsional Hall viscosity can be calculated on the underlying space lattice via the Kubo formula [232]

$$\eta_{\mathrm{H}}^{\mathrm{t}} = \lim_{p_0 \to 0} \frac{1}{p_0} \frac{1}{V} \int \mathrm{d}x^0 \, \mathrm{e}^{\mathrm{i}p_0 x^0} \left\langle \left[T_{11}^{\mathrm{lattice}}(x_0), T_{12}^{\mathrm{lattice}}(0) \right] \right\rangle \tag{4.363}$$
$$= -\frac{2}{V} \, \mathrm{Im} \sum_{\nu(\nu') \in (\mathrm{un})\mathrm{occupied}} \frac{\left\langle \nu \left| T_{11}^{\mathrm{lattice}} \right| \nu' \right\rangle \left\langle \nu' \left| T_{12}^{\mathrm{lattice}} \right| \nu \right\rangle}{\left(E_{\nu'} - E_{\nu}\right)^2} \ ,$$

where V is the area of the system. Our result is shown in Fig. 4.21(b) for different values

[a] The authors of Ref. [233] found a nonphysical discontinuity in the torsional Hall viscosity at the topological phase transition points, which originates from an additional factor of two in their lattice integrals.

of $A \in \{0.25, 0.5, 1, 2\}$. In order to compare the functional dependency of $\eta_{\mathrm{H}}^{\mathrm{t}}$ to the system's lattice Chern number, Fig. 4.21(a) shows the latter quantity as it was illustrated in Fig. 4.19.

Essentially, we identify the same features which we have already obtained in the continuum limit in Sec. 4.3.3. The torsional Hall viscosity is directly proportional to the system's Chern number, which dictates the sign and the topological phase transitions of $\eta_{\mathrm{H}}^{\mathrm{t}}$. Moreover, the torsional Hall viscosity is a continuous quantity. It vanishes at the phase transition points, as in their vicinity it is proportional to the Dirac mass terms of those Hamiltonians which close their gaps at the corresponding values of m/B.

5

Summary, Conclusions and Outlook

In the course of thesis we shed light on the parity-odd ballistic- as well as hydrodynamic transport features of two-dimensional electron systems. We clarified in which sense the transport coefficients of Dirac-like materials in 2+1 space-time dimensions are related to the parity anomaly of planar quantum electrodynamics.

In the first part of this thesis, we have analyzed the physics of two-dimensional quantum anomalous Hall (QAH) insulators in the context of the parity anomaly in 2+1 space-time dimensions. In Chap. 2 we have presented a self contained introduction into the quantum Hall effect, as well as into the field theoretic description of 2+1 dimensional quantum electrodynamics (QED_{2+1}). We have in particular discussed how the parity anomaly of QED_{2+1} arises in the calculation of the effective action and in which way this anomaly is related to the chiral anomaly if the system is confined on a 2+1 dimensional manifold with a 1+1 dimensional boundary. In such a system the Callan-Harvey mechanism becomes apparent. Moreover, in Sec. 3.1 we have introduced and explained the solid-state concepts of two-dimensional topological insulators, quantum anomalous Hall insulators, the Bernevig-Hughes-Zhang (BHZ) as well as the Haldane model, and the concept of two-dimensional Chern insulators. We have shown that the low-energy physics of two-dimensional QAH insulators like (Hg,Mn)Te quantum wells or magnetically doped (Bi,Sb)Te thin films can be described by the combined response of two 2+1 space-time dimensional Chern insulators with a linear dispersion in momentum. Due to their Dirac-like spectra, each of those Chern insulators is directly related to the parity anomaly of planar quantum electrodynamics. Based on these theoretical principles we worked out in which sense the recent progress in condensed matter physics, namely the verification of two-dimensional Dirac-like materials and their experimental control, enables the observation of signatures of the parity anomaly in the solid-state lab.

More specifically, in Sec. 3.2 we related the physics originating from the Newtonian mass term of a QAH insulator to the parity anomaly of planar quantum electrodynamics. We have in particular shown that before renormalization the Newtonian $B|\mathbf{k}|^2$ mass term acts similar to a parity-breaking high-energy regulator in the calculation of the quantum effective action. As a direct consequence, we clarified that this mass term is directly related to the regularization of QED_{2+1} and, as such, to the parity anomaly itself. It was proven that the Newtonian mass alone does not render the effective action UV finite, but ensures an integer quantized DC Hall conductivity which ensures the gauge-invariance of the associated effective Chern-Simons action. Our comparison of the Newtonian mass term to several QED_{2+1} regularization schemes has demonstrated that before renormalization, the $B|\mathbf{k}|^2$ term acts similar to a Wilson mass term, which avoids the fermion doubling in a lattice approach. Moreover, during our calculation of the effective action, we have derived the AC Hall conductivity of QAH insulators described by the BHZ Hamiltonian. We have in particular shown that the leading order AC correction to the DC Hall conductivity contains a term proportional to the Chern number. This term originates from the broken Lorentz symmetry, and, therefore,

from the Newtonian mass term. It was proven that this correction can be measured by purely electrical means, or by determining the leading order frequency corrections to the associated DC Faraday- and Kerr angles. We revealed that the $B|\mathbf{k}|^2$ mass term significantly changes the resonance structure of the AC Hall conductivity in comparison to pure Dirac systems such as graphene.

In Sec. 3.3, we extended our field theoretical analysis to quantizing out-of-plane magnetic fields: In a nutshell, we revealed three novel transport features directly originating from the parity anomaly of planar quantum electrodynamics:

(*i*) A violation of the Onsager relation for chemical potentials in the Dirac mass gap.

(*ii*) A special type of charge pumping in the QAH phase, the so-called anomaly inflow, with an increasing out-of-plane magnetic field. This charge pumping significantly differs from the corresponding charge flow described by conventional QH physics.

(*iii*) For large out-of-plane magnetic fields [$H > H_{\text{crit}}$] we found the formation of counter-propagating QH and QAH edge states if the chemical potential is placed in the conduction- or in the valance band, depending on the sign of the magnetic field.

In summary these three hallmarks underline the different physical origin of the QH- and QAH phase. In particular our results can be used to make these two phases experimentally distinguishable, even though they are described by the same Chern number [$\mathcal{C} \in \mathbb{Z}$]. For instance, as a smoking-gun of the QAH effect in finite out-of-plane magentic fields, we predicted a transition from the $\sigma_{\text{xy}} = -\text{e}^2/\text{h}$ plateau [QAH effect] to a noisy QH plateau with increasing magnetic field strength. By using a Landau-Büttiker approach, it was shown that the average value of this noisy plateau significantly depends on the physical details of the QH-QAH edge state scattering [e.g. asymmetric charge-puddle scattering].

All of the aforementioned results do not incorporate finite temperature effects. In order to shed light on such phenomena, we further analyzed in Sec. 3.4 the finite temperature Hall response of 2+1 dimensional Chern insulators under the combined influence of a chemical potential and an out-of-plane magnetic field. As mentioned several times throughout this thesis, this non-dissipative transport coefficient is directly related to the parity anomaly of planar quantum electrodynamics as it persists in the parity-symmetric limit at zero magnetic fields [$m, B \to 0^{\pm}$]. Due to this crucial property we were able to show that the parity anomaly itself is not renormalized by finite temperature effects. Instead, it was proven that the parity anomaly induces two terms of different physical origin in the effective action of a single Chern insulator, which together define the total Hall conductivity of the entire QAH system:

(*i*) The first term is temperature and chemical potential independent and only defines the intrinsic topological response of the QAH phase.

(*ii*) The second term characterizes the non-topological thermal response of the associated conduction- and valence band excitations.

In our analysis we have rigorously proven that in the topologically nontrivial phase, an increasing relativistic mass term m of a Chern insulator counteracts finite temperature effects, whereas an increasing non-relativistic mass term $B|\mathbf{k}|^2$ instead enhances these corrections. On the other hand, in the topologically trivial phase, both of these mass terms counteract the finite temperature broadening of the Fermi-Dirac distribution as the Newtonian mass cannot cause a camel-back gap-structure in this topological phase. Last but not least, we have derived the thermal response of single Chern insulators in an out-of-plane magnetic field and clarified their relation to the spectral asymmetry. It was explicitly shown that this peculiar quantity is a measure of the parity anomaly in finite out-of-plane magnetic fields.

We have in particular derived in which way the thermal LL response renormalizes the parity anomalous part of the Hall conductivity in magnetic fields. Especially in the Dirac mass gap, this response superimposes the otherwise quantized and temperature independent part of the Hall conductivity arising from the parity anomaly. Most remarkably, it was demonstrated that the anomalous part of the Hall response in the Dirac mass gap of a QAH insulator is much more robust than the common LL contributions with respect to finite temperature effects.

As we have mentioned several times throughout this thesis all of the aforementioned results are in principle verifiable in QAH insulators like (Hg,Mn)Te quantum wells, magnetically doped (Bi,Sb)Te thin films, or bilayer structures of three-dimensional topological- and ferromagnetic insulators.

Let us close the first part of our summary by giving an outlook of exceptionally interesting future research directions. As the classification of three-dimensional topological insulators is also given by the interplay between their Dirac- and Newtonian mass terms, a natural extension of our work would be to derive the effective action of 4+1 space-time dimensional Dirac-like systems including both, a Dirac as well as a momentum-dependent term. This will shed light on the anomaly induced transport described by a $4+1$ dimensional Chern-Simons theory [43]. Another interesting extension would be to study signatures of quantum anomalies beyond the BHZ model in various space-time dimensions. For instance, the chiral-, the gravitational-, and the conformal anomaly should not depend on thermal effects. However, similar to the parity anomaly, these anomalies are expected to induce a temperature dependence in the quantum effective action. Last but not least, another promising future direction of our analysis would be to study the physics originating from counter-propagating QH and QAH edge states in greater depth, in order to further understand the response of QAH insulators in an electromagnetic background. Our predictions are also expected to be of significant relevance for fractional Chern insulators. The response of these systems in the presence of quantizing out-of-plane magnetic fields will give rise to fundamentally new insights into the relation between non-commutative geometries, non-abelian statistics and the parity anomaly in 2+1 space-time dimensions. As this possible extension has a highly innovative and field-opening character, its development is currently in progress.

In the second part of this thesis, we have studied the hydrodynamic transport of two-dimensional electron systems with a broken time-reversal and parity symmetry. In Sec. 4.1, we gave a coherent introduction into the properties of different hydrodynamic solid-state materials. We pedagogically elucidated both, the hydrodynamic features of two-dimensional Fermi liquids like GaAs, as well as the corresponding properties of Dirac fluids, such as graphene, in which the dispersion is linear in momentum. This attribute enables the observation of relativistic hydrodynamics in the solid-state lab. In Sec. 4.1.2, we derived the non-relativistic Navier-Stokes equations from the relativistic conservation laws for the particle current and the energy-momentum tensor. In the scope of this analysis we derived in which way the quantum critical-, as well as the quantum anomalous Hall conductivity contribute to the hydrodynamic response of non-relativistic fluid profiles.

Moreover, in Sec. 4.2, we derived the hydrodynamic transport in Fermi liquids which originates from a peculiar non-dissipative transport coefficient, namely from the Hall viscosity. More specifically, we analyzed the solutions of the non-relativistic Navier-Stokes equations for Fermi liquids in external out-of-plane magnetic fields. In such fields the parity-odd Hall viscosity generates a Hall viscous force which directly competes against the Lorentz force. While together both of these forces contribute to the entire Hall voltage in charged Fermi

liquids, we present a way of how to unambiguously distinguish the Hall viscous- from the Lorentz force contributions to the entire Hall voltage in a two-dimensional channel geometry. It was shown that this distinction relies on the different scaling of both voltage contributions with the corresponding system parameters. We elucidated that the ratio of the Hall viscous- to the Lorentz force induced voltage contribution is negative, and that in clean systems its modulus decreases with the width, slip-length and the carrier density. In contrast, this modulus increases with the electron-electron mean free path. For typical Fermi liquids such as GaAs, we found that the Hall viscous signal dominates over the Lorentz force contribution up to a critical magnetic field, which is on the order of a few tens of millitesla. At this field, the total Hall voltage vanishes, which is a smoking-gun signature of Hall viscosity induced transport. Moreover, we have shown that the identification of both voltage contributions is possible by measuring the system's local Hall voltage. We predicted the for the setup under consideration the total Hall electric field is parabolic in the transverse channel coordinate. This property has been recently measured in Ref. [97]. While the curvature of this parabola essentially originates from Lorentz force, its offset is substantially characterized by the Hall viscosity. All in all, our predictions pave the way to experimentally identify Hall viscous effects. As such, they can be used to identify the electron-electron interaction strength in the systems considered. Hitherto, we performed our analysis solely for Fermi liquids in the non-relativistic fluid velocity limit. Based on the theoretical principles presented in Sec. 4.1, the extension of our Fermi liquid analysis towards the Dirac liquid regime is currently in progress.

Let us close this thesis by giving an outlook of exceptionally interesting future hydrodynamic research directions. On the one hand, we are currently extending of our analysis towards the (gap-less) Dirac fluid phase for instance in graphene, where quantum critical effects become most relevant. In order to experimentally confirm our theoretical predictions, this work is developed in close collaboration with the group of Prof. Dr. Amir Yacoby at the Harvard University. Another highly interesting possible future direction of our approach is to generalize our analysis towards anomaly driven systems in 2+1 space-time dimensions. Relying on our results in the first part of this thesis, an extension towards two-dimensional QAH insulators would be of extraordinary relevance. As a consequence a broken parity and time-reversal symmetry even at zero magnetic fields, the hydrodynamic transport of these systems is characterized by a special Hall viscous effect, namely by the torsional Hall viscosity [85, 227]. Relying on this property, the predicted extension will shed light onto possible signatures of the parity anomaly in 2+1 dimensional hydrodynamic electron transport.

6 Appendix

6.1 Hall Conductivity of Chern Insulators in Magnetic Fields: A Solid-State Perspective

It is the goal of the present appendix to support our field theoretic calculations in Sec. 3.3 by a solid-state approach for determining the Hall conductivity of a single Chern insulator in quantizing out-of-plane magnetic fields **H**. The present analysis will mainly follow the line of reasoning in Ref. [158]. We are in particular deriving Eq. (3.146a) of the main text from a solid-state perspective, by using the Kubo formula [50, 99]. For this reason, the subsequent analysis might by enlightening for condensed matter physicists, which are more familiar with the Kubo formalism in comparison to our field theoretic calculations in Sec. 3.3. This appendix should make our theoretical findings for QAH insulators in quantizing out-of-plane magnetic fields more comprehensible for an interdisciplinary community.

6.1.1 Hamiltonian and Eigen-System

In Sec. 3.1.2, we have studied the eigen-system as well as the Chern number of a single Chern insulator in 2+1 space-time dimensions. In what follows, we are incorporating in our analysis a quantizing out-of-plane magnetic field, which is implemented in the Landau gauge

$$\mathbf{A} = (-Hx_2, 0, 0) \ . \tag{6.1}$$

As explained in Sec. 3.3, the Hamiltonian of a Chern insulator in such a background field is given by [163][b]

$$\mathcal{H}_+(a, a^\dagger) = \begin{pmatrix} m_+ + \omega_+ \left(a^\dagger a + \frac{1}{2} \right) & \alpha \, a^\dagger \\ \alpha \, a & -m_+ + \omega_- \left(a^\dagger a + \frac{1}{2} \right) \end{pmatrix} \ , \tag{6.2}$$

where $\alpha = \sqrt{2}A/l_H, \omega_\pm = \delta \pm \beta, \beta = -2B/l_H^2, \delta = -2D/l_H^2$, and l_H is the magnetic length[c]. Within the present analysis, we are considering positive magnetic field strength with $\mathrm{sgn}(\mathrm{e}H) = 1$. As explained in Sec. 3.3.1, the Hamiltonian in Eq. (6.2) has been obtained form the zero-field model by Peierls substituting the momenta and by introducing the ladder operators a and $a^\dagger$ [cf. Eq. (2.14)]. The degenerated Landau level eigen-energies in

[b] Notice, that in comparison to Sec. 3.3, we changed the sign of β and δ in order to enable an easy comparison of our calculation to the one which is presented in Ref. [158].

[c] In the scope of this analysis we are only considering the (pseudo-)spin up block of the BHZ model. Analogous results for the (pseudo-)spin down block can be derived by inverting the sign of the mass terms $(m_+, B) \to (-m_-, -B)$, as it has been shown in Eq. (3.48).

the momentum k_1 of Eq. (6.2) are given by [cf. Eqs (3.107), (3.108)] [158, 163]

$$E_{n,k_1,s} = \frac{1}{2}\left(\beta + 2n\delta + s\sqrt{\left(\delta + 2(m_+ + n\beta)\right)^2 + 4n\alpha^2}\right) , \tag{6.3}$$

$$E_{0,k_1} = m_+ + \frac{1}{2}(\beta + \delta) . \tag{6.4}$$

For the corresponding eigen-states, we made the ansatz [cf. Eqs. (3.105) and (3.106)]

$$|\psi^s_{n,k_1}\rangle = \begin{pmatrix} C^{n,s}|n,k_1\rangle \\ S^{n,s}|n-1,k_1\rangle \end{pmatrix} \quad \text{for} \quad n \in \mathbb{N} \quad \wedge \quad |\psi_{0,k_1}\rangle = \begin{pmatrix} |0,k_1\rangle \\ 0 \end{pmatrix} \quad \text{for} \quad n = 0 . \tag{6.5}$$

6.1.2 Chern Number and Hall Conductivity

In what follows, we calculate the Chern number $\mathcal{C}_{\mathrm{CI}}$ associated to the Hamiltonan in Eq. (6.2) from a solid-state perspective via the Kubo formula [50, 158]

$$\mathcal{C}_{\mathrm{CI}} = -\frac{2\pi\hbar^2}{V}\sum_{k_1,k_1'}\sum_{n,s\neq n',s'} \frac{\mathrm{Im}\left[v_{1;ns,n's'}v_{2;n's',ns}\right]\left[f(E_{n,k_1,s}-\mu) - f(E_{n',k_1',s'}-\mu)\right]}{\left(E_{n,k_1,s} - E_{n',k_1',s'}\right)^2} . \tag{6.6}$$

Here, V is the system's area and we introduced the matrix elements

$$v_{i;ns,n's'} \equiv \langle n,k_1,s|v_i|n',k_1,s'\rangle , \tag{6.7}$$

which consist of the velocity operators [158]

$$v_1 = \hbar^{-1}\partial_{k_1}H_0[k] = -\frac{l_H}{\sqrt{2}\hbar}\begin{pmatrix} \omega_+(a^\dagger + a) & \alpha \\ \alpha & \omega_-(a^\dagger + a)\end{pmatrix} , \tag{6.8}$$

$$v_2 = \hbar^{-1}\partial_{k_2}H_0[k] = \frac{\mathrm{i}l_H}{\sqrt{2}\hbar}\begin{pmatrix} \omega_+(a^\dagger - a) & -\alpha \\ \alpha & \omega_-(a^\dagger - a)\end{pmatrix} . \tag{6.9}$$

In the second equality of each line we again used the Peierls substitution and introduced the ladder operators a and $a^\dagger$. In what follows, we are neglecting finite temperature effects and assume $T = 0$. We are in addition considering a chemical potential in the system's mass gap at charge neutrality $\mu = E_{\mathrm{z}} = -mD/B$ [cf. Sec. 3.3.2]. Hence, we assume that all conduction band Landau levels with $s = +$ are unoccupied, whereas all valence band Landau levels with $s = -$ are occupied. This is essentially encoded by the Fermi-Dirac distribution functions

$$f(E_{n,k_1,+} - E_{\mathrm{z}}) = 0 \quad \wedge \quad f(E_{n,k_1,-} - E_{\mathrm{z}}) = 1 \qquad \forall n \in \mathbb{N} . \tag{6.10}$$

All Landau levels with $n \in \mathbb{N}$ come in pairs, one level in the conduction band and one level in the valence band, respectively. The single zeroth Landau level is special. For $E_{0,k_1} > E_{\mathrm{z}}$ it belongs to the conduction band, whereas for $E_{0,k_1} < E_{\mathrm{z}}$ it belongs to the valence band.

In Eq. (6.6), the summation over k_1 can be performed trivially, as all summands are degenerated in this momentum. One solely needs to take into account the degeneracy $\mathbb{D} = V/(2\pi l_H^2)$ of each Landau level [cf. Eq. (2.23)], which implies

$$\mathcal{C}_{\mathrm{CI}} = -\frac{\hbar^2}{l_H^2}\sum_{n,n'}\left(\frac{\mathrm{Im}\left[v_{1;n-,n'+}v_{2;n'+,n-}\right]}{\left(E_{n,k_1,-} - E_{n',k_1,+}\right)^2} - \frac{\mathrm{Im}\left[v_{1;n+,n'-}v_{2;n'-,n+}\right]}{\left(E_{n,k_1,+} - E_{n',k_1,-}\right)^2}\right) \tag{6.11}$$

$$= -\frac{2\hbar^2}{l_H^2}\sum_{n,n'}\frac{\mathrm{Im}\left[v_{1;n-,n'+}v_{2;n'+,n-}\right]}{\left(E_{n,k_1,-}-E_{n',k_1,+}\right)^2}\ .$$

In the last equality we used

$$\mathrm{Im}\left[\sum_{n,n'}\langle n,k_1,s|v_1|n',k_1,s'\rangle\langle n',k_1,s'|v_2|n,k_1,s\rangle\right] \tag{6.12}$$
$$= \left[\mathrm{Im}\left[\sum_{n,n'}\langle n,k_1,s|v_1|n',k_1,s'\rangle\langle n',k_1,s'|v_2|n,k_1,s\rangle\right]\right]^\dagger\ ,$$

which can be further simplified to

$$= -\mathrm{Im}\left[\sum_{n,n'}\left(\langle n,k_1,s|v_1|n',k_1,s'\rangle\langle n',k_1,s'|v_2|n,k_1,s\rangle\right)^\dagger\right] \tag{6.13}$$
$$= -\mathrm{Im}\left[\sum_{n,n'}\langle n,k_1,s|v_1|n',k_1,s'\rangle^\dagger\langle n',k_1,s'|v_2|n,k_1,s\rangle^\dagger\right]$$
$$= -\mathrm{Im}\left[\sum_{n,n'}\langle n',k_1,s'|v_1^\dagger|n,k_1,s\rangle\langle n,k_1,s|v_2^\dagger|n',k_1,s'\rangle\right]$$
$$= -\mathrm{Im}\left[\sum_{n,n'}\langle n',k_1,s'|v_1|n,k_1,s\rangle\langle n,k_1,s|v_2|n',k_1,s'\rangle\right]$$
$$= -\mathrm{Im}\left[\sum_{n,n'}\langle n,k_1,s'|v_1|n',k_1,s\rangle\langle n',k_1,s|v_2|n,k_1,s'\rangle\right]\ .$$

In Eq. (6.12) we have explicitly inserted the assumption in Eq. (6.10). After having performed the summations over s and k_1, we are left with the summation over the Landau level index n in Eq. (6.11). To this end, we need to distinguish several cases. We start with the calculation of the matrix elements associated to $n>1$ and $n'>1$:

$$\begin{aligned}
v_{1;ns,n's'} &= -\frac{l_H}{\sqrt{2}\hbar}\Big(\langle n|C^{n,s},\langle n-1|S^{n,s}\Big)\begin{pmatrix}\omega_+(a^\dagger+a) & \alpha\\ \alpha & \omega_-(a^\dagger+a)\end{pmatrix}\begin{pmatrix}C^{n',s'}|n'\rangle\\ S^{n',s'}|n'-1\rangle\end{pmatrix}\\
&= -\frac{l_H}{\sqrt{2}\hbar}\Big(\langle n|C^{n,s},\langle n-1|S^{n,s}\Big)\begin{pmatrix}\omega_+(a^\dagger+a)C^{n',s'}|n'\rangle+\alpha S^{n',s'}|n'-1\rangle\\ \alpha C^{n',s'}|n'\rangle+\omega_-(a^\dagger+a)S^{n',s'}|n'-1\rangle\end{pmatrix}\\
&= -\frac{l_H}{\sqrt{2}\hbar}\Big[\langle n|C^{n,s}\Big(\omega_+(a^\dagger+a)C^{n',s'}|n'\rangle+\alpha S^{n',s'}|n'-1\rangle\Big) \qquad (6.14)\\
&\qquad +\langle n-1|S^{n,s}\Big(\alpha C^{n',s'}|n'\rangle+\omega_-(a^\dagger+a)S^{n',s'}|n'-1\rangle\Big)\Big]\\
&= -\frac{l_H}{\sqrt{2}\hbar}\Big[\omega_+C^{n,s}C^{n',s'}\langle n|(a^\dagger+a)|n'\rangle+\alpha C^{n,s}S^{n',s'}\langle n|n'-1\rangle\\
&\qquad +\alpha S^{n,s}C^{n',s'}\langle n-1|n'\rangle+\omega_-S^{n,s}S^{n',s'}\langle n-1|(a^\dagger+a)|n'-1\rangle\Big]\ .
\end{aligned}$$

Here and in the following we are neglecting the k_1 index as we have already incorporated the corresponding degeneracy. Due to the assumption $n,n'>1$, we can simplify this expression further by using the identities

$$\langle n|(a^\dagger+a)|n'\rangle=\sqrt{n'+1}\langle n|n'+1\rangle+\sqrt{n'}\langle n|n'-1\rangle=\sqrt{n'+1}\delta_{n,n'+1}+\sqrt{n'}\delta_{n,n'-1}$$

$$= \sqrt{n'+1}\delta_{n-1,n'} + \sqrt{n'}\delta_{n+1,n'} \ ,$$

$$\langle n-1|(a^\dagger + a)|n'-1\rangle = \sqrt{n'}\delta_{n-1,n'} + \sqrt{n'-1}\delta_{n+1,n'} \ , \tag{6.15}$$

$$\begin{aligned}\langle n'|(a^\dagger - a)|n\rangle &= \sqrt{n+1}\langle n'|n+1\rangle - \sqrt{n}\langle n'|n-1\rangle = \sqrt{n+1}\delta_{n',n+1} - \sqrt{n}\delta_{n',n-1} \\ &= \sqrt{n+1}\delta_{n',n+1} - \sqrt{n}\delta_{n',n-1} \ ,\end{aligned}$$

$$\langle n'-1|(a^\dagger - a)|n-1\rangle = \sqrt{n}\delta_{n',n+1} - \sqrt{n-1}\delta_{n',n-1} \ ,$$

which imply

$$\begin{aligned}v_{1;ns,n's'} = -\frac{l_H}{\sqrt{2}\hbar}\Big[&\omega_+ C^{n,s}C^{n',s'}(\sqrt{n'+1}\delta_{n-1,n'} + \sqrt{n'}\delta_{n+1,n'}) + \alpha C^{n,s}S^{n',s'}\delta_{n+1,n'} \\ &+ \alpha S^{n,s}C^{n',s'}\delta_{n-1,n'} + \omega_- S^{n,s}S^{n',s'}(\sqrt{n'}\delta_{n-1,n'} + \sqrt{n'-1}\delta_{n+1,n'})\Big] \ .\end{aligned} \tag{6.16}$$

Analogously, we can evaluate the matrix element

$$\begin{aligned}v_{2;n's',ns} &= \frac{\mathrm{i}l_H}{\sqrt{2}\hbar}\left(\langle n'|C^{n',s'}, \langle n'-1|S^{n',s'}\right)\begin{pmatrix}\omega_+(a^\dagger - a) & -\alpha \\ \alpha & \omega_-(a^\dagger - a)\end{pmatrix}\begin{pmatrix}C^{n,s}|n\rangle \\ S^{n,s}|n-1\rangle\end{pmatrix} \\ &= \frac{\mathrm{i}l_H}{\sqrt{2}\hbar}\left(\langle n'|C^{n',s'}, \langle n'-1|S^{n',s'}\right)\begin{pmatrix}\omega_+(a^\dagger - a)C^{n,s}|n\rangle - \alpha S^{n,s}|n-1\rangle \\ \alpha C^{n,s}|n\rangle + \omega_-(a^\dagger - a)S^{n,s}|n-1\rangle\end{pmatrix} \\ &= \frac{\mathrm{i}l_H}{\sqrt{2}\hbar}\Big[\langle n'|C^{n',s'}\left(\omega_+(a^\dagger - a)C^{n,s}|n\rangle - \alpha S^{n,s}|n-1\rangle\right) \\ &\qquad + \langle n'-1|S^{n',s'}\left(\alpha C^{n,s}|n\rangle + \omega_-(a^\dagger - a)S^{n,s}|n-1\rangle\right)\Big] \\ &= \frac{\mathrm{i}l_H}{\sqrt{2}\hbar}\Big[\omega_+ C^{n',s'}C^{n,s}\langle n'|(a^\dagger - a)|n\rangle - \alpha C^{n',s'}S^{n,s}\langle n'|n-1\rangle \\ &\qquad + \alpha S^{n',s'}C^{n,s}\langle n'-1|n\rangle + \omega_- S^{n',s'}S^{n,s}\langle n'-1|(a^\dagger - a)|n-1\rangle\Big] \\ &= \frac{\mathrm{i}l_H}{\sqrt{2}\hbar}\Big[\omega_+ C^{n',s'}C^{n,s}(\sqrt{n+1}\delta_{n',n+1} - \sqrt{n}\delta_{n',n-1}) - \alpha C^{n',s'}S^{n,s}\delta_{n',n-1} \\ &\qquad + \alpha S^{n',s'}C^{n,s}\delta_{n',n+1} + \omega_- S^{n',s'}S^{n,s}(\sqrt{n}\delta_{n',n+1} - \sqrt{n-1}\delta_{n',n-1})\Big] \ .\end{aligned} \tag{6.17}$$

Thus, we obtain in combination:

$$\begin{aligned}\mathrm{i}\frac{2\hbar^2}{l_H^2}\sum_{n,n'>1} v_{1;ns,n's'}v_{2;n's',ns} = \\ \sum_{n'}\Big[&\omega_+ C^{n,s}C^{n',s'}(\sqrt{n'+1}\delta_{n-1,n'} + \sqrt{n'}\delta_{n+1,n'}) + \alpha C^{n,s}S^{n',s'}\delta_{n+1,n'} \\ &+ \alpha S^{n,s}C^{n',s'}\delta_{n-1,n'} + \omega_- S^{n,s}S^{n',s'}(\sqrt{n'}\delta_{n-1,n'} + \sqrt{n'-1}\delta_{n+1,n'})\Big] \\ \times\Big[&\omega_+ C^{n',s'}C^{n,s}(\sqrt{n+1}\delta_{n',n+1} - \sqrt{n}\delta_{n',n-1}) - \alpha C^{n',s'}S^{n,s}\delta_{n',n-1} \\ &+ \alpha S^{n',s'}C^{n,s}\delta_{n',n+1} + \omega_- S^{n',s'}S^{n,s}(\sqrt{n}\delta_{n',n+1} - \sqrt{n-1}\delta_{n',n-1})\Big] \ .\end{aligned} \tag{6.18}$$

To further simplify this expression, let us analyze the terms proportional to $\delta_{n',n-1}$. For these

terms, we obtain

$$\begin{aligned}
&\sum_{n>2,n'>1} \delta_{n',n-1} \left(\omega_+ C^{n,s} C^{n',s'} \sqrt{n'+1} + \alpha S^{n,s} C^{n',s'} + \omega_- S^{n,s} S^{n',s'} \sqrt{n'}\right) \\
&\qquad \times \left[-\omega_+ C^{n',s'} C^{n,s} \sqrt{n} - \alpha C^{n',s'} S^{n,s} - \omega_- S^{n',s'} S^{n,s} \sqrt{n-1}\right] \\
&= \sum_{n>2} - \left(\omega_+ C^{n,s} C^{n-1,s'} \sqrt{n} + \alpha S^{n,s} C^{n-1,s'} + \omega_- S^{n,s} S^{n-1,s'} \sqrt{n-1}\right) \\
&\qquad \times \left[\omega_+ C^{n-1,s'} C^{n,s} \sqrt{n} + \alpha C^{n-1,s'} S^{n,s} + \omega_- S^{n-1,s'} S^{n,s} \sqrt{n-1}\right] \\
&= \sum_{n>2} - \left(\omega_+ C^{n,s} C^{n-1,s'} \sqrt{n} + \alpha S^{n,s} C^{n-1,s'} + \omega_- S^{n,s} S^{n-1,s'} \sqrt{n-1}\right)^2 .
\end{aligned} \tag{6.19}$$

Analogously, we can simplify all contributions coming along with $\delta_{n',n+1}$:

$$\begin{aligned}
&\sum_{n,n'>1} \delta_{n',n+1} \left(\omega_+ C^{n,s} C^{n',s'} \sqrt{n'} + \alpha C^{n,s} S^{n',s'} + \omega_- S^{n,s} S^{n',s'} \sqrt{n'-1}\right) \\
&\qquad \times \left[\omega_+ C^{n',s'} C^{n,s} \sqrt{n+1} + \alpha S^{n',s'} C^{n,s} + \omega_- S^{n',s'} S^{n,s} \sqrt{n}\right] \\
&= \sum_{n>1} \left(\omega_+ C^{n,s} C^{n+1,s'} \sqrt{n+1} + \alpha C^{n,s} S^{n+1,s'} + \omega_- S^{n,s} S^{n+1,s'} \sqrt{n}\right) \\
&\qquad \times \left[\omega_+ C^{n+1,s'} C^{n,s} \sqrt{n+1} + \alpha S^{n+1,s'} C^{n,s} + \omega_- S^{n+1,s'} S^{n,s} \sqrt{n}\right] \\
&= \sum_{n>1} \left(\omega_+ C^{n,s} C^{n+1,s'} \sqrt{n+1} + \alpha C^{n,s} S^{n+1,s'} + \omega_- S^{n,s} S^{n+1,s'} \sqrt{n}\right)^2 .
\end{aligned} \tag{6.20}$$

So all in all, we found the expression

$$\begin{aligned}
&\mathrm{i}\frac{2\hbar^2}{l_H^2} \sum_{n,n'>1}^{\infty} \frac{v_{1;n-,n'+} v_{2;n'+,n-}}{\left(E_{n,-} - E_{n',+}\right)^2} = \\
&\sum_{n>1} \frac{1}{\left(E_{n,-} - E_{n+1,+}\right)^2} \left(\omega_+ C^{n,-} C^{n+1,+} \sqrt{n+1} + \alpha C^{n,-} S^{n+1,+} + \omega_- S^{n,-} S^{n+1,+} \sqrt{n}\right)^2 \\
&- \sum_{n>2} \frac{1}{\left(E_{n,-} - E_{n-1,+}\right)^2} \left(\omega_+ C^{n,-} C^{n-1,+} \sqrt{n} + \alpha S^{n,-} C^{n-1,+} + \omega_- S^{n,-} S^{n-1,+} \sqrt{n-1}\right)^2 .
\end{aligned} \tag{6.21}$$

Next, we analyze the contribution to Eq. (6.11) originating from $n > 0$ and $n' = 0$. We therefore need to consider the matrix elements:

$$\begin{aligned}
v_{1;ns,0s'} &= -\frac{l_H}{\sqrt{2}\hbar} \left(\langle n|C^{n,s}, \langle n-1|S^{n,s}\right) \begin{pmatrix} \omega_+(a^\dagger + a) & \alpha \\ \alpha & \omega_-(a^\dagger + a) \end{pmatrix} \begin{pmatrix} |0\rangle \\ 0 \end{pmatrix} \\
&= -\frac{l_H}{\sqrt{2}\hbar} \left(\langle n|C^{n,s}, \langle n-1|S^{n,s}\right) \begin{pmatrix} \omega_+(a^\dagger + a)|0\rangle \\ \alpha|0\rangle \end{pmatrix} \\
&= -\frac{l_H}{\sqrt{2}\hbar} \left[\langle n|C^{n,s}\omega_+(a^\dagger + a)|0\rangle + \langle n-1|S^{n,s}\alpha|0\rangle\right] \\
&= -\frac{l_H}{\sqrt{2}\hbar} \left[C^{n,s}\omega_+\langle n|1\rangle + S^{n,s}\alpha\langle n-1|0\rangle\right] \\
&= -\frac{l_H}{\sqrt{2}\hbar} \left[C^{n,s}\omega_+\delta_{n,1} + S^{n,s}\alpha\delta_{n,1}\right] = -\frac{l_H}{\sqrt{2}\hbar} \left[C^{n,s}\omega_+ + S^{n,s}\alpha\right]\delta_{n,1} ,
\end{aligned} \tag{6.22}$$

$$
\begin{aligned}
v_{2;0s',ns} &= \frac{\mathrm{i}l_H}{\sqrt{2}\hbar}\left(\langle 0|,0\right)\begin{pmatrix}\omega_+(a^\dagger-a) & -\alpha\\ \alpha & \omega_-(a^\dagger-a)\end{pmatrix}\begin{pmatrix}C^{n,s}|n\rangle\\ S^{n,s}|n-1\rangle\end{pmatrix} \\
&= \frac{\mathrm{i}l_H}{\sqrt{2}\hbar}\left(\langle 0|,0\right)\begin{pmatrix}\omega_+(a^\dagger-a)C^{n,s}|n\rangle-\alpha S^{n,s}|n-1\rangle\\ \alpha C^{n,s}|n\rangle+\omega_-(a^\dagger-a)S^{n,s}|n-1\rangle\end{pmatrix} \\
&= \frac{\mathrm{i}l_H}{\sqrt{2}\hbar}\left[\langle 0|\left(\omega_+(a^\dagger-a)C^{n,s}|n\rangle-\alpha S^{n,s}|n-1\rangle\right)\right] \\
&= \frac{\mathrm{i}l_H}{\sqrt{2}\hbar}\Big[\omega_+C^{n,s}\langle 0|(a^\dagger-a)|n\rangle-\alpha S^{n,s}\langle 0|n-1\rangle \\
&= \frac{\mathrm{i}l_H}{\sqrt{2}\hbar}\left(-\sqrt{n}\omega_+C^{n,s}-\alpha S^{n,s}\right)\delta_{n,1}\ .
\end{aligned}
\tag{6.23}
$$

In combination, this implies

$$
\begin{aligned}
\mathrm{i}\frac{2\hbar^2}{l_H^2}\sum_{n>0}^{\infty}v_{1;ns,0s'}v_{2;0s',ns} &= \sum_{n>0}^{\infty}\left[C^{n,s}\omega_+ + S^{n,s}\alpha\right]\delta_{n,1}\left(-\omega_+C^{n,s}-\alpha S^{n,s}\right)\delta_{n,1} \\
&= \sum_{n>0}^{\infty}-\left(C^{n,s}\omega_+ + S^{n,s}\alpha\right)^2\delta_{n,1} = \sum_{n=1}^{1}-\left(C^{n,s}\omega_+\sqrt{n} + S^{n,s}\alpha\right)^2\ .
\end{aligned}
\tag{6.24}
$$

Next, we analyze the contributions to Eq. (6.11) originating from $n=0$ and $n'>0$. We therefore need to consider the matrix elements:

$$
\begin{aligned}
v_{1;0s,n's'} &= -\frac{l_H}{\sqrt{2}\hbar}\left(\langle 0|,0\right)\begin{pmatrix}\omega_+(a^\dagger+a) & \alpha\\ \alpha & \omega_-(a^\dagger+a)\end{pmatrix}\begin{pmatrix}C^{n',s'}|n'\rangle\\ S^{n',s'}|n'-1\rangle\end{pmatrix} \\
&= -\frac{l_H}{\sqrt{2}\hbar}\left(\langle 0|,0\right)\begin{pmatrix}\omega_+(a^\dagger+a)C^{n',s'}|n'\rangle+\alpha S^{n',s'}|n'-1\rangle\\ \alpha C^{n',s'}|n'\rangle+\omega_-(a^\dagger+a)S^{n',s'}|n'-1\rangle\end{pmatrix} \\
&= -\frac{l_H}{\sqrt{2}\hbar}\left[\langle 0|\left(\omega_+(a^\dagger+a)C^{n',s'}|n'\rangle+\alpha S^{n',s'}|n'-1\rangle\right)\right] \\
&= -\frac{l_H}{\sqrt{2}\hbar}\left[\omega_+C^{n',s'}\langle 0|(a^\dagger+a)|n'\rangle+\alpha S^{n',s'}\langle 0|n'-1\rangle\right] \\
&= -\frac{l_H}{\sqrt{2}\hbar}\left[\omega_+C^{n',s'}\langle 0|(\sqrt{n'+1}|n'+1\rangle+\sqrt{n'}|n'-1\rangle)+\alpha S^{n',s'}\delta_{n',1}\right] \\
&= -\frac{l_H}{\sqrt{2}\hbar}\left[\omega_+C^{n',s'}+\alpha S^{n',s'}\right]\delta_{n',1}\ ,
\end{aligned}
\tag{6.25}
$$

$$
\begin{aligned}
v_{2;n's',0s} &= \frac{\mathrm{i}l_H}{\sqrt{2}\hbar}\left(\langle n'|C^{n',s'},\langle n'-1|S^{n',s'}\right)\begin{pmatrix}\omega_+(a^\dagger-a) & -\alpha\\ \alpha & \omega_-(a^\dagger-a)\end{pmatrix}\begin{pmatrix}|0\rangle\\ 0\end{pmatrix} \\
&= \frac{\mathrm{i}l_H}{\sqrt{2}\hbar}\left(\langle n'|C^{n',s'},\langle n'-1|S^{n',s'}\right)\begin{pmatrix}\omega_+(a^\dagger-a)|0\rangle\\ \alpha|0\rangle\end{pmatrix} \\
&= \frac{\mathrm{i}l_H}{\sqrt{2}\hbar}\left[\langle n'|C^{n',s'}\omega_+(a^\dagger-a)|0\rangle+\langle n'-1|S^{n',s'}\alpha|0\rangle\right] \\
&= \frac{\mathrm{i}l_H}{\sqrt{2}\hbar}\left[C^{n',s'}\omega_+ + S^{n',s'}\alpha\right]\delta_{n',1}\ .
\end{aligned}
\tag{6.26}
$$

Thus, in combination, we found

$$
\mathrm{i}\frac{2\hbar^2}{l_H^2}\sum_{n'>0}^{\infty}v_{1;0s,n's'}v_{2;n's',0s} = \sum_{n'>0}^{\infty}\left[\omega_+C^{n',s'}+\alpha S^{n',s'}\right]\left[C^{n',s'}\omega_+ + S^{n',s'}\alpha\right]\delta_{n',1}
$$

$$= \sum_{n'>0}^{\infty} \left(\omega_+ C^{n',s'} + \alpha S^{n',s'}\right)^2 \delta_{n',1} \ . \tag{6.27}$$

In contrast the contribution to Eq. (6.11) originating from $n = 0$ and $n' = 0$ vanishes, as

$$\begin{aligned} v_{1;0s,0s'} &= -\frac{l_H}{\sqrt{2}\hbar} \left(\langle 0|, 0\right) \begin{pmatrix} \omega_+(a^\dagger + a) & \alpha \\ \alpha & \omega_-(a^\dagger + a) \end{pmatrix} \begin{pmatrix} |0\rangle \\ 0 \end{pmatrix} \\ &= -\frac{l_H}{\sqrt{2}\hbar} \left(\langle 0|, 0\right) \begin{pmatrix} \omega_+(a^\dagger + a)|0\rangle \\ \alpha|0\rangle \end{pmatrix} = -\frac{l_H}{\sqrt{2}\hbar} \left[\langle 0|\omega_+(a^\dagger + a)|0\rangle\right] = 0 \ , \end{aligned} \tag{6.28}$$

and therefore

$$\mathrm{i}\frac{2\hbar^2}{l_H^2} v_{1;0s,0s'} v_{2;0s',0s} = 0 \ . \tag{6.29}$$

The contribution to Eq. (6.11) originating from $n = 1$ and $n' = 1$ vanishes as well, due to

$$\begin{aligned} v_{1;1s,1s'} = -\frac{l_H}{\sqrt{2}\hbar} \Big[&\omega_+ C^{1,s} C^{1,s'} \langle 1|(a^\dagger + a)|1\rangle + \alpha C^{1,s} S^{1,s'} \langle 1|0\rangle + \alpha S^{1,s} C^{1,s'} \langle 0|1\rangle \\ &+ \omega_- S^{1,s} S^{1,s'} \langle 0|(a^\dagger + a)|0\rangle \Big] = 0 \ . \end{aligned} \tag{6.30}$$

In contrast, for $n = 2$ and $n' = 1$, we find

$$\begin{aligned} v_{1;2s,1s'} &= -\frac{l_H}{\sqrt{2}\hbar} \Big[\omega_+ C^{2,s} C^{1,s'} \langle 2|(a^\dagger + a)|1\rangle + \alpha C^{2,s} S^{1,s'} \langle 2|0\rangle + \alpha S^{2,s} C^{1,s'} \langle 1|1\rangle \\ &\qquad + \omega_- S^{2,s} S^{1,s'} \langle 1|(a^\dagger + a)|0\rangle \Big] \\ &= -\frac{l_H}{\sqrt{2}\hbar} \Big[\omega_+ C^{2,s} C^{1,s'} \langle 2|a^\dagger|1\rangle + \alpha S^{2,s} C^{1,s'} + \omega_- S^{2,s} S^{1,s'} \langle 1|a^\dagger|0\rangle \Big] \\ &= -\frac{l_H}{\sqrt{2}\hbar} \Big[\omega_+ C^{2,s} C^{1,s'} \sqrt{2} + \alpha S^{2,s} C^{1,s'} + \omega_- S^{2,s} S^{1,s'} \Big] \ , \end{aligned} \tag{6.31}$$

which in particular implies

$$\begin{aligned} v_{2;1s',2s} &= \frac{\mathrm{i} l_H}{\sqrt{2}\hbar} \Big[\omega_+ C^{1,s'} C^{2,s} \langle 1|(a^\dagger - a)|2\rangle - \alpha C^{1,s'} S^{2,s} \langle 1|1\rangle + \alpha S^{1,s'} C^{2,s} \langle 0|2\rangle \\ &\qquad + \omega_- S^{1,s'} S^{2,s} \langle 0|(a^\dagger - a)|1\rangle \Big] \\ &= \frac{\mathrm{i} l_H}{\sqrt{2}\hbar} \Big[\omega_+ C^{1,s'} C^{2,s} \langle 1|(-a)|2\rangle - \alpha C^{1,s'} S^{2,s} + \omega_- S^{1,s'} S^{2,s} \langle 0|(-a)|1\rangle \Big] \\ &= \frac{\mathrm{i} l_H}{\sqrt{2}\hbar} \Big[-\omega_+ C^{1,s'} C^{2,s} \sqrt{2} - \alpha C^{1,s'} S^{2,s} - \omega_- S^{1,s'} S^{2,s} \Big] \ . \end{aligned} \tag{6.32}$$

Hence, one obtains the following contribution to Eq. (6.11) for this case:

$$\begin{aligned} \mathrm{i}\frac{2\hbar^2}{l_H^2} v_{1;2s,1s'} v_{2;1s',2s} &= \Big[\omega_+ C^{2,s} C^{1,s'} \sqrt{2} + \alpha S^{2,s} C^{1,s'} + \omega_- S^{2,s} S^{1,s'} \Big] \\ &\qquad \times \Big[-\omega_+ C^{1,s'} C^{2,s} \sqrt{2} - \alpha C^{1,s'} S^{2,s} - \omega_- S^{1,s'} S^{2,s} \Big] \\ &= -\left(\omega_+ C^{2,s} C^{1,s'} \sqrt{2} + \alpha S^{2,s} C^{1,s'} + \omega_- S^{2,s} S^{1,s'}\right)^2 \end{aligned} \tag{6.33}$$

$$= -\sum_{n=2}^{2} \left(\omega_+ C^{2,s} C^{1,s'} \sqrt{n} + \alpha S^{2,s} C^{1,s'} + \omega_- S^{2,s} S^{1,s'} \sqrt{n-1}\right)^2 .$$

Last but not least, let us analyze the contribution to Eq. (6.11) which originates from the Landau level indices $n = 1$ and $n' = 2$. In this case, one in particular obtains

$$\begin{aligned} v_{1;1s,2s'} &= -\frac{l_H}{\sqrt{2}\hbar}\Big[\omega_+ C^{1,s} C^{2,s'} \langle 1|(a^\dagger + a)|2\rangle + \alpha C^{1,s} S^{2,s'} \langle 1|1\rangle + \alpha S^{1,s} C^{2,s'} \langle 0|2\rangle \\ &\qquad + \omega_- S^{1,s} S^{2,s'} \langle 0|(a^\dagger + a)|1\rangle\Big] \\ &= -\frac{l_H}{\sqrt{2}\hbar}\Big[\omega_+ C^{1,s} C^{2,s'} \langle 1|a|2\rangle + \alpha C^{1,s} S^{2,s'} + \omega_- S^{1,s} S^{2,s'} \langle 0|a|1\rangle\Big] \\ &= -\frac{l_H}{\sqrt{2}\hbar}\Big[\omega_+ C^{1,s} C^{2,s'} \sqrt{2} + \alpha C^{1,s} S^{2,s'} + \omega_- S^{1,s} S^{2,s'}\Big] , \end{aligned} \tag{6.34}$$

and

$$\begin{aligned} v_{2;2s',1s} &= \frac{\mathrm{i} l_H}{\sqrt{2}\hbar}\Big[\omega_+ C^{2,s'} C^{1,s} \langle 2|(a^\dagger - a)|1\rangle - \alpha C^{2,s'} S^{1,s} \langle 2|0\rangle + \alpha S^{2,s'} C^{1,s} \langle 1|1\rangle \\ &\qquad + \omega_- S^{2,s'} S^{1,s} \langle 1|(a^\dagger - a)|0\rangle\Big] \\ &= \frac{\mathrm{i} l_H}{\sqrt{2}\hbar}\Big[\omega_+ C^{2,s'} C^{1,s} \langle 2|a^\dagger|1\rangle + \alpha S^{2,s'} C^{1,s} + \omega_- S^{2,s'} S^{1,s} \langle 1|a^\dagger|0\rangle\Big] \\ &= \frac{\mathrm{i} l_H}{\sqrt{2}\hbar}\Big[\omega_+ C^{2,s'} C^{1,s} \sqrt{2} + \alpha S^{2,s'} C^{1,s} + \omega_- S^{2,s'} S^{1,s}\Big] . \end{aligned} \tag{6.35}$$

Thus, one obtains the entire contribution:

$$\begin{aligned} \mathrm{i}\frac{2\hbar^2}{l_H^2} v_{1;1s,2s'} v_{2;2s',1s} &= \Big[\omega_+ C^{1,s} C^{2,s'} \sqrt{2} + \alpha C^{1,s} S^{2,s'} + \omega_- S^{1,s} S^{2,s'}\Big] \\ &\qquad \times \Big[\omega_+ C^{2,s'} C^{1,s} \sqrt{2} + \alpha S^{2,s'} C^{1,s} + \omega_- S^{2,s'} S^{1,s}\Big] \\ &= \left(\omega_+ C^{1,s} C^{2,s'} \sqrt{2} + \alpha C^{1,s} S^{2,s'} + \omega_- S^{1,s} S^{2,s'}\right)^2 \\ &= \sum_{n=1}^{1} \left(\omega_+ C^{n,s} C^{n+1,s'} \sqrt{n+1} + \alpha C^{n,s} S^{n+1,s'} + \omega_- S^{n,s} S^{n+1,s'} \sqrt{n}\right)^2 . \end{aligned} \tag{6.36}$$

As the above calculation has been lengthy and sophisticated, let us briefly summarize our intermediate result. Altogether, we have determined the following contributions to Eq. (6.11) originating from the Landau level indices $n, n' > 0$:

$$\begin{aligned} &\mathrm{i}\frac{2\hbar^2}{l_H^2} \sum_{n,n'>0}^{\infty} \frac{v_{1;n-,n'+} v_{2;n'+,n-}}{\left(E_{n,-} - E_{n',+}\right)^2} \\ &= \sum_{n>0} \frac{1}{\left(E_{n,-} - E_{n+1,+}\right)^2} \left(\omega_+ C^{n,-} C^{n+1,+} \sqrt{n+1} + \alpha C^{n,-} S^{n+1,+} + \omega_- S^{n,-} S^{n+1,+} \sqrt{n}\right)^2 \\ &- \sum_{n>1} \frac{1}{\left(E_{n,-} - E_{n-1,+}\right)^2} \left(\omega_+ C^{n,-} C^{n-1,+} \sqrt{n} + \alpha S^{n,-} C^{n-1,+} + \omega_- S^{n,-} S^{n-1,+} \sqrt{n-1}\right)^2 \\ &= \sum_{n=1} \frac{1}{\left(E_{n,-} - E_{n+1,+}\right)^2} \left(\omega_+ C^{n,-} C^{n+1,+} \sqrt{n+1} + \alpha C^{n,-} S^{n+1,+} + \omega_- S^{n,-} S^{n+1,+} \sqrt{n}\right)^2 \\ &- \sum_{n=1} \frac{1}{\left(E_{n+1,-} - E_{n,+}\right)^2} \left(\omega_+ C^{n+1,-} C^{n,+} \sqrt{n+1} + \alpha S^{n+1,-} C^{n,+} + \omega_- S^{n+1,-} S^{n,+} \sqrt{n}\right)^2 . \end{aligned} \tag{6.37}$$

Notice, that in the last line we shifted the index of summation. A remaining task of our calculation is to include the contribution of the zeroth Landau level. If it is part of the valence band, for $E_0 < E_z$, this contribution is given by

$$\begin{aligned}
&\mathrm{i}\frac{2\hbar^2}{l_H^2}\sum_{n'>0}^{\infty}\frac{v_{1;0-,n'+}v_{2;n'+,0-}}{\left(E_{0,-}-E_{n',+}\right)^2} = \sum_{n'>0}^{\infty}\frac{1}{\left(E_{0,-}-E_{n',+}\right)^2}\left(\omega_+ C^{n',+}+\alpha S^{n',+}\right)^2\delta_{n',1}\\
&=\sum_{n=0}^{0}\frac{1}{\left(E_{n,-}-E_{n+1,+}\right)^2}\left(\omega_+ C^{n+1,+}\sqrt{n+1}+\alpha S^{n+1,+}\right)^2\\
&=\sum_{n=0}^{0}\frac{1}{\left(E_{n,-}-E_{n+1,+}\right)^2}\left(\omega_+ C^{n,-}C^{n+1,+}\sqrt{n+1}+\alpha C^{n,-}S^{n+1,+}+\omega_- S^{n,-}S^{n+1,+}\sqrt{n}\right)^2,
\end{aligned} \tag{6.38}$$

where we defined

$$S^{0,+}=0 \quad \wedge \quad C^{0,+}=1 \quad \wedge \quad S^{0,-}=0 \quad \wedge \quad C^{0,-}=1\ . \tag{6.39}$$

If the zeroth Landau level is part of the conduction band, for $E_0 > E_z$, this contribution is instead given by

$$\begin{aligned}
&\mathrm{i}\frac{2\hbar^2}{l_H^2}\sum_{n>0}^{\infty}\frac{v_{1;n-,0+}v_{2;0+,n-}}{\left(E_{n,-}-E_{0,+}\right)^2} = -\sum_{n>0}^{\infty}\frac{1}{\left(E_{n,-}-E_{0,+}\right)^2}\left(\omega_+ C^{n,-}+\alpha S^{n,-}\right)^2\delta_{n,1}\\
&=-\sum_{n=1}^{1}\frac{1}{\left(E_{n,-}-E_{0,+}\right)^2}\left(\omega_+ C^{n,-}\sqrt{n}+\alpha S^{n,-}\right)^2\\
&=-\sum_{n=0}^{0}\frac{1}{\left(E_{n+1,-}-E_{n,+}\right)^2}\left(\omega_+ C^{n+1,-}\sqrt{n+1}+\alpha S^{n+1,-}\right)^2\\
&=-\sum_{n=0}^{0}\frac{1}{\left(E_{n+1,-}-E_{n,+}\right)^2}\left(\omega_+ C^{n+1,-}C^{n,+}\sqrt{n+1}+\alpha S^{n+1,-}C^{n,+}+\omega_- S^{n+1,-}S^{n,+}\sqrt{n}\right)^2.
\end{aligned} \tag{6.40}$$

All in all, we therefore found the following expression for the Kubo formula in Eq. (6.11):

$$\begin{aligned}
&\mathrm{i}\frac{2\hbar^2}{l_H^2}\sum_{n,n'=0}^{\infty}\frac{v_{1;n-,n'+}v_{2;n'+,n-}}{\left(E_{n,-}-E_{n',+}\right)^2}\\
&=\underbrace{\sum_{n=0}^{\infty}\frac{1}{\left(E_{n,-}-E_{n+1,+}\right)^2}\left(\omega_+ C^{n,-}C^{n+1,+}\sqrt{n+1}+\alpha C^{n,-}S^{n+1,+}+\omega_- S^{n,-}S^{n+1,+}\sqrt{n}\right)^2}_{\text{valence band states}}\\
&\underbrace{-\sum_{n=0}^{\infty}\frac{1}{\left(E_{n+1,-}-E_{n,+}\right)^2}\left(\omega_+ C^{n+1,-}C^{n,+}\sqrt{n+1}+\alpha S^{n+1,-}C^{n,+}+\omega_- S^{n+1,-}S^{n,+}\sqrt{n}\right)^2}_{\text{conduction band states}}.
\end{aligned} \tag{6.41}$$

Let us emphasize again that the zeroth Landau level solely contributes to one of the sums. If it belongs to the valence band, it contributes to the first sum. If it belongs to the conduction band, it contributes to the second sum.

In order to further simplify Eq. (6.41), we make use of the system's explicit eigen-states, introduced in Eq. (6.5). In particular, we can rewrite these states in terms of [158]

$$|\psi_n^+\rangle = \begin{pmatrix}\cos\left(\Theta_n\right)|n\rangle\\ \sin\left(\Theta_n\right)|n-1\rangle\end{pmatrix} \quad \wedge \quad |\psi_n^-\rangle = \begin{pmatrix}-\sin\left(\Theta_n\right)|n\rangle\\ \cos\left(\Theta_n\right)|n-1\rangle\end{pmatrix} \quad \wedge \quad |\psi_0\rangle = \begin{pmatrix}|0\rangle\\ 0\end{pmatrix}\ , \tag{6.42}$$

where we have defined the generalized angle Θ_n which is implicitly defined by

$$\cos(\Theta_n) = \sqrt{\frac{1}{2}\left[1 + \frac{\delta + 2(m_+ + n\beta)}{\sqrt{(\delta + 2(m_+ + n\beta))^2 + 4n\alpha^2}}\right]}\ , \tag{6.43}$$

$$\sin(\Theta_n) = \sqrt{\frac{1}{2}\left[1 - \frac{\delta + 2(m_+ + n\beta)}{\sqrt{(\delta + 2(m_+ + n\beta))^2 + 4n\alpha^2}}\right]}\ . \tag{6.44}$$

In particular, this angle allows us to rewrite the amplitudes $C^{n,\pm}$ and $S^{n,\pm}$ for $n > 0$ via

$$C^{n,+} = \cos(\Theta_n) \quad \wedge \quad S^{n,+} = \sin(\Theta_n)\ , \tag{6.45}$$

$$C^{n,-} = -\sin(\Theta_n) \quad \wedge \quad S^{n,-} = \cos(\Theta_n)\ . \tag{6.46}$$

Inserting those identities into Eq. (6.41) implies [158]

$$\begin{aligned}\mathcal{C}_{\mathrm{CI}} = &-\sum_{n=0}^{\infty} \frac{1}{(E_{n+1,+} - E_{n,-})^2} \\ &\times \Big(\omega_+ \cos(\Theta_{n+1})\sin(\Theta_n)\sqrt{n+1} - \omega_- \sin(\Theta_{n+1})\cos(\Theta_n)\sqrt{n} + \alpha \sin(\Theta_{n+1})\sin(\Theta_n)\Big)^2 \\ &+ \sum_{n=0}^{\infty} \frac{1}{(E_{n+1,-} - E_{n,+})^2} \\ &\times \Big(\omega_+ \cos(\Theta_n)\sin(\Theta_{n+1})\sqrt{n+1} - \omega_- \sin(\Theta_n)\cos(\Theta_{n+1})\sqrt{n} - \alpha \cos(\Theta_n)\cos(\Theta_{n+1})\Big)^2 .\end{aligned} \tag{6.47, 6.48}$$

From now on, we assume a particle-hole symmetric Chern insulator with $D = 0$, which in particular implies $\mu = E_z = 0$. As explained in Sec. 3.1.2, the $\mathrm{D}|\mathbf{k}|^2\sigma_0$ term in the Hamiltonian of a single Chern insulator is even under parity-transformations. As such, it cannot contribute to the system's zero-field Chern number. In Sec. 3.3 we have shown that this property extends to quantizing out-of-plane magnetic fields for chemical potentials in the Dirac mass gap. We have analyzed the effects of a particle-hole asymmetry in detail in Ref. [P3]. The assumption of $D = 0$ simplifies the eigen-energies of the Hamiltonian (6.2) in Eq. (6.3):

$$E_{n,s} = \frac{\beta}{2} + s\,\epsilon_n \quad \wedge \quad E_0 = m_+ + \beta/2\ , \tag{6.49}$$

with

$$\epsilon_n = \sqrt{(m_+ + n\beta)^2 + n\alpha^2}\ . \tag{6.50}$$

Consequently, one obtains the following identities

$$\epsilon_n^2 = (m_+ + n\beta)^2 + n\alpha^2\ , \tag{6.51}$$

$$\epsilon_{n+1}^2 - \epsilon_n^2 = \alpha^2 + \beta(2m_+ + (2n+1)\beta)\ , \tag{6.52}$$

$$\epsilon_{n+1}^2 + \epsilon_n^2 = (2n+1)\alpha^2 + (m_+ + n\beta)^2 + (m_+ + (n+1)\beta)^2\ , \tag{6.53}$$

as well as

$$E_{n+1,+} - E_{n,-} = \left(\frac{\beta}{2} + \epsilon_{n+1}\right) - \left(\frac{\beta}{2} - \epsilon_n\right) = (\epsilon_{n+1} + \epsilon_n)\ , \tag{6.54}$$

$$E_{n+1,-} - E_{n,+} = \left(\frac{\beta}{2} - \epsilon_{n+1}\right) - \left(\frac{\beta}{2} + \epsilon_n\right) = -\left(\epsilon_{n+1} + \epsilon_n\right) \ , \tag{6.55}$$

$$\left(E_{n+1,+} - E_{n,-}\right)^2 = \left(E_{n+1,-} - E_{n,+}\right)^2 = \left(\epsilon_{n+1} + \epsilon_n\right)^2 \ . \tag{6.56}$$

These identities enable us to simplify the Θ_n-angles in Eq. (6.43) for $D = 0$. In particular, we obtain

$$\cos\left(\Theta_n\right) = \sqrt{\frac{1}{2}\left[1 + \frac{2\left(m_+ + n\beta\right)}{\sqrt{\left(2\left(m_+ + n\beta\right)\right)^2 + 4n\alpha^2}}\right]} \ , \tag{6.57}$$

$$\sin\left(\Theta_n\right) = \sqrt{\frac{1}{2}\left[1 - \frac{2\left(m_+ + n\beta\right)}{\sqrt{\left(2\left(m_+ + n\beta\right)\right)^2 + 4n\alpha^2}}\right]} \ , \tag{6.58}$$

with

$$\cos^2\left(\Theta_n\right) = \frac{\epsilon_n + \left(m_+ + n\beta\right)}{2\epsilon_n} \quad \wedge \quad \sin^2\left(\Theta_n\right) = \frac{\epsilon_n - \left(m_+ + n\beta\right)}{2\epsilon_n} \ , \tag{6.59}$$

and thus

$$\begin{aligned}\cos^2\left(\Theta_n\right)\cos^2\left(\Theta_{n+1}\right) &= \frac{\epsilon_n + \left(m_+ + n\beta\right)}{2\epsilon_n}\frac{\epsilon_{n+1} + \left(m_+ + (n+1)\beta\right)}{2\epsilon_{n+1}} \\ &= \frac{\epsilon_n\epsilon_{n+1} + \left(m_+ + n\beta\right)\epsilon_{n+1} + \left(m_+ + (n+1)\beta\right)\epsilon_n + \left(m_+ + n\beta\right)\left(m_+ + (n+1)\beta\right)}{4\epsilon_n\epsilon_{n+1}} \ ,\end{aligned} \tag{6.60}$$

$$\begin{aligned}\sin^2\left(\Theta_n\right)\sin^2\left(\Theta_{n+1}\right) &= \frac{\epsilon_n - \left(m_+ + n\beta\right)}{2\epsilon_n}\frac{\epsilon_{n+1} - \left(m_+ + (n+1)\beta\right)}{2\epsilon_{n+1}} \\ &= \frac{\epsilon_n\epsilon_{n+1} - \left(m_+ + n\beta\right)\epsilon_{n+1} - \left(m_+ + (n+1)\beta\right)\epsilon_n + \left(m_+ + n\beta\right)\left(m_+ + (n+1)\beta\right)}{4\epsilon_n\epsilon_{n+1}} \ ,\end{aligned} \tag{6.61}$$

$$\begin{aligned}\cos^2\left(\Theta_n\right)\sin^2\left(\Theta_{n+1}\right) &= \frac{\epsilon_n + \left(m_+ + n\beta\right)}{2\epsilon_n}\frac{\epsilon_{n+1} - \left(m_+ + (n+1)\beta\right)}{2\epsilon_{n+1}} \\ &= \frac{\epsilon_n\epsilon_{n+1} + \left(m_+ + n\beta\right)\epsilon_{n+1} - \left(m_+ + (n+1)\beta\right)\epsilon_n - \left(m_+ + n\beta\right)\left(m_+ + (n+1)\beta\right)}{4\epsilon_n\epsilon_{n+1}} \ ,\end{aligned} \tag{6.62}$$

$$\begin{aligned}\sin^2\left(\Theta_n\right)\cos^2\left(\Theta_{n+1}\right) &= \frac{\epsilon_n - \left(m_+ + n\beta\right)}{2\epsilon_n}\frac{\epsilon_{n+1} + \left(m_+ + (n+1)\beta\right)}{2\epsilon_{n+1}} \\ &= \frac{\epsilon_n\epsilon_{n+1} - \left(m_+ + n\beta\right)\epsilon_{n+1} + \left(m_+ + (n+1)\beta\right)\epsilon_n - \left(m_+ + n\beta\right)\left(m_+ + (n+1)\beta\right)}{4\epsilon_n\epsilon_{n+1}} \ ,\end{aligned} \tag{6.63}$$

$$\begin{aligned}\sin^2\left(\Theta_n\right)\cos^2\left(\Theta_{n+1}\right) &= \frac{\epsilon_n - \left(m_+ + n\beta\right)}{2\epsilon_n}\frac{\epsilon_{n+1} + \left(m_+ + (n+1)\beta\right)}{2\epsilon_{n+1}} \\ &= \frac{\epsilon_n\epsilon_{n+1} - \left(m_+ + n\beta\right)\epsilon_{n+1} + \left(m_+ - (n+1)\beta\right)\epsilon_n - \left(m_+ + n\beta\right)\left(m_+ + (n+1)\beta\right)}{4\epsilon_n\epsilon_{n+1}} \ ,\end{aligned} \tag{6.64}$$

$$\begin{aligned}\cos^2\left(\Theta_n\right)\sin^2\left(\Theta_{n+1}\right) &= \frac{\epsilon_n + \left(m_+ + n\beta\right)}{2\epsilon_n}\frac{\epsilon_{n+1} - \left(m_+ + (n+1)\beta\right)}{2\epsilon_{n+1}} \\ &= \frac{\epsilon_n\epsilon_{n+1} + \left(m_+ + n\beta\right)\epsilon_{n+1} - \left(m_+ + (n+1)\beta\right)\epsilon_n - \left(m_+ + n\beta\right)\left(m_+ + (n+1)\beta\right)}{4\epsilon_n\epsilon_{n+1}} \ .\end{aligned} \tag{6.65}$$

Consequently, we found the following identities:

$$\begin{aligned}
\omega_+^2 \cos^2(\Theta_n)\sin^2(\Theta_{n+1}) - \omega_+^2 \sin^2(\Theta_n)\cos^2(\Theta_{n+1}) &= 2\omega_+^2 \frac{(m_+ + n\beta)(\epsilon_{n+1}-\epsilon_n) - \beta\epsilon_n}{4\epsilon_n\epsilon_{n+1}}, \\
\omega_-^2 \sin^2(\Theta_n)\cos^2(\Theta_{n+1}) - \omega_-^2 \cos^2(\Theta_n)\sin^2(\Theta_{n+1}) &= -2\omega_-^2 \frac{(m_+ + n\beta)(\epsilon_{n+1}-\epsilon_n) - \beta\epsilon_n}{4\epsilon_n\epsilon_{n+1}}, \\
\alpha^2 \cos^2(\Theta_n)\cos^2(\Theta_{n+1}) - \alpha^2 \sin^2(\Theta_n)\sin^2(\Theta_{n+1}) &= 2\alpha^2 \frac{(m_+ + n\beta)(\epsilon_{n+1}+\epsilon_n) + \beta\epsilon_n}{4\epsilon_n\epsilon_{n+1}} \ .
\end{aligned} \tag{6.66}$$

Equipped with these identities, we can evaluate the square brackets in Eq. (6.41). This leads to the six different terms

$$(1): \quad \omega_+^2 \Big(\cos^2(\Theta_n)\sin^2(\Theta_{n+1}) - \cos^2(\Theta_{n+1})\sin^2(\Theta_n)\Big)(n+1) \ , \tag{6.67}$$

$$(2): \quad \omega_-^2 \Big(\sin^2(\Theta_n)\cos^2(\Theta_{n+1}) - \sin^2(\Theta_{n+1})\cos^2(\Theta_n)\Big)\, n \ , \tag{6.68}$$

$$(3): \quad \alpha^2 \Big(\cos^2(\Theta_n)\cos^2(\Theta_{n+1}) - \sin^2(\Theta_{n+1})\sin^2(\Theta_n)\Big) \ , \tag{6.69}$$

$$\begin{aligned}
(4): \quad & \omega_+\omega_-\Big(\left[\cos(\Theta_n)\sin(\Theta_{n+1})\sin(\Theta_n)\cos(\Theta_{n+1})\right] \\
& - \left[\cos(\Theta_{n+1})\sin(\Theta_n)\sin(\Theta_{n+1})\cos(\Theta_n)\right]\Big)\sqrt{n}\sqrt{n+1} = 0 \ ,
\end{aligned} \tag{6.70}$$

$$\begin{aligned}
(5): \quad & -\omega_+\alpha\Big(\left[\cos(\Theta_n)\sin(\Theta_{n+1})\cos(\Theta_n)\cos(\Theta_{n+1})\right] \\
& + \left[\cos(\Theta_{n+1})\sin(\Theta_n)\sin(\Theta_{n+1})\sin(\Theta_n)\right]\Big)\sqrt{n+1} \\
&= -\omega_+\alpha\left(\left[\sin(\Theta_{n+1})\cos(\Theta_{n+1})\right] + \left[\cos(\Theta_{n+1})\sin(\Theta_{n+1})\right]\right)\sqrt{n+1} \\
&= -2\omega_+\alpha\left(\left[\sin(\Theta_{n+1})\cos(\Theta_{n+1})\right]\right)\sqrt{n+1} = -2\sqrt{n+1}\omega_+\alpha\frac{\sqrt{n+1}\alpha}{2\epsilon_{n+1}} = -\frac{(n+1)\omega_+\alpha^2}{\epsilon_{n+1}},
\end{aligned} \tag{6.71}$$

$$\begin{aligned}
(6): \quad & \omega_-\alpha\Big(\left[\sin(\Theta_n)\cos(\Theta_{n+1})\cos(\Theta_n)\cos(\Theta_{n+1})\right] \\
& + \left[\sin(\Theta_{n+1})\cos(\Theta_n)\sin(\Theta_{n+1})\sin(\Theta_n)\right]\Big)\sqrt{n} \\
&= 2\omega_-\alpha\left(\sin(\Theta_n)\cos(\Theta_n)\right)\sqrt{n} = 2\omega_-\alpha\sqrt{n}\frac{\sqrt{n}\alpha}{2\epsilon_n} = \frac{n\omega_-\alpha^2}{\epsilon_n} \ .
\end{aligned} \tag{6.72}$$

Here, we used that

$$\begin{aligned}
\sin(\Theta_n)\cos(\Theta_n) &= \sqrt{\frac{\epsilon_n - (m_+ + n\beta)}{2\epsilon_n}\frac{\epsilon_n + (m_+ + n\beta)}{2\epsilon_n}} = \sqrt{\frac{\epsilon_n^2 - (m_+ + n\beta)^2}{4\epsilon_n^2}} \\
&= \frac{\sqrt{\epsilon_n^2 - (m_+ + n\beta)^2}}{2\epsilon_n} = \frac{\sqrt{\epsilon_n^2 - (\epsilon_n^2 - n\alpha^2)}}{2\epsilon_n} = \frac{\sqrt{n\alpha^2}}{2\epsilon_n} = \frac{\sqrt{n}\alpha}{2\epsilon_n} \ ,
\end{aligned} \tag{6.73}$$

with $\epsilon_n^2 = (m_+ + n\beta)^2 + n\alpha^2$. Analogously, one finds

$$\sin(\Theta_{n+1})\cos(\Theta_{n+1}) = \frac{\sqrt{n+1}\alpha}{2\epsilon_{n+1}} \ . \tag{6.74}$$

As a last step, we are using the identity

$$\omega_\pm = \pm\omega_1 + \omega_2 = \pm\beta \Rightarrow \omega_+^2 = \omega_-^2 = \beta^2 \tag{6.75}$$

in order to derive an explicit, simplified expression for Eq. (6.41):

$$
\begin{aligned}
\sum_{i=1}^{6}(i) &= 2\beta^2\frac{(m_+ + n\beta)\,(\epsilon_{n+1}-\epsilon_n)-\beta\epsilon_n}{4\epsilon_n\epsilon_{n+1}} \\
&\quad + 2\alpha^2\frac{(m_+ + n\beta)\,(\epsilon_{n+1}+\epsilon_n)+\beta\epsilon_n}{4\epsilon_n\epsilon_{n+1}} - \frac{(n+1)\beta\alpha^2}{\epsilon_{n+1}} - \frac{n\beta\alpha^2}{\epsilon_n} \\
&= \frac{2\beta^2\left((m_+ + n\beta)\,(\epsilon_{n+1}-\epsilon_n)-\beta\epsilon_n\right)}{4\epsilon_n\epsilon_{n+1}} \\
&\quad + \frac{2\alpha^2\left((m_+ + n\beta)\,(\epsilon_{n+1}+\epsilon_n)+\beta\epsilon_n\right)}{4\epsilon_n\epsilon_{n+1}} - \frac{4(n+1)\beta\alpha^2\epsilon_n}{4\epsilon_n\epsilon_{n+1}} - \frac{4n\beta\alpha^2\epsilon_{n+1}}{4\epsilon_n\epsilon_{n+1}} \\
&= \frac{1}{4\epsilon_n\epsilon_{n+1}}\Big[2\beta^2\left((m_+ + n\beta)\,(\epsilon_{n+1}-\epsilon_n)-\beta\epsilon_n\right) \\
&\quad + 2\alpha^2\left((m_+ + n\beta)\,(\epsilon_{n+1}+\epsilon_n)+\beta\epsilon_n\right) - 4(n+1)\beta\alpha^2\epsilon_n - 4n\beta\alpha^2\epsilon_{n+1}\Big] \\
&= \frac{1}{4\epsilon_n\epsilon_{n+1}}\Big[2\beta^2\,(m_+ + n\beta)\,(\epsilon_{n+1}-\epsilon_n) - 2\beta^3\epsilon_n \\
&\quad + 2\alpha^2\,(m_+ + n\beta)\,(\epsilon_{n+1}+\epsilon_n) + 2\alpha^2\beta\epsilon_n - 4n\beta\alpha^2\,(\epsilon_n+\epsilon_{n+1}) - 4\beta\alpha^2\epsilon_n\Big] \\
&= \frac{1}{4\epsilon_n\epsilon_{n+1}}\Big[2\beta^2\,(m_+ + n\beta)\,(\epsilon_{n+1}-\epsilon_n) - 2\beta^3\epsilon_n + 2\alpha^2\,(m_+ - n\beta)\,(\epsilon_{n+1}+\epsilon_n) - 2\alpha^2\beta\epsilon_n\Big] \\
&= \frac{1}{(\epsilon_{n+1}+\epsilon_n)^2}\Big[\frac{\epsilon_{n+1}-\epsilon_n}{4\epsilon_n\epsilon_{n+1}}\left(\alpha^2\beta + (2m_+ + (2n+1)\beta)\beta^2\right) \\
&\qquad\qquad + \frac{\epsilon_{n+1}+\epsilon_n}{4\epsilon_n\epsilon_{n+1}}\left(\alpha^2(2m_+ - (2n+1)\beta) - \beta^3\right)\Big] \\
&= \frac{1}{(\epsilon_{n+1}+\epsilon_n)^2}\Big[\frac{\epsilon_{n+1}-\epsilon_n}{4\epsilon_n\epsilon_{n+1}}\left(\beta[\alpha^2 + \beta(2m_+ + (2n+1)\beta)]\right) \\
&\qquad\qquad + \frac{\epsilon_{n+1}+\epsilon_n}{4\epsilon_n\epsilon_{n+1}}\left(\alpha^2(2m_+ - (2n+1)\beta) - \beta^3\right)\Big] \\
&= \frac{1}{(\epsilon_{n+1}+\epsilon_n)^2}\left[\frac{\epsilon_{n+1}-\epsilon_n}{4\epsilon_n\epsilon_{n+1}}\left(\beta[\epsilon_{n+1}^2 - \epsilon_n^2]\right) + \frac{\epsilon_{n+1}+\epsilon_n}{4\epsilon_n\epsilon_{n+1}}\left(2m_+\alpha^2 - (2n+1)\alpha^2\beta - \beta^3\right)\right] \\
&= \frac{1}{(\epsilon_{n+1}+\epsilon_n)^2}\left[\frac{(\epsilon_{n+1}-\epsilon_n)^2}{4\epsilon_n\epsilon_{n+1}}\left(\beta[\epsilon_{n+1}+\epsilon_n]\right) + \frac{\epsilon_{n+1}+\epsilon_n}{4\epsilon_n\epsilon_{n+1}}\left(2m_+\alpha^2 - (2n+1)\alpha^2\beta - \beta^3\right)\right] \\
&= \frac{\beta(\epsilon_{n+1}-\epsilon_n)^2 + 2\alpha^2 m_+ - \beta^3 - (2n+1)\beta\alpha^2}{4\epsilon_n\epsilon_{n+1}(\epsilon_{n+1}+\epsilon_n)}\,.
\end{aligned}
\tag{6.76}
$$

In the sixth equality, we used that

$$
-2\beta^3\epsilon_n - 2\alpha^2\beta\epsilon_n = (\epsilon_{n+1}-\epsilon_n)(2\beta^3\epsilon_n + 2\alpha^2\beta\epsilon_n) + (\epsilon_{n+1}+\epsilon_n)(-2\beta^3\epsilon_n - 2\alpha^2\beta\epsilon_n)\,.
$$

This expression for the Chern number can be further simplified by using the identity

$$
\begin{aligned}
&\omega_1(\epsilon_{n+1}-\epsilon_n)^2 + 2\eta^2 m_+ - \omega_1^3 - (2n+1)\omega_1\eta^2 \\
&\quad = 2\left[(m_+ + n\omega_1)\epsilon_{n+1}(\epsilon_n+\epsilon_{n+1}) - m_+\left[m_+ + (n+1)\omega_1\right]\epsilon_n(\epsilon_n+\epsilon_{n+1})\right]\,,
\end{aligned}
\tag{6.77}
$$

since

$$
\begin{aligned}
&\omega_1(\epsilon_{n+1}-\epsilon_n)^2 + 2\eta^2 m_+ - \omega_1^3 - (2n+1)\omega_1\eta^2 \\
&= \omega_1(\epsilon_n^2 + \epsilon_{n+1}^2 - 2\epsilon_n\epsilon_{n+1}) + 2\eta^2 m_+ - \omega_1^3 - (2n+1)\omega_1\eta^2 \\
&= \omega_1\left[(2n+1)\eta^2 + (m_+ + n\omega_1)^2 + (m_+ + (n+1)\omega_1)^2\right]
\end{aligned}
\tag{6.78}
$$

$$
\begin{aligned}
&- 2\omega_1\epsilon_n\epsilon_{n+1} + 2\eta^2 m_+ - \omega_1^3 - (2n+1)\omega_1\eta^2 \\
&= 2\left[m_+^2\omega_1 + n(n+1)\omega_1^3 + m_+\left(\eta^2 + (1+2n)\omega_1^2\right) - \omega_1\epsilon_n\epsilon_{n+1}\right] ,
\end{aligned}
$$

and

$$
\begin{aligned}
&(m_+ + n\omega_1)\epsilon_{n+1}(\epsilon_n + \epsilon_{n+1}) - m_+\left[m_+ + (n+1)\omega_1\right]\epsilon_n(\epsilon_n + \epsilon_{n+1}) \\
&= m_+(\epsilon_n^2 + \epsilon_{n+1}^2) - \omega_1\epsilon_n\epsilon_{n+1} + \omega_1\left[n\epsilon_{n+1}^2 - (n+1)\epsilon_n^2\right] \\
&= m_+[\eta^2 + \omega_1(2m_+ + \omega_1 + 2n\omega_1)] - \omega_1\epsilon_n\epsilon_{n+1} + \omega_1\left[-m_+^2 + n(n(1+n)\omega_1^2)\right] \\
&= m_+^2\omega_1 + n(n+1)\omega_1^3 + m_+[\eta^2 + \omega_1^2(2n+1)] - \omega_1\epsilon_n\epsilon_{n+1} .
\end{aligned} \tag{6.79}
$$

With Eq. (6.77), we find the following Chern number contribution originating from all Landau levels with $n \in \mathbb{N}$ [158]:

$$
\mathcal{C}_{\mathrm{CI}}^{n>0} = \frac{1}{2}\sum_{n=1}^{\infty}\left(\frac{m_+ + n\beta}{\epsilon_n} - \frac{m_+ + (n+1)\beta}{\epsilon_{n+1}}\right) . \tag{6.80}
$$

However, for the entire Chern number, we still need to include the contribution originating from the zeroth Landau level. If it belongs to the valence band, this contribution is given by

$$
\begin{aligned}
&- \frac{f(E_0)}{(E_{1,+} - E_0)^2}\left(\omega_+ C^{1,+} + \alpha S^{1,+}\right)^2 = -\frac{f(E_0)}{(E_{1,+} - E_0)^2}\left(\omega_+\cos(\Theta_1) + \alpha\sin(\Theta_1)\right)^2 \\
&= -\frac{f(E_0)}{\left(\left(\frac{\beta}{2} + \epsilon_1\right) - \left(\frac{\beta}{2} + m_+\right)\right)^2}\left(\omega_+\cos(\Theta_1) + \alpha\sin(\Theta_1)\right)^2 \\
&= -\frac{f(E_0)}{(\epsilon_1 - m_+)^2}\left(\omega_+\cos(\Theta_1) + \alpha\sin(\Theta_1)\right)^2 \\
&= -\frac{f(E_0)}{(\epsilon_1 - m_+)^2}\left(\omega_1^2\cos^2(\Theta_1) + 2\omega_1\alpha\cos(\Theta_1)\sin(\Theta_1) + \alpha^2\sin^2(\Theta_1)\right) \\
&= -\frac{f(E_0)}{(\epsilon_1 - m_+)^2}\left(\omega_1^2\frac{\epsilon_1 + (m_+ + \beta)}{2\epsilon_1} + 2\omega_1\alpha\frac{\alpha}{2\epsilon_1} + \alpha^2\frac{\epsilon_1 - (m_+ + \beta)}{2\epsilon_1}\right) \\
&= -\frac{f(E_0)}{2\epsilon_1(\epsilon_1 - m_+)^2}\left(\beta^2(\epsilon_1 + m_+ + \beta) + 2\beta\alpha^2 + \alpha^2(\epsilon_1 - m_+ - \beta)\right) \\
&= -\frac{f(E_0)}{2\epsilon_1(\epsilon_1 - m_+)^2}\left(\beta^2(\epsilon_1 - m_+) + \alpha^2(\epsilon_1 - m_+) + \beta^3 + 2\beta^2 m_+ + 2\beta\alpha^2 - \beta\alpha^2\right) \\
&= -\frac{f(E_0)}{2\epsilon_1(\epsilon_1 - m_+)^2}\left(\beta^2(\epsilon_1 - m_+) + \alpha^2(\epsilon_1 - m_+) + \beta\left(\beta^2 + 2\beta m_+ + \alpha^2\right)\right) \\
&= -\frac{f(E_0)}{2\epsilon_1(\epsilon_1 - m_+)^2}\left(\beta^2(\epsilon_1 - m_+) + \alpha^2(\epsilon_1 - m_+) + \beta\left(\epsilon_1^2 - m_+^2\right)\right) \\
&= -\frac{f(E_0)}{2\epsilon_1(\epsilon_1 - m_+)}\left(\beta^2 + \alpha^2 + \beta(\epsilon_1 + m_+)\right) \\
&= -\frac{f(E_0)}{2\epsilon_1(\epsilon_1 - m_+)}\left((\beta^2 + \alpha^2 + 2\beta m_+) + \beta(\epsilon_1 - m_+)\right) \\
&= -\frac{f(E_0)}{2\epsilon_1(\epsilon_1 - m_+)}\left((\epsilon_1^2 - m_+^2) + \beta(\epsilon_1 - m_+)\right) \\
&= -\frac{f(E_0)(\epsilon_1 + m_+ + \beta)}{2\epsilon_1} = -f(E_0)\left[\frac{1}{2} + \frac{m_+ + \beta}{2\epsilon_1}\right] ,
\end{aligned} \tag{6.81}
$$

where we used that $\epsilon_1^2 = (m_+ + \beta)^2 + \alpha^2 = m_+^2 + \beta^2 + 2m_+\beta + \alpha^2$ twice.
In contrast, if the zeroth Landau level belongs to the conduction band, one obtains

$$\begin{aligned}
&\frac{1-f(E_0)}{(E_{1,-}-E_0)^2}\left(\omega_+ C^{1,-} + \alpha S^{1,-}\right)^2 = \frac{1-f(E_0)}{(E_{1,-}-E_0)^2}\left(-\omega_+ \sin(\Theta_1) + \alpha\cos(\Theta_1)\right)^2 \qquad (6.82)\\
&= \frac{1-f(E_0)}{(E_{1,-}-E_0)^2}\left(\beta^2\sin^2(\Theta_1) - 2\beta\alpha\sin(\Theta_1)\cos(\Theta_1) + \alpha^2\cos^2(\Theta_1)\right)\\
&= \frac{1-f(E_0)}{(\epsilon_1+m_+)^2}\left(\beta^2\frac{\epsilon_1-(m_++\beta)}{2\epsilon_1} - 2\beta\alpha\frac{\alpha}{2\epsilon_1} + \alpha^2\frac{\epsilon_1+(m_++\beta)}{2\epsilon_1}\right)\\
&= \frac{1-f(E_0)}{2\epsilon_1(\epsilon_1+m_+)^2}\left(\beta^2(\epsilon_1-m_+-\beta) - 2\beta\alpha^2 + \alpha^2(\epsilon_1+m_++\beta)\right)\\
&= \frac{1-f(E_0)}{2\epsilon_1(\epsilon_1+m_+)^2}\left(\beta^2(\epsilon_1+m_+) + \alpha^2(\epsilon_1+m_+) - 2\beta\alpha^2 + \beta\alpha^2 - \beta^3 - 2\beta^2 m_+\right)\\
&= \frac{1-f(E_0)}{2\epsilon_1(\epsilon_1+m_+)^2}\left(\beta^2(\epsilon_1+m_+) + \alpha^2(\epsilon_1+m_+) - \beta\left(\alpha^2+\beta^2+2\beta m_+\right)\right)\\
&= \frac{1-f(E_0)}{2\epsilon_1(\epsilon_1+m_+)^2}\left(\beta^2(\epsilon_1+m_+) + \alpha^2(\epsilon_1+m_+) - \beta\left(\epsilon_1^2-m_+^2\right)\right)\\
&= \frac{1-f(E_0)}{2\epsilon_1(\epsilon_1+m_+)}\left(\beta^2+\alpha^2-\beta(\epsilon_1-m_+)\right)\\
&= \frac{1-f(E_0)}{2\epsilon_1(\epsilon_1+m_+)}\left(\left[\beta^2+\alpha^2+2\beta m_+\right] - \beta(\epsilon_1+m_+)\right)\\
&= \frac{1-f(E_0)}{2\epsilon_1(\epsilon_1+m_+)}\left(\left[\epsilon_1^2-m_+^2\right] - \beta(\epsilon_1+m_+)\right)\\
&= \frac{1-f(E_0)}{2\epsilon_1}(\epsilon_1-m_+-\beta) = 1-f(E_0)\left[\frac{1}{2}+\frac{m_++\beta}{2\epsilon_1}\right] .
\end{aligned}$$

So the general zeroth Landau level contribution to the system's Chern number is given by

$$\mathcal{C}_{\mathrm{CI}}^{n=0} = -f(E_0)\left[\frac{1}{2}+\frac{m_++\beta}{2\epsilon_1}\right] + (1-f(E_0))\left[\frac{1}{2}-\frac{m_++\beta}{2\epsilon_1}\right] = \frac{1}{2}\left[1-2f(E_0)-\frac{m_++\beta}{2\epsilon_1}\right]. \qquad (6.83)$$

Thus, in total we found

$$\begin{aligned}
\sigma_{\mathrm{xy}} &= \sigma_{\mathrm{xy}}^{n=0} + \sigma_{\mathrm{xy}}^{n>0} = \frac{\mathrm{e}^2}{\mathrm{h}}\mathcal{C}_{\mathrm{CI}}^{n=0} + \frac{\mathrm{e}^2}{\mathrm{h}}\mathcal{C}_{\mathrm{CI}}^{n>0} \qquad (6.84)\\
&= \frac{\mathrm{e}^2}{2\mathrm{h}}\left(\left[1-2f(E_0)-\frac{m_++\beta}{2\epsilon_1}\right] + \sum_{n=1}^{\infty}\left[\frac{m_++n\beta}{\epsilon_n} - \frac{m_++(n+1)\beta}{\epsilon_{n+1}}\right]\right)\\
&= \frac{\mathrm{e}^2}{2\mathrm{h}}\left(1-2f(E_0) - \lim_{n\to\infty}\frac{m_++(n+1)\beta}{\epsilon_{n+1}}\right)\\
&= \frac{\mathrm{e}^2}{2\mathrm{h}}\left(1-2\Theta\left[-\beta/2-m_+\right] - \lim_{n\to\infty}\frac{m_++(n+1)\beta}{\epsilon_{n+1}}\right)\\
&= \frac{\mathrm{e}^2}{2\mathrm{h}}\left(\mathrm{sgn}(m_++\beta/2) + \mathrm{sgn}(B)\right)\\
&= \frac{\mathrm{e}^2}{2\mathrm{h}}\left(\mathrm{sgn}(m_+ - B/l_H^2) + \mathrm{sgn}(B)\right) . \qquad (6.85)
\end{aligned}$$

Here, we used the properties of the telescoping series in the third line and introduced the Heavyside Theta function $f(E_0) = \Theta(-E_0)$ in the fourth line. Notice, that Eq. (6.85) exactly matches Eq. (3.146a) of the main text.

Bibliography

[1] K. v. Klitzing, G. Dorda, and M. Pepper, New method for high-accuracy determination of the fine-structure constant based on quantized Hall resistance, Phys. Rev. Lett. **45**, 494–497 (1980).

[2] D. J. Thouless, M. Kohmoto, M. P. Nightingale, and M. den Nijs, Quantized Hall conductance in a two-dimensional periodic potential, Phys. Rev. Lett. **49**, 405–408 (1982).

[3] A. P. Schnyder, S. Ryu, A. Furusaki, and A. W. W. Ludwig, Classification of topological insulators and superconductors in three spatial dimensions, Phys. Rev. B **78**, 195125 (2008).

[4] C.-K. Chiu, J. C. Y. Teo, A. P. Schnyder, and S. Ryu, Classification of topological quantum matter with symmetries, Rev. Mod. Phys. **88**, 035005 (2016).

[5] X.-L. Qi and S.-C. Zhang, Topological insulators and superconductors, Rev. Mod. Phys. **83**, 1057–1110 (2011).

[6] M. Nakahara and M. Delbrück, *Differentialgeometrie, Topologie und Physik* (Springer Berlin Heidelberg, 2015).

[7] C. L. Kane and E. J. Mele, Quantum spin Hall effect in graphene, Phys. Rev. Lett. **95**, 226801 (2005).

[8] B. A. Bernevig, T. L. Hughes, and S.-C. Zhang, Quantum spin hall effect and topological phase transition in HgTe Quantum Wells, Science **314**, 1757–1761 (2006).

[9] M. König, S. Wiedmann, C. Brüne, A. Roth, H. Buhmann, L. W. Molenkamp, X.-L. Qi, and S.-C. Zhang, Quantum Spin Hall Insulator State in HgTe Quantum Wells, Science **318**, 766 (2007).

[10] L. Fu, C. L. Kane, and E. J. Mele, Topological insulators in three dimensions, Phys. Rev. Lett. **98**, 106803 (2007).

[11] C. Liu, T. L. Hughes, X.-L. Qi, K. Wang, and S.-C. Zhang, Quantum spin hall effect in inverted type-II semiconductors, Phys. Rev. Lett. **100**, 236601 (2008).

[12] R. Roy, Topological phases and the quantum spin Hall effect in three dimensions, Phys. Rev. B **79**, 195322 (2009).

[13] D. Hsieh, D. Qian, L. Wray, Y. Xia, Y. S. Hor, R. J. Cava, and M. Z. Hasan, A topological Dirac insulator in a quantum spin Hall phase (experimental realization of a 3D Topological Insulator), Nature **452**, 970 (2008).

[14] Y. Xia, D. Qian, D. Hsieh, L. Wray, A. Pal, H. Lin, A. Bansil, D. Grauer, Y. Hor, R. Cava, and M. Hasan, Observation of a large-gap topological-insulator class with a single dirac cone on the surface, Nature Physics **5**, 398–402 (2009).

[15] Y. L. Chen, J. G. Analytis, J.-H. Chu, Z. K. Liu, S.-K. Mo, X. L. Qi, H. J. Zhang, D. H. Lu, X. Dai, Z. Fang, S. C. Zhang, I. R. Fisher, Z. Hussain, and Z.-X. Shen, Experimental realization of a three-dimensional topological insulator, Bi_2Te_3, Science

325, 178–181 (2009).

[16] I. Knez, R.-R. Du, and G. Sullivan, Evidence for helical edge modes in inverted InAs/GaSb quantum wells, Phys. Rev. Lett. **107**, 136603 (2011).

[17] X. Wan, A. M. Turner, A. Vishwanath, and S. Y. Savrasov, Topological semimetal and fermi-arc surface states in the electronic structure of pyrochlore iridates, Phys. Rev. B **83**, 205101 (2011).

[18] G. Xu, H. Weng, Z. Wang, X. Dai, and Z. Fang, Chern semimetal and the quantized anomalous Hall effect in $HgCr_2Se_4$, Phys. Rev. Lett. **107**, 186806 (2011).

[19] S. Borisenko, Q. Gibson, D. Evtushinsky, V. Zabolotnyy, B. Büchner, and R. J. Cava, Experimental realization of a three-dimensional dirac semimetal, Phys. Rev. Lett. **113**, 027603 (2014).

[20] Z. K. Liu, J. Jiang, B. Zhou, Z. J. Wang, Y. Zhang, H. M. Weng, D. Prabhakaran, S. K. Mo, H. Peng, P. Dudin, T. Kim, M. Hoesch, Z. Fang, X. Dai, Z. X. Shen, D. L. Feng, Z. Hussain, and Y. L. Chen, A stable three-dimensional topological Dirac semimetal Cd_3As_2, Nature Materials **13**, 677–681 (2014).

[21] Z. K. Liu, B. Zhou, Y. Zhang, Z. J. Wang, H. M. Weng, D. Prabhakaran, S.-K. Mo, Z. X. Shen, Z. Fang, X. Dai, Z. Hussain, and Y. L. Chen, Discovery of a three-dimensional topological dirac semimetal, Na_3Bi, Science **343**, 864–867 (2014).

[22] M. Neupane, S.-Y. Xu, R. Sankar, N. Alidoust, G. Bian, C. Liu, I. Belopolski, T.-R. Chang, H.-T. Jeng, H. Lin, A. Bansil, F. Chou, and M. Z. Hasan, Observation of a three-dimensional topological Dirac semimetal phase in high-mobility Cd_3As_2, Nature Communications **5**, 3786 (2014).

[23] G. W. Semenoff, Condensed-matter simulation of a three-dimensional anomaly, Phys. Rev. Lett. **53**, 2449–2452 (1984).

[24] E. Fradkin, E. Dagotto, and D. Boyanovsky, Physical realization of the parity anomaly in condensed matter physics, Phys. Rev. Lett. **57**, 2967 (1986).

[25] F. D. M. Haldane, Model for a quantum Hall effect without Landau levels: Condensed-matter realization of the "parity anomaly", Phys. Rev. Lett. **61**, 2015–2018 (1988).

[26] X. Huang, L. Zhao, Y. Long, P. Wang, D. Chen, Z. Yang, H. Liang, M. Xue, H. Weng, Z. Fang, X. Dai, and G. Chen, Observation of the chiral-anomaly-induced negative magnetoresistance in 3D Weyl semimetal TaAs, Phys. Rev. X **5**, 031023 (2015).

[27] Q. Li, D. E. Kharzeev, C. Zhang, Y. Huang, I. Pletikosic, A. V. Fedorov, R. D. Zhong, J. A. Schneeloch, G. D. Gu, and T. Valla, Chiral magnetic effect in $ZrTe_5$, Nat. Phys. **12**, 550 (2016).

[28] C.-L. Zhang, S.-Y. Xu, I. Belopolski, Z. Yuan, Z. Lin, B. Tong, G. Bian, N. Alidoust, C.-C. Lee, S.-M. Huang, T.-R. Chang, G. Chang, C.-H. Hsu, H.-T. Jeng, M. Neupane, D. S. Sanchez, H. Zheng, J. Wang, H. Lin, C. Zhang, H.-Z. Lu, S.-Q. Shen, T. Neupert, M. Z. Hasan, and S. Jia, Signatures of the adler–bell–jackiw chiral anomaly in a weyl fermion semimetal, Nat. Commun. **7**, 10735 (2016).

[29] B. Yan and C. Felser, Topological materials: Weyl semimetals, Annu. Rev. Condens. Matter Phys. **8**, 337 (2017).

[30] J. Gooth, A. C. Niemann, T. Meng, A. G. Grushin, K. Landsteiner, B. Gotsmann, F. Menges, M. Schmidt, C. Shekhar, V. Süß, R. Hühne, B. Rellinghaus, C. Felser, B. Yan, and K. Nielsch, Experimental signatures of the mixed axial–gravitational

anomaly in the weyl semimetal NbP, Nature **547**, 324 (2017).

[31] K. Fujikawa, Path integral for gauge theories with fermions, Phys. Rev. D **21**, 2848 (1980).

[32] R. A. Bertlmann, *Anomalies in Quantum Field Theory* (Oxford University Press, 1996).

[33] A. J. Niemi and G. W. Semenoff, Axial-anomaly-induced fermion fractionization and effective gauge-theory actions in odd-dimensional space-times, Phys. Rev. Lett. **51**, 2077 (1983).

[34] A. J. Niemi and G. W. Semenoff, Spectral asymmetry on an open space, Phys. Rev. D **30**, 809–818 (1984).

[35] R. Jackiw, Fractional charge and zero modes for planar systems in a magnetic field, Phys. Rev. D **29**, 2375 (1984).

[36] A. J. Niemi, Topological solitons in a hot and dense fermi gas, Nucl. Phys. B **251**, 155 (1985).

[37] A. N. Redlich, Parity violation and gauge noninvariance of the effective gauge field action in three dimensions, Phys. Rev. D **29**, 2366 (1984).

[38] D. Boyanovsky, R. Blankenbecler, and R. Yahalom, Physical origin of topological mass in 2+1 dimensions, Nucl. Phys. **B270**, 483 (1986).

[39] A. M. J. Schakel, Relativistic quantum hall effect, Phys. Rev. D **43**, 1428–1431 (1991).

[40] J. Xu, Q. Gu, and E. J. Mueller, Realizing the haldane phase with bosons in optical lattices, Phys. Rev. Lett. **120**, 085301 (2018).

[41] W. Liu, Z. Lin, Z. D. Wang, and Y. Chen, Generalized Haldane models on laser-coupling optical lattices, Sci. Rep. **8**, 12898 (2018).

[42] C.-X. Liu, X.-L. Qi, X. Dai, Z. Fang, and S.-C. Zhang, Quantum anomalous Hall effect in $Hg_{1-y}Mn_yTe$ quantum wells, Phys. Rev. Lett. **101**, 146802 (2008).

[43] X.-L. Qi, T. L. Hughes, and S.-C. Zhang, Topological field theory of time-reversal invariant insulators, Phys. Rev. B **78**, 195424 (2008).

[44] R. Yu, W. Zhang, H.-J. Zhang, S.-C. Zhang, X. Dai, and Z. Fang, Quantized anomalous Hall effect in magnetic topological insulators, Science **329**, 61–64 (2010).

[45] C.-Z. Chang, J. Zhang, X. Feng, J. Shen, Z. Zhang, M. Guo, K. Li, Y. Ou, P. Wei, L.-L. Wang, Z.-Q. Ji, Y. Feng, S. Ji, X. Chen, J. Jia, X. Dai, Z. Fang, S.-C. Zhang, K. He, Y. Wang, L. Lu, X.-C. Ma, and Q.-K. Xue, Experimental observation of the quantum anomalous Hall effect in a magnetic topological insulator, Science **340**, 167 (2013).

[46] J. G. Checkelsky, R. Yoshimi, A. Tsukazaki, K. S. Takahashi, Y. Kozuka, J. Falson, M. Kawasaki, and Y. Tokura, Trajectory of the anomalous Hall effect towards the quantized state in a ferromagnetic topological insulator, Nature Phys. **10**, 731 (2014).

[47] C.-Z. Chang, W. Zhao, D. Y. Kim, P. Wei, J. K. Jain, C. Liu, M. H. W. Chan, and J. S. Moodera, Zero-field dissipationless chiral edge transport and the nature of dissipation in the quantum anomalous hall state, Phys. Rev. Lett. **115**, 057206 (2015).

[48] A. J. Bestwick, E. J. Fox, X. Kou, L. Pan, K. L. Wang, and D. Goldhaber-Gordon, Precise quantization of the anomalous hall effect near zero magnetic field, Phys. Rev. Lett. **114**, 187201 (2015).

[49] C.-X. Liu, S.-C. Zhang, and X.-L. Qi, The quantum anomalous hall effect: Theory and

experiment, Annual Review of Condensed Matter Physics **7**, 301 (2016).

[50] H.-Z. Lu, W.-Y. Shan, W. Yao, Q. Niu, and S.-Q. Shen, Massive dirac fermions and spin physics in an ultrathin film of topological insulator, Phys. Rev. B **81**, 115407 (2010).

[51] A. Coste and M. Lüscher, Parity anomaly and fermion-boson transmutation in 3-dimensional lattice QED, Nucl. Phys. B **323**, 631 (1989).

[52] A. N. Redlich, Gauge Noninvariance and Parity Violation of Three-Dimensional Fermions, Phys. Rev. Lett. **52**, 18 (1984).

[53] R. E. Gamboa Saravi, G. L. Rossini, and F. A. Schaposnik, The Zeta function answer to parity violation in three-dimensional gauge theories, Int. J. Mod. Phys. **A11**, 2643–2660 (1996).

[54] Y. Nagahama, One-loop induced topological term in QED_3, Zeitschrift für Physik C Particles and Fields **31**, 583–590 (1986).

[55] Y. Nagahama, Higher Derivative Regularization and Chiral Anomaly, Progress of Theoretical Physics **75**, 427–433 (1986).

[56] T. Kimura, A Parity invariant regularization in 3-D quantum electrodynamics, Prog. Theor. Phys. **92**, 693–698 (1994).

[57] G. V. Dunne, Aspects of Chern-Simons theory, in *Topological Aspects of Low-dimensional Systems: Proceedings, Les Houches Summer School of Theoretical Physics, Session 69: Les Houches, France, July 7-31 1998* (1998) arXiv:hep-th/9902115 .

[58] G. Dunne, K. Lee, and C. Lu, Finite temperature chern-simons coefficient, Physical Review Letters **78**, 3434–3437 (1997).

[59] A. Sissakian, O. Shevchenko, and S. Solganik, Chiral and parity anomalies at finite temperature and density, Nuclear Physics B **518**, 455–472 (1998).

[60] F. S. Nogueira and I. Eremin, Thermal screening at finite chemical potential on a topological surface and its interplay with proximity-induced ferromagnetism, Phys. Rev. B **90**, 014431 (2014).

[61] C.-T. Ma, Parity anomaly and duality web, Fortschritte der Physik **66**, 1800045 (2018).

[62] S. Deser, L. Griguolo, and D. Seminara, Gauge invariance, finite temperature, and parity anomaly in D=3, Physical Review Letters **79**, 1976–1979 (1997).

[63] C. D. Fosco, G. L. Rossini, and F. A. Schaposnik, Induced parity-breaking term at finite temperature, Physical Review Letters **79**, 1980–1983 (1997).

[64] C. D. Fosco, G. L. Rossini, and F. A. Schaposnik, Abelian and non-abelian induced parity-breaking terms at finite temperature, Physical Review D **56**, 6547–6555 (1997).

[65] M. Hott and G. Metikas, Effective action for QED in $2 + 1$ dimensions at finite temperature, Phys. Rev. D **60**, 067703 (1999).

[66] L. Salcedo, Parity breaking in $2 + 1$ dimensions and finite temperature, Nuclear Physics B **549**, 98–144 (1999).

[67] C. D. Fosco, G. L. Rossini, and F. A. Schaposnik, Induced parity breaking term in arbitrary odd dimensions at finite temperature, Phys. Rev. D **59**, 085012 (1999).

[68] C. G. Beneventano, P. Giacconi, E. M. Santangelo, and R. Soldati, Planar QED at finite temperature and density: Hall conductivity, berry's phases and minimal conductivity of graphene, Journal of Physics A: Mathematical and Theoretical **42**, 275401 (2009).

[69] C. D. Fosco and F. A. Schaposnik, Induced parity-odd effective action for a Dirac field on $S^2 \times S^1$, Phys. Rev. D **95**, 105011 (2017).

[70] F. Katmis, V. Lauter, F. S. Nogueira, B. A. Assaf, M. E. Jamer, P. Wei, B. Satpati, J. W. Freeland, I. Eremin, D. Heiman, P. Jarillo-Herrero, and J. S. Moodera, A high-temperature ferromagnetic topological insulating phase by proximity coupling, Nature **533**, 513–516 (2016).

[71] C. Tang, C.-Z. Chang, G. Zhao, Y. Liu, Z. Jiang, C.-X. Liu, M. R. McCartney, D. J. Smith, T. Chen, J. S. Moodera, and J. Shi, Above 400-K robust perpendicular ferromagnetic phase in a topological insulator, Science Advances **3**, e1700307 (2017).

[72] T. Yokoyama, J. Zang, and N. Nagaosa, Theoretical study of the dynamics of magnetization on the topological surface, Phys. Rev. B **81**, 241410 (2010).

[73] F. S. Nogueira and I. Eremin, Fluctuation-induced magnetization dynamics and criticality at the interface of a topological insulator with a magnetically ordered layer, Phys. Rev. Lett. **109**, 237203 (2012).

[74] Y. Tserkovnyak and D. Loss, Thin-film magnetization dynamics on the surface of a topological insulator, Phys. Rev. Lett. **108**, 187201 (2012).

[75] M. M. Otrokov, I. I. Klimovskikh, H. Bentmann, D. Estyunin, A. Zeugner, Z. S. Aliev, S. Gaß, A. U. B. Wolter, A. V. Koroleva, A. M. Shikin, M. Blanco-Rey, M. Hoffmann, I. P. Rusinov, A. Y. Vyazovskaya, S. V. Eremeev, Y. M. Koroteev, V. M. Kuznetsov, F. Freyse, J. Sánchez-Barriga, I. R. Amiraslanov, M. B. Babanly, N. T. Mamedov, N. A. Abdullayev, V. N. Zverev, A. Alfonsov, V. Kataev, B. Büchner, E. F. Schwier, S. Kumar, A. Kimura, L. Petaccia, G. Di Santo, R. C. Vidal, S. Schatz, K. Kißner, M. Ünzelmann, C. H. Min, S. Moser, T. R. F. Peixoto, F. Reinert, A. Ernst, P. M. Echenique, A. Isaeva, and E. V. Chulkov, Prediction and observation of an antiferromagnetic topological insulator, Nature **576**, 416–422 (2019).

[76] R. C. Vidal, A. Zeugner, J. I. Facio, R. Ray, M. H. Haghighi, A. U. B. Wolter, L. T. Corredor Bohorquez, F. Caglieris, S. Moser, T. Figgemeier, T. R. F. Peixoto, H. B. Vasili, M. Valvidares, S. Jung, C. Cacho, A. Alfonsov, K. Mehlawat, V. Kataev, C. Hess, M. Richter, B. Büchner, J. van den Brink, M. Ruck, F. Reinert, H. Bentmann, and A. Isaeva, Topological electronic structure and intrinsic magnetization in $MnBi_4Te_7$: A Bi_2Te_3 derivative with a periodic Mn sublattice, Phys. Rev. X **9**, 041065 (2019).

[77] M. J. M. de Jong and L. W. Molenkamp, Hydrodynamic electron flow in high-mobility wires, Phys. Rev. B **51**, 13389–13402 (1995).

[78] L. Molenkamp and M. de Jong, Observation of Knudsen and Gurzhi transport regimes in a two-dimensional wire, Solid-State Electronics **37**, 551 – 553 (1994).

[79] L. W. Molenkamp and M. J. M. de Jong, Electron-electron-scattering-induced size effects in a two-dimensional wire, Phys. Rev. B **49**, 5038–5041 (1994).

[80] A. Lucas and K. C. Fong, Hydrodynamics of electrons in graphene, Journal of Physics: Condensed Matter **30**, 053001 (2018).

[81] D. Bandurin, I. Torre, R. K. Kumar, M. B. Shalom, A. Tomadin, A. Principi, G. Auton, E. Khestanova, K. Novoselov, I. Grigorieva, L. Ponomarenko, A. Geim, and M. Polini, Negative local resistance caused by viscous electron backflow in graphene, Science **351**, 1055–1058 (2016).

[82] R. Krishna Kumar, D. A. Bandurin, F. M. D. Pellegrino, Y. Cao, A. Principi, H. Guo, G. Auton, M. Ben Shalom, L. A. Ponomarenko, G. Falkovich, K. Watan-

abe, T. Taniguchi, I. Grigorieva, L. S. Levitov, M. Polini, and A. Geim, Superballistic flow of viscous electron fluid through graphene constrictions, Nature Physics **13**, 1182 (2017).

[83] P. J. W. Moll, P. Kushwaha, N. Nandi, B. Schmidt, and A. P. Mackenzie, Evidence for hydrodynamic electron flow in $PdCoO_2$, Science **351**, 1061–1064 (2016).

[84] J. E. Avron, R. Seiler, and P. G. Zograf, Viscosity of Quantum Hall Fluids, Phys. Rev. Lett. **75**, 697–700 (1995).

[85] C. Hoyos, Hall viscosity, topological states and effective theories, Int. J. Mod. Phys. B **28**, 1430007 (2014).

[86] P. Alekseev, Negative magnetoresistance in viscous flow of two-dimensional electrons, Phys. Rev. Lett. **117**, 166601 (2016).

[87] J. M. Link, B. N. Narozhny, E. I. Kiselev, and J. Schmalian, Out-of-bounds hydrodynamics in anisotropic Dirac fluids, Phys. Rev. Lett. **120**, 196801 (2018).

[88] F. Pena-Benitez, K. Saha, and P. Surowka, Berry curvature and Hall viscosities in an anisotropic Dirac semimetal, Phys. Rev. B **99**, 045141 (2019).

[89] C. Copetti and K. Landsteiner, Anomalous hall viscosity at the weyl-semimetal–insulator transition, Phys. Rev. B **99**, 195146 (2019).

[90] G. M. Gusev, A. D. Levin, E. V. Levinson, and A. K. Bakarov, Viscous transport and hall viscosity in a two-dimensional electron system, Phys. Rev. B **98**, 161303 (2018).

[91] G. M. Gusev, A. D. Levin, E. V. Levinson, and A. K. Bakarov, Viscous electron flow in mesoscopic two-dimensional electron gas, AIP Advances **8**, 025318 (2018).

[92] A. D. Levin, G. M. Gusev, E. V. Levinson, Z. D. Kvon, and A. K. Bakarov, Vorticity-induced negative nonlocal resistance in a viscous two-dimensional electron system, Phys. Rev. B **97**, 245308 (2018).

[93] A. I. Berdyugin, S. G. Xu, F. M. D. Pellegrino, R. Krishna Kumar, A. Principi, I. Torre, M. Ben Shalom, T. Taniguchi, K. Watanabe, I. V. Grigorieva, M. Polini, A. K. Geim, and D. A. Bandurin, Measuring hall viscosity of graphene's electron fluid, Science **364**, 162–165 (2019).

[94] L. V. Delacrétaz and A. Gromov, Transport signatures of the hall viscosity, Phys. Rev. Lett. **119**, 226602 (2017), Phys. Rev. Lett. **120**, 079901.

[95] F. M. D. Pellegrino, I. Torre, and M. Polini, Nonlocal transport and the Hall viscosity of two-dimensional hydrodynamic electron liquids, Phys. Rev. B **96**, 195401 (2017).

[96] T. Holder, R. Queiroz, and A. Stern, Unified description of the classical hall viscosity, Phys. Rev. Lett. **123**, 106801 (2019).

[97] J. A. Sulpizio, L. Ella, A. Rozen, J. Birkbeck, D. J. Perello, D. Dutta, M. Ben-Shalom, T. Taniguchi, K. Watanabe, T. Holder, and et al., Visualizing poiseuille flow of hydrodynamic electrons, Nature **576**, 75–79 (2019).

[98] P. Drude, Zur Elektronentheorie der Metalle, Annalen der Physik **306**, 566–613 (1900).

[99] G. Czycholl, *Theoretische Festkörperphysik Band 1* (Springer Berlin Heidelberg, 2016).

[100] D. Tong, Lectures on the quantum hall effect (2016), arXiv:1606.06687 [hep-th] .

[101] K. von Klitzing, The quantized hall effect, Rev. Mod. Phys. **58**, 519–531 (1986).

[102] R. Nakai, S. Ryu, and K. Nomura, Laughlin's argument for the quantized thermal hall effect, Phys. Rev. B **95**, 165405 (2017).

[103] P. S. Laplace, Mémoire sur les intégrales définies et leur application aux probabilités, et spécialement a la recherche du milieu qu'il faut choisir entre les résultats des observations, Mémoires de l'Académie des Sciences **58**, 279–347 (1810).

[104] P. Chebyshev, Sur le développement des fonctions à une seule variable, Bull. Ph.-Math., Acad. Imp. Sc. St. Pétersbourg **1**, 193–200 (1859).

[105] C. Hermite, Sur un nouveau développement en série de fonctions, C. R. Acad. Sci. Paris **58**, 93–100 (1864).

[106] P. Streda, Theory of quantised Hall conductivity in two dimensions, Journal of Physics C: Solid State Physics **15**, L717–L721 (1982).

[107] E. Reyes-Gómez, N. Porras-Montenegro, C. A. Perdomo-Leiva, H. S. Brandi, and L. E. Oliveira, Electron Landé g factor in GaAs–(Ga,Al)As quantum wells under applied magnetic fields: Effects of Dresselhaus spin splitting, Journal of Applied Physics **104**, 023704 (2008).

[108] R. B. Laughlin, Quantized Hall conductivity in two dimensions, Phys. Rev. B **23**, 5632 (1981).

[109] M. E. Peskin and D. V. Schroeder, *An introduction to quantum field theory* (Addison-Wesley, Reading, USA, 1995).

[110] M. D. Schwartz, *Quantum Field Theory and the Standard Model* (Cambridge University Press, 2014).

[111] A. A. Abrikosov, I. Dzyaloshinskii, L. P. Gorkov, and R. A. Silverman, *Methods of quantum field theory in statistical physics* (Dover, New York, NY, 1975).

[112] A. Pilaftsis, *Lectures on Symmetries in Physics, http://www.hep.man.ac.uk/u/pilaftsi/SYM/sym.pdf*, Tech. Rep. (University of Manchester, 2000).

[113] D. Tong, *Quantum Field Theory, http://www.damtp.cam.ac.uk/user/tong/qft.html*, Tech. Rep. (University of Cambridge, 2007).

[114] R. Bertlmann, *Anomalies in Quantum Field Theory*, International Series of Monographs on Physics (Oxford University Press, 2000).

[115] D. Tong, *Gauge Theory, http://www.damtp.cam.ac.uk/user/tong/gaugetheory.html*, Lecture Note (University of Cambridge, 2018).

[116] E. Gava, K. Narain, S. Randjbar-Daemi, E. Sezgin, and Q. Shafi, eds., *Proceedings, Summer School in High-energy Physics and Cosmology: Trieste, Italy, June 17-August 9, 1991. Vol. 1, 2* (World Scientific, Singapore, Singapore, 1992) 339-342.

[117] E. Noether, Invariante Variationsprobleme, Nachrichten von der Gesellschaft der Wissenschaften zu Göttingen, Mathematisch-Physikalische Klasse , 235–257 (1918).

[118] J. Cardy, *Introduction to Quantum Field Theory*, Tech. Rep. (University of Oxford, 2010).

[119] D. Blaschke, *Introduction to Quantum Field Theory and Matter under Extreme Conditions*, Tech. Rep. (University of Wroclaw, 2007).

[120] H. P. Büchler, *Seminar Script: Quantum Field Theory*, Tech. Rep. (Institut für Theo-

retische Physik III Universität Stuttgart, 2013).

[121] E. Fradkin, *Field Theories Of Condensed Matter Physics* (Cambridge University Press, 2013).

[122] T. Ohl, *Lecture Script: Quantum Field Theory 2.0*, Tech. Rep. (Julius-Maximilians-Universität Würzburg, 2016).

[123] A. Zee, *Quantum field theory in a nutshell*, second edition ed. (Princeton University Press, 2010).

[124] A. Zee, Quantum hall fluids, in *Field Theory, Topology and Condensed Matter Physics*, edited by H. B. Geyer (Springer Berlin Heidelberg, Berlin, Heidelberg, 1995) pp. 99–153.

[125] A. Altland and B. D. Simons, *Condensed Matter Field Theory*, 2nd ed. (Cambridge University Press, 2010).

[126] S. L. Adler, Axial-Vector Vertex in Spinor Electrodynamics, Physical Review **177**, 2426–2438 (1969).

[127] J. Bell and R. Jackiw, A PCAC puzzle: $\pi^0 \to \gamma\gamma$ in the σ model, Nuovo Cim. A **60**, 47–61 (1969).

[128] K. Fujikawa, Chiral anomaly and the Wess-Zumino condition, Phys. Rev. D **31**, 341–351 (1985).

[129] M. Stone, Gravitational anomalies and thermal Hall effect in topological insulators, Phys. Rev. B **85**, 184503 (2012).

[130] N. Maeda, Chiral anomaly and effective field theory for the quantum hall liquid with edges, Phys. Lett. B **376**, 142 (1996).

[131] C. G. Callan and J. A. Harvey, Anomalies and fermion zero modes on strings and domain walls, Nucl. Phys. B **250**, 427 (1985).

[132] A. Neagu and A. M. Schakel, Induced quantum numbers in the (2+1)-dimensional electron gas, Phys. Rev. D **48**, 1785–1791 (1993).

[133] A. M. J. Schakel, *Boulevard of Broken Symmetries* (World Scientific, 2008).

[134] J. Fröhlich and T. Kerler, Universality in quantum Hall systems, Nucl. Phys. B **354**, 369–417 (1991).

[135] J. Fröhlich and A. Zee, Large scale physics of the quantum hall fluid, Nuclear Physics B **364**, 517 – 540 (1991).

[136] J. Fröhlich, A. Chamseddine, F. Gabbiani, T. Kerler, C. Kling, P. Marchetti, U. Studer, and E. Thiran, The Fractional Quantum Hall Effect, Chern-Simons Theory, and Integral Lattices, in *Proceedings of the International Congress of Mathematicians*, edited by S. D. Chatterji (Birkhäuser Basel, Basel, 1995) pp. 75–105.

[137] C. L. Kane and E. J. Mele, Z_2 topological order and the quantum spin hall effect, Phys. Rev. Lett. **95**, 146802 (2005).

[138] H. Min, J. E. Hill, N. A. Sinitsyn, B. R. Sahu, L. Kleinman, and A. H. MacDonald, Intrinsic and rashba spin-orbit interactions in graphene sheets, Phys. Rev. B **74**, 165310 (2006).

[139] S. Wu, V. Fatemi, Q. D. Gibson, K. Watanabe, T. Taniguchi, R. J. Cava, and P. Jarillo-Herrero, Observation of the quantum spin hall effect up to 100 kelvin in a monolayer crystal, Science **359**, 76–79 (2018).

[140] F. Reis, G. Li, L. Dudy, M. Bauernfeind, S. Glass, W. Hanke, R. Thomale, J. Schäfer, and R. Claessen, Bismuthene on a SiC substrate: A candidate for a high-temperature quantum spin hall material, Science **357**, 287–290 (2017).

[141] F. Herman, C. D. Kuglin, K. F. Cuff, and R. L. Kortum, Relativistic corrections to the band structure of tetrahedrally bonded semiconductors, Phys. Rev. Lett. **11**, 541–545 (1963).

[142] J. W. Nicklas and J. W. Wilkins, Accurate electronic properties for (Hg,Cd)Te systems using hybrid density functional theory, Phys. Rev. B **84**, 121308 (2011).

[143] B. Bernevig and T. Hughes, *Topological Insulators and Topological Superconductors* (Princeton University Press, 2013).

[144] A. Das, *Lectures on quantum field theory (Second Edition)* (World Scientific Publishing Company, 2020).

[145] R. Narayanan and J. Nishimura, Parity-invariant lattice regularization of a three-dimensional gauge-fermion system, Nuclear Physics B **508**, 371–387 (1997).

[146] W.-K. Tse and A. H. MacDonald, Giant magneto-optical Kerr effect and universal Faraday effect in thin-film Topological Insulators, Phys. Rev. Lett. **105**, 057401 (2010).

[147] W.-K. Tse and A. H. MacDonald, Magneto-optical Faraday and Kerr effects in topological insulator films and in other layered quantized Hall systems, Phys. Rev. B **84**, 205327 (2011).

[148] W. Beugeling, C. X. Liu, E. G. Novik, L. W. Molenkamp, and C. Morais Smith, Reentrant topological phases in Mn-doped HgTe quantum wells, Physical Review B **85** (2012).

[149] C. M. Morris, R. V. Aguilar, A. V. Stier, and N. P. Armitage, Polarization modulation time-domain terahertz polarimetry, Optics Express **20**, 12303 (2012).

[150] A. Hill, A. Sinner, and K. Ziegler, Valley symmetry breaking and gap tuning in graphene by spin doping, New Journal of Physics **13**, 035023 (2011).

[151] A. Hill, A. Sinner, and K. Ziegler, Optical Hall conductivity of systems with gapped spectral nodes, The European Physical Journal B **86**, 1–5 (2013).

[152] R. M. Lutchyn, P. Nagornykh, and V. M. Yakovenko, Frequency and temperature dependence of the anomalous ac hall conductivity in a chiral $p_x + ip_y$ superconductor with impurities, Phys. Rev. B **80**, 104508 (2009).

[153] T. U. München, *Integraltabelle - Integration von Rationale Funktionen, Irrationale Funktionen, Trigonometrische* (Technische Universität München, Höhere Mathematik 1 (MA9501), 2018).

[154] J. B. Kogut and L. Susskind, Hamiltonian Formulation of Wilson's Lattice Gauge Theories, Phys. Rev. **D11**, 395–408 (1975).

[155] S. Capitani, Lattice perturbation theory, Physics Reports **382**, 113–302 (2003).

[156] H. So, Induced Chern-Simons Class with Lattice Fermions, Progress of Theoretical Physics **73**, 528–532 (1985).

[157] H. So, Induced topological invariants by lattice fermions in odd dimensions, Prog. Theor. Phys. **74**, 585 (1985).

[158] S.-B. Zhang, Y.-Y. Zhang, and S.-Q. Shen, Robustness of quantum spin hall effect in

an external magnetic field, Physical Review B **90** (2014).

[159] C. K. Tutschku, *Topological Quantum Computing Using Nanowire Devices*, Master's thesis, Julius-Maximilians-Universität Würzburg (2016).

[160] J. F. Böttcher, *Fate of Topological States of Matter in the Presence of External Magnetic Fields*, Ph.D. thesis, Julius-Maximilians-Universität Würzburg (2020).

[161] B. Scharf, A. Matos-Abiague, and J. Fabian, Magnetic properties of HgTe quantum wells, Phys. Rev. B **86**, 075418 (2012).

[162] B. Zhou, H.-Z. Lu, R.-L. Chu, S.-Q. Shen, and Q. Niu, Finite size effects on helical edge states in a quantum spin-hall system, Phys. Rev. Lett. **101**, 246807 (2008).

[163] M. König, H. Buhmann, L. W. Molenkamp, T. Hughes, C.-X. Liu, X.-L. Qi, and S.-C. Zhang, The quantum spin hall effect: Theory and experiment, Journal of the Physical Society of Japan **77**, 031007 (2008).

[164] S. Deser, R. Jackiw, and S. Templeton, Topologically massive gauge theories, Ann. Phys. **140**, 372 (1982).

[165] X. G. Wen, Gapless boundary excitations in the quantum hall states and in the chiral spin states, Phys. Rev. B **43**, 11025 (1991).

[166] S. Chandrasekharan, Anomaly cancellation in 2+1 dimensions in the presence of a domain wall mass, Phys. Rev. D **49**, 1980 (1994).

[167] M. Stone and F. Gaitan, Topological charge and chiral anomalies in fermi superfluids, Ann. Phys. **178**, 89 (1987).

[168] E. G. Novik, A. Pfeuffer-Jeschke, T. Jungwirth, V. Latussek, C. R. Becker, G. Landwehr, H. Buhmann, and L. W. Molenkamp, Band structure of semimagnetic $Hg_{1-y}Mn_yTe$ quantum wells, Phys. Rev. B **72**, 035321 (2005).

[169] C. Brüne, C. X. Liu, E. G. Novik, E. M. Hankiewicz, H. Buhmann, Y. L. Chen, X. L. Qi, Z. X. Shen, S. C. Zhang, and L. W. Molenkamp, Quantum hall effect from the topological surface states of strained bulk HgTe, Phys. Rev. Lett. **106**, 126803 (2011).

[170] Y. Baum, J. Böttcher, C. Brüne, C. Thienel, L. W. Molenkamp, A. Stern, and E. M. Hankiewicz, Self-consistent $\mathrm{k} \cdot \mathrm{p}$ calculations for gated thin layers of three-dimensional topological insulators, Phys. Rev. B **89**, 245136 (2014).

[171] A. Messiah, *Quantum Mechanics Vol. 2*, Quantum Mechanics (Elsevier Science, 1981).

[172] S. Shamim, W. Beugeling, J. Böttcher, P. Shekhar, A. Budewitz, P. Leubner, L. Lunczer, E. M. Hankiewicz, H. Buhmann, and L. W. Molenkamp, Emergent quantum Hall effects below 50 mT in a two-dimensional topological insulator, Science Advances **6**, eaba4625 (2020).

[173] J. Wang, B. Lian, H. Zhang, and S.-C. Zhang, Anomalous edge transport in the quantum anomalous hall state, Phys. Rev. Lett. **111**, 086803 (2013).

[174] M. Büttiker, Role of quantum coherence in series resistors, Phys. Rev. B **33**, 3020–3026 (1986).

[175] M. Büttiker, Absence of backscattering in the quantum Hall effect in multiprobe conductors, Phys. Rev. B **38**, 9375–9389 (1988).

[176] J. I. Väyrynen, M. Goldstein, and L. I. Glazman, Helical edge resistance introduced by charge puddles, Phys. Rev. Lett. **110**, 216402 (2013).

[177] L. Lunczer, P. Leubner, M. Endres, V. L. Müller, C. Brüne, H. Buhmann, and L. W. Molenkamp, Approaching quantization in macroscopic quantum spin hall devices through gate training, Phys. Rev. Lett. **123**, 047701 (2019).

[178] A. Roth, C. Brüne, H. Buhmann, L. W. Molenkamp, J. Maciejko, X.-L. Qi, and S.-C. Zhang, Nonlocal transport in the quantum spin hall state, Science **325**, 294 (2009).

[179] D. G. Rothe, R. W. Reinthaler, C. X. Liu, L. W. Molenkamp, S.-C. Zhang, and E. M. Hankiewicz, Fingerprint of different spin-orbit terms for spin transport in HgTe quantum wells, New J. Phys. **12**, 065012 (2010).

[180] J. K. Furdyna, Diluted magnetic semiconductors, J. Appl. Phys. **64**, R29 (1988).

[181] G. E. Volovik, An analog of the quantum hall effect in a superfluid ^{3}He film, Soviet Physics - JETP (English Translation) **67**, 1804–1811 (1988).

[182] J. Erdmenger, I. Matthaiakakis, R. Meyer, and D. R. Fernández, Strongly coupled electron fluids in the Poiseuille regime, Phys. Rev. B **98**, 195143 (2018).

[183] T. Scaffidi, N. Nandi, B. Schmidt, A. P. Mackenzie, and J. E. Moore, Hydrodynamic electron flow and Hall viscosity, Phys. Rev. Lett. **118**, 226601 (2017).

[184] M. Müller, L. Fritz, and S. Sachdev, Quantum-critical relativistic magnetotransport in graphene, Phys. Rev. B **78**, 115406 (2008).

[185] M. Müller and S. Sachdev, Collective cyclotron motion of the relativistic plasma in graphene, Phys. Rev. B **78**, 115419 (2008).

[186] N. Borghini, Lecture script: Hydrodynamics II, https://www.physik.uni-bielefeld.de/ borghini/Teaching/Hydro-II/ (2020), Universität Bielefeld, Fakultät für Physik.

[187] B. N. Narozhny, Electronic hydrodynamics in graphene, Annals of Physics **411**, 167979 (2019).

[188] S. A. Hartnoll, P. K. Kovtun, M. Muller, and S. Sachdev, Theory of the Nernst effect near quantum phase transitions in condensed matter, and in dyonic black holes, Phys. Rev. B **76**, 144502 (2007).

[189] K. Jensen, M. Kaminski, P. Kovtun, R. Meyer, A. Ritz, and A. Yarom, Parity-violating hydrodynamics in 2 + 1 dimensions, Journal of High Energy Physics **2012** (2012).

[190] B. Bradlyn, M. Goldstein, and N. Read, Kubo formulas for viscosity: Hall viscosity, ward identities, and the relation with conductivity, Phys. Rev. B **86**, 245309 (2012).

[191] M. Kaminski and S. Moroz, Nonrelativistic parity-violating hydrodynamics in two spatial dimensions, Phys. Rev. B **89**, 115418 (2014).

[192] Y. Nam, D.-K. Ki, D. Soler-Delgado, and A. F. Morpurgo, Electron–hole collision limited transport in charge-neutral bilayer graphene, Nature Physics **13**, 1207–1214 (2017).

[193] L. Fritz, J. Schmalian, M. Müller, and S. Sachdev, Quantum critical transport in clean graphene, Physical Review B **78**, 085416 (2008).

[194] C. S. Küppersbusch, *Magnetic Oscillations in two-dimensional Dirac Systems and Shear Viscosity and Spin Diffusion in a two-dimensional Fermi Gas*, Ph.D. thesis, Universität zu Köln (2015).

[195] M. Sherafati, A. Principi, and G. Vignale, Hall viscosity and electromagnetic response

of electrons in graphene, Phys. Rev. B **94**, 125427 (2016).

[196] I. V. Tokatly and G. Vignale, Lorentz shear modulus of a two-dimensional electron gas at high magnetic field, Phys. Rev. B **76**, 161305 (2007).

[197] E. I. Kiselev and J. Schmalian, Boundary conditions of viscous electron flow, Phys. Rev. B **99**, 035430 (2019).

[198] N. Ashcroft and N. Mermin, *Solid State Physics* (Saunders College Publishing, Fort Worth, 1976).

[199] Z. Qian and G. Vignale, Lifetime of a quasiparticle in an electron liquid, Phys. Rev. B **71**, 075112 (2005).

[200] Z. Qian, Lifetime of a quasiparticle in an electron liquid II, Phys. Rev. B **73**, 245112 (2006).

[201] D. S. Novikov, Viscosity of a two-dimensional Fermi liquid, arXiv:0603184 (2006).

[202] R. N. Gurzhi, Minimum of resistance in impurity-free conductors, Sov. Phys. JETP **17**, 521 [Zh. Eksp. Teor. Fiz. 44, 771 (1963)] (1963).

[203] A. Geim and K. Novoselov, The rise of graphene, Nature Materials **6**, 183–191 (2007).

[204] A. J. Leggett, Lecture 5: Graphene: Electronic band structure and dirac fermions, Phys 769: Selected Topics in Condensed Matter Physics (2010).

[205] S. Das Sarma, S. Adam, E. H. Hwang, and E. Rossi, Electronic transport in two-dimensional graphene, Rev. Mod. Phys. **83**, 407–470 (2011).

[206] A. H. Castro Neto, F. Guinea, N. M. R. Peres, K. S. Novoselov, and A. K. Geim, The electronic properties of graphene, Rev. Mod. Phys. **81**, 109–162 (2009).

[207] B. N. Narozhny and M. Schütt, Magnetohydrodynamics in graphene: Shear and hall viscosities, Phys. Rev. B **100**, 035125 (2019).

[208] J. Crossno, J. K. Shi, K. Wang, X. Liu, A. Harzheim, A. Lucas, S. Sachdev, P. Kim, T. Taniguchi, K. Watanabe, and et al., Observation of the dirac fluid and the breakdown of the Wiedemann-Franz law in graphene, Science **351**, 1058–1061 (2016).

[209] P. R. Wallace, The band theory of graphite, Phys. Rev. **71**, 622–634 (1947).

[210] M. S. Foster and I. L. Aleiner, Slow imbalance relaxation and thermoelectric transport in graphene, Phys. Rev. B **79**, 085415 (2009).

[211] A. Lucas, J. Crossno, K. C. Fong, P. Kim, and S. Sachdev, Transport in inhomogeneous quantum critical fluids and in the dirac fluid in graphene, Phys. Rev. B **93**, 075426 (2016).

[212] Q. Li and S. Das Sarma, Finite temperature inelastic mean free path and quasiparticle lifetime in graphene, Phys. Rev. B **87**, 085406 (2013).

[213] A. Principi and G. Vignale, Violation of the Wiedemann-Franz law in hydrodynamic electron liquids, Phys. Rev. Lett. **115**, 056603 (2015).

[214] M. Polini and G. Vignale, The quasiparticle lifetime in a doped graphene sheet, in *No-nonsense Physicist: An overview of Gabriele Giuliani's work and life* (Scuola Normale Superiore, Pisa, 2016) pp. 107–124.

[215] D. C. Elias, R. V. Gorbachev, A. S. Mayorov, S. V. Morozov, A. A. Zhukov, P. Blake, L. A. Ponomarenko, I. V. Grigorieva, K. S. Novoselov, F. Guinea, and et al., Dirac

cones reshaped by interaction effects in suspended graphene, Nature Physics **7**, 701–704 (2011).

[216] A. Principi, G. Vignale, M. Carrega, and M. Polini, Bulk and shear viscosities of the two-dimensional electron liquid in a doped graphene sheet, Phys. Rev. B **93**, 125410 (2016).

[217] R. Franz and G. Wiedemann, Über die Wärme-Leitungsfähigkeit der Metalle, Annalen der Physik **165**, 497–531 (1853).

[218] L. Lorenz, Bestimmung der Wärmegrade in absolutem Maasse, Annalen der Physik **223**, 429–452 (1872).

[219] A. Sommerfeld and H. Bethe, Elektronentheorie der Metalle, in *Aufbau Der Zusammenhängenden Materie* (Springer Berlin Heidelberg, Berlin, Heidelberg, 1933) pp. 333–622.

[220] C. Hoyos and D. T. Son, Hall viscosity and electromagnetic response, Phys. Rev. Lett. **108**, 066805 (2012).

[221] M. Müller, J. Schmalian, and L. Fritz, Graphene: A nearly perfect fluid, Phys. Rev. Lett. **103**, 025301 (2009).

[222] L. Landau and E. Lifshitz, *Fluid Mechanics*, 2nd ed., Course of Theoretical Physics (Butterworth-Heinemann, 1987).

[223] P. Romatschke, New developments in relativistic viscous hydrodynamics, International Journal of Modern Physics E **19**, 1–53 (2010).

[224] O. Z. Luciano Rezzolla, *Relativistic Hydrodynamics* (Oxford University Press, 2013).

[225] R. Moessner, N. Morales-Durán, P. Surówka, and P. Witkowski, Boundary-condition and geometry engineering in electronic hydrodynamics, Phys. Rev. B **100**, 155115 (2019).

[226] G. F. Giuliani and J. J. Quinn, Lifetime of a quasiparticle in a two-dimensional electron gas, Phys. Rev. B **26**, 4421–4428 (1982).

[227] T. L. Hughes, R. G. Leigh, and O. Parrikar, Torsional anomalies, hall viscosity, and bulk-boundary correspondence in topological states, Phys. Rev. D **88**, 025040 (2013).

[228] T. L. Hughes, R. G. Leigh, and E. Fradkin, Torsional response and dissipationless viscosity in topological insulators, Phys. Rev. Lett. **107**, 075502 (2011).

[229] O. Parrikar, T. L. Hughes, and R. G. Leigh, Torsion, parity-odd response, and anomalies in topological states, Phys. Rev. D **90**, 105004 (2014).

[230] O. Parrikar, *Topics in quantum field theory and holography*, Ph.D. thesis, Illinois U., Urbana (2016).

[231] G. Nakova, Differential geometry for physicists and mathematicians: Moving frames and differential forms: From euclid past riemann by Jose G. Vargas, J. Geom. Symmetry Phys. **38**, 109–113 (2015).

[232] H. Shapourian, T. L. Hughes, and S. Ryu, Viscoelastic response of topological tight-binding models in two and three dimensions, Phys. Rev. B **92**, 165131 (2015).

[233] M. Barkeshli, S. B. Chung, and X.-L. Qi, Dissipationless phonon hall viscosity, Phys. Rev. B **85**, 245107 (2012).

List of Publications

[P1] Jan Böttcher*, **Christian Tutschku***, Laurens W. Molenkamp, and Ewelina M. Hankiewicz. *Survival of the Quantum Anomalous Hall Effect in Orbital Magnetic Fields as a Consequence of the Parity Anomaly*. Phys. Rev. Lett. **123**, 226602 (2019).

[P2] Ioannis Matthaiakakis*, David Rodríguez Fernández*, **Christian Tutschku***, Ewelina M. Hankiewicz, Johanna Erdmenger, and René Meyer. *Functional dependence of Hall viscosity induced transverse voltage in two-dimensional Fermi liquids*. Phys. Rev. B **101**, 045423 (2020).

[P3] Jan Böttcher, **Christian Tutschku**, and Ewelina M. Hankiewicz. *Fate of Quantum Anomalous Hall Effect in the Presence of External Magnetic Fields and Particle-Hole Asymmetry*. Phys. Rev. B **101**, 195433 (2020).

[P4] **Christian Tutschku**, Jan Böttcher, René Meyer, and Ewelina M. Hankiewicz. *Momentum-Dependent Mass and AC Hall Conductivity of Quantum Anomalous Hall Insulators and Their Relation to the Parity Anomaly*. Phys. Rev. Res. **2**, 033193 (2020).

[P5] **Christian Tutschku**, Flavio S. Nogueira, Christian Northe, Jeroen van den Brink, and Ewelina M. Hankiewicz. *Temperature and chemical potential dependence of the parity anomaly in quantum anomalous Hall insulators*. Phys. Rev. B **102**, 205407 (2020).

[P6] **Christian Tutschku**, Rolf W. Reinthaler, Chao H. Lei, Allan H. McDonald, and Ewelina M. Hankiewicz. *Majorana-based quantum computing in nanowire devices*. Phys. Rev. B **102**, 125407 (2020).

---

* Authors contributed equally to this work.

Acknowledgements

'You are the average of the five people you spend the most time with.'

Jim Rohn - Motivational Speaker

It is unquestionable that our social environment contributes to our personal- as well as professional development. More than five years ago I became a member of the department for theoretical physics at the University of Würzburg. During this time, I met several outstanding personalities to whom I am indebted to. This includes both, internal as well as external collaborators. I am extremely grateful to met any on the following personalities who formed my self-development and, therefore, made me the researcher I am today.

First and foremost let me express my special thanks to Prof. Dr. Ewelina M. Hankiewicz. It is owed to her enthusiasm that I changed my field of research from a purely high-energetic perspective towards the corresponding applications in condensed-matter physics at the end of my master's program. This decision defined the starting point of my academic career and, in particular, allowed me to conduct research at the frontier between different areas of physics. For this reason the present thesis has only become possible due to the continuous and pleasant supervision of Prof. Dr. Ewelina M. Hankiewicz. I am more than grateful for our great working relationship and for her personal support in the last half-decade.

Moreover, let me express my deepest gratitude to my closest collaborators: Dr. Jan Böttcher, Prof. Dr. Laurens W. Molenkamp, Dr. René Meyer, Ioannis Matthaiakakis, Dr. David Rodríguez Fernández, Prof. Dr. Johanna Erdmenger, Dr. Christian Northe and Sven Danz, who are not listed by relevance. However, I would like to specially thank Dr. Jan Böttcher for our longstanding collaboration and his personal support in the last four years.

I also would like thank my collaborators in Dresden: Due to several fruitful discussions with Dr. Flavio S. Nogueira, I was able to embed my theoretical results into a much broader and interdisciplinary context. In addition, our common project strongly benefited from the target-oriented and efficient working mode of Prof. Dr. Jeroen van den Brink.

Even though I did not directly collaborate with the following colleagues they strongly supported myself during the last five years on a professional, as well as personal level. On the one hand, I would like to thank Prof. Dr. Björn Trauzettel and Dr. Benedikt Scharf for fruitful discussions. One the other hand, I would like to thank Nelia Meyer and Danijela Sturm-Kirchgassner for any support regarding organizational questions. Moreover, I would like to thank my office colleague Alexander Bauer for his personal support.

Last but not least let me thank my parents Uwe and Vera Tutschku to whom I dedicated this work. Words can not express how grateful I am for the unreserved support of my family.